UNIVERSITY OF OKLAHOMA

GRADUATE COLLEGE

ADVANCES USING THE ADCIRC HYDRODYNAMIC MODEL: PARAMETER ESTIMATION AND ASPECTS OF COUPLED HYDROLOGIC-HYDRODYNAMIC FLOOD INUNDATION MODELING

A DISSERTATION

SUBMITTED TO THE GRADUATE FACULTY

in partial fulfillment of the requirements for the

Degree of

DOCTOR OF PHILOSOPHY

By

EVAN MEREDITH TROMBLE
Norman, Oklahoma
2011

ADVANCES USING THE ADCIRC HYDRODYNAMIC MODEL:
PARAMETER ESTIMATION AND ASPECTS OF COUPLED HYDROLOGIC-
HYDRODYNAMIC FLOOD INUNDATION MODELING

A DISSERTATION APPROVED FOR THE
SCHOOL OF CIVIL ENGINEERING AND ENVIRONMENTAL SCIENCE

BY

_____
Dr. Randall L. Kolar, Chair

_____
Dr. Baxter E. Vieux

_____
Dr. Kendra M. Dresback

_____
Dr. Yang Hong

_____
Dr. Jonathan J. Gourley

_____
Dr. S. Lakshmivarahan

For Jennifer, Andrew, and Lucas

Acknowledgements

A great number of people contributed to this dissertation both during my time in graduate school at the University of Oklahoma and in my more formative years in Juneau, AK. I am not so presumptuous as to believe that I will be able to adequately recognize everyone who had a hand in this endeavor. But, I would be remiss not to attempt to acknowledge some of the most prominent influences in the process.

First and foremost, I have to thank my wife Jennifer for her unwavering love and support through a long, and sometimes arduous, process. I also have to recognize our son Andrew for allowing me to miss time at the park, trips to the zoo, etc., to work on finishing my dissertation, while also providing previously unimaginable distractions. Perhaps, in time, you will understand the topics that engrossed your father for the first two years of your life. While on the subject of family, I have to thank my siblings, Dr. Tanya Tromble and Dr. Roy Tromble for their friendship, assistance, and commiseration throughout life, but especially during the last few years. My brother's expertise in math and computer science was a great help on a number of occasions, while my sister's English competency, undoubtedly, reduced the number of grammatical errors and increased the readability of the text. Additionally, I have to thank my parents for their love and support over the years; I know it was not always easy. Finally, I would like to acknowledge members of my extended family, from my grandparents to my aunts and uncles, who have always been supportive, as well as my in-laws who have welcomed me with open arms, despite attending a rival school.

I owe a great thanks to my adviser, Dr. Kolar, for guiding me along my journey over the last seven years and keeping me on the payroll. I do not feel appreciably more intelligent now than I did when I started at OU, but I hope that is because I have confronted challenging problems during my studies. I feel very fortunate that Dr. Dresback has been available and willing to assist on a wide-variety of issues over the years, and I should thank Dr. Szpilka for providing feedback on my DG hydraulic routing code that did not make it into this dissertation. Also, I am thankful for the willingness of my other committee members to serve on my dissertation committee. I have learned a great deal from each of you through course work and discussions.

I am appreciative of the vigor with which Dr. Varahan has approached the application of the forward sensitivity method to analyze *G*. Dr. Kolar suggested I analyze the variable *G* algorithm based on Dr. John Atkinson's dispersion analysis work as a Master's project during my first year in graduate school. I decided to skip the Master's step, partially due to the inability to make headway on the problem. During the fall of 2004, I never would have imagined that one of my first graduate courses, scientific computing with Dr. Varahan, would lead into such a large portion of my dissertation.

On the subject of teachers, I would like to acknowledge my elementary and middle school math teachers, Mrs. Sewell and Mrs. Borthwick. At the time, I probably took for granted your exceptional efforts to challenge me in class every day. Now, however, I have begun to understand your personal sacrifices to contribute to my academic success.

Finally, I would like to thank many of the other people who have enriched my time at the University of Oklahoma. I have been blessed to work with fantastic graduate students under Dr. Kolar, specifically Dr. Casey Dietrich helping me get started, Ian Toohey sharing

lab space during the middle years, and Casey Dick sharing the laborious task of finishing up. The CEES support staff, namely Audre, Brenda, Molly, and Susan, have always been eager to assist with any problem, including getting my tuition and fees paid during semesters when I may not have turned in the required paperwork in the most timely manner; I also appreciate the efforts of Dr. Miller and Dr. Cerato serving as the CEES Graduate Liaison during my tenure and helping me navigate hurdles from time to time. Additionally, I am grateful for the Engineering in Practice fellowship that generously funded my studies for two years, initiated my friendships with Dr. Danny Krier, Dr. Jesse Bell, Dr. Kristen Savage, and Tiffani Wilke, and allowing me to work with two wonderful, dedicated high school teachers, Adam Carr and Daneice Foster. I have also benefitted from courses and/or guidance from a great number of professors both at OU and the Colorado School of Mines, including Candace Sulzbach, Dr. Mooney, Dr. Nanny, Dr. Kibbey, Dr. Wildeman, Dr. Muralee and Dr. Laubach.

Table of Contents

List of Tables

List of Figures

Abstract

The ADCIRC hydrodynamic model has been used extensively for coastal modeling applications over the last twenty years. Within the last decade, modeling of hurricane storm surge has become one of its principal applications. Utilization of ADCIRC for these problems has required additional model development. Two areas for model development are focused on in this dissertation. First, the numerical parameter, *G*, is analyzed in ADCIRC. Then, aspects of coupled hydrologic-hydrodynamic modeling for coastal flood inundation are explored using ADCIRC.

The numerical parameter, *G*, in the generalized wave continuity equation, which is one of the governing equations in ADCIRC, is analyzed using dispersion analysis results as a guide for parameter selection. Results show traditional analysis techniques, which are limited to linear systems, do not produce optimal results for non-linear problems. Therefore, application of the Forward Sensitivity Method (FSM) to ADCIRC, in 1-D, is explored. Results show model sensitivity to G computed using the FSM is equivalent to numerical analog values using model results. Additionally, the data assimilation step in the FSM can be used to successfully recover target G values using the model errors and sensitivity values. However, due to the variability of the sensitivities, recovery of target values depends on the initial coefficient set specification. Furthermore, sensitivity results show generation of spurious oscillations in the elevation and velocity results when G is set too high.

The preliminary model coupling is completed using 1-D channel routing and

ADCIRC models to analyze the impact of the location of the coupling, the types of boundary conditions used for the models, and the complexity of the momentum equation approximation in the channel routing model. Results show one-way coupling of a model with kinematic wave channel routing to ADCIRC is acceptable if the hand-off point is placed upstream of major backwater effects. Additionally, ADCIRC results are best when flux values are used at the upstream boundary.

Finally, a one-way coupled model system using output from a hydrologic model as the upstream boundary condition in ADCIRC is implemented. The target area for this 2-D application is coastal North Carolina, specifically the Tar-Pamlico and Neuse River basins and Pamlico Sound. The hand-off points on the rivers are placed tens of km inland from the Pamlico Sound to ensure ADCIRC handles areas impacted by tides and storm surge. Results show ADCIRC accurately represents specified boundary discharges at the upstream extents of the rivers and can model inundation of the coastal plain due to the combined effects of rainfall-runoff and hurricane storm surge. A hindcast of Hurricane Isabel shows the coupled system accurately models total water level at the USGS location at Washington where the Tar-Pamlico River discharges into the Pamlico Sound. However, inadequate resolution and issues with the wet/dry algorithm in ADCIRC give rise to some mass balance problems in the river reaches that limit the accuracy of results in the downstream portions of the rivers.

CHAPTER 1. Study Background and Motivation

1.1 Introduction

The goal of this study is to improve the capabilities of modeling coastal flood inundation, specifically using the code ADCIRC (ADvanced CIRCulation model [*Luettich* 1992, 2004; *Westerink* 1994]). ADCIRC is a system of computer programs that solves free surface circulation problems. ADCIRC uses a finite element discretization in space that allows for use of the highly unstructured grids necessary to resolve intricate geographical features along the coasts. The continuous Galerkin (CG) finite element method is applied to the shallow water equations, as shown in (2.1) - (2.3). Specifically, the generalized wave continuity equation (GWCE) formulation of the vertically-integrated continuity equation is solved to determine changes in the free surface elevation, and the depth-averaged velocities are determined through solution of the vertically-integrated momentum equations [*Luettich* 2004]. ADCIRC is applied for numerous modeling purposes including tide- and wind-driven circulation; hurricane storm surge and inundation; baroclinic transport for Naval fleet operations; sediment transport and coastal dredging feasibility; and larval and oil spill conveyance [*Kolar* 2000].

1.2 Coastal Flood Inundation

The United States coastlines along the Gulf of Mexico and bordering the Atlantic Ocean are susceptible to storm surge inundation from tropical cyclones and nor'easters. In the last decade, the Louisiana Gulf Coast has been impacted by Hurricanes Katrina, Rita

and Ike, as well as many lesser storms. During Hurricane Katrina, the peak storm surge, ranging from 7 to 10 m, occurred along the Mississippi coastline 20-80 km east of the center of the storm and affected areas up to 20 km inland along water bodies [*Fritz* 2007].

In addition to storm surge, flooding due to rainfall-runoff can be severe and extensive. In 2009, a coastal low-pressure system that included the remnants of Hurricane Ida produced almost 12 in. of rainfall in Chesapeake and Hampton, VA [*Gutro* 2009]. In June 2001, Tropical Storm Allison produced 15 in. of rainfall over large sections of Brays Bayou and downtown Houston, TX in a three-hour period, leading to flooding that resulted in approximately $5 billion in damages [*Bedient* 2003]. In 1999, Hurricane Floyd produced a record 24-hour rainfall at Wilmington, NC of 15.06 in. and a storm total of 19.06 in [*Pasch* 1999]. Rainfall from Hurricanes Dennis, Floyd and Irene produced 500-year flows in every major river basin in North Carolina except one (the Lumber River Basin in southeastern North Carolina bordering South Carolina). Following Floyd, the flow rate on the Tar River at Tarboro was almost twice as much as the previously recorded high flow, and the peak stage was nearly 3 m higher than the former maximum [*Bales* 2000, 2003].

1.2.1 History of Coastal Flood Inundation Modeling

While there have been significant efforts undertaken to predict hurricane storm surge in a number of coastal areas, e.g. [*Fleming* 2008; *Mattocks* 2008], and precipitation-induced river flood forecasting is also common, e.g. [*Bedient* 2003], relatively few efforts have been made to combine storm surge and rainfall-runoff for prediction of flood inundation. As noted in *Van Cooten et al.* [2011], there is a NOAA service gap in the coastal plain

as "over 90 percent of these CDAs[a] do not receive any hydrologic information regarding water level and timing of flood crest from the NWS[b]." Hydrologic models do not predict storm surge, and many models are incapable of accurately representing flood inundation in the coastal plain because of the assumptions used in model development. On the other hand, hydrodynamic models often do not model precipitation-induced flooding. Thus, to achieve a more holistic representation of coastal inundation, it is necessary to couple a hydrologic model to a hydrodynamic model to generate a total water level product, which consists of the water surface elevation taking into account the combination of tides, storm surge, wind waves and riverine flows.

1.2.2 Coastal Flood Inundation Using ADCIRC

Recently, ADCIRC has been used to simulate hurricane storm surge, e.g. [*USACE* 2009; *Bunya* 2010; *Dietrich* 2010a]. *Westerink et al.* [2008] detail use of ADCIRC to hindcast Hurricanes Betsy and Andrew. The triangular, unstructured grid used to discretize the spatial domain for those hindcasts has significant local refinement of the southern Louisiana coastal floodplain including, generally, "five or more nodes across the major rivers and inlets with grid sizes of 100-200 m" to minimize errors caused by under-resolution, which can significantly reduce conveyance of waterways. That manuscript provides significant detail on applying ADCIRC to model storm surge. The two most relevant elements to the current study are as follows: they apply a constant flow rate at the upstream boundary of each river in the model that is representative of the flow during a particular storm and

a. From *Van Cooten et al.* [2011], "NOAA (2010) defines a CDA as 'that component of an entire watershed that meets the following three criteria: 1) it is not part of any estuary drainage area; 2) it drains directly into an ocean, an estuary, or the Great Lakes; and 3) it is composed only of the downstream-most HUC in which the head-of-tide is found.'"
b. National Weather Service

employ a radiation boundary condition to prevent reflection of tides and surge waves that are propagating upriver; simulations are performed using spatially variable G, which is sometimes referred to as τ_0, with higher values in shallow and overland areas and a lower value in deeper areas, all determined by experience and empirical rules guided by analysis of the linear system.

1.2.3 River Flood Prediction and Inundation

Hydrology deals with the movement, distribution and quality of surface and ground water. Thus, hydrologic models are comprised of some combination of the following components: precipitation, interception, evaporation and evapotranspiration, infiltration, unsaturated flow, saturated flow, soil moisture, surface runoff, channel routing, and erosion and export. One main aspect of hydrologic modeling is predicting the flow rate (or discharge) of a river, stream or channel.

There are innumerable hydrologic models which fall along the spectrum of the two extremes in watershed modeling. At one end are lumped, parametric rainfall-runoff models. At the other end are distributed, physics-based models. Generally, physics-based models, e.g. V*flo* [*Vieux* 2002, 2004], TREX [*Velleux* 2006], MIKE SHE [*Abbott* 1986a,b; *Refsgaard* 1995], PIHM [*Qu* 2005, 2007], and WASH123D [*Yeh* 2005], are distributed models that use governing equations of overland and channel flow, along with detailed information about topography and land use, to route rainfall to the basin outlet. Parametric models, e.g. HL-RDHM [*Koren* 2004; *Smith* 2004; *Reed* 2004; *Moreda* 2006; *Hydrology Laboratory* 2008], HRC-DHM [*Carpenter* 2004, 2006], and HEC-HMS [*Feldman* 2000], can often be applied on a range of scales, from lumped to distributed, with the parameters being calibrated at a given modeling scale. Generally, physics-based models utilize available data

sets, e.g. digital elevation, land-use/cover and soil classification maps, to define model parameters [*Vieux* 2001], while lumped, parametric models rely on historical data for parameter calibration. However, as is the case with HL-RDHM, the parameters can be estimated from distributed physical data sets. Additionally, HL-RDHM, HRC-DHM and HEC-HMS are all capable of physics-based channel routing.

The calculated discharge from a hydrologic model can be used to generate a river stage using a stage-discharge relationship. In turn, the river stage is an indicator of flood inundation potential. Alternatively, the discharge can be input into a hydraulic code to produce river stage and inundation results for a particular reach. *Fang et al.* [2008] describe a flood alert system that uses discharge results from the lumped model HEC-1 and the distributed model V*flo*. They developed a floodplain map library based on rainfall patterns, with the flood inundation prediction based on steady-state flow theory. The 1-D hydraulic code HEC-RAS [*Brunner* 2001, 2002] accepted the peak flow rate for a given rainfall event and generated the water surface elevation for the corresponding cross-sections. Finally, floodplain maps were generated using GIS to process the water surface elevation profiles.

Another approach is to model river and floodplain flow using a 2-D model. *Bates and Anderson* [1993] developed a two-dimensional finite element model that solves the depth-averaged Reynolds equations and applied it to an 11 km reach of the River Culm, Devon, U.K. *Bates et al.* [1998] validated TELEMAC-2D [*Galland* 1991; *Hervouet* 1996], a two-dimensional finite element code, on five river reaches using discharge/elevation as the upstream/downstream boundary conditions. *Horritt and Bates* [2002] compared 1-D and 2-D numerical models for predicting river flood inundation on a 60 km reach of the Severn River, UK and found similar accuracy levels for HEC-RAS, LISFLOOD-FP [*Bates*,

2000] and Telemac-2D at optimal calibration.

1.3 Current Deficiencies in Coastal Flood Inundation

In this study, the main objective is to create a total water level product for the coastal plain, which is subject to significant flood effects from both rainfall-runoff and storm surge. The ADCIRC hydrodynamic model has been used extensively for coastal storm surge modeling, but it does not ingest precipitation data or include the elements necessary to model all the types of rivers encountered in modeling of coastal systems. Therefore, coupling of ADCIRC to a hydrologic model is necessary.

Hydrologic models differ in the level of complexity of the momentum equation approximation used in channel routing. Many models, e.g. V*flo* and HL-RDHM, use the kinematic wave approximation to the momentum equation. Others, including TREX, use the diffusive wave approximation. Still others have been developed with multiple routing options. For example, the PIHM has both kinematic and diffusive wave routing options and both WASH123D and MIKE SHE include kinematic, diffusive and dynamic wave routing algorithms. The approximation to the momentum equation has implications in applicability of models to the coastal plain. Generally, the kinematic wave approximation is more adept at simulating flow in steeper areas because of the assumption that the friction slope is equivalent to the bottom slope. The diffusive and dynamic wave approximations both incorporate depth of flow and, thus, are able to simulate backwater effects and allow water to travel upstream, which is a possibility in rivers in the coastal plain. The momentum equation approximation and location of the boundary between the hydrologic and hydrodynamic models are investigated using a 1-D framework, as presented in Chapter 5 of this

study.

The target region for this study is the area of coastal North Carolina that includes the Tar-Pamlico (Tar) and Neuse Rivers and the Pamlico Sound. The Tar and Neuse Rivers are much smaller than the rivers discretized in the grid for storm surge simulations for Louisiana, notably the Mississippi and Atchafalaya Rivers. The Tar and Neuse Rivers are approximately 40 m wide, whereas the Mississippi and Atchafalaya Rivers are hundreds of meters wide. Additionally, the bottoms of the rivers in Louisiana are well below sea level in the entire ADCIRC domain; the bottom of the Mississippi River is 17.5 m below sea level at Baton Rouge, LA in the ADCIRC grid and the bottom of the Atchafalaya River is about 7 m below sea level at the grid boundary, a comparable distance (approximately 120 km) inland. In contrast, the bottoms of the rivers in the North Carolina grid are about 8 m above sea level approximately 60 km inland from the Pamlico Sound. Thus, implementation issues related to discretization and initialization of the North Carolina rivers in ADCIRC, along with the river boundary condition specification, must be addressed. This work is presented in Chapter 6, along with application to historical storms.

In addition to the coastal inundation-specific aspects of this work, the numerical parameter, G, in the GWCE is investigated in Chapter 2, Chapter 3 and Chapter 4. Due to the impact of G on ADCIRC simulation stability and results, as well as the time and expertise necessary to systematically adjust G, an automated selection routine is desirable. Generally, more complex flow fields, such as those experienced during storm surge applications, require more intricate G specification in order to maintain stability and accuracy.

1.4 Dissertation Roadmap

The hypothesis driving this work is that systematic improvements and additions to the ADCIRC hydrodynamic model can improve forecasting and hindcasting of coastal flood inundation, as well as be useful in future studies of theoretical storms. The subsequent five chapters of the dissertation can be divided into two sections. The first three chapters are focused on analysis of G. The last two body chapters are focused on development of a coupled modeling system composed of a hydrologic model and ADCIRC.

Chapter 2 details work towards a spatially and temporally variable algorithm for automatic selection of the G parameter in the GWCE using idealized test cases and Fourier analysis. Chapter 3 explains application of the Forward Sensitivity Method (FSM) to the linearized 1-D ADCIRC equations and shows how data assimilation can be used to estimate G. The application of FSM is extended to the non-linear 1-D ADCIRC equations in Chapter 4. Additionally, non-constant parameterizations for G are analyzed.

Chapter 5 is focused on determining the proper boundary condition, type and location, for use in coupling ADCIRC with hydrologic models. This is accomplished using a 1-D version of ADCIRC. Extension of the 1-D study to the Tar and Neuse River basins is presented in Chapter 6. Specifically, a procedure is developed for modeling rivers in 2-D ADCIRC based on inputs from a hydrologic model, and results for hindcasts of tropical systems are presented, including a total water level hindcast of Hurricane Isabel.

CHAPTER 2. Analysis of G Using Traditional Techniques

2.1 Introduction

Finite element solutions to the primitive shallow water equations (primitive continuity and conservative momentum), given by *Pritchard* [1971] and shown in (2.1) and (2.2), are subject to spurious oscillations. *Lynch and Gray* [1979] formulated the wave continuity equation (WCE), (2.3), by differentiating the primitive continuity equation with respect to time, substituting the conservative momentum equation for the $(\partial H\mathbf{v})/(\partial t)$ term, and substituting the primitive continuity equation for the $\nabla \cdot (H\mathbf{v})$ term. They found that by using the WCE in conjunction with the conservative momentum equation, accurate modeling of longer physical waves was possible while suppressing (or not generating) the spurious oscillations inherent to finite element solutions of the primitive equations.

$$L = \frac{\partial H}{\partial t} + \nabla \cdot (H\mathbf{v}) = 0 \tag{2.1}$$

$$\mathbf{M}^C = \frac{\partial H\mathbf{v}}{\partial t} + \nabla \cdot (H\mathbf{v}\mathbf{v}) + gH\nabla\zeta + \mathbf{f} \times H\mathbf{v} + \tau H\mathbf{v} - H\psi = 0 \tag{2.2}$$

$$W = \frac{\partial^2 H}{\partial t^2} + \tau\frac{\partial H}{\partial y} - (\nabla \cdot [\nabla \cdot (H\mathbf{v}\mathbf{v}) + gH\nabla\zeta + \mathbf{f} \times H\mathbf{v} - H\psi]) - (H\mathbf{v} \cdot \nabla\tau) = 0 \tag{2.3}$$

In the above equations, L denotes the primitive continuity equation (2.1), $\mathbf{M}^C$ is a symbol for the conservative form of the momentum equation (2.2), and W represents the WCE (2.3). Additionally, H is total water depth, which is equal to the sum of the bathymetry, h, and the water surface elevation, ζ, while t is time, $\mathbf{v}$ is the 2-D fluid velocity, g is the magnitude of gravity, $\mathbf{f}$ is the Coriolis parameter, τ is the bottom friction term, and ψ

accounts for wind stress and atmospheric pressure variations. Furthermore, ∇ is the nabla (grad) operator, $\nabla\bullet$ is the divergence operator, and ∂ denotes a partial differential. Appendix A is a nomenclature reference for commonly used symbols in this work.

Kinnmark [1986] showed that the WCE can be generalized by replacing the bottom friction parameter, τ, with a numerical parameter, G. As in *Kolar et al.* [1994], this is easily expressed by presenting the equations in operator notation. The WCE is given by (2.4), while the generalized wave continuity equation (GWCE), denoted by W^G, is shown in (2.5).

$$W \equiv \frac{\partial L}{\partial t} + \tau L - (\nabla \cdot \mathbf{M}^C) = 0 \qquad \textbf{(2.4)}$$

$$W^G \equiv \frac{\partial L}{\partial t} + GL - (\nabla \cdot \mathbf{M}^C) = 0 \qquad \textbf{(2.5)}$$

The ADCIRC hydrodynamic model [*Luettich* 1992, 2004; *Westerink* 2004] is based on a continuous Galerkin finite element discretization of the GWCE and momentum (either conservative or non-conservative momentum) equation. The numerical parameter, G, affects the behavior of the governing equations for the ADCIRC model. As G increases, the GWCE tends toward a primitive (hyperbolic) form of the continuity equation. When G is reduced, the GWCE moves toward a pure wave form of the continuity equation. Empirical studies by *Kolar et al.* [1994] show G should be 1-10τ. Dispersion analysis supported empirical findings and showed the GWCE has a monotonic dispersion relationship for $G = \tau$.

By analyzing the discrete equations in both 1-D and 2-D, *Atkinson et al.* [2004] show the GWCE is approximately equivalent to the Quasi-Bubble formulation used in

TELEMAC 2D [*Galland* 1991; *Hervouet* 1996] if the appropriate formula is used to compute G. The Quasi-Bubble scheme solves the primitive continuity equation but uses an enriched velocity field to avoid generation of spurious oscillations. The equations for G that make the GWCE approximately equivalent to the Quasi-Bubble formulation are slightly different in 1-D and 2-D, given by (2.6) and (2.7), respectively, where ω is the wave frequency and ι is the imaginary unit.

$$\text{1-D: } G = \frac{\iota\omega + 4\tau}{3} \tag{2.6}$$

$$\text{2-D: } G = \frac{\iota\omega + 3\tau}{2} \tag{2.7}$$

Using the appropriate formula for G, the equations (not shown) for elevation in the two models are equivalent. The difference between the two formulations (GWCE-based and Quasi-Bubble) is in the mass matrix terms for the momentum equation. The momentum equation does not depend on G, and using a lumped formulation for the mass matrix terms would make the equations identical. *Atkinson et al*. [2004] found that the formulas, (2.6) and (2.7), improve the dispersion characteristics of the GWCE formulation over using $G = \tau$.

Constant G values tend to produce reasonable results for simple applications. However, more complex problems require more sophisticated specification of the numerical parameter. The equations suggested by the dispersion analysis point towards a spatially and temporally variable algorithm for G. Unfortunately, dispersion analysis is limited to linear behavior, so the above equations may not produce optimal results for non-linear applications, such as hurricane storm surge.

Simulations comparing results using constant and variable G formulations are

explored in the next two sections, with non-moving boundary domains utilized in Section 2.2 and an application requiring wetting and drying in Section 2.3. Subsequently, Fourier analysis is performed on the GWCE in Section 2.4. Conclusions based on analyses in this chapter are provided in Section 2.5.

2.2 Comparison of Constant and Variable G

Simulations were performed using both constant and variable G (based on *Atkinson et al.* [2004]) formulations. Results are shown for three domains: a 1-D slice of the east coast of the United States, a 2-D quarter annular harbor, and a 2-D Bahamas domain. The error metric for these comparisons is mass balance error, which has been shown to be a good surrogate for truncation error [*Dietrich* 2008]. Following *Dietrich et al.* [2008], conservation of mass for an element over one time step is given by (2.8), where the first term is the accumulation term and the second term is the net flux term. Additionally, A_e is the area of an element, the net flux out of the element is represented by Q_{net}, and Δt denotes the change in time.

$$(\overline{\zeta_{t+\Delta t} - \zeta_t})A_e + \frac{1}{2}(Q_{net}^{t+\Delta t} + Q_{net}^{t})\Delta t = 0 \qquad \textbf{(2.8)}$$

The mass balance residual, ε_v, is calculated (as in *Dietrich et al.* [2008]) as the sum of the accumulation and net flux terms, as (2.9) shows.

$$\varepsilon_v = (\overline{\zeta_{t+\Delta t} - \zeta_t})A_e + \frac{1}{2}(Q_{net}^{t+\Delta t} + Q_{net}^{t})\Delta t \qquad \textbf{(2.9)}$$

This treatment of mass balance is based on the finite volume flux and was also used in *Kolar et al.* [1994]. *Massey and Blain* [2005] investigated different methods for computing flux for GWCE-based finite element models and concluded that the finite volume flux

gives realistic results, even though it is not consistent with the finite element formulation with the GWCE.

2.2.1 1-D East Coast

The domain for these simulations is a 1-D slice of the east coast, shown in Figure 2.1, that transitions from the deep ocean to the continental rise, then up to the continental shelf. This domain was used by *Hagen et al.* [2000], *Dresback* [2005], and *Dietrich et al.* [2008]. The simulations share the following parameters: 65 nodes; domain length of 2,000 km; constant node spacing of 31.25 km; $\Delta t = 1.0$ s; bottom friction coefficient, C_f, of 0.1; and a lateral eddy viscosity of zero. The ocean boundary forcing is a 1.0 m tide with a M_2 period of 44712.0 s. The duration of the simulations is just over 15 tidal cycles (671,000 s) and values are saved every 1,000 s for the last 5 tidal cycles.

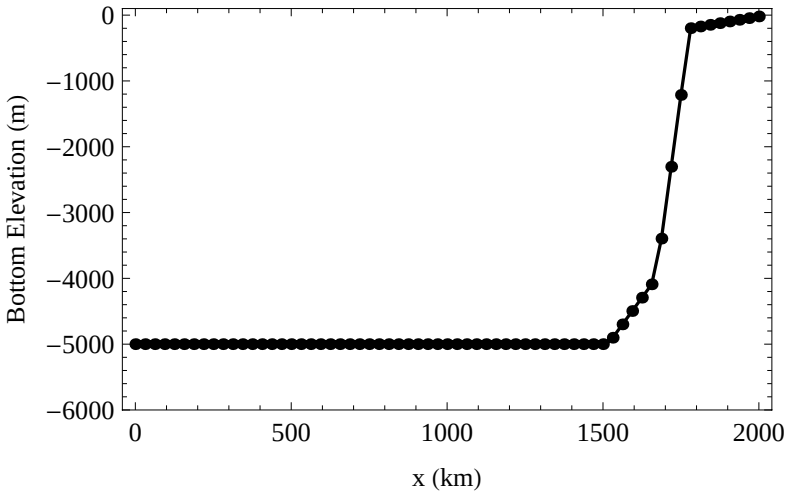

Figure 2.1 Bathymetry and node locations for east coast domain.

The bottom friction, τ, is calculated using the Chezy formula, (2.10), where u_j^k is the depth-averaged velocity in the x-direction at spatial location j and time k.

$$\tau_j^k = C_f\left(\frac{\left|u_j^k\right|}{H_j^k}\right) \tag{2.10}$$

The friction coefficient was selected to produce an average τ value near 0.0001 s^{-1} at the break between the continental rise and continental shelf. The friction value is used to calculate the G value based on the work of *Atkinson et al.* [2004], referred to herein as Atkinson's formula, according to (2.11). The wave frequency is calculated from the tidal forcing period, T, as $\omega = (2\pi)/T$.

$$G_j^k = \alpha_{JHA}\sqrt{\left(\frac{\omega}{3}\right)^2 + \left(\frac{4\tau_j^k}{3}\right)^2} \tag{2.11}$$

Use of Atkinson's formula with an α_{JHA} value of unity will be referred to as the base Atkinson G formulation. For reference, for the east coast domain problem, $\omega = 0.0001405\ s^{-1}$. Thus, there is a lower limit on G of $\omega/3 = 0.00004684\ s^{-1}$.

For this domain, four simulations were performed. Two simulations were with constant G values and the other two used the Atkinson formula for computing G. The two constant G values were 0.001 s^{-1} (which is the value used by *Dietrich et al.* [2008]) and 0.000084355 s^{-1}, which is the mean G value from the base Atkinson simulation. The two variable G simulations use the base Atkinson formulation and the Atkinson formula with an α_{JHA} value of 12.0 which results in a mean G value near 0.001 s^{-1}. The mass residual was computed for each output record, and the average elemental mass residual was calculated as the mean of the absolute values of the residuals for a given element, j, according to (2.12), where n is the number of records used in the computation.

$$(\overline{\varepsilon_v})_j = \left(\frac{1}{n}\sum|\varepsilon_v|\right)_j \tag{2.12}$$

Additionally, the maximum norm for the mass residuals is computed for each element.

The average and maximum mass residuals for each element are shown in Figure 2.2

for each of the four simulations. As Figure 2.2 readily shows, specification of G has a substantial effect on mass residual results. Higher values of G (right panels) drastically reduce the peak local mass balance errors that occur over the continental rise (which consists of elements 49-57), as compared to the lower values of G, regardless of whether the constant or variable G formulation is used.

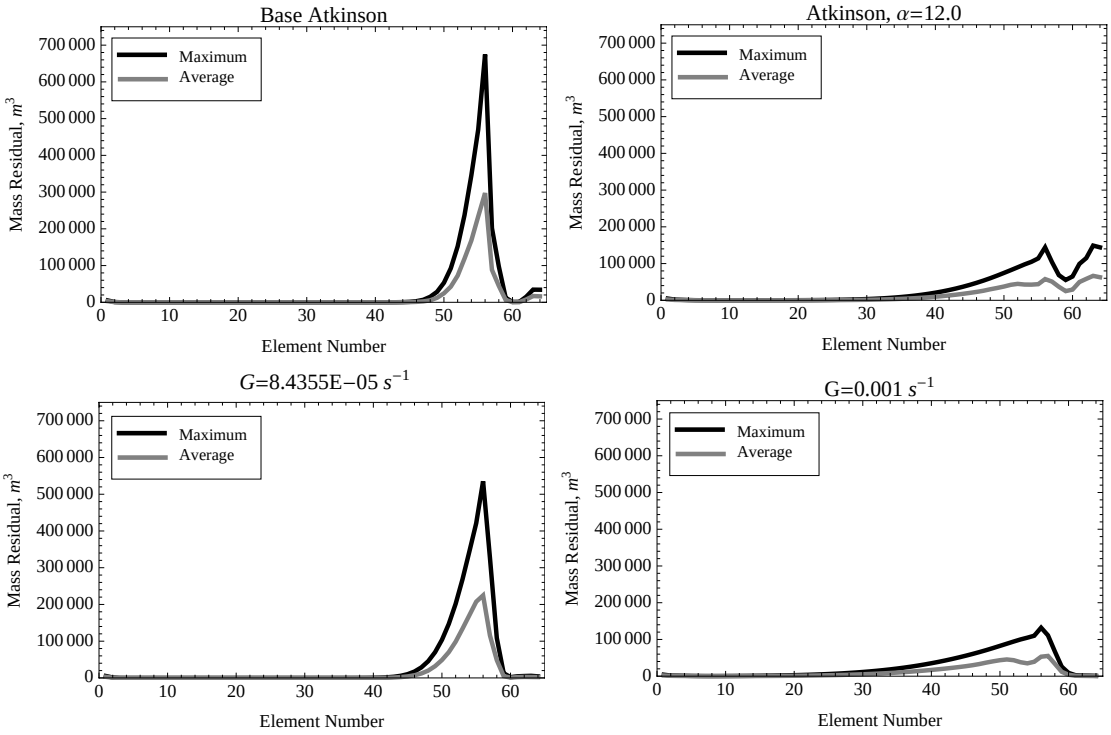

Figure 2.2 Local mass residual plots for simulations on the east coast grid; upper panels are for variable G simulations, while lower panels show results for constant G simulations.

The variable G formulation implemented for these runs only increases the mean nodal G value above the overall simulation mean G value at seven nodes (nodes 58-64). The first of these nodes is at the break between the continental rise and the continental shelf. Thus, the only nodes where the mean G value is larger than the constant G value for the comparisons are on the continental shelf.

The boundary condition on the right side of the domain fixes the velocity at zero at the last node in the domain. Therefore, the G value for that node is at the minimum value,

computed as $\alpha_{JHA}(\omega/3)$, which is thirty times less than the maximum average value for the variable G simulation with $\alpha_{JHA} = 12.0$. A plot of the mean G value for each node for the variable G simulation with $\alpha_{JHA} = 12.0$ is shown in Figure 2.3. The base Atkinson simulation, in contrast, has minimum and maximum mean G values of 4.69 E-05 s^{-1} and 8.22 E-04 s^{-1} and the ratio of the mean G values at the last two nodes is about 17.6. This discrepancy in G near the boundary may be the cause of the rise in the mass residual near the land boundary for the variable G simulations that does not occur for the constant G simulations.

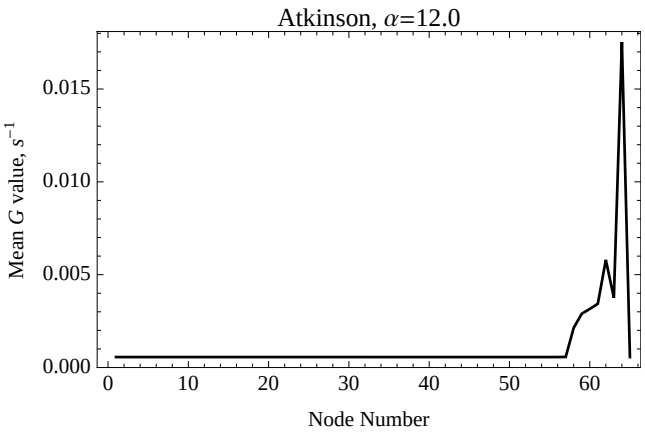

Figure 2.3 Mean G value for each node in the east coast domain for a variable G simulation with $\alpha_{JHA} = 12.0$.

2.2.2 2-D Quarter Annular Harbor

The second domain is a quarter annular harbor that is shown in Figure 2.4 and was used previously by *Lynch and Gray* [1979] and *Dresback* [2005]. Eleven equally spaced arcs (30,000 ft apart with the first at a radius of 200,000 ft) and radii (9° apart) define the 121 nodes in the domain that create 200 elements. The duration of the simulations on the quarter annular harbor domain was 2.0 days, with a 0.5 day ramp on the 1.0 ft elevation boundary condition at the outer boundary. The tidal forcing has a M_2 period of 44712.0 s. The inner boundary was treated as a no-flow land boundary. The other common parameters

are $\Delta t = 10$ s and $C_f = 0.003$. The Coriolis effect was neglected. For the last day of the simulation, the results were recorded every 100 s.

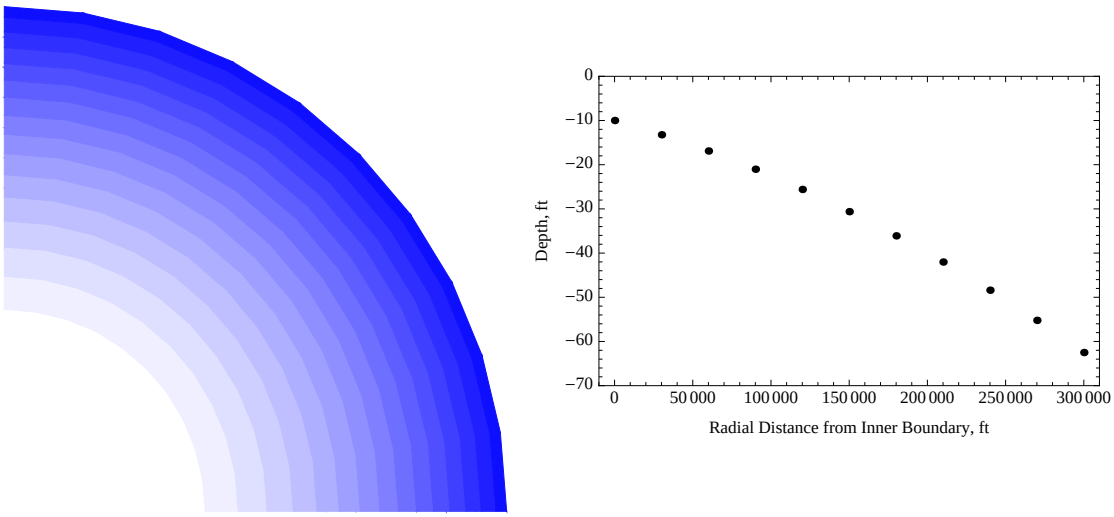

Figure 2.4 Quarter annular harbor domain with bathymetry ranging from 10.0 ft at the inner boundary to 62.5 ft at the outer boundary.

The two simulations are 1) a variable G simulation using the 2-D base Atkinson formula, (2.13),

$$G_j^k = \sqrt{\left(\frac{\omega}{2}\right)^2 + \left(\frac{3\tau_j^k}{2}\right)^2} \qquad \textbf{(2.13)}$$

and 2) a constant G simulation with $G = 0.0001\ \text{s}^{-1}$, which is slightly less than the average G value from the variable G simulation, 1.10E-04 s^{-1}. The global net flux and accumulation values, computed for the last day of the simulations, are shown in Figure 2.5. In contrast to (2.9), where a zero mass residual results when the accumulation and net flux are the same magnitude but opposite signs, a zero mass residual exists for these results when the accumulation and net flux values are the same. This is due to the sign on the net flux term being switched for graphing purposes. The mass residual is the difference between the accumulation and net flux at a given time. The global mass residual is similar

to the elemental value. However, the global mass accumulation consists of the sum of the elemental accumulations. The global net flux is simply the net flux across the domain boundaries because the fluxes across interior element faces cancel, i.e., the flux out of one element is the flux into the adjacent element.

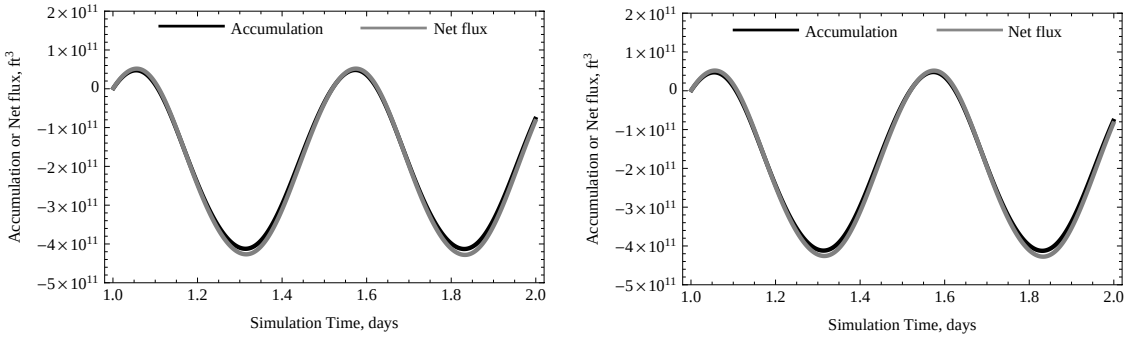

Figure 2.5 Global net flux and accumulation for quarter annular harbor domain simulations. Results on the left are for constant *G*, while results on the right are for variable *G*.

The global mass balance results, presented in Figure 2.5, show similar general trends for the constant and variable G simulations. The accumulation and net flux are set at zero one day into the simulation and allowed to vary from that point forward. For each simulation, the range of the accumulation and net flux terms is about 5.0 E11 ft^3. The range of the mass residual is about 2.0 E10 ft^3 for each simulation, with an average global mass residual of 7.84 E09 ft^3 for the variable G simulation and 7.77 E09 ft^3 for the constant G simulation. Additionally, the variable G simulation had slightly larger accumulation and net flux values at most times during the simulations than the constant G simulation. However, the magnitude of the differences between the terms for the two simulations was on the order of 10^8 ft^3, which is significantly less than the average mass residuals.

Throughout the variable G simulation, the minimum value of G is approximately 7.0 E-05 s^{-1} (given by $\omega/2$), while the maximum value is about 2.3 E-04 s^{-1}. The temporally-averaged G values for the variable G simulation are shown in Figure 2.6. The G

values are a minimum at the inner and outer boundaries for different, yet related, reasons. In both areas, the velocities are low; the non-constant portion of the variable G formula is dependent on velocity. The velocity is close to zero at the inner boundary because the flow is generally along the radial direction and the radial component at the inner boundary is zero (no flow is allowed past that string of nodes). The relatively low velocities at the outer boundary are due to the relatively large depths and arc lengths. The large arc length produces a relatively low unit flux across the arc, as compared to arcs closer to the land boundary. Additionally, the bottom friction value is inversely proportional to the depth.

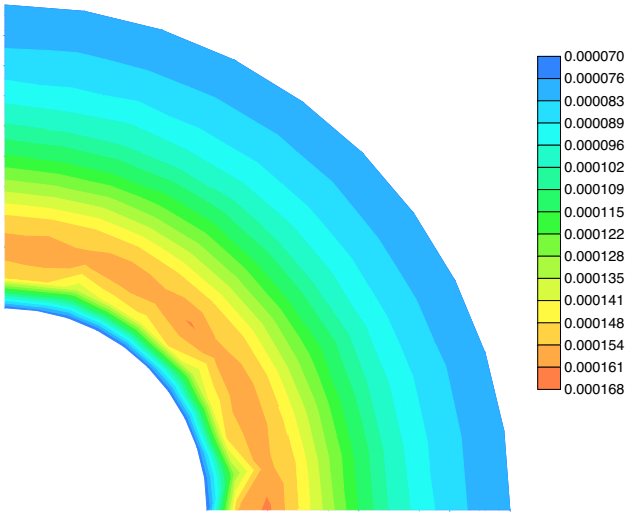

Figure 2.6 Spatial distribution of temporally-averaged G values for the variable G simulation.

A comparison of the local mass balance results is shown in Figure 2.7. The cumulative mass residual is computed for each element and the values at the end of the simulation are used to produce Figure 2.7. The nodal values, ε_n, for local mass balance are computed using the elemental values according to (2.14), where nne is the number of elements surrounding a given node.

$$(\varepsilon_n)_j = \left(\sum_{e=1}^{nne} (\varepsilon_v)_e A_e \right) \Big/ \left(\sum_{e=1}^{nne} A_e \right) \qquad \textbf{(2.14)}$$

The nodal local mass residuals from the two simulations are used to compute the nodal residual difference values, ε_d, used in Figure 2.7 using (2.15), where ε_{n1} values are from the variable G simulation and ε_{n2} values are from the constant G simulation.

$$(\varepsilon_d)_j = \operatorname{sgn}(\varepsilon_{n1} - \varepsilon_{n2})_j \log\left|(\varepsilon_{n1} - \varepsilon_{n2})_j\right| \quad \textbf{(2.15)}$$

Thus, when the nodal residual from the variable G simulation is smaller than its counterpart from the constant G simulation, the nodal residual difference is negative. Therefore, negative values in Figure 2.7 correspond to locations where the variable G simulation has less mass balance error. Conversely, locations on the plot with positive values are areas where the constant G simulation has less mass balance error than the variable G simulation.

The intensity of the color (red or blue) captures the magnitude of the difference in error between the two simulations. Regions where the color is light red, white, or light blue are areas where the log of the absolute value of the difference is small. In these areas, the local mass balance error was approximately equal between the two simulations. Near the interior boundary of the grid, the color is mostly dark blue. Thus, the variable G simulation produces much better mass balance results in this region. Generally, the variable G simulation shows better results at the inner and outer boundaries. However, the constant G simulation has less mass balance error through the majority of the middle of the domain. Relating Figure 2.6 and Figure 2.7, the highest G values for the variable G simulation are found in the same area as the best relative local mass balance results for the variable G simulation.

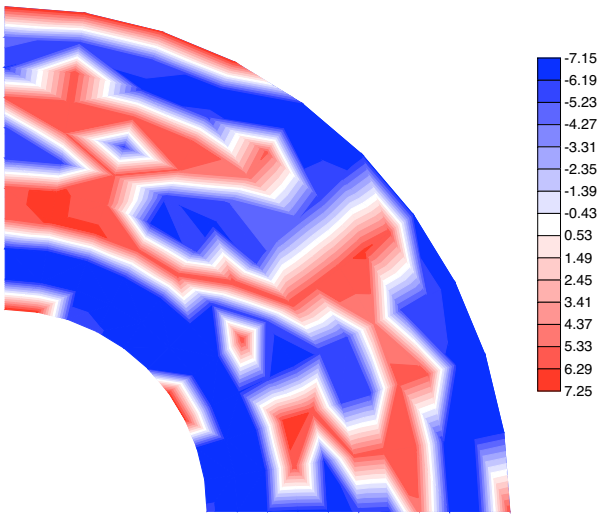

Figure 2.7 Spatial distribution of difference in local mass balance error between the variable *G* simulation and the constant *G* simulation. The magnitude is the log of the absolute value of the difference at each node and the sign is determined by the sign of the computed difference. Areas where the variable *G* simulation have less error are shown in blue, while red areas denote locations where the constant *G* simulation has less error.

2.2.3 2-D Bahamas

The third domain used to compare constant and variable G results is a 2-D Bahamas domain, shown in Figure 2.8 [*Dresback* 2005; *Kolar* 1994; *Massey* 2005]. The domain consists of 926 nodes, defining 1696 elements, with a bathymetry range of 1.0 - 9.0 m. The simulations on this domain were 15.0 days with a 5.0 day ramp on the elevation boundary forcing which consisted of 5 tidal signals (O1, K1, N2, M2, and S2), and the results for the last 5.0 days were output every 4 minutes. The other common parameters were a time step of 60 s, $C_f = 0.009$, and a Coriolis parameter of 5.9 E-05 s^{-1}. Three simulations were performed using this domain: 1) variable G with the base Atkinson formula, 2) constant G of 4.225E-04 s^{-1} which is the average value from the variable G simulation, and 3) constant G of 0.001 s^{-1}.

The elevation and velocity results throughout the domain are similar for the constant and variable G simulations. To illustrate this point, Figure 2.9 shows a compar-

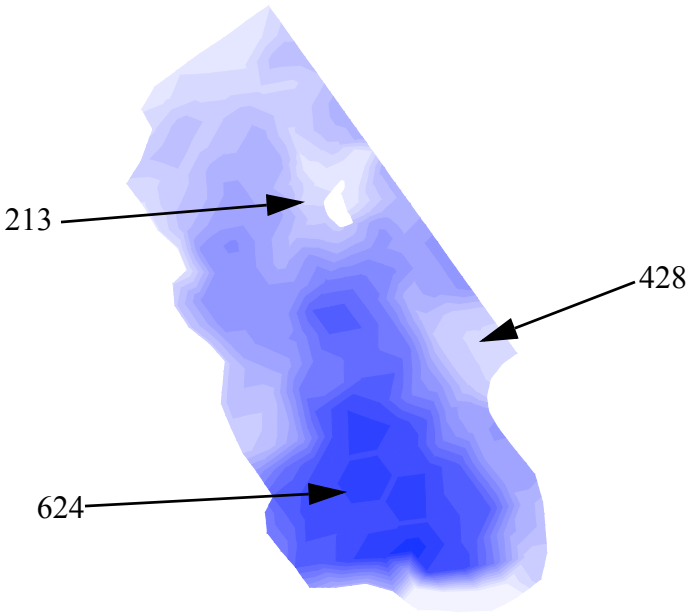

Figure 2.8 Bathymetry for Bahamas domain (dark is deep, light is shallow), which ranges from 1.0-9.0 m. Three arrows are shown corresponding to node locations where results are compared for the constant and variable G simulations. The numbers are the node number for reference to results plots.

ison of flow variables (water surface elevations and depth-averaged velocities) from the constant G simulation using a value of 0.001 s^{-1} to results from the variable G simulation. There is very little difference in either the elevation or velocity results. The peak elevation difference is about 0.5 cm for each of the three nodes analyzed. Note that node 624 is in the deep portion of the domain away from the open boundary, which is the straight line on the top right side of the plot. The other two locations are in shallower areas near the boundary.

While G specification has limited impact on elevation and velocity results, the mass balance is affected more significantly by the choice of G. The global mass balance results are shown in Figure 2.10. As before, each graph corresponds to one particular simulation and the time series are the accumulation and net flux for the entire domain. Again, the difference between the two lines at a given time is the mass balance error. The simulation with the higher constant G value and the variable G simulation show similar error

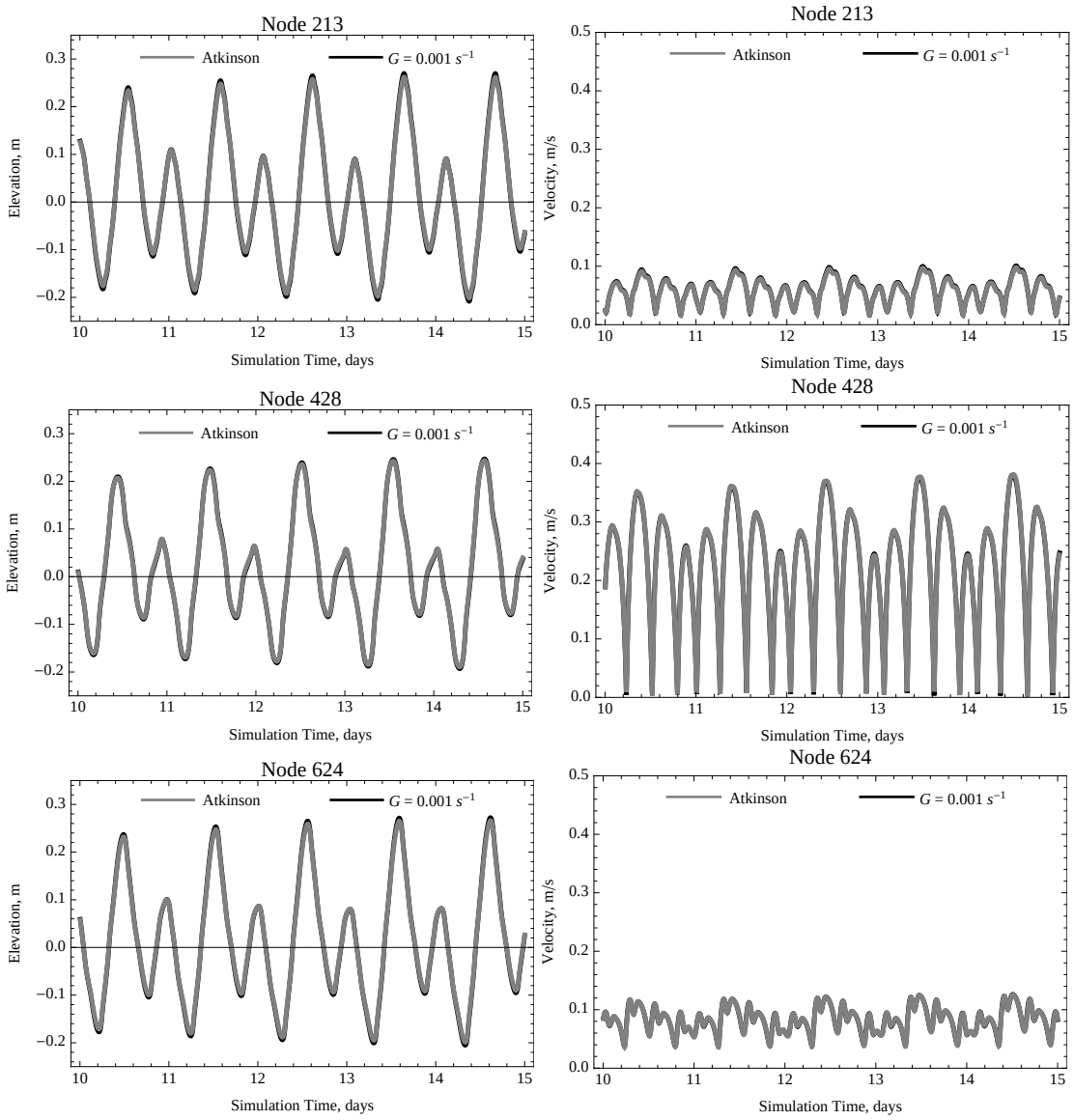

Figure 2.9 Elevation (left) and velocity magnitude (right) time series for the Bahamas domain for nodes 213, 428 and 624.

values. The results with a constant G value of 0.001 s^{-1} show larger errors when the accumulation and net flux are at maximum values than when they are minimums. This trend is also seen in the results for the lower constant G value, 4.225 E-04 s^{-1}. The main difference between the results for the two constant G simulations is that the error is greater for the simulation with the lower G value. It is important to note that the maximum global mass errors grow with time for both constant G simulations, whereas the errors for the variable G simulation do not exhibit that trend from one period to the next.

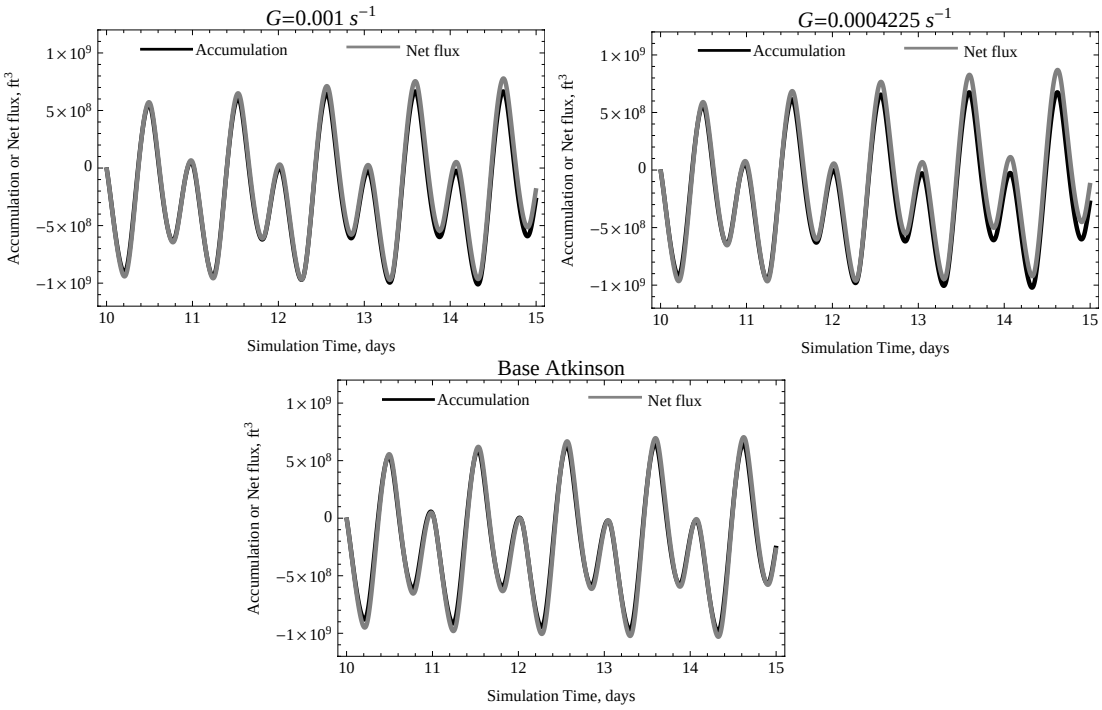

Figure 2.10 Global net flux and accumulation for Bahamas domain. The error in mass balance is the difference between accumulation and net flux.

The range of G values in the simulation using the base Atkinson formula is just over 0.00007 s^{-1} to approximately 0.0027 s^{-1}. The highest values are an order of magnitude higher than the maximum G values for the quarter annular harbor simulation with the base Atkinson formula for G. The mean nodal G values for the base Atkinson simulation are shown in Figure 2.11. The shallower areas generally have higher average G values than the deeper areas due to the higher friction values, with the highest values being located near the bottom right side of the boundary and the top left side of the island.

The local mass balance graphic comparing the results for the variable G simulation to the results for the constant G simulation with the lower G value are shown in Figure 2.12. Near the open boundary (on the top right), the variable G simulation generally shows less local mass balance. However, away from the open boundary, the constant G simulation has less local mass balance error for most locations. Essentially, there is a high correlation

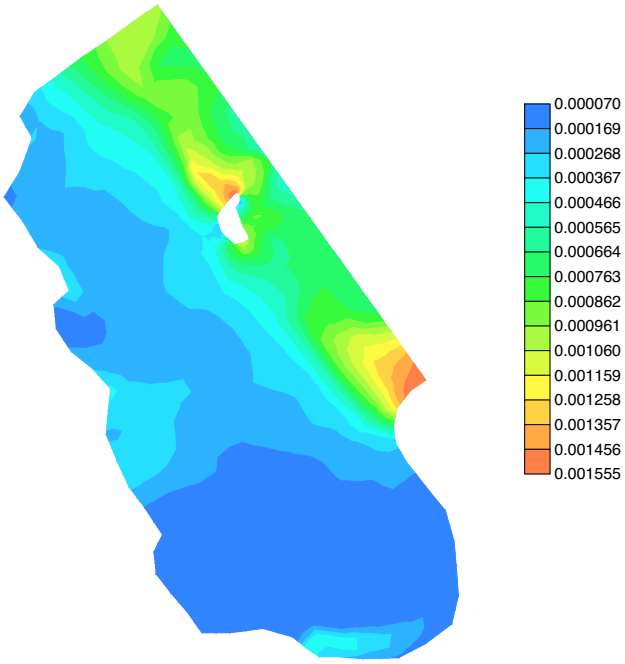

Figure 2.11 Spatial distribution of temporally-averaged G values for the variable G simulation on the Bahamas domain.

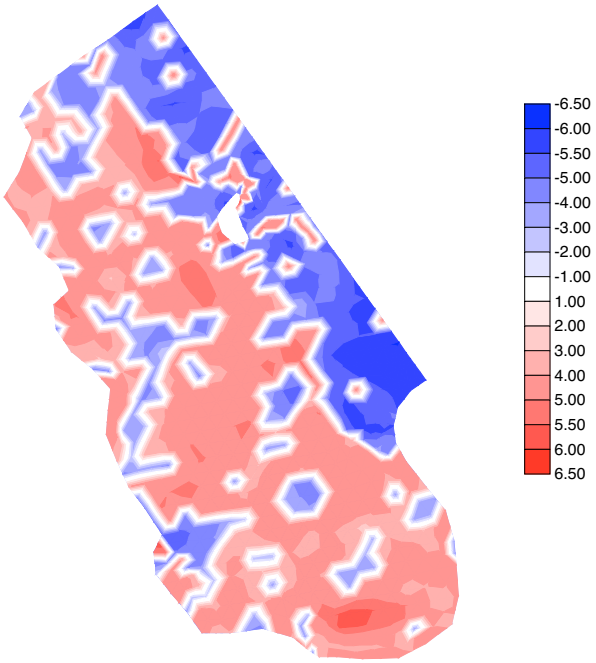

Figure 2.12 Spatial distribution of difference in local mass balance error between the variable G simulation and the constant $G = 0.0004225$ s^{-1} simulation on the Bahamas domain. The magnitude is the log of the absolute value of the difference at each node and the sign is determined by the sign of the computed difference. Areas where the variable G simulation have less error are shown in blue, while red areas denote locations where the constant G simulation has less error.

between the local average G value and local mass balance error. The transition from predominantly blue to predominantly red in Figure 2.12 corresponds to the shift in the average values from the variable G simulation from higher than the overall average (which is the value used in the constant G simulation to which results are being compared) to lower than the overall average.

2.3 Back Bay Problem

Recently, ADCIRC has been used to model hurricane storm surge, particularly in the southeastern United States, with an emphasis on the impacts to southern Louisiana and coastal North Carolina [*Bunya* 2010; *Dietrich* 2010a; *Fleming* 2008; *Mattocks* 2008; *Westerink* 2008]. Accurate modeling of inundation requires wetting and drying as the tides and surge interact with areas of elevation near mean sea level. In order to assess the impact of G selection on these types of problems, a domain was used that has one portion that is always wet and a second section that receives water when a dividing feature is overtopped. A slice of the domain is shown in Figure 2.13. The domain is discretized using a 91 by 7 (x- and y-directions) node grid with constant grid spacing of 16.67 m in each direction, which makes the domain 1.5 km long and 100 m wide. The bathymetry for the 1-D slice is the same as the bathymetry along each of the seven lines of nodes, from ocean boundary to land boundary, in the 2-D grid. The results along the centerline of the simulations were used for comparison purposes.

2.3.1 G Specification

For the continuous Galerkin version of ADCIRC, three types of G specification were examined. The first two, used previously, are constant G and variable G using the

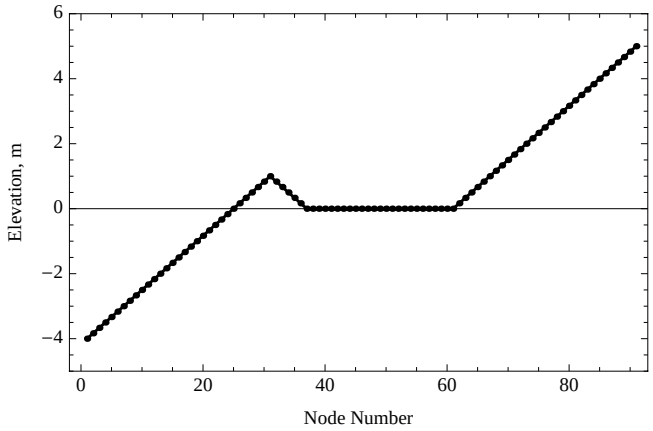

Figure 2.13 One-dimensional slice of the 2-D back bay grid.

base Atkinson formula. The third is an alternate variable G formulation, based on suggestions from Westerink [personal communication, July 2006]. This specification, which will be referred to as the Westerink variable formula, calculates G at each node based on nodal variable using (2.16) and (2.17).

$$G^* = G_0 + \frac{(A_{JJW})\tau|u|}{H} \tag{2.16}$$

$$G = 1 - e^{(-G^*)} \tag{2.17}$$

G_0 is a base value that depends on depth (0.005 for deep areas and 0.02 for shallow areas), while A_{JJW} is a coefficient multiplier on the temporally-variable term in (2.16). For this domain, all the nodes are "shallow", so the G_0 value is always 0.02. The exponential function is used in order to cap the values of the parameter at a maximum of 1.0 as G^* approaches infinity. The relationship between G and G^* for the Westerink variable formula is shown in Figure 2.14. The ratio G/G^* is close to unity for small G^* values. Specifically, when G^* is the base shallow value, 0.02, the ratio is 0.99. The ratio decreases to about 0.95 and 0.90 for G^* values of 0.1 and 0.2, respectively. Thus, the main effect of the transformation from G^* to G is to set a cap on G. This allows areas with less than maximal $(\tau|u|)/H$ values to receive values of G near 1.0 s^{-1} without generating exces-

sively large G values in other parts of the domain.

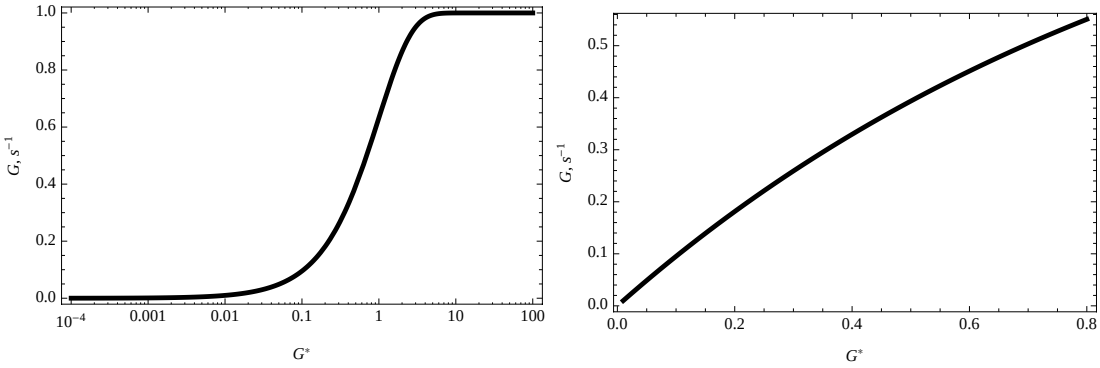

Figure 2.14 Relationship between G and G^* for the Westerink variable formulation; the left panel uses a logarithmic scale for the abscissae, while the right panel shows a limited range of the data in the left panel.

2.3.2 Simulation Set-up

The simulations used a 1.0 m elevation forcing at the ocean boundary and a 0.1 second time step, which is well within the stable range for the G value specifications that produce reasonable results, which will be addressed in subsequent sections. Simulations were 0.2 days, with a ramp over the first 0.01 days and output recorded every 1000 time steps (100 seconds), so there were 172 records of elevation and velocity. The other common parameters were $\varepsilon = 10.0\ \mathrm{m^2/s}$; the friction parameters $C_{f_{min}} = 0.003$, $H_{break} = 2.0$ m, $\theta_f = 10$, and $\gamma_f = 1.333$; and an elevation boundary forcing frequency of $0.01\ \mathrm{days^{-1}}$. As outlined in *Westerink et al.* [2008], the bottom-friction coefficient is computed using (2.18) if the depth is below H_{break}.

$$C_f = C_{f_{min}}\left[1 + \left(\frac{H_{break}}{H}\right)^{\theta_f}\right]^{\gamma_f/\theta_f} \qquad \textbf{(2.18)}$$

The standard Chezy friction law, (2.10), is used when the depth is greater than the break depth.

2.3.3 Stability

The impact on stability was assessed by determining the maximum stable time step. The maximum stable time step using the base Atkinson formula, approximately 0.7 s, was equivalent to the highest maximum stable time steps using constant G values (over the range 0.005 to 1000.0 s^{-1}) or the Westerink variable G formula with a range of A_{JJW} values from 1-1000. The impact of low G values on the stability is significant, with an abrupt decrease in maximum stable time step occurring over a small change in G. For the constant G value simulations, a G value of at least 0.04 s^{-1} is necessary to have the simulation complete with a time step of 0.7 seconds. However, the maximum stable time step for $G = 0.03\ s^{-1}$ is about 0.2 s and is around 0.1 s for $G = 0.01\ s^{-1}$. This result differs from the trend seen on the Bahamas domain (not subject to wetting and drying) where the maximum stable time step reduces from 450 seconds to 390 seconds when the constant G value is increased from 4.225 E-04 s^{-1} to 1.00 E-03 s^{-1}. For the Westerink variable G formula, increasing A_{JJW} from 1 to 3 increases the maximum stable time step from just under 0.2 s to the maximum value of approximately 0.7 s.

2.3.4 Full-Domain Elevation and Velocity Errors

In this section, the elevation and velocity fields will be used to compute root mean square error (RMSE) values. In general, the RMS value of a set of n numbers, $\{c_1, c_2, \ldots, c_n\}$, is given by (2.19).

$$c_{rms} = \sqrt{\frac{\sum_{i=1}^{n} (c_i)^2}{n}} \tag{2.19}$$

The analyses herein will use errors as the set of values. The error value, at spatial location

j and time k, is the difference between values from the two sets of numbers. For instance, the water surface elevation error, $\Delta\zeta_j^k$, is given by (2.20), where the subscripts 1 and 2 refer to two sets (i.e., model and true solution).

$$\Delta\zeta_j^k = (\zeta_j^k)_1 - (\zeta_j^k)_2 \tag{2.20}$$

The order of the difference computation is inconsequential as the error value is squared in the RMSE computation. Generally, however, error is calculated by subtracting the model solution from the true solution.

The elevation RMSE in space, $RMSE_x(\zeta)$, uses the errors at a given time, k, to compute the error metric. At time k, the elevation RMSE in space is given by (2.21) using error computations at n spatial locations.

$$(RMSE_x(\zeta))^k = \sqrt{\frac{\sum_{j=1}^{n} (\Delta\zeta_j^k)^2}{n}} \tag{2.21}$$

The elevation RMSE in time, $RMSE_t(\zeta)$, uses the errors at a given spatial location, j, to compute the error metric. At location j, the elevation RMSE in time is given by (2.22) using error computations at $nrecs$ temporal levels.

$$(RMSE_t(\zeta))_j = \sqrt{\frac{\sum_{k=1}^{nrecs} (\Delta\zeta_j^k)^2}{nrecs}} \tag{2.22}$$

The elevation RMSE in time and space, $RMSE_{xt}(\zeta)$, uses the $RMSE_x(\zeta)$ value for each time record to compute the error metric as shown in (2.23).

$$RMSE_{xt}(\zeta) = \sqrt{\frac{\sum_{k=1}^{nrecs} ((RMSE_x(\zeta))^k)^2}{nrecs}} \quad \textbf{(2.23)}$$

The velocity RMSE values are computed using the same procedure as the elevation RMSE values.

A new version of ADCIRC solves the primitive continuity and momentum equations using discontinuous Galerkin (DG) finite elements [*Dawson* 2010; *Kubatko* 2006]. The DG ADCIRC solution was used as the "true" solution. The reason for using the DG code as the "true" solution is two-fold. First, the DG version of ADCIRC does not use the GWCE. Thus, G specification is not necessary in the DG code. Second, the DG model is better suited to handle this type of problem, where the solution may change rapidly from one node to the next. The DG solution on the 91 x 7 grid was compared to results from a DG simulation using a split-by-four version of the grid that has double the resolution in each direction and, therefore, four times the number of elements.

To compare two simulations (e.g., the two DG simulations at different resolutions or the DG and CG simulations with the same resolution), only the nodes that were wet in both simulations were used to compare elevations and velocities. For example, if the node at the peak of the divide between the ocean and the back bay is wet in one simulation and dry in the other simulation, the node is ignored in error computations. Each simulation has one value of velocity error, $RMSE_{xt}(u)$, and one value of elevation error, $RMSE_{xt}(\zeta)$, associated with it. The elevation error between the original DG simulation and the DG simulation on the split-by-four grid was less than 0.01 m.

The elevation and velocity $RMSE_{xt}$ values for the CG simulations are plotted in

Figure 2.15 and Figure 2.16, respectively. Note the error metric is $RMSE_{xt}$ and the A_{JJW} value is referred to as simply A in the plot label. The constant G results show a steep decrease in error as G is increased up to the breakpoint value of 0.04 s^{-1}, where subsequent increases in G do not result in substantial decreases in error (which coincides with the G value necessary to achieve the largest maximum stable time step, as noted in Section 2.3.3). The minimum error values for the constant G simulations occur when G is 5.0 s^{-1}, although the values for $G = 1.0\ s^{-1}$ are near the minimum. The minimum elevation and velocity error values for the constant G simulations are approximately 0.02 m and 0.09 m/s, respectively.

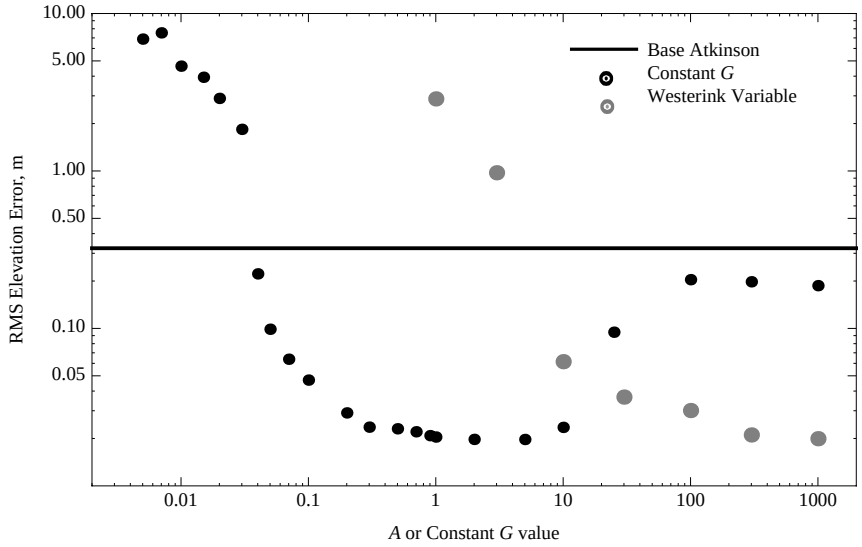

Figure 2.15 Elevation error, $RMSE_{xt}(\zeta)$, for the back bay domain for CG simulations compared to the DG simulation. The error value for the base Atkinson G formula is shown with a solid line. The x-axis denotes the constant G value or the value of A_{JJW} used in the Westerink variable G formula for each run.

Using the base Atkinson formula, the error values are approximately 0.3 m and 0.3 m/s, respectively. These values are comparable to the values achieved using a constant G value of 0.04 s^{-1}. Simulations using the Westerink variable G formula were performed with A_{JJW} values of 1, 3, 10, 30, 100, 300 and 1000. In this case, the breakpoint where

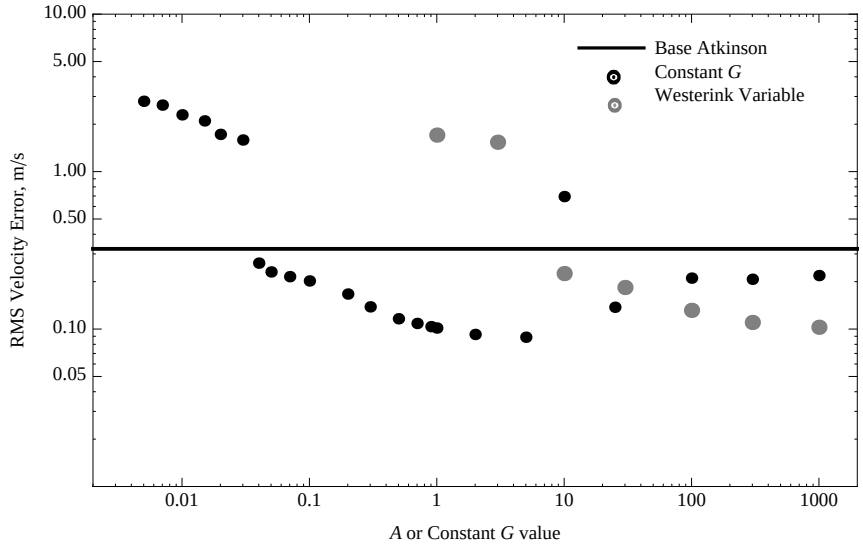

Figure 2.16 Velocity error, $RMSE_{xt}(u)$, for the back bay domain for CG simulations compared to the DG simulation. The error value for the base Atkinson G formula is shown with a solid line. The x-axis denotes the constant G value or the value of A_{JJW} used in the Westerink variable G formula for each run.

subsequent increases to G (in this case through increases to the coefficient multiplier on the velocity part of the equation) do not dramatically decrease elevation and velocity errors occurs at a slightly higher value, $A_{JJW} = 10$, than where the maximum stable time step plateaus. The minimum error values occur with the highest A_{JJW} value used for this set of simulations and are in the same range as the minimum error values for the best constant G simulations. It is important to note that the G values based on the Westerink formula are capped (i.e., the maximum values approach 1.0 s^{-1}). Based on the error reducing as A_{JJW} is increased, it does not appear that variability of G, in space and time, is important for minimizing error. This may be a consequence of using the DG simulation result as the true solution.

2.3.5 Extent of Wetting and Drying

In computing error values for elevations and velocities between the CG and DG ADCIRC simulations, nodes where the wet/dry status was not consistent between the two

simulations were ignored. In order to account for these nodes, the number of instances of wet/dry inconsistencies were counted and are presented in Table 2.1, Table 2.2 and Table 2.3. The three tables contain the results for the constant G simulations, the base Atkinson simulation, and the simulations using the Westerink variable G formula, respectively.

The results for the comparisons of constant G runs to the DG results are similar to the results for the variable G runs using the Westerink formula. This is not particularly surprising based on previous metrics. For both sets, the vast majority of the inconsistencies occur for cases when a node is wet in the CG simulation and dry in the DG simulation. The minimum number is near 700 and the average, calculated by dividing the total by the number of records analyzed, is about 4 nodes per record. The values used for specifying G that produced minimum error values also produce the fewest numbers of discrepancies. While this is not necessarily surprising, as the extent of the wetting is highly dependent on the elevation field, it does suggest that the solution in the areas near the wetting extent are similar, whereas the elevation error calculation is a measure of the solution over the entire domain.

For extremely high constant G values, the less frequent inconsistency (with a node wet in the DG solution and dry in the CG simulation) occurs more often. There is only one DG simulation result, so the shift from higher to lower values in column two of Table 2.1 results from a sequential reduction in the extent of the wet area in the CG simulations as G is increased. This reduction in wet area in the CG simulation results in times when the DG simulation is wet in areas that are dry in the CG simulation and, thus, non-zero values in the third column of the table.

Table 2.1 Comparison of the wetting and drying in constant G CG simulations and the DG simulation.

Constant G Value, s^{-1}	DG Dry, CG Wet[a]	DG Wet, CG Dry[b]	Total[c]
0.005	4715	0	4715
0.01	4713	0	4713
0.02	4711	0	4711
0.03	4689	0	4689
0.04	1295	0	1295
0.05	790	0	790
0.1	720	0	720
0.3	683	0	683
0.5	685	0	685
1.0	683	1	684
5.0	676	1	677
10.0	671	0	671
25.0	603	25	628
100.0	538	141	679

a. This column contains the number of instances in the elevation output files where a DG node is dry and the same node is wet in the CG simulation.
b. This column contains the number of instances in the elevation output files where a DG node is wet and the same node is dry in the CG simulation.
c. This column is the sum of the previous two columns; it contains the total number of instances of inconsistent wet/dry values between the CG and DG simulations.

Table 2.2 Comparison of the wetting and drying in the base Atkinson CG simulation and the DG simulation. The columns are consistent with those in Table 2.1.

DG Dry, CG Wet	DG Wet, CG Dry	Total
480	274	754

The base Atkinson formula for G results in the highest ratio, 0.57, of "DG Wet, CG Dry" to "DG Dry, CG Wet" of any of the simulations. While the total number of inconsistencies between wetting and drying is slightly higher for this case than the minimum values using either constant G or the alternate variable G simulation, the bias towards too much

Table 2.3 Comparison of the wetting and drying in CG simulations with the Westerink variable G formula and the DG simulation. The columns are consistent with those in Table 2.1.

Coefficient Value, A_{JJW}	DG Dry, CG Wet	DG Wet, CG Dry	Total
1	4705	0	4705
3	4682	0	4682
10	728	0	728
30	691	0	691
100	683	0	683
300	683	0	683
1000	682	0	682

wet extent is less than for the other G specifications, which suggests better general mass balance.

2.3.6 Nodal Errors and G Values

The nodal elevation and velocity errors were computed for each node in the domain using the RMSE in time, $RMSE_t$, as per (2.22). As before, only instances where the node was wet in both the CG and DG ADCIRC simulations were used in the RMSE computations. Additionally, the arithmetic average (in time) of the G values was computed for each node in the domain. Again, values were only used when the node was wet in both simulations. The nodal $RMSE_t$ values for the constant G simulation with $G = 0.04$ s^{-1} are shown in Figure 2.17. The line in the left panel shows the $RMSE_t(\zeta)$ is approximately 0.3 m in the back bay and an order of magnitude less, 0.03 m, oceanward of the dividing feature. Combined with prior knowledge about the wet extent of the simulations, this suggests too much water is moving into the back bay for the constant G simulations. The elevations, and thus the wet extent, are high compared to the DG simulation.

The results for a constant G simulation with a G value of 1.0 s^{-1} are shown in

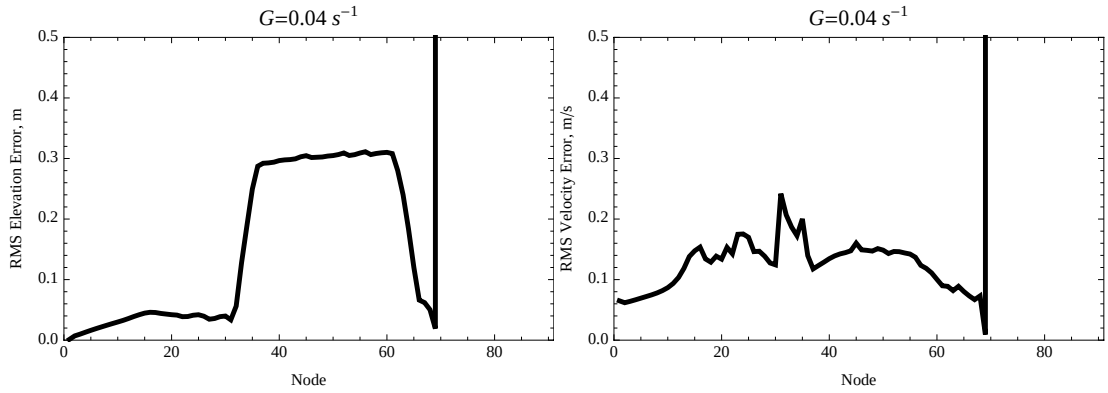

Figure 2.17 Nodal elevation and velocity RMSE in time, $RMSE_t$, for the back bay domain for a constant G simulation using a value of 0.04 s^{-1}. The nodal temporal arithmetic average G value, 0.04 s^{-1} for this simulation, is also shown. The vertical line in each plot shows the maximum extent of inundation during the simulation.

Figure 2.18 to illustrate the impact of increasing G. Noting that the scales differ between the plots in Figure 2.17 and Figure 2.18, the large decrease in the $RMSE_t(\zeta)$ in the back bay portion of the domain is obvious. The maximum nodal value for $RMSE_t(\zeta)$ is on the order of 0.02 m with constant $G = 1.0\ \mathrm{s}^{-1}$. The $RMSE_t(u)$ is dramatically reduced as well, from a peak of about $0.25\ \mathrm{m/s}$ for the simulation using $G = 0.04\ \mathrm{s}^{-1}$ to less than $0.1\ \mathrm{m/s}$ for all nodes in the domain for the simulation using $G = 1.0\ \mathrm{s}^{-1}$.

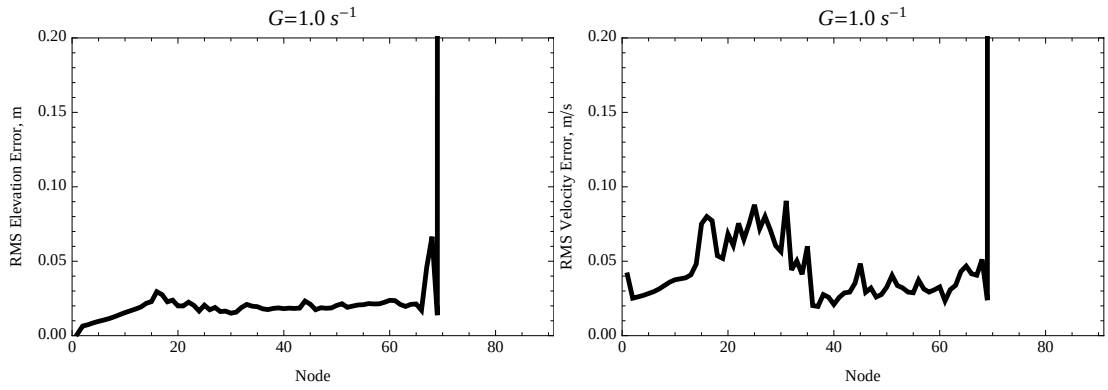

Figure 2.18 Nodal elevation and velocity RMSE in time, $RMSE_t$, for the back bay domain for a constant G simulation using a value of 1.0 s^{-1}. The vertical line in each plot shows the maximum extent of inundation during the simulation.

Using the base Atkinson formula produces the results shown in Figure 2.19. Similar to the results for the constant G run using 0.04 s^{-1}, the majority of the elevation error is in

the back bay portion of the domain. Consistent with many of the simulations, the highest $RMSE_t(u)$ occur just before and over the dividing feature. Use of the base Atkinson variable G formula results in the highest G values occurring just to the right of the peak in the divide. In fact, the only mean nodal G values that are greater than 0.04 s^{-1} (the lowest constant G value that produces reasonable results) occur at nodes 31-34. The average G values for nodes 32-34 are all about 0.075 s^{-1}. Consistent with results for other domains, similar quality results are obtained using a much lower average G value by selectively increasing G at certain instances of space and time.

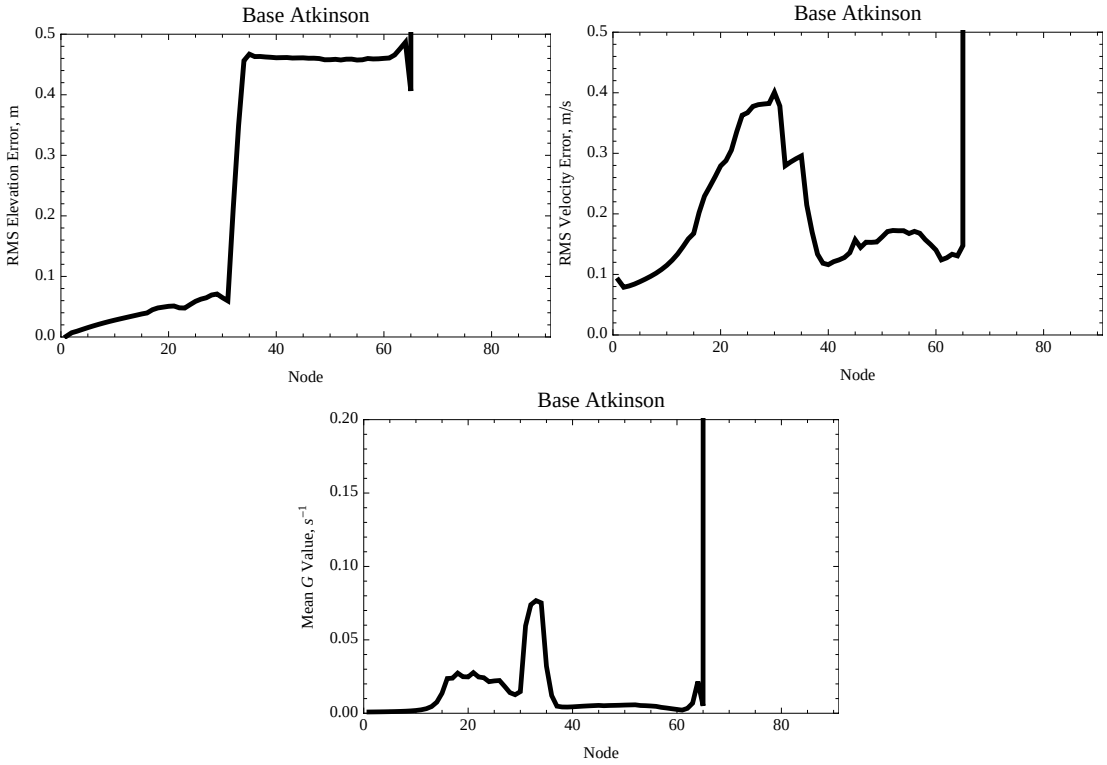

Figure 2.19 Nodal elevation and velocity $RMSE_t$ values for the back bay domain for the variable G simulation using the base Atkinson formula, as well as the mean G value for each node. The vertical line depicts the maximum extent of inundation.

The first reasonable results using the Westerink variable formula to calculate G occur with an A_{JJW} value of 10. The range of average G values for this simulation was 0.023-0.074 s^{-1}. The $RMSE_t$ and average G value plots for the simulation with

$A_{JJW} = 10$ are shown in Figure 2.20. While the maximum average G value for this simulation is similar to the maximum value for the base Atkinson variable G simulation, the location of the maximum is different. The values greater than 0.07 s^{-1} occur just oceanward of the divide, at nodes 29-31, with a drop to just over 0.05 s^{-1} at node 32 and a decrease to less than 0.04 s^{-1} at node 33. Oceanward of the divide, the average G values are greater than 0.04 s^{-1} at and to the right of node 16. Results show the maximum $RMSE_t(u)$ on the bay side and over the transition, with increases in the coefficient A_{JJW} decreasing the magnitude of errors.

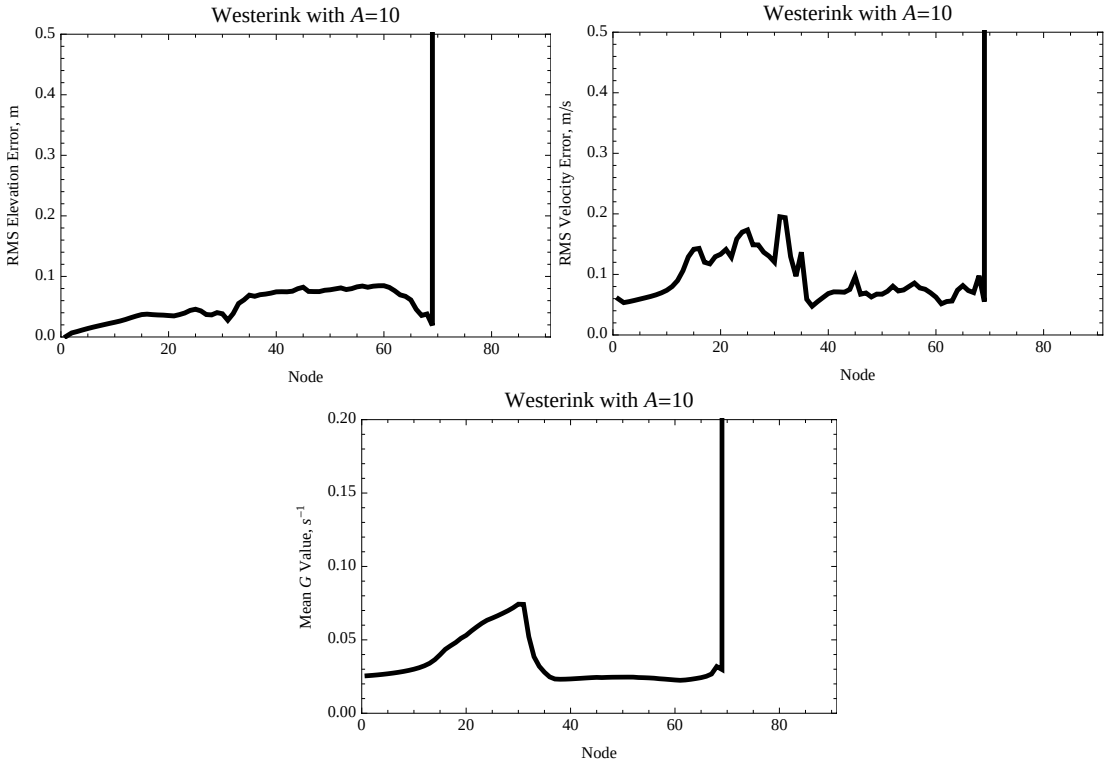

Figure 2.20 Nodal elevation and velocity $RMSE_t$ values for the back bay domain for the simulation using the Westerink variable G formula with $A_{JJW} = 10.0$, as well as the mean G value for each node. The vertical line depicts the maximum extent of inundation.

The results for an A_{JJW} value of 100 are shown in Figure 2.21. Increasing the coefficient multiplier in the Westerink formula for G results in decreased $RMSE_t$ values, although the minimum $RMSE_t$ levels achieved with constant G simulations are not

reached using the Westerink variable G formula. Because there is an upper limit on G using the Westerink variable G formula, the largest G values approach, but cannot exceed, 1.0 s^{-1}. Thus, the average G values at the divide, for simulations with sequentially larger coefficient multiplier values, approach 1.0 s^{-1}. The maximum average G value exceeds 0.98 s^{-1} with an A_{JJW} value of 1000, while it approaches 0.46 s^{-1} with an A_{JJW} value of 100. The influence on the minimum values is even more dramatic. The minimum average G value is about 0.04 s^{-1} with an A_{JJW} value of 100; however, increasing A_{JJW} by a factor of 10 increases the minimum average G value above 0.20 s^{-1}. Subsequent increases to A_{JJW}, above 1000, would simply result in the simulation nearing the simulation using a constant G value of 1.0 s^{-1}.

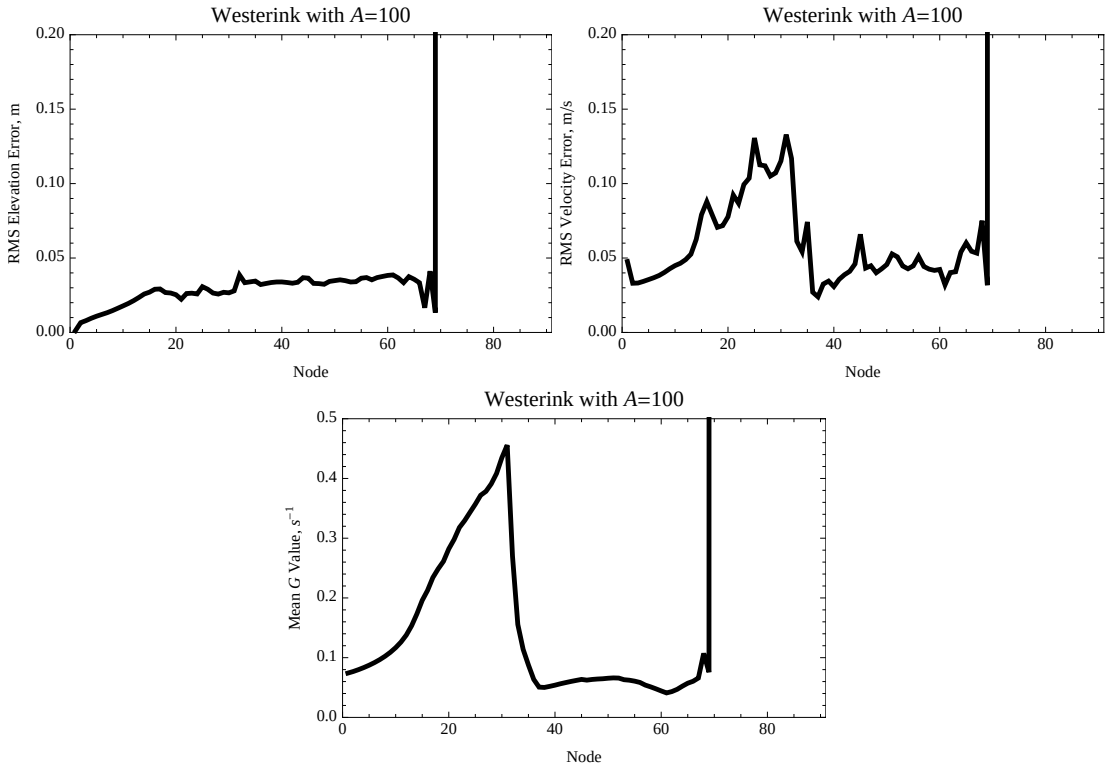

Figure 2.21 Nodal elevation and velocity $RMSE_t$ values for the back bay domain for the simulation using the Westerink variable G formula with A_{JJW} = 100.0, as well as the mean G value for each node. The vertical line depicts the maximum extent of inundation.

2.4 Fourier Analysis

Fourier analysis is used to analyze the stability and propagation characteristics of a numerical algorithm [*Tannehill* 1997]. The ratio of the solution for elevations and velocities at the future time level to the current time level is referred to as the propagation factor. For the linear shallow water equations, the propagation factor, λ, should be one for all wavelengths (assuming frictionless and inviscid). The magnitude of λ should be one and there should not be any change in phase. This study utilizes the analytical Fourier relationship derivation work of *Szpilka* [2005].

2.4.1 Staggered Finite Difference

The staggered finite difference approximation to the shallow water equations allows for a more simple introduction to Fourier analysis than the ADCIRC model we will examine subsequently. Using weighted Euler time stepping and assuming constant bathymetry, *Szpilka* [2005] finds the discrete propagation factors, λ', for this approximation to be the complex conjugates given by (2.24).

$$\lambda' = 1 + \frac{2S\theta - \tau\Delta t T \pm \sqrt{(\tau\Delta t T)^2 + 4ST}}{2(T(1 + \tau\Delta t\theta) - S\theta^2)}, \text{ where} \quad \textbf{(2.24)}$$

$$S = (e^{\iota\sigma\Delta x} - 1)2\iota \sin\left(\frac{\sigma\Delta x}{2}\right) gh\left(\frac{\Delta t}{\Delta x}\right)^2 \text{ and} \quad \textbf{(2.25)}$$

$$T = e^{(\iota\sigma\Delta x)/2} \quad \textbf{(2.26)}$$

Forward Euler, Crank-Nicolson and Backward Euler correspond to θ values of 0.0, 0.5 and 1.0, respectively.

By selecting a parameter set, the amplification factor, λ_d, and phase change per time step, θ_d, can be calculated for different wave number values using (2.27) and (2.28),

respectively.

$$\lambda_d = |\lambda'| \tag{2.27}$$

$$\theta_d = \text{atan}\frac{\text{Im}(\lambda')}{\text{Re}(\lambda')} \tag{2.28}$$

Using a depth of 10.0 m, gravitational constant of 9.81 m/s^2, Δx of 50.0 m and Δt of 1.0 s, the amplification factor and phase have been computed; the results are plotted, against dimensionless wave number, in Figure 2.22 using the three different time-weighting values (Forward Euler, Crank-Nicolson, and Backward Euler). The dimensionless wave number is given by (2.29), where m is the number of elements used to represent the wave.

$$\sigma\Delta x = (2\pi)/m \tag{2.29}$$

The minimum resolvable wave has a length of $2\Delta x$ and corresponds to the Nyquist frequency. This wave has the largest dimensionless wave number, π.

The phase values are similar for each of the time discretization methods. Additionally, the amplification factor is similar for dimensionless wave numbers less than $\pi/10$. However, for the large wave numbers (associated with the shortest wave lengths), the amplification factor is highly dependent on the time-weighting.

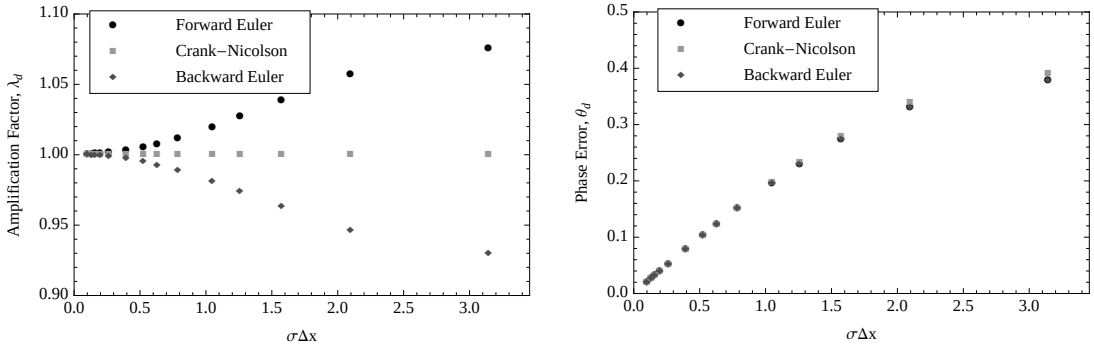

Figure 2.22 Amplification and phase plots for the staggered finite-difference approximation to the shallow water equations for different values of θ and σΔ*x*, the dimensionless wave number.

The forward Euler, which is fully explicit, has amplification factors greater than unity for high wave numbers (which correspond to the shortest wave lengths) and this parameter set. Thus, simulations will be unstable as the water surface elevation disturbances grow progressively with time unless enough artificial or physical damping is introduced. Conversely, the fully implicit backward Euler method artificially damps propagation of waves of the highest numbers. The Crank-Nicolson method produces propagation factors just under unity (approximately 0.99995) for the range of wave numbers presented. The propagation factors for the staggered finite difference approximation to the shallow water equations are complex conjugates. Thus, the amplification factors for the two propagation factors are the same. The difference between the two is in the phase plots; for a given wave number, the amplification factors are the same but the phase errors have opposite signs. Changing the parameters used causes changes to the propagation factor. However, the general trends present in Figure 2.22 persist.

2.4.2 ADCIRC

Szpilka [2005] does not provide explicit equations for the propagation factors for ADCIRC. However, the system of equations and the cubic polynomial resulting from setting the determinant of the matrix equal to zero are given. Solving the cubic polynomial yields three roots, which are the propagation factors for the ADCIRC model approximation to the shallow water equations. As in the case for the staggered finite difference approximation, two of the roots are complex conjugates and are the physical modes for propagation. The third root is a computational mode resulting from the three time-level discretization of the GWCE in ADCIRC that, in turn, is due to the time derivative of the continuity equation that is taken during the model formulation.

Using the same parameters as for the staggered finite difference case presented above, the propagation and phase for G values of 1.0 E-04, 1.0 E-03, 1.0 E-02 and 1.0 E-01 s^{-1} are shown in Figure 2.23. Note that the scales in the left panels vary while the scales in the right panels are consistent. The propagation factors with the lowest G value shown are almost equivalent to the ones for the staggered finite difference with Crank-Nicolson time discretization. The phase values are similar as well, although the maximum value is higher than is found with the staggered finite difference. Thus, the imaginary component is greater for ADCIRC, with this G value, than for the equivalent staggered finite difference.

There are notable trends as G increases. First, the amplification factor for the physical modes at high wave numbers decreases, resulting in increased damping over time; with a G value of 0.1 s^{-1}, the amplification factors are similar to the values for the staggered finite difference using backward Euler time stepping. Additionally, the amplification factors for all wave numbers for the computational mode decrease as G increases until they reach minimums near zero with $G = 2.0\ s^{-1}$. This may be due to the GWCE trending towards the primitive continuity equation as G increases. The primitive continuity equation does not have a third (computational) mode. Thus, it seems reasonable that the computational mode associated with the GWCE will become less prevalent for higher G values.

The graphs in the bottom row in Figure 2.23 show another facet of increasing G. The plots, for a G value of 0.1 s^{-1}, look similar to the plots for lower G values for dimensionless wave numbers greater than $\pi/10$. Specifically, for the physical modes, the amplification factors for the high wave numbers increase towards unity while the amplification factor for the computational mode decreases with decreasing wave number, that is, as you move from the right edge of the plot to the left. However, starting with a dimensionless

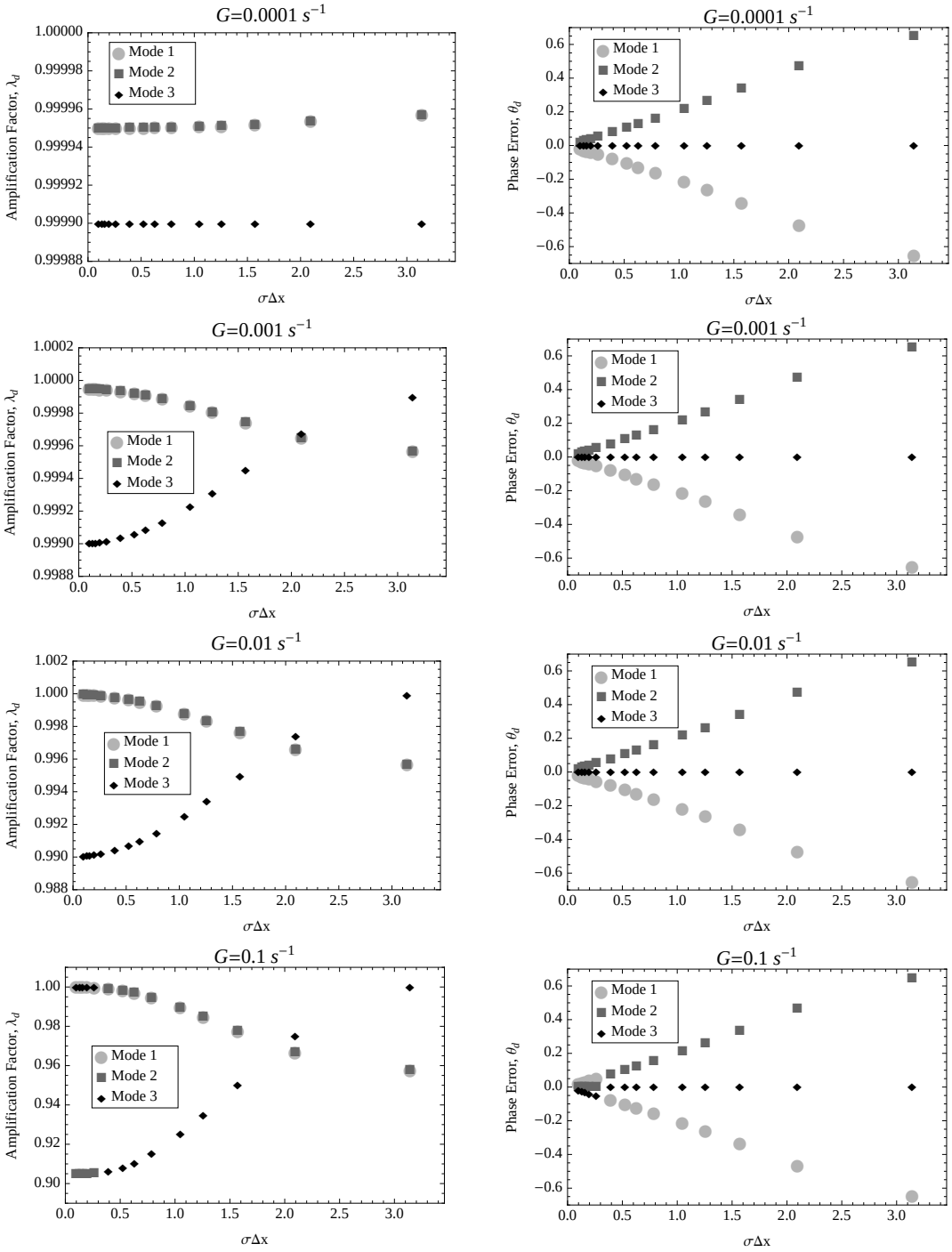

Figure 2.23 Amplification and phase plots for ADCIRC for four different G values.

wave number of $\pi/12$ the second and third modes switch places. For high wave numbers, as well as in the plots with lower G values, the first and second roots produced the complex conjugate physical modes and the third root was the non-physical, computational mode.

Increasing G results in an increase in wave number where this switch between modes takes place. For instance, the switch occurs between dimensionless wave numbers $(2\pi)/3$ and π with $G = 1.0\ \mathrm{s}^{-1}$.

2.4.3 Comparison to Dispersion Analysis for Bahamas

Kolar et al. [1994] show results for a 1-D dispersion analysis using $h = 2$ m, $\tau = 0.01\ \mathrm{s}^{-1}$ and $\Delta x = 2700$ m. These parameters are consistent with values for the Bahamas domain used previously. For large values of G ($> 0.05\ \mathrm{s}^{-1}$), the dispersion curve folds, giving two wave numbers for the same frequency. The result of a folding dispersion curve is the generation of spurious, short-wavelength noise in the solution.

The Fourier analysis for the 1-D ADCIRC equations, using the same parameter set with a $\Delta t = 1.0$ s, results in amplification factors (for all three modes) near unity and phase error values near zero for all wave numbers with $G = 0.001\ \mathrm{s}^{-1}$. As G is increased, the amplification factor for the computational mode tends towards zero.

Increasing Δt to 100 s, while holding the other parameters constant, results in a mode shift for high wave numbers, even when low values of G are used. The switch occurs for dimensionless wave numbers greater than $\pi/2$ when $G = 0.0001\ \mathrm{s}^{-1}$. Additionally, at the lowest wave numbers, the physical modes do not have the exact same amplification factors.

2.5 Conclusions

The analyses presented in this chapter demonstrate that application of variable G schemes can improve behavior of ADCIRC on certain applications. Careful selection of G can result in realistic elevation and velocity fields that produce smaller mass balance resid-

uals than those that result from an arbitrary selection of G. Additionally, use of variable G schemes allows G to be increased at certain combinations of space and time where a larger G value is necessary to help maintain stability and mass balance, while still allowing a relatively low value to be used throughout the domain to avoid spurious oscillations resulting from high G values.

However, while the base Atkinson formula for G may give near optimal dispersion results for the linear equations, it is not optimal for the highly non-linear conditions present under hurricane storm surge and wetting and drying applications. The Westerink variable G formula, which is similar in form and function to the Atkinson formula, produces decent results for the back bay wetting and drying problem.

The use of the Westerink variable G formula points to a difficulty in modeling with the GWCE. Traditional analysis techniques, like dispersion and Fourier analysis, are solely applicable to the linear equations. However, there is a need to apply ADCIRC to non-linear problems. Therefore, it is desirable to utilize techniques that allow for analysis of non-linear equations. The next two chapters focus on such an effort through the application of the forward sensitivity method to the 1-D ADCIRC model.

CHAPTER 3. Application of the Forward Sensitivity Method to Linear 1-D ADCIRC with Constant G

3.1 Introduction

The specification of the numerical parameter G in ADCIRC has primarily been guided by linear analyses and experience. Over time, the complexity of specification schemes has evolved as applications have become more complex. *Kolar et al.* [1994] details assessment of different constant G simulations. Currently, variable G implementations are routinely used [*Westerink* 2008]. However, other than traditional linear analysis techniques, which provide limited guidance for the highly non-linear problems that typically require more sophisticated G schemes, assessment of the results generated from a particular simulation has been the main tool for evaluation.

Recently, *Lakshmivarahan and Lewis* [2010] outlined a methodology for determining corrections to control parameters. The forward sensitivity method (FSM) combines sensitivity function analysis with the solution of an inverse problem. The evolution of the sensitivity of the solution to the control parameters is computed. Then, the inverse problem is solved using a least-squares approach. Control parameters include initial and boundary conditions as well as physical, empirical and numerical parameters. In this chapter, the FSM is applied to the numerical parameter, G, in the generalized wave continuity equation (GWCE).

The analysis in this chapter is limited to the linearized 1-D shallow water equation

system consisting of the GWCE and the non-conservative momentum equation (NCM). However, the FSM is applicable to non-linear systems, as will be considered in Chapter 4. The linear case was selected as the starting point for purposes of simplicity. Additionally, this chapter is limited to constant G analyses, where G is constant in both space and time. Both semi-implicit (referred to herein as simply "implicit") and explicit time-marching schemes are analyzed.

To begin, the governing equations and discretizations are presented in Section 3.2. Then, the sensitivity equations and sensitivity results for two applications are presented in Section 3.3. Subsequently, in Section 3.4, the FSM sensitivities to G are compared to a numerical analog for the sensitivities where the difference in the results for two simulations, with slightly different G values, are used to compute the sensitivity. Next (Section 3.5), the corrections to G, using the solution to the inverse problem, are assessed. Sequential optimization for corrections to G (Section 3.6) and a comparison of FSM to dispersion analysis (Section 3.7) complete the analysis for the chapter. Finally, conclusions are made based on the 1-D constant G analyses. Additionally, details of the discrete time formulation of the FSM are included in Appendix B.

3.2 1-D Discretizations

3.2.1 Governing Equations

The 1-D linear inviscid generalized wave continuity and momentum equations are given by (3.1) and (3.2), respectively, where the subscripts refer to space or time derivatives, e.g., $\zeta_{tt} = (\partial^2 \zeta)/(\partial t^2)$.

$$\zeta_{tt} + G\zeta_t + (G-\tau)hu_x - gh\zeta_{xx} = 0 \tag{3.1}$$

$$u_t + \tau u + g\zeta_x = 0 \tag{3.2}$$

3.2.2 Continuous Galerkin Finite Element Discretization

Application of the continuous Galerkin finite element method using constant grid spacing results in the following equations for the GWCE, (3.3), and momentum equations, (3.4):

$$\mathbf{M}_{i,j}\frac{\partial^2 \zeta_j}{\partial t^2} + G\mathbf{M}_{i,j}\frac{\partial \zeta_j}{\partial t} - (G-\tau)h_j\mathbf{B}_{i,j}u_j + gh\mathbf{S}_{i,j}\zeta_j = 0 \tag{3.3}$$

$$\mathbf{M}^L_{i,j}\frac{\partial u_j}{\partial t} + \tau\mathbf{M}^L_{i,j}u_j + g\mathbf{B}^T_{i,j}\zeta_j = 0 \tag{3.4}$$

where $\mathbf{M}_{i,j} = \Delta x\begin{bmatrix}1/3 & 1/6\\ 1/6 & 1/3\end{bmatrix}$, $\mathbf{M}^L_{i,j} = \Delta x\begin{bmatrix}1/2 & 0\\ 0 & 1/2\end{bmatrix}$, $\mathbf{B}_{i,j} = \begin{bmatrix}-1/2 & -1/2\\ 1/2 & 1/2\end{bmatrix}$, $\mathbf{B}^T_{i,j} = \begin{bmatrix}-1/2 & 1/2\\ -1/2 & 1/2\end{bmatrix}$ and $\mathbf{S}_{i,j} = \frac{1}{\Delta x}\begin{bmatrix}1 & -1\\ -1 & 1\end{bmatrix}$.

3.2.3 Finite Difference Time Discretization

Application of a three-level scheme centered at k for the GWCE and a two-level scheme centered at $k+1/2$ for the momentum equation results in the following set of equations, (3.5) and (3.6).

$$\frac{1}{\Delta t^2}\mathbf{M}_{i,j}(\zeta_j^{k+1} - 2\zeta_j^k + \zeta_j^{k-1}) + \frac{G}{2\Delta t}\mathbf{M}_{i,j}(\zeta_j^{k+1} - \zeta_j^{k-1}) - (G-\tau)h_j\mathbf{B}_{i,j}u_j^k + \tag{3.5}$$

$$\frac{1}{\Delta t}\mathbf{M}^{L}_{i,j}(u_j^{k+1} - u_j^k) + \frac{\tau}{2}\mathbf{M}^{L}_{i,j}(u_j^{k+1} + u_j^k) + \frac{g}{2}\mathbf{B}^{T}_{i,j}(\zeta_j^{k+1} + \zeta_j^k) = 0 \qquad \textbf{(3.6)}$$

The $\alpha_i's$ are the time-weight parameters subject to $\alpha_1 + \alpha_2 + \alpha_3 = 1.0$.

3.2.4 Semi-Implicit Scheme

Using the unlumped mass matrices, for both the GWCE and momentum equations, and equal values ($\alpha_i = 1/3$) for the time-weighting coefficients in the GWCE results in a semi-implicit scheme. With lumping, the Crank-Nicolson time discretization of the momentum equation can be solved directly using the new elevations calculated from the current time step. The system can be written symbolically as shown in (3.7), where **A**, **B**, and **C** are coefficient matrices for the future, current, and past time levels, respectively; the **c** vectors contain the nodal water surface elevation and velocity values; and $\mathbf{f}_{bc}^{k+1}$ is the specified boundary forcing.

$$\mathbf{A}(G)\mathbf{c}^{k+1} = \mathbf{B}(G)\mathbf{c}^{k} + \mathbf{C}(G)\mathbf{c}^{k-1} + \mathbf{f}_{bc}^{k+1} \qquad \textbf{(3.7)}$$

Discretizing the domain with $n = 5$ nodes results in the following coefficient matrix and unknown vector components, with the appropriate modifications made to account for a specified (i.e., Dirichlet) elevation on the first node and a specified velocity on the last node:

$$\mathbf{A}(G) = \begin{bmatrix} 1 & 0 & 0 & 0 & 0 & 0 & 0 & 0 & 0 & 0 \\ E_1 & F_2 & E_2 & 0 & 0 & 0 & 0 & 0 & 0 & 0 \\ 0 & E_2 & F_3 & E_3 & 0 & 0 & 0 & 0 & 0 & 0 \\ 0 & 0 & E_3 & F_4 & E_4 & 0 & 0 & 0 & 0 & 0 \\ 0 & 0 & 0 & E_4 & F_4^* & 0 & 0 & 0 & 0 & 0 \\ -r & r & 0 & 0 & 0 & q & 0 & 0 & 0 & 0 \\ -r & 0 & r & 0 & 0 & 0 & 2q & 0 & 0 & 0 \\ 0 & -r & 0 & r & 0 & 0 & 0 & 2q & 0 & 0 \\ 0 & 0 & -r & 0 & r & 0 & 0 & 0 & 2q & 0 \\ 0 & 0 & 0 & 0 & 0 & 0 & 0 & 0 & 0 & 1 \end{bmatrix} \tag{3.8}$$

$$\mathbf{B}(G) = \begin{bmatrix} 0 & 0 & 0 & 0 & 0 & 0 & 0 & 0 & 0 & 0 \\ I_1 & J_2 & I_2 & 0 & 0 & dh_1 & 0 & -dh_3 & 0 & 0 \\ 0 & I_2 & J_3 & I_3 & 0 & 0 & dh_2 & 0 & -dh_4 & 0 \\ 0 & 0 & I_3 & J_4 & I_4 & 0 & 0 & dh_3 & 0 & -dh_5 \\ 0 & 0 & 0 & I_4 & J_4^* & 0 & 0 & 0 & dh_4 & dh_5 \\ r & -r & 0 & 0 & 0 & s & 0 & 0 & 0 & 0 \\ r & 0 & -r & 0 & 0 & 0 & 2s & 0 & 0 & 0 \\ 0 & r & 0 & -r & 0 & 0 & 0 & 2s & 0 & 0 \\ 0 & 0 & r & 0 & -r & 0 & 0 & 0 & 2s & 0 \\ 0 & 0 & 0 & 0 & 0 & 0 & 0 & 0 & 0 & 0 \end{bmatrix} \tag{3.9}$$

$$\mathbf{C}(G) = \begin{bmatrix} 0 & 0 & 0 & 0 & 0 & 0 & 0 & 0 & 0 & 0 \\ K_1 & L_2 & K_2 & 0 & 0 & 0 & 0 & 0 & 0 & 0 \\ 0 & K_2 & L_3 & K_3 & 0 & 0 & 0 & 0 & 0 & 0 \\ 0 & 0 & K_3 & L_4 & K_4 & 0 & 0 & 0 & 0 & 0 \\ 0 & 0 & 0 & K_4 & L_4^* & 0 & 0 & 0 & 0 & 0 \\ 0 & 0 & 0 & 0 & 0 & 0 & 0 & 0 & 0 & 0 \\ 0 & 0 & 0 & 0 & 0 & 0 & 0 & 0 & 0 & 0 \\ 0 & 0 & 0 & 0 & 0 & 0 & 0 & 0 & 0 & 0 \\ 0 & 0 & 0 & 0 & 0 & 0 & 0 & 0 & 0 & 0 \\ 0 & 0 & 0 & 0 & 0 & 0 & 0 & 0 & 0 & 0 \end{bmatrix} \tag{3.10}$$

$$\mathbf{c}^k = \begin{bmatrix} \zeta_1^k & \zeta_2^k & \zeta_3^k & \zeta_4^k & \zeta_n^k & u_1^k & u_2^k & u_3^k & u_4^k & u_n^k \end{bmatrix}^T \tag{3.11}$$

$$\mathbf{f}_{bc}^{k+1} = \begin{bmatrix} \zeta_{1,\,bc}^{k+1} & 0 & 0 & 0 & 0 & 0 & 0 & 0 & 0 & u_{n,\,bc}^{k+1} \end{bmatrix}^T \tag{3.12}$$

where $E_i = a + b - eh_{e_i}$, $F_i = 4(a+b) + e(h_{e_{i-1}} + h_{e_i})$, $F_i^* = 2(a+b) + eh_{e_i}$,

$I_i = 2a + eh_{e_i}$, $J_i = 8a - e(h_{e_{i-1}} + h_{e_i})$, $J_i^* = 4a - eh_{e_i}$, $K_i = -(a-b) + eh_{e_i}$,

$L_i = -4(a-b) - e(h_{e_{i-1}} + h_{e_i})$, $L_i^* = -2(a-b) - eh_{e_i}$, $a = \frac{\Delta x}{6\Delta t^2}$, $b = \frac{G\Delta x}{12\Delta t}$,

$d = \frac{G-\tau}{2}$, $e = \frac{g}{3\Delta x}$, $q = \frac{\Delta x}{2}\left(1 + \frac{\tau\Delta t}{2}\right)$, $r = \frac{g\Delta t}{4}$ and $s = \frac{\Delta x}{2}\left(1 - \frac{\tau\Delta t}{2}\right)$.

3.2.5 Explicit Scheme

By using the lumped mass matrix for the first two terms in the GWCE, (3.5), and setting $\alpha_1 = 0$ and $\alpha_2 = \alpha_3 = 1/2$, the GWCE system becomes explicit. Additionally, the elevation term in the momentum equation, (3.6), was treated explicitly so the only terms on the left-hand side of the system are on the diagonal. The system is of the same form as the semi-explicit scheme outlined above, with slightly different coefficient matrices (**A***, **B***, and **C***), as shown below.

$$\mathbf{A}^*(G) = \begin{bmatrix} 1 & 0 & 0 & 0 & 0 & 0 & 0 & 0 & 0 & 0 \\ 0 & 2(a'+b') & 0 & 0 & 0 & 0 & 0 & 0 & 0 & 0 \\ 0 & 0 & 2(a'+b') & 0 & 0 & 0 & 0 & 0 & 0 & 0 \\ 0 & 0 & 0 & 2(a'+b') & 0 & 0 & 0 & 0 & 0 & 0 \\ 0 & 0 & 0 & 0 & a'+b' & 0 & 0 & 0 & 0 & 0 \\ 0 & 0 & 0 & 0 & 0 & q & 0 & 0 & 0 & 0 \\ 0 & 0 & 0 & 0 & 0 & 0 & 2q & 0 & 0 & 0 \\ 0 & 0 & 0 & 0 & 0 & 0 & 0 & 2q & 0 & 0 \\ 0 & 0 & 0 & 0 & 0 & 0 & 0 & 0 & 2q & 0 \\ 0 & 0 & 0 & 0 & 0 & 0 & 0 & 0 & 0 & 1 \end{bmatrix} \quad \textbf{(3.13)}$$

$$\mathbf{B}^*(G) = \begin{vmatrix} e'h_{e_1} & N_2 & e'h_{e_2} & 0 & 0 & dh_1 & 0 & -dh_3 & 0 & 0 \\ 0 & 2a'+e'h_{e_2} & N_3 & e'h_{e_3} & 0 & 0 & dh_2 & 0 & -dh_4 & 0 \\ 0 & 0 & e'h_{e_3} & N_4 & e'h_{e_4} & 0 & 0 & dh_3 & 0 & -dh_5 \\ 0 & 0 & 0 & e'h_{e_4} & N_4^* & 0 & 0 & 0 & dh_4 & dh_5 \\ -r' & r' & 0 & 0 & 0 & s & 0 & 0 & 0 & 0 \\ -r' & 0 & r' & 0 & 0 & 0 & 2s & 0 & 0 & 0 \end{vmatrix} \qquad \textbf{(3.14)}$$

$$\mathbf{C}^*(G) = \begin{vmatrix} e'h_{e_1} & O_2 & e'h_{e_2} & 0 & 0 & 0\,0\,0\,0\,0 \\ 0 & e'h_{e_2} & O_3 & e'h_{e_3} & 0 & 0\,0\,0\,0\,0 \\ 0 & 0 & e'h_{e_3} & O_4 & e'h_{e_4} & 0\,0\,0\,0\,0 \\ 0 & 0 & 0 & e'h_{e_4} & O_4^* & 0\,0\,0\,0\,0 \\ 0 & 0 & 0 & 0 & 0 & 0\,0\,0\,0\,0 \\ 0 & 0 & 0 & 0 & 0 & 0\,0\,0\,0\,0 \end{vmatrix} \qquad \textbf{(3.15)}$$

where $N_i = 2a' - e'(h_{e_{i-1}} + h_{e_i})$, $N_i^* = 2a' - e'h_{e_i}$,

$O_i = -2(a'-b') - e'(h_{e_{i-1}} + h_{e_i})$, $O_i^* = -(a'-b') - e'h_{e_i}$, $a' = \frac{\Delta x}{2\Delta t^2}$, $b' = \frac{G\Delta x}{4\Delta t}$,

$d = \frac{G-\tau}{2}$, $e' = \frac{g}{2\Delta x}$, $q = \frac{\Delta x}{2}\left(1+\frac{\tau\Delta t}{2}\right)$, $r' = -\frac{g\Delta t}{2}$ and $s = \frac{\Delta x}{2}\left(1-\frac{\tau\Delta t}{2}\right)$.

3.3 Sensitivity to G

Given the system described above, the sensitivity to G can be found by taking the derivative with respect to G, as shown in (3.16).

$$\frac{\partial}{\partial G}[\mathbf{A}(G)\mathbf{c}^{k+1}] = \frac{\partial}{\partial G}[\mathbf{B}(G)\mathbf{c}^{k} + \mathbf{C}(G)\mathbf{c}^{k-1} + \mathbf{f}_{bc}^{k+1}] \tag{3.16}$$

By applying the product rule and noting that the boundary forcing is independent of G, the sensitivity is described by (3.17).

$$\frac{\partial \mathbf{A}(G)}{\partial G}\mathbf{c}^{k+1} + \mathbf{A}(G)\frac{\partial \mathbf{c}^{k+1}}{\partial G} = \frac{\partial \mathbf{B}(G)}{\partial G}\mathbf{c}^{k} + \mathbf{B}(G)\frac{\partial \mathbf{c}^{k}}{\partial G} + \frac{\partial \mathbf{C}(G)}{\partial G}\mathbf{c}^{k-1} + \mathbf{C}(G)\frac{\partial \mathbf{c}^{k-1}}{\partial G} \tag{3.17}$$

Defining the sensitivity to G at a given time, $\mathbf{w}^{k} = \partial \mathbf{c}^{k} / (\partial G)$, allows the system to be simplified and rearranged for solution of the new, unknown sensitivity vector based on the previous sensitivities and computed elevation and velocity fields according to (3.18).

$$\mathbf{A}(G)\mathbf{w}^{k+1} = -\frac{\partial \mathbf{A}(G)}{\partial G}\mathbf{c}^{k+1} + \frac{\partial \mathbf{B}(G)}{\partial G}\mathbf{c}^{k} + \frac{\partial \mathbf{C}(G)}{\partial G}\mathbf{c}^{k-1} + \mathbf{B}(G)\mathbf{w}^{k} + \mathbf{C}(G)\mathbf{w}^{k-1} \tag{3.18}$$

The three time-level scheme requires sets of initial values at times k and $k-1$. Results herein have cold start initial conditions, where the initial elevation and velocity fields are zero throughout the domain. The initial conditions do not depend on G; therefore, the initial conditions for the sensitivity are $\mathbf{w}^{-1} = \mathbf{w}^{0} = \begin{bmatrix} 0 & 0 & 0 & 0 & 0 & 0 & 0 & 0 & 0 & 0 \end{bmatrix}^{T}$.

3.3.1 Sensitivity of Implicit Scheme

The derivatives with respect to G of the matrices are necessary to compute the evolution of the sensitivity to G in time (cf. (3.18)). The derivatives of the matrices for the implicit scheme are as follows:

$$\frac{\partial \mathbf{A}(G)}{\partial G} = \frac{\partial \mathbf{C}(G)}{\partial G} = \begin{bmatrix} 0 & 0 & 0 & 0 & 0 & 0 & 0 & 0 & 0 & 0 \\ \frac{\Delta x}{12\Delta t} & \frac{\Delta x}{3\Delta t} & \frac{\Delta x}{12\Delta t} & 0 & 0 & 0 & 0 & 0 & 0 & 0 \\ 0 & \frac{\Delta x}{12\Delta t} & \frac{\Delta x}{3\Delta t} & \frac{\Delta x}{12\Delta t} & 0 & 0 & 0 & 0 & 0 & 0 \\ 0 & 0 & \frac{\Delta x}{12\Delta t} & \frac{\Delta x}{3\Delta t} & \frac{\Delta x}{12\Delta t} & 0 & 0 & 0 & 0 & 0 \\ 0 & 0 & 0 & \frac{\Delta x}{12\Delta t} & \frac{\Delta x}{6\Delta t} & 0 & 0 & 0 & 0 & 0 \\ 0 & 0 & 0 & 0 & 0 & 0 & 0 & 0 & 0 & 0 \\ 0 & 0 & 0 & 0 & 0 & 0 & 0 & 0 & 0 & 0 \\ 0 & 0 & 0 & 0 & 0 & 0 & 0 & 0 & 0 & 0 \\ 0 & 0 & 0 & 0 & 0 & 0 & 0 & 0 & 0 & 0 \\ 0 & 0 & 0 & 0 & 0 & 0 & 0 & 0 & 0 & 0 \end{bmatrix} \tag{3.19}$$

$$\frac{\partial \mathbf{B}(G)}{\partial G} = \begin{bmatrix} 0 & 0 & 0 & 0 & 0 & 0 & 0 & 0 & 0 & 0 \\ 0 & 0 & 0 & 0 & 0 & \frac{h_1}{2} & 0 & -\frac{h_3}{2} & 0 & 0 \\ 0 & 0 & 0 & 0 & 0 & 0 & \frac{h_2}{2} & 0 & -\frac{h_4}{2} & 0 \\ 0 & 0 & 0 & 0 & 0 & 0 & 0 & \frac{h_3}{2} & 0 & -\frac{h_5}{2} \\ 0 & 0 & 0 & 0 & 0 & 0 & 0 & 0 & \frac{h_4}{2} & \frac{h_5}{2} \\ 0 & 0 & 0 & 0 & 0 & 0 & 0 & 0 & 0 & 0 \\ 0 & 0 & 0 & 0 & 0 & 0 & 0 & 0 & 0 & 0 \\ 0 & 0 & 0 & 0 & 0 & 0 & 0 & 0 & 0 & 0 \\ 0 & 0 & 0 & 0 & 0 & 0 & 0 & 0 & 0 & 0 \\ 0 & 0 & 0 & 0 & 0 & 0 & 0 & 0 & 0 & 0 \end{bmatrix} \tag{3.20}$$

3.3.2 Sensitivity of Explicit Scheme

The derivatives of the matrices, with respect to G, for the explicit scheme are shown below:

$$\frac{\partial \mathbf{A}^*(G)}{\partial G} = \frac{\partial \mathbf{C}^*(G)}{\partial G} = \begin{bmatrix} 0 & 0 & 0 & 0 & 0 & 0 & 0 & 0 & 0 & 0 \\ 0 & \frac{\Delta x}{2\Delta t} & 0 & 0 & 0 & 0 & 0 & 0 & 0 & 0 \\ 0 & 0 & \frac{\Delta x}{2\Delta t} & 0 & 0 & 0 & 0 & 0 & 0 & 0 \\ 0 & 0 & 0 & \frac{\Delta x}{2\Delta t} & 0 & 0 & 0 & 0 & 0 & 0 \\ 0 & 0 & 0 & 0 & \frac{\Delta x}{4\Delta t} & 0 & 0 & 0 & 0 & 0 \\ 0 & 0 & 0 & 0 & 0 & 0 & 0 & 0 & 0 & 0 \\ 0 & 0 & 0 & 0 & 0 & 0 & 0 & 0 & 0 & 0 \\ 0 & 0 & 0 & 0 & 0 & 0 & 0 & 0 & 0 & 0 \\ 0 & 0 & 0 & 0 & 0 & 0 & 0 & 0 & 0 & 0 \\ 0 & 0 & 0 & 0 & 0 & 0 & 0 & 0 & 0 & 0 \end{bmatrix} \tag{3.21}$$

$$\frac{\partial \mathbf{B}^*(G)}{\partial G} = \begin{bmatrix} 0 & 0 & 0 & 0 & 0 & 0 & 0 & 0 & 0 & 0 \\ 0 & 0 & 0 & 0 & 0 & \frac{h_1}{2} & 0 & -\frac{h_3}{2} & 0 & 0 \\ 0 & 0 & 0 & 0 & 0 & 0 & \frac{h_2}{2} & 0 & -\frac{h_4}{2} & 0 \\ 0 & 0 & 0 & 0 & 0 & 0 & 0 & \frac{h_3}{2} & 0 & -\frac{h_5}{2} \\ 0 & 0 & 0 & 0 & 0 & 0 & 0 & 0 & \frac{h_4}{2} & \frac{h_5}{2} \\ 0 & 0 & 0 & 0 & 0 & 0 & 0 & 0 & 0 & 0 \\ 0 & 0 & 0 & 0 & 0 & 0 & 0 & 0 & 0 & 0 \\ 0 & 0 & 0 & 0 & 0 & 0 & 0 & 0 & 0 & 0 \\ 0 & 0 & 0 & 0 & 0 & 0 & 0 & 0 & 0 & 0 \\ 0 & 0 & 0 & 0 & 0 & 0 & 0 & 0 & 0 & 0 \end{bmatrix} \tag{3.22}$$

3.3.3 Sensitivity Results for Tidal Problem on the Linear Sloping Domain

The parameters for the first test case are outlined in Table 3.1, and the bathymetry and node locations for the linear sloping domain are shown in Figure 3.1. Simulations were run for 10.0 days with results (elevations, velocities and sensitivities) recorded every 5.0

minutes (60 time steps). The ramp function for the open boundary elevation is a hyperbolic tangent function. At the end of the ramp, its value is 0.964. Thus, there is a small disruption in the results at the end of the ramp because of the small jump in the forcing due to the ramp specification. This artificial disturbance quickly dissipates. A larger coefficient can be used in the hyperbolic tangent function, but that increases the rate of change of the forcing at early times, which increases potential for instability at the outset of the simulation.

Table 3.1 Parameters for linear sloping bottom test case.

Parameter	Value
Bathymetry value at open boundary	20.0 m
Bottom slope	1.25E-04 m/m
Domain length	40.0 km
Δx	2.0 km
τ	0.001 s^{-1}
Forcing amplitude	1.0 m
Forcing period	44714.8 s
Time step	5.0 s
Ramp duration	1.0 days

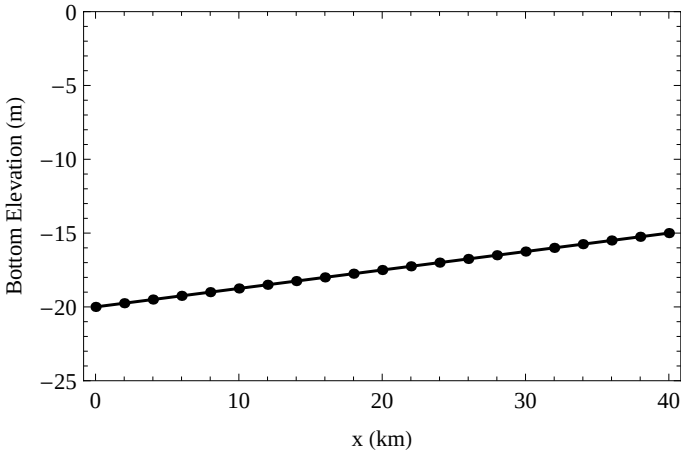

Figure 3.1 Bathymetry and node locations for the linear sloping domain.

For both the implicit and explicit schemes, elevation sensitivity results for the 11th node in the domain over the last two days of the simulations with $G = 0.001\ s^{-1}$ are shown in Figure 3.2. The units for elevation and velocity sensitivities to constant G are ms (meter-seconds) and m, respectively. The results at the 11th node are consistent with the results for the other nodes in the domain, with the exception of the open boundary node,

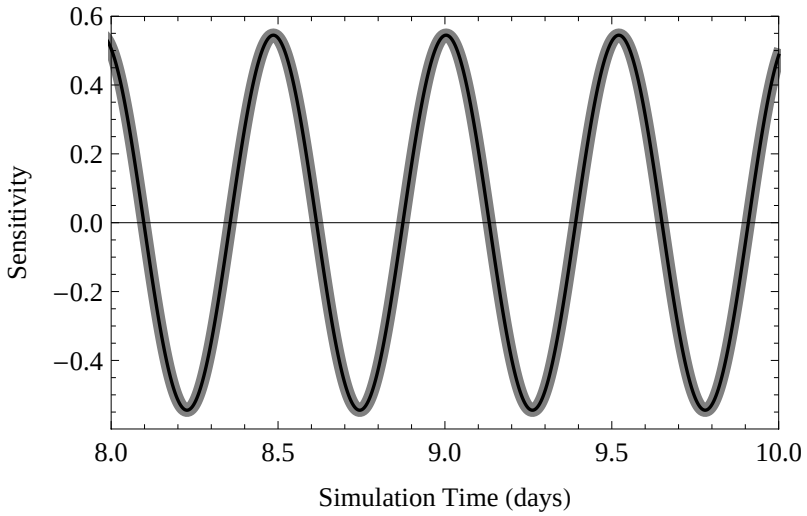

Figure 3.2 Elevation sensitivity results for the last two days of the simulation with $G = 0.001$ s^{-1} for the 11th node in the linear sloping domain. The results for the implicit scheme are shown in black, while the explicit results are shown in gray.

which is inherently insensitive to G because the specified elevation at the boundary is independent of the numerical parameter and simulation results.

Plots like Figure 3.2 are prevalent in this chapter so detailed discussion is warranted. This plot shows the temporal evolution of the FSM elevation sensitivity to G for the 11th node in the domain. There are two lines; the black line shows the evolution of the sensitivity during the simulation using the implicit scheme, and the gray line shows the evolution of the sensitivity during the simulation using the explicit scheme. The gray line has a larger thickness so results are not obscured when the sensitivities are equivalent. Nine days into the simulation with $G = 0.001\ \text{s}^{-1}$, the elevation sensitivity to G is at a maximum near 0.53 ms. This means that if there is a small increase to G, the results from the new simulation will have a higher elevation value at node 11 than the results with $G = 0.001\ \text{s}^{-1}$.

In contrast to the sensitivity results for the simulations with $G = 0.001\ \text{s}^{-1}$, the results for simulations with $G = 0.01\ \text{s}^{-1}$ show wide variations for elevation sensitivities

for different locations in the domain. For the majority of the domain, the peak magnitude of the elevation sensitivity to G is about 0.006-0.008 ms. This is depicted in Figure 3.3, a graph of the elevation sensitivities for the last two days of the run at the 11th node in the domain. However, nodes 2-7 show a large variation in sensitivity from one node to the next.

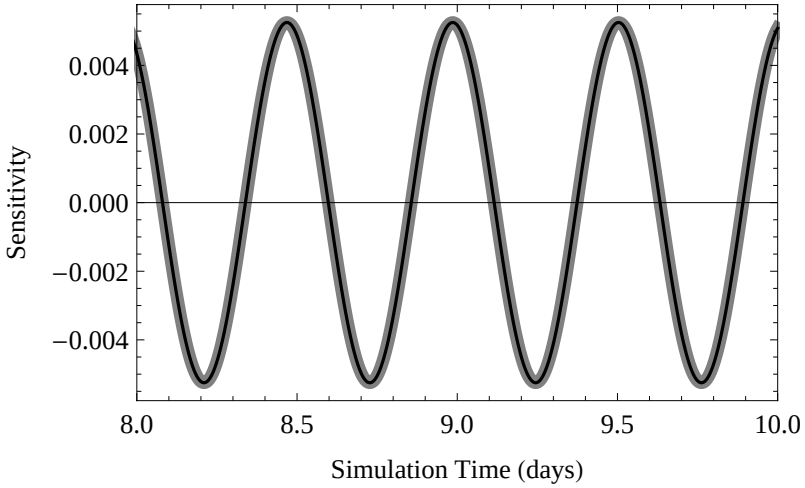

Figure 3.3 Elevation sensitivity results for the last two days of the simulation with $G = 0.01$ s^{-1} for the 11th node in the linear sloping domain. The results for the implicit scheme are shown in black, while the explicit results are shown in gray.

The variation is especially apparent for the 3rd and 5th nodes in the domain, which have sensitivities that are out-of-phase with the sensitivities in the rest of the domain. Out-of-phase means that the sensitivity for a node is negative at a time when it is positive for other nodes and vice versa. Additionally, the peak amplitude of the sensitivity is variable; the maximum sensitivity for node 2 is approximately 0.018 ms while the maximum sensitivity at node 5 is only about 0.0014 ms, as seen in Figure 3.4 and Figure 3.5, respectively. The general trends in the sensitivities continue for the case where $G = 0.1$ s^{-1}. For these simulations, the magnitude of the elevation sensitivity is about 0.001 ms, which is about 50 times less than with a G value an order of magnitude lower. Additionally, while the amplitude is similar for all nodes, the sign of the sensitivity at a given time alternates from node

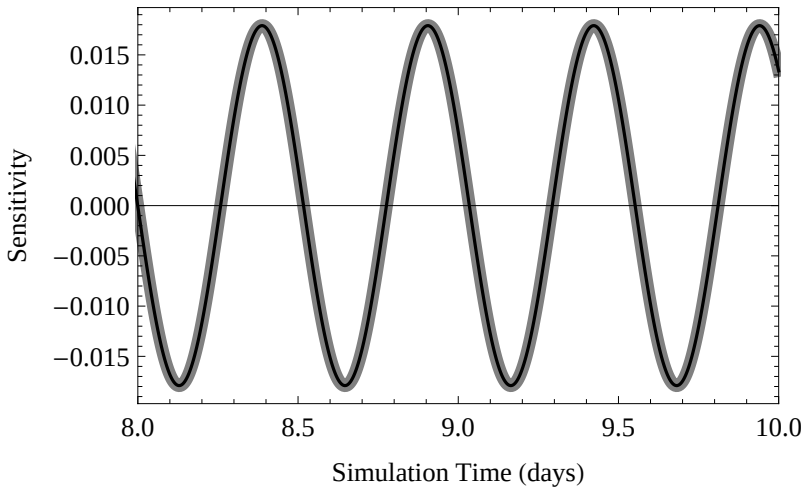

Figure 3.4 Elevation sensitivity results for the last two days of the simulation with $G = 0.01$ s^{-1} for the 2nd node in the linear sloping domain. The results for the implicit scheme are shown in black, while the explicit results are shown in gray.

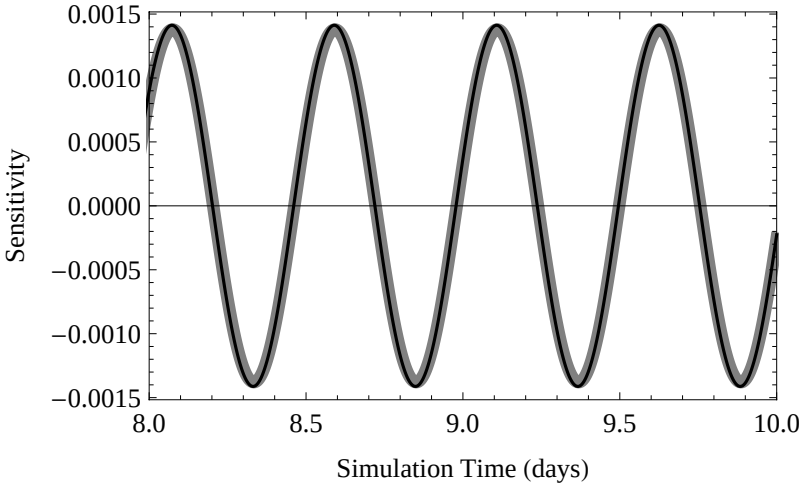

Figure 3.5 Elevation sensitivity results for the last two days of the simulation with $G = 0.01$ s^{-1} for the 5th node in the linear sloping domain. The results for the implicit scheme are shown in black, while the explicit results are shown in gray.

to node throughout the entire domain when $G = 0.1\ \text{s}^{-1}$, rather than just near the open boundary with $G = 0.01\ \text{s}^{-1}$.

The impact of G on sensitivities at a given node can be shown by graphing the sensitivities from multiple simulations on the same plot. The elevation sensitivity results at node 2 for five simulations with different G values are shown in Figure 3.6. The second-

lightest color shows the results for the simulation with $G = 0.01\ s^{-1}$. The black line in Figure 3.4 shows the same values as the second-lightest color in Figure 3.6. The maximum sensitivity values near 0.018 ms occur at approximately 8.4, 8.9, 9.4 and 9.9 days into the simulation. The log scale was necessary for the sensitivities because the maximum sensitivities vary over orders of magnitude for different values of G. Generally, the gaps in Figure 3.6 correspond to times when the sensitivity is negative, which is problematic with a log scale. The log scale was used for the sensitivities because the maximum sensitivities vary over orders of magnitude for different values of G.

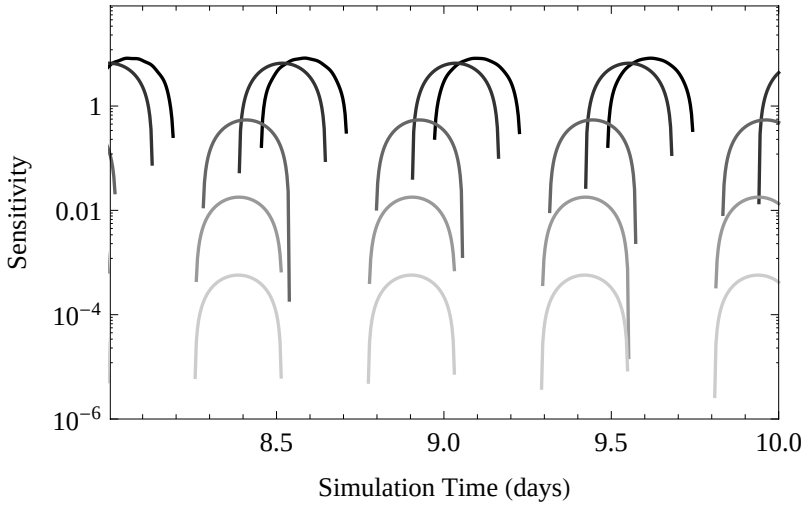

Figure 3.6 Elevation sensitivity to G at node 2 for implicit simulations on the linear sloping domain. The darkness of the lines decreases for increasing G for the following set of constant G values: {0.00001, 0.0001, 0.001, 0.01, 0.1} s^{-1}.

The impact of G on elevation sensitivities at nodes 2-7 is shown in Figure 3.7. Increasing G from 0.00001 to 0.001 s^{-1} results in the sensitivity decreasing in magnitude, but also shifting to the left. Thus, the peak elevation sensitivity to a change in G occurs earlier in time for a higher G value. These trends continue as G is increased further, although the shift becomes less pronounced between consecutive values.

The change of signs at high G values can be seen by comparing the plot for node 2

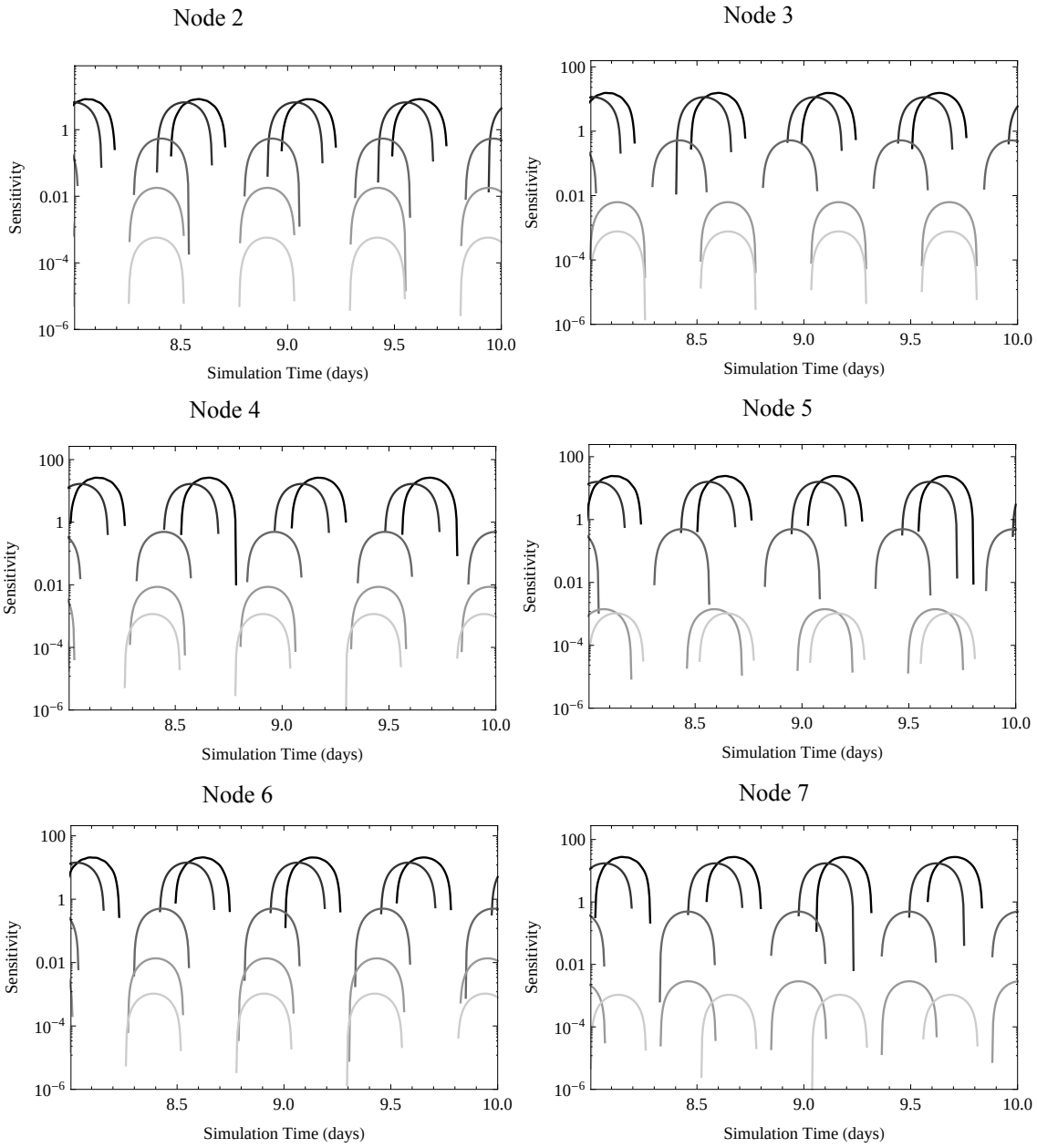

Figure 3.7 Elevation sensitivity to G for implicit runs on the linear sloping domain. The darkness decreases with increasing G for the following set of values: {0.00001, 0.0001, 0.001, 0.01, 0.1} s^{-1}.

to the one for node 3. The results are similar for the three lowest G values. In the plot for node 2, the sensitivities for the two highest G values plot almost directly beneath the values for $G = 0.001\ s^{-1}$. However, the positive sensitivities for the two highest G values at node 3 appear in the void for $G = 0.001\ s^{-1}$ (when the sensitivities to $G = 0.001\ s^{-1}$ are negative). The plots for nodes 4 and 6 are similar to the plot for node 2, while the plot for

node 5 shows the same trend as the one for node 3. The plot for node 7 still has the sensitivities for the $G = 0.1\ \text{s}^{-1}$ simulation primarily in the void for the results with $G = 0.001\ \text{s}^{-1}$. Conversely, the sensitivities for $G = 0.01\ \text{s}^{-1}$ are back in line with the results for the lower G values, signifying the end of the node-to-node sign oscillations for that G value.

The GWCE was introduced for CG finite element modeling to control spurious $2\Delta x$ oscillations present in solutions of the shallow water equations using the primitive continuity equation. Increasing G shifts the GWCE toward the primitive continuity equation. The elevation sensitivity results show $2\Delta x$ oscillations in the sensitivity to G for values of the numerical parameter of $0.01\ \text{s}^{-1}$ and larger, suggesting those values result in the GWCE becoming "too primitive." This idea will be explored in more detail in Section 3.7 where the FSM results are compared to dispersion analysis results.

The decrease in the magnitude of the sensitivity to G as G increases also makes sense. When G is zero, the GWCE is a close to a pure wave equation. Introduction of non-zero G values results in the primitive continuity portion of the GWCE contributing. Eventually, when G gets to values resulting in the GWCE becoming "too primitive," the system reduces to (3.23) because the primitive continuity equation term is dominant.

$$GL \approx 0 \tag{3.23}$$

Thus, further increases in G will have only minimal impacts on the solution, as demonstrated by the FSM, which shows the magnitude of the sensitivity approaching zero for larger G values. However, there is no absolute upper limit on G. The primitive continuity equation is recovered when $G = \infty$. Thus, even though the sensitivity to G is low for the high G values under consideration, use of the primitive equations may equate to a large

incremental sum of $2\Delta x$ oscillations.

The velocity sensitivity to G follows the same general trends as the elevation sensitivity, although the velocity sensitivity is non-zero at node 1 and zero at the last node because the velocity is specified at the right-side domain boundary. Specifically, the sensitivities are similar between nodes, for the same G value, as long as G is less than 0.01 s^{-1}. For values above that threshold, the sensitivities begin to have opposite signs when successive nodes are compared, with the portion of the domain adversely affected growing with increasing G. Again, the effects are seen initially near the specified elevation boundary (lower node numbers). Additionally, the magnitude of the velocity sensitivity decreases as the G value is increased, as shown in Figure 3.8, which is a log plot of the velocity sensitivities at nodes 2-7 for five simulations with different G values. As with the elevation sensitivities, increasing G in the low range causes the peak velocity sensitivities to occur earlier.

The velocity sensitivities calculated for the 4th and 5th nodes, for both implicit and explicit schemes, with $G = 0.01$ s^{-1} are shown in Figure 3.9 and Figure 3.10, respectively. These are the velocity counterparts to the elevation sensitivity results (Figure 3.4 and Figure 3.5) shown previously, except the plot for the 4th node has been used for the velocities whereas the plot for the 2nd node was used for elevation sensitivity results. This change in the nodes used to generate figures was to highlight the difference in sign between results for consecutive nodes. For the velocity results, the results for node 2 are similar to the results for node 5. As was the case with the elevation sensitivities, the choice of scheme (implicit vs. explicit) has minimal effect on the computed velocity sensitivity to G.

The elevation and velocity results and sensitivities for 11 nodes in the linear sloping

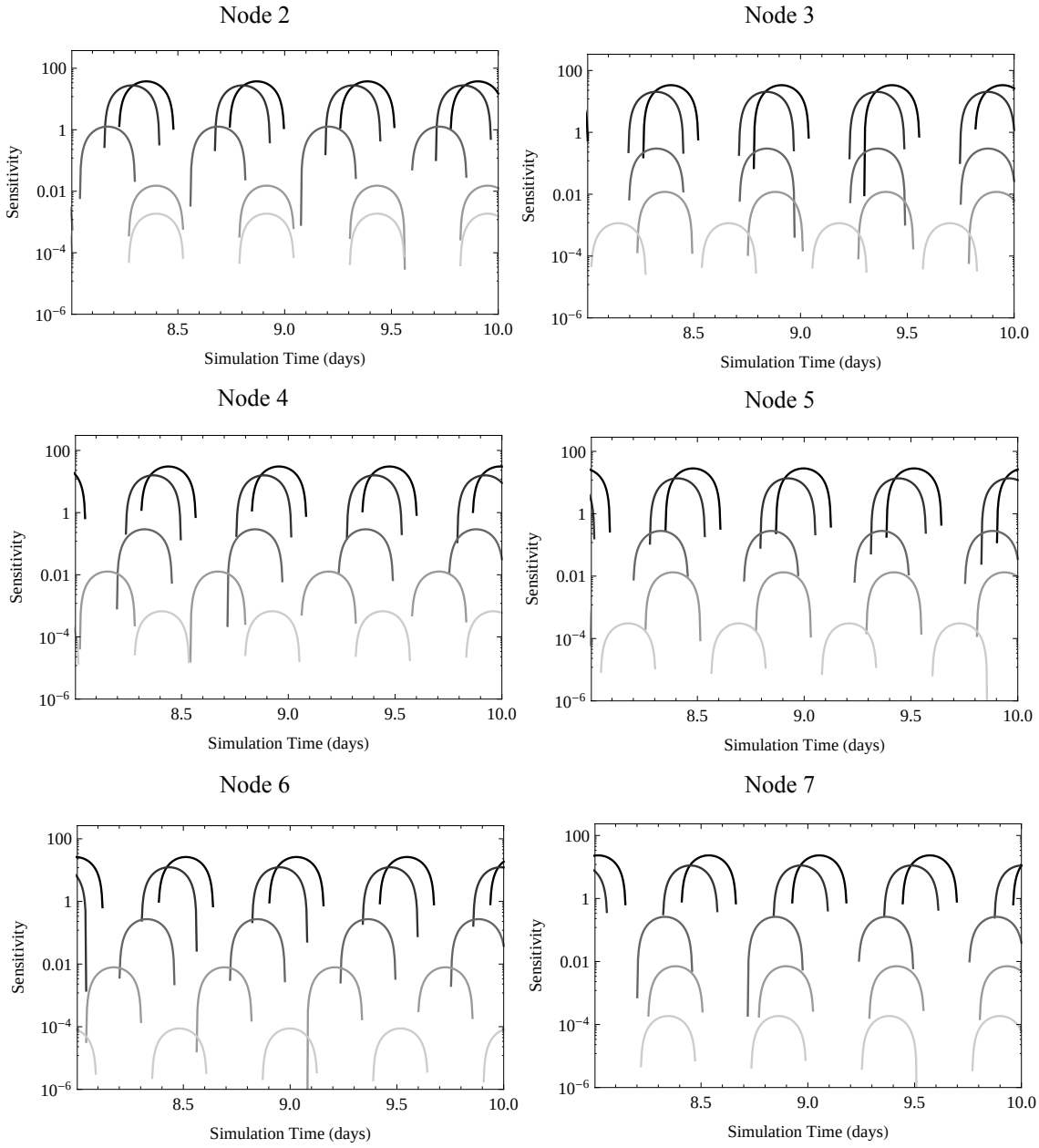

Figure 3.8 Velocity sensitivity to G for implicit runs on the linear sloping domain. The darkness decreases with increasing G for the following set of values: {0.00001, 0.0001, 0.001, 0.01, 0.1} s^{-1}.

domain are shown in Appendix C.1.1 (elevation) and Appendix C.1.2 (velocity) using $G = 0.001\ s^{-1}$. By plotting the elevation and elevation sensitivity results on the same plot, it is readily apparent that the maximum elevation sensitivity to G occurs later in time than the maximum elevation values during a tidal cycle. The peak elevation sensitivity occurs at approximately the time when the elevation is at the equilibrium position for the first time

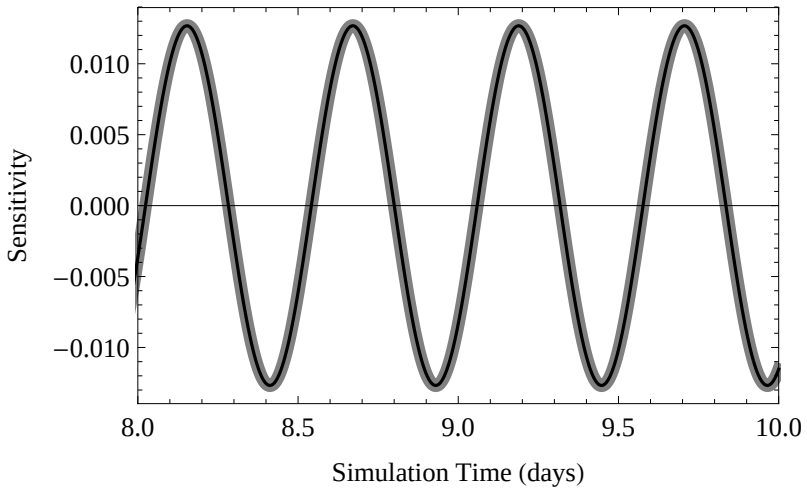

Figure 3.9 Velocity sensitivity results for the last two days of the simulation with $G = 0.01\ s^{-1}$ for the 4th node in the linear sloping domain. The results for the implicit scheme are shown in black, while the explicit results are shown in gray.

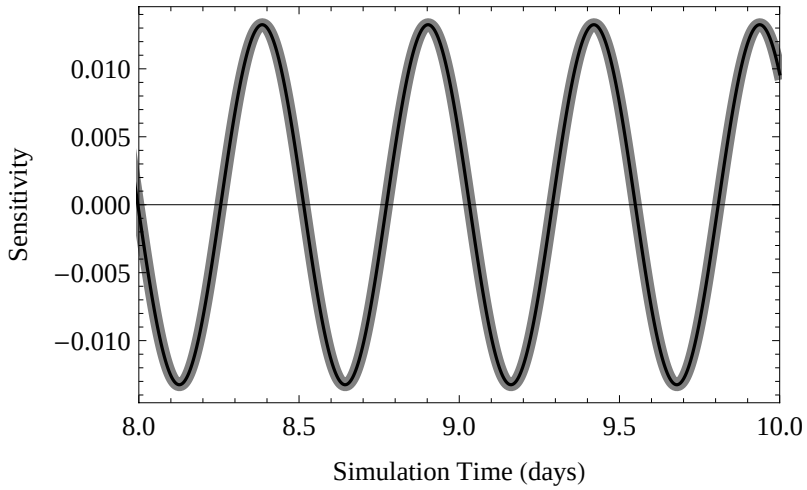

Figure 3.10 Velocity sensitivity results for the last two days of the simulation with $G = 0.01\ s^{-1}$ for the 5th node in the linear sloping domain. The results for the implicit scheme are shown in black, while the explicit results are shown in gray.

following the occurrence of the maximum. The minimum elevation sensitivity occurs at approximately the same time as the water surface elevation returns to mean sea level in the transition from the minimum WSE value back to a maximum. These results are consistent throughout the domain.

In each of the plots with the elevations and elevation sensitivities, there are four sets of results. The four sets correspond to four different grid discretizations. The base linear

sloping domain grid has 21 nodes. The other grids have 11, 41 and 81 nodes. The results show the elevation time series are indistinguishable from one simulation to the next. However, the elevation sensitivity to G is highly dependent on the grid spacing. For the grid with 11 nodes, the peak elevation sensitivity to G varies from about 2 ms near the ocean boundary to approximately 3 ms at the land boundary. For the base grid, containing 21 nodes, the range of peak elevation sensitivities to G is about 0.5-0.7 ms. The two finer grids have ranges of 0.15-0.2 and 0.03-0.04 ms, respectively.

The velocity and velocity sensitivity results show trends that are similar to those for elevations. That is, the maximum velocity sensitivities occur when the velocity is at zero in the transition from a peak positive velocity to a peak negative velocity. Likewise, the minimum velocity sensitivities occur when the velocity is at zero in the transition from a peak negative velocity to a peak positive velocity. However, the occurrence of the peak elevation and peak velocity do not coincide. As such, the timing of the peak elevation sensitivity is offset from the peak velocity sensitivity.

The exception to the general trend for the velocity results is near the boundary. At the ocean boundary node, the timing of the peak velocity sensitivity is much closer to the occurrence of the peak velocity value than for locations away from the ocean boundary. Additionally, the magnitude of the sensitivity at the specified elevation boundary condition location is significantly larger than for interior locations. And, as stated previously, the velocity sensitivity is zero at the land boundary due to the no-flow boundary condition.

The relationship between peak velocity sensitivity magnitude and grid resolution is consistent with results for elevation sensitivities. Decreasing the element size, by increasing the number of elements, reduces the velocity sensitivity to G. Using the 11 node

grid, the peak velocity sensitivity at the mid-point of the domain is about 0.85 m^2s. The peak sensitivities for the 21, 41 and 81 node domains at the same spatial location are 0.21, 0.053 and 0.013 m^2s, respectively.

As mentioned briefly in the introduction to this chapter, the FSM can be applied to analyze initial conditions. This involves computing the sensitivity of the elevation and velocity fields to the initial conditions (the elevation and velocity fields specified at the beginning of the simulation). For the system under analysis, the sensitivity to the initial condition goes to zero as time increases. Thus, use of the cold start initial conditions does not adversely impact the analyses herein. Specifically, for the linear sloping domain case presented here, the magnitude of the maximum sensitivity of one element of the solution to a change in the initial condition is 0.112 after the first time step. After 12 hours, the magnitude of the maximum sensitivity is 1.52 E-06 and the magnitude reduces to 6.99 E-12 at the end of the first day. The sensitivities to the initial condition continue to decrease as the simulation time increases.

3.3.4 Sensitivity Results for Tidal Problem Over a Seamount

The set-up parameters for the second test case are similar to those for the first. The major difference is the bathymetry, which is shown in Figure 3.11. Additionally, this domain consists of 31 nodes, whereas the linear sloping domain contains only 21 nodes. Simulations were performed for a duration of 5.0 days with a one-day ramp.

For the seamount domain, the explicit code is unstable at $\Delta t = 5.0$ s with $G = 0.001\ s^{-1}$, so results comparing implicit and explicit sensitivities are shown for the simulation with $G = 0.01\ s^{-1}$. The elevation sensitivities are shown for the last day for

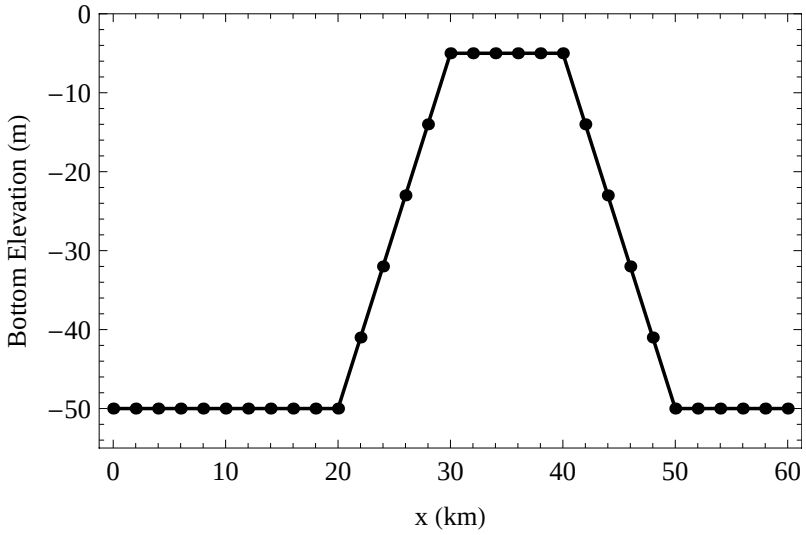

Figure 3.11 Bathymetry and node locations for the seamount domain.

three different nodes: node 6 (Figure 3.12) is in the deep flat portion of the domain, node 18 (Figure 3.13) resides on the plateau of the seamount, and node 26 (Figure 3.14) is at the transition between the linear increase in bathymetry and the flat area in the back bay. As can be seen, there is no discernible difference between the implicit and explicit results.

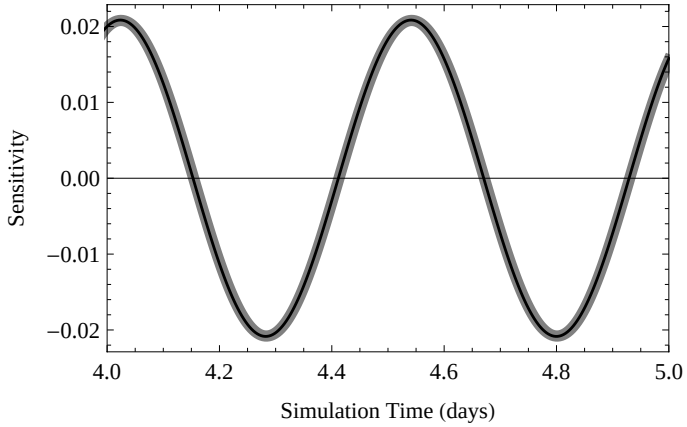

Figure 3.12 Elevation sensitivity results for the last day of the simulation with $G = 0.01\ s^{-1}$ for the 6th node in the seamount domain for the implicit (black) and explicit (gray) codes.

The implicit code is stable for lower G values (using the same time step), which allows analysis of the sensitivities over a wider range of G values. Log plots of the elevation sensitivities for nodes 2-5 over the last day of simulation with different G values are

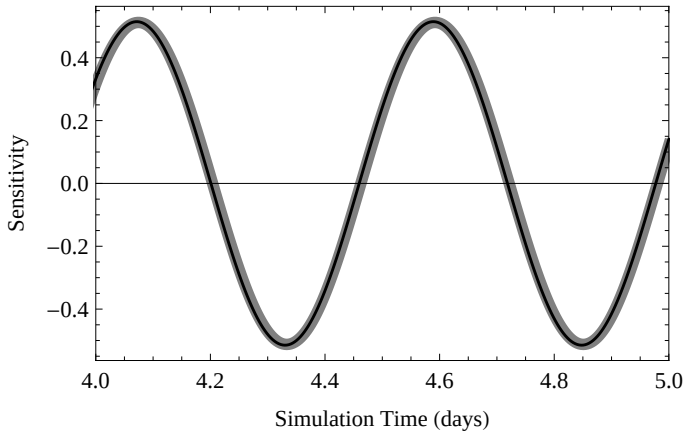

Figure 3.13 Elevation sensitivity results for the last day of the simulation with $G = 0.01$ s^{-1} for the 18th node in the seamount domain for the implicit (black) and explicit (gray) codes.

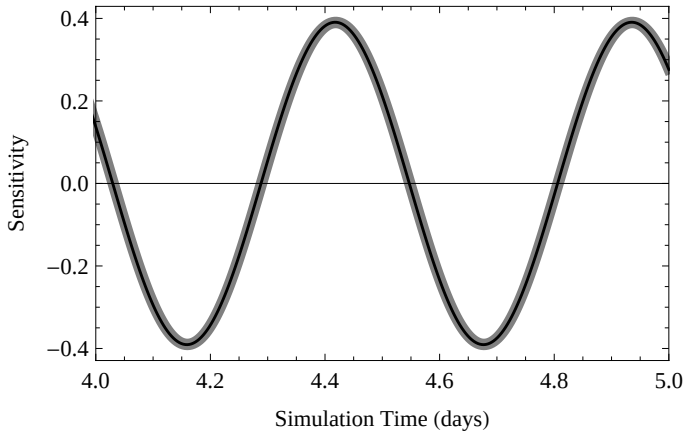

Figure 3.14 Elevation sensitivity results for the last day of the simulation with $G = 0.01$ s^{-1} for the 26th node in the seamount domain for the implicit (black) and explicit (gray) codes.

shown in Figure 3.15. The general trends present for simulations on the linear sloping domain also apply for the seamount domain. Specifically, the magnitude of the sensitivity decreases with increasing G, and the peak sensitivities occur earlier in time for higher G values (although the timing trend is not seen for node 2). The node-to-node oscillation in the sensitivities for the highest G value used in this set of simulations, $0.1\ \text{s}^{-1}$, is readily apparent. The sensitivities for the even nodes (2 and 4) are different from the ones for the odd nodes (3 and 5).

Close inspection of the results shows a general trend of increasing peak elevation

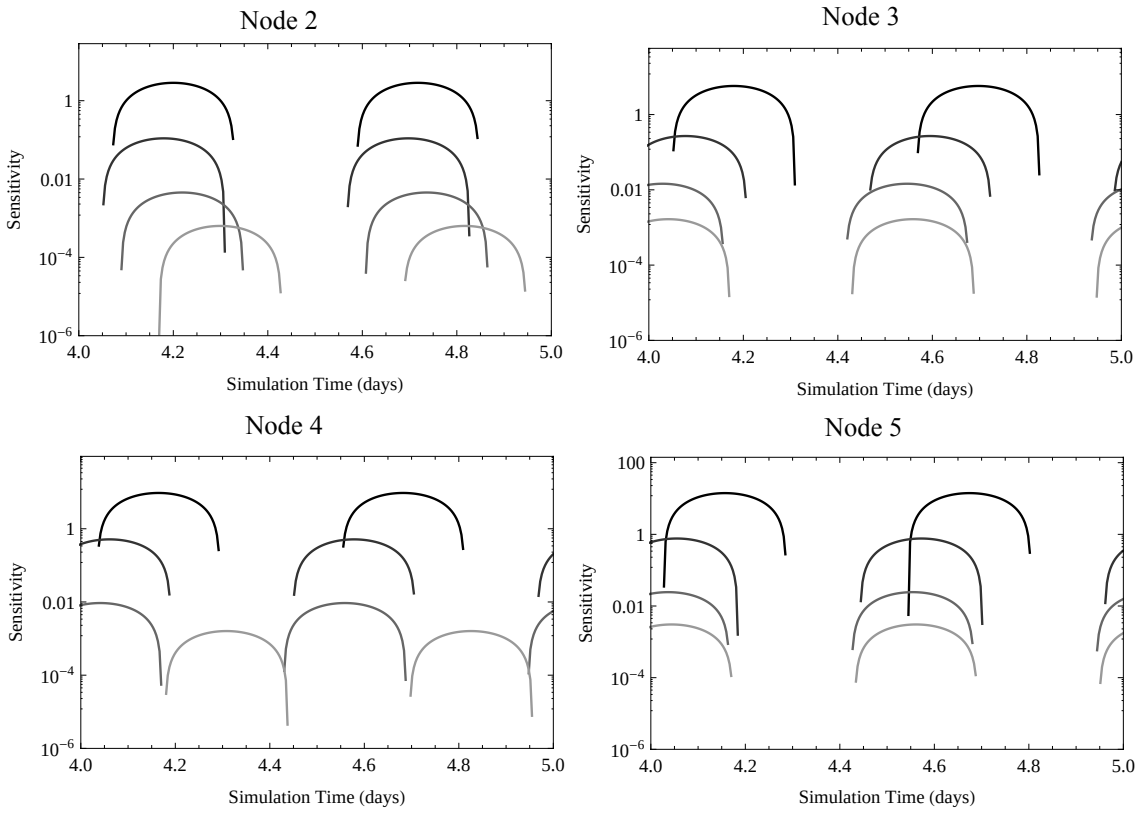

Figure 3.15 Elevation sensitivity to *G* for implicit runs on the seamount domain. The darkness decreases with increasing *G* for the following set of values: {0.0001, 0.001, 0.01, 0.1} s^{-1}.

sensitivity to G as you move away from the specified elevation boundary. The peak elevation sensitivity for each node in the domain for simulations with a range of G values is shown in Figure 3.16. The second-lightest set of dots, from results with $G = 0.01\ s^{-1}$, shows an oscillation in the magnitude of the peak sensitivity for a substantial portion of the domain. This indicates the G value is too high, resulting in the GWCE becoming "too primitive," even though the sign of the sensitivity has not been affected, as it has for $G = 0.1\ s^{-1}$. The plot of the peak velocity sensitivity (not shown) contains a smooth set of points for the back bay with $G = 0.1\ s^{-1}$, while results with $G = 0.01\ s^{-1}$ show oscillations in the magnitude of the peak. However, a smooth set of points is not a sufficient condition to conclude the G value is below the "too primitive" threshold. Inspection of the sign of the velocity sensitivities for the higher G value reveals the node-to-node switching

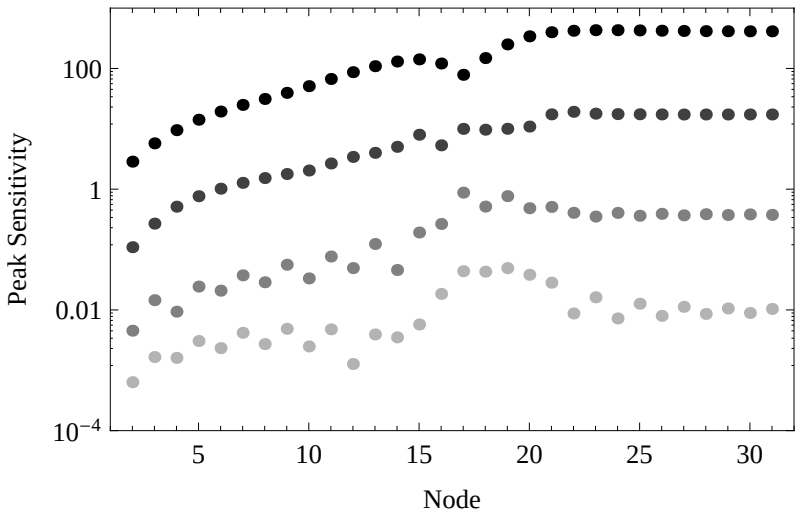

Figure 3.16 Peak elevation sensitivity to G for implicit runs on the seamount domain. The darkness decreases with increasing G for the following set of values: {0.0001, 0.001, 0.01, 0.1} s^{-1}.

of signs on the sensitivities ($2\Delta x$ oscillations) for the higher G value that does not have peak magnitude oscillations.

The elevation and velocity results with the explicit code using $G = 0.001\ s^{-1}$ for the seamount domain are shown in Appendix C.2.1 (elevation) and Appendix C.2.2 (velocity). For these simulations, the time step was reduced to 1 second. The smaller time step (previous simulations on the seamount domain were with a 5 second time step) allowed simulations to complete with lower G values. The elevation and velocity results with the explicit code using $G = 0.01\ s^{-1}$ for the seamount domain are shown in Appendix C.3.1 (elevation) and Appendix C.3.2 (velocity). Unlike the detailed results in Appendix C.1 (for the linear sloping domain) and Appendix C.2 (seamount domain) that were generated with a G value below the threshold where oscillations appear in the solution and sensitivities, $G = 0.01\ s^{-1}$ is in the "too primitive" range for the seamount domain, as stated previously. This scenario is worth analyzing, despite the relatively high G value, because it is a realistic problem. Increased G values are necessary with the explicit code for stability purposes. Unfortunately, spurious oscillations may be introduced.

However, before analyzing the results for the higher G value, comments will be made about the results for the lower G value on the seamount domain with the explicit code. With $G = 0.001\ s^{-1}$, the elevation and elevation sensitivity results near the ocean boundary are similar to the results for the linear sloping domain. The maximum elevation sensitivity coincides with the equilibrium water surface elevation during the transition from a maximum elevation to a minimum. The minimum sensitivity also occurs when the water surface elevation is at mean sea level; the minimum sensitivity occurs when the change in elevation with time is positive. The elevation sensitivity is zero when the elevation is at a maximum or minimum. Additionally, while the elevation results are visually indistinguishable for 16, 31 and 61 node grids, the elevation sensitivity decreases significantly with increased resolution (decreased element size).

Over the rise, the relationship between the timing of the elevations and elevation sensitivities changes. The results for the rise (labeled "Node 13," "Node 14" and "Node 16") show the maximum sensitivity coincides with the maximum elevation values. Likewise, the minimum values coincide and so do the zero values. For "Node 18," on the top of the seamount, the relationship between the elevation results and elevation sensitivities are similar to the relationship in the deep portion of the domain near the boundary. Then, for nodes on the landward side of the seamount, the maximum sensitivities occur when elevations are at minimum values and the minimum sensitivities occur when the elevations are at maximum values. This is opposite the behavior over the rise. Throughout the domain, the elevation sensitivity to G decreases with increasing resolution.

The trends for the relationship between velocity and velocity sensitivity are less prevalent than those for elevations. In the portion of the domain oceanward of the

seamount, the maximum sensitivity occurs, generally, when the velocity is zero during the transition from a minimum velocity to a maximum velocity. Then, throughout much of the rest of the domain, the velocities and velocity sensitivities are 180 degrees out-of-phase. The maximum velocity sensitivities coincide with minimum velocities and the minimum sensitivities coincide with instances of maximum velocity.

This situation, when elevations and elevation sensitivities (or velocities and velocity sensitivities) are 180 degrees out-of-phase, is interesting. If the sensitivity of a quantity to G is a minimum when the quantity is a maximum and vice-versa, that means that increasing G will result in decreased amplitude maxima and minima of the solution. For the case of out-of-phase velocities and velocity sensitivities, increasing G will reduce the range of velocities encountered in the domain. Conversely, decreasing G will increase the range of velocities. When the quantity and the quantity sensitivity are 90 degrees out-of-phase, the zero sensitivity values align with the maximum quantity values. In this case, increasing G will not have an impact on range of the quantity through the simulation. However, changing G will affect the timing of the zero quantity values.

The results for the seamount domain with the higher G value are more difficult to summarize generally because the results are not consistent for nodes in the same area of the domain. Additionally, there is a lack of consistency for spatial locations from one grid resolution to the next. Nevertheless, for the "non-primitive" G values, the timing of the sensitivity results were similar between resolutions with the magnitude of the sensitivity decreasing with increasing resolution. However, using $G = 0.01\ \mathrm{s}^{-1}$ on the seamount domain, the results for "Node 13" show the elevation sensitivity to G is greater in magnitude for the 31 node grid than for the 16 node grid. Additionally, the elevation sensitivities

using those two grids have opposite signs for that spatial location. At the transition between the rise and the seamount, the elevation sensitivities for the 16 and 31 node grids are comparable in timing and magnitude. Near the middle of the seamount, the elevation sensitivities for those two grids are 180 degrees out-of-phase.

The velocity sensitivities also show a high level of variation between spatial locations and resolutions. The velocity sensitivities for the transition from the flat portion near the boundary to the rise are similar in timing and magnitude for all three grid resolutions. For the location of node 18 in the 31 node grid, the peak velocity sensitivity is actually lower for the coarsest grid than for the finest grid, with the largest peak (for the three grids) occurring with the 31 node grid.

One implication of the seamount domain sensitivity results is that analysis of sensitivities, and thus the implications of changes in the elevation and velocity fields resulting from changes in G, is complicated by G values that transition into the "too primitive" range. Additionally, though, the results for the simulations with $G = 0.01\ \mathrm{s}^{-1}$ show that elevation and velocity results can depend on G even for grids with significant resolution.

The results with $G = 0.001\ \mathrm{s}^{-1}$, on both the linear sloping domain and the seamount domain, showed the sensitivity to G tending towards zero with increasing grid resolution. These results suggested the possibility of generating solutions that are independent of G if sufficient resolution is achieved. Obviously, the definition of sufficient in "sufficient resolution" would depend on the level of *G*-independence desired for a given application. The seamount domain results with $G = 0.01\ \mathrm{s}^{-1}$ suggest that results for certain portions of the domain will remain dependent on G specification regardless of the level of resolution achieved.

3.4 Comparison of FSM and Numerical Analog Sensitivities

The FSM sensitivity results presented previously predict the changes in the solution (elevations or velocities) that result from a change in the numerical parameter, G. In order to validate the procedure, the numerical sensitivity can be calculated using finite differences. In particular, by comparing the results from two simulations with slightly different G values, an estimate of the sensitivity to G can be calculated using the difference between the two solutions and the difference in the G values, as shown in (3.24).

$$\frac{\partial \zeta}{\partial G} \approx \frac{\Delta \zeta}{\Delta G} = \frac{(\zeta_j^k)_2 - (\zeta_j^k)_1}{G_2 - G_1} \tag{3.24}$$

Figure 3.17 compares the sensitivity using the FSM with that using the numerical analog for the 11th node in the linear sloping domain with a G value of 0.001 s^{-1}. For the second solution used to compute the numerical analog sensitivities, a G value of 0.0011 s^{-1} was used. Thus, the difference in the specified G values, ΔG, was 0.0001 s^{-1}. The comparison of sensitivities for the same set-up with a larger difference for G, $\Delta G = 0.001$ s^{-1}, is shown in Figure 3.18. For this comparison, the same base G value, 0.001 s^{-1}, was used while the second value was 0.002 s^{-1}. Cases such as these, where the second value of G used to generate the numerical analog is larger than the value of G for which the sensitivity is desired, are referred to herein as forward numerical analogs. The equations for forward and backward numerical analogs are shown in (3.25) and (3.26), respectively.

$$\frac{\Delta \zeta}{\Delta G} = \frac{\zeta(G + \Delta G) - \zeta(G)}{\Delta G} \tag{3.25}$$

$$\frac{\Delta \zeta}{\Delta G} = \frac{\zeta(G) - \zeta(G - \Delta G)}{\Delta G} \tag{3.26}$$

The magnitude of the numerical analog sensitivity in each of the cases referenced

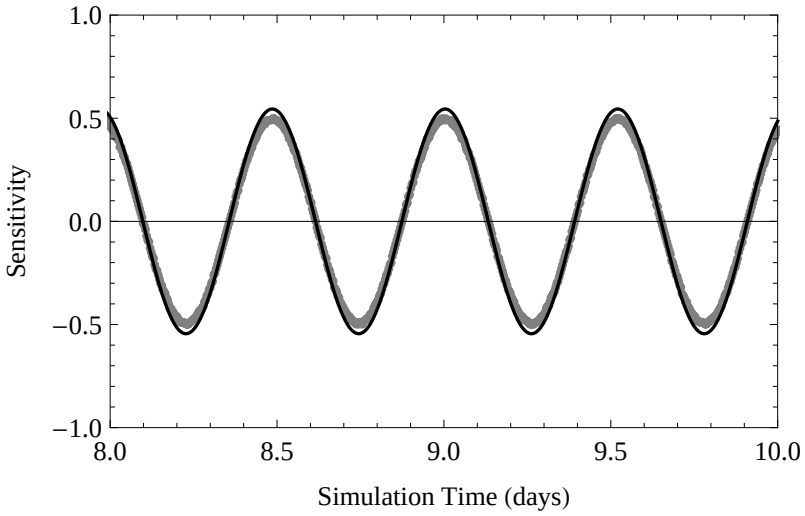

Figure 3.17 Comparison of elevation sensitivity results for the last two days of an explicit model simulation with $G = 0.001\ s^{-1}$ at the 11th node in the linear sloping domain. The FSM results are shown in black, while the gray depicts the numerical analog finite-difference sensitivities calculated using $\Delta G = 0.0001\ s^{-1}$.

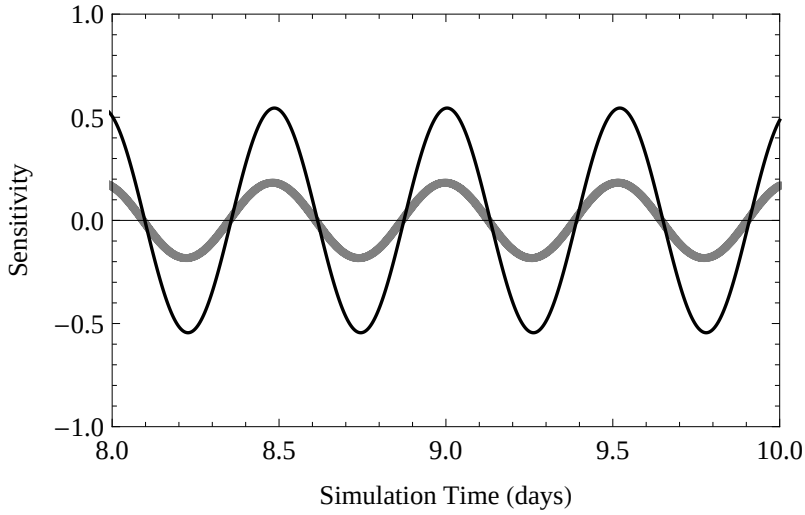

Figure 3.18 Comparison of elevation sensitivity results for the last two days of an explicit model simulation with $G = 0.001\ s^{-1}$ at the 11th node in the linear sloping domain. The FSM results are shown in black, while the gray depicts the numerical analog finite-difference sensitivities calculated using $\Delta G = 0.001\ s^{-1}$.

above is lower than the magnitude calculated using the FSM. This is a result of using a forward difference to compute the numerical analog sensitivity. The sensitivity to G decreases as G increases. Thus, over a given span of G values, the maximum sensitivity occurs for the minimum G value. Therefore, the average sensitivity given by the forward

numerical analog sensitivity calculation is less than the value from the FSM method. The numerical sensitivity is only a good approximation for small values of ΔG because the sensitivity to G changes rapidly with G (cf. Figure 3.17 and Figure 3.18). An order of magnitude change in G often results in a change in the magnitude of the sensitivity to G of a factor of 30-50 (e.g., Figure 3.7, Figure 3.8, and Figure 3.16). Backward numerical analog sensitivities occur in the section on data assimilation, with Figure 3.25 showing that the magnitude of the backward numerical analog sensitivity to G is greater than the FSM sensitivity.

The results presented above show that the sensitivities computed using the FSM are equivalent to the sensitivities calculated using the numerical as ΔG goes to zero. This is to be expected because the sensitivity is defined as the ratio of the change in one entity with respect to the change in another one. Therefore, if treated appropriately, the two methods should produce equivalent results. The comparison of FSM and the numerical analog confirms that the behavior predicted by the FSM actually occurs as G varies. Additionally, the FSM presents an opportunity to perform data assimilation based on errors between observations and the results from a model run with a given value of G, although one could alternatively use a numerical analog approach to compute sensitivities for use in data assimilation.

The equivalence of the FSM and numerical analog gives rise to the following question: What is the benefit of FSM over a reasonably simple and straightforward numerical finite difference calculation? In this chapter, constant G simulations are analyzed. In this case, using the numerical analog for the analysis would require a similar amount of computational effort as FSM. Instead of calculating the sensitivities using the FSM during one

ADCIRC simulation, two ADCIRC simulations would be performed and the output would be used to calculate numerical analog sensitivities. In the next chapter, however, a variable G parameterization will be analyzed. Using the numerical analog approach, $n + 1$ simulations would need to be performed to calculate the elevation and/or velocity sensitivities to n parameters, with one base run and one simulation with a small change in each parameter. However, the FSM allows the sensitivity of the solution to each parameter to be calculated during the same simulation.

3.5 Data Assimilation using Forward Sensitivities

Application of the FSM results in a sensitivity value that can also be used to adjust the value of G based on some error metric. As presented by *Lakshmivarahan and Lewis* [2010], using a first-order approach where only the first term in the Taylor series expansion is retained, the error (defined as the difference between the observation and model result) is equal to the product of the sensitivity and the correction, as given by (3.27), where **e** is the error, **z** is the observation, **c** is the model result, and **w** is the sensitivity.

$$\mathbf{e}(x, t, G) = \mathbf{z}(x, t) - \mathbf{c}(x, t, G) = (\Delta G)\mathbf{w}(x, t, G) \qquad \textbf{(3.27)}$$

The correction to the numerical parameter is ΔG, and the correction depends on the sensitivity vector and error in the model results.

The correction can be computed in a variety of ways. The most simple correction calculation would be to use an observation at one point in space (x_j) at one time (t_k), along with the model results for the same location in space and time. The correction, ΔG, to a specified value, G_0, based on this one observation is shown in (3.28).

$$\Delta G(G_0) = \frac{e(x_j, t_k, G_0)}{w(x_j, t_k, G_0)} \tag{3.28}$$

Least-squares minimization is a more sophisticated approach that allows for use of multiple observations in space or time. For the results herein, least-squares minimization will be applied on a nodal basis. In other words, the observations and model results for a given point in space, over a range of time, will be used to compute a least-squares correction to G. This is analogous to the real-world situation where a buoy collects water surface elevation data at a fixed location in the domain over a range of times. Conversely, least-squares minimization could be applied on a temporal basis, where errors throughout the domain at a given time are used to generate a correction.

The least-squares correction for node j using $nrecs$ values in time requires the vector of sensitivities shown in (3.29), and the error vector shown in (3.30).

$$\mathbf{H}_j = \{w_j^1, w_j^2, \ldots, w_j^{nrecs}\}^T \tag{3.29}$$

$$\mathbf{e}_j = \{(z_j^1 - c_j^1), (z_j^2 - c_j^2), \ldots, (z_j^{nrecs} - c_j^{nrecs})\}^T \tag{3.30}$$

The optimal least-squares correction, adapted from *Lakshmivarahan and Lewis* [2010] for a scalar parameter, is given by (3.31).

$$(\Delta G)_j = \frac{\mathbf{H}_j^T \mathbf{e}_j}{\mathbf{H}_j^T \mathbf{H}_j} \tag{3.31}$$

The optimal least-squares correction is a standard result that is presented proficiently in the text referenced above, as well as in *Lewis et al*. [2006], which provides additional detail about the origins of the analysis technique.

3.5.1 Correction to 2-D CG Results on the Linear Sloping Domain

Corrections require computation of errors. A set of observations, to which the model result is compared, is necessary to generate error values. For this study, observations were created using the 2-D CG version of ADCIRC on a rectangular grid that is uniform in the y-direction. In other words, the observations used for evaluating the 1-D model are simulation results using the 2-D version of ADCIRC. Specifically, the 1-D domains presented previously were extended "into the paper" to create 2-D domains to use with the ADCIRC production code in linear mode. The 2-D CG code was run implicitly with the same parameters as the 1-D code. The 2-D domain consists of 11 nodes in the y-direction for each of the 21 nodes in the x-direction for the linear sloping domain. Results for the 6th line of nodes (the centerline) from a simulation with $G = 0.001\ \mathrm{s}^{-1}$ are used as the observations. In this way, there is a set of observations from a node in the 2-D domain to compare to 1-D model results. Furthermore, the x-component of the velocity is used as the observation to compare to the 1-D velocity results; the y-component of the velocity is ignored, but is generally several orders of magnitude less than the x-component (and close to zero).

The root mean square error in space, $RMSE_x$, is calculated for each output record during the comparison period. Then, the temporal mean of these values is calculated to determine the average value of the root mean square error. The computation for $\overline{RMSE_x(\zeta)}$ is given by (3.32), which is the error metric used in this section.

$$\overline{RMSE_x(\zeta)} = \frac{1}{nrecs} \sum_{k=1}^{nrecs} (RMSE_x(\zeta))^k \qquad \textbf{(3.32)}$$

The elevation error results are shown in Figure 3.19, while the velocity error results are shown in Figure 3.20.

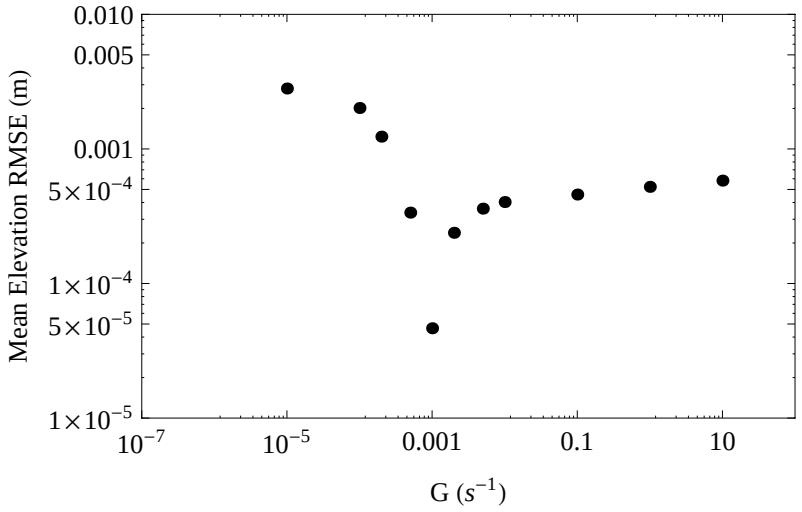

Figure 3.19 $\overline{RMSE}_x(\zeta)$ results compared to G for the last two days of the 10.0 day simulations on the linear sloping domain.

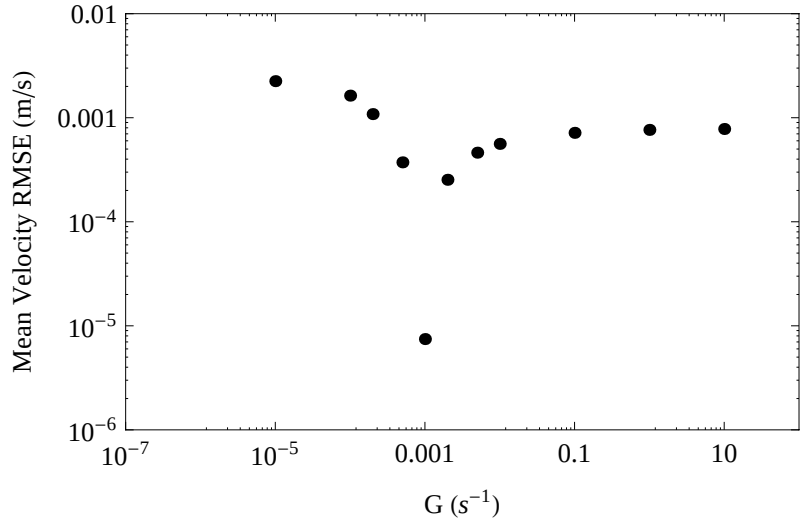

Figure 3.20 $\overline{RMSE}_x(u)$ results compared to G for the last two days of the 10.0 day simulations on the linear sloping domain.

The results show that the minimum error occurs when the same G value is used in the 1-D model as was used in the 2-D model to create the observations. This is not a surprising result because the 1-D results are sensitive to G, so increasing or decreasing G will cause the results to differ, thus introducing an error. The low error values for the case where $G = 0.001\ \text{s}^{-1}$ suggest the 2-D model is, essentially, a 1-D problem, at least along

the centerline.

The value of G that minimizes the error (i.e. $G = 0.001\ \text{s}^{-1}$) is the value of G that we would hope to identify using data assimilation. Generally, elevation observations are more prevalent in the field than velocity observations, so we will focus on using the elevation results and observations to calculate the correction to G using (3.31), although the procedure can be similarly applied using velocity results when available. The sensitivity, $\mathbf{H}$, and error, $\mathbf{e}$, vectors can include any subset of information available. When available, elevation data is often in the form of time series at discrete locations. Thus, unless otherwise specified, a time series of elevation observations will be used in this study to calculate the errors. Then, the correction will be computed using the errors and the corresponding time series of sensitivity values for the selected node.

The correction varies for a given run depending on which node is used to calculate the correction. For example, the corrections based on results from the run with $G = 0.0001\ \text{s}^{-1}$ are shown in Figure 3.21. The sensitivity of the elevation result to G for the left boundary node is zero due to the elevation being a specified value in that location. Thus, it does not make sense to attempt to correct G based on results at that node. However, the correction can be calculated for each of the other nodes in the domain, as seen in Figure 3.21.

The results show the correction to be just greater than $0.0001\ \text{s}^{-1}$ for each of the nodes. However, we know the optimal correction is close to $0.0009\ \text{s}^{-1}$, based on the values of G used for the runs to generate the model and observation results. It makes sense that the predicted correction is less than the actual optimal correction because the magnitude of the sensitivity varies so greatly with G. The sensitivity calculated for $G = 0.0001\ \text{s}^{-1}$ is

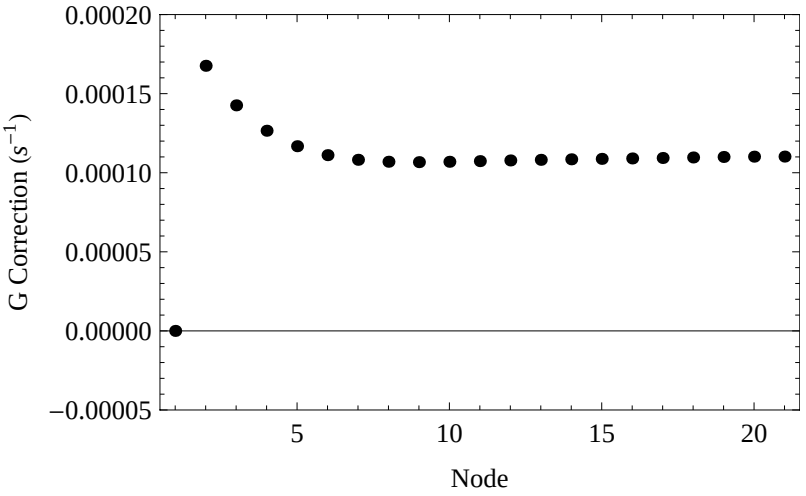

Figure 3.21 Nodal least-squares correction, ΔG, for each node based on results for an implicit simulation with $G = 0.0001$ s^{-1} using output from the last two days of the simulation. Observations are from the 2-D CG ADCIRC code with $G = 0.001$ s^{-1}.

much greater than the sensitivity for $G = 0.001\ \text{s}^{-1}$. Thus, the correction calculated using the sensitivity from the run with $G = 0.0001\ \text{s}^{-1}$ is expectedly low. Referring back to (3.31), it is apparent that large sensitivities cause the denominator on the RHS to be large, resulting in relatively small corrections. However, as the correction is in the proper direction, multi-step optimization could be employed to reach the optimal G value for this situation, as will be shown in Section 3.6.

In order to show how the correction varies with G, the maximum, minimum and mean of the nodal corrections were calculated for runs with a wide range of G values. Referring back to Figure 3.21, which shows a set of nodal least-squares corrections, the maximum correction is the one calculated for node 2, $\Delta G = 0.000168\ \text{s}^{-1}$. The minimum correction comes from results at node 9, $\Delta G = 0.000107\ \text{s}^{-1}$. The mean correction is calculated as the arithmetic mean of the nodal corrections for nodes 2-21. The results are shown in Figure 3.22 (maximum), Figure 3.23 (minimum) and Figure 3.24 (mean). The black points, which are indicative of positive corrections, show that when the G value is

low, data assimilation using FSM suggests increasing G. Conversely, the gray points, indicating negative corrections, denote that data assimilation suggests decreasing G. Therefore, for this application, sequential data assimilation using the forward sensitivity method would result in discovery of the optimal G value, as long as the original G value is not too high.

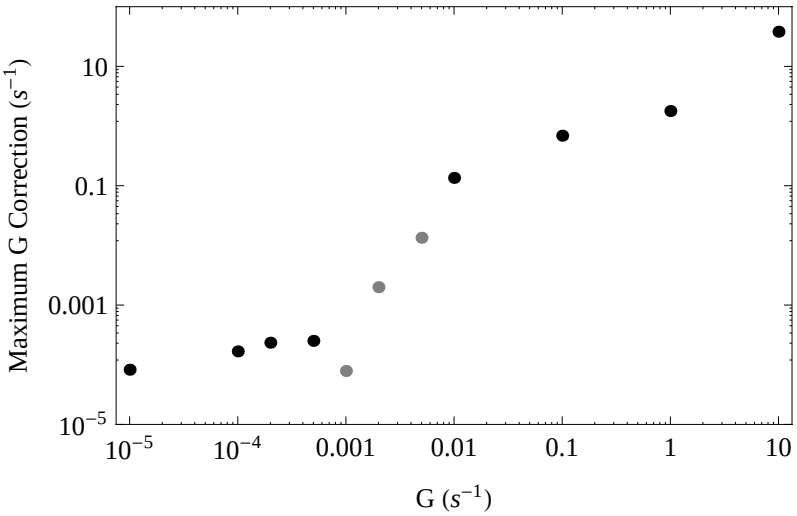

Figure 3.22 Maximum nodal least-squares correction, ΔG, for simulations over a range of G values using output from the last two days of the simulation. The magnitude of the correction is shown on the y-axis. The color of the dot corresponds to the sign of the correction. Positive corrections are shown in black, while negative corrections are shown in gray.

As Figure 3.22, Figure 3.23, and Figure 3.24 show, for a given G value, the maximum, minimum and mean corrections are similar if G is less than $0.005\ s^{-1}$. However, for both $G = 0.002\ s^{-1}$ and $G = 0.005\ s^{-1}$, the mean correction is negative and larger in magnitude than the value of G used for the simulation. For example, the mean correction for $G = 0.005\ s^{-1}$ is $\Delta G = -0.0289\ s^{-1}$. Thus, use of the mean correction to compute a new G value would result in the new G value being less than zero. Furthermore, the maximum correction, which corresponds to the least negative value, for $G = 0.005\ s^{-1}$ is $\Delta G = -0.0134\ s^{-1}$. This correction, too, would result in a negative value for G in

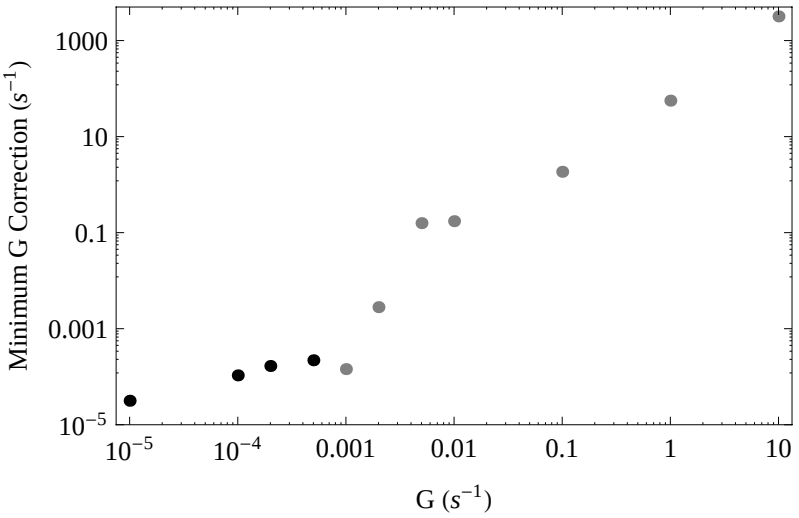

Figure 3.23 Minimum nodal least-squares correction, ΔG, for simulations over a range of G values using output from the last two days of the simulation. The magnitude of the correction is shown on the y-axis. The color of the dot corresponds to the sign of the correction. Positive corrections are shown in black, while negative corrections are shown in gray.

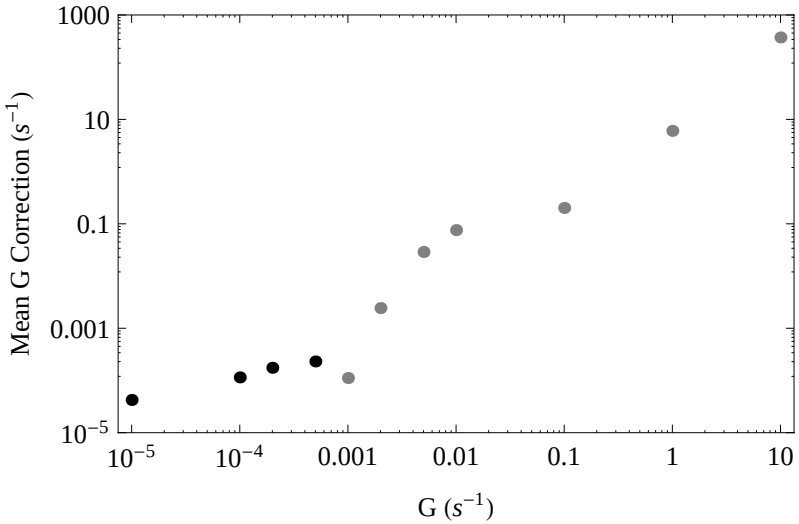

Figure 3.24 Mean nodal least-squares correction, ΔG, for simulations over a range of G values using output from the last two days of the simulation. The magnitude of the correction is shown on the y-axis. The color of the dot corresponds to the sign of the correction. Positive corrections are shown in black, while negative corrections are shown in gray.

the next model iteration. This "overcorrection" problem is a result of the magnitude of the sensitivity to G decreasing as G increases. The decrease in sensitivity magnitude with increases in G causes the correction size to be too small for low G values and too large for high G values, as per (3.31).

Furthermore, for G values of 0.01 s^{-1} and above some of the corrections are positive, which is opposite in sign from the mean corrections (cf. Figure 3.22). Therefore, if a node that suggests a positive correction is used to generate the correction, the resulting new G value, given by adding the correction to the previous value of G, will actually be farther from the target value than the previous value. Obviously, this is not the optimal scenario, i.e., a divergent algorithm.

In this study, the presence of positive and negative corrections for the same simulation is a result of the equations becoming "too primitive." The initial appearance (lowest G value that experiences oscillations) corresponds to the G threshold above which spurious oscillations are generated. When the solution becomes "too primitive," the sensitivities start to become irregular (e.g., Figure 3.4 and Figure 3.5). Rather than being similar from one node to the next, the sensitivities for successive nodes are opposite in sign or have varying magnitudes of the same sign. This transition from a normal pattern to an irregular one produces the aberrant correction results.

To illustrate the difficulties in generating corrections, even for this simple system, it is informative to return to the comparison between the FSM sensitivity and the numerical analog sensitivity. For the following plots (Figure 3.25 - Figure 3.29), the numerical analog sensitivity is calculated using the results from the 1-D model with $G = 0.001\ s^{-1}$ as the target. The error calculations, presented previously in Figure 3.19 and Figure 3.20, show the 1-D and 2-D simulations are almost equivalent when the same G value is used. Thus, in this case, the numerical analog sensitivity will provide a reasonable estimate of the average sensitivity to G over the range from the current G value to the target value, which is the sensitivity value that would result in a near optimal correction (using a first-order

approach). Note, that this numerical analog, while equivalent in the way it is computed, is slightly different conceptually than the numerical analogs calculated previously. In this case, the numerical analog is the average sensitivity and gives information about the sensitivity to G over a range of G values. In contrast, previously the numerical analog was computed to give an estimate of the rate of change of the solution to small changes in G value, in order to validate the FSM sensitivity calculations.

For a G value of 0.002 s^{-1} and a target of $G = 0.001\ s^{-1}$, as Figure 3.25 shows, the calculated backward numerical analog sensitivity, given by (3.33), is greater than the FSM sensitivity value for the run with $G = 0.002\ s^{-1}$.

$$\frac{\Delta\zeta}{\Delta G} = \frac{\zeta(G^*) - \zeta(G_{opt})}{\Delta G} \tag{3.33}$$

In (3.33), G^* is the current parameter value, G_{opt} is the optimal value, and ΔG is the difference $G^* - G_{opt}$. However, the shape of the curves is similar. The two sets of sensitivities are in-phase and have the same sign. Returning focus to the concept of overcorrection mentioned above, the corrections using results from the simulation with $G = 0.002\ s^{-1}$ were too large because the FSM sensitivities are lower than the average sensitivities over the ΔG range. This is opposite the previously shown situation (i.e., Figure 3.17 and Figure 3.18) where a forward difference is used to calculate the numerical analog sensitivity, resulting in the numerical analog sensitivities being lower in magnitude than the sensitivities calculated with the FSM.

The problem of positive and negative corrections produced using results from different nodes for the same simulation, discussed previously, occurs for values of G equal to or greater than 0.01 s^{-1} for the current application. For most of the nodes in the domain,

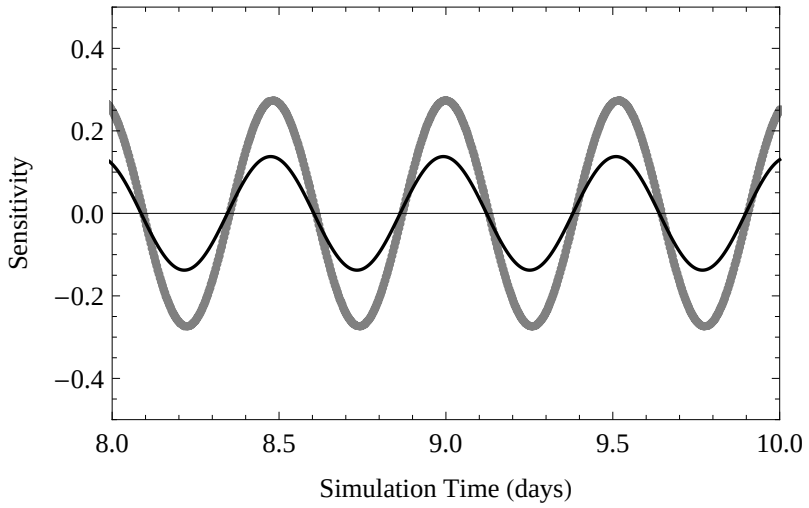

Figure 3.25 Numerical analog sensitivity (gray) between implicit 1-D results with $G = 0.001$ s^{-1} and $G = 0.002$ s^{-1} and FSM sensitivity (black) for $G = 0.002$ s^{-1} for the 11th node in the linear sloping domain.

the numerical analog and FSM sensitivities are in-phase, although the magnitudes for the FSM sensitivities are much lower than their numerical analog counterparts. The results for the 11th node in the domain, using $G = 0.01$ s^{-1} to generate model results, are shown in Figure 3.26. In comparison to Figure 3.25 (which is for results from a simulation with a G value below the primitive threshold), the shape of the sensitivities (FSM and numerical analog) is the same in each graph. The difference is that the disparity in magnitude of the sensitivities is less in Figure 3.25 than in Figure 3.26.

With $G = 0.002$ s^{-1}, the results for the 3rd node in the domain are similar to the results for the 11th node. The main difference is a shift of the results from the 11th node to the left. Specifically, the zero sensitivity occurring at about 8.2 days in the plot for the 11th node occurs just over 8.0 days into the simulation at the 3rd node. Figure 3.27 shows the results for the 3rd node with $G = 0.01$ s^{-1}. The difference between this plot and previous ones is striking. Again, the magnitude of the FSM sensitivity is much lower than the numerical analog sensitivity. The difference is that the sign of the FSM and numerical analog

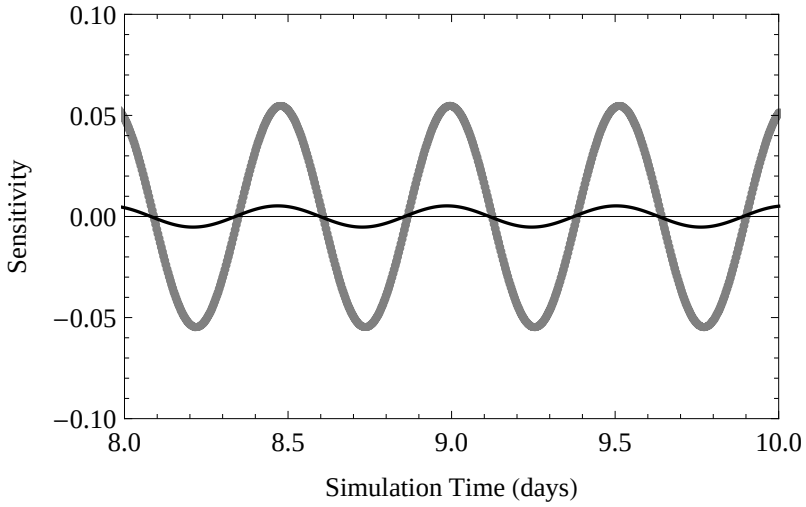

Figure 3.26 Numerical analog sensitivity (gray) between implicit 1-D results with $G = 0.001$ s^{-1} and $G = 0.01$ s^{-1} and FSM sensitivity (black) for $G = 0.01$ s^{-1} for the 11th node in the linear sloping domain.

sensitivities is different. The numerical analog sensitivity is calculated from the results of two simulations, with the difference between observations and model results divided by the difference in the G values used to generate the two data sets (e.g., (3.25) and (3.26)). In this case, the difference in the parameter used, $\Delta G = 0.010 - 0.001 = -0.009$ s^{-1}, was negative. Thus, when the numerical analog sensitivity is negative, the error value must be positive. Conversely, when the error value is negative, the numerical analog sensitivity is calculated as positive. For the early times in Figure 3.27, the error is positive (the numerical analog sensitivity is negative). At these times, the sensitivity calculated using the FSM is also positive. Therefore, the correction calculated using the error and the FSM sensitivities will also be positive, which is obviously incorrect.

Further increase in the G value results in further degradation of the solution and corrections. Specifically, the portion of the domain influenced by the model becoming "too primitive" increases as G increases. Figure 3.28 shows the FSM sensitivities are out-of-phase with the numerical analog sensitivities for the 11th node when $G = 0.1$ s^{-1} is used

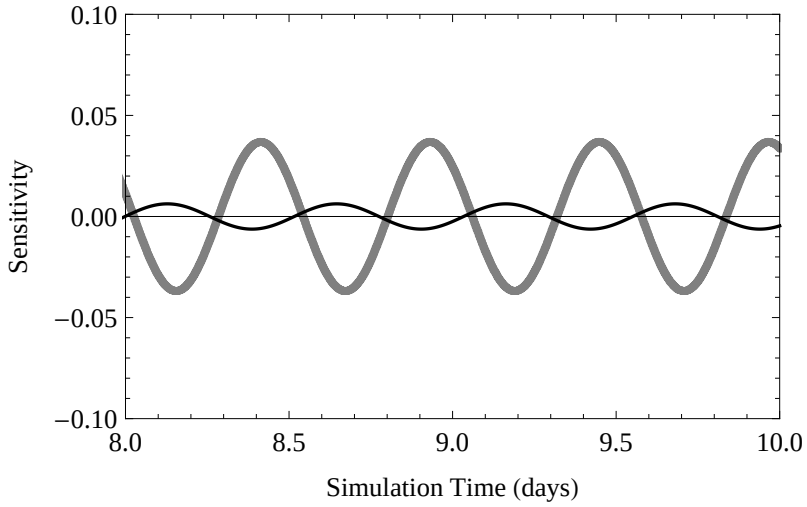

Figure 3.27 Numerical analog sensitivity (gray) between implicit 1-D results with $G = 0.001$ s^{-1} and $G = 0.01$ s^{-1} and FSM sensitivity (black) for $G = 0.01$ s^{-1} for the 3rd node in the linear sloping domain.

for the simulation. Compared to previous figures for the 11th node (Figure 3.25 and Figure 3.26), the numerical analog sensitivities maintain a similar shape. The magnitude is reduced because ΔG is an order of magnitude larger and the errors are similar in magnitude. The difference is in the sensitivity calculated using the FSM. With this increased G value, the sign of the FSM sensitivity is generally opposite the sign of the numerical analog sensitivity for this location in the domain. Therefore, the correction will be the wrong sign. In fact, the correction for node 11 with $G = 0.1$ s^{-1} is $\Delta G = 0.329$ s^{-1}. Conversely, the correction for the 12th node is $\Delta G = -0.549$ s^{-1}. The numerical analog and FSM sensitivities for the 12th node with $G = 0.1$ s^{-1} are shown in Figure 3.29. Comparing the results for the 11th and 12th nodes, the numerical analog sensitivities are similar. However, the FSM sensitivities are opposite in sign.

In summary, it is important to understand the system and the nature of the FSM sensitivities when attempting to generate corrections. For this system, the accuracy of the correction is highly dependent on the initial parameter specification. When G is too high

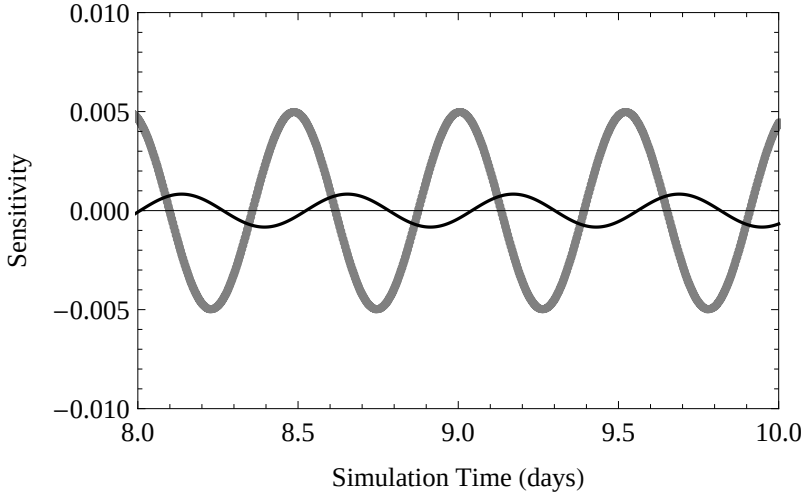

Figure 3.28 Numerical analog sensitivity (gray) between implicit 1-D results with $G = 0.001$ s^{-1} and $G = 0.1$ s^{-1} and FSM sensitivity (black) for $G = 0.1$ s^{-1} for the 11th node in the linear sloping domain.

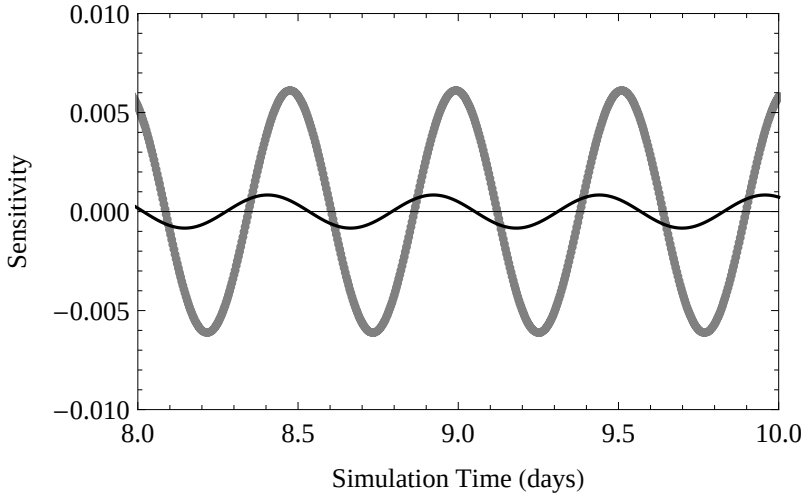

Figure 3.29 Numerical analog sensitivity (gray) between implicit 1-D results with $G = 0.001$ s^{-1} and $G = 0.1$ s^{-1} and FSM sensitivity (black) for $G = 0.1$ s^{-1} for the 12th node in the linear sloping domain.

and the equation becomes "too primitive," the corrections will generally not be useful in recovering the target parameter value. However, recovery of a target value is possible if the initial specification is within a certain range and will be explored in more detail in Section 3.6. Furthermore, while analysis and discussion focused on corrections using elevation sensitivities in this section, the same pattern holds for corrections using velocity sensitivi-

ties.

3.5.2 Correction to 2-D CG Results on the Seamount Domain

The previous section details attempts to correct the G value based on observations from the 2-D CG model for the linear sloping domain. For the seamount domain, observations were also generated with the 2-D CG model. Once again, the observations were model results from the 2-D model with a G value of 0.001 s^{-1}. The simulation conditions are the same as for the simulations in Section 3.3.4.

The $\overline{RMSE_x}$ for elevations and velocities, for a range of G values using the implicit 1-D model, are shown in Figure 3.30 and Figure 3.31, respectively. The counterparts of these plots using the explicit 1-D model are shown in Figure 3.32 and Figure 3.33. The implicit results show error minima when the G value in the 1-D model is set to the value used in the 2-D model to generate the observations. This is consistent with results from the linear sloping domain. There is not a well-defined minimum error value for either of the explicit error graphs because the explicit code is unstable at $G = 0.001\ s^{-1}$, as well as for lower values. However, it is readily apparent that the error decreases as G is lowered towards the optimal value that coincides with the value used to generate the observations, as long as G is not reduced so much as to make the model unstable. While it may not be readily apparent, because of the scales used on the figures, the results for the implicit and explicit codes, with the same G value, are similar. For example, the temporal mean nodal root mean square elevation error for the last day of the simulation is 0.009051 m for the implicit code with $G = 0.01\ s^{-1}$, while it is 0.009100 m for the explicit code with the same value of G. The error results suggest corrections to the G value used to generate the observations should be possible, assuming the model is stable at the target G value, which

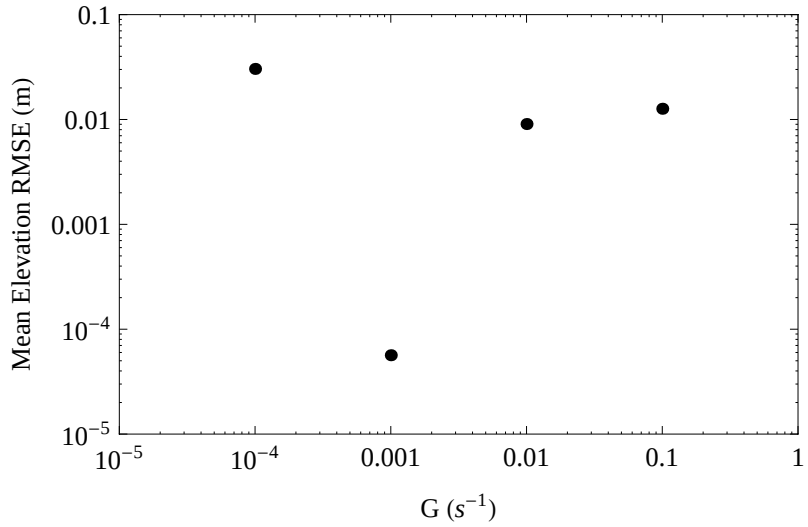

Figure 3.30 Implicit 1-D model temporal mean nodal root mean square elevation error results compared to G for the last day of the 5.0 day simulations on the seamount domain using the 2-D CG result as the true solution.

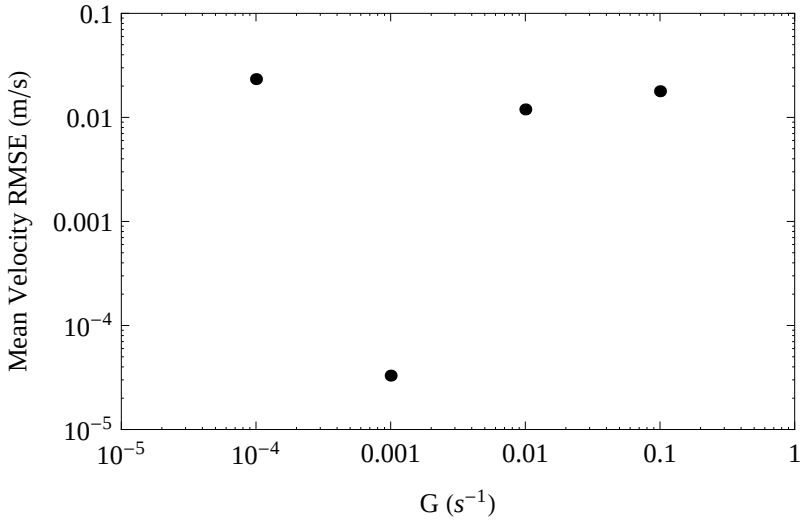

Figure 3.31 Implicit 1-D model temporal mean nodal root mean square velocity error results compared to G for the last day of the 5.0 day simulations on the seamount domain using the 2-D CG result as the true solution.

is not the case for the explicit model at the current time step.

The maximum, minimum and mean nodal least-squares corrections, ΔG, using the implicit model are shown in Figure 3.34, Figure 3.35, and Figure 3.36. The corrections for the G value that is too low, $G = 0.0001\ \text{s}^{-1}$, are positive regardless of the node used to

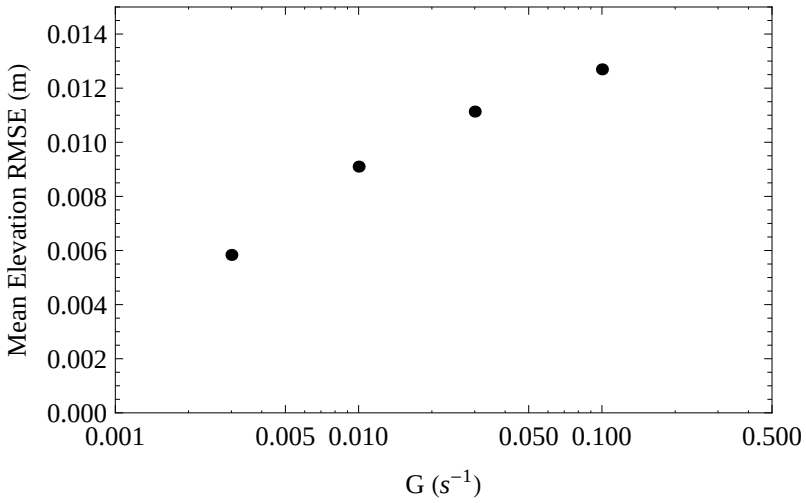

Figure 3.32 Explicit 1-D model temporal mean nodal root mean square elevation error results compared to *G* for the last day of the 5.0 day simulations on the seamount domain using the 2-D CG result as the true solution.

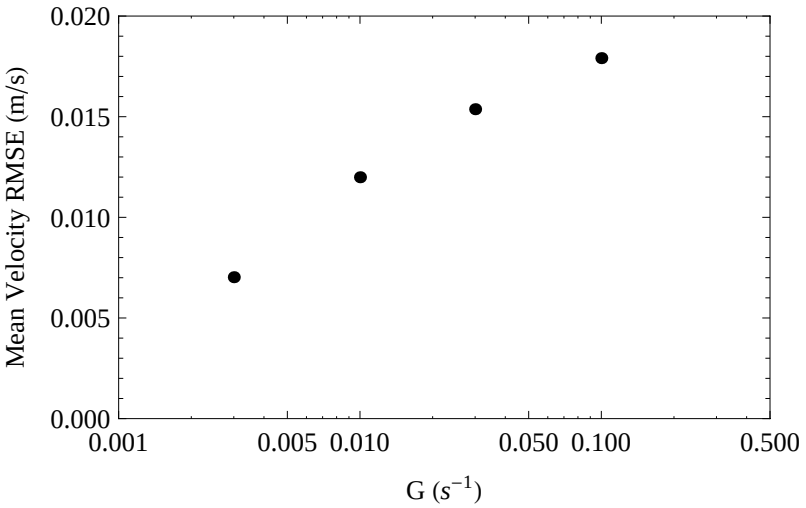

Figure 3.33 Explicit 1-D model temporal mean nodal root mean square velocity error results compared to *G* for the last day of the 5.0 day simulations on the seamount domain using the 2-D CG result as the true solution.

generate the correction. This is consistent with results from the linear sloping domain. The corrections are also lower than the optimal correction of $\Delta G = 0.0009\ \text{s}^{-1}$. In fact, the corrections range from a minimum of 7.755×10^{-6} at node 17 to a maximum of 0.0001640 s^{-1} at node 15. Generally, however, there is not a large deviation from node to node, as shown in Figure 3.37. Note that the correction has been set to zero for the specified eleva-

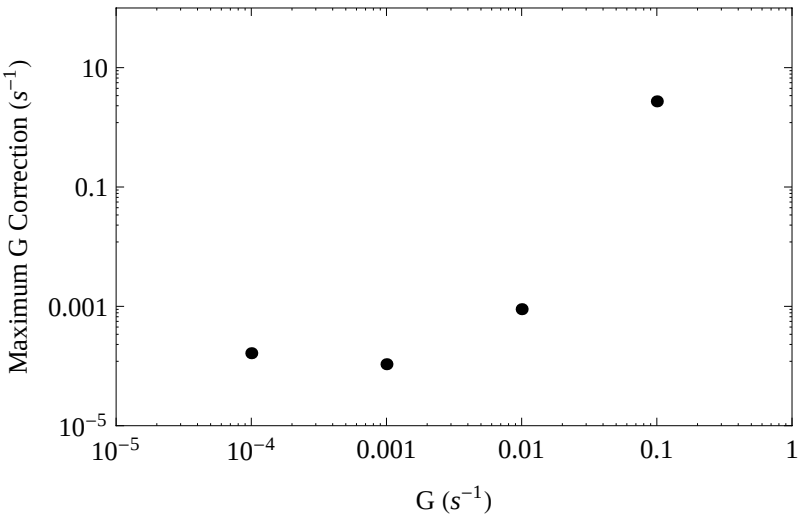

Figure 3.34 Maximum nodal least-squares correction, Δ*G*, for the seamount domain simulations over a range of *G* values using output from the last day of the implicit simulations and 2-D results as observations. The magnitude of the correction is shown on the y-axis. The color of the dot corresponds to the sign of the correction. Positive corrections are shown in black, and negative corrections are shown in gray.

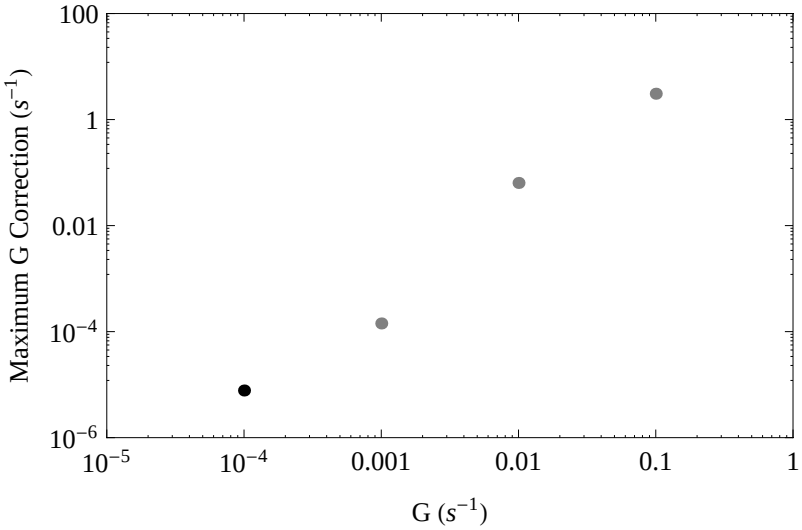

Figure 3.35 Minimum nodal least-squares correction, Δ*G*, for the seamount domain simulations over a range of *G* values using output from the last day of the implicit simulations and 2-D results as observations. The magnitude of the correction is shown on the y-axis. The color of the dot corresponds to the sign of the correction. Positive corrections are shown in black, and negative corrections are shown in gray.

tion boundary node (node 1) because the sensitivity and error are both zero.

The magnitude of the corrections when $G = 0.001\ \text{s}^{-1}$ in the 1-D model are small

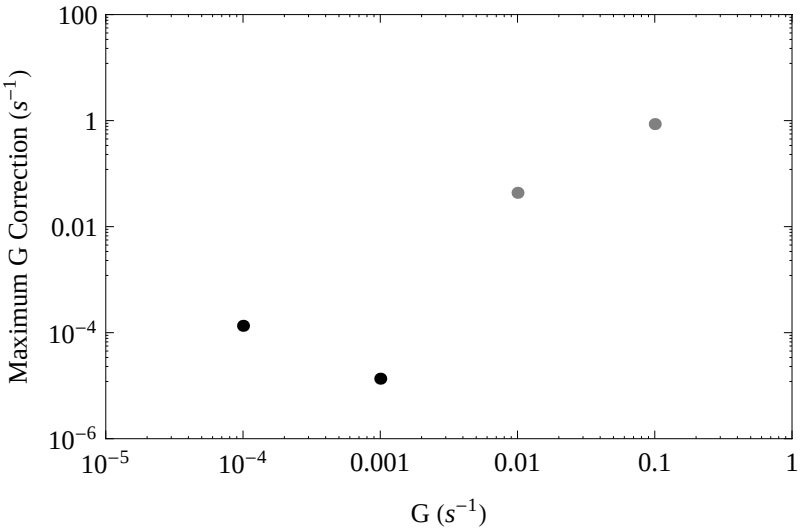

Figure 3.36 Mean nodal least-squares correction, Δ*G*, for the seamount domain simulations over a range of *G* values using output from the last day of the implicit simulations and 2-D results as observations. The magnitude of the correction is shown on the y-axis. The color of the dot corresponds to the sign of the correction. Positive corrections are shown in black, and negative corrections are shown in gray.

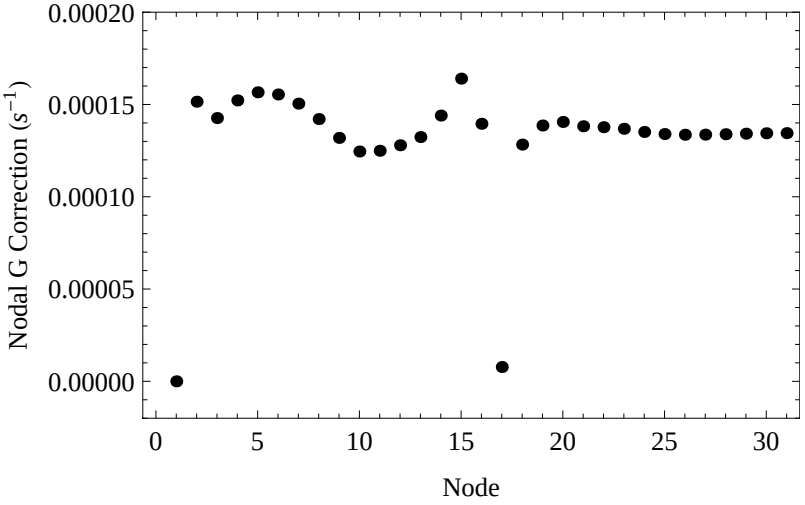

Figure 3.37 Nodal least-squares corrections, Δ*G*, for the seamount domain simulation with G = 0.0001 s^{-1} using output from the last day of the implicit simulation and 2-D results as observations.

because the error is small. The only negative value occurs at node 2, with positive corrections in the rest of the domain with the magnitude decreasing as you move away from the specified elevation boundary towards the no-flow boundary. When $G = 0.01\ s^{-1}$, the corrections (not shown) are negative with the exception of the one generated using results

for node 18. However, the magnitude of the correction is too large (mean correction is $-0.064\ \text{s}^{-1}$ whereas the optimal correction is approximately $-0.009\ \text{s}^{-1}$), a result of the decreasing magnitude of the sensitivity with increasing G. When $G = 0.1\ \text{s}^{-1}$, the GWCE becomes "too primitive," resulting in corrections that show a $2\Delta x$ oscillation, as seen in Figure 3.38. This is consistent with the plot of the peak elevation sensitivity (Figure 3.16) at each node in the domain for different G values. The line of peak elevation sensitivity for the two lowest G values in Figure 3.16 is fairly smooth. There is a general increase in amplitude as you move away from the specified elevation boundary, and there is also a dip in the sensitivity over the top of the seamount, which resides from node 16 to node 21. However, there are $2\Delta x$ oscillations in peak sensitivity amplitude for the two higher G values.

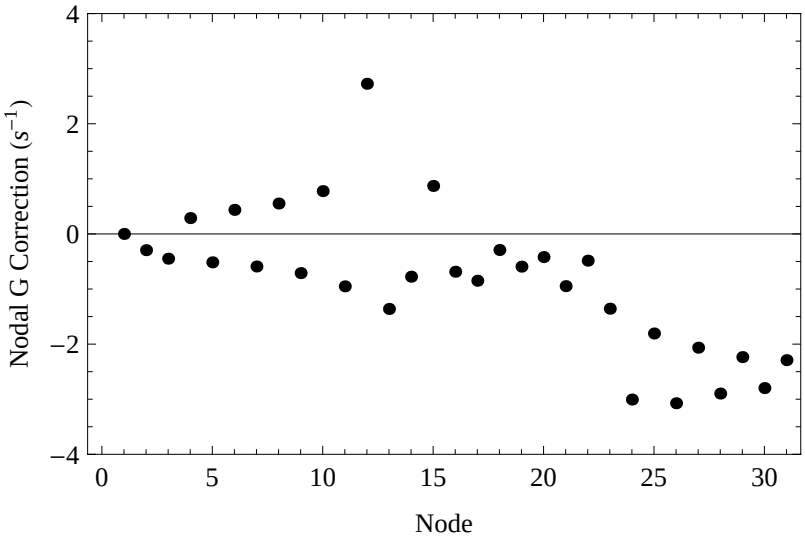

Figure 3.38 Nodal least-squares corrections, ΔG, for the seamount domain simulation with $G = 0.1\ \text{s}^{-1}$ using output from the last day of the implicit simulation and 2-D results as observations.

3.6 Sequential Optimization

In the previous section, corrections to G have been calculated based on model errors and sensitivities to G. In this section, the correction, ΔG, is added to the previous

G value to determine the next G value. This process is continued until the new correction is below a certain threshold, which signifies the optimization process has converged at the target value.

The linear sloping domain presented in Section 3.3.3 is used for this proof-of-concept application. The simulation parameters are the same as those used previously, with the exception that the run is only 5.0 days long and corrections are generated using the results from the last day of the simulation. The observations are the elevation results along the centerline of the 2-D ADCIRC simulation with $G = 0.001\ \text{s}^{-1}$. The correction, ΔG, is the mean of the nodal corrections using the elevation results to compute the errors.

The first test, using the explicit code, had a starting G value of $0.0005\ \text{s}^{-1}$ and a convergence threshold for ΔG of 1.0 E-10 s^{-1}. As expected, specification of an initial value that is less than the target value resulted in each correction being in the appropriate direction (positive) with less than optimal magnitude, as shown in Table 3.2. The target value for the simulation is not the G value used in the 2-D CG simulation; the target value is the value at which the sequential optimization finishes, 8.98 E-04 s^{-1}. However, it is close to the value used in the 2-D model to create the observations. The ratio of the correction to the optimal correction is notable. As the G value approaches the target value, the correction approaches the optimal correction. This is logical because as ΔG goes to zero, the numerical analog and FSM sensitivities converge, assuming the target G value is not in the primitive range. If the numerical analog and FSM sensitivities are equal, the correction will be optimal.

A second test was performed using the implicit 1-D code, which allows for a lower starting G value. The test was initialized with a G value of 1.00 E-06 s^{-1} and concluded

Table 3.2 Sequential optimization of G for the linear sloping domain compared to the 2-D CG simulation with $G = 0.001\ s^{-1}$. The units for each of the columns, except for the fourth column, are s^{-1}. The ratios in the fourth column are dimensionless.

G Value	Mean Nodal Correction, ΔG	Optimal Correction, ΔG_{opt}	$\frac{\Delta G}{\Delta G_{opt}}$	New G Value, $G + \Delta G$
5.00E-04	2.24E-04	3.98E-04	0.564	7.24E-04
7.24E-04	1.39E-04	1.74E-04	0.801	8.63E-04
8.63E-04	3.28E-05	3.46E-05	0.948	8.96E-04
8.96E-04	1.78E-06	1.81E-06	0.983	8.98E-04
8.98E-04	3.10E-08	3.14E-08	0.984	8.98E-04
8.98E-04	4.81E-10	4.88E-10	0.986	8.98E-04
8.98E-04	7.02E-12	7.02E-12	1.000	8.98E-04

when the magnitude of ΔG fell below 1.00 E-05 s^{-1}. The implicit and explicit codes give slightly different results, so the target G value, 9.48 E-04 s^{-1}, was slightly higher for this simulation. The G values for this optimization were {1.00 E-06, 2.38 E-05, 7.41 E-05, 1.69 E-04, 3.31 E-04, 5.61 E-04, 7.97 E-04, 9.26 E-04, 9.48 E-04, 9.48 E-04} s^{-1}, with the ratio of the first correction step to the optimal correction of just 0.024 and the final correction ratio approaching unity.

Finally, tests were performed with initial G values greater than the target value. As expected, specification of a value larger than the target, but still below the primitive threshold, results in an overcorrection in the first step. For the explicit code with an initial value of 1.20 E-03 s^{-1}, the mean correction for the first step is –3.94 E-04 s^{-1}, resulting in a new G value of 8.06 E-04 s^{-1}. From there, the corrections bring the G value up to the target value. However, if the initial specification is significantly higher than the target, the overcorrection can result in negative G values. For instance, the mean correction with G of 0.002 s^{-1} is –2.38 E-03 s^{-1}, which is larger than the previous G value. Thus, in prac-

tice, constraints on G would have to be put into the optimization algorithm.

3.7 Comparison of FSM to Dispersion Analysis

Kolar et al. [1994] performed a dispersion analysis of the 1-D shallow water equations using the GWCE for the Bight of Abaco, Bahamas. A dispersion plot similar to the one included in the paper is shown in Figure 3.39. The authors note spurious $2\Delta x$ oscillations do not occur if the dispersion curve is monotonic. The frequency for the M_6 tide is delineated in Figure 3.39, and monotonic dispersion relations exist as long as G does not exceed 0.075 s^{-1}. The frequency of the M_2 tide is one third the frequency for the M_6 tide, and G must be less than approximately 0.3 s^{-1} to ensure the solution remains free of spurious, short-wavelength oscillations for the M_2 frequency.

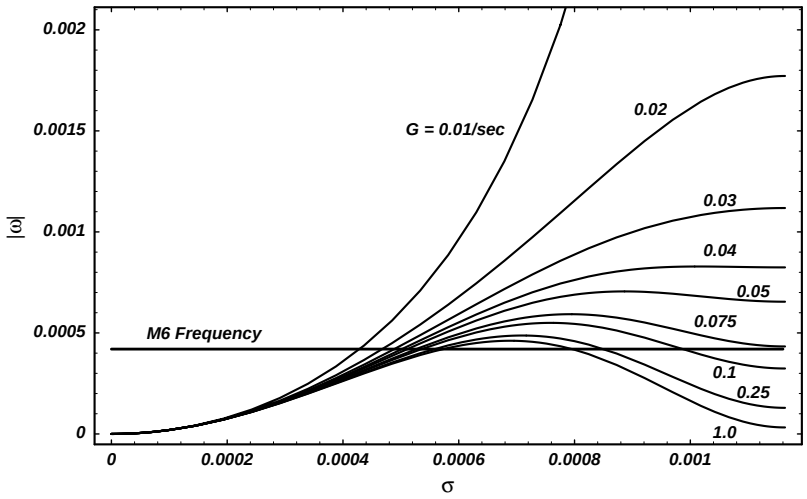

Figure 3.39 Based on work from *Kolar et al.* [1994], dispersion curve for the Bight of Abaco, Bahamas for various values of G; h = 2 m.

The dispersion analysis used a bathymetry value of 2.0 meters, an element size of 2700 meters and a bottom friction value of 0.01 s^{-1}. For this study, these parameters were also used in 1-D simulations in a flat bottom domain consisting of 21 nodes. The time step

size for the 1-D simulations is 5.0 seconds. Larger time steps result in differences in the calculated sensitivities, whereas the sensitivities were consistent between simulations with time steps of 2.5 and 5.0 seconds. It should also be noted that dispersion analysis is restricted to interior nodes. The 1-D simulations herein include boundaries that are treated as stated previously (specified elevation on the left, zero velocity on the right).

For the 1-D simulations with the boundary forcing with an M_6 tide, the dispersion analysis predicts spurious oscillations for G values greater than 0.075 s^{-1}. The elevation FSM sensitivity results are free of $2\Delta x$ oscillations with $G = 0.01\ s^{-1}$. With $G = 0.03\ s^{-1}$, the sensitivity results show $2\Delta x$ oscillations for the first 4 elements in from the left boundary. However, the interior of the domain is not impacted. Further increase of G causes increases to the fraction of the domain where the oscillations are present in the FSM sensitivities.

Using an M_2 tide as the boundary forcing, the dispersion analysis predicts spurious oscillations will appear for simulations in which G is greater than or equal to approximately 0.3 s^{-1}. Again, oscillations with the FSM do not occur with $G = 0.01\ s^{-1}$ and occur only near the open boundary with $G = 0.03\ s^{-1}$. Similar to the case for the M_6 forcing, the oscillations become more prevalent as G increases, although the M_2 forcing simulations generally have less prominent $2\Delta x$ noise than the simulations with the M_6 forcing. This is consistent with results suggested by the dispersion analysis. However, with a G value of 0.1 s^{-1}, the entire domain experiences $2\Delta x$ oscillations.

The FSM sensitivities and dispersion analysis do not produce the same values of G for the initial appearance of $2\Delta x$ oscillations in the solution (which signifies that the G value is too high, resulting in the GWCE becoming “too primitive”). Given the underlying

differences (e.g., dispersion analysis is confined to interior nodes and continuous time) in the analysis techniques, this is not an entirely surprising result. However, the similarity between the results for the two techniques points to FSM being a useful tool in analysis of problems (non-linear equations, non-constant bathymetry, etc.) where dispersion analysis is not valid.

3.8 Conclusions

The FSM was successfully applied to the linearized, 1-D version of ADCIRC with constant G. The FSM is useful in determining the sensitivity, both in space and time, to G. In particular, the sensitivity of the elevation and velocity fields to changes in G varies greatly with G. The sensitivity is much greater at low values of G than at higher values where the GWCE effectively approaches the primitive continuity equation. Additionally, as G increases, the sensitivities from the FSM show the $2\Delta x$ oscillations that plague the continuous Galerkin solution when the primitive continuity equation is used instead of the GWCE. Additionally, the maximum G threshold, above which the GWCE becomes "too primitive" and results in generation of spurious $2\Delta x$ oscillation, can be identified through analysis of the FSM sensitivities. In that sense, FSM can be used as a tool like dispersion analysis to predict folding of dispersion relations, with the advantage of being applicable to non-constant bathymetry and non-linear equations.

The corrections, ΔG, calculated using the FSM are intrinsically tied to the sensitivities. The change in sensitivity over the range of possible G values makes direct estimation of the optimal correction difficult using first-order methods. At high G values, the corrections are also hindered by the $2\Delta x$ oscillations in the sensitivities. However, sequential

optimization should be possible as long as care is taken in specification of the starting point for optimization. Specifically, use of a low initial value is optimal because the corrections are less than optimal when G is low, whereas the magnitude of the correction is often too high for high G values due to the variation in sensitivity magnitude with G. The next chapter will extend the FSM analysis to the case of variable G on the non-linear, 1-D shallow water equations.

CHAPTER 4. Extension of the Forward Sensitivity Method to Non-linear 1-D ADCIRC with Variable G

4.1 Introduction

In the previous chapter, the FSM was applied to analyze the linearized, 1-D shallow water equations with constant G parameterization for the GWCE. The results suggest the FSM is a viable tool for both the analysis of the system, specifically regarding whether the G specification causes spurious oscillations to be generated as a result of the GWCE becoming "too primitive," and the obtention of the optimal value of G by generating corrections using the sensitivities and model errors.

In this chapter, the analyses in the previous chapter are extended to the non-linear, 1-D shallow water equations with variable G parameterization for the GWCE. Whereas both implicit and explicit discretizations were analyzed in the previous chapter, this chapter will be limited to an explicit discretization. This decision was made due to computational concerns. For the implicit system, calculation of the sensitivities requires solution of an inverse problem. For the implicit linear case of Chapter 3, LU-decomposition (described in [*Lewis et al.* 2006]) was applied to the matrix for the $k+1$ time level. The LU factors, which were constant in time, were used in the solution of the inverse problem throughout the entire simulation. For the non-linear case, the LU factors vary in time and must be recalculated each time step. The extra stability of the implicit scheme did not warrant the computational burden of the implicit scheme, especially considering the two schemes produced

similar results for the linear case.

The discretization, as in the previous chapter, will be addressed first, followed by presentation of the sensitivities. The simulation set-up is given in Section 4.4. Sensitivity results are analyzed in Section 4.5 and data assimilation is explored in Section 4.6. Section 4.7 is focused on application of the FSM to analyze the impact of G on mass residuals. Finally, the conclusions section closes the chapter.

4.2 1-D Discretizations

4.2.1 Governing Equations

The non-linear 1-D generalized wave continuity equation (GWCE) and non-conservative momentum equation (NCM) are given by (4.1) and (4.2), respectively, where ε is the lateral eddy viscosity.

$$\frac{\partial^2 \zeta}{\partial t^2} + G\frac{\partial \zeta}{\partial t} - Hu\frac{\partial G}{\partial x} - \frac{\partial}{\partial x}\left[\frac{\partial}{\partial x}(Huu) + gH\frac{\partial \zeta}{\partial x} + \varepsilon\frac{\partial^2 \zeta}{\partial x \partial t} + (\tau - G)Hu\right] = 0 \qquad \textbf{(4.1)}$$

$$\frac{\partial u}{\partial t} + u\frac{\partial u}{\partial x} + \tau u + g\frac{\partial \zeta}{\partial x} - \frac{\varepsilon}{H}\frac{\partial^2 (Hu)}{\partial x^2} = 0 \qquad \textbf{(4.2)}$$

4.2.2 Continuous Galerkin Finite Element Discretization

Application of the continuous Galerkin finite element method results in the following equations for the GWCE (4.3) and NCM (4.4) equations.

$$0 = \langle\frac{\partial^2 \zeta}{\partial t^2}, \phi_i\rangle + \langle G\frac{\partial \zeta}{\partial t}, \phi_i\rangle - \langle Hu\frac{\partial G}{\partial x}, \phi_i\rangle + \langle\frac{\partial}{\partial x}(Huu), \frac{\partial \phi_i}{\partial x}\rangle + \langle gh\frac{\partial \zeta}{\partial x}, \frac{\partial \phi_i}{\partial x}\rangle + \qquad \textbf{(4.3)}$$
$$\langle\frac{g\partial^2 \zeta}{2\partial x^2}, \frac{\partial \phi_i}{\partial x}\rangle + \langle\varepsilon\frac{\partial^2 \zeta}{\partial x \partial t}, \frac{\partial \phi_i}{\partial x}\rangle + \langle(\tau - G)Hu, \frac{\partial \phi_i}{\partial x}\rangle + Boundary$$

$$0 = \langle \frac{\partial u}{\partial t}, \phi_i \rangle + \langle u \frac{\partial u}{\partial x}, \phi_i \rangle + \langle \tau u, \phi_i \rangle + \langle g \frac{\partial \zeta}{\partial x}, \phi_i \rangle + \varepsilon \langle \frac{\partial (Hu)}{\partial x}, \frac{\partial (\phi_i / H)}{\partial x} \rangle \qquad \textbf{(4.4)}$$

The boundary terms, which are normal flux values, are omitted from here on, because the specified elevation boundary condition used on the ocean (left) boundary makes the boundary flux term irrelevant on one edge of the domain. The land (right) boundary is a no-flow boundary, which means that the flux is zero and does not need to be carried through the derivation. Additionally, lumping is used selectively to generate an explicit set of equations.

4.2.3 Finite Difference Time Discretization

Application of an explicit, three-level scheme centered at k for the GWCE (except for the eddy viscosity term which is centered at $k - 1/2$) and an explicit, two-level scheme for the momentum equation results in the following set of elemental equations for constant grid spacing, (4.5) and (4.6):

$$\left(1 + \frac{G\Delta t}{2}\right)\mathbf{M}^L_{i,j}\zeta^{k+1}_j = 2\mathbf{M}^L_{i,j}\zeta^k_j + \left(\frac{G\Delta t}{2} - 1\right)\mathbf{M}^L_{i,j}\zeta^{k-1}_j + \Delta t^2 (Hu)_e (G)^k_j \mathbf{M}^5_{i,j} - \qquad \textbf{(4.5)}$$
$$\Delta t^2 (Huu)^k_j \mathbf{M}^3_{i,j} - g\Delta t^2 \mathbf{M}^2_{i,j}\zeta^k_j - \frac{g\Delta t^2}{2}(\zeta^2)^k_j \mathbf{M}^3_{i,j} - \varepsilon\Delta t \mathbf{M}^3_{i,j}\zeta^k_j + \varepsilon\Delta t \mathbf{M}^3_{i,j}\zeta^{k-1}_j +$$
$$\Delta t^2 [(G - \tau)(Hu)]^k_j \mathbf{M}^4_{i,j}$$

$$\left(1 + \frac{\tau\Delta t}{2}\right)\mathbf{M}^L_{i,j}u^{k+1}_j = \left(1 - \frac{\tau\Delta t}{2}\right)\mathbf{M}^L_{i,j}u^k_j - \frac{\Delta t}{2}(u^2)^k_j \mathbf{M}^5_{i,j} - g\Delta t^2 \zeta^k_j \mathbf{M}^5_{i,j} - \varepsilon\Delta t \mathbf{M}^3_{i,j}u^k_j \qquad \textbf{(4.6)}$$

where $\mathbf{M}^L_{i,j} = \Delta x \begin{bmatrix} 1/2 & 0 \\ 0 & 1/2 \end{bmatrix}$, $\mathbf{M}^2_{i,j} = \frac{h_j + h_{j+1}}{2\Delta x}\begin{bmatrix} 1 & -1 \\ -1 & 1 \end{bmatrix}$, $\mathbf{M}^3_{i,j} = \frac{1}{\Delta x}\begin{bmatrix} 1 & -1 \\ -1 & 1 \end{bmatrix}$,

$\mathbf{M}^4_{i,j} = \frac{1}{2}\begin{bmatrix} -1 & -1 \\ 1 & 1 \end{bmatrix}$ and $\mathbf{M}^5_{i,j} = \frac{1}{2}\begin{bmatrix} -1 & 1 \\ -1 & 1 \end{bmatrix}$.

4.2.4 Explicit Equations for Interior Nodes

The linear system, analyzed in the previous chapter, could be written in terms of time-independent coefficient matrices multiplied by the vectors of elevations and velocities. The non-linear system could be written in a similar form, with the major difference being that the matrices would contain time-dependent terms. For instance, the finite amplitude term $(\frac{g\Delta t^2}{2}(\zeta^2)_j^k \mathbf{M}_{i,j}^3)$ in the GWCE would be split, and one ζ term would be in the matrix and another would be in the solution vector for the current time. Rather than provide the equations in that form, the non-linear system can be written symbolically as shown in (4.7), where j is the index over each of the entities in the unknown vector (elevations and velocities).

$$\beta_j(G)c_j^{k+1} = M_{1j}(\mathbf{c}^k, G) + M_{2j}(\mathbf{c}^{k-1}, G) \quad \textbf{(4.7)}$$

The $\beta_j(G)$ values are the coefficients on the new unknowns and $M_{1j}(\mathbf{c}^k, G)$ and $M_{2j}(\mathbf{c}^{k-1}, G)$ are the known right-hand side values corresponding to the time levels k and $k-1$, respectively. The applicable boundary condition values have been absorbed into $M_{1j}(\mathbf{c}^k, G)$. Equations for general interior nodes for the GWCE (4.8) and NCM (4.9) equations are shown below.

$$2\left(1+\frac{G_j^k\Delta t}{2}\right)\zeta_j^{k+1} = 4\zeta_j^k + 2\left(\frac{G_j^k\Delta t}{2}-1\right)\zeta_j^{k-1} - a\left(-\zeta_{j-1}^k + 2\zeta_j^k - \zeta_{j+1}^k\right) - \tag{4.8}$$

$$b\left(-(h_{j-1}+h_j)\zeta_{j-1}^k + 2(h_{j-1}+2h_j+h_{j+1})\zeta_j^k - (h_j+h_{j+1})\zeta_{j+1}^k\right) +$$

$$a\left(-\zeta_{j-1}^{k-1} + 2\zeta_j^{k-1} - \zeta_{j+1}^{k-1}\right) - r\left(-(Huu)_{j-1}^k + 2(Huu)_j^k - (Huu)_{j+1}^k\right) +$$

$$\frac{f}{2}\left(-\left((Hu)_{j-1}^k + (Hu)_j^k\right)G_{j-1}^k + \left((Hu)_{j-1}^k - (Hu)_{j+1}^k\right)G_j^k + \left((Hu)_j^k + (Hu)_{j+1}^k\right)G_{j+1}^k\right) -$$

$$b\left(-(\zeta^2)_{j-1}^k + 2(\zeta^2)_j^k - (\zeta^2)_{j+1}^k\right) + f\left((GHu)_{j-1}^k - (GHu)_{j+1}^k\right) - f\left((\tau Hu)_{j-1}^k - (\tau Hu)_{j+1}^k\right)$$

$$2\left(1+\frac{\tau\Delta t}{2}\right)u_j^{k+1} = 2\left(1-\frac{\tau\Delta t}{2}\right)u_j^k - \frac{d}{2}\left(-(u^2)_{j-1}^k + (u^2)_{j+1}^k\right) - \tag{4.9}$$
$$e\left(-\zeta_{j-1}^k + \zeta_{j+1}^k\right) - a\left(-u_{j-1}^k + 2u_j^k - u_{j+1}^k\right)$$

where $a = \frac{2\varepsilon\Delta t}{\Delta x^2}$, $b = \frac{g\Delta t^2}{\Delta x^2}$, $d = \frac{\Delta t}{2\Delta x}$, $e = \frac{g\Delta t}{\Delta x}$, $f = \frac{\Delta t^2}{\Delta x}$, and $r = \frac{2\Delta t^2}{\Delta x^2}$. The system of equations can be found in Appendix D.

4.3 Sensitivity to G

As mentioned in the introduction to this chapter, the major differences between this chapter and the previous one are the inclusion of non-linear terms in the equation and consideration of variable G parameterizations. For the studies herein, a three-coefficient parameterization of G based on total water depth and velocity will be utilized, as described by (4.10).

$$G_j^k = \left(\alpha_0 + \frac{\alpha_1}{H} + \alpha_2|u|\right)_j^k \tag{4.10}$$

Note, the α values in the parameterization are unrelated to the time-weighting coefficients in the GWCE. Additionally, while G varies in space and time according to (4.10), the α values are constant for a given simulation. This parameterization is based on past analyses (e.g. [*Atkinson* 2004; *Westerink* 2008]) that show G should be inversely proportional to water depth and proportional to velocity. It should be noted that the constant G case can be recovered by setting α_0 to the desired constant G value, while simultaneously setting the other two coefficients to zero. The sensitivity to G will now be evaluated by the sensitivities to the coefficients in the parameterization for G.

Given the system described in (4.7), the sensitivity to G can be found by taking the derivative with respect to each of the α values, as shown in (4.11).

$$\frac{\partial}{\partial \alpha_i}[\beta_j(G)c_j^{k+1}] = \frac{\partial}{\partial \alpha_i}[M_{1j}(\mathbf{c}^k, G) + M_{2j}(\mathbf{c}^{k-1}, G)] \quad \textbf{(4.11)}$$

By applying the product rule, the sensitivity is described by (4.12). As was the case in the previous chapter, the boundary forcing is independent of G. Additionally, a more detailed presentation of the terms in (4.12) can be found in Appendix D.

$$\frac{\partial \beta(G)}{\partial \alpha_i}\mathbf{c}^{k+1} + \beta(G)\frac{\partial \mathbf{c}^{k+1}}{\partial \alpha_i} = D_c(M_1)\frac{\partial \mathbf{c}^k}{\partial \alpha_i} + D_{\alpha_i}(M_1) + D_c(M_2)\frac{\partial \mathbf{c}^{k-1}}{\partial \alpha_i} + D_{\alpha_i}(M_2) \quad \textbf{(4.12)}$$

where $D_c(M_1) = [\partial M_{1i}/\partial c_j] \in R^{2n \times 2n}$, $D_c(M_2) = [\partial M_{2i}/\partial c_j] \in R^{2n \times 2n}$, $D_{\alpha_i}(M_1) = [\partial M_{1j}/\partial \alpha_i] \in R^{2n}$, and $D_{\alpha_i}(M_2) = [\partial M_{2j}/\partial c_i] \in R^{2n}$.

Defining the sensitivity to coefficient α_i at a given time k as $\mathbf{w}_i^k = \partial \mathbf{c}^k/(\partial \alpha_i)$ allows the system to be simplified and rearranged for solution of the new, unknown sensitivity based on the previous sensitivities and computed Jacobians according to (4.13).

$$\beta(G)\mathbf{w}_i^{k+1} = -\frac{\partial\beta(G)}{\partial\alpha_i}\mathbf{c}^{k+1} + D_c(M_1)\mathbf{w}_i^k + D_{\alpha_i}(M_1) + D_c(M_2)\mathbf{w}_i^{k-1} + D_{\alpha_i}(M_2) \quad \textbf{(4.13)}$$

The three time-level scheme requires two sets of initial values at times k and $k-1$. Results herein have cold start initial conditions, where the initial elevation and velocity fields are zero throughout the domain. The initial conditions do not depend on G; therefore, the initial conditions for the sensitivity, to each α_i coefficient, are vectors, $\mathbf{w}_i^{-1}, \mathbf{w}_i^0 \in R^{2n}$ containing only zeroes.

Application of the chain rule, $\frac{\partial}{\partial\alpha_i} = \frac{\partial}{\partial G}\frac{\partial G}{\partial\alpha_i}$, when taking the derivative with respect to α_i, simplifies calculations. The derivative with respect to G is independent of the parameterization, so it is the same for each of the coefficients. Therefore, increasing the complexity of the parameterization for G is simple.

4.4 Set-Up for Tidal Problem on East Coast Domain

The parameters for the test case are outlined in Table 4.1 and the domain is shown in Figure 4.1. The domain is the east coast domain utilized in Chapter 2. Simulations were run for 3.0 days with results (elevations, velocities and sensitivities) recorded every 5.0 minutes (60 time steps). The bathymetry value for the first 49 nodes in the domain is 5000 m. The bottom elevation rises up to a bathymetry value just above 4000 m over the next 5 nodes. The rise continues dramatically over the next four nodes, with the bathymetry value being just under 200 m at node 58. This change in bathymetry is representative of the continental rise off the east coast of the United States. The minimum bathymetry value, 20.0 m, occurs at node 65, on the right boundary of the domain. This domain allows for a reasonable solution using the non-linear equations with a linear specified elevation boundary condition because the non-linear terms are not significant near the open boundary.

Table 4.1 Parameters for east coast domain test case.

Parameter	Value
Number of nodes	65
Domain length	2000 km
Δx	31.25 km
τ	0.001 s^{-1}
Forcing amplitude	1.0 m
Forcing period	44714.8 s
Time step	5.0 s
Ramp duration	1.0 days

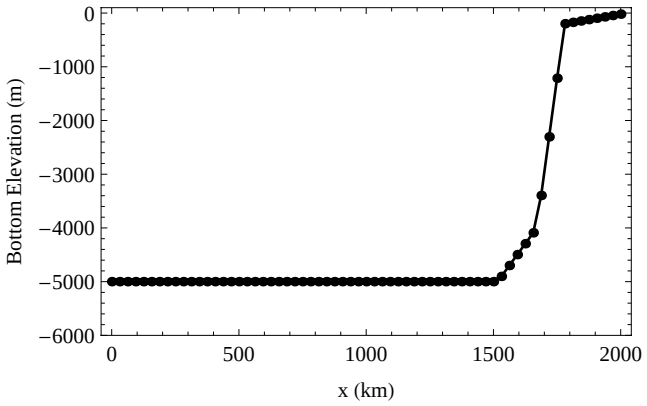

Figure 4.1 Bathymetry and node locations for east coast domain.

The time step and simulation duration were not arbitrary choices. Ten-day simulations were performed with a constant value of $G = 0.001\ s^{-1}$ with different time step values. Results show the sensitivities do not vary significantly, from forcing period to forcing period, after the ramp phase, as seen in Figure 4.2. There is a small disturbance at the end of the ramp phase (1.0 days into the simulation) due to a small, abrupt jump in the forcing resulting from the equation used in the ramp function. However, it quickly dissipates. Thus, a three-day simulation, using results from the last day for analyses, is long enough that the initial condition and ramp do not play any role in the results. The sensitivities were also used to determine the time step. The sensitivities were almost identical for the runs with $\Delta t = 2.5$ s and $\Delta t = 5.0$ s, as seen in Figure 4.3. However, when the time step was increased, the sensitivities started to diverge, as shown in Figure 4.4, which compares results with $\Delta t = 5.0$ s and $\Delta t = 10.0$ s.

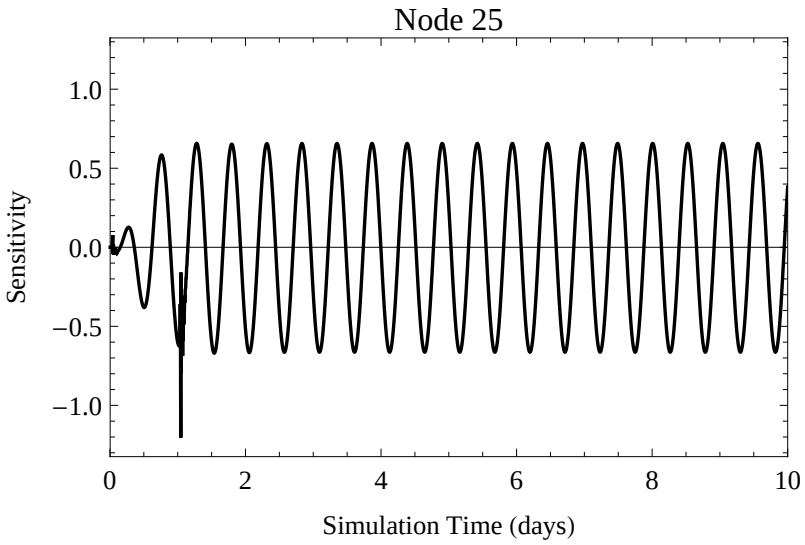

Figure 4.2 FSM elevation sensitivities to α_0 for a simulation with $G = \alpha_0$, where $\alpha_0 = 0.001$ s^{-1} at node 25 in the east coast domain.

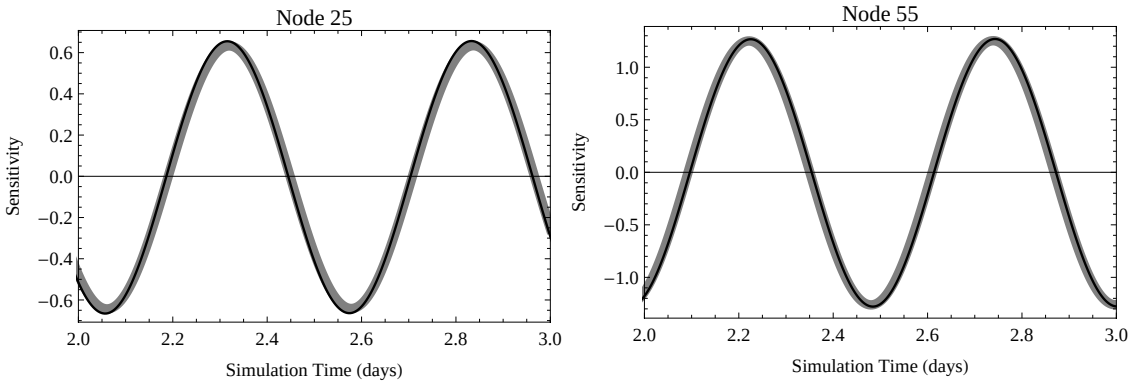

Figure 4.3 FSM elevation sensitivities to α_0 for a simulation with $G = \alpha_0$, where $\alpha_0 = 0.001$ s^{-1}. The black line shows results from a simulation with a time step of 5.0 s, while the gray line shows results using 2.5 s for the time step.

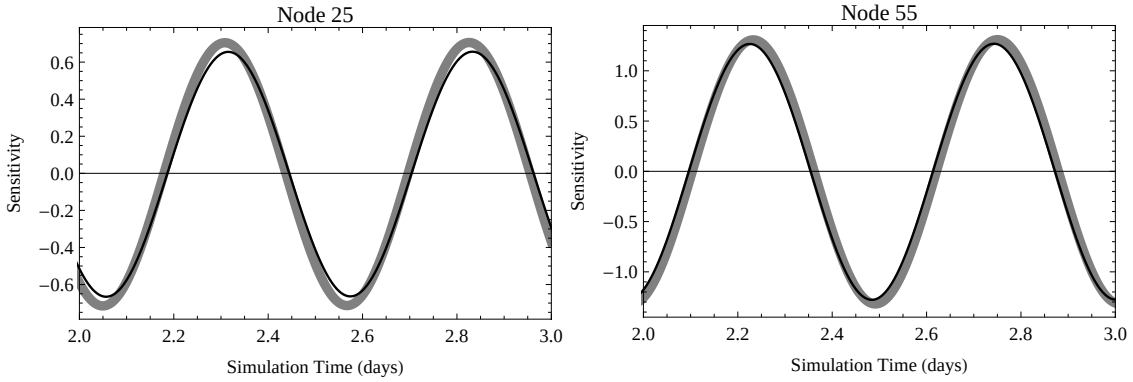

Figure 4.4 FSM elevation sensitivities to α_0 for a simulation with $G = \alpha_0$, where $\alpha_0 = 0.001$ s^{-1}. The black line shows results from a simulation with a time step of 5.0 s, while the gray line shows results using 10.0 s for the time step.

4.5 Sensitivity for Tidal Problem on East Coast Domain

The G parameterization requires sensitivity to G to be analyzed in terms of sensitivity of the solution to the coefficients in the parameterization. Therefore, for the initial analysis of the non-linear, variable G simulations, attempts will be made to isolate individual coefficients to determine their influence. For example, sensitivity to α_0 will be analyzed first, with α_1 and α_2 set to zero. This G parameterization is simply the constant G parameterization, addressed in the previous chapter, applied to the non-linear system. Then, with α_0 held constant, sensitivity to α_1 will be assessed. Finally, with the first two coefficients held constant, the sensitivity to α_2 will be examined. However, before the sensitivity studies commence, comparisons will be made between the FSM sensitivities and the numerical analog sensitivities to verify that the sensitivities predicted by the FSM, for the case under investigation, match the numerical analogs when small perturbations are applied to the coefficient values.

4.5.1 Comparison Between FSM and Numerical Analog Sensitivities

To compare the FSM sensitivities to the numerical analog sensitivities, a base run was performed using the following parameter set: $\alpha_0 = 0.001\ \mathrm{s}^{-1}$, $\alpha_1 = 0.1\ \mathrm{m/s}$, $\alpha_2 = 0.1\ \mathrm{m}^{-1}$. The coefficients have different units in order to make the units, s^{-1}, for each of the terms in the variable G parameterization consistent. Then, each of the coefficients were perturbed, one each run, and the numerical analog sensitivities were calculated. The numerical analog sensitivity for α_0 is computed using finite differences according to (4.14).

$$\frac{\partial \zeta_j^k}{\partial \alpha_0} = \frac{\zeta(G(\alpha_0 + \Delta\alpha_0, \alpha_1, \alpha_2))_j^k - \zeta(G(\alpha_0, \alpha_1, \alpha_2))_j^k}{\Delta\alpha_0} \quad \textbf{(4.14)}$$

The numerical analog sensitivities to other parameters are computed as in (4.14) with different $\Delta\alpha_i$ values. The perturbations, $\Delta\alpha_i$, were one-tenth of the value of coefficients used in the base run (e.g., $\Delta\alpha_0 = 0.0001\ \text{s}^{-1}$). For each case, the elevation sensitivities are shown for node 25 (the mid-point of the deep, flat portion of the domain), node 55 (on the continental rise), node 58 (at the transition from the rise to the shelf) and node 62 (on the shelf). The units for the sensitivities vary. The units for the elevation sensitivities to $\alpha_0, \alpha_1, \alpha_2$ are ms, s, m^2, respectively.

The comparisons between the FSM and numerical analog (forward) sensitivities are shown in Figure 4.5 (α_0), Figure 4.6 (α_1), and Figure 4.7 (α_2). In each of the plots, the

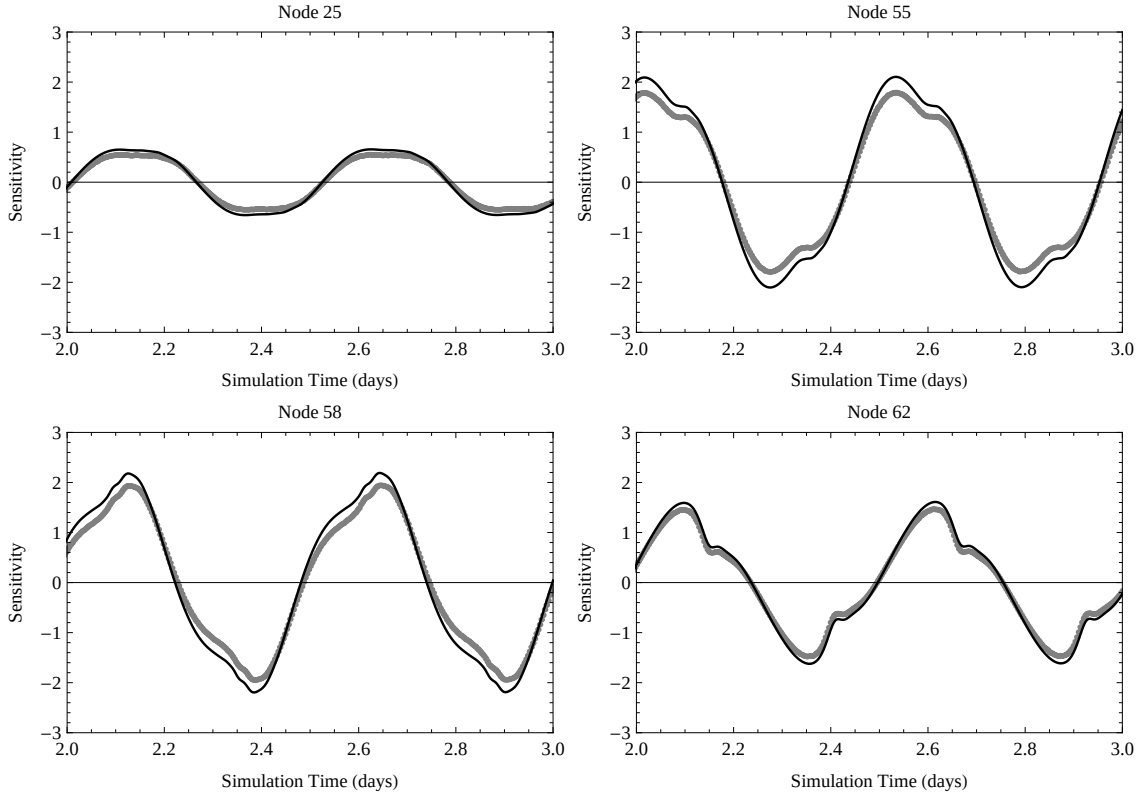

Figure 4.5 Comparison of FSM (black) and numerical analog (gray) elevation sensitivities to α_0 in the variable *G* parameterization at various nodes in the east coast domain.

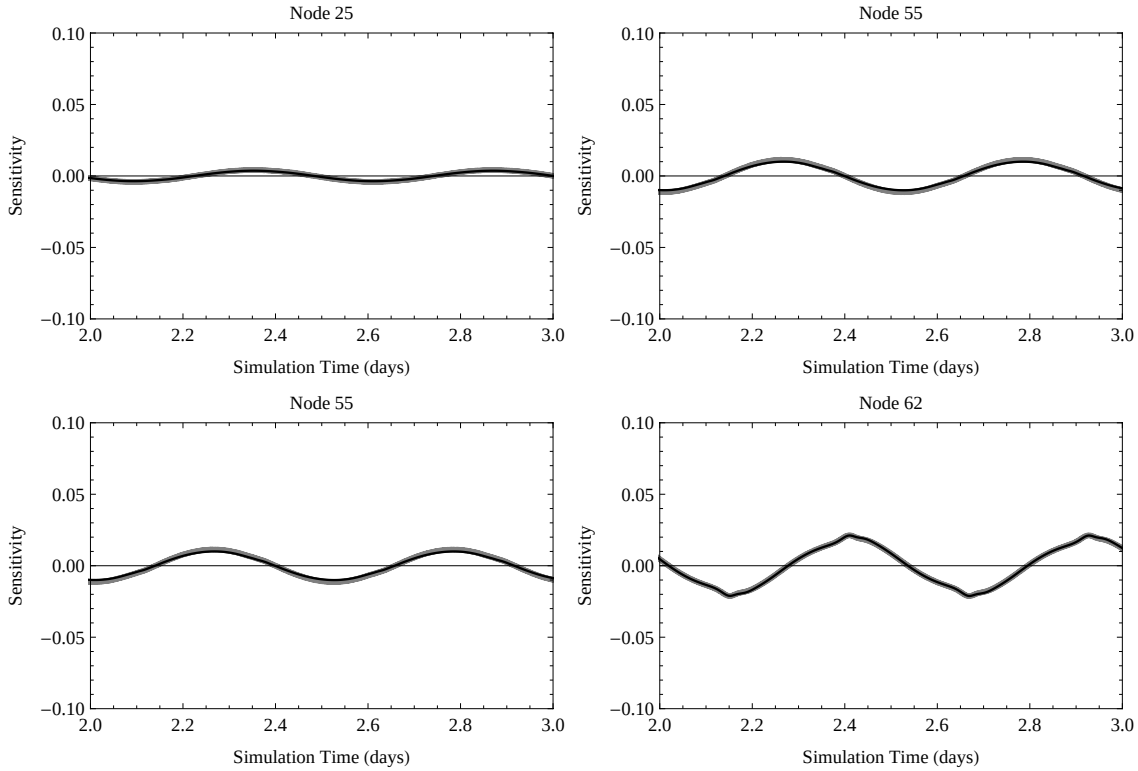

Figure 4.6 Comparison of FSM (black) and numerical analog (gray) elevation sensitivities to α_1 in the variable G parameterization at various nodes in the east coast domain.

black line shows the evolution in time of the FSM sensitivity to a given coefficient. The gray line shows the numerical analog sensitivity to the same coefficient.

The comparison shows that the sensitivities are very similar. As expected, based on results from the previous chapter, the numerical analog sensitivity to the constant coefficient is slightly lower than the same FSM sensitivity. This is a result of the use of the forward numerical analog because the magnitude of the sensitivity to constant G decreases as the constant G value increases, and the magnitude of the difference between the two is a function of the step size. However, in the comparisons of the sensitivity to both α_1 and α_2, the numerical analog is generally larger (in magnitude) than the FSM sensitivity. This suggests the sensitivity to these coefficients increases as their value is increased, at least in the range examined in this comparison. These sensitivities will receive more attention later

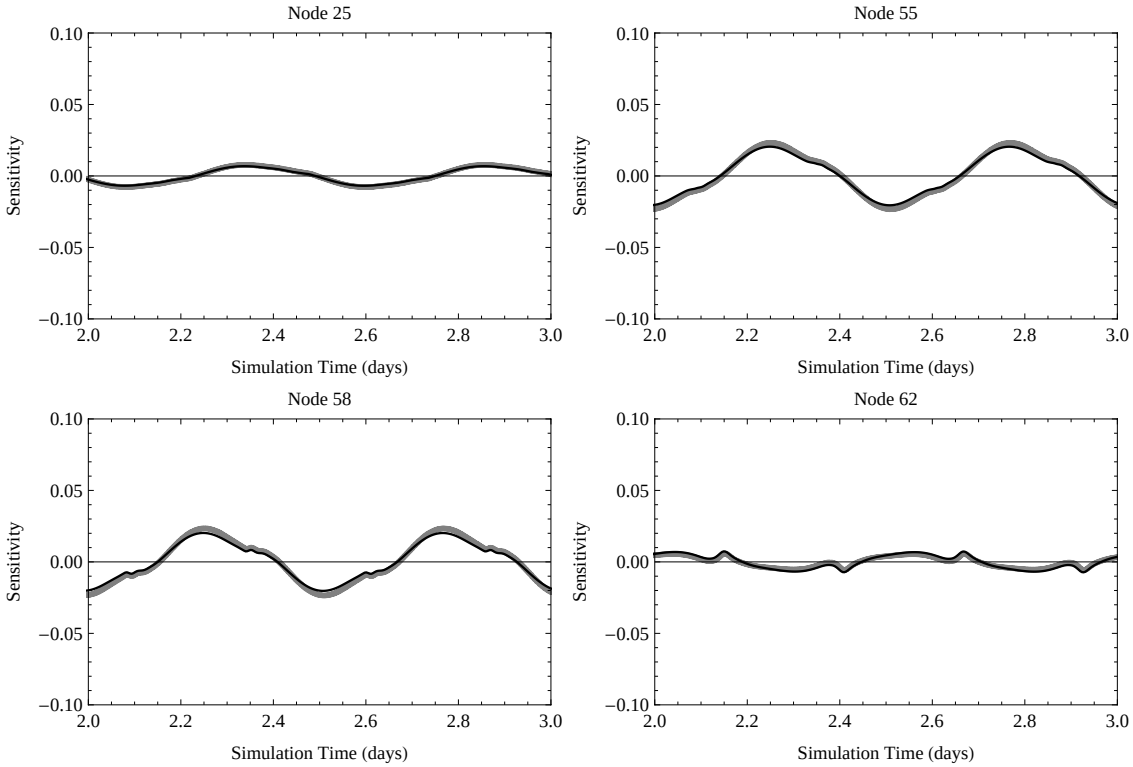

Figure 4.7 Comparison of FSM (black) and numerical analog (gray) elevation sensitivities to α_2 in the variable G parameterization at various nodes in the east coast domain.

in this section.

The sensitivities to each of the coefficients in the parameterization for G have different units, which makes intercomparison difficult. However, we can use the chain rule to normalize the sensitivities. For the elevation sensitivities, application of the chain rule results in (4.15).

$$\frac{\partial \zeta}{\partial \alpha_i} = \frac{\partial \zeta}{\partial G}\frac{\partial G}{\partial \alpha_i} \tag{4.15}$$

The normalized sensitivity, $(\partial\zeta)/(\partial G)$, due to change in a coefficient, α_i, can be calculated, as in (4.16), by dividing the sensitivity of the elevation or velocity to the coefficient by the sensitivity of G to the coefficient.

$$\left.\frac{\partial \zeta}{\partial G}\right|_{\alpha_i} = \left(\frac{\partial \zeta}{\partial \alpha_i}\right) \Big/ \left(\frac{\partial G}{\partial \alpha_i}\right) \tag{4.16}$$

The normalized sensitivities have the same units as the sensitivities to the constant G term, α_0. The units for the normalized elevation sensitivities are ms. A comparison of normalized sensitivities is shown at the beginning of Section 4.5.3.

4.5.2 Sensitivity to α_0

The sensitivity to the constant coefficient, α_0, was assessed with the other coefficients set to zero, resulting in a constant G parameterization. Results from five simulations, with $\alpha_0 = \{0.0001, 0.001, 0.01, 0.1, 1.0\}\ \text{s}^{-1}$, are shown. Use of constant G values less than or equal to $10^{-5}\ \text{s}^{-1}$, with the explicit discretization, results in instability at the current time step size.

The FSM elevation sensitivity to α_0, for nodes 25, 55, 58 and 62 is shown in Figure 4.8. This type of graph is explained thoroughly in Section 3.3.3. The results are consistent with the linear, constant G results presented in Chapter 3. Specifically, the magnitude of the sensitivity decreases with increase in α_0. Additionally, there is a phase shift between sensitivities for the simulations with the lowest α_0 values (the darkest line) and those with slightly higher values. Furthermore, while most of the sensitivities approximately line up vertically at node 55, this is not the case at nodes 58 and 62. The curves for the simulations with the highest α_0 values become shifted out from underneath the curves for the simulations with lower values. This suggests the highest α_0 values are in the "too primitive" range. This concept is discussed in detail in Section 3.3 and Section 3.4 of the previous chapter, but is reviewed briefly below.

Locations where $2\Delta x$ oscillations in the sensitivities may exist can be found by

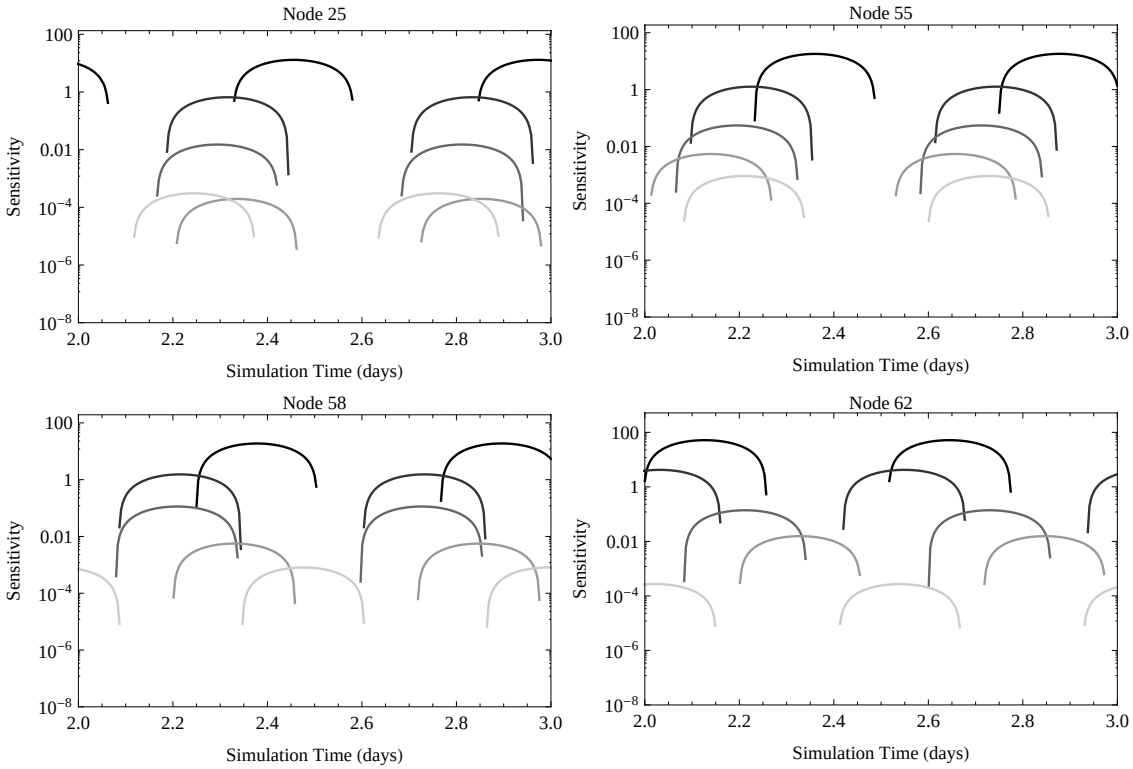

Figure 4.8 FSM elevation sensitivities to α_0 at nodes 25, 55, 58 and 62 in the east coast domain for simulations with α_0 = {0.0001, 0.001, 0.01, 0.1, 1.0} s^{-1}. The darkest line corresponds to the lowest coefficient value. The lines get progressively lighter for each increase in α_0.

overlaying plots of sensitivities for successive nodes. In a regular sensitivity plot, a primitive G value will result in the sensitivities for consecutive nodes being approximately mirror images of each other. On a logarithmic plot, the negative sensitivities are neglected because the minimum value on the plot is greater than zero. Therefore, on logarithmic plots there are gaps in the curves when the sensitivities drop out of the range of the plot. The elevation sensitivities to α_0 for the node pair (25,26) are shown for a range of α_0 values in Figure 4.9. For the lowest α_0 values (which have the largest magnitude sensitivities), there is not very much node-to-node variation in sensitivity. Therefore, the curves for nodes 25 and 26 are very similar and plot close to one another. At nodes 25 and 26, the sensitivities are nearly indistinguishable for α_0 values from 0.0001 to 0.01 s^{-1}. On the other hand, by overlaying curves for multiple nodes on the same logarithmic plot, if the sensitivities at

successive nodes are mirror images, the gap in the curve for one node will be filled by the positive values from the adjacent node, suggesting short-wavelength oscillations. With $\alpha_0 = 1.0\ s^{-1}$, the gap in the lines for node 25 is almost perfectly filled by the lines for the sensitivities at node 26.

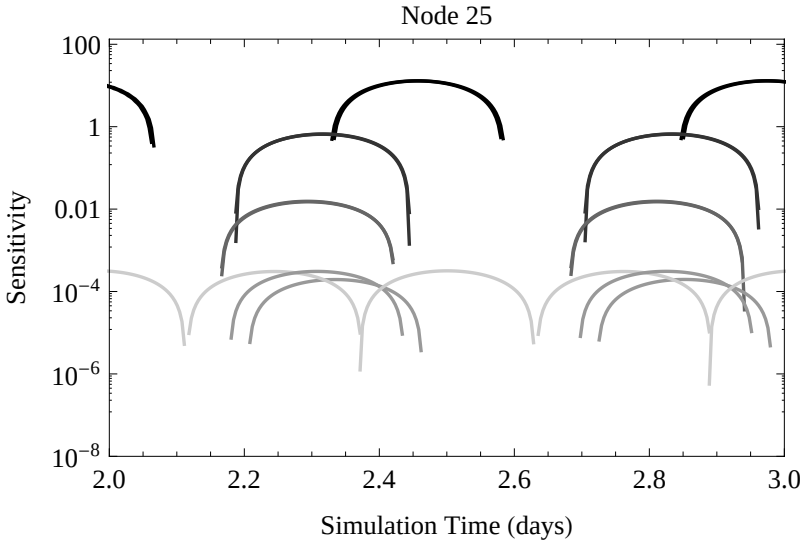

Figure 4.9 FSM elevation sensitivities to α_0 for the node pair (25,26) in the east coast domain for simulations with $\alpha_0 = \{0.0001, 0.001, 0.01, 0.1, 1.0\}\ s^{-1}$. The darkest line corresponds to the lowest coefficient value. The lines get progressively lighter for each increase in α_0.

The FSM elevation sensitivities to α_0 for successive nodes are plotted in Figure 4.10. The node number listed on each of the graphs is the lower node number in the pair (e.g. "Node 25" is the label for the comparison of nodes 25 and 26). For the first pair (nodes 25 and 26), the sensitivities for the three lowest α_0 values are almost indistinguishable. For the second lightest line, from the simulation with $\alpha_0 = 0.1\ s^{-1}$, the peak magnitude of the sensitivity is different, suggesting the parameterization is resulting in G becoming "too primitive." The highest α_0 value is certainly well beyond the primitive threshold. As described above, the gaps for one node are almost perfectly filled by the curve for the next node which signifies a node-to-node oscillation in sensitivity.

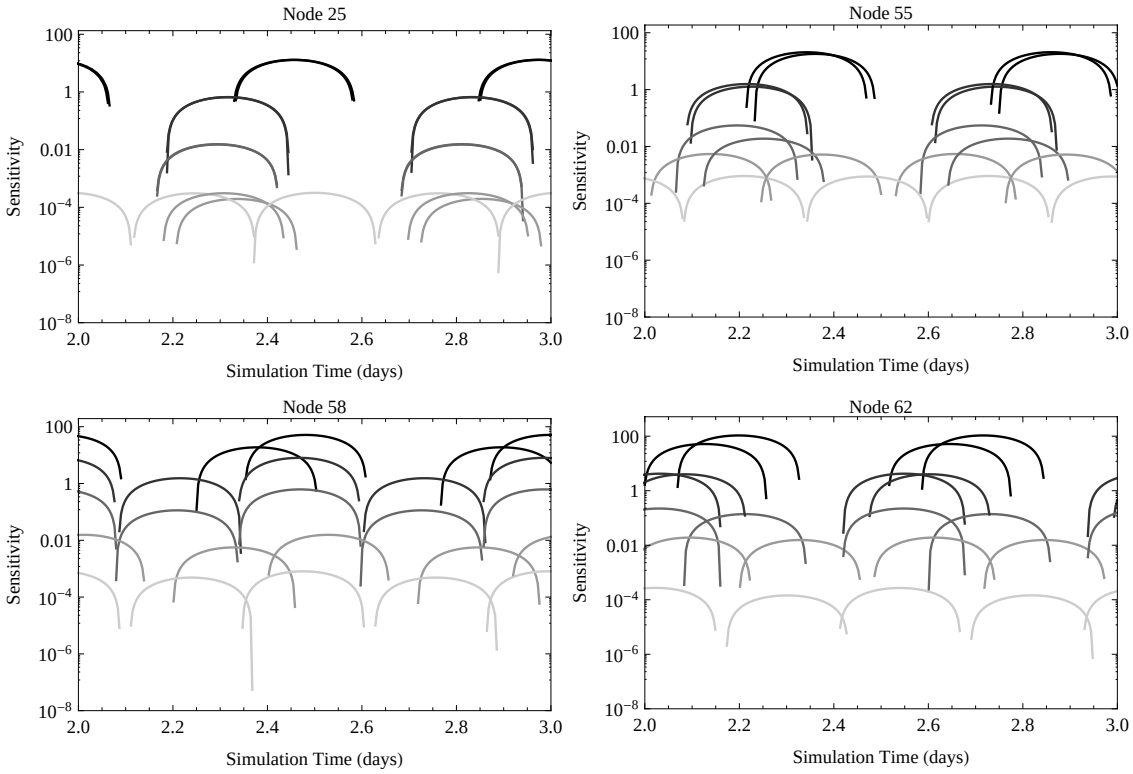

Figure 4.10 FSM elevation sensitivities to α_0 at successive node pairs: (25, 26), (55, 56), (58, 59) and (62,63) in the east coast domain for simulations with α_0 = {0.0001, 0.001, 0.01, 0.1, 1.0} s^{-1}. The darkest line corresponds to the lowest coefficient value. The lines get progressively lighter for each increase in α_0.

For the next pair of nodes, 55 and 56, the sensitivities for the two lowest α_0 values are also similar. With an α_0 value of 0.01 s^{-1}, the sensitivities have different magnitudes, which indicates the G value is becoming "too primitive." The two highest α_0 values show the classic node-to-node oscillation resulting from the G value becoming too large.

Skipping ahead to the last set of nodes, 62 and 63, the results for $\alpha_0 = 0.001$ s^{-1} look the best. There is very little phase shift between the nodes and the peak magnitudes are almost exactly the same. Once again, the sensitivities for the values of α_0 greater than or equal to 0.01 s^{-1} are almost exactly 180 degrees out-of-phase for successive nodes. For the lowest α_0 value, there are phase and magnitude differences that are larger than with $\alpha_0 = 0.001$ s^{-1}. This implies that some values of G may be too small, which is evident

because there is a G threshold between 10^{-5} and 10^{-4} s^{-1} below which runs are unstable.

Comments on the results for nodes 58 and 59, near the shelf break, were saved for last because of the seemingly aberrant results. For this pairing, the sensitivity results for $\alpha_0 = 0.001$ s^{-1} suggest a constant value of 0.001 s^{-1} is too large because the sensitivities at nodes 58 and 59 have opposite signs. However, analysis of the actual elevation results at this point suggests this is the correct behavior of the sensitivities. Additionally, while there is a node-to-node oscillation, there is not a $2\Delta x$ oscillation. Specifically, the opposite signs occur for consecutive nodes only for the 58-59 pairing. The signs are the same for node pairs 57-58 and 59-60. Thus, there is not a pattern of $2\Delta x$ oscillations, there is just one sign swap between nodes 58 and 59. The consistency of the FSM elevation sensitivity results is apparent by looking at the results for the last four nodes on the continental rise, which are shown in Figure 4.11.

Close inspection shows that the signs are consistent, although the magnitudes of the sensitivities are not. However, while the magnitudes are different, they do not follow a $2\Delta x$ pattern either. The magnitude of the sensitivities at nodes 56 and 58 are similar, while the magnitude at node 55 is the lowest of the four nodes and the magnitude is largest at node 57. The results on the continental shelf (node numbers 58 and larger) are also consistent in sign between nodes for $\alpha_0 = 0.001$ s^{-1}, rather than being plagued by $2\Delta x$ oscillations that occur with higher constant G values.

4.5.3 Sensitivity to α_1

Before delving into an analysis of sensitivity to the first coefficient on the variable terms in the G parameterization, it is worthwhile to revisit the idea of normalized sensi-

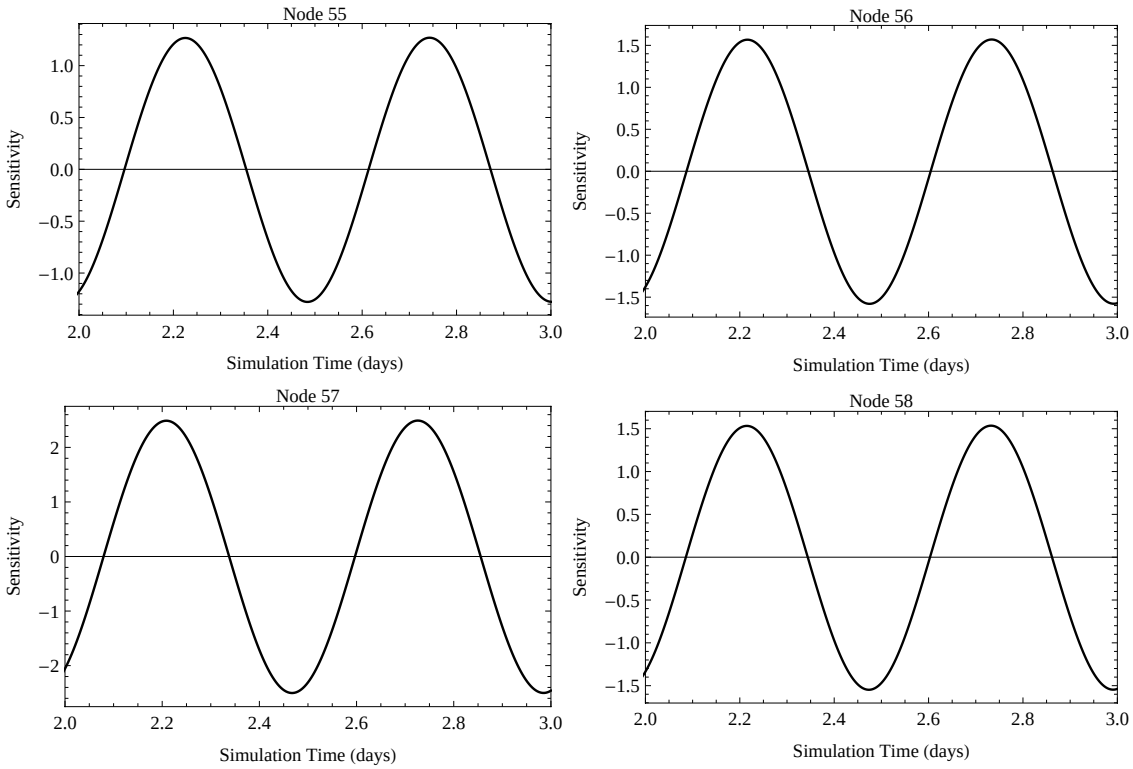

Figure 4.11 FSM elevation sensitivities to α_0 at nodes 55, 56, 57 and 58 in the east coast domain for the simulations with $\alpha_0 = 0.001$ s^{-1}.

tivity. The second term in the G parameterization, α_1 / H, varies over orders of magnitude in the east coast domain because the bathymetry varies by a factor of 250 from the open boundary to the land boundary. The term also varies temporally, as the elevations change, but the temporal variation is minimal, especially in the deep portions of the domain. Therefore, the term involving α_1 essentially increases G in the shallow areas of the domain while allowing it to stay at a low value in deep areas. Thus, the comparison of normalized sensitivities to α_0 or α_1, while the other two parameters are held at zero, is fairly straightforward. In contrast, attempting to use only α_2, while holding the other coefficients at zero, would prove difficult due to the presence of occasional instances where the velocity is zero, which would result in a zero G value. Furthermore, the magnitude of the velocity at a node is not approximately constant throughout the simulation.

Two simulations were performed using α_1 values of 5.0 and 0.1 m/s, with the other coefficients set to 0.0. These values were chosen so that areas of the domain would have G values of approximately 0.001 s^{-1}, making them comparable to the constant G results with $\alpha_0 = 0.001\ s^{-1}$. The larger α_1 value results in a G value of approximately 0.001 s^{-1} in the deep portion of the domain and 0.050 s^{-1} on the shelf, while the smaller value results in a G value on the order of 0.001 s^{-1} in the shallow areas and 0.00002 s^{-1} in the deep portion of the domain. Comparisons for the two simulations using only α_1 values to sensitivities to constant G runs with an α_0 value of 0.001 s^{-1} ($\alpha_1, \alpha_2 = 0.0$) are shown in Figure 4.12 (deep area equivalence) and Figure 4.13 (shallow area equivalence), respectively.

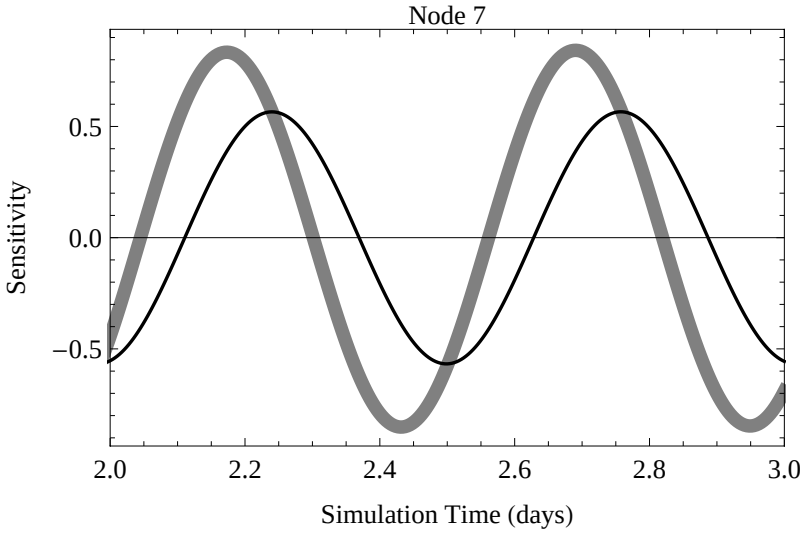

Figure 4.12 Comparison of normalized FSM elevation sensitivities at node 7 in the east coast domain for simulations with $G = \alpha_0$, where $\alpha_0 = 0.001\ s^{-1}$ (black); and $G = \alpha_1 / H$, where $\alpha_1 = 5.0$ m / s (gray).

The sensitivities are not equivalent for the simulations because, while the coefficient selection results in similarities in G for certain portions of the domain, there are portions of the domain where the G value differs greatly between the two simulations. Using the higher α_1 value, the relatively high G in the shallow portion of the domain

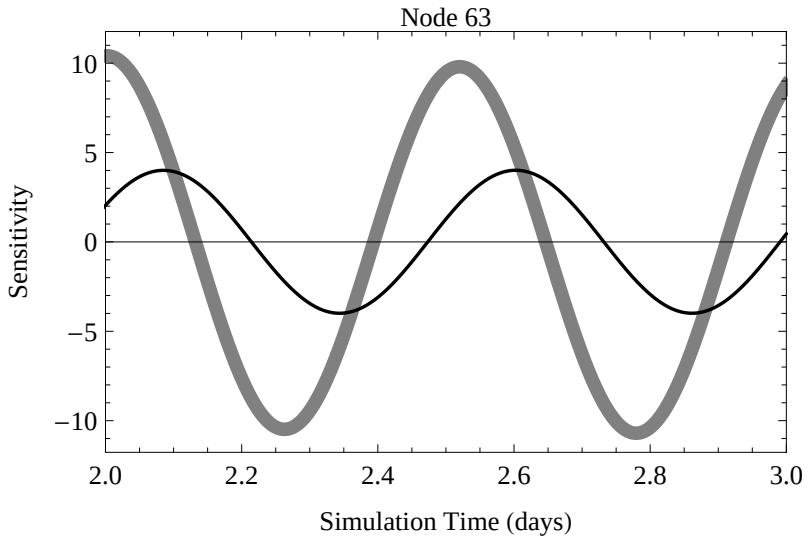

Figure 4.13 Comparison of normalized FSM elevation sensitivities at node 63 in the east coast domain for simulations with $G = \alpha_0$, where $\alpha_0 = 0.001$ s^{-1} (black); and $G = \alpha_1 / H$, where $\alpha_1 = 0.1$ m / s (gray).

results in the normalized sensitivity being much lower in that region than for the constant G case. However, despite G values around 0.025-0.25 s^{-1} on the shelf, the sensitivities do not suggest that the G parameterization is "too primitive," which would be the case if a value in that range was applied to the entire domain.

With the lower α_1 value, the sensitivities are similar on the shelf. However, the sensitivities to G for the simulation using the lower α_1 value are much larger in the deep ocean and continental rise portions of the domain than they are for the run with the constant $\alpha_0 = 0.001\ s^{-1}$. This is a consequence of the G value being approximately 0.00002 s^{-1} in the deep ocean. However, the normalized sensitivity, shown in Figure 4.12 and Figure 4.13, allows a reasonable comparison to be made on the sensitivity to G based on a change in a given coefficient value, whereas comparisons of the actual sensitivities to the change in the parameters would be difficult due to the dimensional issues.

In fact, with some idealized test cases, the normalized sensitivities are nearly iden-

tical. This is the case when a simulation is performed on a flat bottom domain with a constant bathymetry value of 5000 m. Using a constant G value of 0.001 s^{-1}, the normalized sensitivity to α_0 and α_1 is the same throughout space and time. This makes sense because, whether you change α_0 or α_1 to modify G by ΔG, the resulting elevation and velocity fields should be practically equivalent because the bathymetry is the same throughout the domain, hence G is approximately constant. Note this is because the ratio $(\Delta H)/H$ is small.

In general, increases in α_1 do not change G by a constant amount throughout the domain. Therefore, even when the sensitivity is normalized, the simulation dynamics related to the sensitivity to G result in the sensitivities to α_0 and α_1 behaving very differently. Sensitivities are almost the same for very early times during the ramp period (starting from zero, which is the initial sensitivity due to the cold start initial conditions), but they quickly diverge as time continues.

Simulations to assess the sensitivity to the second coefficient in (4.10), α_1, were performed with α_0 set to either 0.0001 s^{-1} or 0.001 s^{-1} and α_2 held at zero. The α_0 values used as the base values are in the stable range, and they are below the threshold where the GWCE becomes "too primitive." For each of the base values, the following set of α_1 values was used: $\{0.1, 1.0, 10.0, 100.0, 1000.0\}$ m/s. For these sets of simulations, the regular (not normalized) sensitivities to α_1 will be shown. While the normalized sensitivities are useful for comparing sensitivities to different coefficients, they can be misleading when comparing how the elevation (or velocity) field is impacted by changes to one coefficient. For instance, if the time series of the elevation sensitivity to α_1 is the same at every node in a domain, we expect a consistent change to the elevation based on

change in α_1. However, if the normalized sensitivities are examined, the time series will differ for different nodes because the water depth varies in space (assuming a constant bathymetry domain is not being used).

The sensitivities for the four node pairs shown previously, {(25, 26), (55, 56), (58, 59), (62, 63)}, are shown in Figure 4.14. The constant coefficient value for these simulations is $\alpha_0 = 0.0001\ s^{-1}$ and the α_1 values are $\{0.1, 1.0, 10.0, 100.0, 1000.0\}\,m/s$. The results for the first pair of nodes are consistent with other nodes in the deep portion of the domain. There is little node-to-node variation in sensitivity to α_1 for all but the highest coefficient value.

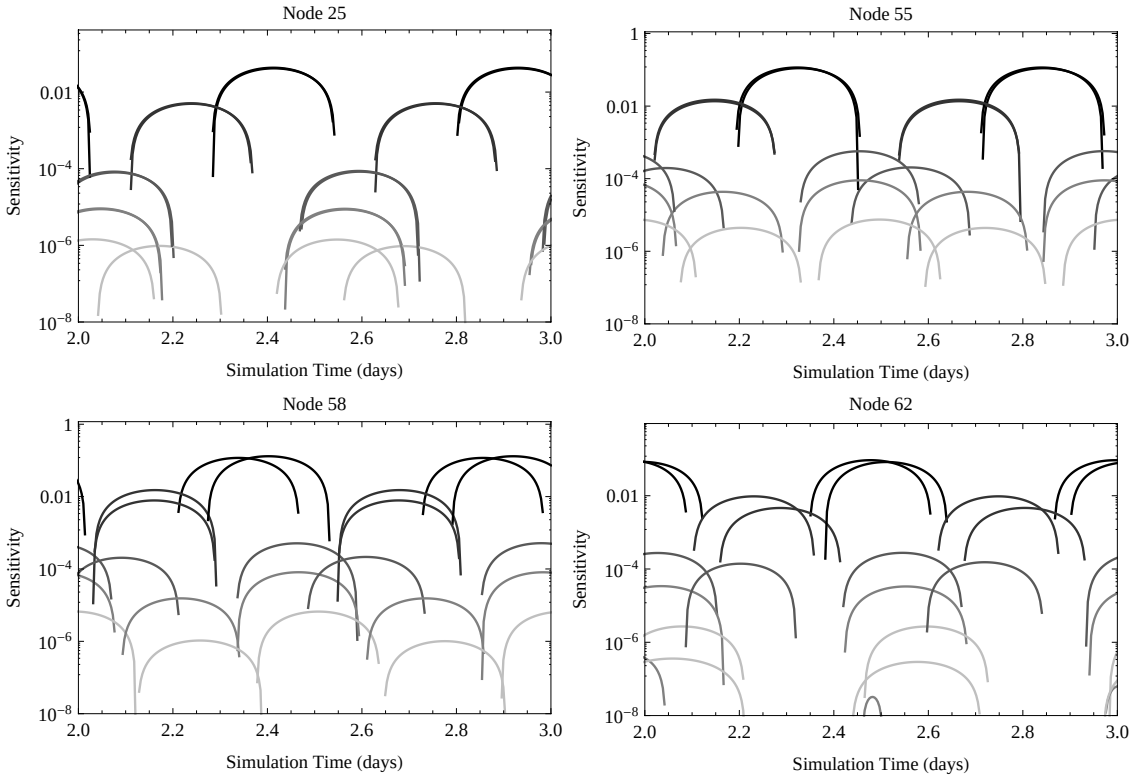

Figure 4.14 FSM elevation sensitivities to α_1 at successive node pairs: (25, 26), (55, 56), (58, 59) and (62,63) in the east coast domain for simulations with $\alpha_0 = 0.0001\ s^{-1}$ and $\alpha_1 = \{0.1, 1.0, 10.0, 100.0, 1000.0\}$ m / s. The darkest line corresponds to the lowest coefficient value and the lines get progressively lighter for each increase in α_1.

For the next set of nodes (55 and 56), $2\Delta x$ oscillations are seen for the two highest α_1 values, while the sensitivities remain consistent between nodes for the two lowest α_1 values. The two pairs of nodes on the shelf show a similar behavior to the pair on the rise. However, the oscillations for node 62 and 63 are in the magnitude of the sensitivity at the highest α_1 values, rather than being out-of-phase like the sensitivities for nodes 55 and 56. This suggests an upper limit of α_1 between 1.0 and 10.0 m/s for this application, when a constant value of 0.0001 s^{-1} is used, to avoid generation of spurious oscillations.

Results for the same four node pairs and the same range of α_1 values, with an α_0 value of 0.001 s^{-1}, are shown in Figure 4.15. Again, for the deep portions of the domain, only the highest α_1 value produces $2\Delta x$ oscillations in the sensitivities. The sensitivities for the two lowest α_1 are almost identical. This is due to the constant, base G value being larger than in the previous set of simulations, which results in the lowest α_1 values not producing a significant change to the overall G value. In the deep portions of the domain, the bathymetry is 5000 m, so the α_1/H term is on the order of 0.00002 s^{-1} for the lowest α_1 value and 0.0002 s^{-1} when $\alpha_1 = 1.0\ m/s$. Thus, the total G value is close to the α_0 value for those two runs, whereas the α_1/H term is greater than the α_0 term throughout the domain when any of the three highest α_1 values are used.

However, over the continental rise and landward, $2\Delta x$ oscillations in the sensitivities occur in the results for the three highest α_1 values. The sensitivities for the two lowest α_1 values become different as the domain gets more shallow. Also, comparing the results for the simulations with $\alpha_1 = 10.0\ m/s$ for the two base G coefficient values, the G parameterization appears to be more primitive (due to the sensitivities being 180 degrees out-of-phase) with $\alpha_0 = 0.001\ s^{-1}$ than with $\alpha_0 = 0.0001\ s^{-1}$.

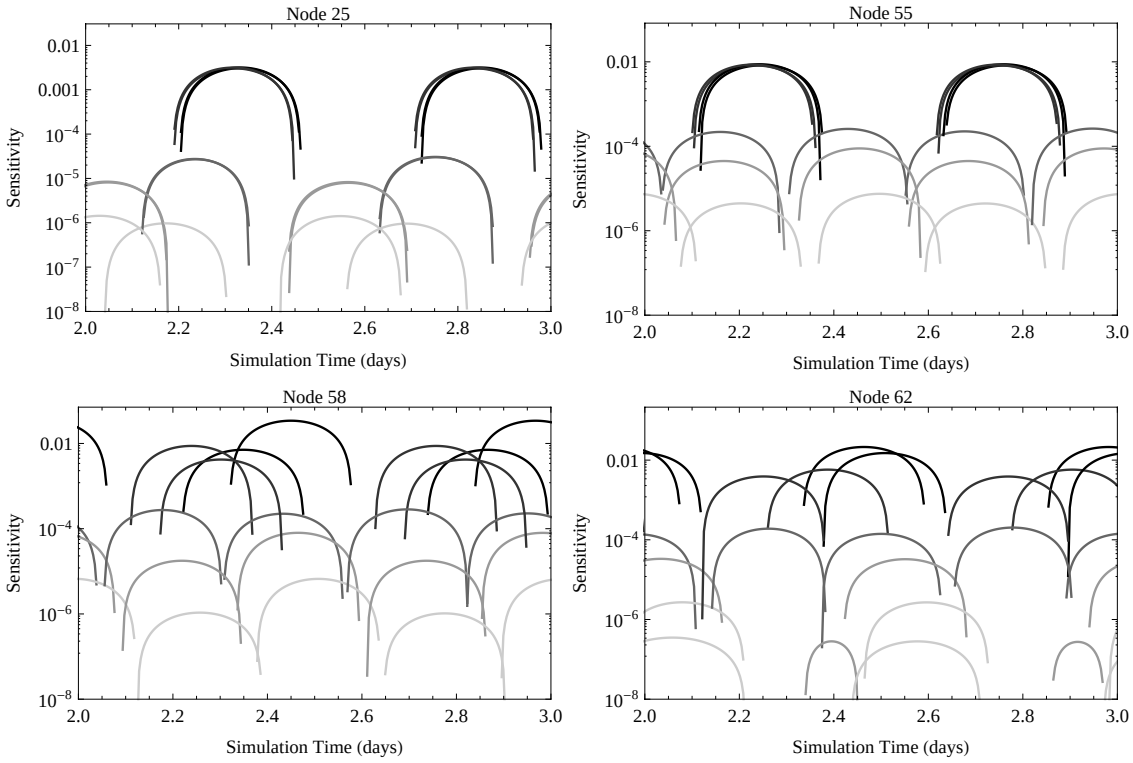

Figure 4.15 FSM elevation sensitivities to α_1 at successive node pairs: (25, 26), (55, 56), (58, 59) and (62,63) in the east coast domain for simulations with $\alpha_0 = 0.001$ s^{-1} and $\alpha_1 = \{0.1, 1.0, 10.0, 100.0, 1000.0\}$ m / s. The darkest line corresponds to the lowest coefficient value and the lines get progressively lighter for each increase in α_1.

4.5.4 Sensitivity to α_2

The third coefficient was analyzed using two combinations for the first two coefficients. Both combinations had α_0 set to 0.0001 s^{-1}. The α_1 values differed for the two sets, with the lower value being 1.0 m/s and the higher value being 5.0 m/s, which is close to the threshold that results in G becoming "too primitive." Simulations were run with a wide range of α_2 values: $\{0.01, 0.1, 1.0, 10.0, 100.0\}$ m^{-1}. However, results will not be shown for the highest α_2 value because that coefficient value results in the simulation becoming unstable for both combinations of α_0 and α_1.

The results for the elevation sensitivities for the simulations with the lower α_1 value are shown in Figure 4.16, while the results for simulations with the higher α_1 value

are shown in Figure 4.17. The general trend is for the sensitivity to decrease as α_2 increases. However, as the plot for nodes 25 and 26 in Figure 4.16 shows, the sensitivity is larger with an α_2 value of 0.1 m^{-1} than with a value of 0.01 m^{-1}. The magnitude of the sensitivity is also greater when the lower α_1 value is used. Referring back to (4.10), a smaller α_1 value results in lower G values throughout the domain. Lower G values are generally associated with larger sensitivity magnitudes.

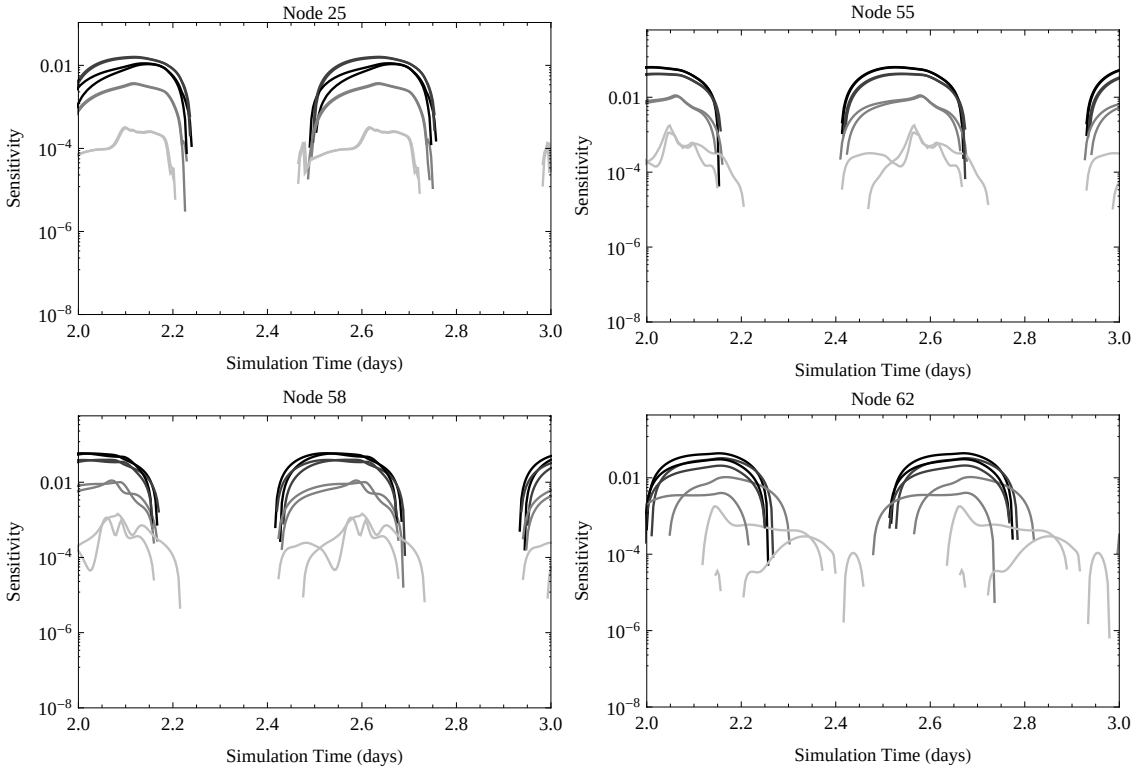

Figure 4.16 FSM elevation sensitivities to α_2 at successive node pairs, (25, 26), (55, 56), (58, 59) and (62,63), in the east coast domain for simulations with $\alpha_0 = 0.0001\ s^{-1}$, $\alpha_1 = 1.0\ m / s$ and $\alpha_2 = \{0.01, 0.1, 1.0, 10.0\}\ m^{-1}$. The darkest line corresponds to the lowest coefficient value and the lines get progressively lighter for each increase in α_2.

In general, the sensitivity results to α_2 do not show the precise 180° out-of-phase $2\Delta x$ oscillations seen previously for large α_0 and α_1 values, although more jagged oscillations can be seen in the results on the shelf for the higher α_2 values when the smaller α_1 value is used, as is evident in the comparison of nodes 62 and 63 in Figure 4.17 to the same

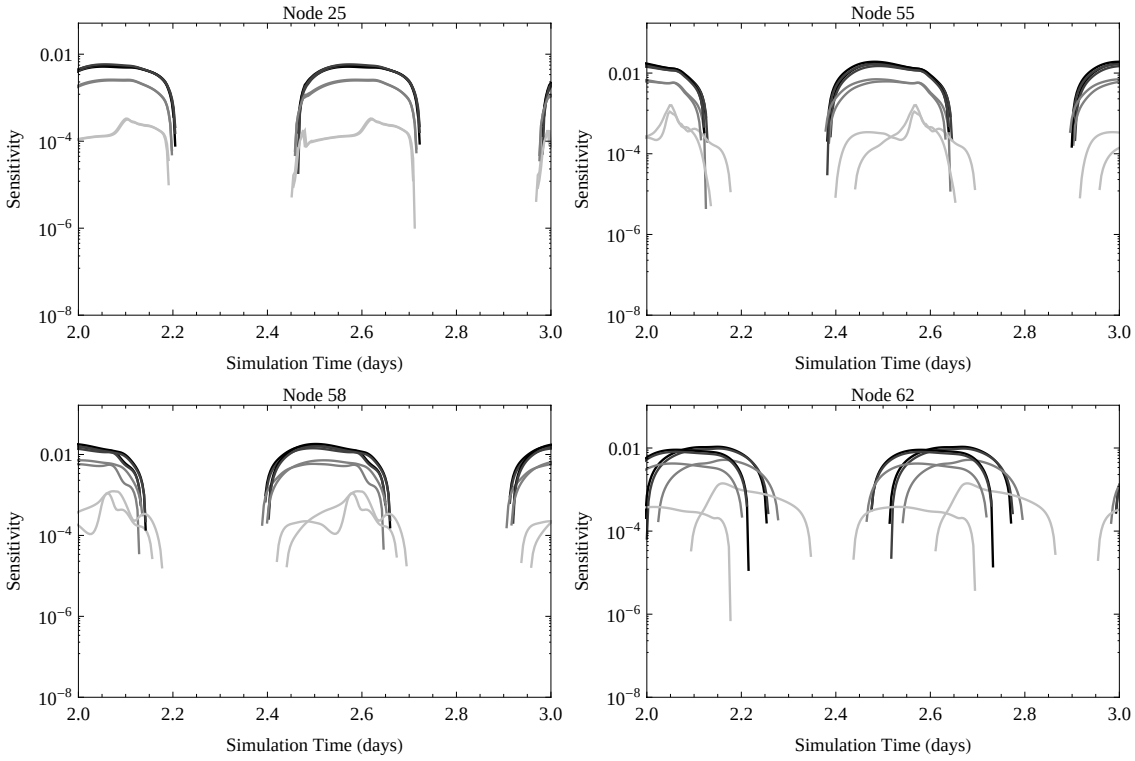

Figure 4.17 FSM elevation sensitivities to α_2 at successive node pairs, (25, 26), (55, 56), (58, 59) and (62,63), in the east coast domain for simulations with $\alpha_0 = 0.0001\ s^{-1}$, $\alpha_1 = 5.0$ m / s and $\alpha_2 = \{0.01, 0.1, 1.0, 10.0\}\ m^{-1}$. The darkest line corresponds to the lowest coefficient value and the lines get progressively lighter for each increase in α_2.

panel (lower right) in Figure 4.16. However, while higher α_2 values do not necessarily result in the G specification becoming "too primitive," the extreme variation of the sensitivities in time coupled with instability for the largest α_2 values suggests high values of α_2 may cause model instability.

4.6 Data Assimilation for Tidal Problem on East Coast Domain

The least-squares correction for the coefficients for the variable G formulation differs from the scalar parameter case of Chapter 3; it is given by (4.17) [*Lakshmivarahan* 2010], where ΔG is the optimal least-squares correction, $\mathbf{H}$ is the sensitivity matrix, and $\mathbf{z}$ is the error vector.

$$\Delta G = (\mathbf{H}^T\mathbf{H})^{-1}\mathbf{H}^T\mathbf{z} \tag{4.17}$$

A detailed derivation of the least-squares correction is provided in Chapter 5 of *Lewis et al.* [2006]. For completeness, the key steps will be included here.

The system currently under investigation is given in (4.18).

$$\mathbf{z} = \mathbf{H}(\Delta G) \tag{4.18}$$

The residual vector, $\mathbf{r}$, can be defined as the difference between $\mathbf{z}$ (the error vector) and $\mathbf{H}(\Delta G)$ (the product of the sensitivity and the correction, or change in the G parameterization coefficient vector) as in (4.19).

$$\mathbf{r} = \mathbf{z} - \mathbf{H}(\Delta G) \tag{4.19}$$

The least-squares problem is to find an ΔG that minimizes $f(\Delta G)$ in (4.20).

$$f(\Delta G) = \|\mathbf{r}\|^2 = \|\mathbf{z} - \mathbf{H}(\Delta G)\|^2 \tag{4.20}$$

Then, by choosing the Euclidean/2-norm, (4.20) becomes (4.21).

$$f(\Delta G) = (\mathbf{z} - \mathbf{H}(\Delta G))^T(\mathbf{z} - \mathbf{H}(\Delta G)) \tag{4.21}$$

By expanding and rearranging (4.21), the expression can be written in a quadratic form for ΔG. The new expression for the error norm is shown in (4.22).

$$f(\Delta G) = \mathbf{z}^T\mathbf{z} - 2\mathbf{z}^T\mathbf{H}(\Delta G) + (\Delta G)^T(\mathbf{H}^T\mathbf{H})(\Delta G) \tag{4.22}$$

Setting the gradient of the error norm to zero and equating the two remaining terms yields (4.23).

$$(\mathbf{H}^T\mathbf{H})(\Delta G) = \mathbf{H}^T\mathbf{z} \tag{4.23}$$

Finally, the optimal least-squares value, ΔG^*, is found by multiplying both sides by the inverse of $\mathbf{H}^T\mathbf{H}$, as shown in (4.24), which is essentially the same as (4.17).

$$\Delta G^* = (\mathbf{H}^T\mathbf{H})^{-1}\mathbf{H}^T\mathbf{z} \quad \textbf{(4.24)}$$

The least-squares correction attempts to minimize the gradient of the error of the Euclidean norm between the error vector and the product of the sensitivities to G and the G corrections.

4.6.1 Data Assimilation for Small Perturbation

In Section 4.5.1, the FSM sensitivities to each of the three coefficients in the G parameterization (α_0, α_1 and α_2) were compared to numerical analog sensitivities. In order to isolate the coefficients, they were perturbed by a small amount one at a time. The results from these simulations provide a good set by which to verify the effectiveness of multi-parameter correction estimations using the data assimilation step in the FSM because the multi-parameter corrections should have one dominant value and two that are close to zero for these perturbation sets.

The base values used for the parameterization of G are $\alpha_0 = 0.001\ \text{s}^{-1}$, $\alpha_1 = 0.1\ \text{m/s}$, and $\alpha_2 = 0.1\ \text{m}^{-1}$. In each case, the perturbation was one-tenth of the base coefficient value in the positive direction. Therefore, to compare the sensitivities to α_0, the coefficient was increased to $0.0011\ \text{s}^{-1}$. Thus, the optimal correction is $\Delta\alpha_0 = -0.0001\ \text{s}^{-1}$, while the optimal correction for the other two coefficients is zero. Corrections were computed based on time series of sensitivities and errors at a given node using (4.17). Thus, for the 65 node domain analyzed herein, there are 64 sets of corrections using elevation results. The nodal values were used to generate individual corrections to see the range in corrections throughout the domain. The elevation value is specified at the left boundary, which results in the elevation sensitivity to the G parameterization being zero. The error is zero for this node as well.

The results for the three different perturbations are summarized in Table 4.2. The first column shows the perturbations from the base values for a given simulation. The other columns contain information about the least-squares corrections for each of the coefficients. The bold value is the mean correction to the perturbed parameter (i.e., the mean of all the nodal corrections). The optimal correction is the negative of the perturbation set shown in the first column.

Table 4.2 Perturbations from base coefficient values and nodal least-squares correction results for simulations on the east coast grid varying one coefficient value at a time.

Perturbations $\{\Delta\alpha_0, \Delta\alpha_1, \Delta\alpha_2\}$	Mean, Min, Max Corrections to α_0	Mean, Min, Max Corrections to α_1	Mean, Min, Max Corrections to α_2
{0.0001, 0.0, 0.0}	**-1.09E-04**, -1.14E-04, -9.94E-05	3.05E-04, -1.51E-03, 1.51E-03	-6.96E-04, -1.53E-03, 7.28E-04
{0.0, 0.01, 0.0}	2.20E-06, 4.41E-08, 8.653E-06	**-1.03E-02**, -1.15E-02, -9.43E-03	-1.51E-04, -5.33E-04, 6.88E-04
{0.0, 0.0, 0.01}	5.87E-06, -4.21E-06, 1.10E-05	1.90E-04, -3.11E-03, 2.68E-03	**-1.09E-02**, -1.23E-02, -1.01E-02

In each case, each of the corrections for the perturbed coefficient is close to the optimal correction. The maximum error in the corrections for the first two perturbations are about 15%, while the maximum error is 23% when the perturbation is applied to α_2. Furthermore, the corrections for the coefficients that are held constant are relatively small. The mean corrections to α_0, when the perturbation is to either α_1 or α_2, are on the order of 10^{-6} s^{-1}, so they are more than two orders of magnitude less than the base α_0 value. The mean corrections to α_1 or α_2, when the perturbation is to a different parameter, are on the order of 10^{-4} (m/s or m^{-1}). They, too, are more than two orders of magnitude less than the base coefficient values. Therefore, the methodology is effective for correction estimation for multiple parameters.

4.6.2 Estimation of α_1-Only Parameterization

Up to this point, corrections to coefficients have been calculated to attempt to recover the parameterization used to create the observations. In this subsection, the observations are the model results from a simulation with a constant $G = 0.001\ \mathrm{s}^{-1}$ value (i.e., $\alpha_0 = 0.001$, $\alpha_1 = \alpha_2 = 0.0$). In contrast, the model (to generate the model results) uses a G parameterization where only the α_1 value is non-zero. Furthermore, only the α_1 value is allowed to be corrected. Therefore, the computed sensitivities to α_0 and α_2 are ignored and the sensitivity matrix used in the least-squares correction is just a vector with the sensitivities to α_1. This is equivalent to the scalar correction analyzed for the constant G parameterization in Chapter 3.

The starting point for the iterative optimization was $\alpha_1 = 1.0\ \mathrm{m/s}$. The mean of the nodal corrections based on the results from this simulation was $\Delta\alpha_1 = 0.328\ \mathrm{m/s}$, with the majority of the individual nodal corrections falling between 0.15 and 0.40 $\mathrm{m/s}$, as can be seen in Figure 4.18. The results from the next simulation, with $\alpha_1 = 1.328\ \mathrm{m/s}$, give a mean correction of $\Delta\alpha_1 = 0.970\ \mathrm{m/s}$. The pattern remains similar and the majority of the nodal corrections fall between 0.50 and 1.2 $\mathrm{m/s}$. That mean correction results in a value of $\alpha_1 = 2.298\ \mathrm{m/s}$ for the next simulation. Again, the corrections suggest this value is too low and the new mean correction is $\Delta\alpha_1 = 3.868\ \mathrm{m/s}$. For the majority of the domain, the nodal corrections lie between 1.0 and 4.5 $\mathrm{m/s}$. Using the mean correction leads to an α_1 value of $6.166\ \mathrm{m/s}$ and a subsequent mean correction of $\Delta\alpha_1 = 26.304\ \mathrm{m/s}$. Again, the mean correction is in line with the nodal corrections throughout the majority of the domain. Applying the mean correction brings about a new coefficient value, $\alpha_1 = 32.47\ \mathrm{m/s}$, that is fairly large (the lowest G values during the

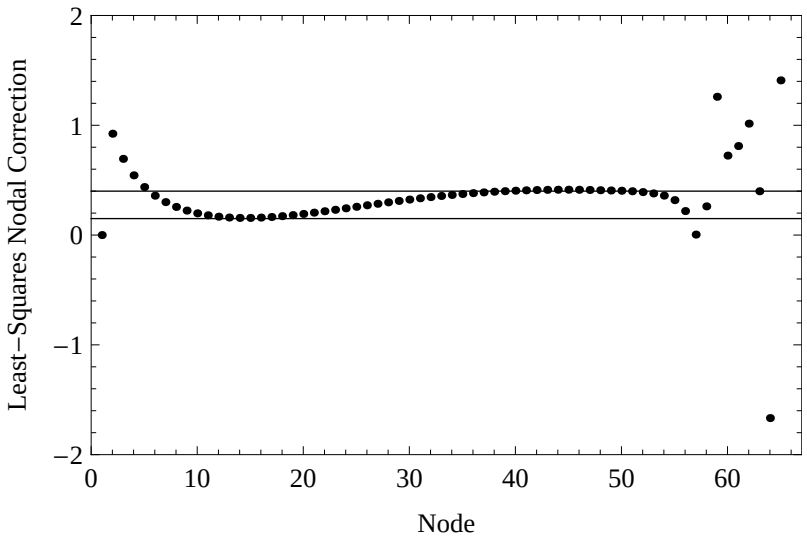

Figure 4.18 Nodal least-squares corrections, $\Delta\alpha_1$, for a simulation with $G = \alpha_1 / H$, where α_1 = 1.0 m / s. This is the starting point for the iterative optimization. The observations are results from a simulation with $G = 0.001\ s^{-1}$. The horizontal lines depict corrections of 0.15 and 0.40 m / s, respectively.

simulation are greater than $0.006\ s^{-1}$). However, the mean nodal correction based on results for this simulation is 239.1 m/s which would result in α_1 being even larger for the next simulation.

Based solely on the growth of $\Delta\alpha_1$, it would appear that the least-squares correction procedure is ineffective on this system because the corrections are resulting in α_1 values in the "too primitive" range. However, as α_1 increases, the elevation error (which is used to compute the corrections) decreases. The $\overline{RMSE_x(\zeta)}$ is 0.0147 m when $\alpha_1 = 1.0$ m/s. After two correction steps, the error is down to 0.0123 m ($\alpha_1 = 2.298\ m/s$). After two more correction steps, the error has reduced to 0.0089 m ($\alpha_1 = 32.47\ m/s$). The corrections to the coefficient are intended to reduce the error in the system. Thus, while α_1 climbs into a range where the G parameterization is beginning to be "too primitive," the errors continue to be reduced.

For the simulation with α_1 equal to 32.47 m/s, $2\Delta x$ oscillations in the sensitivi-

ties occur near the deep ocean boundary (the magnitude of the sensitivity at the odd nodes is lower than the magnitude for even nodes) and landward of node 47. The oscillations near the ocean boundary are consistent with results presented previously. Section 3.7 compares analysis of the generation of oscillations using the FSM to dispersion analysis results. For low G values, the sensitivities are free of $2\Delta x$ oscillations. The short wavelength oscillations appear first near the open boundary as G is increased. Further increase in G results in more of the domain being subject to oscillations.

The oscillations at the higher node numbers start as node-to-node discrepancies in the magnitude of the sensitivity and transition to sensitivities of opposite signs and different magnitudes over the continental rise and shelf. These oscillations in the sensitivities result in less consistent nodal corrections over an increased range of the domain, as Figure 4.19 shows. In contrast to the corrections shown in Figure 4.18, there are node-to-node oscillations in corrections near the left boundary in Figure 4.19. Additionally, there is less consistency in the nodal corrections between nodes in the upper 40s and lower 50s when the higher α_1 value is used.

Using the mean correction step, $\Delta\alpha_1 = 239.1 \text{ m/s}$, and running the next simulation with $\alpha_1 = 271.6 \text{ m/s}$ results in an even smaller mean elevation error. However, the larger coefficient value also increases the $2\Delta x$ oscillations in the sensitivity. Furthermore, while there is generally less elevation error, the right-hand plot of Figure 4.20 shows significant $2\Delta x$ oscillations in the nodal $RMSE_t(\zeta)$. Additionally, while the total error for the simulation is reduced, the most significant reduction is in the deep ocean portion of the domain, as Figure 4.20 shows. The nodal RMS error rises almost linearly from zero at node 1 (because the elevation is specified at that boundary) to 0.0166 m at node 40 for the simu-

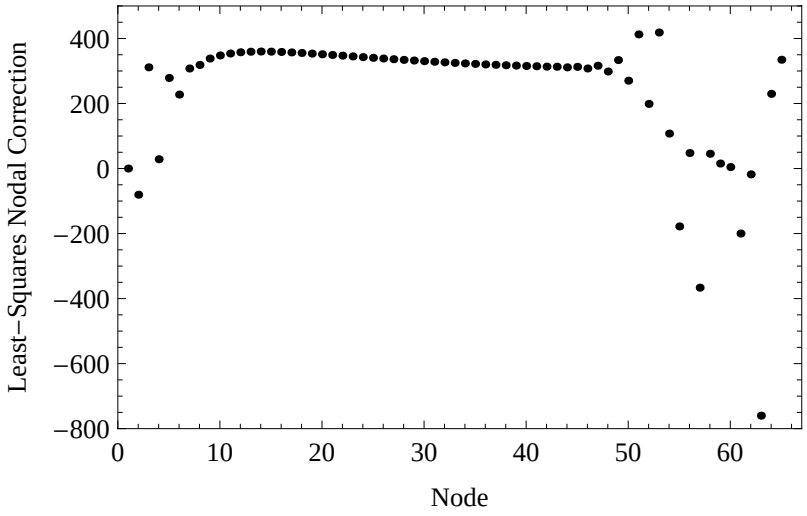

Figure 4.19 Nodal least-squares corrections, $\Delta\alpha_1$, for a simulation with $G = \alpha_1 / H$, where $\alpha_1 = 32.47$ m / s. The observations are results from a simulation with $G = 0.001$ s^{-1}.

lation with $\alpha_1 = 1.0$ m/s. The nodal RMS error at node 40 decreases as the corrections increase α_1, as shown by the error values for the five subsequent runs using α_1 based on corrections: {0.0157, 0.0137, 0.0111, 0.0092, 0.0069} m. This suggests it is important to be selective in the information used to correct the coefficients for the G parameterization. If a parameterization that will give accurate results on the shelf is desired, using observations dominated by values for the deep ocean to generate corrections might not produce the desired results.

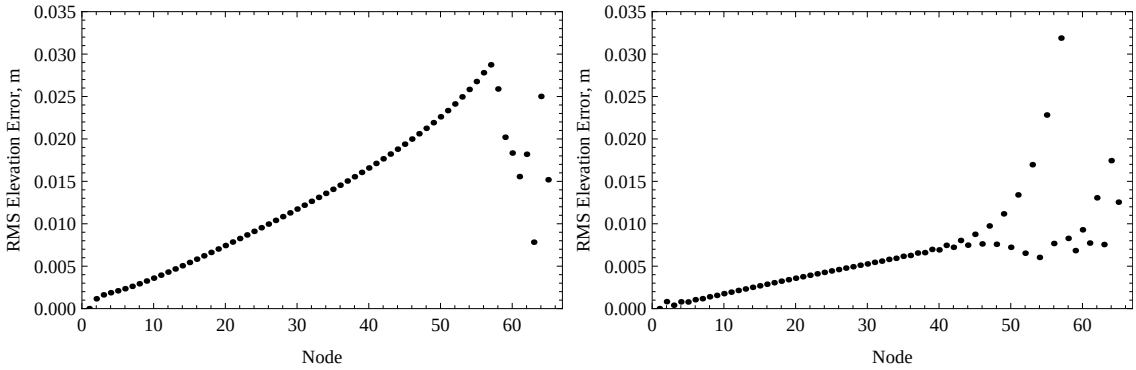

Figure 4.20 Nodal RMS elevation errors for simulations on the east coast domain with $\alpha_1 = 1.0$ m / s (left) and $\alpha_1 = 271.6$ m / s (right). The observations used to compute the errors are the results for a constant G simulation with $G = 0.001$ s^{-1}.

4.6.3 Estimation for Parameterization Using α_1 and α_2

In the previous subsection, simulations were performed using only α_1 for the parameterization of G. The goal in this section is to find an optimal combination of α_1 and α_2 to match results generated by using a different parameterization, in this case a constant G parameterization with $G = 0.001\ \text{s}^{-1}$. The observations were results from a simulation with a constant G value of $0.001\ \text{s}^{-1}$. In this section, the same observations will be used, and both α_1 and α_2 will be used in the G parameterization; α_0 will remain zero, and the sensitivities to α_0 will be ignored in the correction generation process. The sensitivities to α_0 are ignored and α_0 is held at zero because the observations were generated using only α_0. Under ideal conditions, use of the sensitivities to α_0 and correcting α_0 would just recover the α_0-only parameterization used to create the observations.

The following set of α_i values ($\{\alpha_0, \alpha_1, \alpha_2\}$) was used to start the first sequential optimization: $\{0.0, 1.0, 0.0\}$. It should be noted that this is the same starting point as for the sequential optimization of α_1 detailed in the previous subsection. The sequential corrections for this set are shown in Table 4.3. In the previous case, using only α_1, the correction was $\Delta\alpha_1 = 0.328\ \text{m/s}$. However, when the sensitivities to both α_1 and α_2 are used to compute the corrections, the mean nodal corrections are $\Delta\alpha_1 = 0.498\ \text{m/s}$ and $\Delta\alpha_2 = 0.142\ \text{m}^{-1}$. The coefficient set resulting from the third correction yields a parameterization of G that is unstable.

Use of $\{0.0, 1.0, 1.0\}$ as the coefficient set for the start of a second sequential optimization attempt results in a negative $\Delta\alpha_1$ large enough that α_1 is negative in the next coefficient set. This parameterization is also unstable.

From the two sequential optimization attempts, it is obvious that optimization of a

Table 4.3 Mean nodal corrections to α_1 and α_2 using observations from a simulation with constant G = 0.001 s^{-1}.

Simulation #	α_0	α_1	α_2	$\Delta\alpha_0$	$\Delta\alpha_1$	$\Delta\alpha_2$
1	0.000	1.000	0.000	0.000	0.498	0.142
2	0.000	1.498	0.142	0.000	-1.475	0.696
3	0.000	0.023	0.838	0.000	-0.648	0.378
4[a]	0.000	-0.625	1.216			

a. This coefficient set is unstable for the conditions of the simulation. Therefore, it did not create results to compute corrections.

variable G parameterization using only α_1 and α_2, based on observations from a constant G simulation, is not a trivial process. Certainly, there is a parameter set that minimizes the elevation error. Unfortunately, arbitrary specification of initial coefficients does not result in the optimal coefficient set being recovered. The end goal of this study is not to optimize α_1 and α_2 based on constant G observations, so it is not practical to continue this pursuit. However, if the problem at hand was of greater interest (for instance, if it was an actual 2-D application with a true observation set), it would be worth pursuing a wider range of alternative starting points or a different method to compute the correction set (rather than using the mean nodal correction).

4.6.4 Full Variable G Parameter Estimation

Thus far in this chapter, efforts have been confined to perturbations of only one parameter or optimization of the coefficients for the non-constant G terms based on observations from a constant G simulation. In this section, attempts are made to recover the parameter set $\alpha_0 = 0.0001\ s^{-1}$, $\alpha_1 = 2.0\ m/s$ and $\alpha_2 = 0.2\ m^{-1}$.

The starting coefficient set for the first attempt is $\{0.001, 0.0, 0.0\}$. Thus, the

optimal corrections are $\{-0.0009, 2.0, 0.2\}$. However, using the mean of the nodal corrections calculated based on the initial simulation yields the following set of corrections: $\{0.0084, -2.77, -0.036\}$. Rather than decrease α_0 and increase the other coefficients, the data assimilation process gives corrections that further increase α_0 and decrease the coefficients that were initially zero. Application of these corrections results in an unstable second simulation.

A second attempt was made using an initial coefficient set of $\{0.001, 5.0, 1.0\}$. This, too, proved unsuccessful. The correction set, $\{-0.0018, -9.26, -2.22\}$, yielded negative values for all three coefficients for the next simulation.

Rather than continue to guess random coefficient sets to generate corrections, perturbations were made to the base coefficient set. Five perturbations were performed: 1) +10%, 2) +50%, 3) +100%, 4) -10%, and 5) -50%. The percentage was applied to each of the coefficients. Thus, for the first perturbation, the trial coefficient set is $\{0.00011, 2.2, 0.22\}$ and the optimal correction set is $\{-1.0\times10^{-5}, -0.2, -0.02\}$.

For the first perturbation of +10%, the actual mean correction set is $\{-7.37\times10^{-6}, -0.235, -0.015\}$. This is a fairly good correction set. All three corrections are in the appropriate direction. The corrections to α_0 and α_2 are about three-quarters of the optimal value while α_1 is overcorrected by 17.5%. For the second perturbation (+50%), the optimal correction set is $\{-5\times10^{-5}, -1.0, -0.1\}$. The mean correction set for this simulation is $\{-2.38\times10^{-5}, -1.76, -0.099\}$. This correction set follows the same pattern as the previous one, although the correction is almost exactly right for the third coefficient. The optimal and actual corrections for the third run (+100%) are $\{-0.0001, -2.0, -0.2\}$ and $\{1.97\times10^{-5}, -5.13, -0.267\}$, respectively. These mean corrections are significantly worse.

The overcorrection for α_1 is so severe that it causes an increase in α_0, pulling the first coefficient in the wrong direction. The third coefficient is in the appropriate direction and of a reasonable magnitude.

The optimal and actual corrections for the fourth perturbation (-10%) are $\{1.0\times10^{-5}, 0.2, 0.02\}$ and $\{8.36\times10^{-6}, 0.18, 0.013\}$, respectively. Similar to the small perturbation in the positive direction, when the coefficients are perturbed by a relatively small amount in the negative direction, the corrections are fairly good. The corrections, optimal ($\{5.0\times10^{-5}, 1.0, 0.1\}$) and actual ($\{5.99\times10^{-5}, 0.403, 0.040\}$), for the larger negative perturbation of -50% are decent as well. The first coefficient is slightly overcorrected, while the two others are undercorrected by about 60%, but the corrections are all in the correct direction. The undercorrections for the negative perturbations are consistent with results seen previously due to the magnitude of the sensitivity reducing with increasing G (and increasing α values).

The implication is that multi-coefficient corrections can recover an optimal variable G parameterization under certain conditions. However, use of the mean nodal correction based on elevation errors and sensitivities is not a robust correction scheme. Consistent with previous results presented in Chapter 3, the general trend of decreasing sensitivity to a coefficient with increase in that coefficient causes undercorrections when the coefficients are lower than optimal and overcorrections when the coefficients are greater than optimal. Additionally, the correction process is complicated by the feedback between parameters, as was seen with the corrections for the third perturbation.

4.7 Sensitivity of Mass Residual to G

In Chapter 2, mass residual based on the finite volume flux is used as an error metric for evaluating different G specifications. Furthermore, analyses in that chapter show mass balance error is highly dependent on G. In this section, the sensitivity of the mass residual to G is analyzed. Additionally, mass residuals and mass residual sensitivities are used to generate corrections to attempt to minimize local mass balance error.

4.7.1 Derivation of Sensitivity

The mass residual is presented in (2.9) and is equal to the sum of the accumulation and net flux portions of the continuity equation. For an element defined by nodes $j-1$ and j, the accumulation and net flux over one time step, from time level k to $k+1$, are given by (4.25) and (4.26).

$$(accum) = \frac{\Delta x}{2}(\zeta_j^{k+1} + \zeta_{j-1}^{k+1} - \zeta_j^k - \zeta_{j-1}^k) \quad \textbf{(4.25)}$$

$$(netflux) = \frac{\Delta t}{2}(q_j^{k+1} - q_{j-1}^{k+1} + q_j^k - q_{j-1}^k) \quad \textbf{(4.26)}$$

Rewriting the net flux term, (4.26), in terms of water surface elevations and velocities results in (4.27).

$$(netflux) = \frac{\Delta t}{2}(((h+\zeta)u)_j^{k+1} - ((h+\zeta)u)_{j-1}^{k+1} + ((h+\zeta)u)_j^k - ((h+\zeta)u)_{j-1}^k) \quad \textbf{(4.27)}$$

The total accumulation and net flux at a given time are obtained through summation of the values over the time steps. For the accumulation term, the total accumulation (assuming a zero initial accumulation value) is simply a function of the current water surface elevation values, as shown by (4.28).

$$(accum_T)^{k+1} = \frac{\Delta x}{2}(\zeta_j^{k+1} + \zeta_{j-1}^{k+1}) \tag{4.28}$$

The total net flux depends on previous total net flux value and the net flux over the time step according to (4.29).

$$(netflux_T)^{k+1} = (netflux_T)^k + (netflux) \tag{4.29}$$

The sensitivity to G is obtained by calculating the derivative with respect to G. The sensitivity to G will be presented here, but the same procedure is valid for sensitivity to coefficients in a parameterization. For the accumulation term, the sensitivity to G is given by (4.30).

$$\frac{\partial}{\partial G}(accum_T)^{k+1} = \frac{\Delta x}{2}\left(\frac{\partial \zeta_j^{k+1}}{\partial G} + \frac{\partial \zeta_{j-1}^{k+1}}{\partial G}\right) \tag{4.30}$$

The elemental accumulation sensitivity to G is easily computed using nodal elevation sensitivity values, as represented by the terms in the parenthesis.

The sensitivity of the elemental net flux is slightly more complicated. The sensitivity of the total net flux is given by (4.31).

$$\frac{\partial}{\partial G}(netflux_T)^{k+1} = \frac{\partial}{\partial G}(netflux_T)^k + \frac{\partial}{\partial G}(netflux) \tag{4.31}$$

The sensitivity due to the latest time step is computed using (4.32).

$$\begin{aligned}\frac{\partial}{\partial G}(netflux) = \frac{\Delta t}{2}\Bigg(&\left[u\frac{\partial \zeta}{\partial G} + (h+\zeta)\frac{\partial u}{\partial G}\right]_j^{k+1} - \left[u\frac{\partial \zeta}{\partial G} + (h+\zeta)\frac{\partial u}{\partial G}\right]_{j-1}^{k+1} \\ &+ \left[u\frac{\partial \zeta}{\partial G} + (h+\zeta)\frac{\partial u}{\partial G}\right]_j^{k} - \left[u\frac{\partial \zeta}{\partial G} + (h+\zeta)\frac{\partial u}{\partial G}\right]_{j-1}^{k}\Bigg)\end{aligned} \tag{4.32}$$

As with the accumulation sensitivity, the net flux sensitivity can be computed using the variables computed for the earlier studies, specifically the elevation and velocity sensitivi-

ties and the elevation and velocity fields.

4.7.2 Mass Residual Sensitivity to Parameterization Coefficients on East Coast Domain

Before addressing the sensitivity of the mass residual to the coefficients in the G parameterization, it is informative to show the elemental mass residuals under investigation. The elemental mass residuals for six elements in the east coast domain for a simulation with a constant G value of 0.001 s^{-1} are shown in Figure 4.21. For reference, the maximum value of the accumulation term for elements near the ocean boundary is about 30,000 m^2, for elements on the continental rise is about 6,000 m^2, and for elements on the continental shelf is about 3,000 m^2.

The mass residual for element 2 has a decreasing trend. This is due to a negative average net flux. However, the mass error is relatively small. Elements 36 and 47 reside in the deep flat portion of the domain away from the ocean boundary, and results for these elements are consistent with results for elements in the deep portion of the domain that are not in the immediate vicinity of the boundary. The error is consistent from one element to the next and the magnitude of the mass residual is a very small percentage of the total mass passing through the element. If we assume that all the mass residual is due to an error in the accumulation term, the maximum water surface elevation error is on the order of 0.1 mm. Element 50 is in the transition from the deep ocean to the steep continental rise, and the mass residual at element 50 is two orders of magnitude larger than at element 47. Element 57 is the last element on the continental rise and, aside from the boundary element (not shown), is the location of the largest mass residual. Element 62 shows there is less mass error on the continental shelf than over the continental rise for this application.

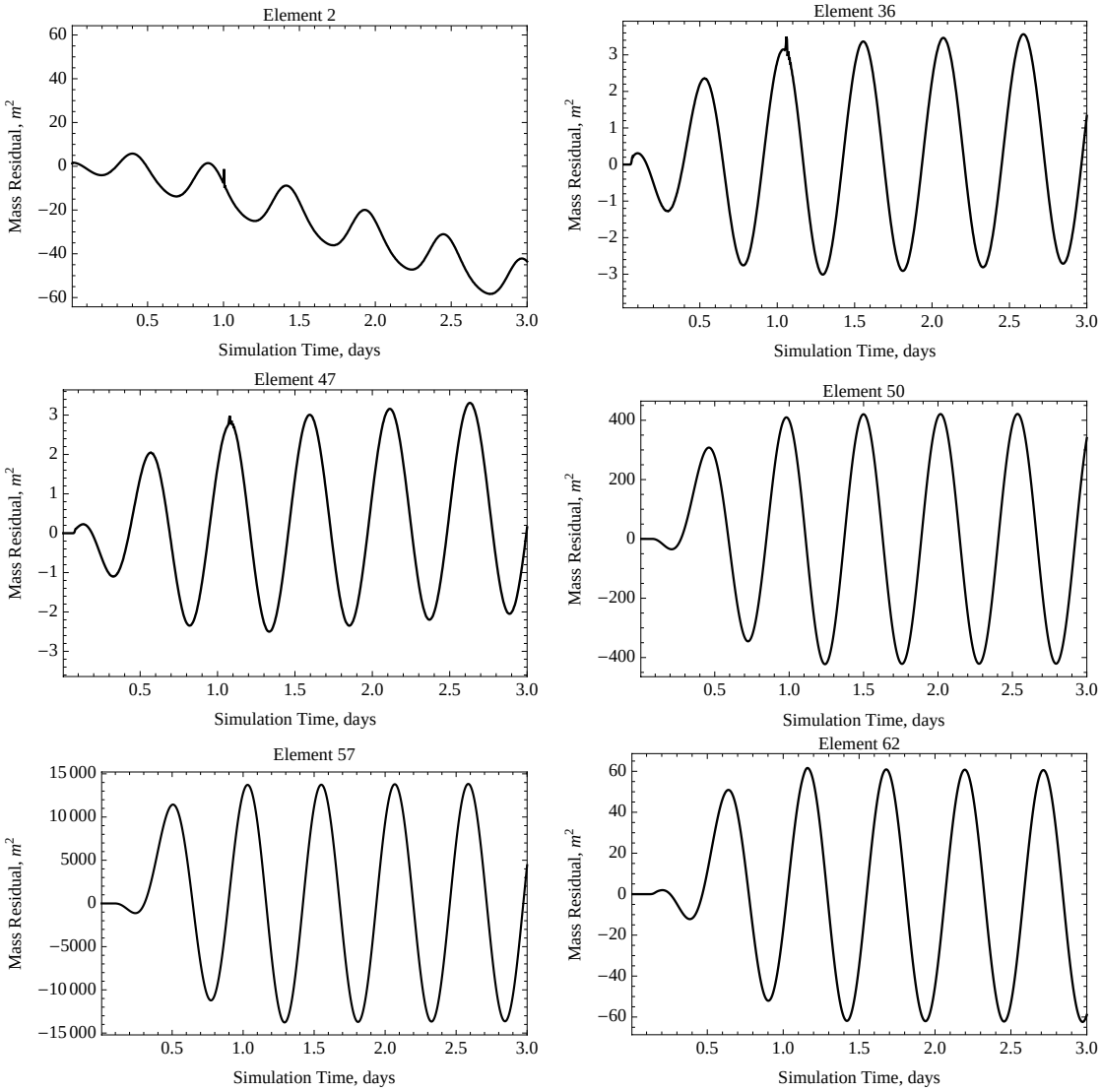

Figure 4.21 Elemental mass residuals for select elements in the east coast domain. The results are for a constant G simulation with $G = 0.001\ s^{-1}$.

The mass residual sensitivity to α_0, for the same six elements, is shown in Figure 4.22. The mass residual sensitivity is a maximum at the ocean boundary, specifically elements 1 and 2. The sensitivity for element 3 is in line with the sensitivity for most of the deep portion of the domain, which can be seen in the graph for element 36. The mass residual sensitivities for elements 47 and 50 show an increase as the deep portion of the domain transitions to the continental rise. Other than at the ocean boundary, the largest mass residual sensitivity values are on the continental rise and shelf, specifically near the

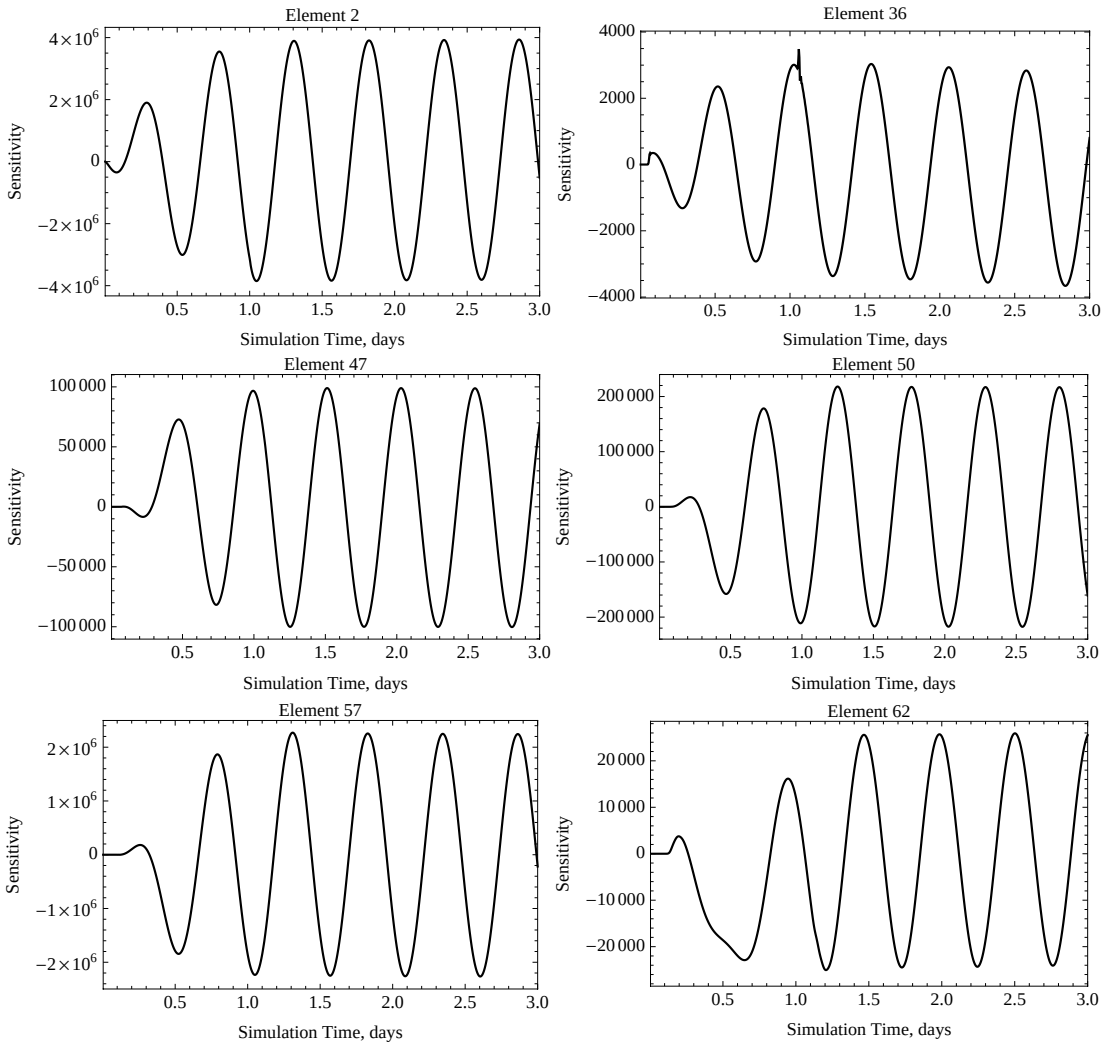

Figure 4.22 Elemental mass residual sensitivity to α_0 for select elements in the east coast domain. The units of the sensitivity are m^2s. These results are for a constant *G* simulation with *G* = 0.001 s^{-1}.

shelf break at node 58 (elements 56, 57 and 59).

For the same set of elements, the mass residual sensitivity to α_1 is shown in Figure 4.23. There are a couple main trends. The sensitivity is large near the ocean boundary, as the results for element 2 show. For the deep portion of the domain not in the immediate vicinity of the ocean boundary, the sensitivities are a minimum (e.g., element 36). The sensitivities increase over the continental rise, with the maximum sensitivity occurring at elements 56, 63 and 64. The sensitivities are also high for elements 57-59,

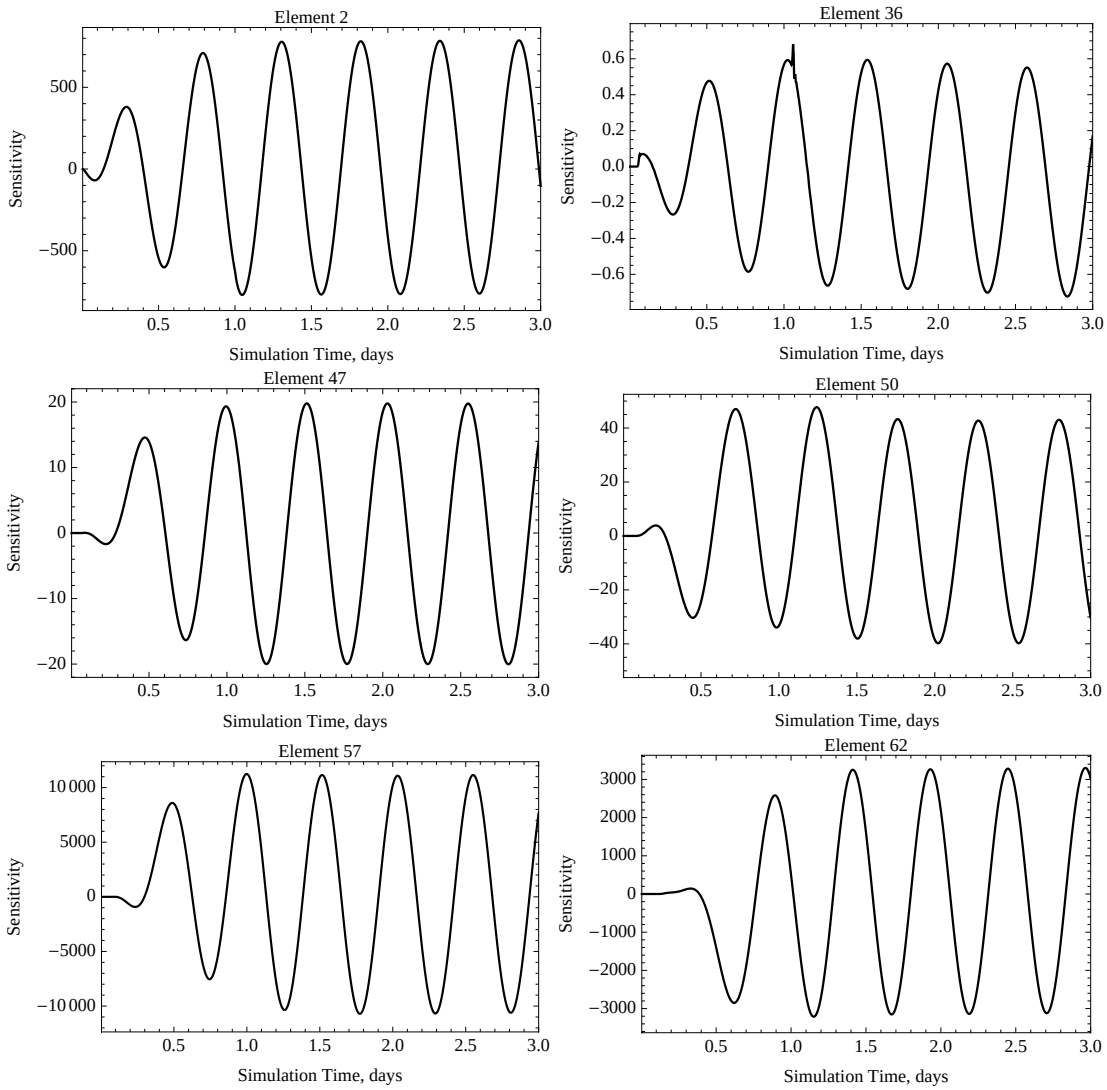

Figure 4.23 Elemental mass residual sensitivity to α_1 for select elements in the east coast domain. The units of the sensitivity are ms. These results are for a constant *G* simulation with $G = 0.001\ s^{-1}$.

which is the range spanning the shelf break. The pattern is consistent with the results for sensitivity to α_0.

Figure 4.24 shows the mass residual sensitivity to α_2 for the same set of elements. The same general trends exist for the sensitivity to α_2 as for the sensitivities to the other coefficients. The sensitivity is high near the ocean boundary, low in the deep ocean, then high again over the continental rise, especially near the shelf break. The plot for element 57

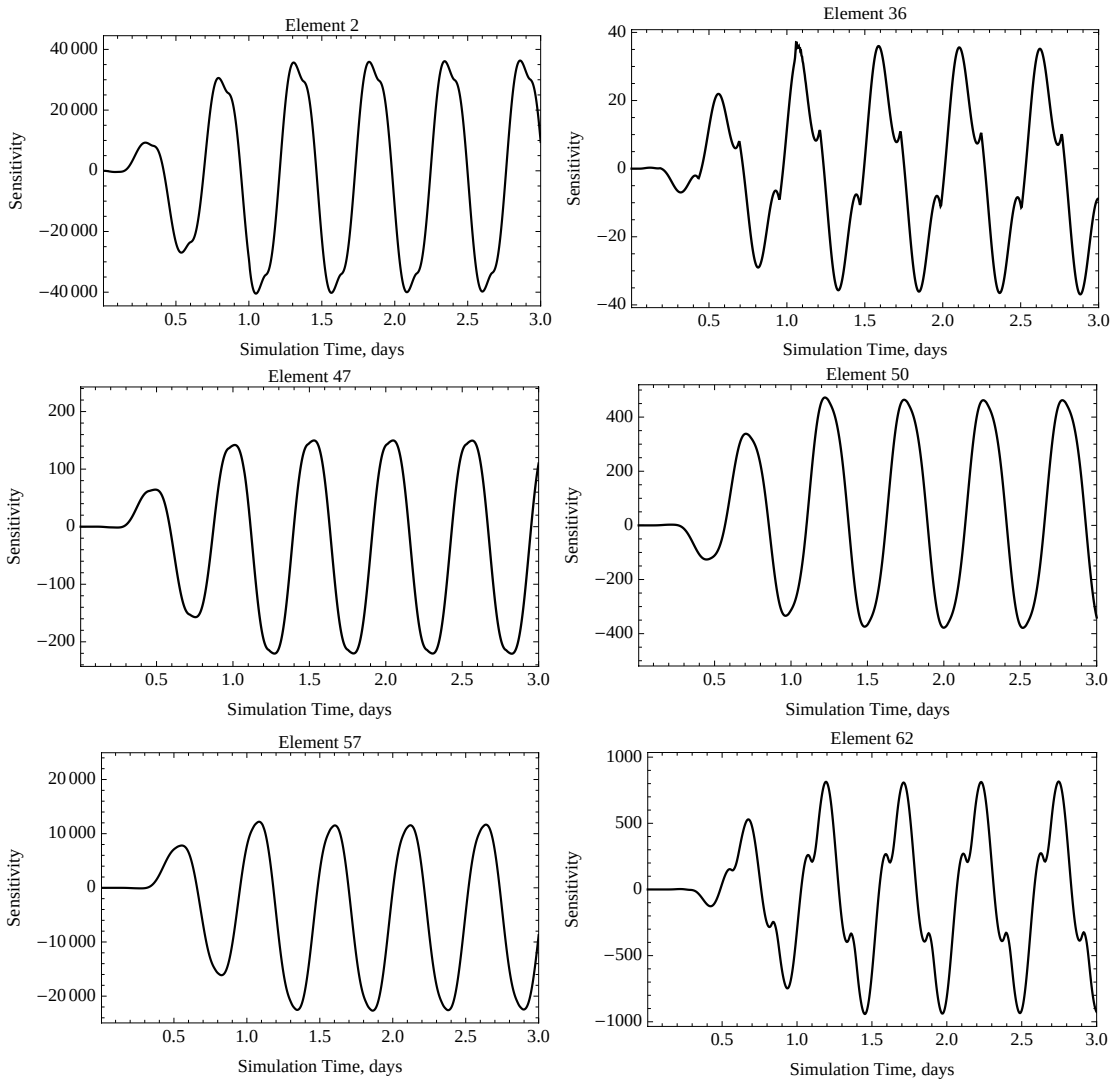

Figure 4.24 Elemental mass residual sensitivity to α_2 for select elements in the east coast domain. The units of the sensitivity are m^3. These results are for a constant G simulation with G = 0.001 s^{-1}.

shows a negative bias. This same bias exists for elements 58 and 59, while element 56 has a positive bias.

4.7.3 Coefficient Corrections Based on Mass Residuals

In order to generate corrections based on mass residuals, the negative of the mass residual is used as the error. This is done because the error is the difference between the observations and model. The observations are taken as zero mass residual. In other words,

it is assumed that conservation of mass, in a finite volume sense, applies to the system under exploration. The least-squares corrections are computed from the mass residual sensitivity to G and the mass residual error vector. The elemental G corrections, based solely on the elemental mass residual and mass residual sensitivity to α_0, are shown in Figure 4.25. For most of the domain, the corrections are small. The magnitude of the corrections are especially small based on results for elements 2 and 47 because the sensitivities are relatively large and the mass residuals are still relatively low. The largest corrections are for elements 57 and 58. These are the elements on either side of the shelf break.

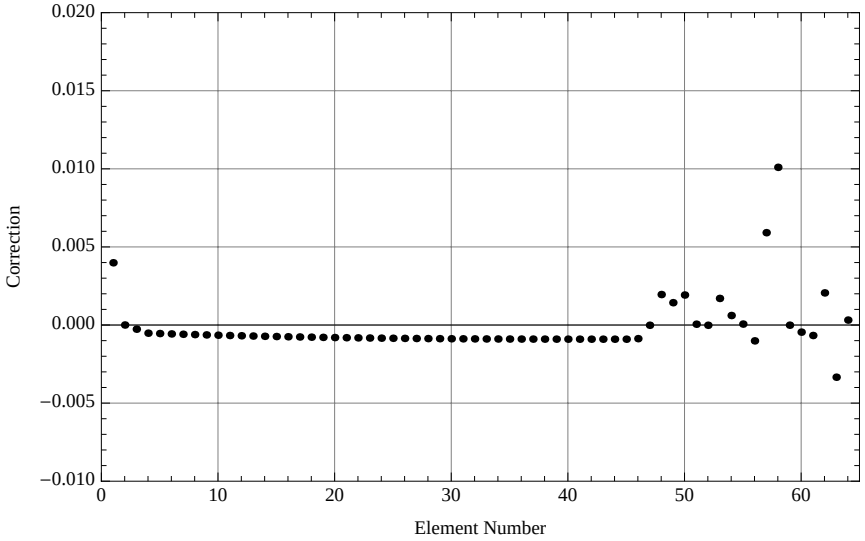

Figure 4.25 Elemental corrections to G based on mass residuals and sensitivity to α_0. The results are for a constant G simulation with $G = 0.001\ s^{-1}$ on the east coast domain.

The elemental G corrections, based solely on the elemental mass residual and mass residual sensitivity to α_1, are shown in Figure 4.26. For most of the deep portion of the domain, the corrections are negative, with a local maximum (magnitude) occurring for element 45. The largest correction in the entire domain is based on the results for element 1 (19.9 m/s) and it is outside the range of the plot. The area from element 48 through element 58 yields a wide range of corrections. The correction for α_1 based on element 57

(the element with the largest mass residual) suggests better mass balance can be achieved by decreasing α_1. However, the majority of the elements on the continental rise yield positive corrections, although there is not a consistent pattern to the corrections. The corrections based on results for elements on the shelf are close to zero.

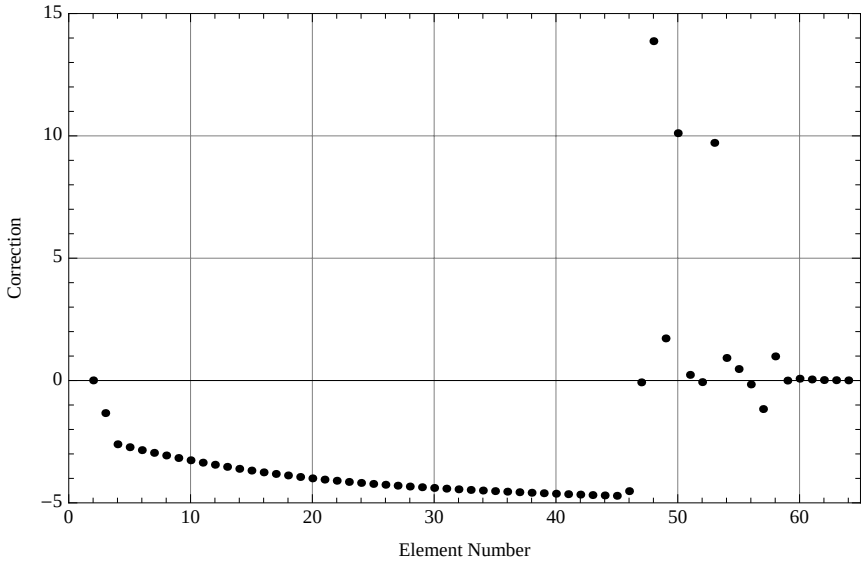

Figure 4.26 Elemental corrections to G based on mass residuals and sensitivity to α_1. The results are for a constant G simulation with $G = 0.001\ s^{-1}$ on the east coast domain.

The elemental G corrections, based solely on the elemental mass residual and mass residual sensitivity to α_2, are shown in Figure 4.27. The results are consistent with the results for the other two coefficients. Specifically, the corrections for the majority of the domain are close to zero. However, there is a range of corrections suggested using the results for elements 48-58, although there is not a consistent trend to the corrections. The maximum positive correction is based on results for element 53 ($\Delta\alpha_2 = 1.28\ m^{-1}$), while the largest negative correction is based on the results from element 57 ($\Delta\alpha_2 = -0.571\ m^{-1}$).

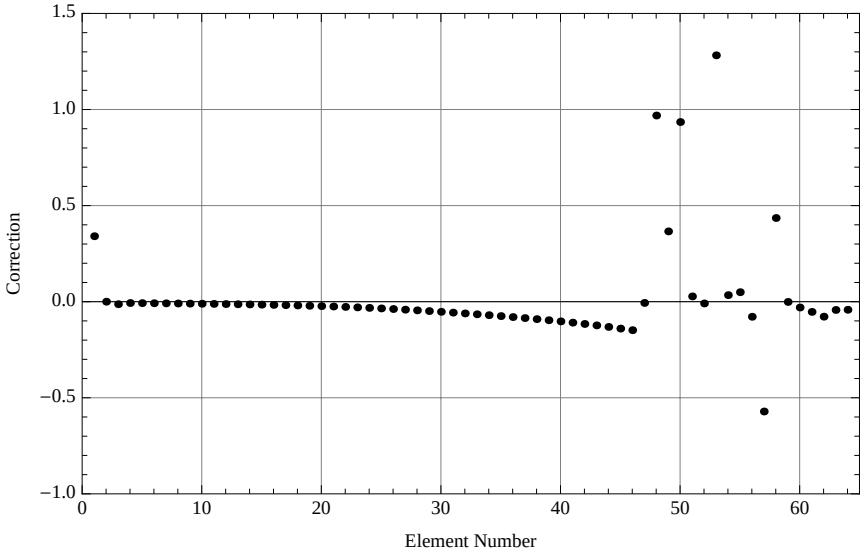

Figure 4.27 Elemental corrections to G based on mass residuals and sensitivity to α_2. The results are for a constant G simulation with $G = 0.001$ s^{-1} on the east coast domain.

4.7.4 Analysis of Errors and Corrections for α_0-Only Simulations

The appropriate correction to attempt to minimize mass residuals, based on the analysis in the previous section, is not readily apparent. In an attempt to shed some light on the interaction between the mass residual sensitivity to G and the mass residual, four constant G simulations were performed with G values of 0.0001, 0.001, 0.01 and 0.1 s^{-1}. The mass residual results for element 47 are presented in Figure 4.28. The mass residual results for element 57 are shown in Figure 4.29. Figure 4.30 contains the results for element 62.

The results for element 47 show that the minimum mass residual occurs with a constant value of $G = 0.001$ s^{-1}. The results for element 47 are consistent with the results throughout the deep portion of the domain. In contrast, the results for element 57 show decreases in mass residual with increases in G over the range of G values used in these simulations. The results for element 62 show a minimum mass residual for this set of simulations with $G = 0.001$ s^{-1}, as well. For this set of simulations, the minimum mass

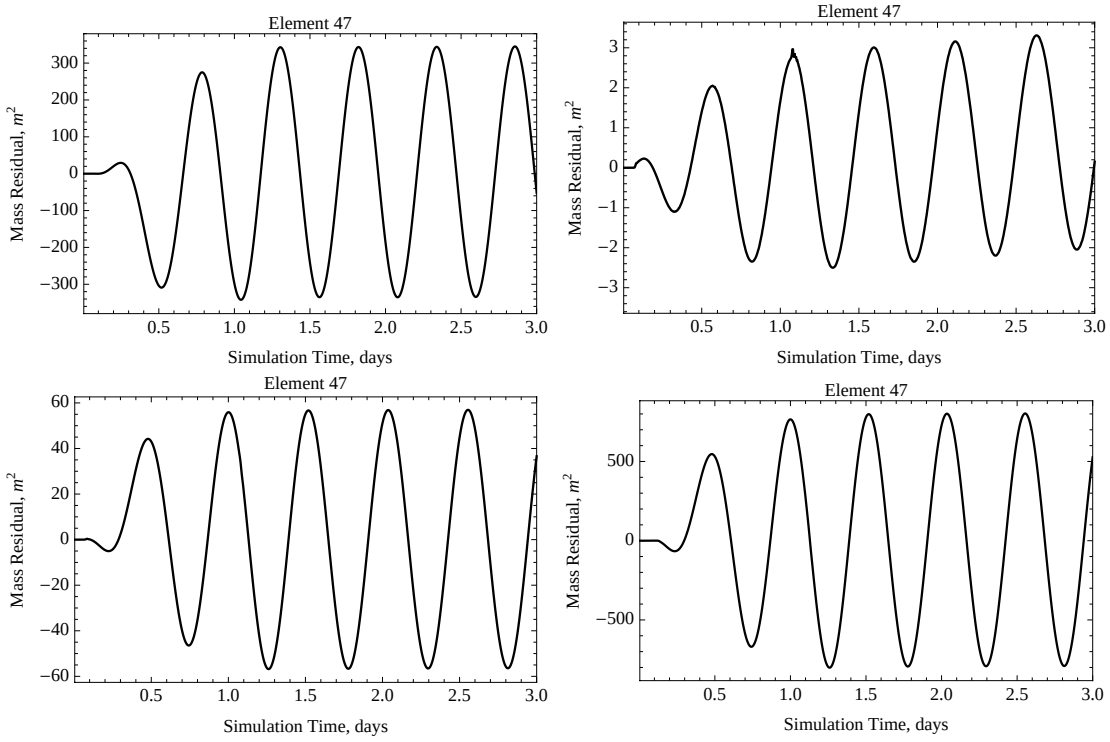

Figure 4.28 Mass residual results for element 47 for simulations with $G = 0.0001$ (top left), 0.001 (top right), 0.01 (bottom left) and 0.1 (bottom right) s^{-1}.

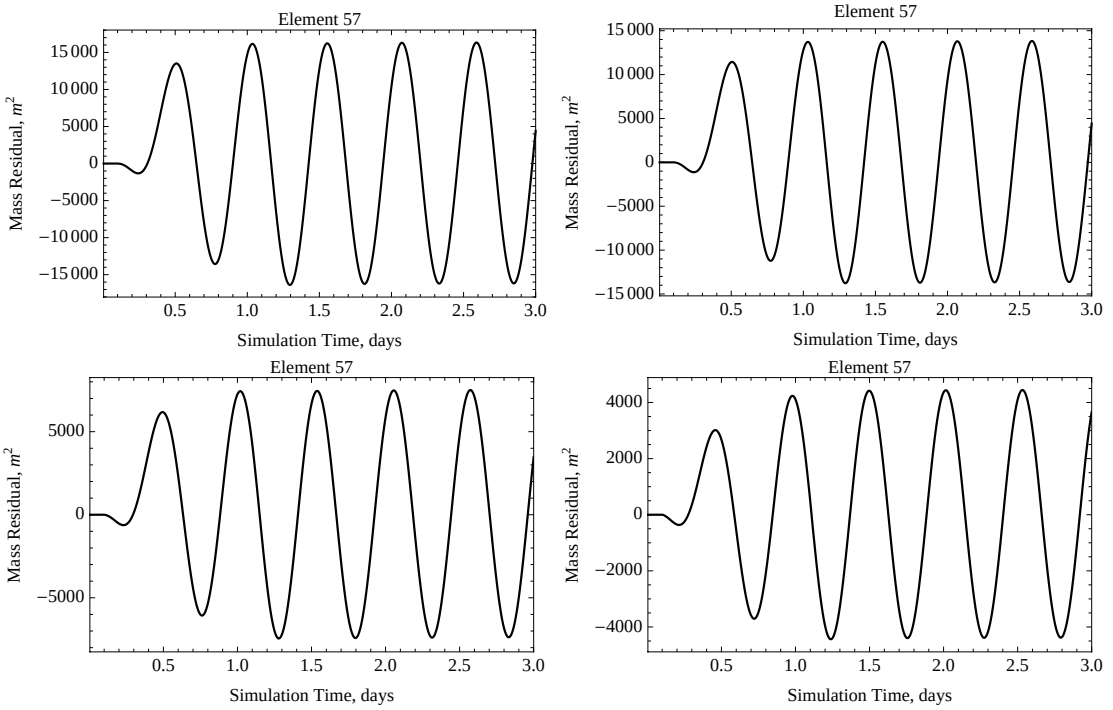

Figure 4.29 Mass residual results for element 57 for simulations with $G = 0.0001$ (top left), 0.001 (top right), 0.01 (bottom left) and 0.1 (bottom right) s^{-1}.

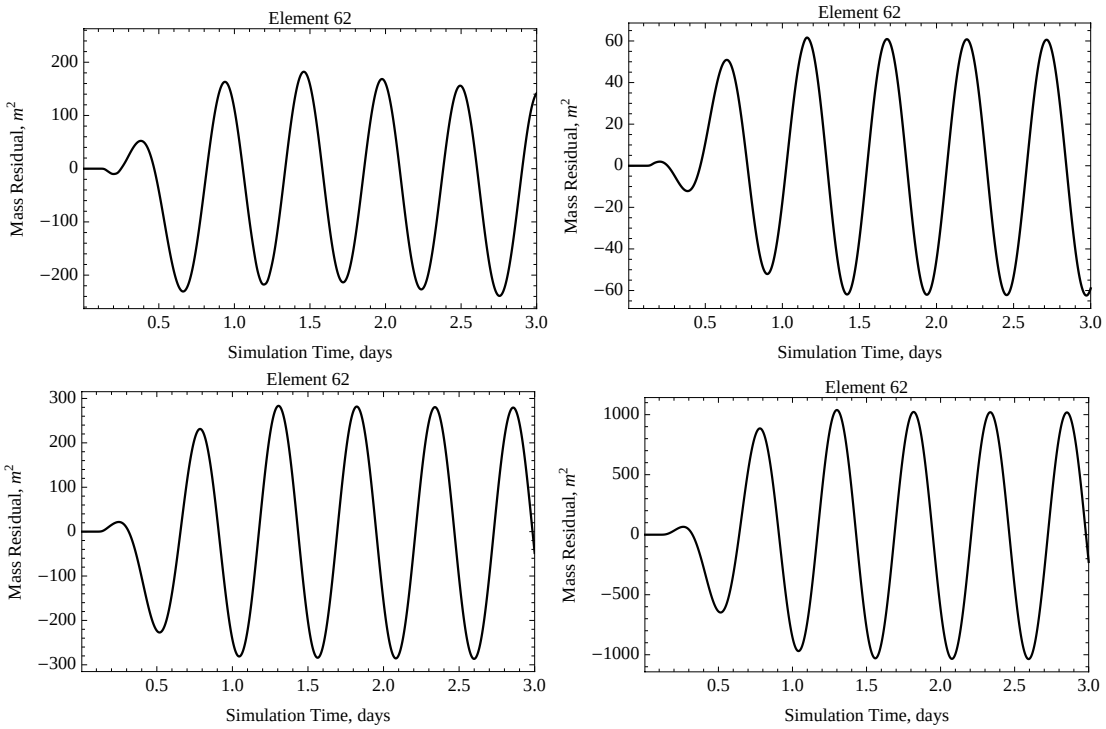

Figure 4.30 Mass residual results for element 62 for simulations with $G = 0.0001$ (top left), 0.001 (top right), 0.01 (bottom left) and 0.1 (bottom right) s^{-1}.

residual for element 50 occurs with $G = 0.01\ s^{-1}$.

Based on the mass residual results for element 47, the correction using the results from the simulation with $G = 0.0001\ s^{-1}$ should be positive while the corrections using the results from the simulations with G values of 0.01 and 0.1 s^{-1} should be negative. This is the case, as seen in Table 4.4. The corrections for element 62 should have the same sign as the ones for element 47. This, too, is the case.

Based on the mass residual results for element 57, the corrections should be positive using sensitivities to α_0 for element 57, at least over the range of constant G values used here. The corrections for the three simulations with the lowest G values are 0.00503, 0.00591 and 0.0247 s^{-1}, respectively. Finally, the corrections for element 50 show positive values when G is less than the value that produces the smallest mass residual, and negative

Table 4.4 Corrections to G value, $\Delta\alpha_0$, based on mass residuals and mass residual sensitivities to α_0 for different elements in the east coast domain. The G value listed is the α_0 parameter value used for the simulation.

Element	$G = 0.0001$	$G = 0.001$	$G = 0.01$	$G = 0.1$
47	0.000142	*minimum*[a]	-0.00640	-0.114
50	0.000213	0.00192	*minimum*	-0.158
57	0.00503	0.00591	0.0247	*minimum*
62	0.0000662	*minimum*	-0.00882	-0.505

a. For a given element, the distinction "*minimum*" denotes the G value (from the set of four values) at which the mass residual is a minimum. The corrections are not identically zero for these elements as the actual minimum mass residual values do not generally occur at the exact G values used for the simulations.

when G is higher than the optimal G value. Based on these results, the sensitivity of the mass residual to G gives insight into how to adjust coefficients to reduce mass balance locally.

4.7.5 Analysis of Errors and Corrections using α_1 Only

For this section, five simulations were performed using $G = \alpha_1 / H$, with α_1 values of 0.1, 0.3, 1.0, 3.0 and 10.0 $\mathrm{m/s}$. These values were considered because they span two orders of magnitude, and the highest value was previously associated with the equations becoming "too primitive." The mean and maximum elemental mass residual for each of the simulations is shown in Figure 4.31. The results for the last day of the simulation were used to compute maximum and mean values (i.e., for a given element, the mean is the average of the elemental mass residual over the last 24 hours of the simulation and the maximum is the highest (magnitude) elemental mass residual during that same time span).

The general trends are similar to the trends seen for the constant G simulations. The error is high at the ocean boundary then decreases to a minimum in the deep ocean away from the boundary. The transition to the continental rise results in an increase in mass

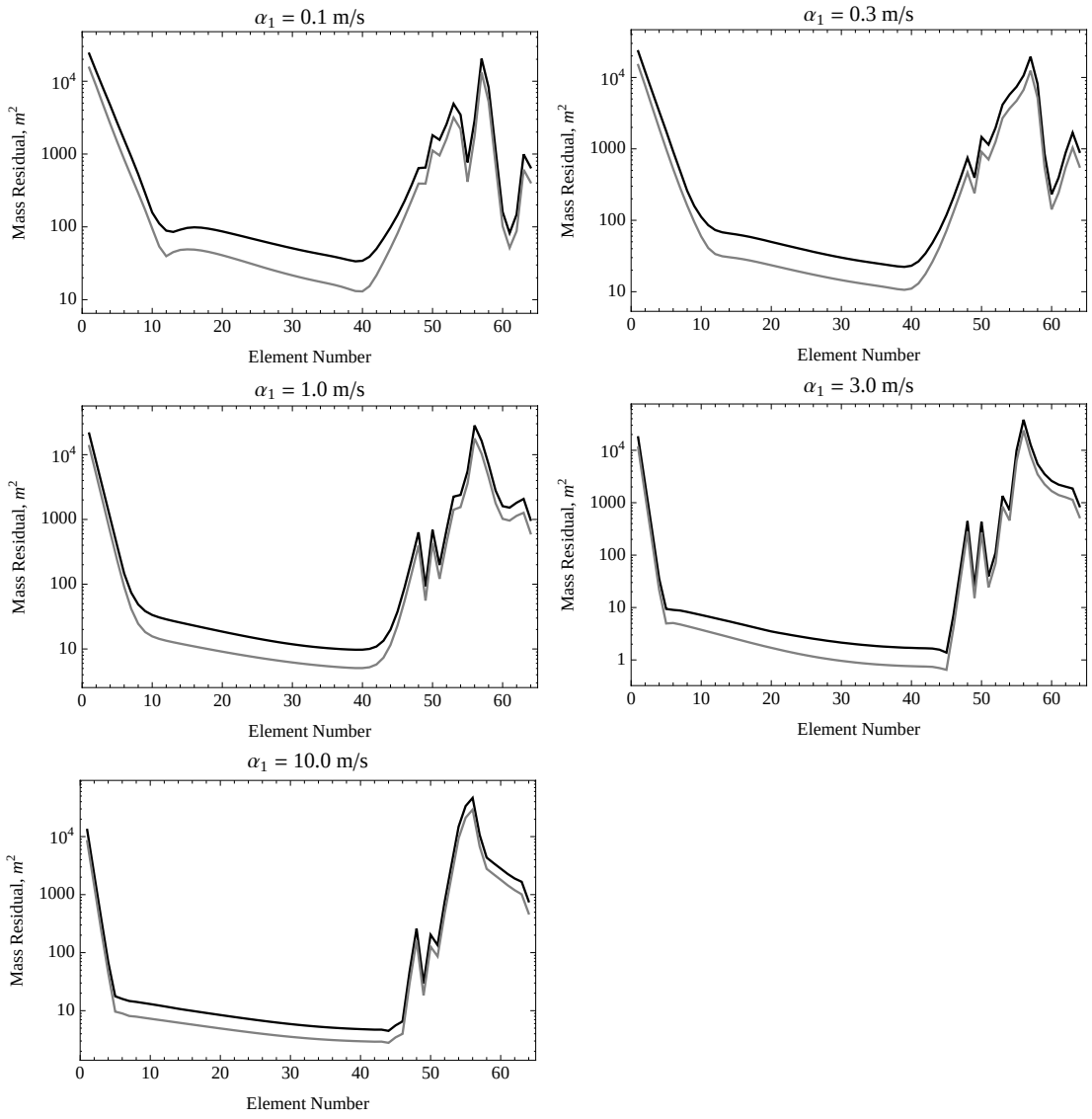

Figure 4.31 Maximum (black) and mean (gray) elemental mass residual for the east coast domain using different values of α_1. The absolute value of the mass residual is used in computation of the maximum and mean values.

residual with the maximum mass error occurring near the transition from the continental rise to the continental shelf.

More specifically, though, the mass residual results show different trends for different areas. For element 2, the mean mass residual decreases with increasing α_1 through most the range with a slight increase in error moving from $\alpha_1 = 3.0$ to $\alpha_1 = 10.0$ m/s. The results for element 30 show the same behavior. Element 50 shows

reduced mass error due to each increase in α_1, which is also the case for the elements on either side of the shelf break (57 and 58). However, elements 56 and 59 have mean mass residuals that generally grow with increasing α_1. The elements on the continental shelf also show a general growth of mean mass residual with increasing α_1.

Based on the discrepancy in mean mass residual trends associated with increasing α_1, it is not surprising that the corrections to α_1 based on mass residual and sensitivity to α_1 show a fair amount of variation throughout the domain. Figure 4.32 shows the elemental corrections to α_1 using mass residual results and sensitivity to α_1 over the last day of the simulation with $\alpha_1 = 1.0\ \mathrm{m/s}$. Focusing on particular data points, the corrections based on results from elements 2, 30, 50, 57 and 58 are all positive, as predicted by analysis of the mean mass residual results. Likewise, the corrections are negative based on results for elements 56 and 59. Table 4.5 shows the corrections using information for the different elements for different simulations. As is readily apparent from analysis of the elemental corrections, the least-squares correction using the elemental mass residuals and mass residual sensitivity to α_1 results in a decrease in the mass residual for the element used to generate the correction. However, the minimization of elemental mass residual at a given element does not necessarily result in improvement in elemental mass residual throughout the domain. In fact, as seen by the results for elements 56-59, a decrease in elemental mass residual for a given element does not even mean the mass residual is improved for the adjacent elements. Furthermore, the results for element 62 show that multiple local minimum mean mass residual values may exist for a given element. And, in that case, the final value of the coefficient resulting from sequential optimization may be influenced by the starting point for the coefficient in the optimization process.

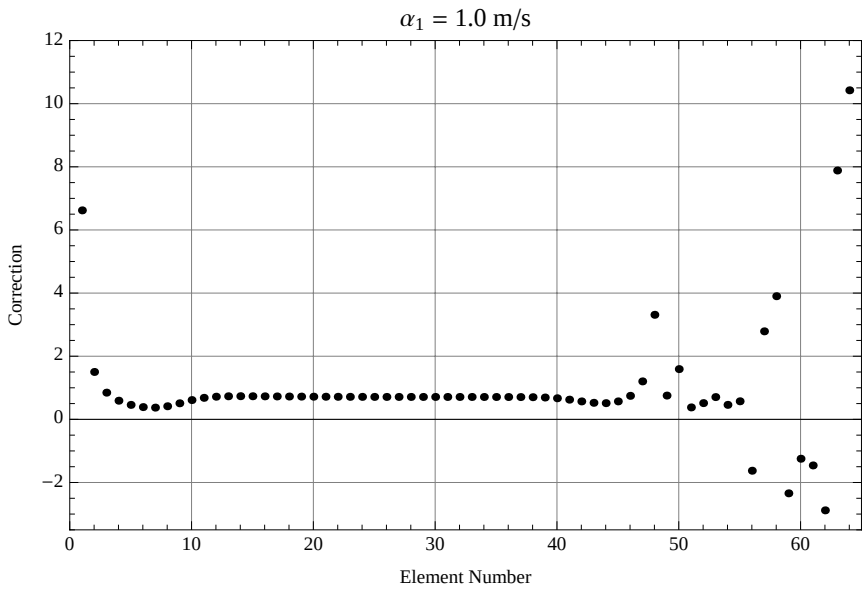

Figure 4.32 Elemental corrections to α_1 based on mass residual and sensitivity of mass residual to α_1 for a simulation with α_1 = 1.0 m / s on the east coast domain.

Table 4.5 Corrections to α_1 based on mass residuals and mass residual sensitivities to α_1 for different elements in the east coast domain.

Element	α_1 = 0.1	α_1 = 0.3	α_1 = 1.0	α_1 = 3.0	α_1 = 10.0
2	1.03	1.16	1.5	*minimum*[a]	-8.82
30	0.182	0.0398	0.710	*minimum*	-26.7
50	0.960	0.608	1.59	6.39	*minimum*
56	*minimum*	-0.204	-1.62	-10.6	-84.3
57	0.0457	1.64	2.79	14.4	*minimum*
59	0.0612	*minimum*	-2.34	-24.2	*local*[b]
62	*minimum*	-0.285	-2.88	0.022	*local*

a. For a given element, the distinction "*minimum*" denotes the coefficient value at which the mass residual is a minimum.

b. For elements 59 and 62, there was a decrease in mean mass residual at high values of α_1 resulting in a local minimum value.

4.7.6 Mass Residuals and Mass Residual Sensitivities for Seamount Domain with Linear ADCIRC

While this chapter is dedicated to analysis of the non-linear shallow water equations, this subsection is included because of the focus on sensitivity of mass residual to G. The mass residuals and sensitivities for the seamount domain with the explicit, linear code are shown in Appendix C.2.3 ($G = 0.001\ s^{-1}$) and Appendix C.3.3 ($G = 0.01\ s^{-1}$). The results for "Element 20" with $G = 0.001\ s^{-1}$ (Figure C.23) are an example of difficulty in attempting to eliminate mass balance error with ADCIRC. For the 31 node domain, the net flux term is positive throughout the time period shown in the plot (the third day of the simulation), and there is an increasing trend from tidal cycle to tidal cycle. The accumulation term is periodic and centered around zero. Thus, there is obviously non-zero mass residual (resulting from the sum of the accumulation and net flux terms).

The logical correction necessary to remedy the mass balance error is to decrease the net flux, rather than decrease the accumulation. The sensitivity of the net flux term to G is generally positive, so the net flux can be decreased by decreasing G. However, the zero sensitivity values in time coincide with the maximum net flux values, suggesting that decreasing G might not be effective in reducing the maximum net flux values to reduce the mass residual at those instances in time.

In Section 3.3.4, it was noted that the velocity sensitivity to G in the seamount domain does not tend towards zero as grid resolution is increased when $G = 0.01\ s^{-1}$. The seamount results with $G = 0.001\ s^{-1}$ show the mass residual does not tend towards zero throughout the domain as grid resolution is increased. Element 15 in the 31 node grid shows a net flux sensitivity value of approximately -2,000,000 m^2s near the end of the third day

of the simulation. Element 30 in the 61 node grid has a corresponding net flux sensitivity value of approximately -1,500,000 m^2s. Per element length, there is actually a larger magnitude sensitivity for the element in the 61 node grid than the corresponding one in the 31 node grid.

4.8 Conclusions

In this chapter, the forward sensitivity method was successfully applied to the 1-D non-linear version of ADCIRC with a three coefficient variable G parameterization. The sensitivity to the coefficients in the G parameterization was validated by comparing the FSM sensitivities to finite difference numerical analog sensitivities using multiple simulation results to compute sensitivities to G. Additionally, corrections to coefficients were calculated using elevation errors or mass residuals; the corrections using mass residuals also used the sensitivity of the mass residuals to G.

The results presented in this chapter show data assimilation using the FSM is useful in minimizing error through corrections to coefficients in the G parameterization. The majority of the focus was on correcting G coefficients using elevation errors because elevation observations are more prevalent than velocity observations for real applications. The α_1 optimization in Section 4.6.2 showed sequential optimization can result in decreasing error. However, that case also showed it is important to focus corrections to important areas. The mean of the nodal corrections was used to compute the new α_1 value for that set of simulations. The majority of the nodes are in the deep ocean portion of the domain. As a result, the mean correction was dominated by the errors and sensitivities in the deep ocean portion, rather than over the continental rise and on the continental shelf,

where it might be more desirable to minimize the error locally.

The analysis in Section 4.6.4 shows that multiple parameter estimation can be performed successfully. However, as in the constant G cases analyzed in Chapter 3, the corrections are highly-dependent on the G resulting from the parameterization. For terms in the G parameterization that increase with increasing coefficient values, the magnitude of the sensitivity to G generally decreases with increasing coefficient value. And, eventually, if the coefficient is increased too much, the resulting G parameterization will become "too primitive" and introduce spurious short-wavelength oscillations into the results and sensitivities.

The implications of the sensitivities for corrections based on elevation errors are similar to the implications noted for the constant G case in the previous chapter. Specifically, sequential optimization is possible, as long as the initial coefficient set is close enough to the target value. Additionally, sequential optimization is more effective if the values in the initial set are too low; coefficient values that are too high generally result in overcorrections and the overcorrections can be extreme if the coefficient set is too far from the target set. When the coefficients result in the specification becoming "too primitive," sensitivities often take the wrong sign (compared to the numerical analog sensitivities). This results in the correction being in the wrong direction.

The sensitivity of the mass residual to G is analyzed in Section 4.7. Results show that the FSM accurately predicts the change in mass residual based on a change in the G parameterization. As a result, it is possible to decrease local mass balance error using elemental least-squares corrections to the G parameter. However, changing G to decrease the mass residual for a given element does not necessarily reduce the overall local mass

balance error. As the results in Section 4.7.4 and Section 4.7.5 demonstrate, the coefficient values that minimize the local mass residual are different for different elements. Thus, changing the coefficients in the G parameterization will, generally, increase the local mass residual at certain instances in the domain. And, as is the case on the east coast domain, decreasing the local mass balance error in the area with the highest mass residuals based on the elemental least-squares correction from element with the highest error may not actually reduce the maximum mass residual. The mass residual will be reduced at the previous peak location. However, a new peak location may arise, and the new maximum may be in the adjacent element.

The majority of the mass balance error results from inconsistent net flux values. The accumulation term, which is simply a function of the current elevations for the nodes defining an element, is fairly consistent from element to element. The net flux term involves the elevations and velocities. Using elevation errors to generate corrections may result in increased mass residuals. Therefore, it is important to understand the goal of a particular G optimization. The G parameterization that produces the optimal elevation field for a hurricane storm surge application may not result in the most mass conservative (locally) elevation and velocity field for a contaminant transport simulation.

CHAPTER 5. 1-D Coupling of Channel Routing Models to ADCIRC

5.1 Introduction

A holistic coastal flood inundation model can be produced by coupling a hydrologic model for overland processes to a hydrodynamic model for coastal processes. There are numerous reasons to couple models and there are multiple ways to do so. One set-up is the coupling of a land surface-hydrology model with a mesoscale model. The land surface-hydrology model supplies surface heat fluxes as boundary conditions to the mesoscale meteorology model MM5 [*Chen* 2001]. That set-up is similar in form to the one followed in this chapter, where different models pass information back and forth across a boundary between them, and it allows models to be combined to create a more comprehensive model. Another form of coupled modeling is nested grid modeling that simulates different parts of the domain with different model set-ups, which may include varying the model, grid resolution and domain extent used. Nested grid models are common in meteorology and allow critical areas to be modeled at high-resolutions without incurring the computational expense of modeling the entire domain at the high-resolution, e.g. [*Frohn* 2002]. Research is currently underway to use a nested approach coupling ADCIRC to HYCOM (Hybrid Coordinate Ocean Model) in order to model baroclinic flow in the Gulf of Mexico and western Atlantic Ocean. This project uses initial and boundary conditions from HYCOM, a global ocean model to drive ADCIRC [*Dresback* 2009]. A nested approach is also used to couple wave models to ADCIRC, e.g. [*Westerink* 2008; *Ziljema* 2010; *Dietrich* 2010b]. Additionally, model coupling can use output from one model as the underlying physics for

another model, as in contaminant transport modeling, e.g. [*Ng* 1996], where the velocity field from a flow model drives the advective transport.

In coupling a hydrologic model to a hydrodynamic model, a location must be specified where information is exchanged. This location (or set of locations if multiple exchanges are required, e.g., for multiple rivers within a single domain) is herein referred to as a "hand-off point" (or hand-off location). The goal of this study is to provide guidance for the location of the hand-off point based on the channel routing algorithm used in the hydrologic model. To this end, 1-D channel routing models have been developed that solve the continuity equation in conjunction with either the kinematic, diffusive or dynamic wave approximation to the momentum equation.

The chapter begins with an overview of the channel routing models developed for the study. Then, the domains for the majority of the testing are presented in Section 5.3, which is followed by a brief comparison of the channel routing model results (Section 5.4). An outline of the coupled simulations is given in Section 5.5, which leads in to the one-way coupling (Section 5.6 through Section 5.8) and two-way coupling (Section 5.9 and Section 5.10) portions of the chapter. The last section contains conclusions based on the 1-D coupling analyses.

5.2 1-D Channel Routing Models

Channel routing is a standard component of distributed hydrologic models that is used to represent river flow through the domain. However, the implementation of channel routing within hydrologic models is far from standard. Even among physics-based models, which use a combination of conservation of mass, momentum and energy equations, there

are a variety of approaches. For this study, we will focus on utilization of conservation of mass and momentum, which is generally the approach adopted for channel routing in physics-based hydrologic models.

Three standard approximations to the momentum equation are employed frequently in hydrologic models. *Yeh et al.* [2005] describe WASH123D, an unstructured grid hydrologic model that can solve the continuity equation in conjunction with any of three momentum equation approximations (kinematic, diffusive or dynamic wave), and note that while the dynamic wave equation completely describes water flow, it is difficult to solve on steep slopes. Conversely, the kinematic and diffusive wave approximations are easier to solve, but errors occur when inertial terms are significant.

The structure of hydrologic models is also highly variable. For example, WASH123D uses a triangular, unstructured grid and solves 1-D channel flow along the edges of triangular elements that are used for 2-D overland flow and 3-D subsurface flow. TREX [*Velleux* 2006] also solves 1-D channel flow in elements along the edges of the 2-D overland cells, but differs in that it uses a structured grid. V*flo* [*Vieux* 2002, 2004], like TREX, is a structured grid model. However, it uses a 1.5-D (1-D network) approach to represent the 2-D domain, with cell-to-cell connections being made using either an overland or channel specification. However, the 1-D coupling study is independent of the treatment of channel routing within the larger 2-D domain and focuses simply on the channel routing component.

5.2.1 Kinematic Wave Approximation

Kinematic wave routing combines the continuity equation with the kinematic wave

approximation to the momentum equation. The continuity equation, assuming no lateral inflow or outflow, is given by (5.1) where h is depth of flow and q is the discharge per unit width, referred to as the "unit discharge" throughout the chapter (this is unrelated to the theory of the unit hydrograph [*Sherman* 1932] that is described in hydrology texts, including [*Bedient* 2002]).

$$\frac{\partial h}{\partial t} + \frac{\partial q}{\partial x} = 0 \tag{5.1}$$

The kinematic wave approximation, (5.2), assumes the friction slope, S_f, is equal to the bottom slope, S_0.

$$S_f = S_0 \tag{5.2}$$

The velocity, u, can be related to the friction slope using Manning's Equation, shown in (5.3), with the hydraulic radius, R, calculated as shown in (5.4), where A is the cross-sectional flow area, P is the wetted perimeter of the cross-section, n is Manning's roughness value, and k_n is the coefficient in Manning's equation (equal to 1.0 for units in meters).

$$u = \frac{k_n}{n} R^{2/3} (S_f)^{1/2} \tag{5.3}$$

$$R = \frac{A}{P} \tag{5.4}$$

In order to create a numerical model for testing purposes, finite difference approximations will be used to discretize the equations. In time, explicit time stepping will be used so the new variable quantities depend only on values from the previous time level. In space, upstream one-sided difference will be used. Using a reference system of the ocean on the left and the river flowing from right to left, discretization of (5.1) results in (5.5).

$$\frac{h_j^{k+1} - h_j^k}{\Delta t} + \frac{q_{j+1}^k - q_j^k}{(\Delta x)_{j+1}} = 0 \qquad \textbf{(5.5)}$$

Rearranging (5.5) to the form shown in (5.6) allows the new depth values to be calculated explicitly, using the depth and unit discharge values from the previous time level.

$$h_j^{k+1} = h_j^k - \frac{\Delta t}{(\Delta x)_{j+1}}(q_{j+1}^k - q_j^k) \qquad \textbf{(5.6)}$$

The numbering scheme for the nodes and elements for the kinematic and diffusive wave models is shown in Figure 5.1.

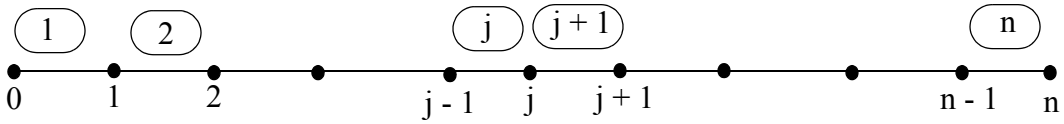

Figure 5.1 Schematic representation of the discretization of nodes and elements for kinematic and diffusive wave channel routing models.

For each time step, the calculation of the new water depths is the first step. Then, these depth values are used to update the velocity and unit discharge values. First, the velocity is calculated using Manning's equation with the simplification of $R = h$, which results from assuming representation of a rectangular channel cross-section with width, b, much greater than depth. The simplification process for R is shown in (5.7) and is consistent with the 1-D approach, assuming no variation "into the paper." The resulting velocity and unit discharge updates are given by (5.8) and (5.9), respectively. The negative sign in (5.8) is necessary because the river flows from right to left (in the negative x-direction).

$$R = \frac{A}{P} = \frac{bh}{b + 2h} \approx \frac{bh}{b} \approx h \qquad \textbf{(5.7)}$$

$$u_j^{k+1} = -\left(\frac{k_n}{n_j}\right)[h_j^{k+1}]^{2/3}[(S_0)_j]^{1/2} \qquad \textbf{(5.8)}$$

$$q_j^{k+1} = u_j^{k+1} h_j^{k+1} \qquad \textbf{(5.9)}$$

5.2.2 Diffusive Wave Approximation

The diffusive wave approximation to the momentum equation differs from the kinematic wave approximation in that it assumes the friction slope is equal to the slope of the water surface rather than the bottom slope. The continuum equation for the diffusive wave approximation to the momentum equation is given by (5.10), where Z is water surface elevation above a horizontal datum. Thus, the diffusive wave approximation allows water to move upstream depending on the gradient of the water surface, as water moves from areas of higher water surface elevation to areas of lower water surface elevation.

$$S_f = S_0 - \frac{\partial h}{\partial x} = -\frac{\partial Z}{\partial x} \tag{5.10}$$

Upstream, one-sided finite differences were used for the continuity equation for the kinematic wave model because this model limits flow to the downslope direction. However, centered finite differences will be used for the continuity equation for the diffusive wave routing model. Application of centered finite differences for the continuity equation, (5.1), using explicit time stepping results in (5.11).

$$h^{k+1} = h^k - \frac{\Delta t}{(\Delta x)_j + (\Delta x)_{j+1}}(q^k_{j+1} - q^k_{j-1}) \tag{5.11}$$

The momentum approximation term, given by (5.10), can be treated using a one-sided or centered finite difference approximation. Using the upstream one-sided difference, the discretized equation is (5.12). Using a centered difference, the discretized equation is (5.13).

$$(S_f)^k_j = -\frac{Z^k_{j+1} - Z^k_j}{(\Delta x)_{j+1}} \tag{5.12}$$

$$(S_f)_j^k = -\frac{Z_{j+1}^k - Z_{j-1}^k}{(\Delta x)_j + (\Delta x)_{j+1}} \quad \textbf{(5.13)}$$

Examination of a wave in the water surface represented by three nodes, as shown in Figure 5.2, shows why the centered difference may be the better choice for this set of equations. The wave will attempt to propagate in both directions, with water moving downstream (left) as well as upstream (right). If one-sided differences are used, the calculation of the friction slope at node j will have one sign (positive) if an upstream difference is used, and the opposite sign (negative) if a downstream difference is used. However, using centered differences, the friction slope at node j will be calculated using values at nodes $j-1$ and $j+1$. The friction slope at node j will be zero, resulting in zero velocity, and the water will move upstream at node $j+1$ and downstream at node $j-1$, which makes sense based on the continuum equations.

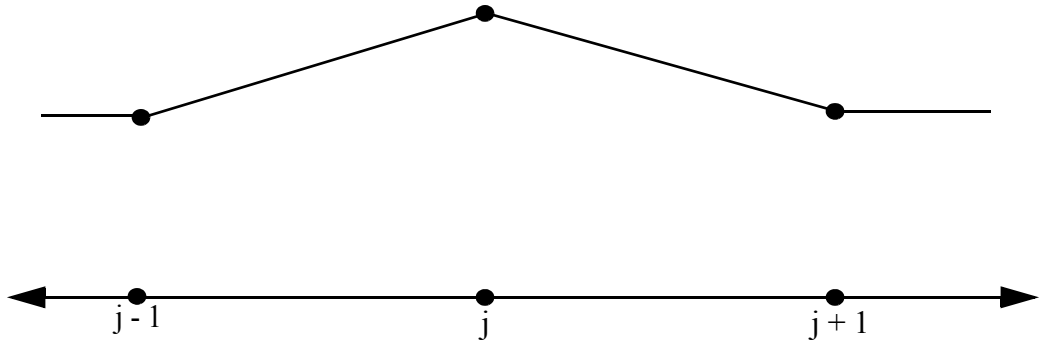

Figure 5.2 Wave in water surface elevation represented by values at three successive nodes.

The velocity for the diffusive wave model depends on the calculated friction slope. The magnitude of the velocity is calculated with Manning's equation using the magnitude of the friction slope; the velocity takes the sign of the friction slope. Using the same approximation for hydraulic radius as for the kinematic wave model, the velocity is given by

(5.14).

$$u_j^{k+1} = Sign[(S_f)_j^{k+1}]\left(\frac{k_n}{n_j}\right)[h_j^{k+1}]^{2/3}\left|(S_f)_j^{k+1}\right|^{1/2} \quad \textbf{(5.14)}$$

The unit discharge is calculated using the same method as for the kinematic wave equation, as shown in (5.9), with the new unit discharge being the product of the new water depth and velocity.

5.2.3 Dynamic Wave Approximation

The dynamic wave approximation to the momentum equation includes the advective terms that are neglected in both the kinematic and diffusive wave approximations. Solution of the dynamic wave equation model requires use of a staggered grid where equations for water depths and velocities are not solved at the same nodes; the finite difference approximation to the dynamic wave equations on a regular grid is inherently unstable [*Chaudhry* 1993]. As the velocities are offset from the water depths, the continuity equation used for the first two models, (5.1), has to be modified to the form found in (5.15), where q has been rewritten as (uh).

$$\frac{\partial h}{\partial t} + \frac{\partial}{\partial x}(uh) = 0 \quad \textbf{(5.15)}$$

Applying the chain rule and moving the spatial derivative terms to the right-hand side results in (5.16).

$$\frac{\partial h}{\partial t} = -u\frac{\partial h}{\partial x} - h\frac{\partial u}{\partial x} \quad \textbf{(5.16)}$$

Use of explicit centered finite difference yields the discretization given in (5.17), where $(u^*)_j^k$ depends on the direction of flow.

$$h_j^{k+1} = h_j^k - (\Delta t)\left\{(u^*)_j^k\left(\frac{h_{j+1}^k - h_{j-1}^k}{(\Delta x)_j + (\Delta x)_{j+1}}\right) + h_j^k\left(\frac{u_{j+1}^k - u_j^k}{((\Delta x)_j + (\Delta x)_{j+1})/2}\right)\right\} \qquad \textbf{(5.17)}$$

The numbering scheme for the dynamic wave model is similar to the one used for the kinematic and diffusive wave models. The difference for the dynamic wave model, as shown in Figure 5.3, is that the velocities use the same numbering as the elements and grid spacing, while the water depths remain at the previous node positions.

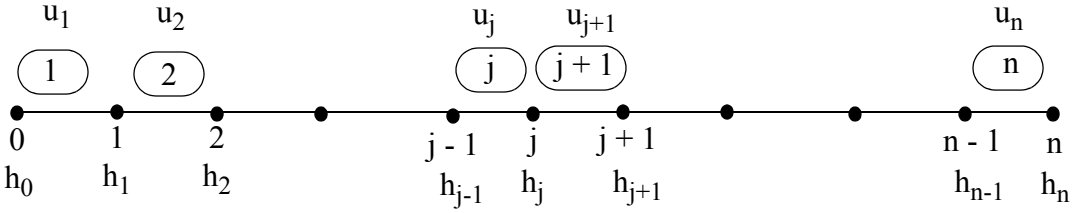

Figure 5.3 Schematic representation of the discretization of nodes and elements for the dynamic wave channel routing model, with velocities and depths staggered for stability.

Updated velocities come from solution of the momentum equation, given in continuum form in (5.18), where the first term on each side of the equations is new (compared to the momentum equation approximation (5.10) for the diffusive wave model).

$$\frac{\partial u}{\partial t} = -u\frac{\partial u}{\partial x} + g\left(-\frac{\partial h}{\partial x} + S_0 - S_f\right) \qquad \textbf{(5.18)}$$

The $(\partial u)/(\partial t)$ term is the local acceleration, while the convective acceleration is represented by the first term on the right-hand side, $-u((\partial u)/(\partial x))$. Assuming constant grid spacing, which will be used for the 1-D simulations, the explicit finite difference equation for the momentum equation is given by (5.19). An upstream, one-sided difference is used for the advective term. The flow is assumed from right to left in the discretization in (5.19). The indexing on the finite difference approximation to the derivative in the advective term would be different for flow from the left to right.

$$u_j^{k+1} = u_j^k + (\Delta t)\left\{ -u_j^k\left(\frac{u_{j+1}^k - u_j^k}{\Delta x}\right) + g\left(-\left(\frac{h_j^{k+1} - h_{j-1}^{k+1}}{\Delta x}\right) + (S_0)_j + (S_f)_j^k\right)\right\} \quad \textbf{(5.19)}$$

The calculations for the bottom and friction slope are given by (5.20) and (5.21), respectively.

$$(S_0)_j = \frac{Z_j - Z_{j-1}}{\Delta x} \quad \textbf{(5.20)}$$

$$(S_f)_j^k = u_j^k\left|u_j^k\right|\left(\frac{(n_j + n_{j-1})/2}{k_n[(h_j^k + h_{j-1}^k)/2]^{2/3}}\right)^2 \quad \textbf{(5.21)}$$

5.3 1-D Domains

Two domains have been created for this study. The first is the linear sloping domain containing 243 nodes shown in Figure 5.4. The total elevation change in the grid is 24.0 m, and the length of the domain is 120 km. Along the x-axis, the distance between nodes is 500 m. The slope is 0.0002 m/m, which is consistent with the slopes of the Tar and Neuse Rivers in coastal North Carolina. This will be the primary domain considered in this chapter.

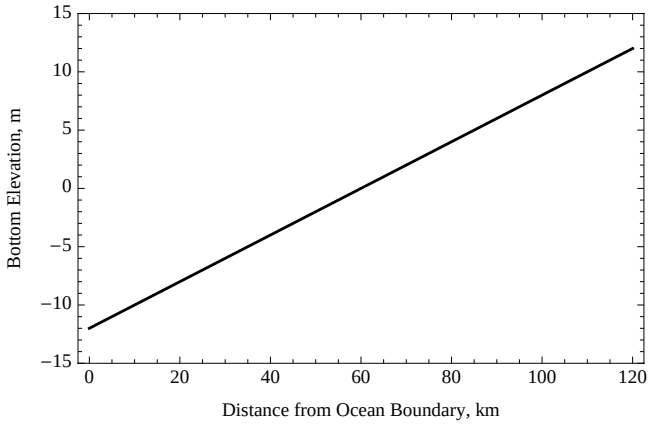

Figure 5.4 Linear sloping domain for 1-D simulations.

The second domain, shown in Figure 5.5, has a linear sloping river discharging into a flat estuary with a depth of 3.0 meters. The flat estuary is similar to the Pamlico Sound at the mouth of the Tar and Neuse Rivers. After 10 km, the flat estuary transitions to a series of linear sloping regions, with the maximum depth of 10.0 m occurring at the ocean boundary 71 km from the upstream boundary. The same node spacing, 500 m, is used for this grid. Therefore, a total of 143 nodes are included in the variable sloping domain.

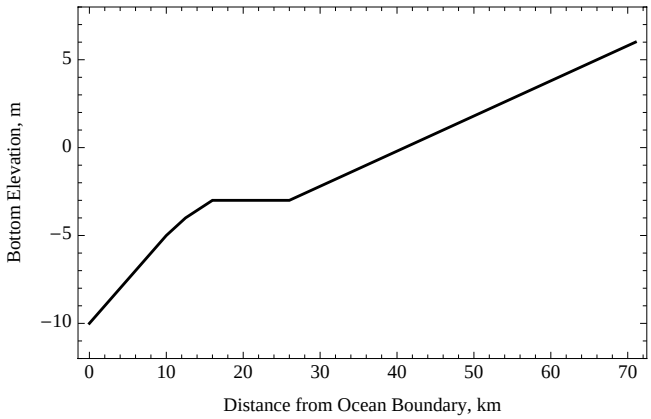

Figure 5.5 Variable sloping domain for 1-D simulations.

5.4 Channel Routing Model Comparison

To test the three channel routing models, which will also be referred to as "hydraulic" models at times throughout this chapter, simulations were performed on the linear sloping domain. The upstream boundary forcing was the unit discharge hydrograph shown in Figure 5.6. The downstream boundary was treated with $(\partial h)/(\partial x) = 0$. The other simulation parameters are given in Table 5.1. The Manning's roughness value was selected so normal depth would be the same in the 1-D ADCIRC and channel routing models with a unit flux of 2.0 m/s.

Table 5.1 Parameters for channel routing test case on linear sloping domain.

$n = 0.01934$	$nn = 241$	$\Delta x = 500$ m	duration = 5.0 days
$\Delta t = 1.0$ s	$S_0 = 0.0002$	output every 15 min	

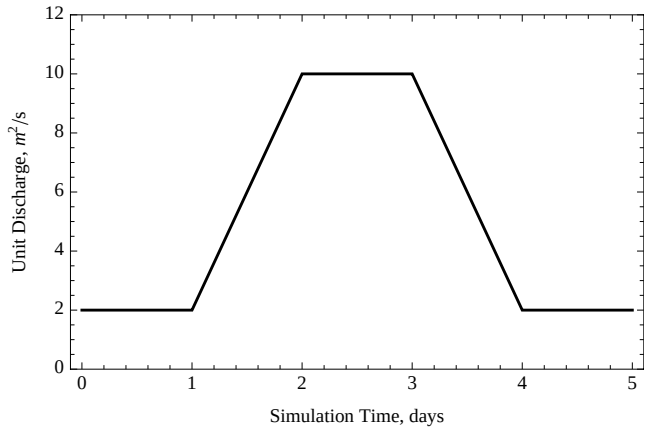

Figure 5.6 Upstream boundary forcing for the channel routing model test.

The unit discharge time series at locations 30, 60 and 90 km from the upstream boundary are shown in Figure 5.7. There is not a large difference in the unit discharge time series for the different models. However, it is apparent that there is a difference between the kinematic wave model and the others near the changes in the forcing; the diffusive and dynamic wave models have smoother transitions between the constant flow rate and the variable flow rate portions of the time series. The diffusive and dynamic wave models attenuate the peak and spread out the hydrograph more than the kinematic wave model does. However, despite the differences, all three models do a sufficiently good job of routing an inflow hydrograph downstream to the outflow from the domain.

5.5 Outline of Coupling Simulations

The first four sections of simulations use the parameters outlined in Table 5.2. The first three sections investigate different variations of one-way coupling, where results from one model are used as boundary conditions for a different model simulation, while the fourth section deals with dynamic two-way coupling, in which information is passed between two models in a single simulation.

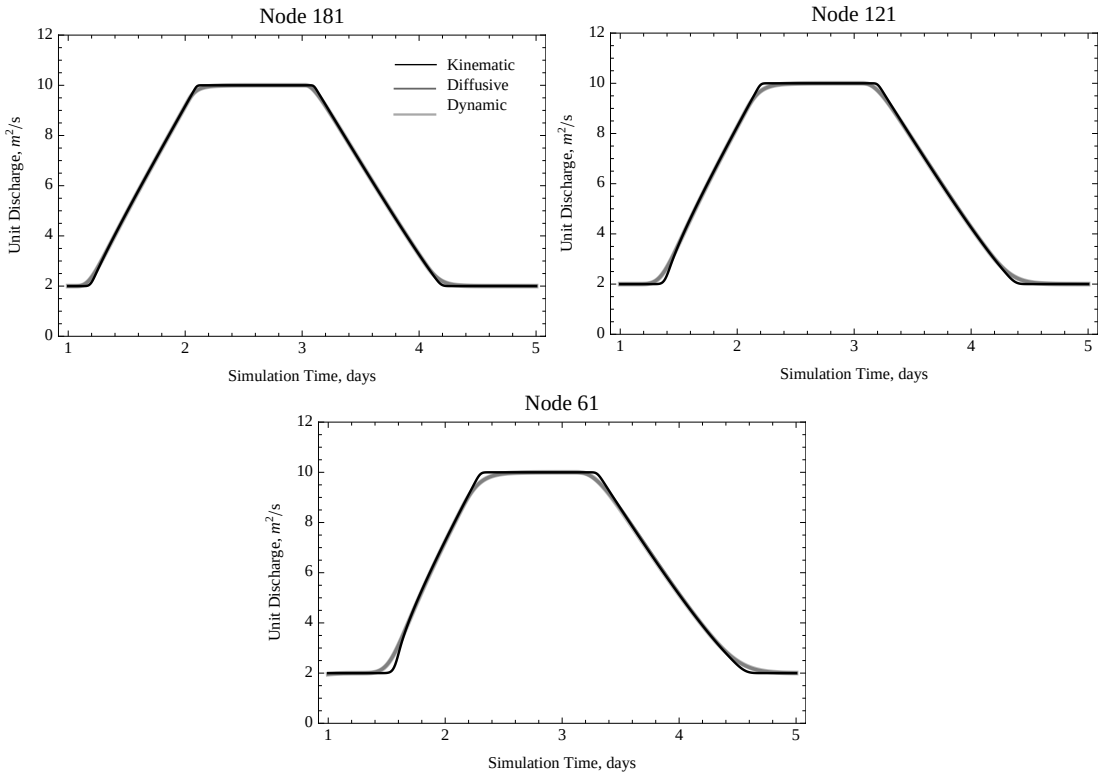

Figure 5.7 Unit discharge results for the three channel routing models at three locations on the linear sloping domain.

Table 5.2 Base simulation parameters for Section 5.6 through Section 5.9.

$n = 0.01934$	$C_f = 0.003$	$G = 0.01$	duration = 2.5 days
$\Delta t = 1.0$ s	$S_0 = 0.0002$	output every 15 min for last 1.5 days	$\varepsilon = 0.0$

The first set of simulations (Section 5.6) uses results from the full-domain ADCIRC model as the downstream boundary condition in hydraulic simulations. The full-domain ADCIRC simulation, as the name suggests, is an ADCIRC simulation performed on the entire domain. In terms of this study, "full-domain" implies forcing with the specified ocean elevation and upstream flow boundary conditions at their respective edges of the domain. Time series of elevations and velocities are output from the model at specified locations to be used as boundary conditions for subsequent partial-domain hydraulic simulations. These hydraulic simulations are performed on varying domain sizes, with the

upstream boundary location held constant. The downstream boundary (hand-off point), where the ADCIRC results are used as boundary conditions, varies between simulations.

The second of these sections (Section 5.7) focuses on partial-domain ADCIRC simulations forced with upstream boundary conditions from full-domain simulations (both ADCIRC and channel routing). The partial-domain ADCIRC runs have a constant oceanward extent, which corresponds to the oceanward extent of the full-domain simulations. However, the inland extent of these simulations varies between simulations as the location of the hand-off point is modified.

The simulations in Section 5.8 do not use full-domain results as the boundary conditions. Instead, partial-domain simulations are used to generate boundary conditions. The term partial-domain is, perhaps, a bit misleading when it is applied to simulations used to generate boundary conditions for one-way coupled simulations. The partial-domain ADCIRC simulation used to generate boundary conditions is actually an ADCIRC simulation run on the entire domain. The difference between the partial-domain and full-domain ADCIRC simulations to produce boundary conditions is that the partial-domain ADCIRC simulation has all portions of the domain above mean sea level initialized as dry and the upstream boundary is treated as a zero flow boundary. Thus, while the partial-domain ADCIRC simulation uses the same grid file as the full-domain ADCIRC simulation, there is no river inflow. Furthermore, portions of the domain are dry in the partial-domain simulation, while the entire domain is wet during the full-domain simulation because there is a river inflow at the right boundary. In contrast, the partial-domain ADCIRC simulations in Section 5.7 do not include the entire extent of the domain, but all the elements within the domain are active (wet) because there is a river flow applied at the upstream boundary.

The partial-domain hydraulic simulations (to produce boundary conditions) also use the same grid file as the full-domain simulations. Furthermore, the entire domain is modeled as wet. Similar to the partial-domain ADCIRC simulation (to produce boundary conditions) described above, the major difference between the partial-domain and full-domain hydraulic simulations is in one of the boundary conditions. In the full-domain hydraulic simulations, the boundary condition on the left side (ocean) boundary is a specified tide and surge elevation time series. In the partial-domain hydraulic simulation to produce boundary conditions for ADCIRC, the boundary condition at the left side boundary is normal depth. This treatment allows water to flow downstream without being subject to the tides and surge that cause backwater effects. Also, the initialization is different between the full- and partial-domain hydraulic simulations because the partial-domain simulation treats the entire domain as a river, with a specified initial depth, whereas the full-domain simulation initializes with a minimum water surface elevation of mean sea level. Therefore, in the areas on the left side of the domain, the initial water surface elevation is lower in the partial-domain hydraulic simulations than in the full-domain hydraulic simulations.

The fourth simulation section (Section 5.9) uses the same grid files, but divides the domain so that ADCIRC models the ocean portion and the dynamic wave hydraulic model computes results on the river portion, although the extent of the domain handled by each model varies between simulations (as the hand-off point is moved). Information is passed from ADCIRC to the hydraulic model at each time step as the downstream boundary condition for the hydraulic model. Similarly, results at the downstream end of the hydraulic model are used as the upstream boundary condition in ADCIRC, i.e., dynamic two-way

coupling.

The final simulation section (Section 5.10) builds on aspects of the previous sections and explores two-way coupling using a different grid and different boundary forcings than were applied previously. Specifically, the elevation ocean forcing time series is an approximation to elevation data captured during Hurricane Isabel. Additionally, the upstream flux forcing is adapted from USGS gauge data for Hurricane Floyd.

5.6 Hydraulic Simulations Using Full-Domain ADCIRC Forcing

In order to assess the impact of the momentum equation approximation on the ability to utilize downstream boundary conditions to model flow in the near-shore reaches of the river, simulations were performed using the three hydraulic models with downstream boundary conditions drawn from a full-domain ADCIRC simulation. This is a one-way coupling application, with information from ADCIRC used as a boundary condition in the hydraulic model. The full-domain ADCIRC simulation is run before the coupled simulation; the ADCIRC simulation utilized the full grid with the elevation ocean boundary condition shown in Figure 5.8, as well as a constant upstream unit discharge value of 2.0 m^2/s into the domain.

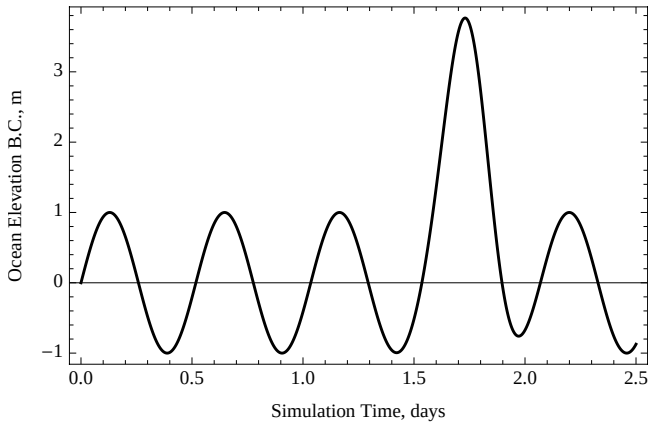

Figure 5.8 Elevation ocean boundary forcing for 1-D simulations.

The downstream boundary conditions used for the one-way coupled hydraulic simulations come from the elevation and velocity fields in ADCIRC. Specifically, at the various hand-off locations chosen for coupling for different simulations (to assess the impacts of the location of the coupling), time series of elevations and velocities are output every time step during the ADCIRC simulation. For elevation downstream boundary forcings, the water surface elevation values from ADCIRC are used as the boundary forcing. For flux forcing at the downstream boundary, the flux (q_{bc}) is the product of the depth from ADCIRC and the ADCIRC velocity at the hand-off point, u_{bc} as shown in (5.22), where the depth is given by the sum of the water surface elevation, ζ_{bc}, and the bathymetry value at the boundary, y_{bc}. This value is applied as the boundary condition for the hydraulic model.

$$q_{bc} = (\zeta_{bc} + y_{bc})u_{bc} \tag{5.22}$$

The channel routing codes are run with a 1.0 second time step, which matches the ADCIRC time step. The upstream boundary condition is the same constant discharge as is used in the full-domain ADCIRC simulation to create the boundary conditions: 2.0 m^2/s into the domain. This unit discharge is consistent with values often experienced by the Tar and Neuse Rivers. The error for the coupled simulation is calculated as the difference between the coupled simulation result and the full-domain ADCIRC simulation at a given location at a given point in time. The elevation RMS error in time, given by (5.23), is calculated in time for each node in the coupled simulation domain for a particular simulation.

$$RMSE_t(\zeta)_j = \sqrt{\frac{\sum_{k=1}^{nrecs} ((\zeta_{adc})_j^k - (\zeta_{hyd})_j^k)^2}{nrecs}} \tag{5.23}$$

Less of the domain contains results for coupled simulations with the downstream boundary (hand-off point) further upstream (to the right). The $RMSE_t(u)$ is computed for each node in the coupled simulation domain, as in (5.23), except the velocity results from the two models are substituted for the water surface elevations.

5.6.1 Kinematic Wave Channel Routing Results

The hydraulic code using the kinematic wave approximation for the momentum equation is independent of the downstream boundary condition except at the downstream boundary node. Thus, only one set of results will be shown for the kinematic wave routing model. Elevations from ADCIRC were applied as the downstream boundary condition, which has the result of creating zero elevation error at the downstream boundary location, as can be seen in Figure 5.9. The velocity error is shown to the right of the elevation error in the same figure.

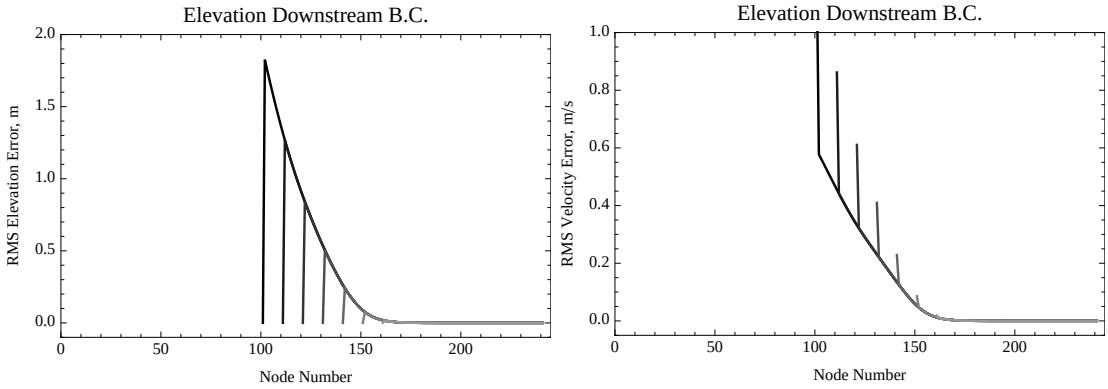

Figure 5.9 Elevation and velocity $RMSE_t$ for the kinematic wave channel routing model on the linear sloping domain, forced with elevation results from ADCIRC at the downstream boundary. The lines decrease in darkness from the results for the simulation with the most oceanward hand-off point to the results for the simulation with the hand-off point farthest upstream.

Graphs similar to those found in Figure 5.9 are prevalent in this chapter, so detailed discussion is warranted. The left panel shows the $RMSE_t$ for elevations in meters and the right graph shows the $RMSE_t$ for velocities in meters per second. There are seven lines,

each corresponding to a different simulation. The only difference in the seven simulations is the extent of the channel routing domain and, therefore, the location of the downstream boundary specification (hand-off point). For the simulations on the linear sloping domain, the first hand-off location is at node 101, which has a bathymetry value of 2.0 m below sea level. The hand-off points occur in 1.0 m elevation intervals (10 node intervals), with the seventh location occurring 4.0 m above sea level at node 161.

A $RMSE_t$ is computed for each node in the coupled simulation domain. The black line in each of the graphs corresponds to the error results from the simulation using the most oceanward boundary location. The lines get successively lighter to denote the results for simulations with hand-off points farther upstream.

Finally, addressing the results shown for the kinematic wave model in Figure 5.9, it is apparent that the boundary condition does not affect the model results except at the boundary. It appears that the black line disappears when the next lighter line starts, then that line disappears when the line for the third boundary location starts, and so on until the lightest line takes over. This is not the case. Instead, the lines simply plot over the top of each other because the same RMS error values occur for each simulation. The number of lines plotted on top of each other increases as one moves upstream. The same situation exists for the velocity errors. The main difference between the elevation and velocity plots is that specified elevation boundary condition causes the elevation error to be zero at the boundary and creates an increased error in the velocity at the boundary. There is a discontinuity in the elevation fields between the models at the downstream boundary. Using Manning's equation, the velocity is directly related to the water depth so there is also a discontinuity in the velocity field, which causes the error for the boundary node to be much

different than the error for the first non-boundary node.

The results for the variable sloping domain are presented in Appendix E.1.1. There are nine hand-off points with the downstream-most location at node 26, the second hand-off point at node 33, and the rest in ten node increments upstream. The results for the variable sloping domain are consistent with results for the linear sloping domain.

The interpretation of the results for the kinematic wave routing algorithm is straightforward. The solution is better as one moves farther inland, away from the areas affected by tidal action and storm surge, which are both combined in the elevation boundary condition at the ocean boundary for the full-domain ADCIRC simulation. The kinematic wave approximation to the momentum equation does not provide a mechanism for "backwater" effects to be handled. As one moves upstream, the "backwater" effects for this simulation become increasingly less important, which results in the kinematic wave model producing better results near the upstream boundary than it does in areas downstream. For node 171 in the linear sloping domain, which is 5.0 m above mean sea level (and 10 nodes upstream of the most inland hand-off point), the RMS errors for elevation and velocity are 0.0031 m and 0.0020 m／s, respectively.

5.6.2 Diffusive Wave Channel Routing Results

There are three sets of results for the diffusive wave model on each domain, corresponding to simulations with a variety of downstream boundary condition specifications: 1) elevation, 2) flux, and 3) velocity. Centered finite difference was used for the diffusive wave approximation to the momentum equation for stability purposes; upstream treatment of the momentum equation produced more prevalent short wavelength oscillations in the

solutions.

The $RMSE_t$ results for the different simulation sets on the linear sloping domain are shown in Figure 5.10. The results for the variable sloping domain can be found in Appendix E.1.2. The results are similar for all three boundary condition specifications. For the linear sloping domain, the RMS elevation error is in the range of 0.05 m, and the RMS velocity error is around 0.03 $\mathrm{m/s}$. However, the boundary condition has an impact on the shape of the error plots. When an elevation downstream boundary condition is used, the elevation error at the most oceanward node is zero. The elevation error increases to a maximum, then returns toward zero in the river upstream of the major backwater effects. The velocity error is a maximum near the boundary and decreases as you move upstream. It is worthwhile to note that there are also errors near the upstream boundary. However, these errors were not cause for major concern because they do not pollute the solution throughout the river. For example, with the elevation specified at the most oceanward hand-off point, the RMS elevation and velocity errors at node 201 are 0.00046 m and 0.000098 $\mathrm{m/s}$, respectively. This study is concerned with the near-coastal interface rather than the channel routing upstream boundary.

When velocity is specified at the downstream boundary, the velocity error is zero at the boundary. However, for non-boundary nodes, the velocity boundary condition does not seem to have a major effect on the velocity errors. When the elevation boundary condition is used, the elevation errors gradually increase from zero at the boundary. However, when the velocity boundary condition is used, the velocity error increase is abrupt. This is a result of the diffusive wave model equations. The velocity boundary condition is used, in conjunction with the calculated depth, to compute the flux at the boundary. The flux, in

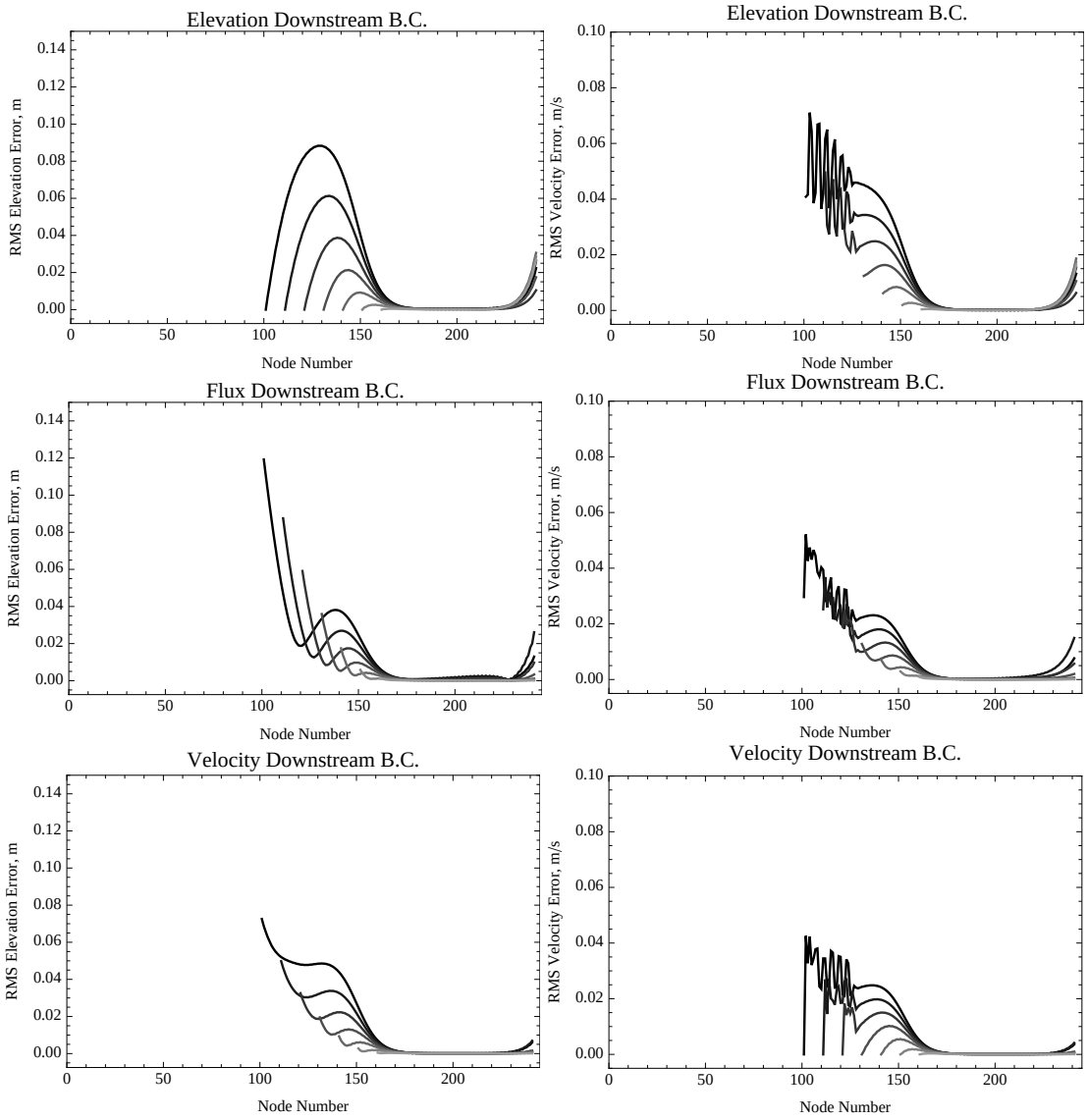

Figure 5.10 Elevation and velocity $RMSE_t$ results for the diffusive wave channel routing model on the linear sloping domain. Boundary conditions come from the full-domain ADCIRC simulation.

turn, is used in the calculation of the new depths at the first two nodes in the domain. However, there is no direct momentum advection due to the specified velocity. The movement of water upstream results only from water surface elevation gradients. Additionally, the elevation errors are a maximum at the boundary. Thus, the flux that is calculated for use in the continuity computations is different than the ADCIRC flux at the location of the boundary.

Use of flux as the downstream boundary condition does not result in either zero elevation or velocity error at the boundary. In fact, it produces the largest elevation error at the boundary. However, it yields the lowest elevation error for nodes in the range of 130-160. The velocity error is less than when the elevation boundary condition is used and on par with the results for simulations with the specified velocity boundary condition.

Overall, several general trends are present. First, regardless of boundary condition and boundary location, the errors tend toward zero as one moves upstream away from the backwater effects (although unrelated errors are present near the upstream boundary). Additionally, moving the boundary farther upstream reduces the error in the simulation. This is not particularly surprising because the presence of adverse velocities (upstream, opposite the direction of the bottom slope) decreases as one moves upstream. Thus, the inertial terms ignored in formulation of the diffusive wave model are less important, and the error from neglecting them is reduced.

The results for the variable sloping domain support the findings from the linear cases. Specifically, solutions using centered differences are better than corresponding results using one-sided differences. Additionally, similar error levels exist regardless of the type of information used at the downstream boundary for the diffusive wave model. The overall error levels are slightly higher, but this is primarily due to the use of more ocean-ward hand-off points for the variable sloping domain.

5.6.3 Dynamic Wave Channel Routing Results

Two sets of simulations were performed using the dynamic wave channel routing model, with the only difference being the information used as the downstream boundary

condition: 1) elevation and 2) velocity. The results for the linear sloping domain are shown in Figure 5.11. The graphs on the left are elevation errors, while the graphs on the right are velocity errors. The ADCIRC velocity applied as the boundary condition is the value from the ADCIRC node that coincides with the first elevation node in the dynamic wave simulation. Due to the staggered finite difference grid, this treatment introduces a small error in the velocity forcing, which is why the velocity error is not zero at the hand-off point.

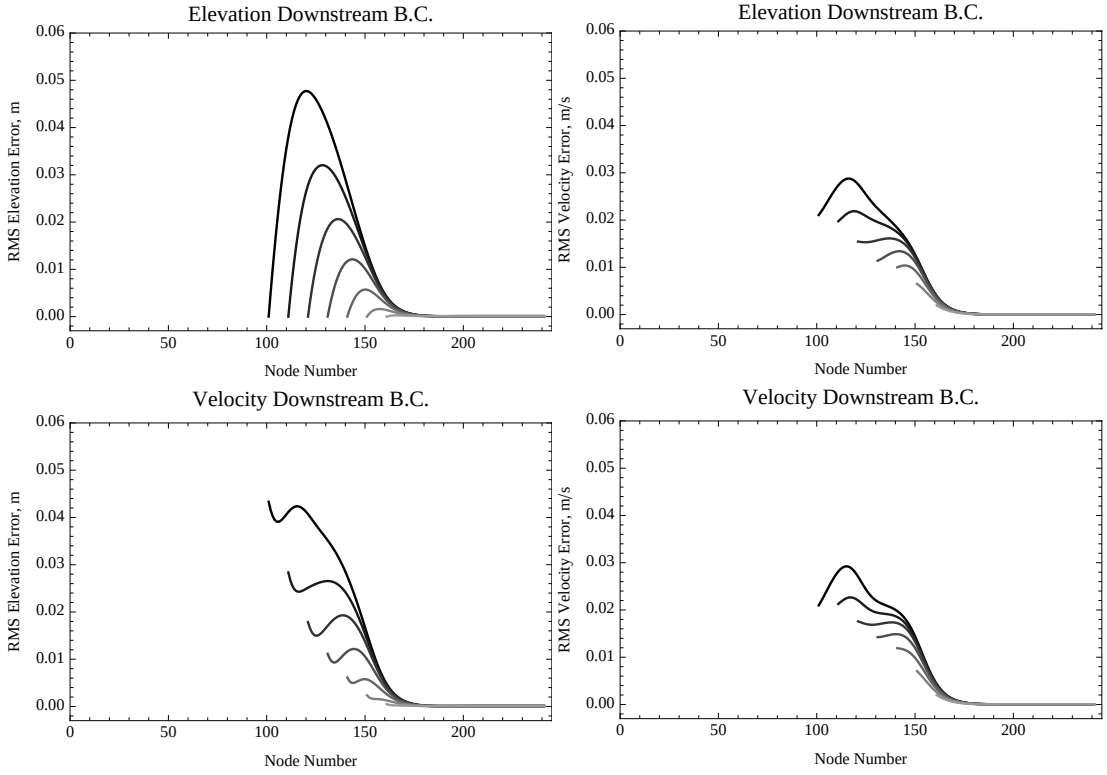

Figure 5.11 Elevation and velocity $RMSE_t$ for the dynamic wave channel routing model simulation sets on the linear sloping domain. The downstream boundary conditions come from a full-domain ADCIRC simulation.

The plots for the dynamic wave channel routing model show similar results for both domains (the variable sloping domain results are presented in Appendix E.1.3), and general patterns seen with the other momentum equation approximations hold for the dynamic wave model as well. However, before addressing the general results, a few graph generation specifics should be noted. First, the error scales are different for the different sets of

results. The range of elevation errors for the dynamic wave results is 0-0.05 m, whereas the range for the diffusive wave results is 0-0.15 m. Additionally, the non-zero velocity errors when velocities are used as the specified boundary condition are a result of the use of a staggered grid. The velocities for the dynamic model are offset from the velocities for ADCIRC by $(\Delta x)/2$. Rather than average the velocities so the locations coincide, the upstream velocity from the dynamic wave results is compared to the ADCIRC result.

Returning focus to analysis of the results, the errors for the dynamic wave simulations are about half as much as the errors for simulations using the diffusive wave approximation to the momentum equation for both domains. Trends that hold from the previous simulations (with the different momentum equation approximations) are that results are better for upstream locations within the domain and simulations with more upstream hand-off locations. Additionally, the choice of information specified at the downstream boundary does not have a significant role in peak errors in elevations or velocities. However, as with the diffusive wave approximation, the shape of the error graphs and the location of the maximum errors is dependent on the boundary condition specification.

5.7 ADCIRC Simulations Using Full-Domain Simulation Forcing

Previously, the effects of changing the downstream boundary condition, hand-off location, and complexity of the momentum equation in the channel routing model were investigated. In this section, a similar investigation will be performed to gain an understanding of the implications of upstream boundary forcings on the 1-D ADCIRC model.

The full-domain channel routing model was run to obtain results to use as the upstream boundary forcing for the ADCIRC simulations. The overall boundary forcings for

this investigation are the same as for the previous inquiry. Specifically, a constant upstream flux of 2.0 m^2/s into the domain is used and a tidal signal with a surge wave superimposed is used as the elevation forcing at the ocean boundary. A total of six sets of simulations result from using both domains (linear sloping and variable sloping) with the three hydraulic models (kinematic wave, diffusive wave and dynamic wave).

Before examining the effects of the boundary conditions on the ADCIRC model, it may be useful to better understand the information being passed into ADCIRC at the upstream boundary. This was not a major issue in the previous study using ADCIRC results as the boundary conditions because the model used to produce all the boundary conditions was consistent across all the simulations. The plots in Figure 5.12 show the elevation and velocity errors for each of the hydraulic models, as compared to the full-domain ADCIRC results on the linear sloping domain. It is important to note that the error ranges are not consistent between graphs.

As expected, the dynamic wave full-domain results most closely resemble the full-domain results from ADCIRC. The peak error for the dynamic wave elevation results is about one-half the largest elevation error for the diffusive wave results. This is also true for the results on the variable sloping domain shown in Appendix E.2.1. The dynamic wave model excels, compared to the diffusive wave and kinematic wave models, in capturing similar velocity fields to those produced by ADCIRC. This result is not surprising; the kinematic and diffusive wave approximations neglect the acceleration terms found in the dynamic wave approximation. One source of error that may account for a portion of the difference seen between the dynamic wave and ADCIRC solutions is the bottom friction scheme employed. The channel routing models use Manning's equation for friction, which

is different than the scheme used in this particular ADCIRC simulation. The Manning's roughness value was chosen to produce equivalent steady-flow results in the river at the base river inflow, but that value does not produce equivalent results for all locations (i.e., the ocean portion of the domain) in the domain or for different flow rates.

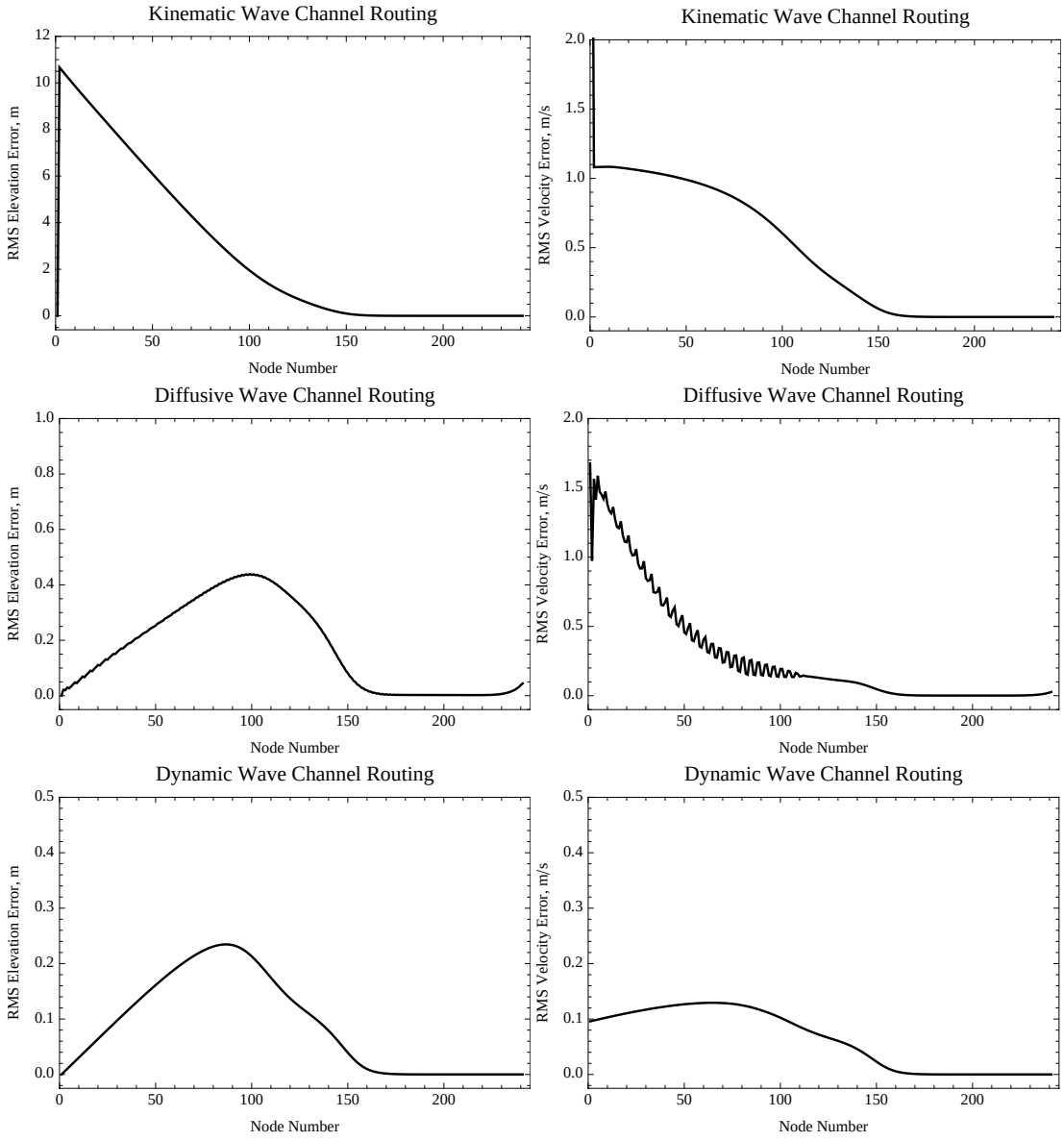

Figure 5.12 Elevation and velocity $RMSE_t$ for the full-domain hydraulic models compared to the full-domain ADCIRC results on the linear sloping domain.

5.7.1 Elevation Upstream Boundary Condition from Hydraulic Models

The first round of simulations using ADCIRC on the partial domain consisted of specifying the elevation from the full-domain hydraulic solutions as the upstream boundary condition. The elevation and velocity $RMSE_t$ results can be seen in Figure 5.13. It is important to note the scales used on the graphs when comparing results between plots. Additionally, the full-domain ADCIRC result is used as the true solution.

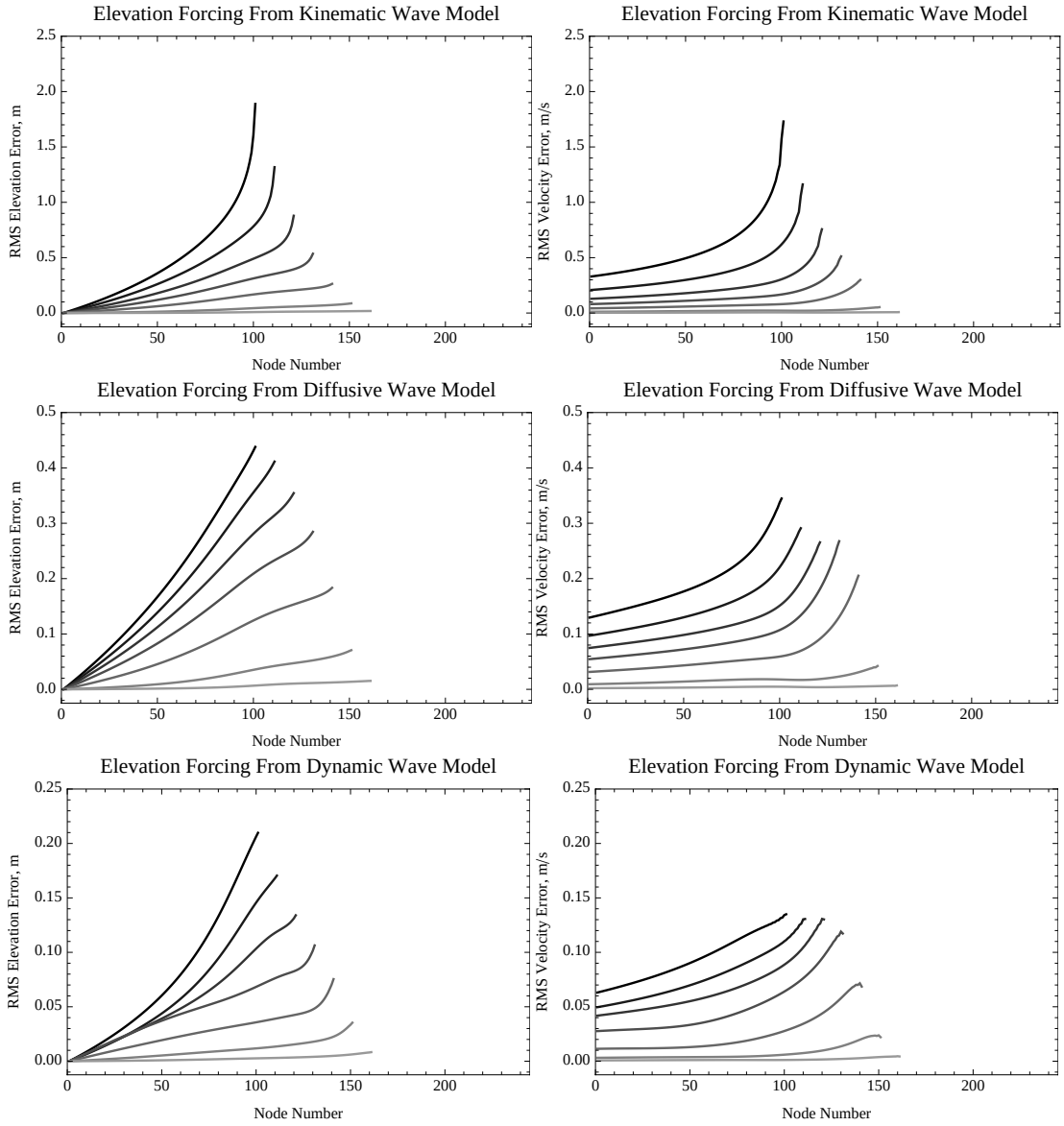

Figure 5.13 Elevation and velocity $RMSE_t$ for ADCIRC on the linear sloping domain using elevation upstream boundary conditions from the three different channel routing models.

Not surprisingly, the higher the error in the boundary conditions, the more error there is in the simulation solution. Thus, the solution is much better when forced with the dynamic wave results at the upstream boundary than with the diffusive wave results. Similarly, ADCIRC produces better results using boundary conditions from the diffusive wave hydraulic model than when boundary conditions from the kinematic wave model are specified. However, if the hand-off point is far enough upstream that the tides and surge do not impact the channel routing solution in that area, boundary conditions from the kinematic wave model can be used to produce satisfactory ADCIRC simulation results.

At the ocean boundary, the elevation boundary condition specification constrains both models (the full-domain ADCIRC and the partial-domain ADCIRC using upstream boundary conditions from the hydraulic routing model), yielding zero $RMSE_t$ error. For each set of elevation error results, the error increases incrementally as one moves upstream until a maximum is reached at the hand-off location, where the elevation boundary condition from the hydraulic model is specified. The velocity errors follow the same trend. They decrease as one moves from the upstream boundary to the ocean boundary. One trend that exists for both the elevation and velocity results is that, for a given node, the elevation and velocity errors are lowest for the simulation with the hand-off point farthest upstream. The error at a given node increases as the upstream boundary location is moved downstream. This is not particularly surprising given the errors shown in Figure 5.12. Over the range of hand-off points, the elevation error between the full-domain hydraulic and full-domain ADCIRC simulations increases from upstream to downstream.

In general, the same trends hold for partial-domain ADCIRC simulations, using elevation upstream boundary conditions, on the variable sloping domain. These results are

presented in Appendix E.2.2. Simulations with boundary conditions from the dynamic wave model produce the best results, whereas using results from the kinematic wave model to force ADCIRC produce the worst set of results. Due to the fact that hand-off locations do not exist as far upstream for the variable sloping domain as they do for the linear sloping domain, the errors using boundary conditions from the kinematic wave model do not approach zero like they do for the linear domain. However, if the boundary was moved upstream, away from locations where tides and surge play a prominent role in the solution, ADCIRC could produce satisfactory results on the variable sloping domain using boundary conditions from the kinematic wave model.

5.7.2 ADCIRC Forced with Upstream Boundary Condition from Dynamic Wave Model

Based on the previous results, the full-domain dynamic wave results are the best choice for limiting ADCIRC error because the dynamic wave algorithm provides the results most consistent with the full-domain ADCIRC results. Thus, for testing the different types of upstream boundary conditions for ADCIRC, the full-domain dynamic wave results will be used. Using the time series elevation and velocity results from the full-domain dynamic wave hydraulic model as upstream boundary conditions, elevation and velocity errors were generated (again comparing to the full-domain ADCIRC solution) for two boundary forcings: 1) specifying elevation, as in the previous section, and 2) specifying flux. The plots for the linear sloping domain can be found in Figure 5.14. The corresponding plots for the variable sloping domain are provided in Appendix E.2.3.

Comparing the results with elevations specified at the upstream boundary to the results with flux specified, the error plots are similar in shape. The results, again, are better

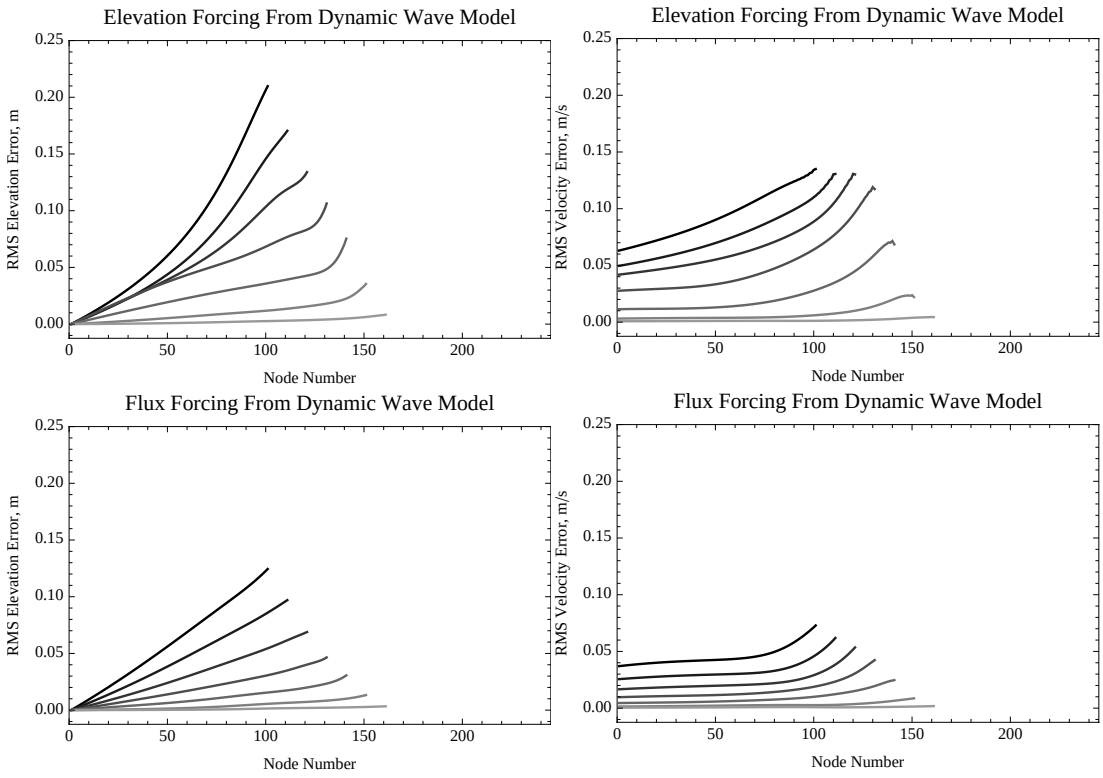

Figure 5.14 Elevation and velocity $RMSE_t$ for ADCIRC using elevation or flux upstream boundary conditions from the dynamic wave hydraulic model on the linear sloping domain.

with the boundary farther upstream. This is reasonable because the full-domain hydraulic results are most like the full-domain ADCIRC results near the upstream boundary of the domain. The error results differ in the magnitudes of the errors. When elevations are specified, the $RMSE_t$ for both elevations and velocity is approximately twice as much as the corresponding error when flux is used as the upstream boundary condition. The error results for the variable sloping domain show the same trends as the results for the linear sloping domain.

Up to this point, elevation and velocity errors have been reported. However, since flux is used as a quantity for boundary condition specification, it seems prudent to use flux $RMSE_t$ as a tool for analyzing both the error in the boundary condition time series and the partial-domain flow fields. Additionally, the discharge is an important quantity for analysis

of river systems. The flux $RMSE_t$ for the full-domain dynamic wave channel routing model on the linear sloping domain, compared to the full-domain ADCIRC model, is shown in Figure 5.15. The flux error is negligible for the most upstream portions of the domain. This is expected due to the constant upstream flux boundary condition used in each of the models.

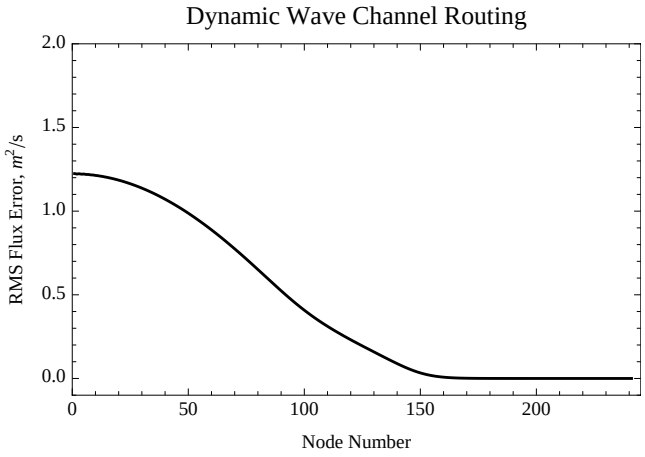

Figure 5.15 Flux $RMSE_t$ for the full-domain dynamic wave channel routing model on the linear sloping domain. The full-domain ADCIRC solution is used as the true solution.

The specified elevation ocean boundary condition constrains neither the velocities nor, by extension, the fluxes. The different numerical schemes introduce some error between the solutions for portions of the domain influenced by tides and surge, and the flux $RMSE_t$ is 1.22 m^2/s at the ocean boundary. Referring back to Figure 5.12, the velocity $RMSE_t$ for the dynamic wave model at the ocean boundary node is 0.096 m/s. These results, fortunately, equate. If the water depth is constant at a location and there is no error in the water depth calculation, the flux $RMSE_t$ value is simply the velocity $RMSE_t$ value multiplied by the depth of flow. The bathymetry value at the ocean boundary is 12 m. The depth is not constant throughout the simulation, but the deviation of the tidal signal is less than 10% (plus or minus) of the bathymetry value. The average depth is greater than the bathymetry value because of the surge signal superimposed on the tidal oscillation.

However, the bathymetry value gives a good estimate of the depth throughout the simulation. The ratio of the RMS flux error to the RMS velocity error is 12.7 m, which is slightly greater than the bathymetry value. Therefore, the flux errors are consistent with the velocity errors.

The flux $RMSE_t$ for the two sets of partial-domain ADCIRC simulations on the linear sloping domain, forced with upstream boundary conditions from the dynamic wave channel routing model, are shown in Figure 5.16. The flux errors for the variable sloping domain are provided in Appendix E.2.3. As is to be expected from the elevation and velocity $RMSE_t$, the flux $RMSE_t$ are smaller when flux is used as the upstream boundary condition than when elevations are specified. The shape of the flux error lines is different than the elevation and velocity error lines for the same simulation sets. Specifically, for the simulations with the most oceanward hand-off points, the RMS flux errors are higher near the boundary than near the hand-off location. The elevation and velocity errors decrease from the maximum values at the hand-off to minimum values at the ocean boundary. This increase in flux error is due to the increasing bathymetry as the ocean boundary is approached.

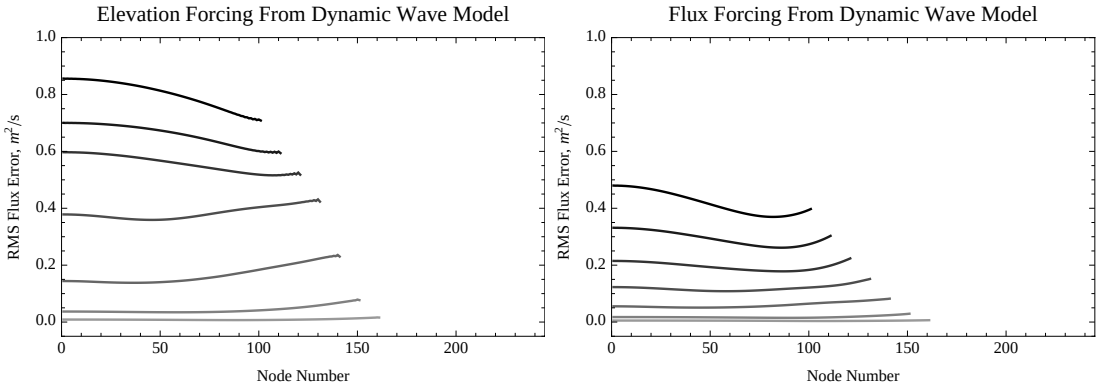

Figure 5.16 Flux $RMSE_t$ for ADCIRC using elevation or flux upstream boundary conditions from the dynamic wave hydraulic model on the linear sloping domain.

5.7.3 ADCIRC Forced with Upstream Boundary Condition from ADCIRC

An alternative for looking at the effect of boundary conditions on ADCIRC is to use the full-domain ADCIRC solution to provide the upstream boundary condition values. The results for the partial-domain simulations on the linear sloping domain, with elevation or flux boundary conditions, are shown in Figure 5.17. The errors for this scenario are directly related to the boundary condition (location and type of information specified), i.e., not due to any internal model differences. Note the error scales are two orders of magnitude lower for these results than for the partial-domain ADCIRC results using upstream boundary conditions from the full-domain dynamic wave hydraulic routing model (c.f. Figure 5.14 and Figure 5.16).

When full-domain ADCIRC results are used as the upstream boundary condition for the partial-domain ADCIRC simulation, the errors are about 80% less when the flux is specified than when the elevation is specified. The scales on the velocity plots make the comparison of the velocity errors somewhat difficult. However, the flux errors at the ocean boundary provide some insight into the relative velocity errors at that location using the simplified relationship between velocity and flux RMS errors mentioned previously. The flux errors differ by a factor of five at the ocean boundary. The velocity errors differ by approximately the same factor. For example, with the hand-off point at node 131, the ratio of the flux $RMSE_t$ values ($RMSE_t$ with elevation forcing divided by $RMSE_t$ with flux forcing) at the boundary is 4.84. The corresponding ratio of velocity $RMSE_t$ values is 4.77.

The results, shown in Appendix E.2.4, are mixed on the variable sloping domain. Specifying flux at the upstream boundary produces significantly better results than speci-

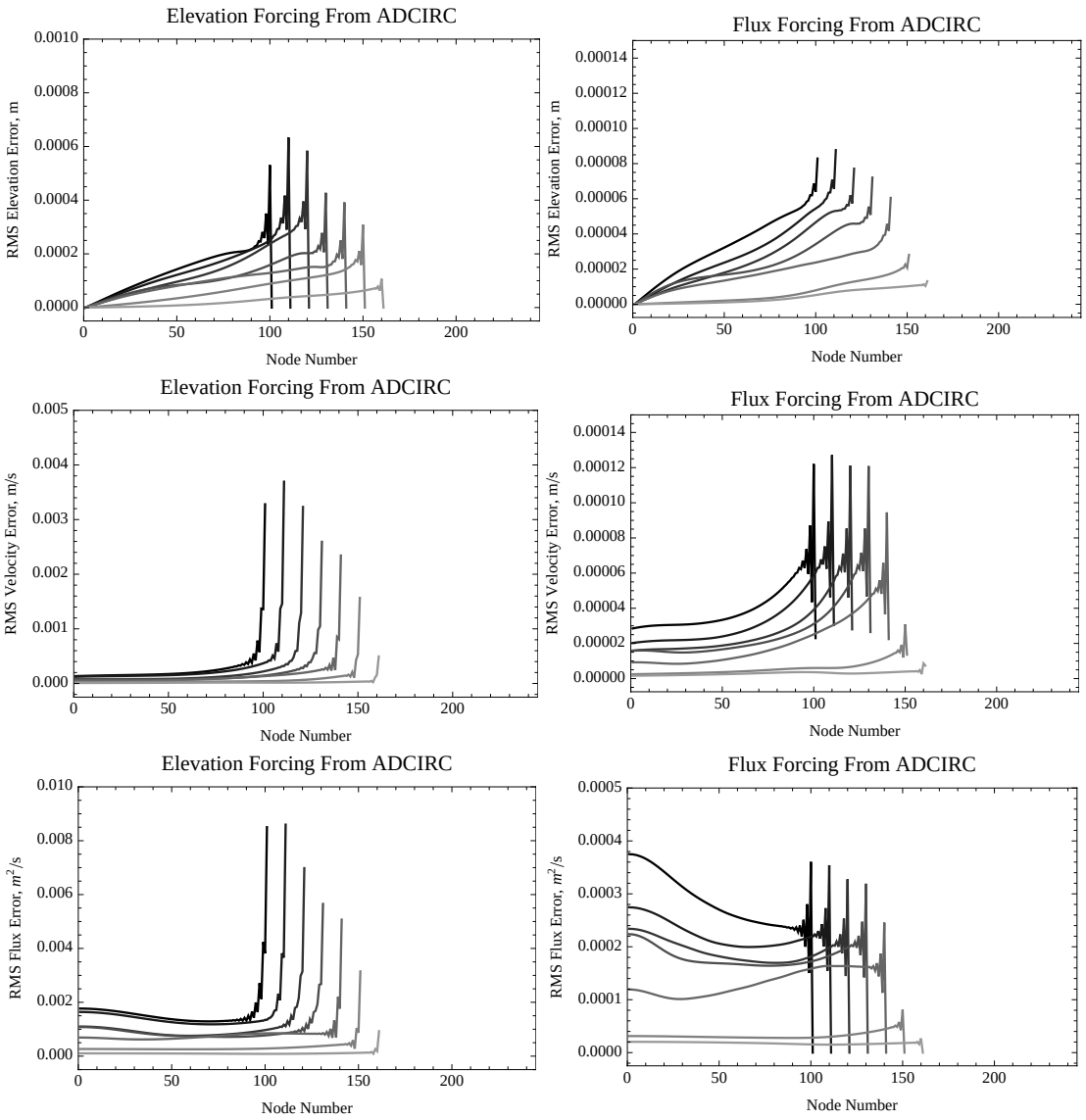

Figure 5.17 Elevation, velocity and flux $RMSE_t$ for ADCIRC using elevation and flux upstream boundary conditions from the full-domain ADCIRC model on the linear sloping domain. Note the scales are not the same.

fying elevations for the boundary locations upstream of the estuary. Additionally, for the one location in the middle of the estuary, the results are significantly better with the flux specification. However, for the boundary locations that occur at changes in the slope of the domain (the two most oceanward locations and the middle location of the seven), the elevation specification produces better results, especially for elevations on either end of the flat estuary.

5.8 Simulations Using Boundary Forcing from Partial-Domain Simulations

Previously, results were shown for simulations using boundary conditions from full-domain simulations. This treatment of the problem, while providing useful insight, is not analogous to real world, one-way coupling of models. Generally, hydraulic routing components within hydrologic models do not cover the ocean and accept ocean elevation boundary conditions. Similarly, hydrodynamic models do not cover significant portions of the river basin system and, thus, do not ingest precipitation forcing to generate river discharges.

For the one-way coupled results presented below, the partial-domain ADCIRC simulations use upstream boundary conditions from the partial-domain dynamic wave hydraulic model results. The hydraulic model run assumes the depth does not vary in space at the downstream boundary, rather than using the tides and surge elevation boundary time series. Despite using the entire 241 node linear sloping grid, it is referred to as a partial-domain simulation because it only receives the forcing information at one of the two boundaries (in this case, the upstream boundary). Revisiting Figure 5.7, the momentum approximation used in the channel routing model has minimal effects on the results on the linear sloping domain when there is not a downstream boundary condition causing backwater effects. Thus, to avoid redundancy, only dynamic wave results will be used to force the partial-domain ADCIRC simulations. However, the simulations could have just as easily been performed using results from the kinematic or diffusive wave models without introducing significant error. Similar to previous simulation sets, the different boundary condition sets for the partial-domain ADCIRC simulations are derived from the results of one hydraulic model run. The elevation and velocity fields are recorded at different hand-off

locations.

Subsequently, the 1-D ADCIRC model is run without any river discharge input at the upstream boundary. The elevations are specified as the ocean boundary condition and ADCIRC handles the problem as a moving boundary problem on the river side, with the extent of the active elements moving in and out with the tides and surge. Results from ADCIRC will be used as downstream boundary conditions for the partial-domain hydraulic simulations.

Simulations for this section have the same parameters as previous simulations. However, the length of the simulations has been changed to 5.0 days, with output recorded every 15 minutes for the last four days. Additionally, the timing of the surge signal on the ocean boundary has been delayed half a day, as seen in Figure 5.18. Finally, a non-constant river discharge is used as the upstream boundary condition. The unit discharge hydrograph is shown in Figure 5.19.

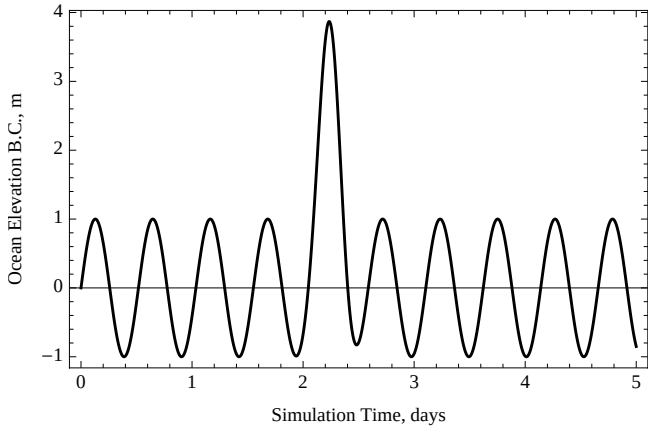

Figure 5.18 Elevation ocean boundary forcing for 1-D simulations.

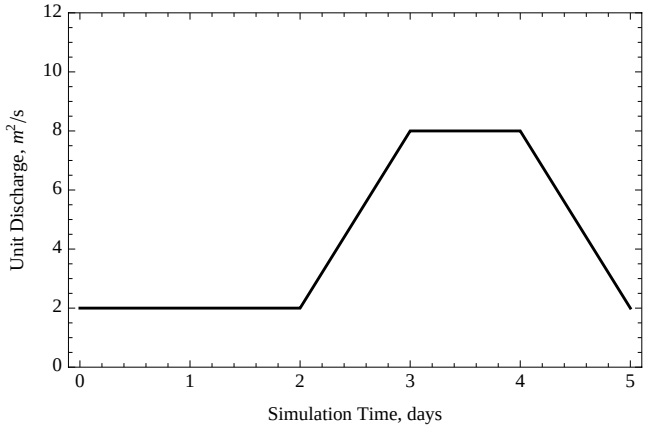

Figure 5.19 Unit discharge hydrograph used as the upstream boundary condition.

5.8.1 ADCIRC Forced with Upstream Boundary Condition from Dynamic Wave Hydraulic Model

The dynamic wave hydraulic model was run on the entire domain using the discharge hydrograph, Figure 5.19, as the upstream boundary condition. However, rather than specify a time series of elevation as the downstream boundary condition, the condition $(\partial h)/(\partial x) = 0$ is used at the downstream boundary. Thus, the elevation depends on the flow at the downstream boundary location. Elevation or flux results from this simulation are used as the upstream boundary condition in the one-way coupled ADCIRC simulations. ADCIRC uses the elevation tides and surge boundary condition as the ocean forcing and results are compared to the full-domain ADCIRC simulation using the elevation ocean boundary condition and the discharge hydrograph upstream boundary condition.

The $RMSE_t$ for the partial-domain ADCIRC simulations on the linear sloping domain are shown in Figure 5.20. The plots clearly show the errors are significantly less when flux is used as the upstream boundary condition forcing for the partial-domain ADCIRC model. The elevation and velocity $RMSE_t$ are generally about 4-5 times larger for the simulations when the elevations from the dynamic wave model are used as the

upstream ADCIRC boundary condition. The flux $RMSE_t$ follow the same trend. For the middle hand-off location (boundary at node 131), the average ratio of nodal flux $RMSE_t$ ($RMSE_t$ with elevation forcing to $RMSE_t$ with flux forcing) is 3.11 with a maximum of 3.40 and a minimum of 2.89.

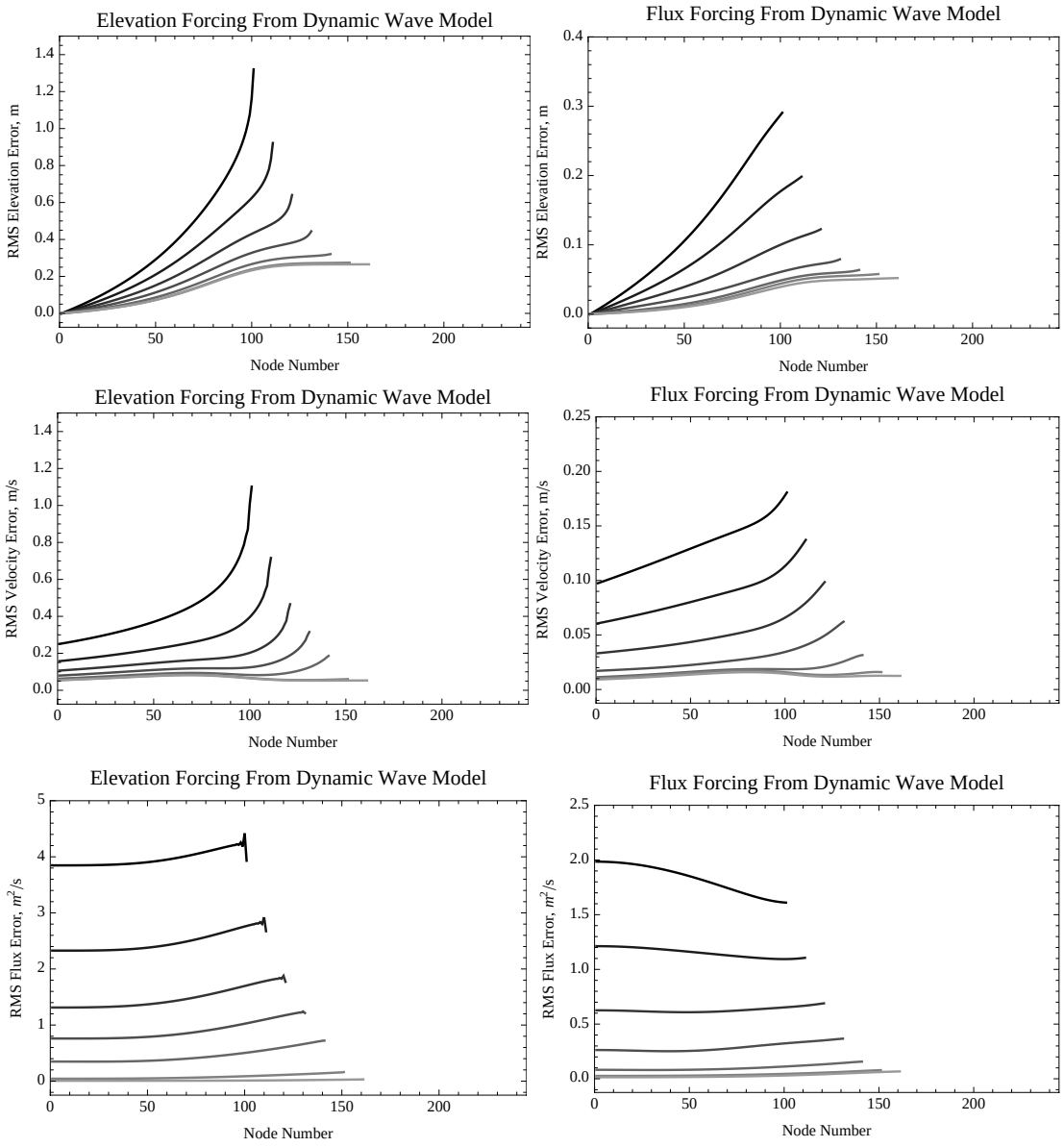

Figure 5.20 Elevation, velocity and flux $RMSE_t$ for ADCIRC using elevation and flux upstream boundary conditions from the partial-domain dynamic wave model on the linear sloping domain. Note the scales are not the same.

Additionally, the results show the partial-domain ADCIRC errors decrease as the hand-off location is placed farther upstream. This is not a new result. The impact of the ocean boundary condition decreases as one moves upstream towards the upstream boundary of the domain. Placing the hand-off location upstream of major backwater effects is particularly important in this scenario because the channel routing model used to create the boundary conditions is not subject to the ocean boundary forcing. Therefore, when the hand-off location is in a region with significant backwater effects, the coupled model result will not accurately represent the full-domain true solution because the upstream boundary condition forcing will not be consistent with the actual hand-off location values. The results for the variable sloping domain, shown in Appendix E.3.1, follow the same trends.

5.8.2 Dynamic Wave Hydraulic Model Forced with Downstream Elevation from ADCIRC

For this set of simulations, the full-domain ADCIRC simulation used the elevation ocean boundary condition time series, Figure 5.18, and allowed wetting and drying to occur on the right side of the domain throughout the simulation. There was no flux input at the upstream boundary of the domain. The elevation results at the different hand-off locations were used to force the dynamic wave hydraulic model at the downstream boundary. When the specified elevation resulted in a flow depth of less than 0.5 m at the boundary, the specified elevation was adjusted so the depth was equal to 0.5 m. The discharge hydrograph, Figure 5.19, was applied to the upstream boundary in the partial-domain dynamic wave hydraulic simulation.

The elevation and velocity $RMSE_t$ results for the partial-domain dynamic wave model simulations on the linear sloping domain are presented in Figure 5.21, while the

results for the variable sloping domain are contained in Appendix E.3.2. The results are not surprising. There is a large amount of error in the elevation boundary conditions used because the ADCIRC simulation used to generate the boundary conditions assumes the river is dry, so the elevations are vastly under-predicted in the regions of the domain that are dominated by river flow. The error in the elevation boundary condition specified at the hand-off, in turn, results in large error values adjacent to the hand-off point. However, the farther one moves away from the boundary, the better the coupled results become. The elevation and velocity $RMSE_t$ do not go to zero at the upstream boundary because the friction parameterizations are not equivalent for the range of flow rates encountered in this set of simulations. However, away from the hand-off point, the $RMSE_t$ reach an asymptotic value.

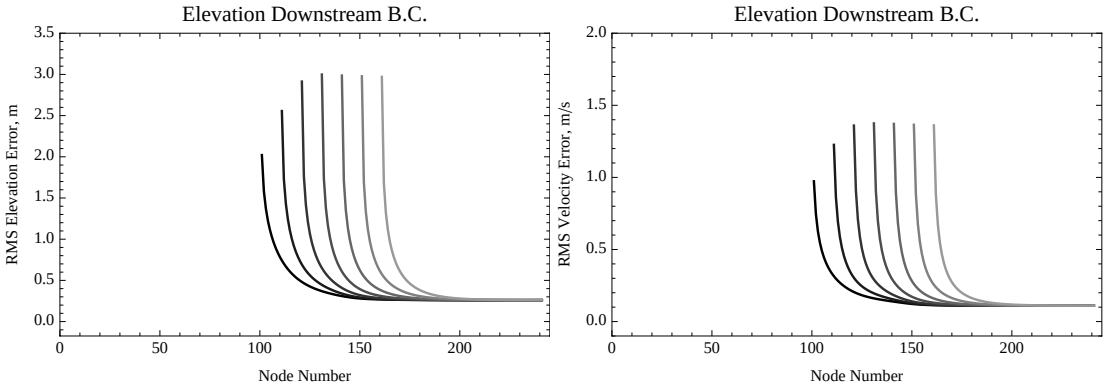

Figure 5.21 Elevation and velocity $RMSE_t$ for the partial-domain dynamic wave model using elevation and downstream boundary conditions from the partial-domain ADCIRC simulation on the linear sloping domain.

5.9 Two-Way Coupling of ADCIRC to the Dynamic Wave Hydraulic Model

The previous simulations were all one-way coupled simulations where one model (either ADCIRC or a hydraulic model) was running and accepting boundary conditions from a previous simulation. Thus, the flow of information was one-way. This section,

examines a series of two-way coupled simulations using ADCIRC and the dynamic wave hydraulic model. At each time step, the flux is passed from the hydraulic model to ADCIRC as the upstream boundary condition. Additionally, the hydraulic model uses elevation results at the hand-off point as its downstream boundary condition. For the first set of simulations, the upstream boundary condition is a constant unit discharge of 2.0 m^2/s into the domain. For the second set, the upstream boundary condition for the hydraulic model is the 5.0 day variable unit discharge time series (Figure 5.19). For both sets, the ocean boundary condition for ADCIRC is the 5.0 day tides and surge elevation time series (Figure 5.18).

Figure 5.22 (constant upstream boundary flux) and Figure 5.23 (non-constant upstream boundary flux) show the elevation and velocity $RMSE_t$, compared to the full-domain ADCIRC simulations, for the two-way coupled simulations on the linear sloping domain. Similar to previous data sets, each line corresponds to a run with a particular hand-off location, with ADCIRC used oceanward of the boundary and the hydraulic model covering the domain upstream of the coupling location. The corresponding figures for the variable sloping domain are provided in Appendix E.4.

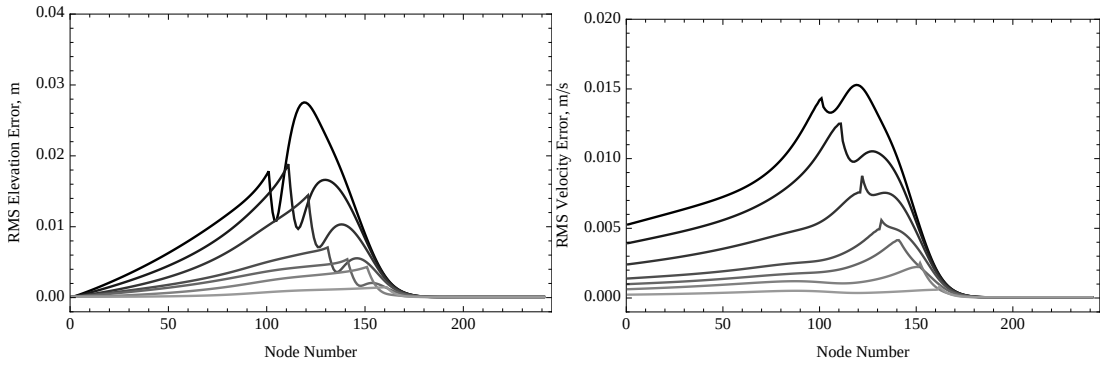

Figure 5.22 Elevation and velocity $RMSE_t$ for the two-way coupled simulations with a constant upstream unit discharge boundary condition of 2.0 m^2 / s into the linear sloping domain. The full-domain ADCIRC simulation is used as the true solution.

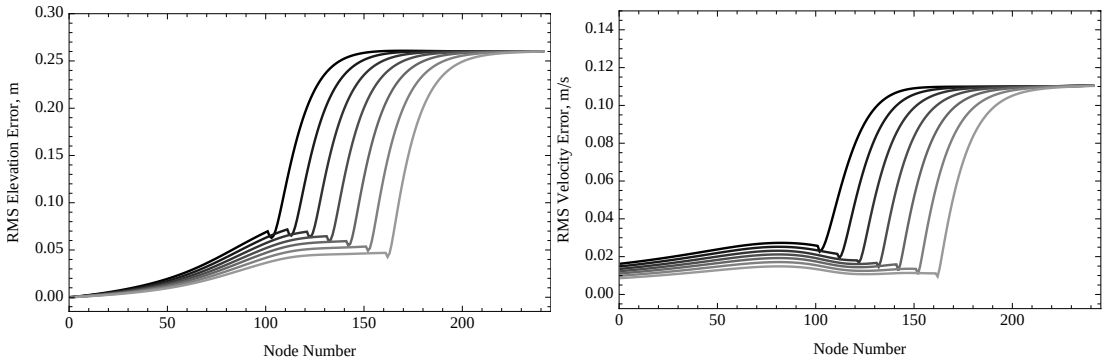

Figure 5.23 Elevation and velocity $RMSE_t$ for the two-way coupled simulations with a non-constant upstream unit discharge boundary condition into the linear sloping domain. The full-domain ADCIRC simulation is used as the true solution.

Throughout the domain, the error tends towards zero as the hand-off location between the models is moved upstream. In other words, given two simulations that are equivalent aside from the hand-off point, the $RMSE_t$ will generally be lower for the simulation with the hand-off point farther upstream. Conversely, the largest errors are found when the coupling boundary is most oceanward. The error is less than the error using the same model set-up but forcing the partial-domain ADCIRC simulations with flux upstream boundary conditions from the full-domain dynamic wave simulation using a one-way coupling. However, the errors are higher than for the partial-domain ADCIRC simulations using full-domain ADCIRC flux results as the upstream boundary condition. The results are better for hand-off locations farther upstream due to the flow field being more uniform in the river than down in the areas influenced by backwater effects, especially when the constant flow rate ($2.0\ \mathrm{m}^2/\mathrm{s}$) used to calibrate the Manning's roughness value is used as the river boundary condition. The full-domain ADCIRC and dynamic wave hydraulic models do not produce the exact same results, so there is some error inherent to the choice of the true solution.

There is more error when the non-constant flux discharge is used for the upstream

boundary forcing. Specifically, the error near the upstream boundary is constant, as in the previous case, but the asymptotic value is non-zero. This is due to the full-domain ADCIRC model producing larger flow depths than the dynamic wave channel routing models for unit discharges above 2.0 m^2/s. The larger flow depths with ADCIRC are a result of the differences in the friction treatment. With the same unit discharge, the larger flow depths for ADCIRC (than for the dynamic wave hydraulic model) result in lower velocities in the river for the true solution than for the coupled simulations.

5.10 Two-Way Coupling Application Using North Carolina Information

In order to further test the two-way coupled model, information from the Tar River and Pamlico Sound domain explored in the next chapter was used to create grid and input files for the 1-D model.

5.10.1 Grid

The Tar and Neuse Rivers discharge into the Pamlico Sound in North Carolina. The sound is separated from the Atlantic Ocean by barrier islands. In order to create a realistic grid for 1-D simulations, elevations from the 2-D ADCIRC grid [*Blanton* 2008] were used as the background to create the bottom profile down the river, through the estuary and out into the Atlantic Ocean. Points were extracted every 5 km along the Tar River in the 2-D ADCIRC grid, starting at the upstream boundary northwest of Tarboro, NC. The profile of the Tar River is shown in Figure 5.24, with a third-order polynomial fit given by (5.24), where x is distance from the upstream boundary in km.

$$Elevation = 8.0 - 0.07x - 0.0025x^2 + 0.000022x^3 \quad \textbf{(5.24)}$$

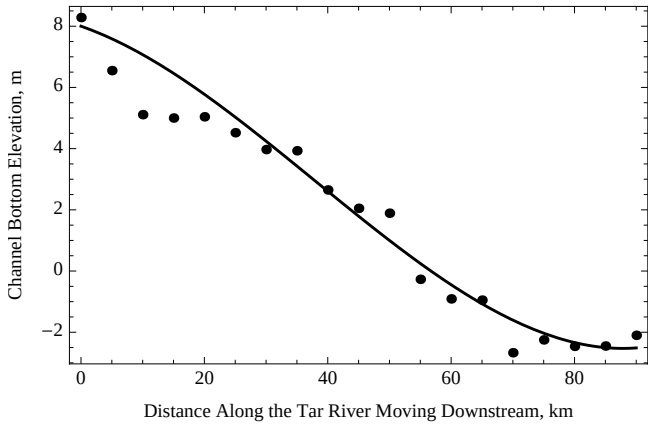

Figure 5.24 Smooth channel (solid line) for generation of 1-D domain points plotted against elevations for the Tar River from the ADCIRC grid (points)

Elevations from the Pamlico Sound through the barrier islands into the Atlantic Ocean can be seen in Figure 5.25, with a fit line given by (5.25), where x is distance from the outlet of the Tar River in km.

$$Elevation = -2.512 - \frac{x^2}{800} \qquad \textbf{(5.25)}$$

Points for the Pamlico Sound and Atlantic Ocean were selected every 10 km. The fit lines do not provide an exact representation of the system, but they pick up the large scale topographic/bathymetric trends and introduce a more realistic domain than the domains used previously.

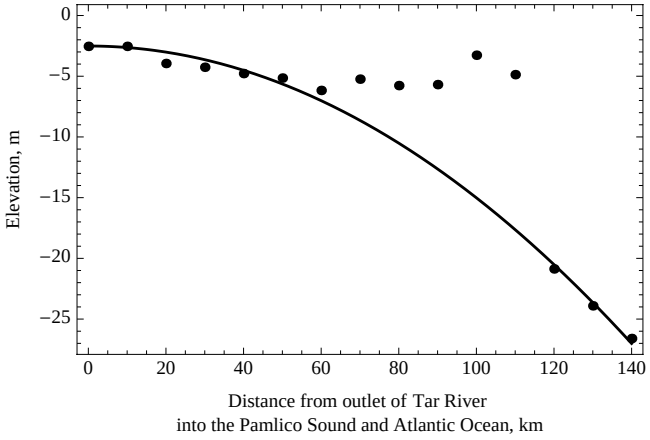

Figure 5.25 Smooth estuary and ocean bottom (solid line) for generation of 1-D domain points plotted against elevations for the Pamlico Sound and Atlantic Ocean from the ADCIRC grid (points).

The bottom elevations for the 1-D grid were created by combining the two elevation functions, reversing the x-coordinate values so the ocean is on the left and the river is on the right, and enforcing a minimum slope of 0.00001 m/m from right to left. The minimum slope criterion was enforced to minimize problems if the kinematic wave model was used (although it was not applied to this domain for this study). With the kinematic wave approximation, the velocity depends on the bottom slope. If the bottom slope is zero, the velocity will also be zero. Thus, the water will not be able to travel past a section of zero or negative slope. Additionally, the grid was extended on the upstream side to 15.0 m using a linear slope of 0.0001 m/m. The bottom elevations for the 1-D grid are shown in Figure 5.26.

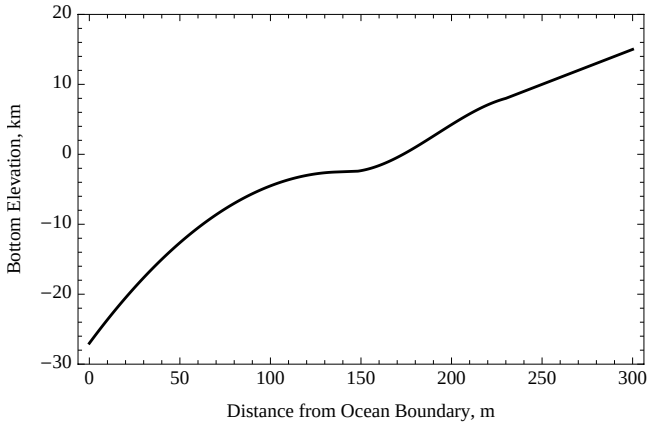

Figure 5.26 Bottom elevations for 1-D North Carolina grid.

5.10.2 Hydrologic Input

The worst riverine flooding on the Tar and Neuse Rivers resulted from rainfall from Hurricane Floyd in 1999 [*Bales* 2000, 2003]. The daily data (discharge and stage) from USGS Station 02083500 for the Tar River at Tarboro is plotted in Figure 5.27. In order to use the data from Hurricane Floyd in a 1-D framework, an estimate of the unit discharge hydrograph must be made so the stage values for the 1-D simulations are similar to the values encountered during the event. Using estimates of bottom slope and Manning's

roughness value of 0.00015 m/m and 0.025, respectively, a reasonable match can be achieved to the USGS flow rates by assuming a 60 meter wide rectangular channel and calculating the flow rate using Manning's equation, with $R = h$, and the USGS stage values. A comparison of the calculated discharges (with this stage-discharge relation) to the actual values is shown in Figure 5.28.

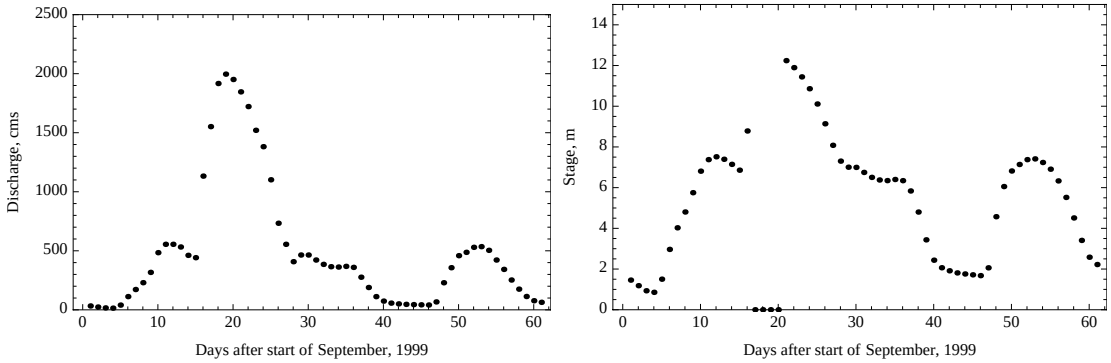

Figure 5.27 Estimated discharge and stage values for the USGS station for the Tar River at Tarboro, NC due to rainfall run-off from Hurricane Floyd.

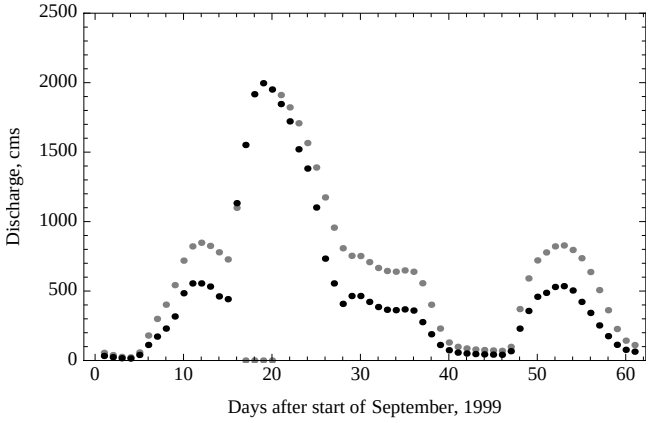

Figure 5.28 Comparison of discharges calculated using USGS stage values assuming uniform flow and a rectangular channel (gray) to the actual USGS daily discharge values (black).

The fifth-order best fit polynomial to the USGS results (black dots) for days 13 through 28 of Figure 5.28 is given by (5.26), where x is the number of days for the data set, and the line for this polynomial is shown in Figure 5.29.

$$Q = 447.43 - 338.65x + 315.59x^2 - 54.19x^3 + 3.507x^4 + 0.0799x^5 \qquad \textbf{(5.26)}$$

Then, the stage for the rectangular section described above can be calculated from the best fit polynomial for the discharge. A comparison of the computed stage for the 1-D system with the actual data is shown in Figure 5.30. Note that no stage values are available for the time period just before the peak. The unit discharge hydrograph for the 1-D simulation system for Hurricane Floyd is shown in Figure 5.31.

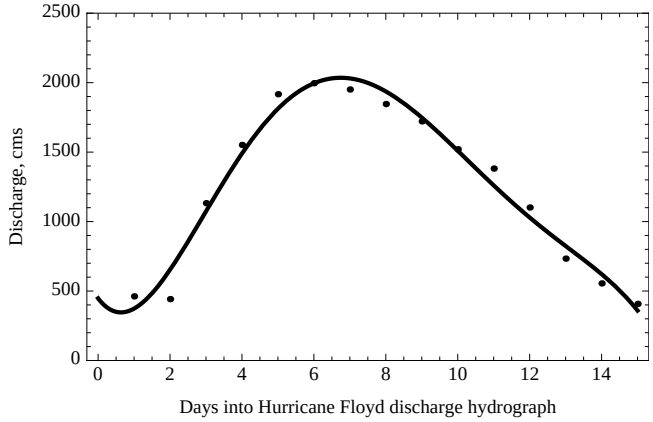

Figure 5.29 Plot of a fifth-order polynomial fit to the USGS Hurricane Floyd discharge hydrograph for the Tar River at Tarboro, NC.

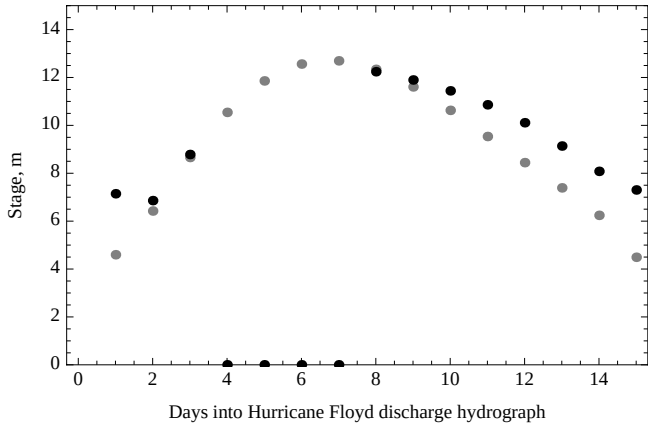

Figure 5.30 Comparison of stages calculated using USGS discharge values, assuming uniform flow and a rectangular channel (gray), to the actual USGS daily stage values (black).

5.10.3 Hurricane Elevation Boundary Forcing

Information from Hurricane Isabel (2003) was used to generate the ocean elevation boundary condition. This storm was chosen because it is a recent hurricane that made land-

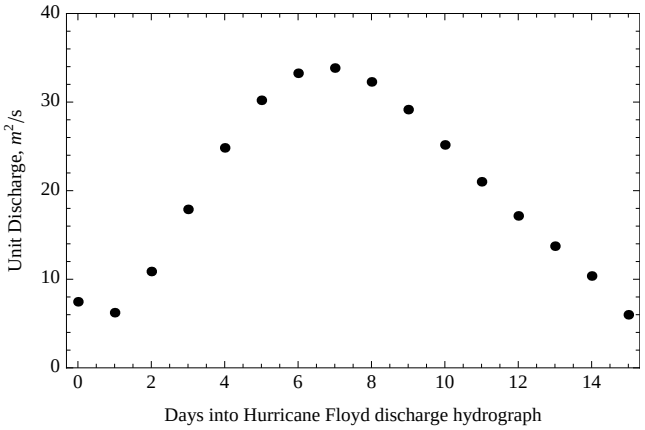

Figure 5.31 Unit discharge hydrograph for Hurricane Floyd for 1-D simulations.

fall in the target study area. Rather than use actual results, an approximate time series was generated that facilitated implementation consistent with the current ocean elevation boundary forcing in the 1-D model. Furthermore, the implementation would allow for simple modifications to the boundary forcing to examine different scenarios (e.g., changes to the amplitude or timing of the storm surge).

The water surface elevation time series from the NOAA gauge at Duck Pier (#8651370) is shown in Figure 5.32. There are two plots corresponding to mean low low water (MLLW) and North American Vertical Datum 1988 (NAVD88) datums. The NAVD88 datum will be used because the 2-D ADCIRC domain elevations are in NAVD88. Additionally, the difference between NAVD88 and MSL is small in North Carolina, whereas the MLLW datum is significantly different than MSL. The MLLW value is 0.667 m above the NAVD88 value at Duck Pier.

The main tidal signal at Duck Pier can be approximated using a sine wave with an amplitude of 0.5 m and a period of 12.4 hours. This is shown in the plot on the left side of Figure 5.33. The portion of the signal that is not represented by the simple sine wave is shown on the right side of Figure 5.33.

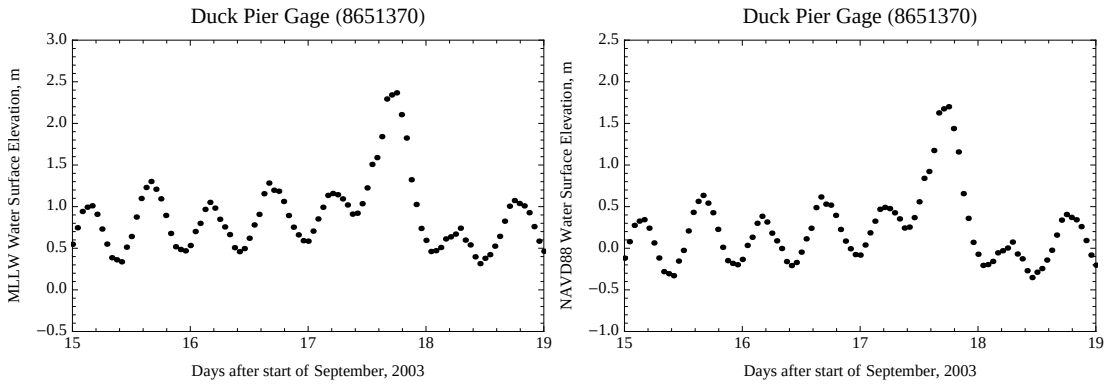

Figure 5.32 Water surface elevation from the NOAA gage at Duck Pier (8651370). The plot on the left is based on mean low low water (MLLW), and the plot on the right is in North American Vertical Datum 1988 (NAVD88). The conversion from MLLW to NAVD88 is -0.667 m at the Duck Pier location.

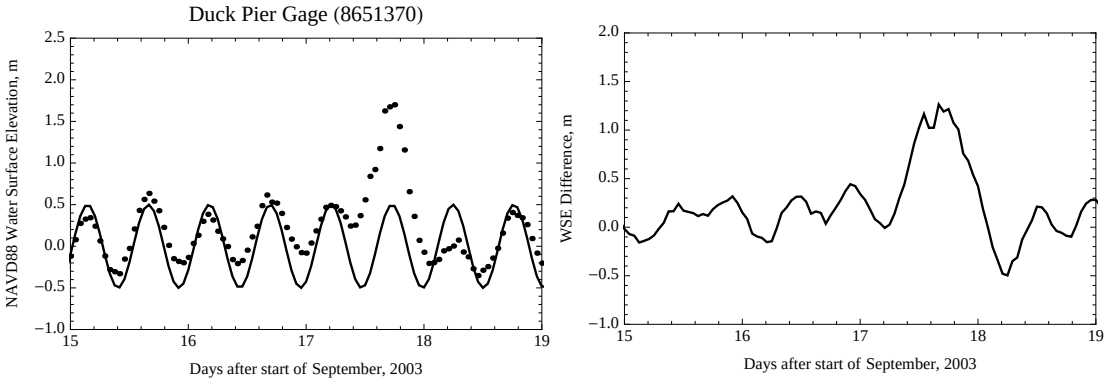

Figure 5.33 Comparison of the NOAA gage values to a sine signal (left graph) and the difference between the two (right graph).

The majority of the signal that is not represented by the sine wave is the surge signal resulting from Hurricane Isabel. The surge signal, ζ_{ISABEL}, can be reasonably represented using (5.27), where x is the number of days into September.

$$\zeta_{Isabel} = -1.25(2.5(17.7 - x))^2 + 1.25 \text{ for } 17.3 \le x \le 18.1 \quad \textbf{(5.27)}$$

Figure 5.34 shows, on the left, the comparison of the surge signal to the difference between the signal and the sine wave. Finally, the combined sine and surge are compared to the gauge data on the right side of Figure 5.34. The water elevations for the Duck Pier gauge are represented reasonably well by the sum of the tidal sine wave and the parabolic surge signal.

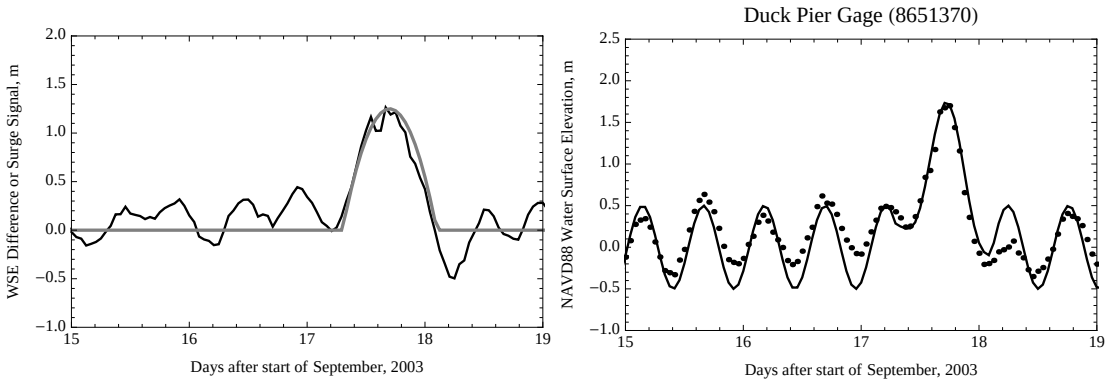

Figure 5.34 The plot on the left shows the surge signal (gray) compared to the difference between the NOAA values and the sine wave (black). The plot on the right is a comparison of the NOAA gage values (points) to the combined sine and surge signal (line).

5.10.4 Two-Way Coupled Simulations

The intent of the simulations based on information from North Carolina was to demonstrate the abilities of the coupled system. Specifically, the 1-D grid is much less idealized than the grids used for previous simulations. Additionally, the ocean and river boundary forcings are based on historical data. However, this is not an attempt to hindcast a particular event or provide an estimate of the maximum inundation level for coastal North Carolina based on a hypothetical combination of boundary forcings.

The base parameters were kept at the values used in previous simulations. The grid contains 1201 nodes with equal spacing of 250 m. The boundary forcings are given in Figure 5.35. The ocean boundary condition consists of a 1.0 m amplitude tide with a period of 12.4 hr. This tidal amplitude is twice the amplitude used to match the historical data at Duck Pier, NC. The 1.0 m amplitude was maintained to be consistent with the tidal forcing used in previous simulations. The 1.25 m surge signal derived from the Hurricane Isabel data at Duck Pier, NC is superimposed on top of the tidal signal. The surge signal is present during the 5th and 6th tidal cycles. The river boundary condition has a linear, two-day ramp. The unit discharge is based on the polynomial expression derived from the Hurricane Floyd

data from the USGS gauge for the Tar River at Tarboro, NC. The Manning's roughness was set at 0.025 (constant). This is a slight increase over the previous value used. However, results from previous simulations suggested that the dynamic wave model needed a higher roughness value to match ADCIRC at higher flows. The higher roughness value decreases the velocity of flow and increases the flow depth.

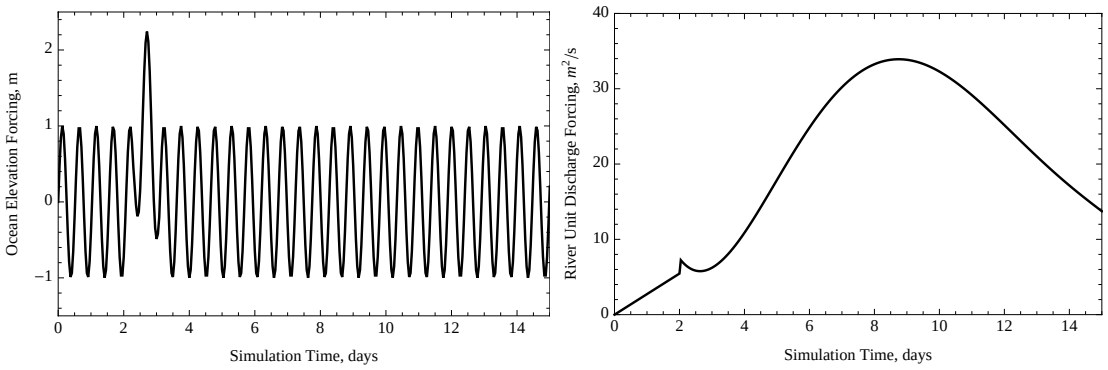

Figure 5.35 Ocean and river boundary forcing time series for the 1-D North Carolina simulations.

Two simulations were performed. Both were 15.0 days in duration with nodal elevation and velocity values output every hour. Additionally, both consisted of ADCIRC coupled with the dynamic wave model. The first simulation placed the hand-off point for the models at node 482. This coincides with a bathymetry value of 3.0 m and is consistent with the bathymetry where the Tar River discharges into the Pamlico Sound. The second simulation places the hand-off location at node 1191. This latter set-up was created to allow ADCIRC to model the majority of the domain while still using the two-way coupled code. This second set-up is used as the true solution in this section, and it is essentially a full-domain ADCIRC simulation for all but the most inland elements in the domain. For generation of a comparison solution, use of the two-way coupled code was preferable over the full-domain ADCIRC model only because use of the regular ADCIRC code for a full-domain ADCIRC simulation would have required implementation of the Hurricane Floyd

river forcing in the ADCIRC code. While this endeavor is trivial, it is also unnecessary because the coupled system can be used (with the hand-off point located near the upstream domain boundary).

The water surface elevations for the first simulation (results from second simulation are not shown because it is the true solution), with the hand-off point at node 482, are shown in Figure 5.36. For reference, the grid bottom elevations are shown in gray on the plots. After one day, the river is still ramping up from the starting conditions of a depth of 0.5 m in the river. After two days, the depths in the entire river have increased substantially from the initial conditions. The third plot is at the time with the largest ocean boundary forcing elevation, near 2.25 m. The surge increases the water surface elevations both in the ADCIRC domain and in the portion of the domain upstream of the hand-off location.

Four days into the simulation, the ocean forcing is simply the sinusoidal tidal signal. However, the unit flux at the upstream boundary is now greater than 10 m^2/s and the flow depth is 7.03 m. The discharge at the upstream boundary reaches a maximum of just under 34 m^2/s at a time 8.75 days into the simulation. This flow rate produces a flow depth exceeding 14 m at the boundary. The water surface profile is influenced both by the flow rate and the channel bottom slope. Larger slopes correspond to more rapid flow and, thus, smaller depths. The presence of larger depths, due to small bottom slopes, can be seen in the area around nodes 500-600, where the river is discharging into the estuary. Additionally, the specified elevation boundary condition at the ocean boundary constrains the elevations. The final figure, twelve days into the simulation, shows the water level in the river has decreased from the peak. It is worthwhile to note that the large flow depths in the estuary area of the domain are unrealistic. The flow depths are higher than would be seen in an

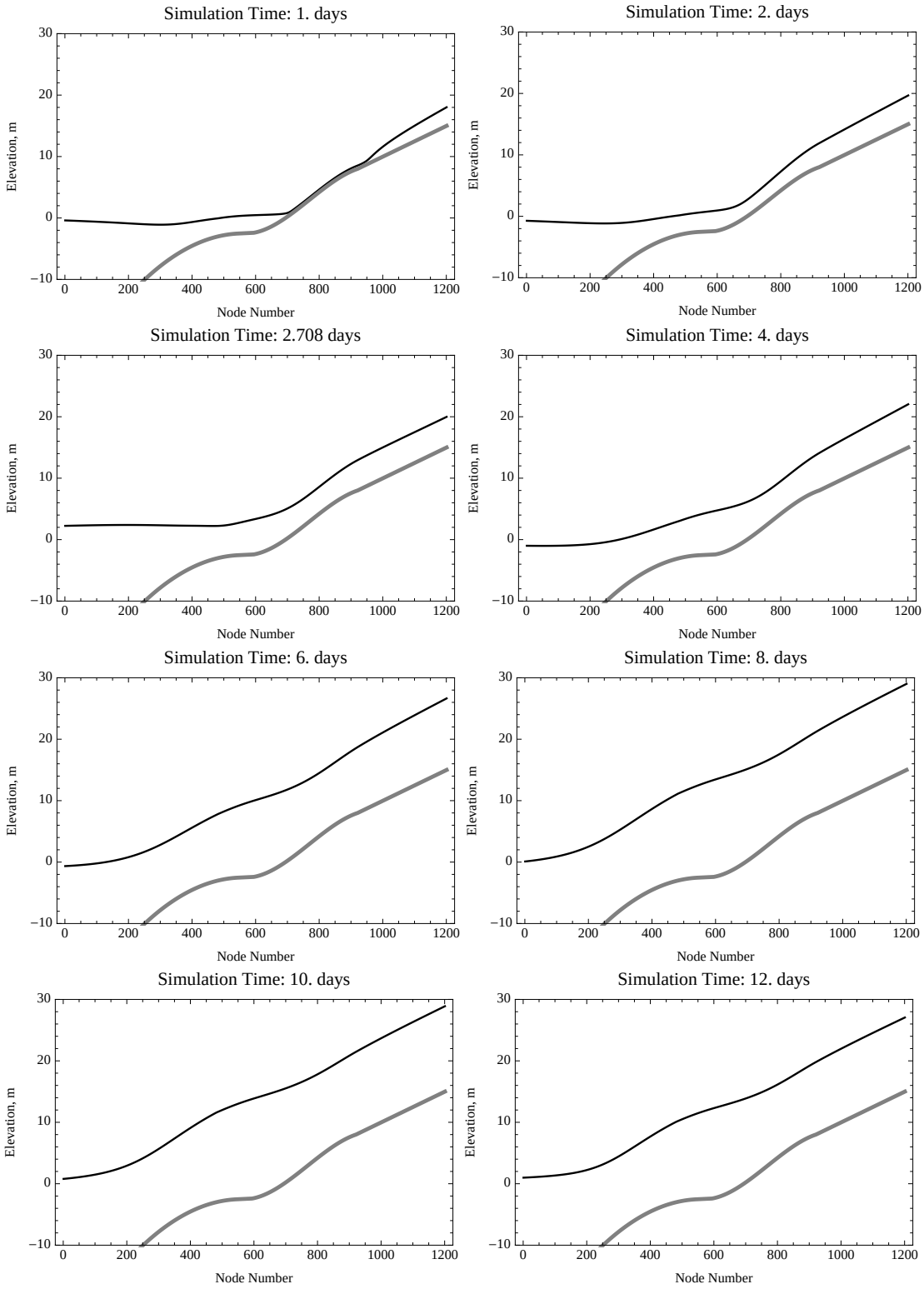

Figure 5.36 Water surface elevation output (black lines) for the entire domain at various times during the coupled simulation with the hand-off location at node 482. The gray lines depict the bathymetry. The peak ocean boundary forcing occurs 2.708 days into the simulation.

actual 2-D application because the unit discharge is too high; the effective flow width increases in the transition from the river to the estuary, so the discharge per unit width decreases. However, in the 1-D model used here, this decrease in discharge per unit width is not taken into account, aside from the changes that occur in space and time within the 1-D model simulation.

The elevation and velocity $RMSE_t$ between the two simulations are shown in Figure 5.37. The results are consistent with results from the previous studies. The dip in error near the upstream boundary corresponds to the hand-off location in the second simulation, which uses ADCIRC to model the vast majority of the domain. The errors are lowest near the ocean boundary. This is the region handled by ADCIRC in both simulations. In addition, it is the area farthest from the hand-off location and nearest to the boundary where the elevation is specified and the elevation error is zero.

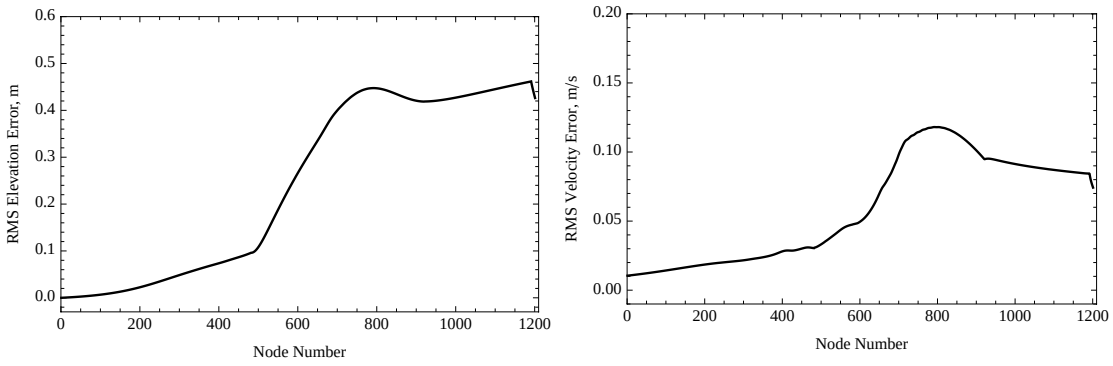

Figure 5.37 Elevation and velocity $RMSE_t$ between the two 1-D North Carolina simulations.

The errors in the river portion of the domain are consistent with errors seen previously. Referring back to the results for the non-constant upstream discharge two-way coupled simulation on the linear sloping domain, Figure 5.23, the asymptotic elevation and velocity RMS error values in the river were about 0.27 m and 0.11 $\mathrm{m/s}$, respectively. The

elevation errors are slightly higher for the NC simulation set, while the velocity errors are similar. However, much larger flows were employed for the latest set of simulations.

5.11 Summary and Conclusions

In this chapter, coupled simulations were performed using a 1-D ADCIRC model and 1-D finite difference hydraulic models using different approximations for the momentum equation. Results show that the dynamic wave approximation for the momentum equation is vastly superior to the diffusive wave approximation for handling backwater effects due to tides and surge in the near-ocean region, while the kinematic wave approximation does not provide a mechanism to handle backwater effects. However, if the boundary for coupling is moved far enough inland that significant backwater effects are handled by ADCIRC, coupling to kinematic and diffusive wave hydraulic routing models provides satisfactory results.

Additionally, while the type of boundary condition specified at the downstream boundary of the hydraulic models did not have a large impact on the results, ADCIRC performs significantly better when flux values are used at the upstream boundary than when elevations are specified. This result is favorable because hydrologic models are primarily interested in correctly calculating discharge values. Thus, discharge is not only a natural quantity to be used as the upstream boundary condition for ADCIRC when coupling to hydrologic models, it is also the optimal quantity for accuracy and ease of implementation.

ADCIRC is able to model flow in the river portion of the domain (above sea level). However, there were errors present when comparisons were made between ADCIRC results and dynamic wave hydraulic results. The difference in treatment of the friction term

in the models contributes to the error. The difference can be minimized for certain flow rates through adjustment of the roughness coefficients in the models. This discrepancy in results highlights an aspect of modeling: The model is supposed to produce a reasonable representation of the physical system. Attempting to produce a reasonable representation of a physical system is a major focus of the next chapter, where the knowledge obtained in this chapter is applied to coastal North Carolina using 2-D ADCIRC.

CHAPTER 6. 2-D Coupling of Hydrologic Models to ADCIRC for Coastal Flood Inundation

6.1 Introduction

The geographical study area for this research is coastal North Carolina, specifically the Tar-Pamlico (Tar) and Neuse River basins, as well as the Pamlico Sound (part of the Croatan-Albemarle-Pamlico Estuary system) and the Atlantic Coast. The two river basins stretch from north of Raleigh, NC, southeast to the southwest section of the Pamlico Sound. The area is subject to flooding due to both rainfall-runoff (Hurricane Floyd, Tropical Storm Alberto) and storm surge (Hurricane Floyd, Hurricane Isabel). The near coastal regions where river flows are affected by tides (and surge) constitute a service gap in forecasts by the National Weather Service [*Van Cooten* 2011].

Initial implementation of the coupled system will use hydrologic models that employ the kinematic wave approximation for channel routing. Use of hydrologic models that use kinematic wave channel routing is primarily due to those models being set-up for the study area, whereas output from models using more complex momentum approximations for channel routing was not readily available at the outset of the project. Thus, the coupled system will be a one-way coupled system with the hydrologic model providing upstream boundary conditions for ADCIRC. Two models have been set up for the Tar and Neuse River basins for the purpose of implementation in a coupled system. These two models are the Hydrology Laboratory Research Distributed Hydrologic Model (HL-

RDHM) [*Koren* 2004; *Smith* 2004; *Reed* 2004; *Moreda* 2006; *Hydrology Laboratory* 2008] and V*flo* [*Vieux* 2002, 2004]. The use of hydrologic models using kinematic wave routing requires the ADCIRC domain to include river regions subject to backwater effects. However, as presented in Chapter 5, the results for one-way coupled simulations are relatively independent of the momentum equation approximation as long as the hand-off point is far enough upstream that backwater effects are not prevalent in the hydrologic model domain.

A study by *Peng et al.* [2004] showed peak surge in excess of 4 m for hypothetical Category 3 storms in this area. In order to ensure enough coverage by ADCIRC, the decision was made to place the boundary of the ADCIRC domain near the 8 m elevation value (ADCIRC grid river bottom elevation) on the Tar and Neuse Rivers. It is not currently desirable to discretize additional (unnecessary) stretches of rivers in the ADCIRC domain above 8 m because ADCIRC does not possess the necessary components to model rainfall-runoff processes. The only mechanism for bringing river flows into the domain is as a boundary condition. Thus, precipitation falling on the portion of the coupled domain allocated to ADCIRC will be lost under the current implementation. Therefore, it is optimal to place the ADCIRC boundary just upstream of prevalent backwater effects that would adversely impact the kinematic wave model solutions. As results from Chapter 5 show, as long as ADCIRC covers enough of the domain to handle the major backwater effects, there is not any increase in coupled model accuracy by modeling additional upstream areas of the river with ADCIRC instead of the hydrologic model. The selection of the hand-off points was conservative to allow for modeling of major storms without having to modify the grid, depending on the storm being modeled.

While rivers have been modeled in ADCIRC previously, including the Mississippi and Atchafalaya Rivers in Louisiana [*Westerink* 2008], the nature of the Tar and Neuse Rivers, besides the fact that they are not defined by levees, presents unique grid, initialization, and boundary flux specification issues that will be explored in future sections. Subsequently, results from application of ADCIRC to tropical events will be presented.

6.2 Grid Modifications and River Initialization

6.2.1 Re-positioning of ADCIRC Grid Boundary

The original ADCIRC grid contained areas in the coastal plain up to at least the 15 m contour line, as shown in Figure 6.1 [*Blanton* 2008]. The Tar and Neuse Rivers were discretized, in most of the domain, using a line of nodes on each side of the river. Additionally, near the upland grid boundary, the river resolution is relaxed to the extent that their definition is lost. Therefore, at the original grid boundary, the rivers are not delineated in the grid. Rather than increase the extent of the fine resolution on the rivers, the decision was made to move the boundary of the ADCIRC domain seaward to locations where adequate river resolution existed. This decision reduced grid modifications, while still maintaining adequate coverage to allow ADCIRC to handle backwater effects. Additionally, the boundary placement avoided the use of increasingly small elements in the upland portions of the rivers, which may have detrimentally affected the maximum stable time step.

The locations of the hand-off points on the Tar and Neuse Rivers, where information will be exchanged between the hydrologic and hydrodynamic models, are shown in Figure 6.2. Additionally, as mentioned earlier, the placement of the boundary near the 8 m elevation contour attempts to minimize the extent of the rivers in ADCIRC while still main-

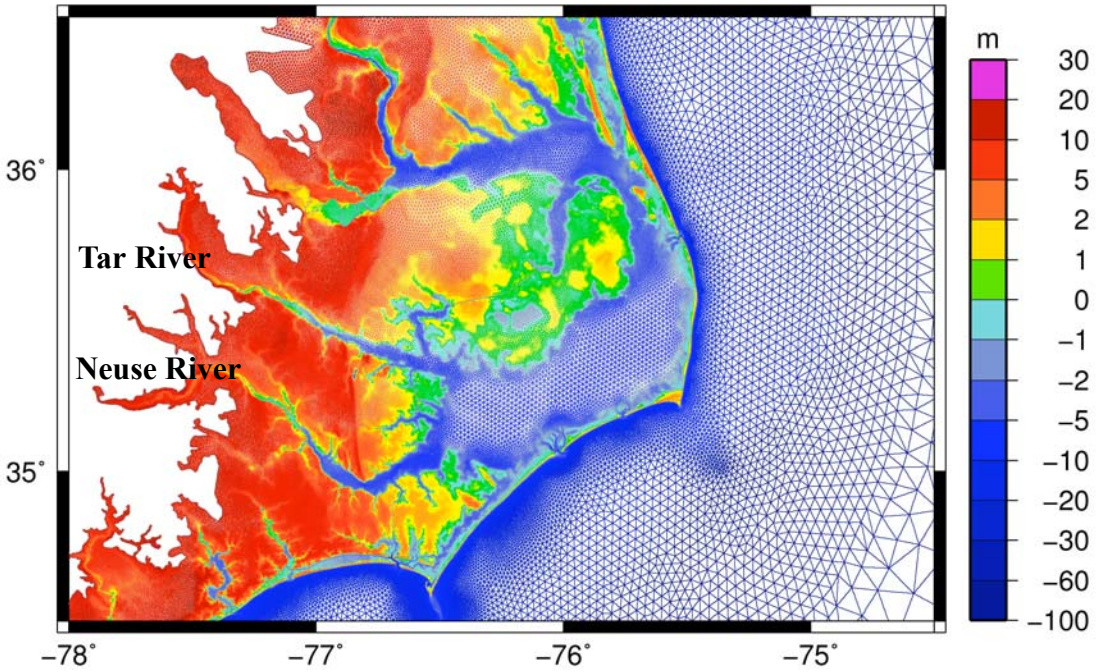

Figure 6.1 ADCIRC v20 grid zoomed in to show the discretization for North Carolina, with the Tar and Neuse Rivers labeled. The rivers are the paths that transition from blue where they discharge into the Pamlico Sound to green, yellow and orange in upstream areas.

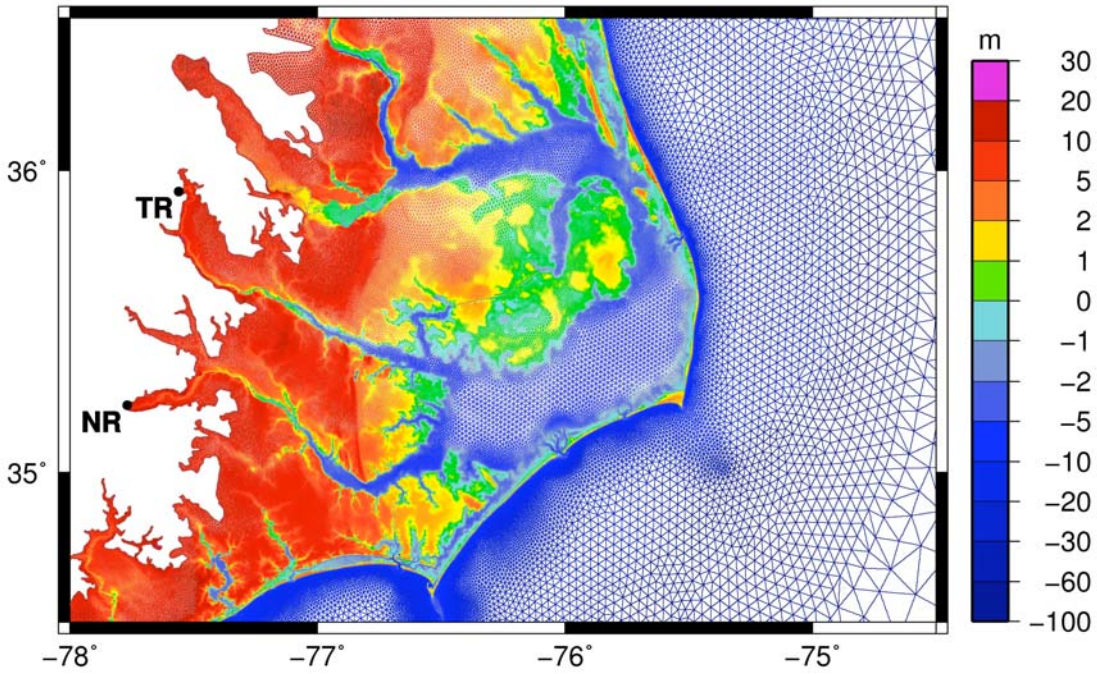

Figure 6.2 Modified ADCIRC grid with the upper extent of the Tar and Neuse Rivers removed. The hand-off points on the Tar River (TR) and Neuse River (NR) are marked on the plot as dots. The areas upstream of the hand-off points, shown in Figure 6.1, have been removed from the ADCIRC modeling domain.

taining enough coverage to account for major surge inundation.

6.2.2 Resolution of River

The main channels of the Tar and Neuse Rivers are discretized using two nodes across, one on each edge of the rivers, with elevations derived from high-resolution LIDAR data. This corresponds to resolution of these rivers on the order of 30-40 m, which is a far different scenario than for larger rivers previously modeled using ADCIRC. *Westerink et al.* [2008] note significant local refinement of the southern Louisiana coastal floodplain including, generally, "five or more nodes across the major rivers and inlets with grid sizes of 100-200 m" to minimize errors caused by under-resolution, which can significantly reduce conveyance of waterways. This discrepancy highlights one difference between the rivers in coastal North Carolina and those in southern Louisiana: the width.

Additionally, the Tar and Neuse Rivers are not confined by levee systems. Therefore, the lateral extent of the rivers is flow dependent, whereas the lateral extent of the Mississippi and Atchafalaya is approximately constant with depth due to the levee systems. Furthermore, the bottom elevations of the Mississippi and Atchafalaya are below sea level significantly inland from the coast; the bottom of the Mississippi is 17.5 m below sea level (in the ADCIRC grid) at Baton Rouge, LA (approximately 120 km inland from New Orleans). Conversely, the ADCIRC grid for the current study has river bottom elevations of approximately 8 m above sea level for the Tar and Neuse Rivers, about 60 km inland from the Pamlico Sound.

6.2.3 Relationship between Channel Resolution and Geometry

The original ADCIRC grid discretizes the bulk of the Tar and Neuse Rivers with

two nodes for the main channel in a given cross-section. An increase in resolution, as in Figure 6.3, can allow grid points (locations between line segments) to better capture channel geometry. However, the implications for accurate modeling of low flows for rivers within ADCIRC are not as obvious. Figure 6.4 shows the flow area for a given discretization based on a given water surface elevation.

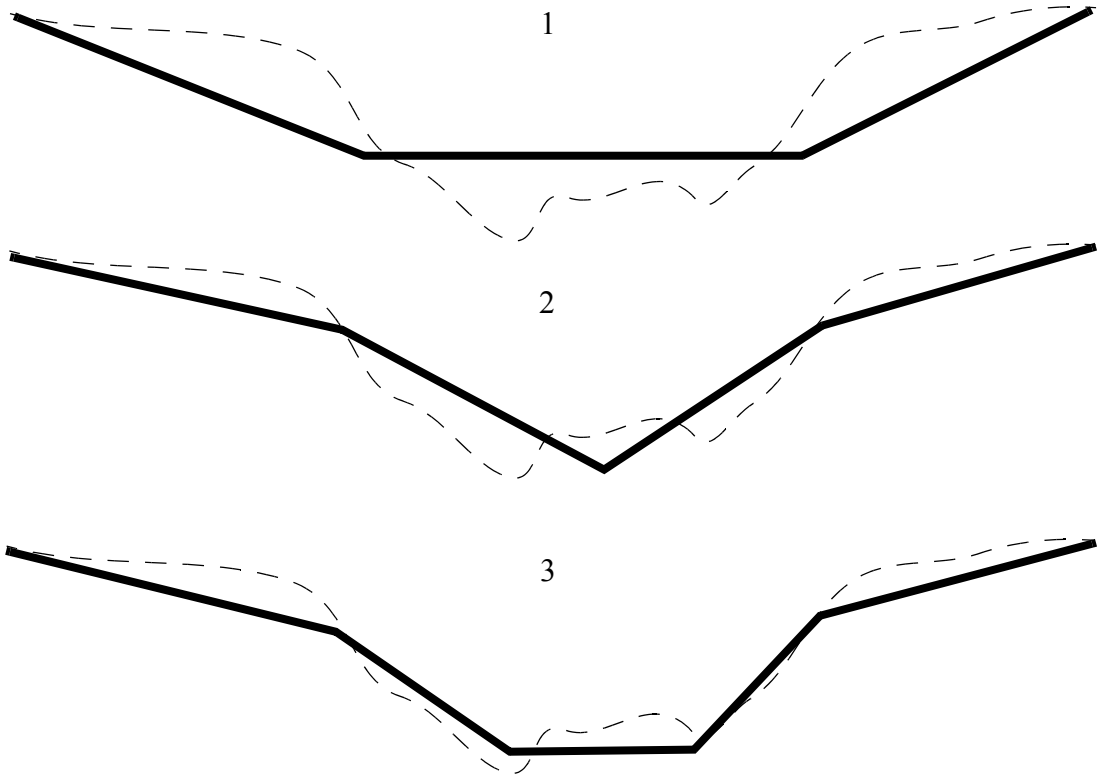

Figure 6.3 River and floodplain geometry representation based on various channel representations: 1) two nodes for the channel, 2) three nodes for the channel, and 3) four nodes for the channel. The dashed line shows a theoretical cross-section, while the solid line depicts the ADCIRC representation based on different discretizations.

Section 1 in Figure 6.3 shows the discretization of the cross-section with two nodes for the channel. Based on this section, it is obvious that ADCIRC cannot model flows at elevations below the river bottom in the grid. For water surface elevations between the river bottom and the elevation of the lowest adjacent floodplain node, the river will resemble a rectangular section (assuming the elevation of both points defining the river bottom is

equal), because ADCIRC only activates an element once the local water surface exceeds a minimum depth for all the nodes for that element. The case of an approximately rectangular cross-sectional flow area is shown in section 1a of Figure 6.4. If the first node on each floodplain is wet, the geometry for the flow is defined by four points, as shown in section 1b of Figure 6.4. The flow area consists of a trapezoidal section in the bottom with a rectangular section on top of it.

The bottom three sections in Figure 6.4 show the implications for adding another node in the middle of the river. Until the water surface elevation exceeds the second-lowest node in the channel section (assuming the lowest nodes in the section are defining the river), ADCIRC will not treat the river as wet. So, despite matching the overall channel geometry better and one of the three nodes in the discretization having a lower elevation than the minimum elevation in section 1, the increased resolution actually results in a larger range of shallow depths that cannot be represented. Certainly, the two nodes on either bank in the refined section could be lowered to the same heights as the corresponding (spatially) nodes in the original discretization. This could, potentially, improve the stage-discharge relationships for these sections if detailed cross-sections existed for the entire extent of the rivers. However, the improvement by increasing the channel resolution by a factor of two (by switching from one element defined by two nodes to two elements defined by three nodes) is marginal. The minimum water surface elevation that can be represented is equal to the sum of second lowest nodal elevation in the section (assuming the two lowest nodes in the section are consecutive and the 3rd node defining the element, which is part of the next section, has a similarly low elevation value) and the defined minimum water elevation for wetting. A non-symmetric cross-section with a flat portion between two nodes near the

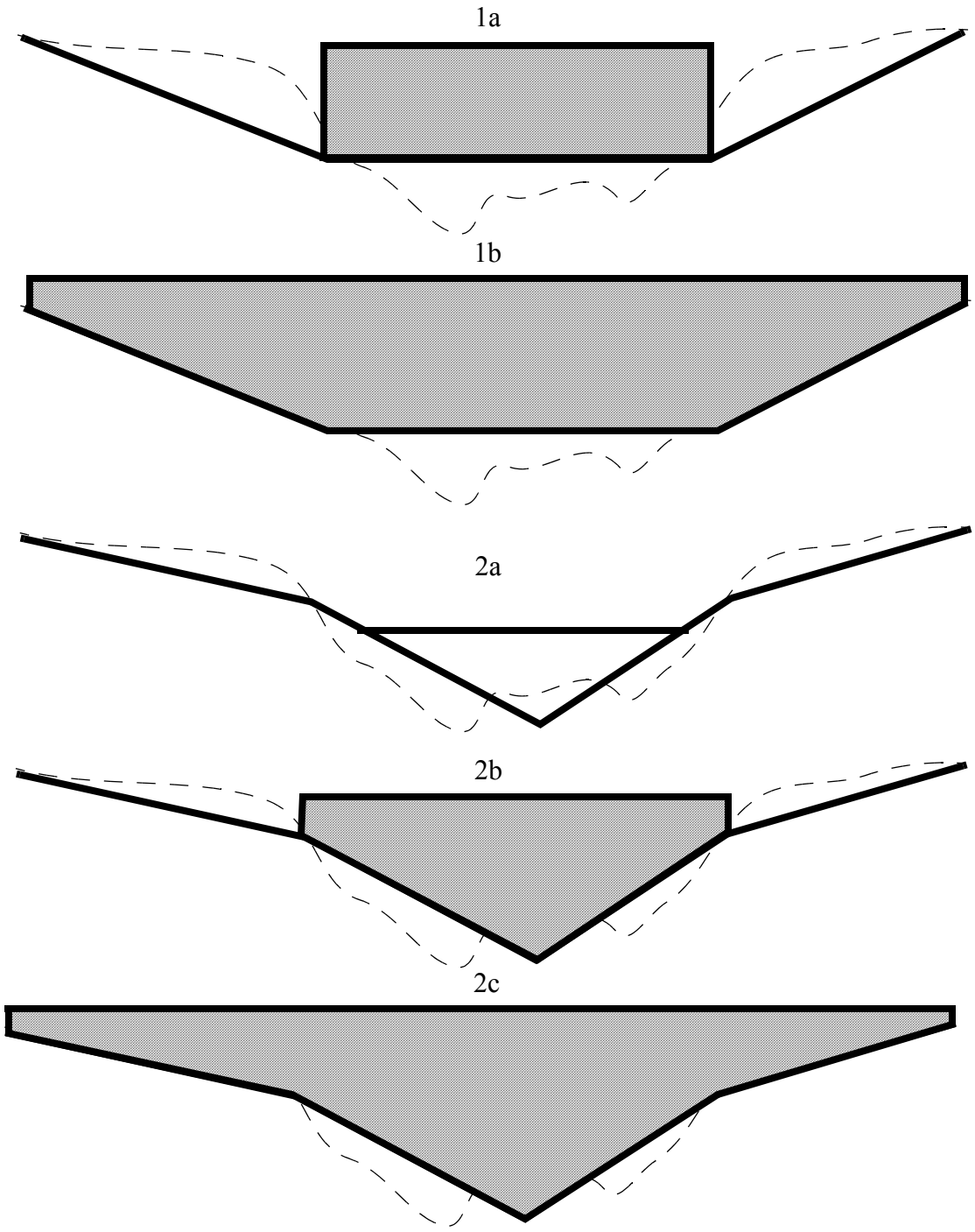

Figure 6.4 Schematic of ADCIRC flow area (filled regions) based on water surface elevation (top horizontal line) for a channel defined by two nodes (1a and 1b) and three nodes (2a, 2b and 2c).

level of the actual channel bottom with a higher third channel node would probably be necessary to improve the stage-discharge relationship for low flows.

Further increase in resolution in the river, by adding a fourth node in the river section (third section in Figure 6.3), allows reasonable overall representation of channel geometry, while also allowing stage at low flows to be modeled accurately. However, this requires grid spacing to be one-third of the spacing in the original discretization and would require significant river bathymetry data for accurate representation. The elements defining the Tar and Neuse Rivers are already among the smallest elements in the grid. A decrease in the grid spacing by a factor of three might adversely impact the time step, as well. Because the focus of this study is flood inundation, which corresponds to high-flow events, the decision was made to use the original spatial discretization and sacrifice accuracy at low flows. With regards to element size and time step, an important application of ADCIRC is operational flood forecasting. Thus, while decreases in stable time step may be tenable for hindcasts or planning simulations, grid modifications that result in simulation run times increasing by a factor of two or three may preclude operational flood forecasting with ADCIRC because of computational resource issues.

6.2.4 Original Channel Representation

The original ADCIRC grid elevations along the Tar and Neuse Rivers' profiles can be seen in Figure 6.5 and Figure 6.6, respectively. In many locations, the left and right sides of the rivers are at approximately the same elevation, which is the situation depicted in the schematic drawing in Figure 6.3. However, there are also a number of locations where there is a significant difference in elevation from one side of the river to the other. As Figure 6.5 shows, the most glaring instances of this along the Tar River are 1, 5, 20, 32, 36 and 51 km

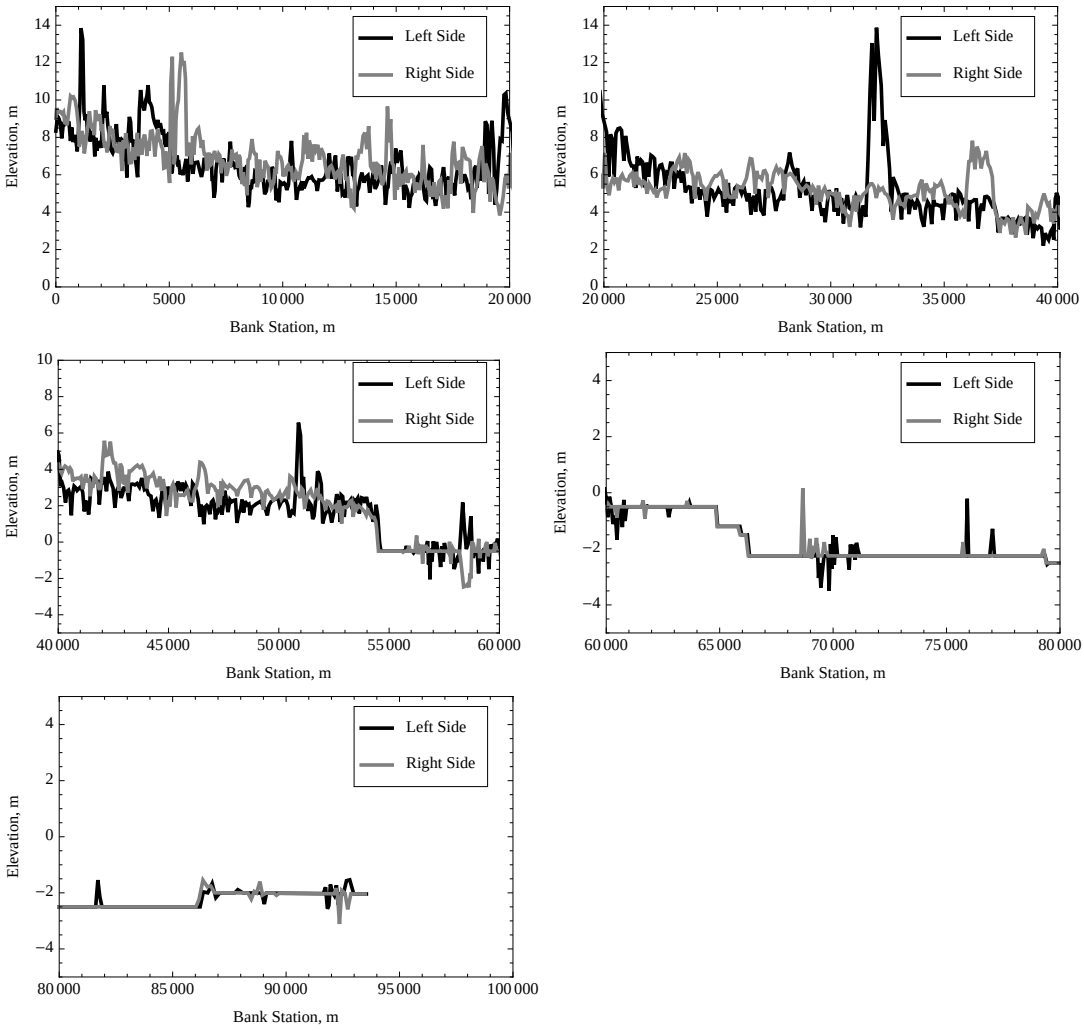

Figure 6.5 Original river node elevations along the Tar River in the ADCIRC grid from the upstream boundary to the Pamlico Sound.

from the upstream boundary. Looking specifically at the elevations 32 km down from the boundary along the Tar River, the water surface elevation would have to approach 14 m in order for the river to be wet in that location. With a water surface elevation of 14 m in that location, one side of the river would barely be wet, while the depth on the other side would be approximately 8 m (the difference between the two lines in the figure at that location). Figure 6.6 shows that discrepancies in nodal elevations, from one side of the river to the other, exist along the Neuse River as well, with the most notable instances 4, 25 and 29 km down from the hand-off point. It is important to remember that, while the main river nodes

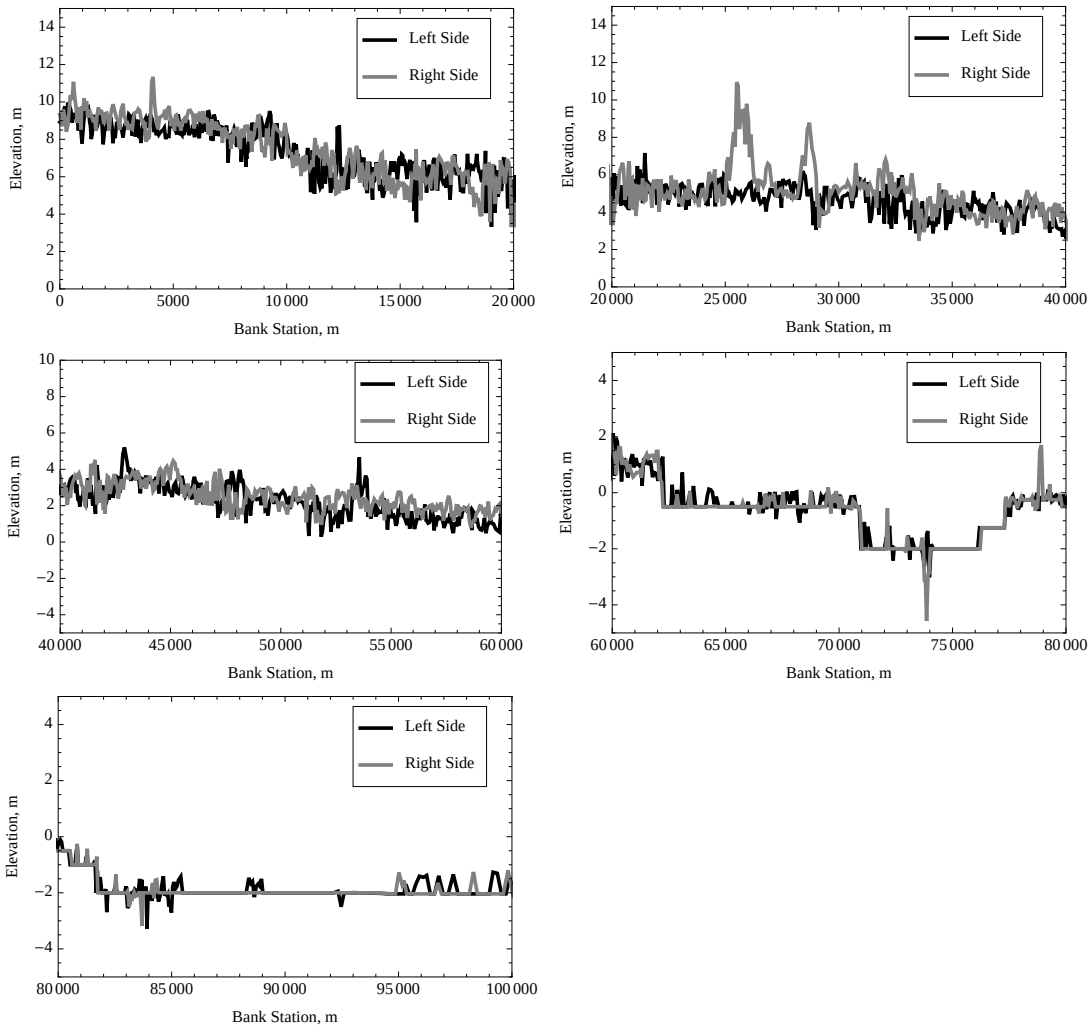

Figure 6.6 Original river node elevations along the Neuse River in the ADCIRC grid from the upstream boundary to the Pamlico Sound.

are located near the banks spatially, the elevations of the main river nodes define the elevation of the channel bottom in the model.

Results from a simulation forced with baseflow rates and using the original river elevations demonstrate the need for modifications to the river elevations. As can be seen in Figure 6.7, the ADCIRC bathymetry, on initial inspection, follows the river in this section. The dark blue areas correspond to the lowest elevations, and these occur along the Tar River. The initial results show a fair amount of flow in the floodplains adjacent to the river, which is due to the initialization for this simulation, but the baseflow should be contained

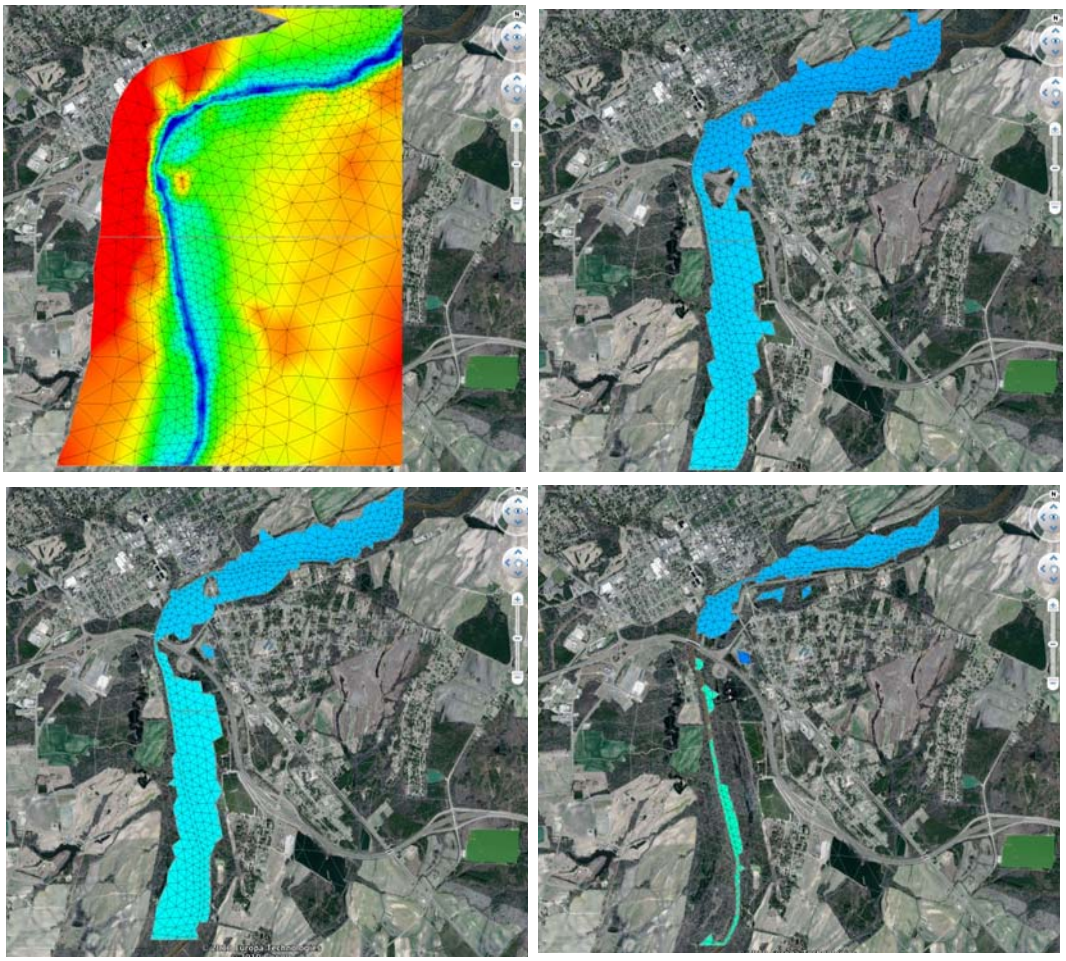

Figure 6.7 Images for the Tar River around Tarboro, NC and Princeville, NC with SMS output overlaid on Google Earth maps: original ADCIRC bathymetry (top left) and ADCIRC elevations at the beginning of the simulation (top right), 6 hours into the simulation (bottom left), and 42 hours into the simulation (bottom right). This location is about 19 km downstream of the hand-off point on the Tar River.

in the main channel. The flooding is due to the initialization procedure, which used the elevations along the channel to determine local high points and ensure the initial water surface was above the channel bottom for the entire length of the river. Subsequently, adjacent areas were initialized wet if they were below the starting water surface elevation in the river. The image at the bottom right of Figure 6.7 shows discontinuities in the wet areas in the domain. By the end of the simulation, the Tar River is a series of ponds. This result clearly demonstrates the need for adjustments to the river portion of the ADCIRC grid.

Even if the river was contiguous from the boundary all the way to the Pamlico Sound, adjustments to the river elevations would still be necessary because of the unphysical river flooding created by efforts to initialize the river as a continuous body of water.

6.2.5 Modifications to River Geometry

The preliminary ADCIRC grid, with bathymetry/topography from high-resolution LIDAR data, was problematic in the rivers because the elevations specified for the nodes along the sides of the Tar and Neuse were not consistent or realistic. Aerially, these nodes were essentially creating the river bottom boundary shown in Figure 6.8 (Figure 6.16 shows a set of images that further illustrates this idea). Each side of the river was defined by a line of grid points and the triangular elements created between these two lines define the river. However, the elevations for these nodes were often comparable to the values in the adjacent floodplains. The nodes that define the river should have lower elevations than the nodes that define the adjacent floodplains. In other words, the main channel for each river was not well-defined. An example of the discrepancy in elevation between one side of the river and the other is shown in Figure 6.8. The black circle outlines a location on the Tar River, upstream of Tarboro, NC, where the nodal elevations on the south edge of the river are about 7 m. The nodal elevations on the north edge of the river are close to 14 m. For reference, this location is about 5 km down from the boundary, and the discrepancy can be seen in the top left panel of Figure 6.5.

In order to create more realistic rivers in the ADCIRC grid, the bathymetry for the rivers needed to be adjusted. The same issue that caused unrealistic flows along the river proved problematic in modifying the bathymetry because river elements could not be clearly identified. Typically, river elements (elements that make up the river at low flows)

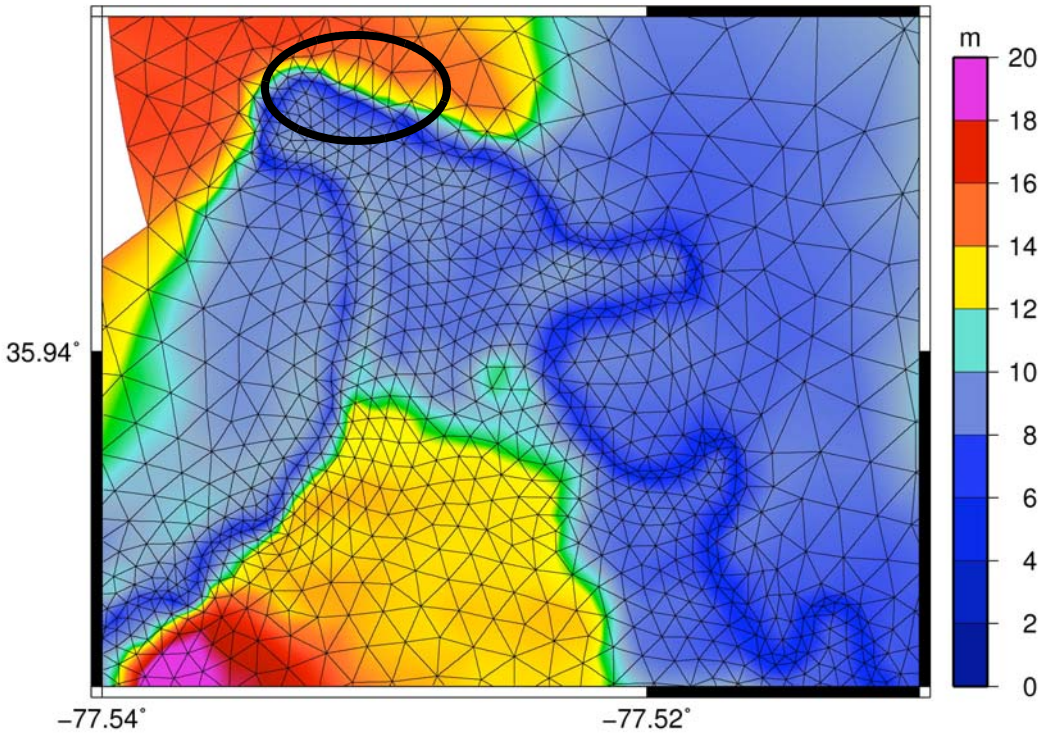

Figure 6.8 ADCIRC v20 grid along a stretch of the Tar River upstream of Tarboro, NC. The black circle outlines a location where the nodal elevations are about 7 m on the north edge of the main river channel than on the south edge.

could be selected based on elevation, i.e., river elements should be lower than adjacent floodplain elements. However, elevation-based criteria in automated selection routines created for this study were often incorrect in selecting the next river element down river for the ADCIRC grid. Similarly, criteria based on grid size (the smallest elements are generally the ones in the river in this domain) and element orientation (locally, the river is usually fairly straight) are helpful for automatic selection, but certainly not infallible.

A pre-processing program was created to select river elements from the ADCIRC boundary down to the ocean. After the most upstream element in the river has been selected, the following main steps are utilized in the program to select river elements.

- Determine the potential river elements that share a face with the last river

element; the term potential river element implies the element has not already been determined to be a river element.

- Calculate the vectors between the areal center of the last river element and the areal centers of the new possibilities, as well as the vector between the last river element and the river element two prior (the element two prior was used because the elements are triangles and this method gives a more consistent direction for the local river path).
- Calculate the dot product between the previous vector and the vectors for the new possibilities.
- A heuristic metric for comparing possibilities was developed by trial-and-error, and is given by (6.1), where p is the vector between the centroid of the last river element and the river element two prior; v_i is the vector between the centroid of the last river element and the centroid of a potential new river element; z_i is the bathymetry of the highest node associated with the potential river element (the addition of 20.0 is to make values positive and is necessary because bathymetry values at the top of the Tar and Neuse Rivers are on the order of -10.0 m, meaning the elevations are 10.0 meters above the datum, which is mean sea level); and A_i is the area of the potential river element. The elevation of the highest node is used, rather than the lowest node, because river elements should have low values for all three nodes, whereas floodplain elements should have at least one node that has a higher elevation than the river node elevation in the vicinity.

$$Metric = \frac{(p \cdot v_i)(z_i + 20.0)^2}{A_i} \tag{6.1}$$

- The new river element is the possible element with the highest metric score (increases in score result from a larger dot product, lower elevation, and smaller element area).

When there are no longer any possibilities for new river elements, or a sufficiently low elevation has been reached, the program produces a file containing one value for nodes associated with selected river elements and a different value for nodes that are not associated with selected river elements. This file, which is written in the same format as the fort.63 (water surface elevation) output file for ADCIRC, can be visualized using SMS,

FigureGen, or a similar program, and an image showing the selected river elements can be exported in KMZ format. The KMZ file can be read into Google Earth and the aerial extent of the selected river elements can be analyzed. Specifically, the string of elements can be compared to actual river geometry. Locations where the selection criterion fails to choose the correct element can be hardwired to do so. Then, the program must be re-run until it produces a complete set of elements for each of the rivers in the domain. In creating the set of river elements for the Tar River, 30 elements were hardwired into the selection routine, while hardwiring of 14 elements was required on the Neuse River. For reference, there are approximately 2500 elements along the Tar River and 3000 along the Neuse River.

Subsequently, the selected river elements were processed to create a more realistic river profile in the ADCIRC grid. For each node belonging to a river element, the nodal elevation was adjusted to the elevation of the lowest node of any of the nodes belonging to the river elements that contain that node. Then, an averaging process was used to smooth the elevations of the nodes that belong to the river elements. The following steps were used during each smoothing iteration:

- Each node is checked to determine if it is a river node.
- If a node is not a river node, it is ignored.
- For each river node, each element is checked to determine the elements to which the current node belongs.
- Each element containing the current river node as one of its three nodes has all three of its nodes (including the current node) flagged.
- The arithmetic average of the elevations of the flagged nodes is calculated and saved as the new elevation of the current river node.

The number of iterations used in the smoothing process is somewhat arbitrary (subsequent iterations repeat the procedure with the most recently adjusted nodal eleva-

tions). For the Tar and Neuse Rivers, one hundred iterations were used. The resulting bottom elevations along each side of the channel can be seen in Figure 6.9 (Tar River) and Figure 6.10 (Neuse River). The result of the modification is that the two lines of nodes defining each river have more consistent elevations. However, the large scale variation in slope throughout the rivers is maintained. Furthermore, no modifications were made to floodplain elevations, although the first line of floodplain elements (one each side of the river) uses one or two river nodes.

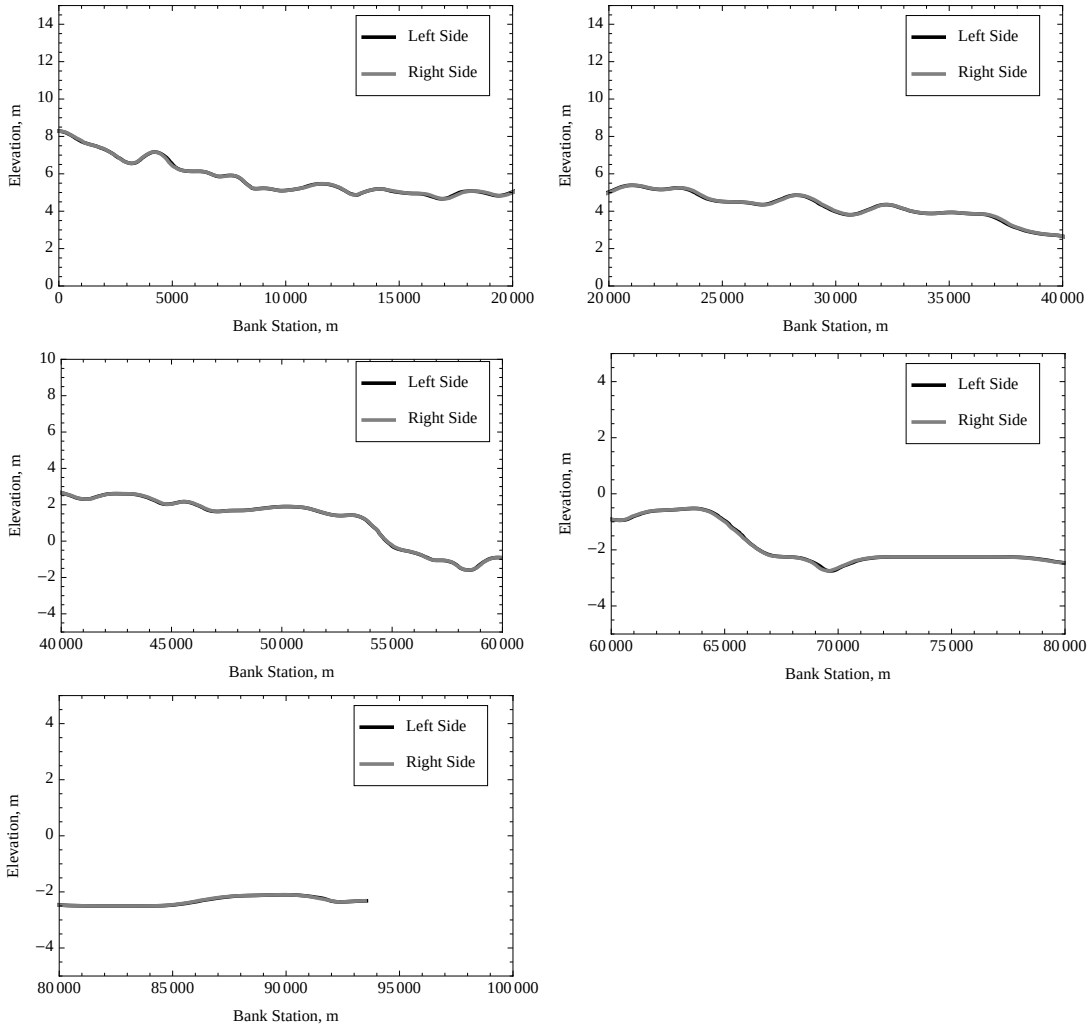

Figure 6.9 River node elevations along the Tar River in the ADCIRC grid from the upstream boundary to the Pamlico Sound after lowering and smoothing.

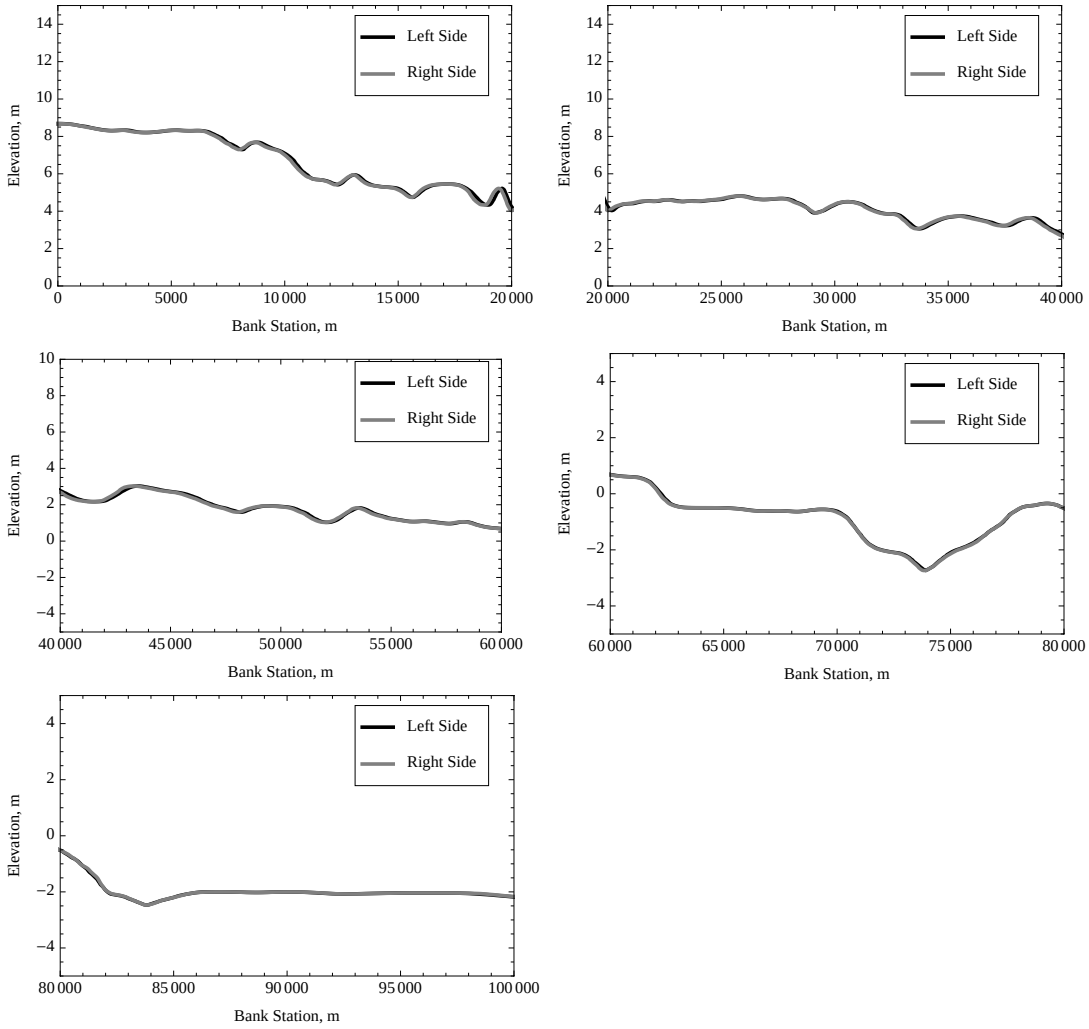

Figure 6.10 River node elevations along the Neuse River in the ADCIRC grid from the upstream boundary to the Pamlico Sound after lowering and smoothing.

The river initialization procedure is the same before and after the grid elevation modifications. The high points in the river are determined and a minimum water depth is assigned at those points. Then, the water surface elevation between consecutive high points varies linearly. Elements that are lower than the local water surface elevation are initialized as wet, including "non-river" elements in some areas. Before the elevation modification, large amounts of the floodplain were initially wet, as seen in Figure 6.7. Following the elevation modification, the areal extent of the river is accurately represented at the start of the simulation, i.e., it stays within the channel banks.

The cross-sections of the rivers in the ADCIRC grid were compared to "real" sections (fine-resolution HEC-RAS [*Brunner* 2001, 2002] sections) provided by the North Carolina Floodplain Mapping Program (NCFMP). These comparisons were done before the modifications previously presented. However, for each cross-section, the ADCIRC calculations were performed both for the original grid geometry and for the original grid geometry with the higher river node lowered to the elevation of the lower river node (similar to the first step in the process to create the smoothed grid).

Plots of water surface elevation versus discharge for sections across the Tar and Neuse Rivers in the ADCIRC grid were compared to equivalent plots for the real sections. In order to focus on the geometric differences in sections for both ADCIRC and NCFMP sections, a bottom slope of 0.00015 m/m and Manning's roughness of 0.025 are used for all computations. Thus, the actual water surface elevation vs. discharge curves will differ from the ones that were created. However, the chosen bottom slope and Manning's roughness are realistic values for these rivers and are useful in assessing the geometry of the river discretization in the ADCIRC grid. The water surface elevation values are based on uniform flow depth for a given flow rate.

The locations analyzed on the Tar and Neuse Rivers are listed in Table 6.1 and Table 6.2, respectively. Additionally, the locations are shown graphically in Appendix F.1. The locations were estimated based on descriptions for the NCFMP cross-sections, which is the reason more precision was not included in the coordinates. The comparisons for the first four sections on the Tar River are shown in Figure 6.11. The ADCIRC water surface elevations differ from NCFMP water surface elevation values at low flows because of resolution constraints (NCFMP HEC-RAS sections on order of meters, ADCIRC on order of

Table 6.1 Locations of cross-sections for comparisons on the Tar River.

Number	Latitude (North)	Longitude (West)
1	35.930	77.559
2	35.939	77.523
3	35.922	77.509
4	35.894	77.528
5	35.873	77.535
6	35.843	77.544
7	35.800	77.549
8	35.784	77.546
9	35.761	77.516
10	35.640	77.417
11	35.618	77.391
12	35.618	77.377
13	35.616	77.367
14	35.609	77.331
15	35.598	77.310
16	35.594	77.271
17	35.609	77.227
18	35.589	77.194
19	35.573	77.170

Table 6.2 Locations of cross-sections for comparisons on the Neuse River.

Number	Latitude (North)	Longitude (West)
1	35.224	77.767
2	35.220	77.740
3	35.226	77.697
4	35.235	77.659
5	35.261	77.619
6	35.241	77.568
7	35.258	77.531
8	35.295	77.496
9	35.324	77.466
10	35.338	77.422
11	35.343	77.394
12	35.334	77.367
13	35.319	77.325
14	35.298	77.294
15	35.261	77.244
16	35.247	77.208
17	35.240	77.179
18	35.216	77.139
19	35.189	77.097
20	35.164	77.087

10's of meters). The rivers in ADCIRC are represented as fixed width until elements on the floodplain become wet. Thus, the cross-sectional flow area for in-channel flow is approximately rectangular, as discussed earlier in Section 6.2.3. Conversely, the actual geometry is represented well in the HEC-RAS sections. Generally, the width of flow increases as the flow rate increases. At high flows, the rating curves for ADCIRC tends to more closely

match the curve for HEC-RAS. Comparisons for all of the sections on the Tar and Neuse Rivers are shown in Appendix F.

The first section available downstream of the hand-off point on the Tar River, section 1 in Figure 6.11, shows agreement within 0.30 m for all flow rates greater than 50 cms. However, there is a large discrepancy (2-3 m) in water surface elevation predicted for low flows. At low flows, which correspond to relatively small flow depths, the water surface elevation is higher for the ADCIRC section because the channel bottom is higher than the minimum channel elevation in the NCFMP HEC-RAS sections.

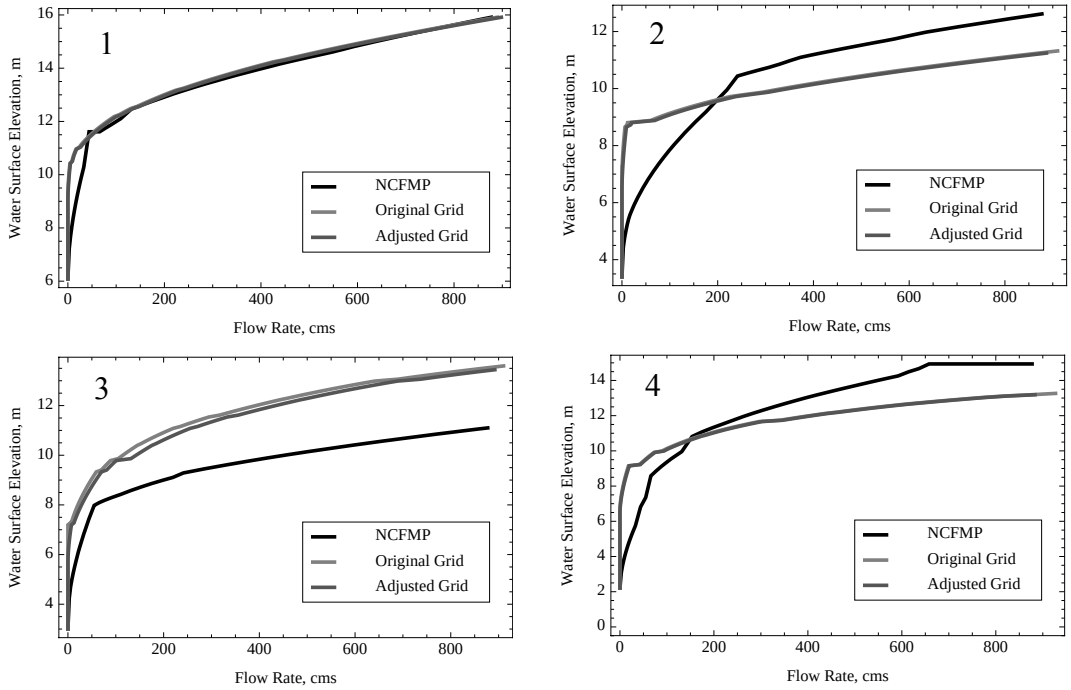

Figure 6.11 Water surface elevation vs. flow rate plots to compare the ADCIRC cross-section to the actual channel cross-sections (from NCFMP data) for the first four locations on the Tar River downstream of the ADCIRC boundary.

Sections 2-4 on the Tar River do not show the same level of agreement between the ADCIRC and NCFMP results as section 1. At sections 2 and 4, ADCIRC underpredicts the water surface elevation for high flows. The transition from ADCIRC overprediction to underprediction occurs at about 200 cms for section 2 and around 150 cms for section 4.

Conversely, ADCIRC overpredicts water surface elevation for all flows for section 3. As expected, at low flows, ADCIRC overpredicts the water surface elevation for all four sections. It should also be noted that there are two ADCIRC lines. Generally, the two ADCIRC sets produce almost identical results. This is the case for sections 1, 2 and 4. There is separation in the two ADCIRC lines for section 3. The darker line corresponds to the adjusted ADCIRC section, with the higher river node lowered to the elevation of the lower river node. This adjustment decreases the water surface for a given flow rate, if there is a discrepancy in the node elevations in the original grid.

The comparisons for the first four sections on the Neuse River are shown in Figure 6.12. As was seen for the results for the Tar River, the ADCIRC water surface elevations are significantly higher than the water surface elevations for the NCFMP sections at low flows. However, there is good agreement for flows greater than 75 cms for sections 1-4 on the Neuse River.

Some locations on the Tar River show errors of more than a meter for high flow rates. However, errors are generally larger for in-channel flows and smaller for out-of-bank flows. The target application of this study is flood forecasting due to tropical and extratropical systems. Therefore, the errors in stage at low flows are acceptable.

A summary of all the sections compared on the Tar River is shown in the left panel of Figure 6.13. Each small black dot is the error between the water surface elevation using the adjusted ADCIRC section data and the water surface elevation using the HEC-RAS section data from the NCFMP. Thus, there are 19 small dots for the Tar River comparison, one for each section. Positive error values occur when the water surface elevation using the ADCIRC section is higher than the corresponding water level using the NCFMP data. The

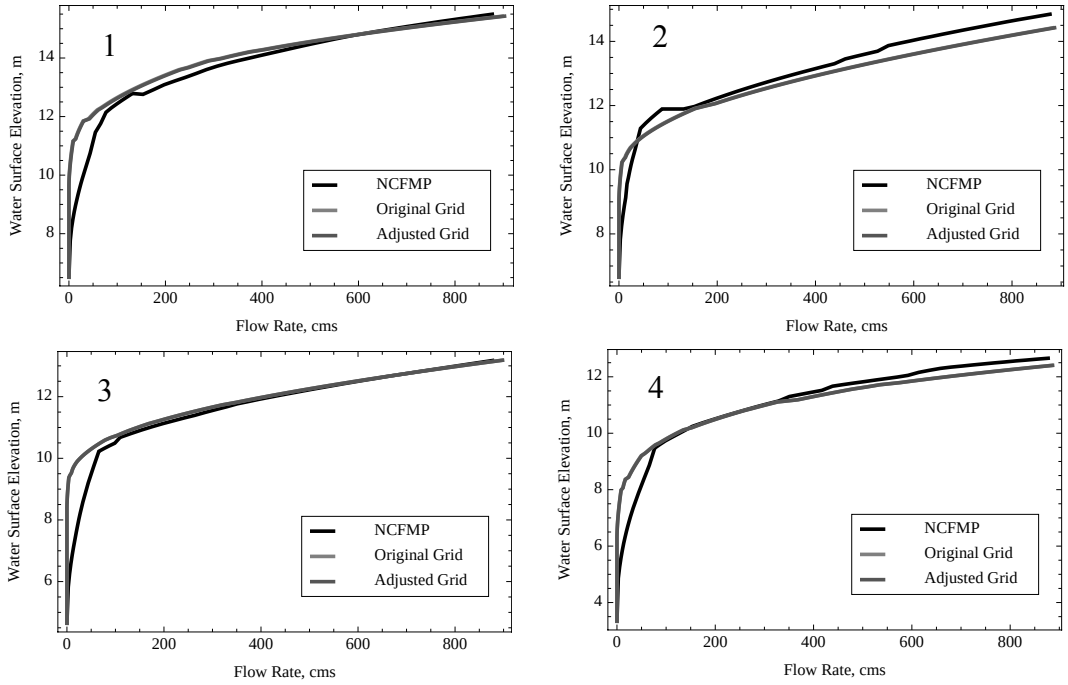

Figure 6.12 Water surface elevation vs. flow rate plots to compare the ADCIRC cross-section to the actual channel cross-sections (from NCFMP data) for the first four locations on the Neuse River downstream of the ADCIRC boundary.

errors were calculated for discharges of 10, 25, 50, 100, 200, 300, and 500 cms. The large dots in each vertical series are the arithmetic average of the individual section errors.

The plot for the Tar River shows that for flows above 100 cms, the average error is close to zero. Thus, on average, for the target flows rates, the predicted water surface elevation using ADCIRC should be fairly accurate, provided the discharge results in ADCIRC correspond to the actual flow rates experienced by the Tar River. For flow rates of 100, 200, 300 and 500 cms, the average errors are 0.27, -0.30, -0.39 and -0.43 m. Thus, the bias for high flows is for ADCIRC to underpredict water surface elevation by 1-1.5 ft. Additionally, for flows equal to or exceeding 200 cms, most of the individual section errors are less than 1.5 m. While this may not be optimal, future work improving the representation of rivers in ADCIRC could further reduce model errors, especially for high flows.

The right panel of Figure 6.13 shows the results for the Neuse River. There are 20

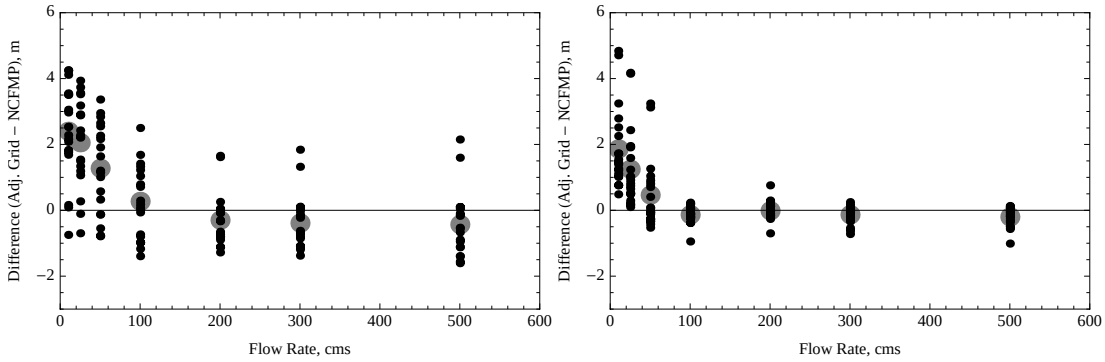

Figure 6.13 Comparison of ADCIRC sections to detailed sections from the NCFMP for the Tar River (left) and Neuse River (right).

small black dots for each flow rate for the Neuse River. Once again, ADCIRC produces unrealistically high water surface elevation levels for low flows, due to the channel discretization. However, for flows equal to or exceeding 100 cms, the average error is close to zero and most of the individual error values are less than 1.0 m. The average errors for flow rates of 100, 200, 300 and 500 cms are -0.14, -0.01, -0.13 and -0.20 m. As was the case for the Tar River results, the bias is for ADCIRC to underpredict water surface elevations at high flows. It is readily apparent, from a comparison of results from the Tar River to those from the Neuse River, that there is substantially less difference for the sections on the Neuse River. This is consistent with the results shown in Figure 6.11 and Figure 6.12. The reason for the better match on the Neuse River is unclear. The two rivers are geometrically similar and handle similar flow rates, although the Neuse is slightly more sinuous. Additionally, the grid generation and analysis tools were consistent for each of the rivers.

The variation in error with respect to distance from the boundary is shown in 6.14 (Tar River) and 6.15 (Neuse River). These figures were created to see if there was a systematic cause for the error. If discernible trends in the difference were present, adjustments could be made to the ADCIRC grid to attempt to reduce the grid-induced error in water surface elevations. The plots for the locations on the Neuse River show low errors for high

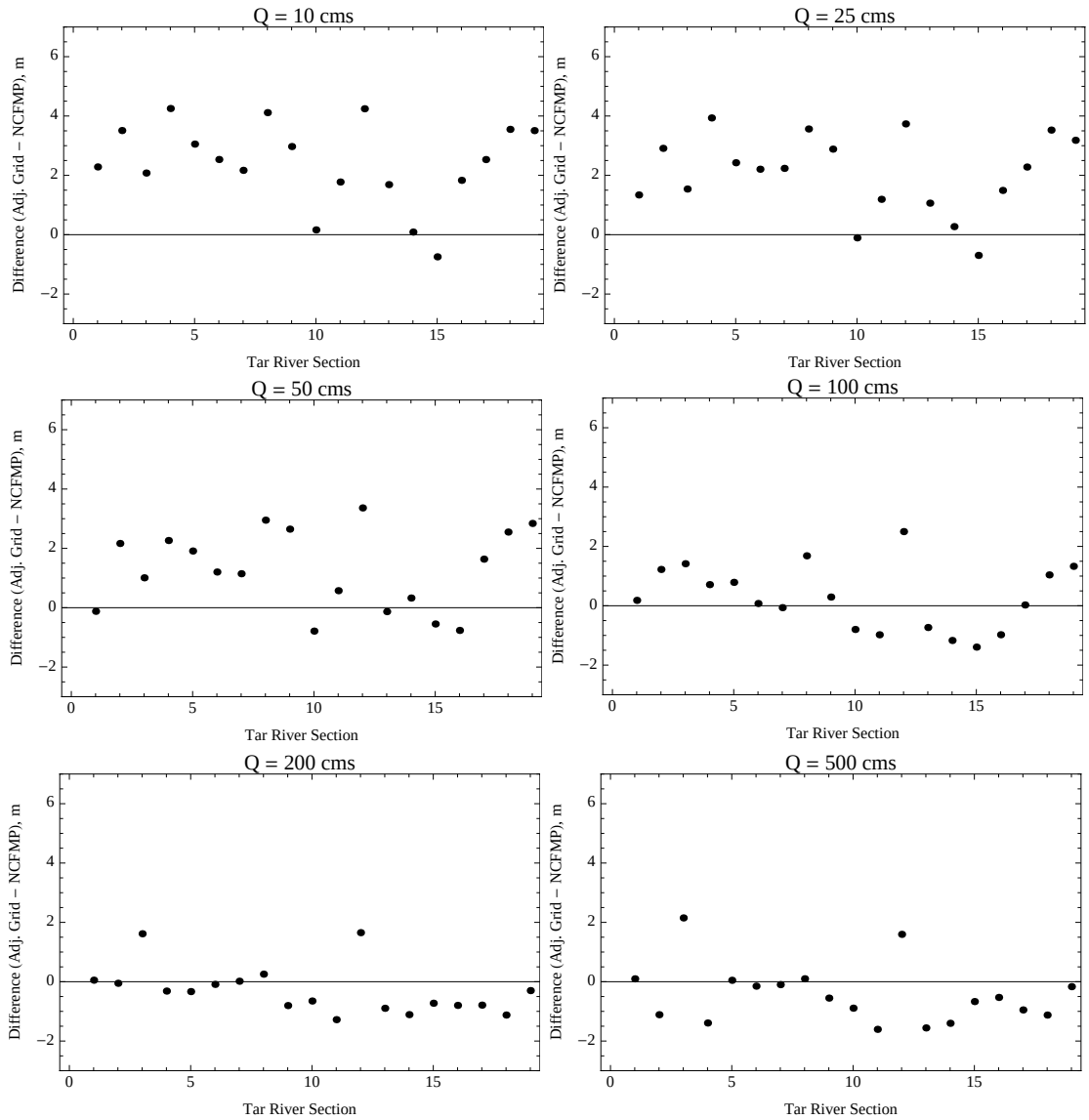

Figure 6.14 Difference in water surface elevation between results with the adjusted ADCIRC grid sections and the NCFMP sections at different locations on the Tar River for six different flow rates.

flows and consistency from section to section.

However, the results are not as good for the Tar River locations. Additionally, there is not a consistent pattern that can be exploited. For example, for flow rates of 200 and 500 cms, the only locations where ADCIRC overpredicts the water surface elevations are at sections 3 and 12. The sections before and after both section 3 and section 12 (sections 2, 4, 11 and 13) all have negative differences for flow rates of 500 cms. Section 8 on the Tar

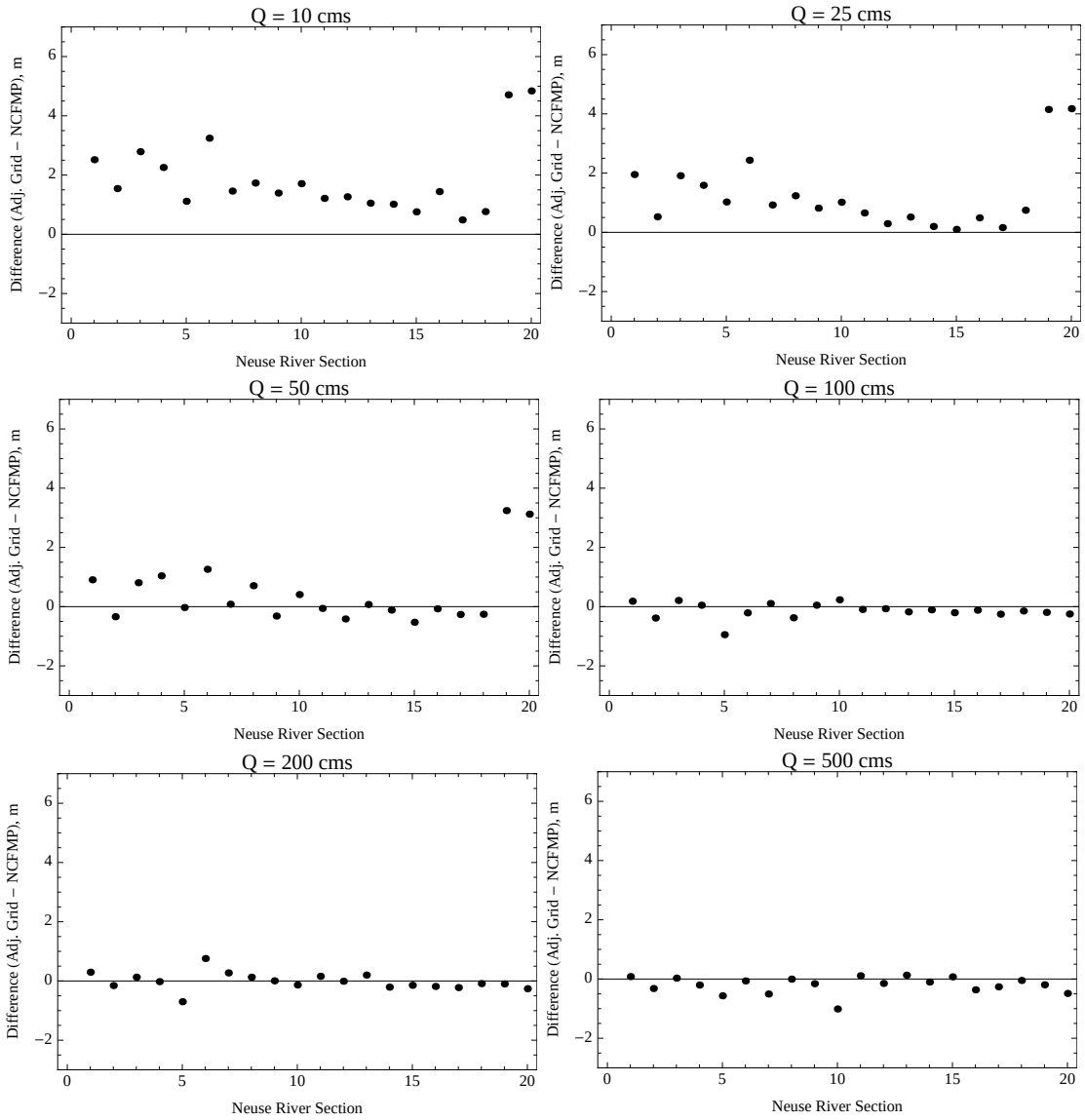

Figure 6.15 Difference in water surface elevation between results with the adjusted ADCIRC grid sections and the NCFMP sections at different locations on the Neuse River for six different flow rates.

River is an example of another difficulty regarding grid modification. The predicted water surface elevations when the flow is 100 cms is about 2 m too high. However, the water surface elevations are good with flows of 200 and 500 cms. Grid modifications to reduce the water surface elevation for a discharge of 100 cms would also have to maintain the water surface elevation for the higher flow values.

A different issue related to grid modification was that resolution was added to the

middle of a horseshoe bend in the Tar River, because the original ADCIRC grid did not have non-river edge nodes in the floodplain in that area. In ADCIRC, if all three nodes for an element are wet, that element is wet. The river nodes are wet at base flows. This resulted in a three-element wide cut-off that allowed water to move down the river without going all the way around the bend. The addition of four nodes on the floodplain created floodplain elements and kept low flows in the actual river. This grid modification is illustrated in Figure 6.16.

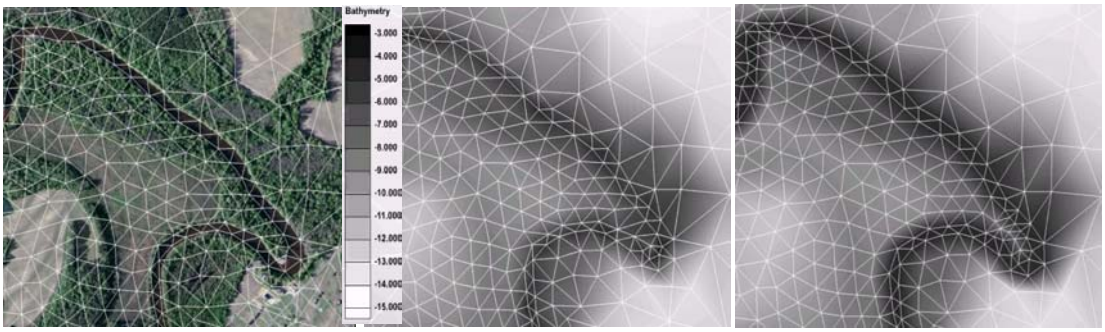

Figure 6.16 Images showing a portion of the ADCIRC grid that illustrates grid issues with sharp river bends: overlain on Google Earth (left), the original bathymetry (middle) and the modified grid and bathymetry (right).

6.2.6 Grid Stability

Along with the initialization problems discussed previously, the grid is also subject to severe stability constraints on the time step. The maximum stable time step is around a half second. This is not a strict criterion, but attempts to use ADCIRC parameters (G, lateral eddy viscosity, advective term options) to increase stability so a one-second time step could be used were unsuccessful. The following sequence of images, Figure 6.17, shows the evolution of the water surface elevations on the Neuse River just upstream of Kinston, NC, for an unstable simulation. This simulation was performed using the regular parameters for runs with the North Carolina grid with two exceptions: a time step of 0.9 seconds and a constant G value of 1.0 s^{-1}. The elevations appear reasonable through the

first three time steps. However, the solution begins to degrade starting with the output for the fourth time step. The errors appear initially near the bottom right side of the “S” curve shown, and the simulation quickly becomes unstable as time evolves further.

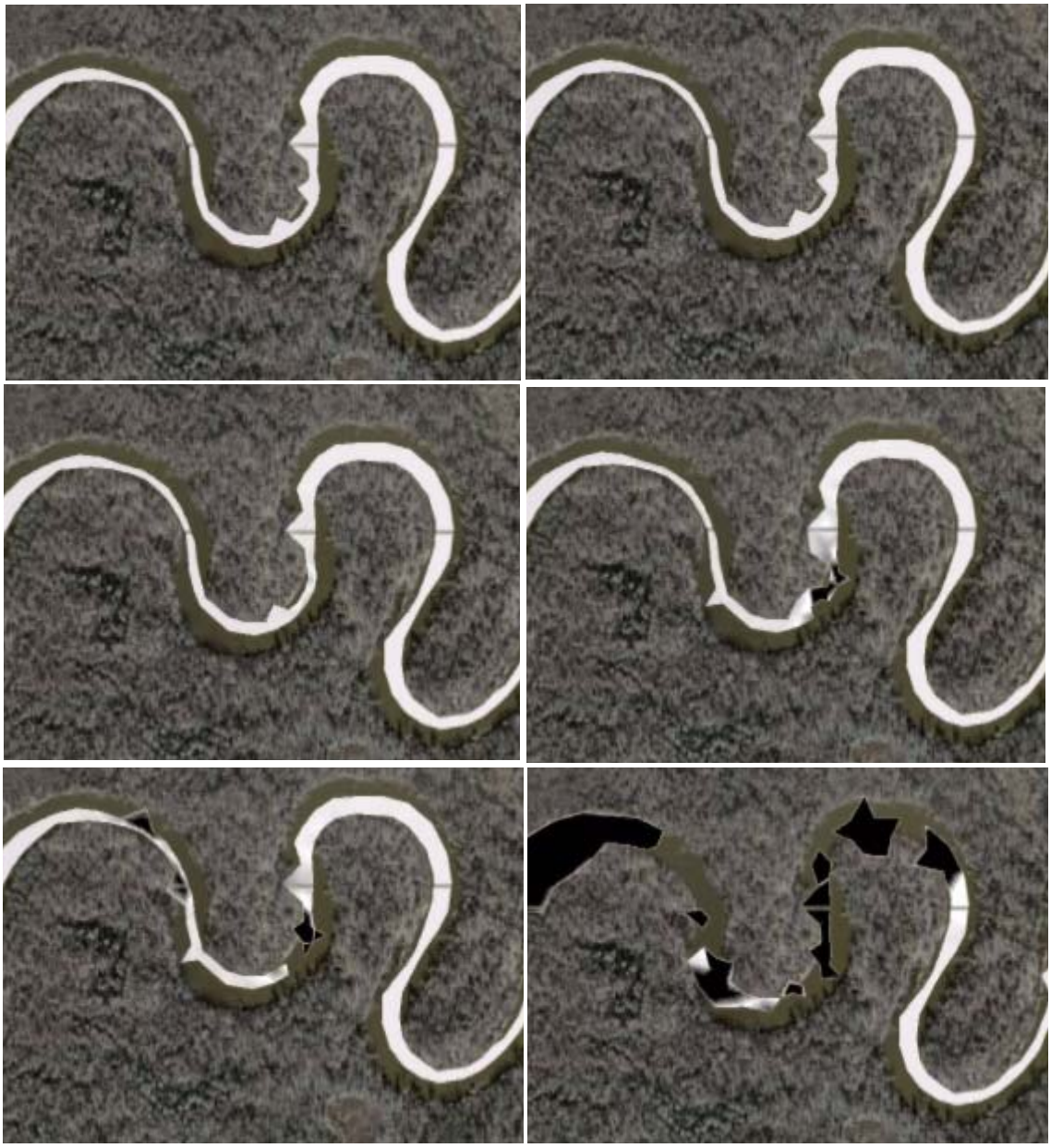

Figure 6.17 Water surface elevations for the six steps of a simulation. Areas shown in white have reasonable values, while black areas have water surfaces ten meters too high.

Attempts to create a more stable grid in order to reduce simulation run times were partially successful. As Figure 6.18 shows, the width of the river varies widely in this

region. For the most part, the main river channel is just a series of single elements (as previously presented) through this section. For this reason, the different widths of the river implies vastly different grid sizes throughout this stretch of the Neuse River. Specifically, the width of the river in the straight stretch near the bottom left of Figure 6.18 is about 60 meters, whereas the width in the "S" curve section is often 10-15 meters.

Figure 6.18 Initial width of the Neuse River just upstream of Kinston, NC.

By sequentially increasing the width through the skinny stretches where stability problems are present, the simulations become more stable. Initially, simulations with a one-second time step always crashed before a minute of simulation time was reached. With limited movement of nodes, the simulation ran for over 6 hours of simulation time with a one-second time step and a constant G value of 0.1 s^{-1}. The simulation using the grid with the nodes moved crashed in the same stretch of the Neuse River as the previous grid,

without being subject to large flows. The specific reason for the instability is unknown. While the end goal of increasing the stable time step (which would have decreased the computational expense of the simulations) was not achieved, the procedure of moving nodes was partially successful. Additional focus on river delineation in the future could result in increased stability at larger time steps. Thus, it is recommended that element sizes be kept approximately constant, when possible, for river delineation.

6.3 Boundary Flux Specification

6.3.1 Reduced River Grid

In order to test the upstream boundary condition for the Tar and Neuse Rivers, a new grid was created from the full ADCIRC grid. The extents of the two grids can be seen in Figure 6.19. For the reduced grid, 90% of the computational nodes were removed. The nodes that remain span the entire extent of the Tar and Neuse Rivers, as well as portions of the Pamlico Sound that connect the two rivers. The reduced grid contains 50,266 nodes, whereas the full domain is discretized by 539,879 nodes. In creating the river grid, the only nodes removed that are upstream of the boundary in the Pamlico Sound are in the higher elevation area between the two rivers down near the sound. These nodes are far (tens of kilometers) from the upstream river boundaries and were removed for computational efficiency.

6.3.2 Boundary Flux Based on Conveyance

Results from Chapter 5 show that, compared to full-domain ADCIRC results, coupled hydraulic-ADCIRC results are better when flux boundary conditions are used. Therefore, in this study, the focus will be on applying discharge values at the upstream

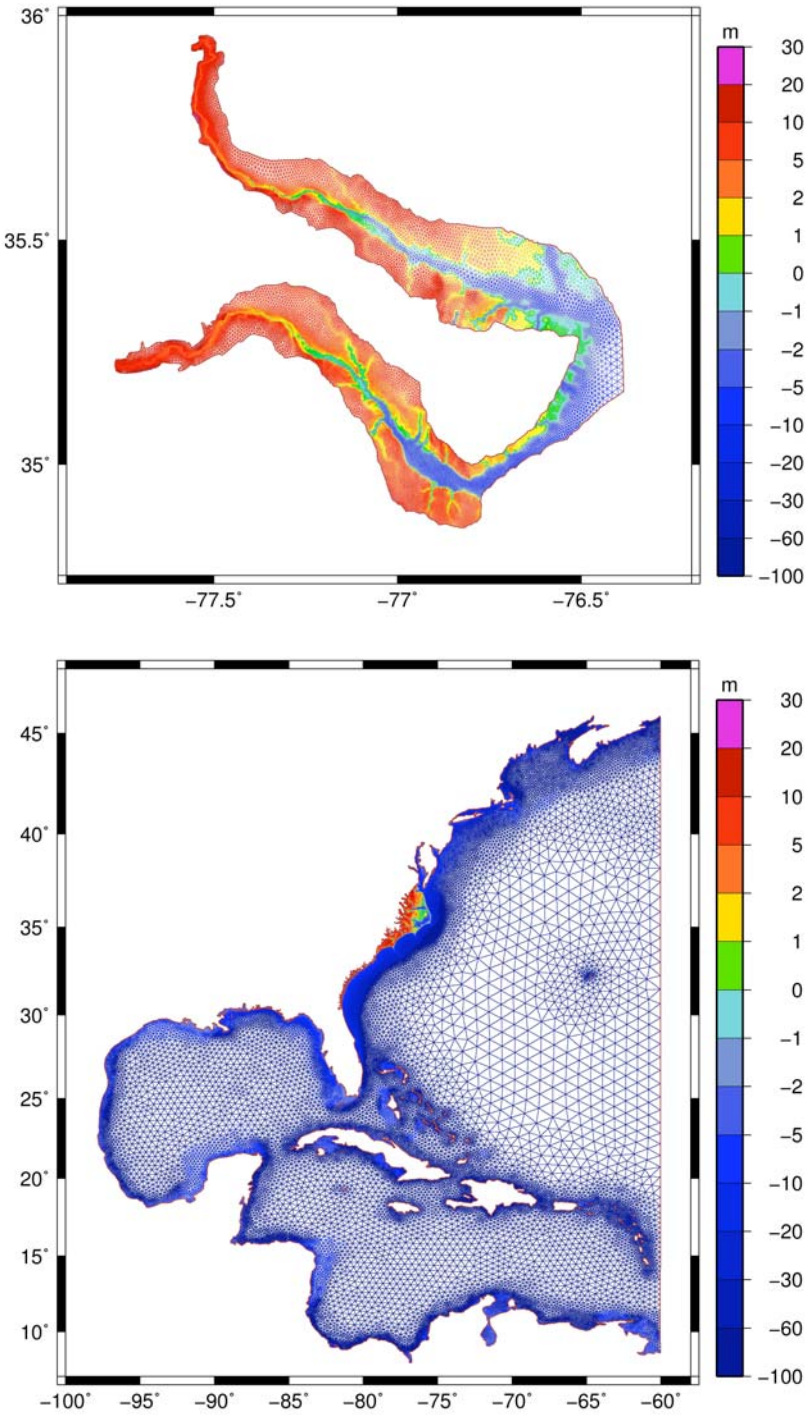

Figure 6.19 Extent of the reduced grid for river testing (top) and the full ADCIRC grid for simulations for North Carolina (bottom).

ADCIRC river boundaries. One method for distributing the discharge at the upstream boundary is by using the conveyance of a given node, shown in (6.2), where C_i is the conveyance of a node along the boundary, n_i is the Manning's roughness value for the node,

w_i is the active flow width (along the boundary) for the node, and h_i is the water depth at the node.

$$C_i = \frac{1}{n_i} w_i (h_i)^{\frac{5}{3}} \tag{6.2}$$

For a dry node (a node that is associated only with dry elements), the active flow width is obviously zero. For a node associated with one wet face (side of an element) along the boundary, the active width is equal to one half the length of that face. For a node between two wet faces, the active width is equal to one half the sum of the lengths of the two adjacent faces.

The total conveyance is calculated through a summation of the nodal conveyances over the nodes along a given boundary segment, as (6.3) states.

$$C_T = \sum_i C_i \tag{6.3}$$

The nodal discharges are calculated using the total discharge, total conveyance and nodal conveyances using (6.4), which essentially assumes discharge for a section is proportional to conveyance.

$$Q_i = Q_T \left(\frac{C_i}{C_T} \right) \tag{6.4}$$

Finally, the discharge per unit width, herein referred to as the "unit discharge," for each node is calculated by dividing the nodal discharge by the active width of a given node, as (6.5) shows.

$$q_i = \frac{Q_i}{w_i} \tag{6.5}$$

Obviously, this calculation is only performed for nodes with a non-zero active width, in order to avoid division by zero. However, the nodal discharge is zero for dry nodes. The summation of conveyances and distribution of discharges is performed separately, at each time step, for each river in the domain.

The specification of boundary flux using conveyance requires the active width for nodes along the upstream river boundaries to be known throughout the simulation. Thus, the lateral extent of the river at the boundary must be known. The current ADCIRC framework requires specification of the nodal unit discharge before the run starts, with non-periodic flows contained in the fort.20 file or periodic flows specified in the fort.15 file. Conversely, code modifications could allow the boundary specification to be done during the simulation.

In order to test the use of conveyance to distribute discharges at the upstream boundary, modifications were made to the serial version of ADCIRC that allow dynamic distribution of boundary discharges. The active width is calculated, and the previously introduced equations, (6.2) through (6.5), are used each time step during the simulation. Two separate implementations were considered: 1) conveyance calculated using the nodal depth (the difference between the computed water surface elevation for the node and the elevation of the node) and 2) conveyance calculated using nodal depth computed as the difference between an average water surface elevation for wet nodes along the boundary and the elevation of the node. Implementation 1 uses (6.2). The conveyance calculation for implementation 2 is of the same form as (6.2), and it is shown in (6.6), where the nodal water depth, h_i, in (6.2) has been replaced by a representative nodal depth that is the sum of the average water surface elevation along the boundary and the bathymetry value for a

node.

$$C_i = \frac{1}{n_i} w_i (h_{avg} + z_i)^{\frac{5}{3}} \quad \textbf{(6.6)}$$

Simulations were performed to assess the ability of ADCIRC to bring the specified boundary discharge into the domain. The simulations used a constant flow rate of 500 cms as the upstream boundary forcing for both the Tar and Neuse Rivers. The total length of each simulation is 0.5 days, with a ramp applied to the boundary forcing for the first half (0.25 days) of the run. The time step for the simulations is 0.5 seconds. The G value is set to 0.1 s^{-1}, and Manning's roughness values and horizontal eddy viscosity values are spatially variable and consistent with normal values used for simulations of the region.

The elevation and velocity fields were post-processed to calculate flux across sections which are 5, 10, 25 and 40 nodes into the domain along each of the two rivers. These locations are shown in Figure 6.20, with the top panel showing the locations on the Tar River and the bottom panel showing the cross-sections on the Neuse River. The results are shown in Figure 6.21 through Figure 6.24.

The discharge hydrograph results for the Tar River, using conveyances calculated with the computed water surface elevations (implementation 1), can be seen in Figure 6.21. The same set of results, using conveyances based on an average boundary water surface elevation (implementation 2), are shown in Figure 6.22. The equivalent sets of graphics for the Neuse River are found in Figure 6.23 (implementation 1) and Figure 6.24 (implementation 2).

The results for the Tar River show the computed discharge across the sections is too

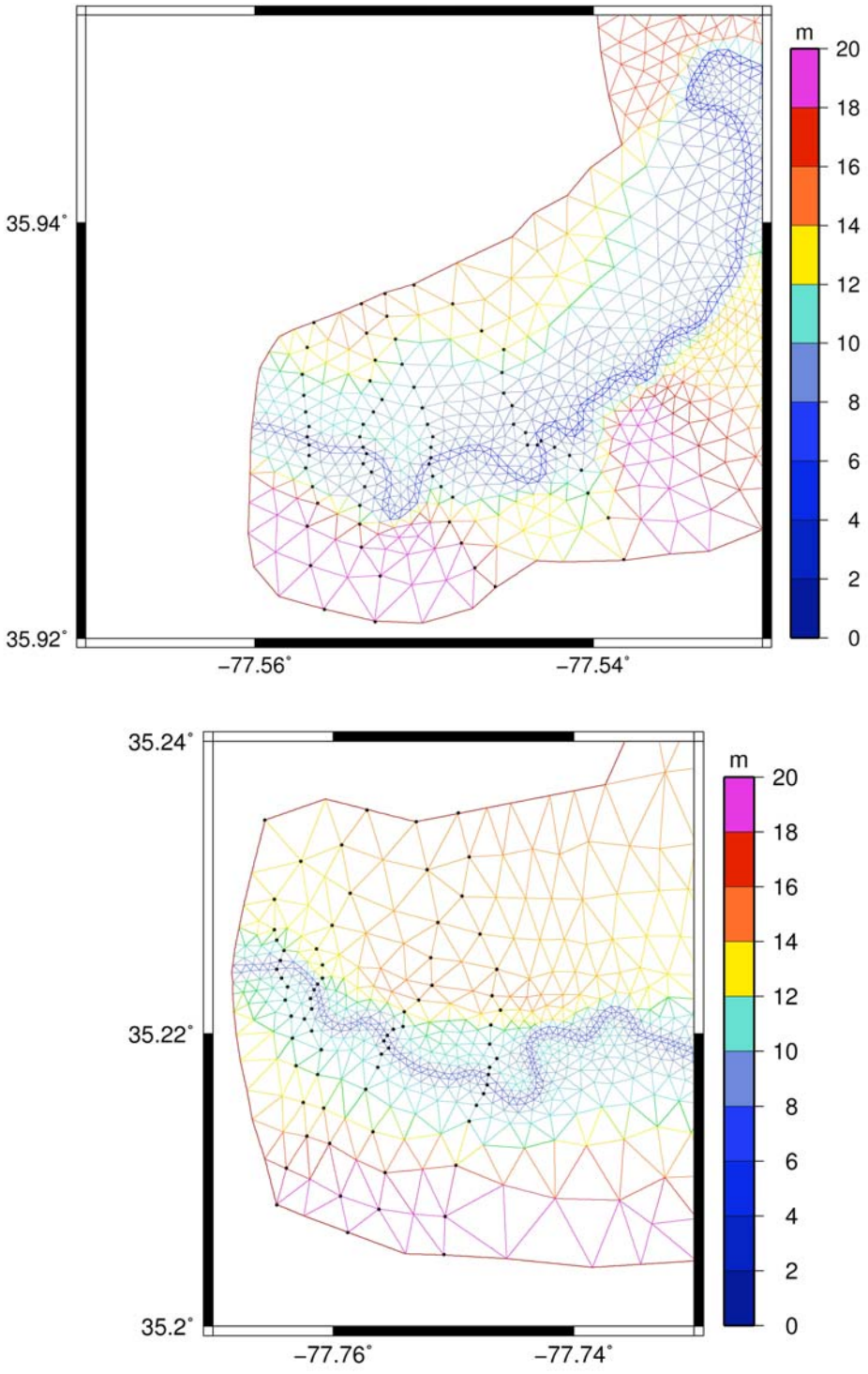

Figure 6.20 Locations of the cross-sections on the Tar River (top panel) and Neuse River (bottom panel) 5, 10, 25 and 40 nodes from the hand-off point on each river. The color of the lines delineating the elements corresponds to the ground elevation value.

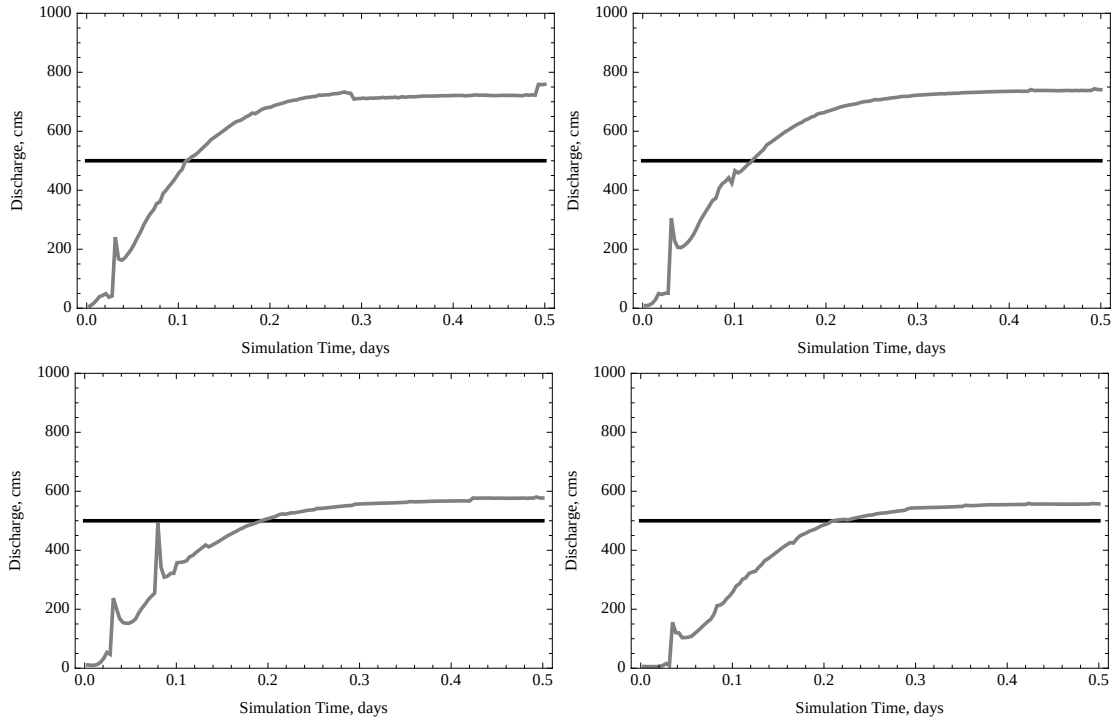

Figure 6.21 Discharge hydrographs for sections which are 5 (top left), 10 (top right), 25 (bottom left) and 40 (bottom right) nodes into the ADCIRC domain along the Tar River using implementation 1. The black line denotes the constant boundary forcing, 500 cms.

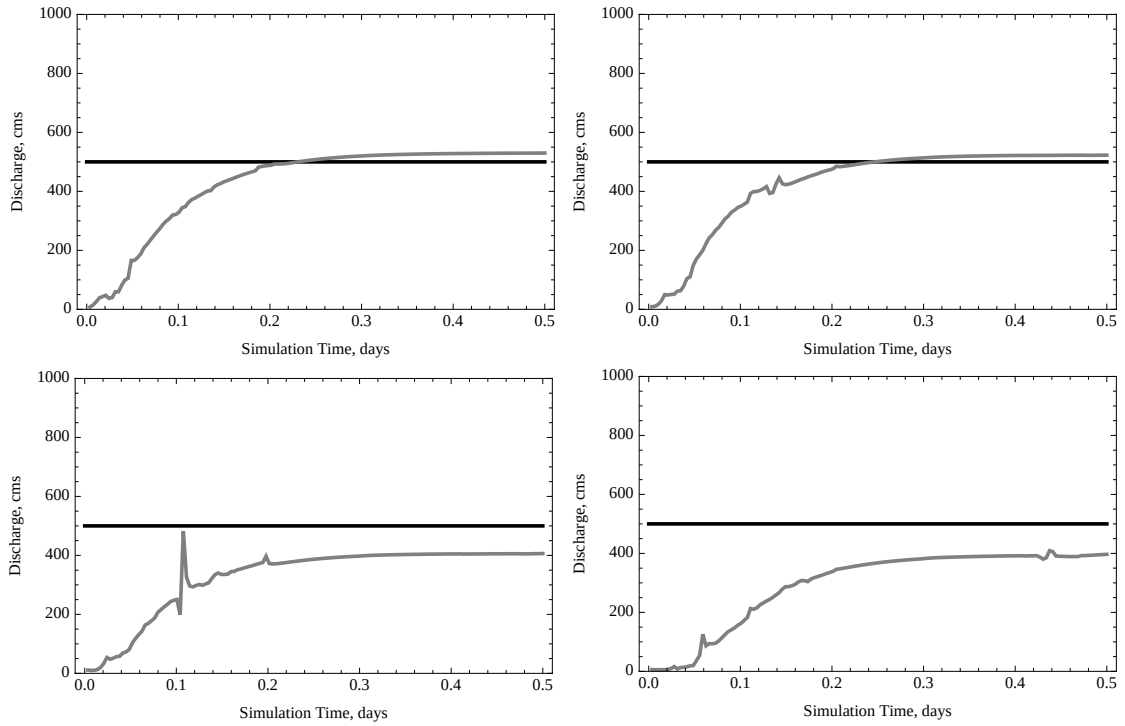

Figure 6.22 Discharge hydrographs for sections which are 5 (top left), 10 (top right), 25 (bottom left) and 40 (bottom right) nodes into the ADCIRC domain along the Tar River using implementation 2. The black line denotes the constant boundary forcing, 500 cms.

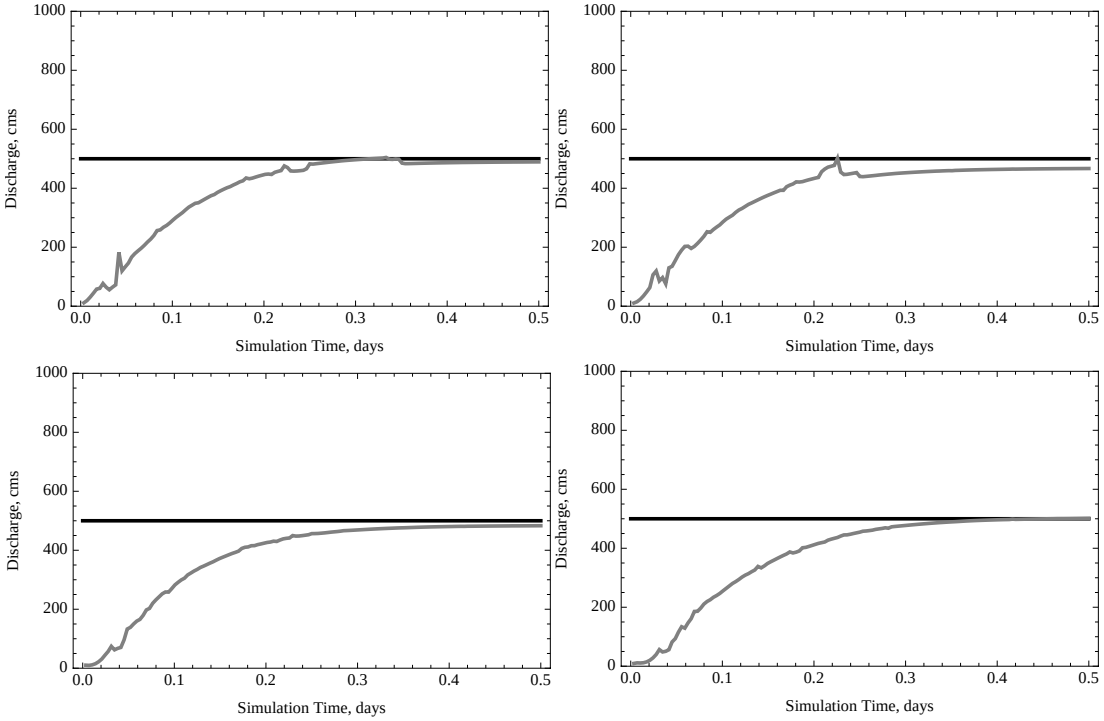

Figure 6.23 Discharge hydrographs for sections which are 5 (top left), 10 (top right), 25 (bottom left) and 40 (bottom right) nodes into the ADCIRC domain along the Neuse River using implementation 1. The black line denotes the constant boundary forcing, 500 cms.

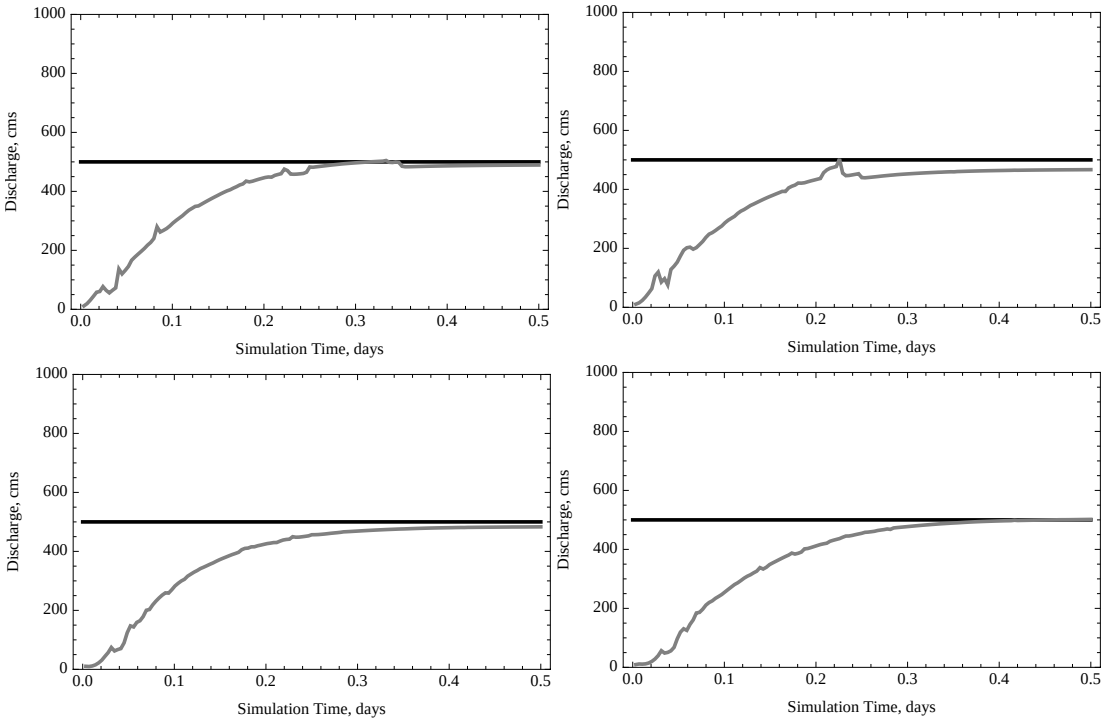

Figure 6.24 Discharge hydrographs for sections which are 5 (top left), 10 (top right), 25 (bottom left) and 40 (bottom right) nodes into the ADCIRC domain along the Neuse River using implementation 2. The black line denotes the constant boundary forcing, 500 cms.

high when the nodal water surface elevations are used to distribute the flow across the boundary. However, when the average water surface elevation at the boundary is used to distribute the boundary flux, the computed discharges near the boundary are a better match to the constant forcing value. For both boundary forcing implementations, the computed discharge is less for sections three and four than for sections one and two. As mentioned briefly in the outline of the simulation set-up, there was a 0.25 day ramp on the discharge boundary forcing, which is why the ADCIRC results underpredict the flow during the initial portions of each time series.

The results for the Neuse River show consistency between results for the two different boundary forcing implementations. At each of the four sections, the discharge nears steady-state at the end of the simulation and approaches the specified constant discharge value. However, there are small differences in the computed discharge from section to section. For both forcing implementations, the discharge is greater for the fourth section than for the other three.

A comparison of the flux across each of the segments in the cross-sections on the Tar River is shown in Figure 6.25. The equivalent set of plots for the Neuse River are presented in Figure 6.26. The results are consistent with the discharge hydrographs for the different sections. The two implementations produce different results on the Tar River, but they produce very consistent results for the Neuse River. The use of nodal elevations (implementation 1) to distribute conveyances results in higher flow rates. The elevated flow rates are fairly consistent from segment to segment. In other words, the discharge across each of the segments on the Tar River is higher with implementation 1 than with implementation 2, except for one segment location 40 nodes into the domain.

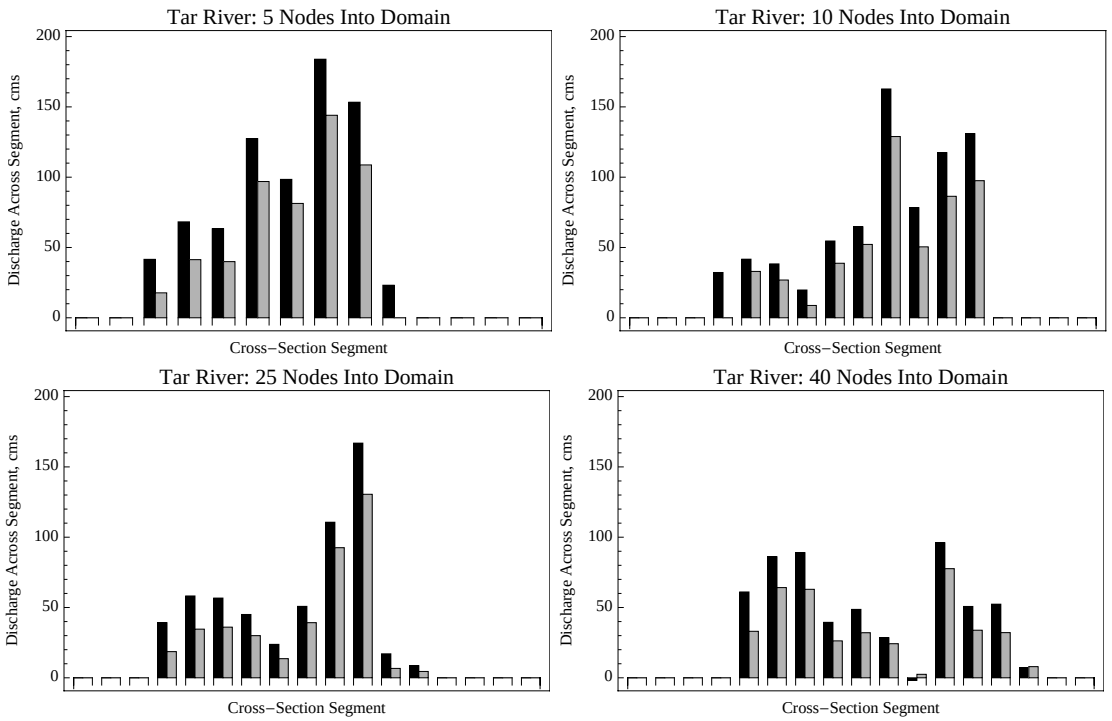

Figure 6.25 A comparison of flux across each of the segments in the cross-sections for the Tar River with boundary forcing implementations 1 (black) and 2 (gray) from above. The results are from the end of the 0.5 day simulations.

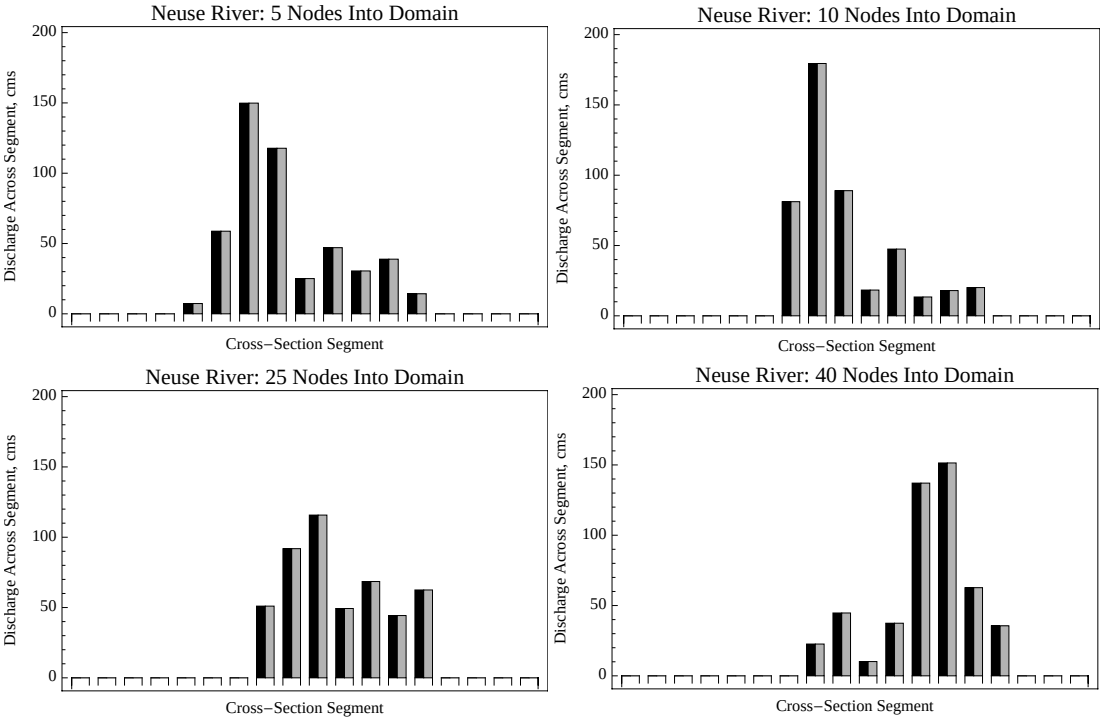

Figure 6.26 A comparison of flux across each of the segments in the cross-sections for the Neuse River with boundary forcing implementations 1 (black) and 2 (gray) from above. The results are from the end of the 0.5 day simulations.

The first implementation should be less stable because there is a positive feedback between water surface elevation and discharge when conveyance is used to calculate boundary forcing. An increase in water surface elevation at a specific node, compared to the rest of the nodes on the boundary, results in an increase in the conveyance associated with that node. Therefore, using implementation 1, the discharge assigned to that node will increase. Subsequently, the higher discharge will tend to further increase the water surface elevation at that node. However, the second implementation uses an average water surface elevation across the entire boundary at a given time step to calculate the nodal depths and conveyances, so local maxima and minima in the water surface along the boundary do not cause unrealistic boundary forcing values and distributions to occur. Thus, it is recommended that implementation 2 be used, rather than implementation 1.

6.3.3 Boundary Flux Applied to Main River Nodes Only

An alternate method to the use of conveyance to assign the discharge at the boundary is the specification of all the discharge to only the two main river nodes. The two main river nodes at the boundary on the Neuse River are shown in Figure 6.27. As the figure shows, the main channel of the Neuse River is lower in elevation (corresponding to a higher bathymetry value) than the adjacent floodplains. Thus, for low flows, only the elements making up the main channel of the river will be wet, and the active width for each of the circled nodes will be one half the distance between those nodes. However, once the river stage reaches a level that causes the elements adjacent to the river to be wet, the active width for each of the nodes circled in Figure 6.27 will increase, as depicted in Figure 6.28. The increase in active width is problematic because the quantity used in the ADCIRC calculations is the unit discharge, which is the nodal discharge divided by the active width.

Thus, if the elements adjacent to the main channel are wet, as well as the main channel elements, the unit discharge needs to be reduced to maintain the correct total discharge specified at the model boundary.

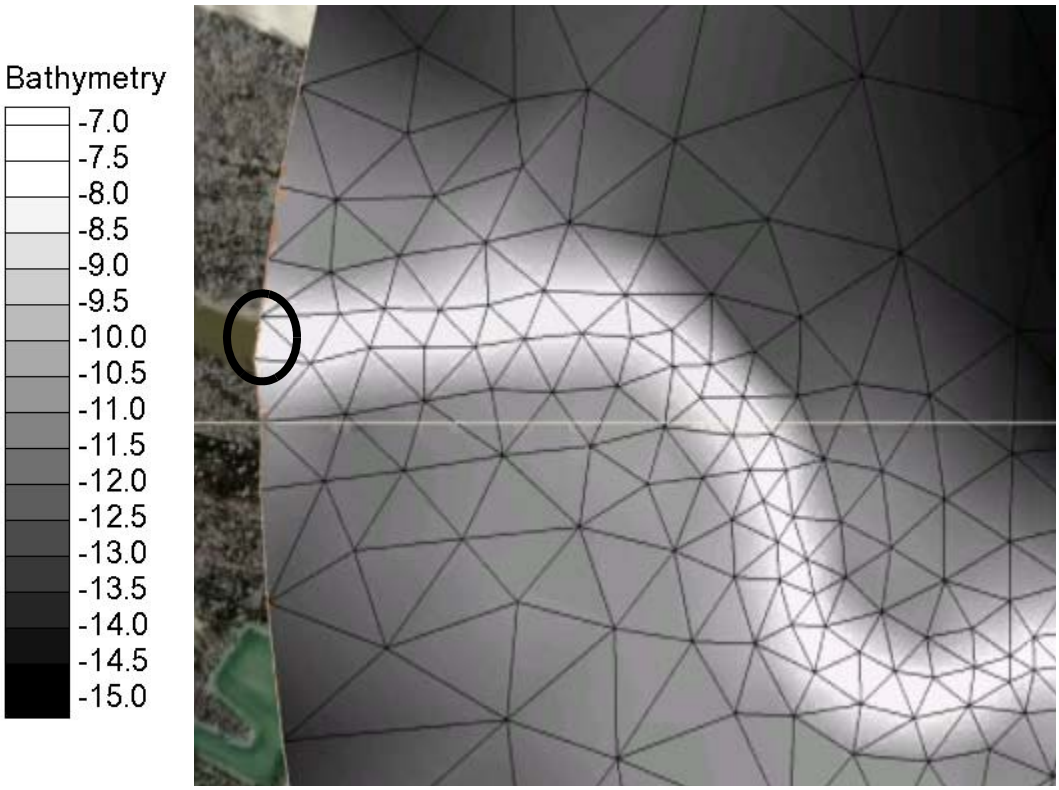

Figure 6.27 Discretization and bathymetry of the ADCIRC grid at the upstream boundary of the Neuse River. The two river nodes at the boundary are circled.

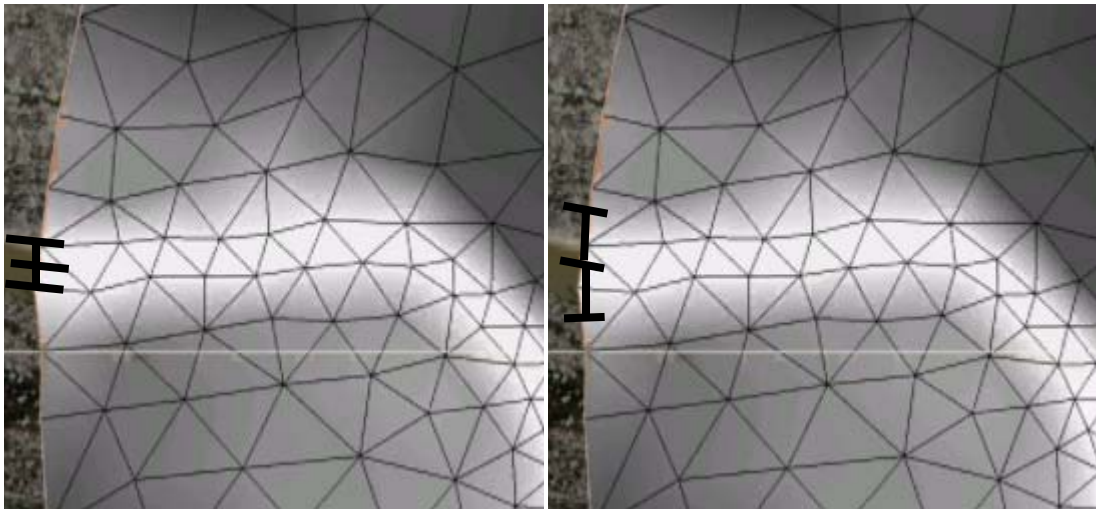

Figure 6.28 Active width for main river boundary nodes for in-channel flow (left) and out-of-bank flow (right).

It seems reasonable to use a stage-discharge relationship for the model channel to generate the pre-run nodal unit discharge specification. The stage-discharge relationship could be easily derived from a series of constant discharge river simulations or a simulation with a wide variation in discharge forcing, although a series of constant discharge simulations would not provide a looped rating curve. The water surface elevation for a given river discharge would give a fairly accurate estimate of the extent of the river at a given time during the simulation. The conveyance, based on the water surface elevation and river extent, could then be used to distribute the river flux across the boundary.

Unfortunately, this procedure could result in major mass balance errors due to the way rivers are represented in ADCIRC. For example, the water surface elevation in the model might be slightly lower than predicted just before the river reaches bank-full conditions. While the simulation has only the main river elements wet, the stage-discharge relationship predicts the first floodplain elements, adjacent to the river on each side, to be wet as well. Therefore, the predicted active width for the two main river nodes, for the purposes of computing the unit discharge, will be approximately twice as large as the actual active width. Thus, the specified unit discharge, based on the predicted water surface elevation and extent, will be approximately half as large as it should be according to the model results. This small error in predicted water surface elevation will result in only half of the necessary boundary flux entering the domain. This error will cause an immediate reduction in the discharge entering the ADCIRC domain. As a result, the water surface elevation will drop and the river may never reach bank-full depth at the boundary because the active width will remain lower than predicted. As the total discharge increases, the amount of discharge applied to floodplain nodes will rise. However, if the floodplain elements are not wet, the

discharge applied to the floodplains will be neglected.

The opposite situation is possible as well. If the active width in the model is greater than expected from the stage-discharge relationship, the mass entering the domain will be too high. For instance, if the river and the first floodplain elements on each side are wet, but the rating curve predicts that only the river will be wet, the amount of flow entering the domain will be too large because the active width is incorrect.

Given these problems, it is desired to use an implementation for discharge at the boundary that uses a fixed width to avoid mass balance problems resulting from the a priori unit discharge assignment. The active width for the two main channel nodes along the boundary can easily be made constant with a minor modification to the ADCIRC grid. This modification process consists of two steps, of which the order is not important. One step is lowering one node along the boundary on each side of the main channel to an elevation that is similar to the elevation of the main channel nodes. The result of this change can be seen in the left panel of Figure 6.29, where the lowered nodes (circled) are now lighter in color, as compared to Figure 6.28. The other step is to make sure the orientation of the elements is such that the elements adjacent to the river elements containing faces along the upstream boundary create a funnel from the boundary into the main channel. The original discretization has this orientation for the element directly south of the main channel. However, the element configuration on the north floodplain must be modified. The result of this modification can be seen in the right panel of Figure 6.29. The adjustment is an application of the "Swap Edges" tool in SMS to the face marked with an "X" in the left panel.

Following this modification, a line of four elements (numbered from north to south) should always be wet. In this way, the active width of the two main channel nodes will be

constant throughout the simulation and the unit discharges can be calculated a priori. This new boundary forcing implementation, with discharge limited to the main river nodes, is tested in the next section. This set-up does not preclude additional elements along the upstream boundary from becoming wet. However, such inundation will not affect the active width of the main channel nodes.

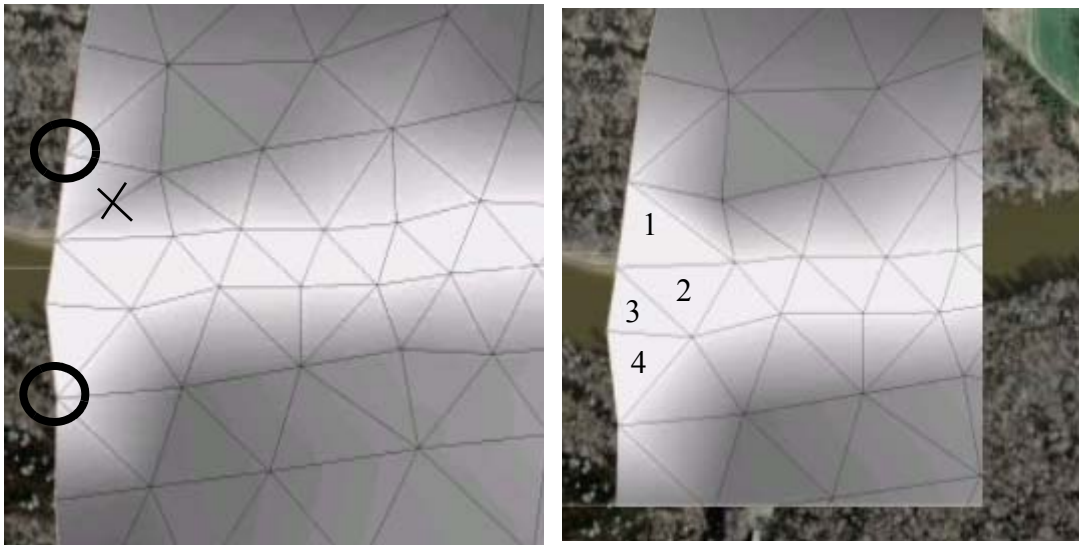

Figure 6.29 Modifications to grid boundary necessary to fix the active width of the main river nodes for discharge specification. The left panel highlights the modification to the elevation for the first node on the floodplain (on each side of the river) along the boundary, as well as the element edge that must be reoriented. The right panel shows the line of four elements along the boundary that will be wet, at baseflow, throughout the simulation.

6.3.4 River Application (Hurricane Floyd)

In order to test the boundary specification, simulations were performed using hydrographs from Hurricane Floyd (1999). USGS discharge values for the Tar River at Tarboro, NC and the Neuse River near Fort Barnwell, NC were used as the upstream forcing on each river, respectively. Simulations were performed using a ramp for the first day of simulation time. Discharge near the boundary is compared to the specified discharge to assess the boundary condition implementation. Theoretically, water surface elevation and discharge hydrographs could be compared to USGS values at select stations to evaluate

the river system. However, the analysis at gauge stations is limited by the nature of the boundary specification. Specifically, because the discharge from USGS data at Tarboro and Fort Barnwell is applied at the ADCIRC grid boundary (Fort Barnwell is about 68 km, along the river, away from the hand-off point on the Neuse River), there is an inherent time lag introduced. Additionally, the flood wave will have an opportunity to be attenuated during the stretch from the boundary to the gauge station. As mentioned previously, ADCIRC does not account for precipitation or lateral inflows over the region discretized in the ADCIRC grid, which also introduces error in comparisons to data from USGS gauge locations.

Simulations using discharge results from Hurricane Floyd were performed using three different boundary forcing implementations: 1) computed water surface elevations used in conveyance calculations, 2) average water surface elevation used in conveyance calculations and 3) discharge applied to two river nodes only. The first two are the same implementations used previously in Section 6.3.2. Implementation 3 has the additional benefit that the current parallel ADCIRC framework can be used without any modifications, because the discharge values are split only between the two river nodes and can be done so a priori. The active width is fixed, so the unit discharge values are just the nodal discharges divided by the active width. The G value for the simulations was a constant value of 0.1 s^{-1}.

The discharge hydrograph results from implementation 1 can be seen in Figure 6.30. The results are consistent with the findings for the constant discharge simulation presented previously (Figure 6.21 and Figure 6.23). Specifically, the Tar River discharge calculated from the ADCIRC results is greater than the amount of flow that is

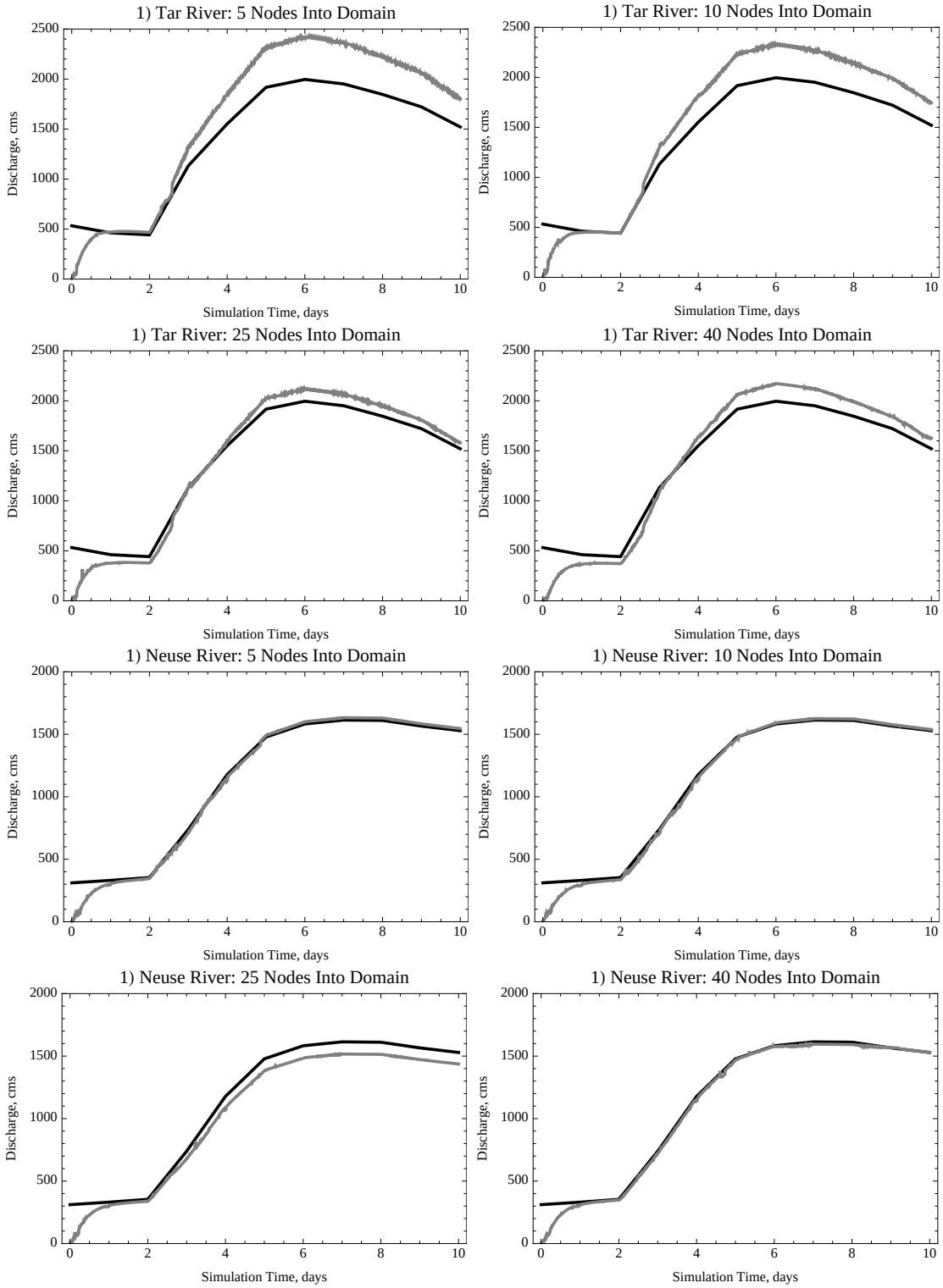

Figure 6.30 Comparison of ADCIRC (gray) to forcing (black) hydrographs for Hurricane Floyd simulations using boundary implementation 1, for both the Tar and Neuse Rivers. Results for the first day of the ADCIRC results include a ramp function to smooth the transition from a cold start.

supposed to be entering the domain. The peak ADCIRC discharge is approximately 20% higher across the first section (5 nodes along the river in from the boundary) than the actual peak forcing used for the boundary condition calculation. However, the ADCIRC results are close to the boundary forcing hydrograph on the Neuse River. Additionally, there are high-frequency oscillations in the discharge results on the Tar River. The oscillations are due to instability related to the use of nodal elevations to compute the nodal discharges to input as the boundary condition.

The results for the Tar River for implementations 2 and 3 are shown in Figure 6.31. The results using implementation 2 are shown in the left panels, while the results using implementation 3 are shown in the right panels. The results are not identical. For instance, the peak discharge at the first section, 5 nodes into the domain, using implementation 3 is 2,090 cms, while the peak discharge using 2 is 2,064 cms; the peak discharge used to generate the forcing is 1,996 cms. However, the results are more consistent for the locations farther downstream.

The results for implementations 2 and 3 on the Neuse River are shown in Figure 6.32. Again, results using implementation 2 are shown in the left panels and the results at the same locations, using implementation 3, are shown in the right panels. The discharge hydrographs for the different boundary implementations are consistent. Additionally, there is not much error compared to the boundary forcing. The computed discharges for the third section on the Neuse are slightly low, regardless of implementation.

The distribution of flow in the cross-section depends on the boundary implementation. The discharge across each segment in each of the four cross-sections, three days into the Hurricane Floyd simulation, is shown in Figure 6.33. Focusing on the comparison

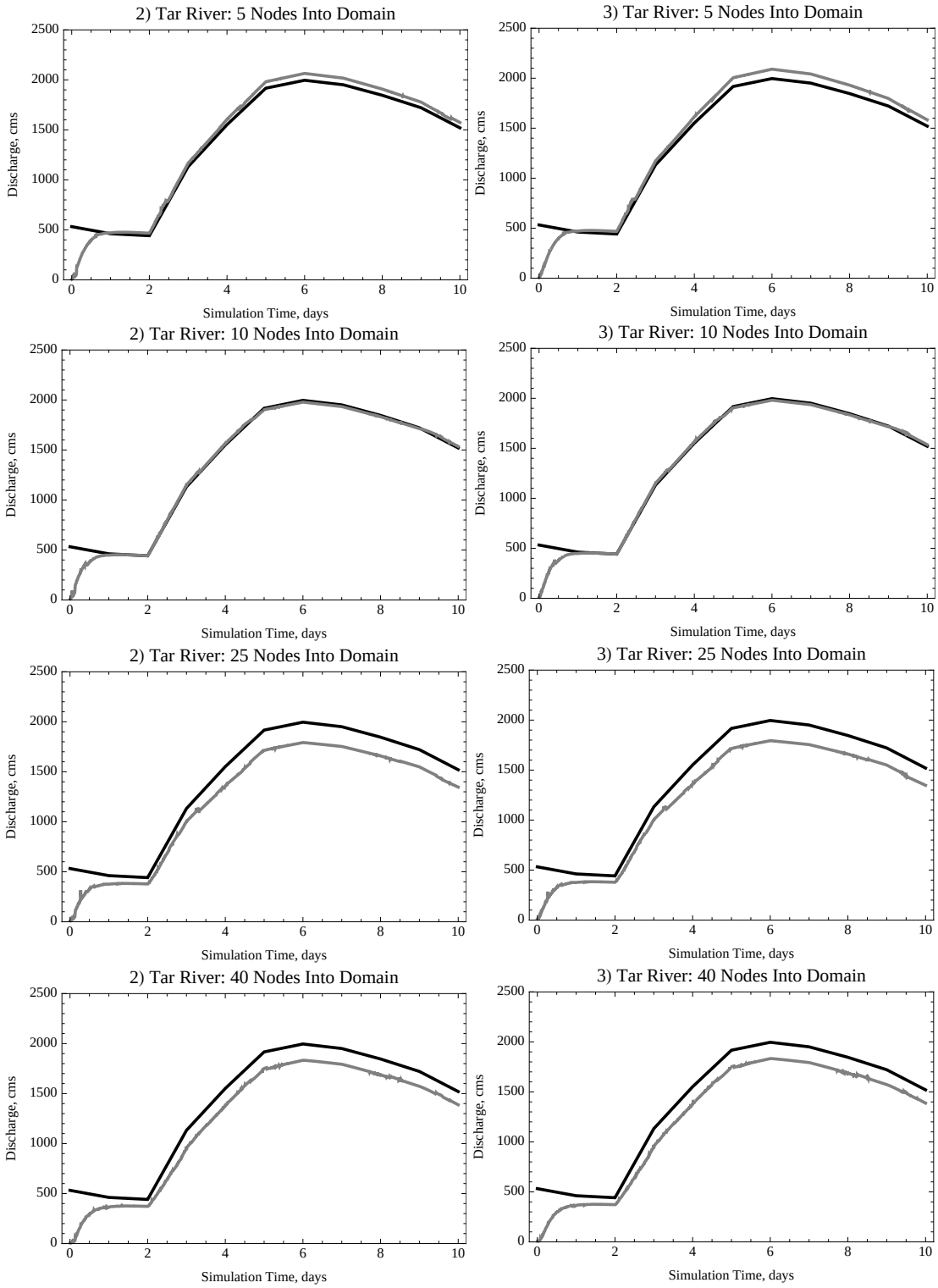

Figure 6.31 Comparison of ADCIRC (gray) to forcing (black) hydrographs on the Tar River for Hurricane Floyd simulations using boundary implementations 2 (left panels) and 3 (right panels). Results for the first day of the ADCIRC results include a ramp function to smooth the transition from a cold start.

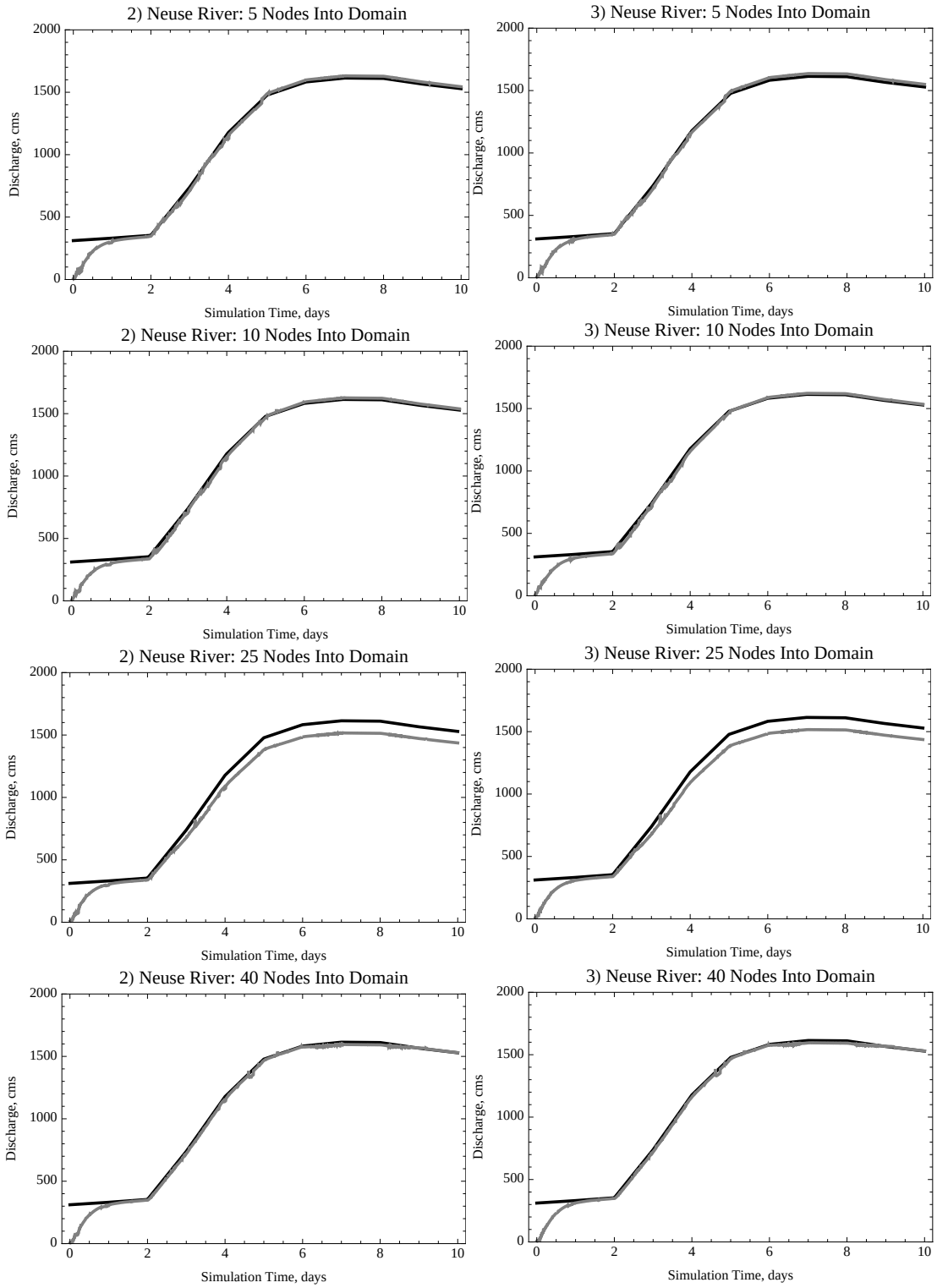

Figure 6.32 Comparison of ADCIRC (gray) to forcing (black) hydrographs on the Neuse River for Hurricane Floyd simulations using boundary implementations 2 (left panels) and 3 (right panels). Results for the first day of the ADCIRC results include a ramp function to smooth the transition from a cold start.

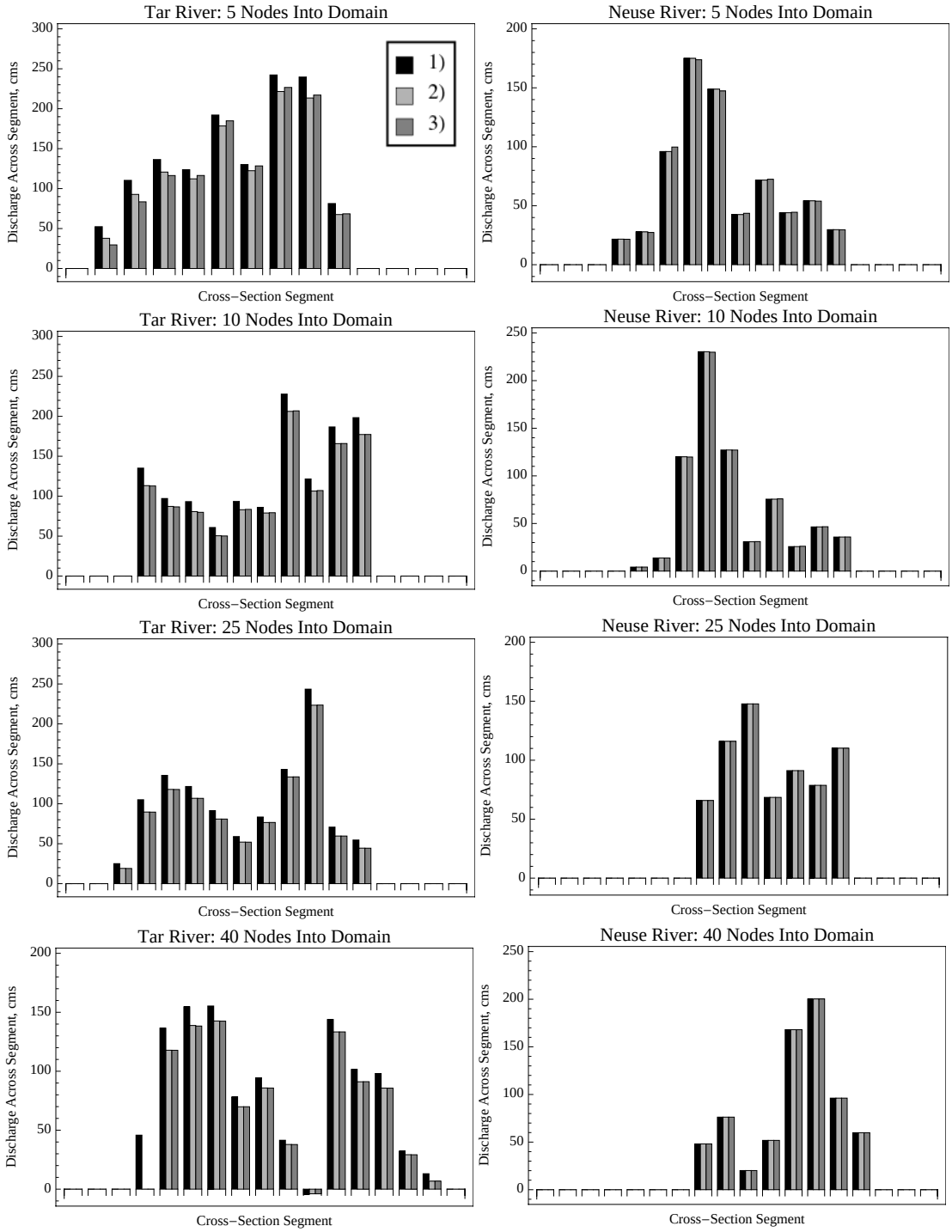

Figure 6.33 Comparison of distribution of discharge, for different boundary forcing implementations, in the sections three days into the Hurricane Floyd simulations. The results for implementation 1 are shown in black, whereas the results for implementations 2 and 3 are shown in light and dark gray respectively. Results for the Tar River are on the left, while the graphs in the right panels show information for the Neuse River.

between implementations 2 and 3, there is a different distribution for the first section on each of the rivers. For the Tar River, the discharge in the second and third segments is lower for implementation 3 than for implementation 2. This result is consistent with analysis of sections near the boundary. Specifying flux only on the main river nodes results in higher flows through the main channel of the river (and lower flows near the extents of the inundation) than when the boundary flux is specified based on conveyance. However, the flux quickly spreads out from the main channel and influences the entire wet extent of the river and floodplain. Just ten nodes into the river, the differences in distribution of discharge is almost indistinguishable for implementations 2 and 3.

The equivalent set of distributions, for results five days into the simulation, is shown in Figure 6.34. Five days into the simulation corresponds to the transition between the rising limb and the peak of the forcing hydrograph. The peak forcings for the Tar and Neuse Rivers are six and seven days into the simulation, respectively. The discharge five days into the simulation is 96.0% of the maximum on the Tar River, while on the Neuse River the forcing at that time is 91.6% of the maximum.

The impact of pushing the entire boundary forcing into the domain through the main channel can easily be seen. Again, analysis will focus on implementations 2 and 3. At the section five nodes into the domain along the Tar River, the maximum flows are found through sections eight and nine, regardless of forcing implementation. The discharges through segments eight and nine are 9.9% and 8.7% larger, respectively, when the entire discharge is input at the main river nodes (implementation 3). However, the discharges through segments one through four are lower when implementation 3 is used, with a decrease in discharge through segments one and two of more than 30%, compared to results

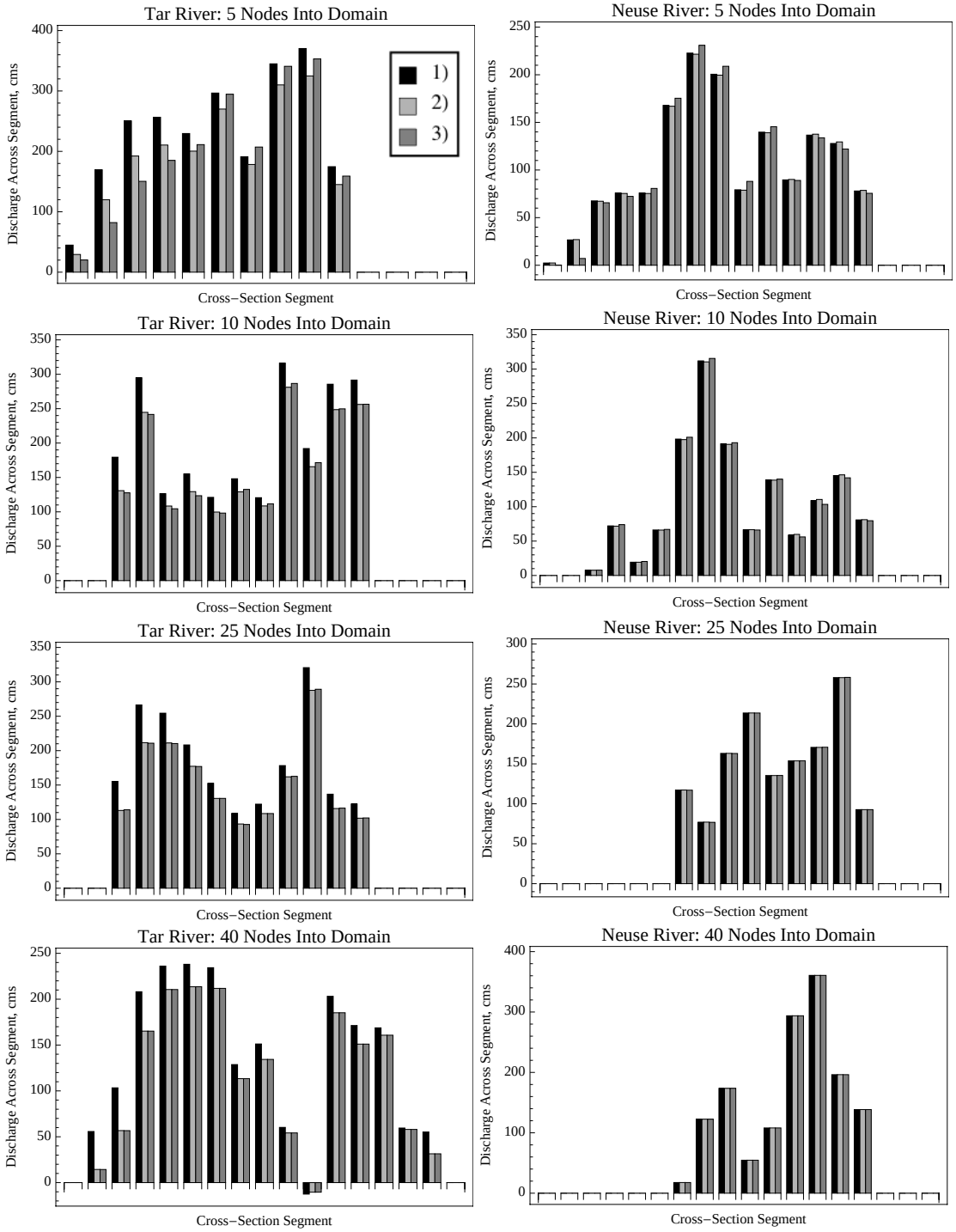

Figure 6.34 Comparison of distribution of discharge, for different boundary forcing implementations, in the sections five days into the Hurricane Floyd simulations. The results for implementation 1 are shown in black, whereas the results for implementations 2 and 3 are shown in light and dark gray respectively. Results for the Tar River are on the left, while the graphs in the right panels show information for the Neuse River.

from implementation 2. These results are not surprising. Near the hand-off point, implementation 3 artificially increases the amount of flow through the main channel while sacrificing flow near the lateral extent of the river.

The results on the Neuse River are consistent with the results on the Tar River. For the section five nodes into the domain, the discharge through the segments near the main channel (five through ten) are higher with implementation 3 than with 2. Towards the lateral boundaries on each side, less discharge is found when 3 is utilized instead of 2.

Contrary to results three days into the simulation, five days into the simulation there is a noticeable difference in the discharge distribution for the section ten nodes into the domain on each river. For the section ten nodes into the domain on the Tar River, the discharge is higher with 3 than with 2 for segments eight through thirteen. This portion of the section corresponds to the area with the higher flow rates. The maximum percentage difference is across segment eleven, where the discharge is 3.5% higher with 3 than with 2. At the section twenty-five nodes into the domain, the discharges between 2 and 3 are within 1% for all segments in the cross-section. The same trends hold true on the Neuse River. For the section ten nodes into the domain, there are overestimates as high as 5.7% and underestimates of 6.5% comparing discharges across segments with 3 to results from 2. The overestimates are near the main channel areas with the highest flow rates. The differences decrease as one moves farther away from the boundary. At the section twenty-five nodes in along the Neuse River, the discharges across segments are all within 0.5% of each other comparing results from 2 and 3.

The results show specifying the entire discharge to the main river nodes does not have a deleterious impact on results. The amount of water entering the domain is consistent

with more physically realistic implementations. Furthermore, while there is an impact in the immediate vicinity of the boundary, the error is relatively small, even for the highest recorded flow rates on the Tar and Neuse Rivers, and even that spreads out 25 nodes into the domain, which is about 1.5-2% of the total river length being simulated. Therefore, it seems that constraining the non-zero boundary unit discharge forcings to the main river nodes is a reasonable practice.

This study does not assess flows in excess of approximately 2,000 cms. However, it does not seem logical to assess the ability of an implementation to handle a non-physical condition that is not necessary, such as forcing the Tar River with a flow rate of 20,000 cms (consistent with the average flow on the Mississippi River).

Rivers that handle larger flows generally have larger main channel widths than the Tar and Neuse Rivers. As such, the main channel would probably be delineated with more nodes in a river cross-section than just the two that define the width of the main channel. This added resolution would reintroduce mass balance issues related to the active width. Certainly, a similar boundary implementation could be used that limits the forcing to two (or a different fixed number) of nodes. However, a better method might be to use a rating curve to distribute the flow with a bias towards the nodes that are wet at low flows, as described below.

Specifically, implementation 3 has four nodes wet at the boundary on the Tar and Neuse Rivers. However, the non-zero unit discharges are limited to the two middle (main channel) nodes. A rating curve could be used to estimate the expected water surface elevation for a given discharge. The expected lateral extent can be obtained from the expected water surface elevation. To be conservative, a threshold (such as 0.5 m) could be used so

the depth at a node, based on the expected water surface elevation, has to be at a certain level before the node will be assumed to be wet. Then, based on the conservative wet extent, the discharge could be specified to all the interior wet nodes (the last wet node on each side of the floodplain will still be given zero unit discharge). Thus, the lateral extent of forcing is variable, but the mass balance issues related to boundary forcing can be mitigated.

6.4 Tributary Additions

Both the Tar and Neuse Rivers have confluences with substantial tributaries within the ADCIRC domain. Fishing Creek empties into the Tar River just upstream of Tarboro, NC, and flow from Contentnea Creek joins the Neuse River upstream of Fort Barnwell, NC. The locations of the confluences are shown in Figure 6.35. Neither Fishing nor Contentnea Creek is adequately resolved in the original ADCIRC grid. However, the discharges experienced by the tributaries are considerable portions of the downstream flows on the Tar and Neuse Rivers, respectively. There are additional, smaller tributaries on both the Tar and Neuse Rivers within the ADCIRC domain. However, the vast majority of flow on the Tar and Neuse Rivers is accounted for by incorporating Fishing and Contentnea Creeks.

The magnitude of flows in Fishing and Contentnea Creeks, compared to the Tar and Neuse Rivers, is shown in Table 6.3. The data presented is the maximum flow at the ADCIRC grid boundary (hand-off location) for each river boundary location from an hourly time series output generated by HL-RDHM. The HL-RDHM results are consistent with the USGS gauge data to which the model has been compared [*Van Cooten* 2011]. For

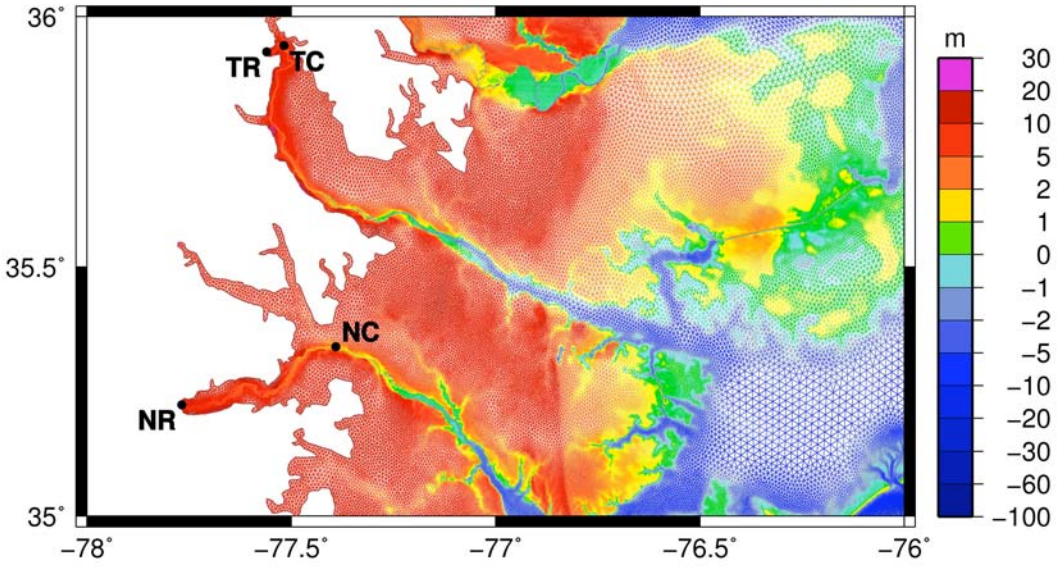

Figure 6.35 Modified ADCIRC grid with the upper extent of the Tar and Neuse Rivers removed. The hand-off points on the Tar River (TR) and Neuse River (NR) are marked on the plot. Additionally, the location of the confluence of the Tar River and Fishing Creek is marked (TC) and the confluence of the Neuse River and Contentnea Creek is shown (NC).

Hurricane Floyd, Hurricane Isabel and Tropical Storm Alberto, the peak flow at the Fishing Creek hand-off is always more than half the peak flow at the Tar River hand-off point. For Hurricane Isabel, the peak flow at the Fishing Creek hand-off point actually exceeds the maximum discharge for the hand-off point on the Tar River, and the peak magnitude at the Fishing Creek boundary during Hurricane Floyd is more than 80% of the peak forcing on the Tar River. Similar trends apply to the Neuse River - Contentnea Creek system. The peak flow at the hand-off point for Contentnea Creek during Hurricanes Floyd and Isabel is about two-thirds of the largest flows at the hand-off point on the Neuse River.

A number of alternatives were considered to handle flows from Fishing and Contentnea Creeks given the ADCIRC framework. If contributions from the tributaries are neglected, the result would be discharges that are substantially lower than they should be downstream of the confluences with those tributaries. The first alternative was to add the

Table 6.3 Peak flow rates (cms) at ADCIRC boundary locations from HL-RDHM simulations producing hourly discharge values.

Event	Tar River Upstream	Fishing Creek	Neuse River Upstream	Contentnea Creek
Hurricane Floyd	1106	915	1195	777
Hurricane Isabel	138	223	301	192
T.S. Alberto	363	214	308	107

flow from Fishing Creek to the flow for the Tar River and apply the combined flow at the ADCIRC boundary on the Tar River. Similarly, the Neuse River and Contentnea Creek flows would be added together and applied at the Neuse River hand-off point.

While this would have been a simple modification in procedure, two main problems exist, both of which are more prevalent on the Neuse River system. First, the distance from the ADCIRC boundary to the confluence is different for the different reaches. The distance along the Neuse River from the boundary to the confluence is much greater than the distance along Contentnea Creek from the boundary. Thus, an inherent time lag will be introduced into the system for the Contentnea Creek flow if it enters at the Neuse River hand-off point. Additionally, the discharge upstream of the confluence would be artificially inflated by the tributary discharge being applied upstream of the actual tributary location. This increased flow rate would have implications on the flow speed, further complicating the discharge timing. Furthermore, the increased discharge rates upstream of the confluence would render flood forecasts in those areas useless, or at least less useful. Therefore, the decision was made to modify the ADCIRC grid to delineate Fishing and Contentnea Creeks.

Two alternatives related to grid modifications were considered. Cross-section data from the NCFMP could have been used to generate nodes for the river and floodplain. However, due to time constraints (as well as the geometric concerns related to discretization), a more simple procedure was used for each tributary:

- Each edge of the tributary was traced using the "Path" tool in Google Earth, with points selected becoming nodes for the tributary addition in the ADCIRC grid; an example of this is shown in Figure 6.36.
- Two paths along each side of the river on each floodplain were selected using the "Path" tool in Google Earth.
- Channel elevations were assigned assuming a constant change in elevation from one node to the next, with the elevation assigned to the node at the confluence based on the ADCIRC grid value in the main river at the confluence location; this creates an approximately linearly sloping tributary.
- Floodplain elevations were assigned in the same manner, with constant change from one node to the next along a line:
    - First floodplain line on each side is 2 m higher than the channel.
    - Second floodplain line on each side is 3 m higher than the channel.
- The XYZ data points were imported into the ADCIRC grid in SMS.
- Nodes in the current ADCIRC grid in regions defined by the new tributary nodes were removed.
- New nodes were triangulated to create elements.
- Selective addition, subtraction and movement of nodes was used to improve the mesh, with nodal elevations of added nodes being generated automatically by SMS based on the elevations of surrounding nodes.

The implementation is consistent with the treatment of the Tar and Neuse Rivers in that the main channels are defined by a line of nodes on each side. Modifications can be made to the elevations of the ADCIRC nodes in the future, as necessary, to have accurate inundation prediction for the tributaries upstream of the confluences. Also, this treatment is not unlike the approach often used in distributed hydrologic models, where the river channel is assumed to have a particular geometric shape (e.g., parabolic).

Figure 6.36 shows the delineation of Fishing Creek for the tributary addition to the original ADCIRC grid. Just to the right of where the white lines connect to the Tar River, it looks like Fishing Creek actually wraps around to the east of the horseshoe bend in the Tar River, so the actual confluence is on the southeast corner of the horseshoe bend. The decision to not follow that path for Fishing Creek was twofold. First, the aerial image shows water throughout a fair amount of that region and it is hard to tell whether or not there is a connection, although it appears that there is a line of trees between Fishing Creek and the Tar River in that location. Regardless, however, it is likely that at high flows, the two channels are connected at the chosen location. Second, and more importantly, the target grid resolution did not allow elements to be added without modifying the path of either the Tar River or Fishing Creek, unless the dividing area was defined as a levee system. While ADCIRC possesses this capability, a levee elevation would have to be defined. Currently, no levee systems exist in this grid and addition for this feature seemed unnecessary for the current application.

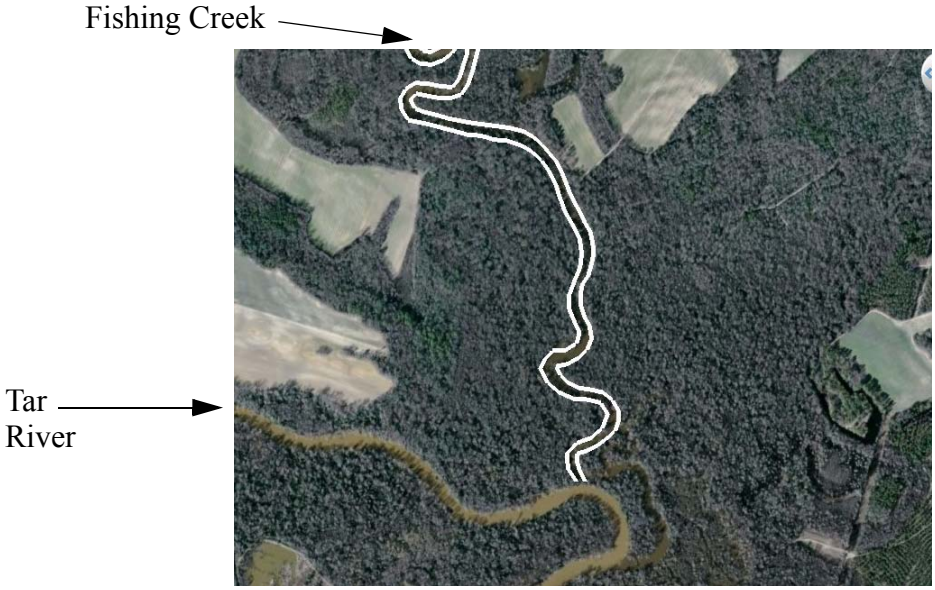

Figure 6.36 Definition of the edges of Fishing Creek just upstream of the confluence with the Tar River using paths in Google Earth.

The original (where Fishing Creek is not considered) and new discretizations of area around Fishing Creek are shown in Figure 6.37. Fishing Creek was not specifically delineated in the v20 ADCIRC grid, although the elevations suggest that there is a waterway in that area. The impact of the modifications can clearly be seen in the image on the right. The elevations are lower in the main channel than in the surrounding areas. The channel elevations and widths are consistent with values for the Tar River in that area.

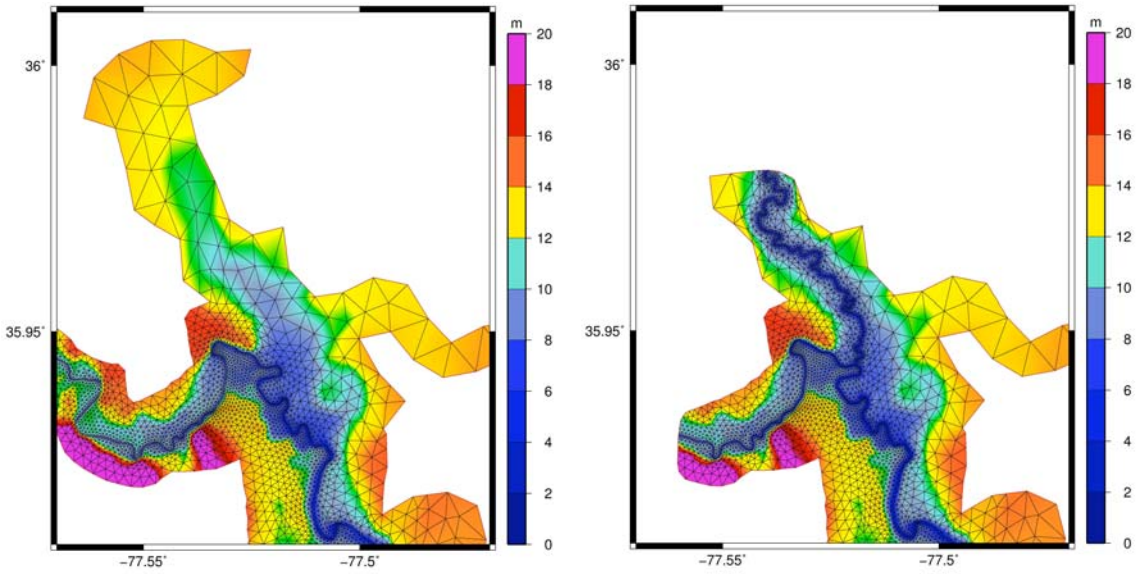

Figure 6.37 Fishing Creek discretization in v20 (left) and in the modified grid (right) for the tropical event hindcasts.

Figure 6.38 shows the modifications to the ADCIRC grid to delineate Contentnea Creek. The upland areas of Contentnea Creek were removed so the hand-off location (location of ADCIRC boundary) on Contentnea Creek was placed just downstream of the confluence on Contentnea Creek, which occurs upstream of Grifton, NC. This allowed one hand-off point to be used for Contentnea Creek. If the ADCIRC grid extended farther up Contentnea Creek, hand-off points would be needed on the main stem of Contentnea Creek (shown on the west side of the left panel of Figure 6.38) and the tributary to Contentnea Creek (shown on the north side of the left panel of Figure 6.38).

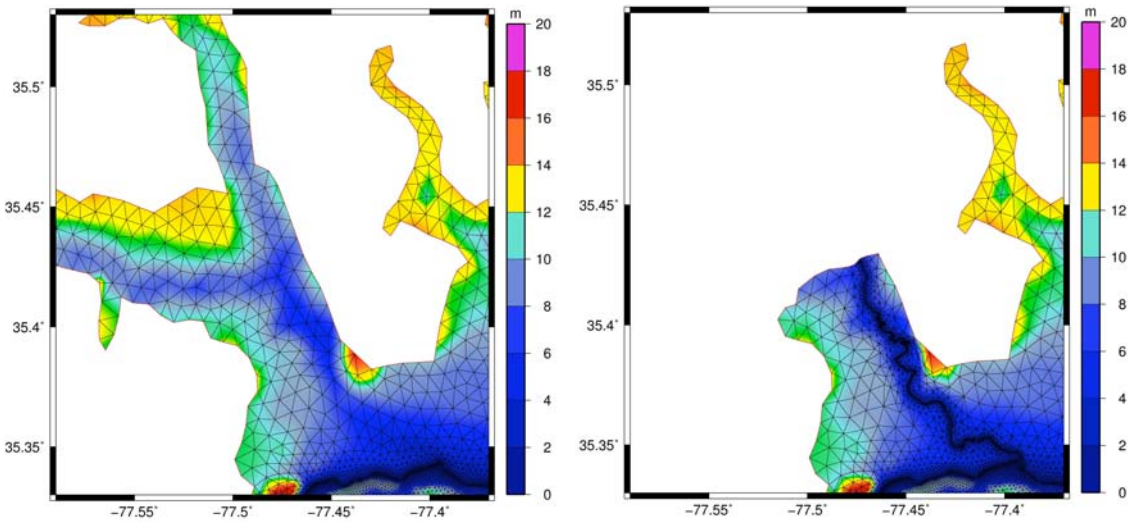

Figure 6.38 Contentnea Creek discretization in v20 (left) and in the modified grid (right) for the tropical event hindcasts.

6.5 Full-domain Hindcasts

Hindcasts of Hurricane Floyd (1999), Hurricane Isabel (2003) and Tropical Storm Alberto (2006) were performed using the full ADCIRC grid with the tributary additions to allow for discharge specification on Fishing and Contentnea Creeks, as well as on the Tar and Neuse Rivers. The discharge hydrographs are hourly time series from HL-RDHM for each of the four hand-off locations at the ADCIRC boundary.

The simulations were all performed using a 20-day ramp on the tides, a 0.25-day ramp on the river forcings and 0.0 for the flux settling time, which is the amount of time the rivers are allowed to ramp up before tidal forcing is initially applied. The time step for the simulations was 0.5 seconds and the G parameter was set to -3, which is a variable G setting. The spatially variable parameters specified in the nodal attributes (fort.13) file for all simulations were Manning's roughness, horizontal eddy viscosity and G.

The main difference between the simulations is that tides, winds and waves

(through use of the coupled ADCIRC+SWAN code, which uses the unstructured version of the wave model SWAN [*Dietrich* 2010b; *Zijlema* 2010] for the period when wind forcing is available, simulation days 45-50.47) were used for the hindcast of Hurricane Isabel, while only tides were used for Floyd and Alberto. The inclusion of winds and waves for the Hurricane Isabel hindcast was to demonstrate the capabilities of the entire system. With the wind forcing applied, nodal attributes for the surface canopy coefficients and surface directional effective roughness length values were also used for Hurricane Isabel. The peak surge during Isabel occurs about 50 days into the simulation, while the peak discharge just downstream of the confluence with Fishing Creek on the Tar River occurs about 56 days into the simulation. Thus, the two factors, surge and river flooding, are fairly decoupled during Hurricane Isabel.

6.5.1 Boundary Forcing

The boundary forcing for each of the four hand-off points for each of the simulations is seen in Figure 6.39 (Hurricane Floyd), Figure 6.40 (Hurricane Isabel) and Figure 6.41 (Tropical Storm Alberto). The black line in each of the graphs shows the values from HL-RDHM used to compute the boundary forcing for ADCIRC. The gray line shows the discharge, calculated from the elevation and velocity results, across an ADCIRC river section just inside the boundary (7 nodes in from the boundary on both the Tar River and Fishing Creek, 5 nodes from the boundary on the Neuse River, and 9 nodes from the boundary on Contentnea Creek). More detail on the HL-RDHM simulations can be found in *Van Cooten et al.* [2011] and *Vergara et al.* [2010].

An important aspect of coupled simulations is that the specified discharge actually enters the ADCIRC domain. Generally, as the values in Table 6.4 and Table 6.5 show, the

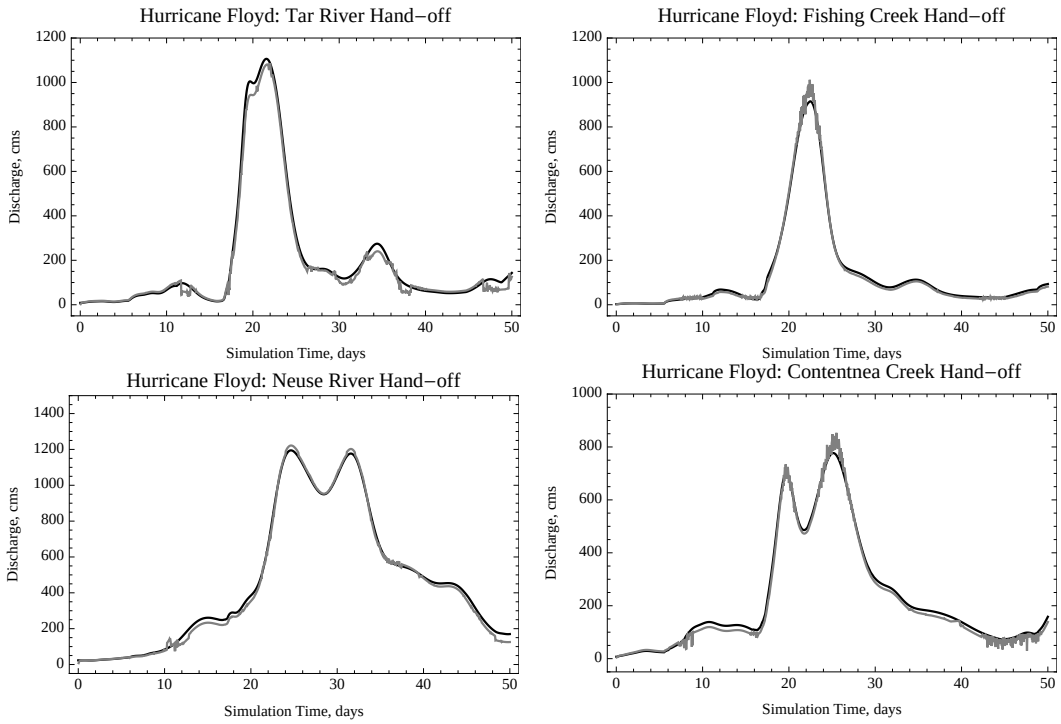

Figure 6.39 Comparison of input (black) and computed discharge (gray) values at the boundary for each of the hand-off points for Hurricane Floyd.

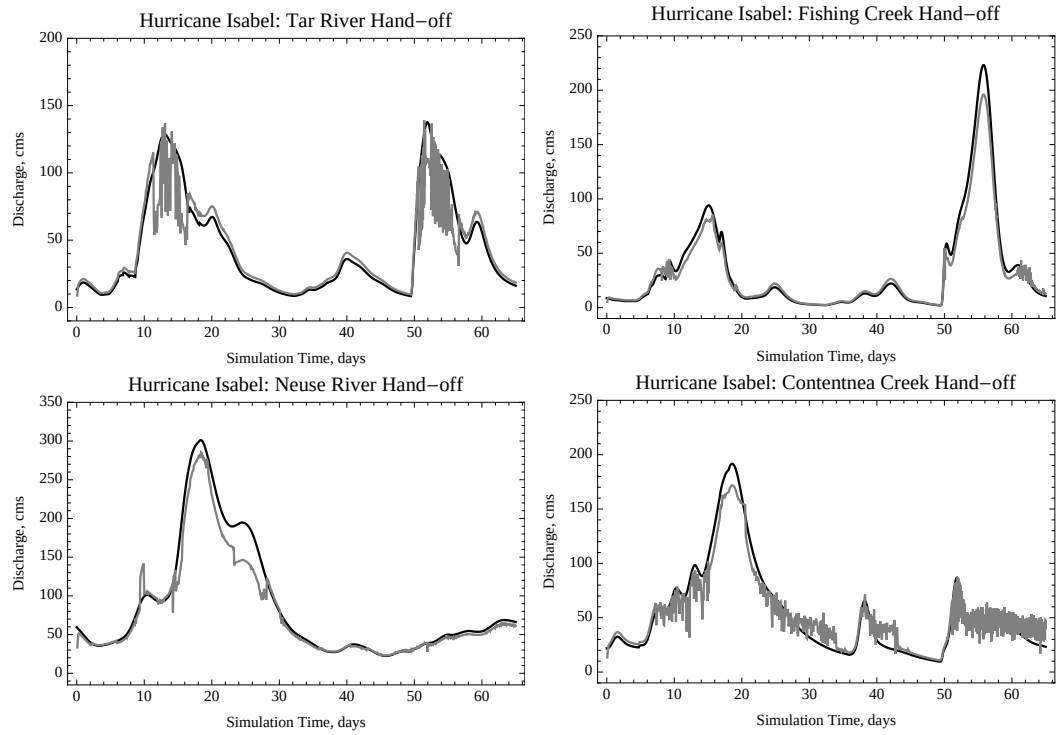

Figure 6.40 Comparison of input (black) and computed discharge (gray) values at the boundary for each of the hand-off points for Hurricane Isabel.

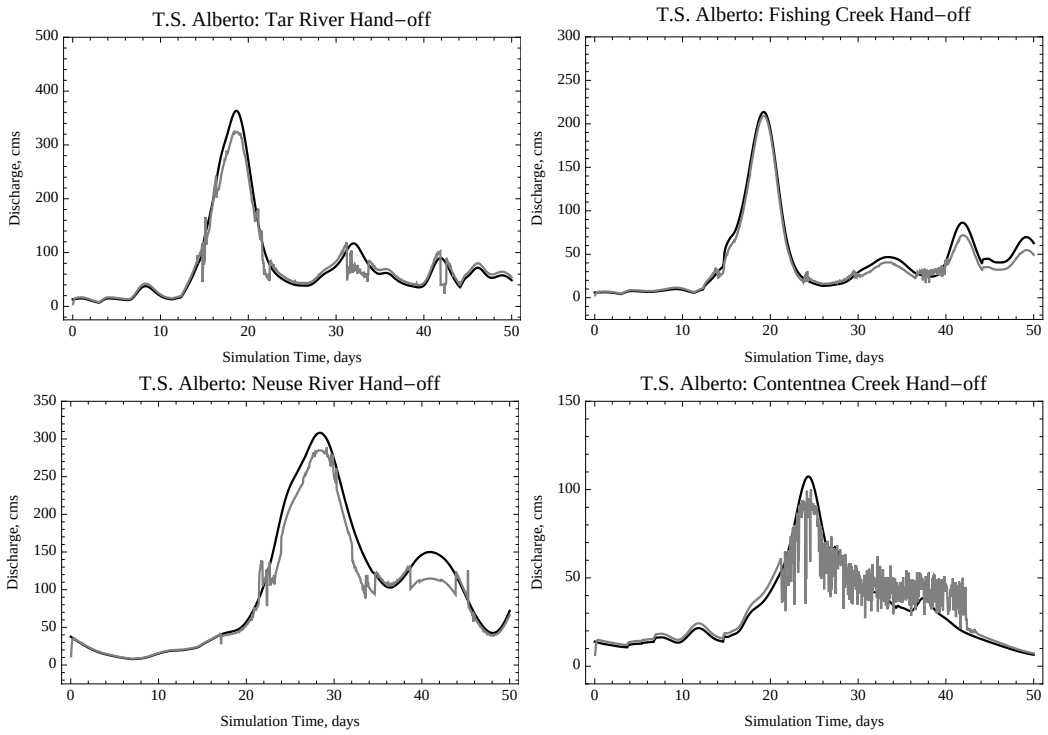

Figure 6.41 Comparison of input (black) and computed discharge (gray) values at the boundary for each of the hand-off points for Tropical Storm Alberto.

total volume of discharge specified approximately equals the total volume calculated using the output water surface elevations and velocities from ADCIRC. The total volume is the area under the discharge hydrograph.

The largest errors occur during different events for different hand-off points. The worst error for the Tar River boundary, -5.7%, occurs for Hurricane Floyd. Fishing Creek reproduces the specified volume very well for Hurricane Floyd, but has errors of approximately -8% for both Hurricane Isabel and Tropical Storm Alberto. On the Neuse River system, Contentnea Creek performs worst for Hurricane Floyd, -3.9%, while the Neuse River has almost perfect mass balance for Hurricane Floyd but has errors close to -10% for both Hurricane Isabel and Tropical Storm Alberto.

Along with the small errors in volume entering the domain, there are short-wave-

Table 6.4 Comparison of specified volume (cubic meters) of boundary forcing to volume calculated near the boundary from ADCIRC output fields for channels in the Tar River system.

Event	Tar Specified	Tar Output	Fishing Specified	Fishing Output
Hurricane Floyd	8.55 E08	8.06 E08	5.92 E08	5.80 E08
Hurricane Isabel	2.44 E08	2.35 E08	1.90 E08	1.75 E08
TS Alberto	3.31 E08	3.23 E08	1.92 E08	1.76 E08

Table 6.5 Comparison of specified volume (cubic meters) of boundary forcing to volume calculated near the boundary from ADCIRC output fields for channels in the Neuse River system.

Event	Neuse Specified	Neuse Output	Contentnea Specified	Contentnea Output
Hurricane Floyd	2.00 E09	1.97 E09	9.92 E08	9.53 E08
Hurricane Isabel	4.81 E08	4.37 E08	3.00 E08	3.00 E08
TS Alberto	4.32 E08	3.88 E08	1.36 E08	1.45 E08

length oscillations in the discharge at some locations.Oscillations in the discharge results are generated during ADCIRC simulations when bank-full depth is exceeded and the initial floodplain wetting occurs. When the flow rates are within a given range for each of the channels, the oscillations occur, which may be caused by elements alternately wetting and drying. The most dramatic instances of this are the Tar River hand-off for Hurricane Isabel (top left panel of Figure 6.40) and the hand-off on Contentnea Creek for both Hurricane Isabel and Tropical Storm Alberto (bottom right panels of Figure 6.40 and Figure 6.41). The oscillations for the Tar River hand-off location occur for flow rates around 100 cms.

Similar oscillations occur for the Tar River location for the other events as well, but they are less noticeable because the flow is not near 100 cms for the entire duration of the event. The oscillations occur at the Contentnea Creek hand-off for flows between 30-100 cms. The oscillations are less prevalent for Hurricane Floyd because the flows are above the range that produces the oscillations for the majority of the event. Also, for Hurricane Isabel, the oscillations disappear when the flow rate passes 100 cms, but they come back after the flow rate drops back under 100 cms. The oscillations are less prevalent during Hurricane Floyd because the flow rates are high enough that the floodplain is inundated for a large portion of the simulation. Additionally, the range of discharges experienced minimizes the oscillations that do occur for the flow rates near bank-full because of the overall scale on the figure.

6.5.2 Confluence

Along with mass balance at the grid boundaries, mass conservation should apply for river confluences. Table 6.6 shows the total volumes calculated upstream and downstream of the confluences on the Tar and Neuse Rivers for the three events. For the Tar River, the upstream value is the sum of the volume calculated on the Tar River upstream of the confluence with the volume calculated on Fishing Creek upstream of the confluence. Similarly, the upstream value for the Neuse confluence is the volume for the Neuse upstream of the confluence added to the volume for Contentnea Creek upstream of the confluence. These values are compared to the total volume calculated for sections on the Tar and Neuse Rivers downstream of the confluences.

The results are fairly consistent in that the downstream total volume always exceeds the total volume upstream of the confluence. The error for the confluence on the Tar River

Table 6.6 Comparison of the sum of the calculated volumes (cubic meters) at sections just upstream of the confluences with the volume calculated just downstream of the confluence on the Tar and Neuse Rivers.

Event	Upstream Tar Plus Fishing	Downstream Tar	Upstream Neuse Plus Contentnea	Downstream Neuse
Hurricane Floyd	1.58 E09	1.59 E09	4.21 E09	4.75 E09
Hurricane Isabel	4.81 E08	5.14 E08	1.94 E09	2.26 E09
T.S. Alberto	5.89 E08	5.97 E08	1.14 E09	1.36 E09

is negligible for Hurricane Floyd and is less than 2% for Tropical Storm Alberto, while the confluence experiences a gain of almost 7% during Hurricane Isabel. The confluence on the Neuse River experiences larger mass balance errors, ranging from 12.8% for Hurricane Floyd to 19.3% for Tropical Storm Alberto.

6.5.3 Overall River Behavior

Thus far, most of the analysis of river behavior has been focused on the locations just downstream of the hand-off locations, with additional attention given to the confluences of the main stems and tributaries. In this section, results from locations throughout the river reaches will be presented.

The total discharge was computed through fifteen sections (combined) on the Tar River and Fishing Creek. Additionally, sixteen total sections were used on the Neuse River and Contentnea Creek. The locations of all the sections for computing discharge can be found in Table 6.7 (Tar River and Fishing Creek) and Table 6.8 (Neuse River and Contentnea Creek). The locations for the cross-sections on the main rivers are shown graphically in Figure 6.51. For each of the three events, the total discharge through each

Table 6.7 Locations of cross-sections on the Tar River and Fishing Creek for calculating discharge from ADCIRC simulations.

Tar Basin ID	Description	Latitude	Longitude
1	Top of Tar River (8 nodes in)	35.9289	-77.5556
2	Tar River 3.6 km from hand-off point	35.9349	-77.5340
3	Tar River upstream of confluence (6.0 km from hand-off point)	35.9458	-77.5269
4	Top of Fishing Creek	35.9777	-77.5390
5	Fishing Creek intermediate location	35.9658	-77.5351
6	Fishing Creek 0.5 km upstream of the confluence with the Tar River	35.9486	-77.5183
7	Tar River downstream of confluence (8.7 km from hand-off point)	35.9357	-77.5168
8	Tar River 11.7 km from hand-off point	35.9194	-77.5105
9	Tar River at Tarboro (18.9 km from hand-off point)	35.8939	-77.5324
10	Tar River 24.6 km from hand-off point	35.8482	-77.5424
11	Tar River 33.7 km from hand-off point	35.7753	-77.5325
12	Tar River 50.0 km from hand-off point	35.6608	-77.4629
13	Tar River at Greenville (62.3 km from hand-off point)	35.6168	-77.3728
14	Tar River near Grimesland (84.8 km from hand-off point)	35.5744	-77.1771
15	Pamlico River at Washington	35.5422	-77.0628

cross-section is shown in Figure 6.42. The total volume comparisons have some inherent error because the rivers are not allowed to reach steady-state discharge conditions at the beginning and end of the volume calculation period. However, this error is relatively small, and it should cause the total discharge volume to decrease with distance downstream from the ADCIRC grid boundary. The error is small because the discharge boundary forcing values at the start of the simulations are low, so they are in the same range as the flow rates

Table 6.8 Locations of cross-sections on the Neuse River and Contentnea Creek for calculating discharge from ADCIRC simulations.

Neuse Basin ID	Description	Latitude	Longitude
1	Top of Neuse River (6 nodes in)	35.2244	-77.7647
2	Neuse River 4.7 km from hand-off point	35.2190	-77.7313
3	Neuse River 10.4 km from hand-off point	35.2281	-77.6927
4	Neuse River 16.9 km from hand-off point	35.2400	-77.6513
5	Neuse River upstream of Kinston gauge (26.8 km from hand-off point)	35.2644	-77.6036
6	Neuse River at Kinston (30.0 km from hand-off point)	35.2532	-77.5873
7	Neuse River downstream of Kinston gauge (30.3 km from hand-off point)	35.2507	-77.5861
8	Neuse River 35.2 km from hand-off point	35.2460	-77.5447
9	Neuse River 45.5 km from hand-off point	35.3007	-77.4876
10	Neuse River upstream of confluence with Contentnea Creek (50.6 km from hand-off point)	35.3256	-77.4651
11	Top of Contentnea Creek	35.4217	-77.4707
12	Contentnea Creek at Grifton (upstream of confluence with Neuse River)	35.3776	-77.4477
13	Neuse River downstream of confluence (60.1 km from hand-off point)	35.3339	-77.3777
14	Neuse River near Fort Barnwell (67.5 km from hand-off point)	35.3137	-77.3039
15	Neuse River 79.9 km from hand-off point	35.2527	-77.2185
16	Neuse River 99.5 km from hand-off point	35.1626	-77.0817

throughout the rivers early in the simulations. Additionally, for most of the hand-off point hydrographs, the discharge is close to zero and decreasing with time near the end of the simulation. This helps offset errors due to higher discharge rates for the uppermost reaches early in the simulation. Furthermore, the large discharge peaks that occur for relatively

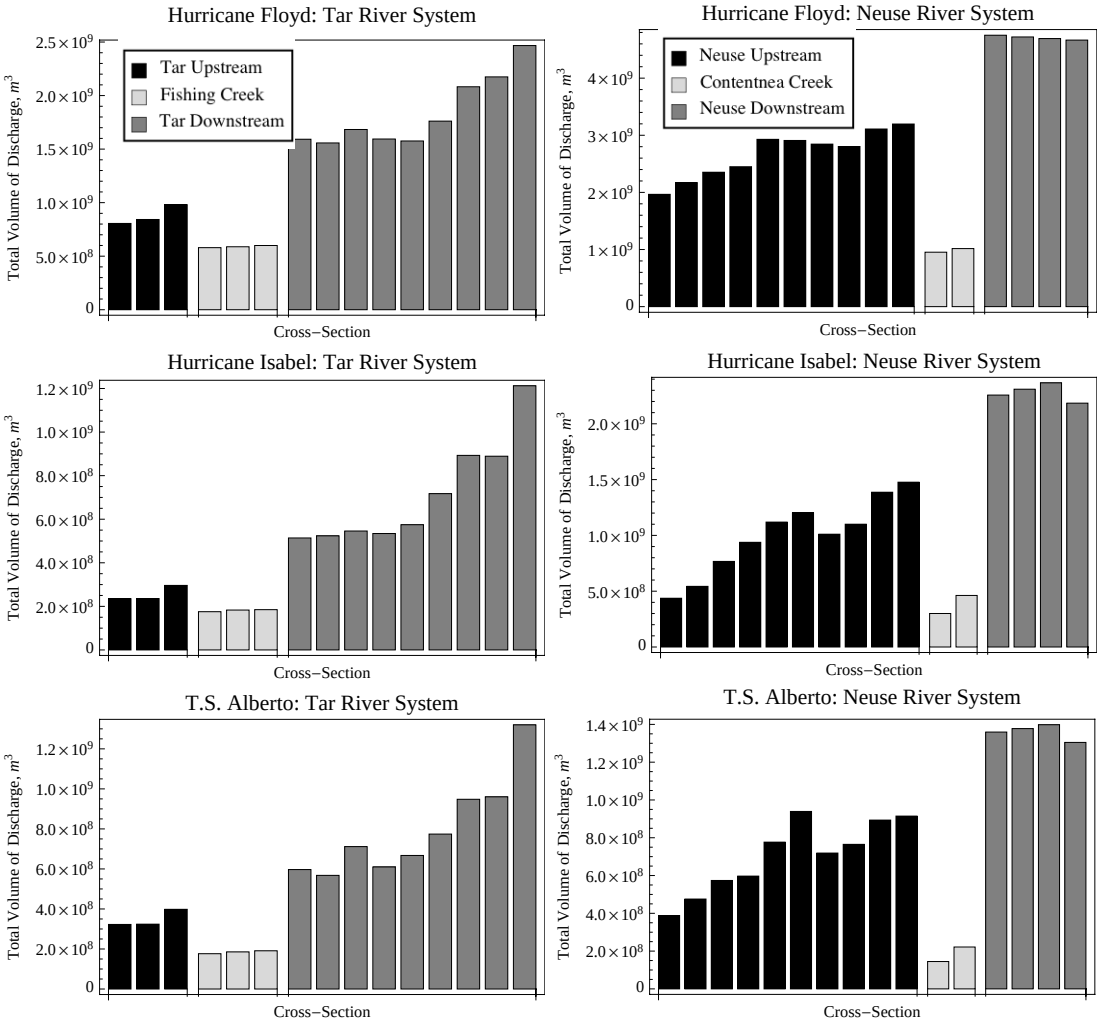

Figure 6.42 Total volume of discharge for different cross-sections on the rivers in the ADCIRC grid for Hurricanes Floyd and Isabel and Tropical Storm Alberto.

large portions of the middle of the simulations account for the majority of the total discharge. The major flood waves for each event are allowed to pass through the entire domain during the simulation.

The general trend shows the discharge volume increases with distance downstream from the grid boundary. This occurs on both the Tar River and Fishing Creek upstream of their confluence, although the mass error is relatively small on Fishing Creek. The most dramatic increase on the Tar River system is downstream of the confluence. The mass balance error (increase in discharge volume) downstream of the confluence is in the same

range as the discharge values just downstream of the confluence. Thus, there is a mass balance error of approximately 100% along the Tar River downstream of the confluence with Fishing Creek.

In the Neuse River system, the majority of the mass balance error occurs on the Neuse River upstream of the confluence. The gain in discharge volume from the Neuse River hand-off point to the cross-section on the Neuse River just upstream of the confluence (cross-section 10 in the Neuse River system) is 238% during the Hurricane Isabel simulation. The increase between those two locations during the Hurricane Floyd simulation is about 62%. It is worth noting that the confluence on the Neuse River occurs significantly farther downstream from the boundary than the confluence on the Tar River.

The cause of the oscillations and mass error is inundation of the river floodplain in ADCIRC. Tests with idealized river domains (prismatic channels) show consistent mass balance throughout the reach for in-channel flows. However, mass balance errors occur when the discharge is increased to induce floodplain inundation. On the idealized domain, the floodplain inundation causes growing mass errors as the inundation moves down the floodplain. Eventually, if the floodplain wetting is not impeded by topography changes (which is the case on the idealized domain), it causes the simulation to crash due to overly large build up of water, creating unrealistic water surface gradients. Attempts to control the mass balance errors and instability with model parameter selections were ineffective. Future endeavors to model rivers with ADCIRC should include a focus on the wetting and drying algorithms, especially as they pertain to river inundation.

6.5.4 Hurricane Isabel Validation

The Hurricane Isabel hindcast is different from the hindcasts for Hurricane Floyd and Tropical Storm Alberto because the Hurricane Isabel simulation included the use of wind fields and computation of wave fields to model the storm surge from the tropical cyclone. Therefore, the Hurricane Isabel validation utilized the following forcing fields: 1) river discharge boundary conditions from HL-RDHM at the four hand-off locations, 2) tidal forcings on the ocean boundary, and 3) wind field forcings from Hurricane Isabel applied as a surface stress within the domain. Additionally, wave radiation stresses are accounted for through use of the coupled ADCIRC+SWAN model.

The wind field was present (in the simulation) for the period of 0:00 UTC on September 14, 2003 to 11:30 UTC on September 19, 2003. The beginning of the wind forcing coincides with a simulation time of 45.0 days. Hurricane Isabel made landfall as a Category 2 storm[a] at approximately 16:00 UTC on September 18, 2003 and the center passed just east of the Tar and Neuse River basins, as shown in Figure 6.43, which is adapted from a figure first published in *Van Cooten et al.* [2011]. The locations of the National Data Center Buoy (NDBC) stations used for validation are also shown in Figure 6.43, with the wave height validation stations on the left panel and the water surface elevation (tidal gauge) validation stations on the right panel.

The coupled ADCIRC+SWAN model provides wave and water level information through time for the entire domain. Snapshots of the significant wave height and water surface elevation fields just prior to Hurricane Isabel making landfall on the outer banks, from *Van Cooten et al.* [2011], are shown in Figure 6.44. The wave field shows the largest

a. On the Saffir Simpson scale

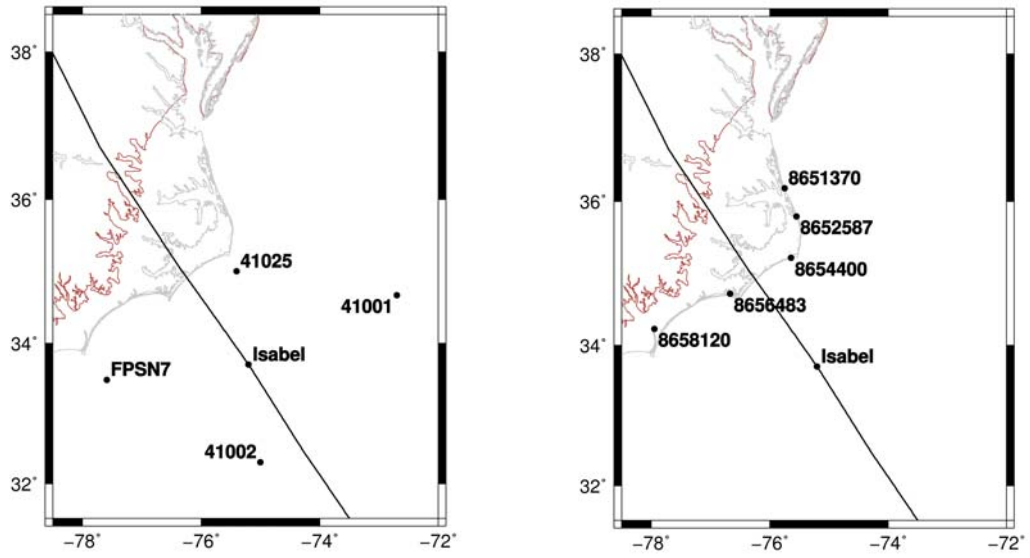

Figure 6.43 Hurricane Isabel track along with wave and tidal gauge locations. The wave height stations are 41001 (East of Cape Hatteras, NC), 41002 (South Cape Hatteras, NC), FPSN7 (Frying Pan Shoals, NC) and 41025 (Diamond Shoals, NC). The tidal stations are 8658120 (Wilmington, NC), 8656483 (Beaufort, NC), 8654400 (Cape Hatteras, NC), 8652587 (Oregon Inlet, NC) and 8651370 (Duck Pier, NC).

waves are on the right side of the hurricane in the region slightly off-shore. The waves break and reduce in amplitude across the continental rise just seaward of the outer banks, and the maximum significant wave heights in the Pamlico Sound are in the 2-3 m range. The water surface elevation field shows 2-3 m water rise along the outer banks, between Beaufort and Cape Hatteras, on the northeast side of the hurricane. There is drawdown on the east side of the Pamlico Sound and water is piling up in the area on the southwest side of the sound, where the Neuse River discharges into the sound.

Water surface elevations from ADCIRC were compared to NOAA tidal station data. A comparison of the results for the tidal stations in North Carolina is shown in Figure 6.45. The comparisons at 8658120, 8656483, 8654400, and 8651370 are included in *Van Cooten et al.* [2010]. The locations in the figure start with the northernmost station, Duck Pier, and end with the southernmost station, Wilmington. Oregon Inlet is on the outer banks about

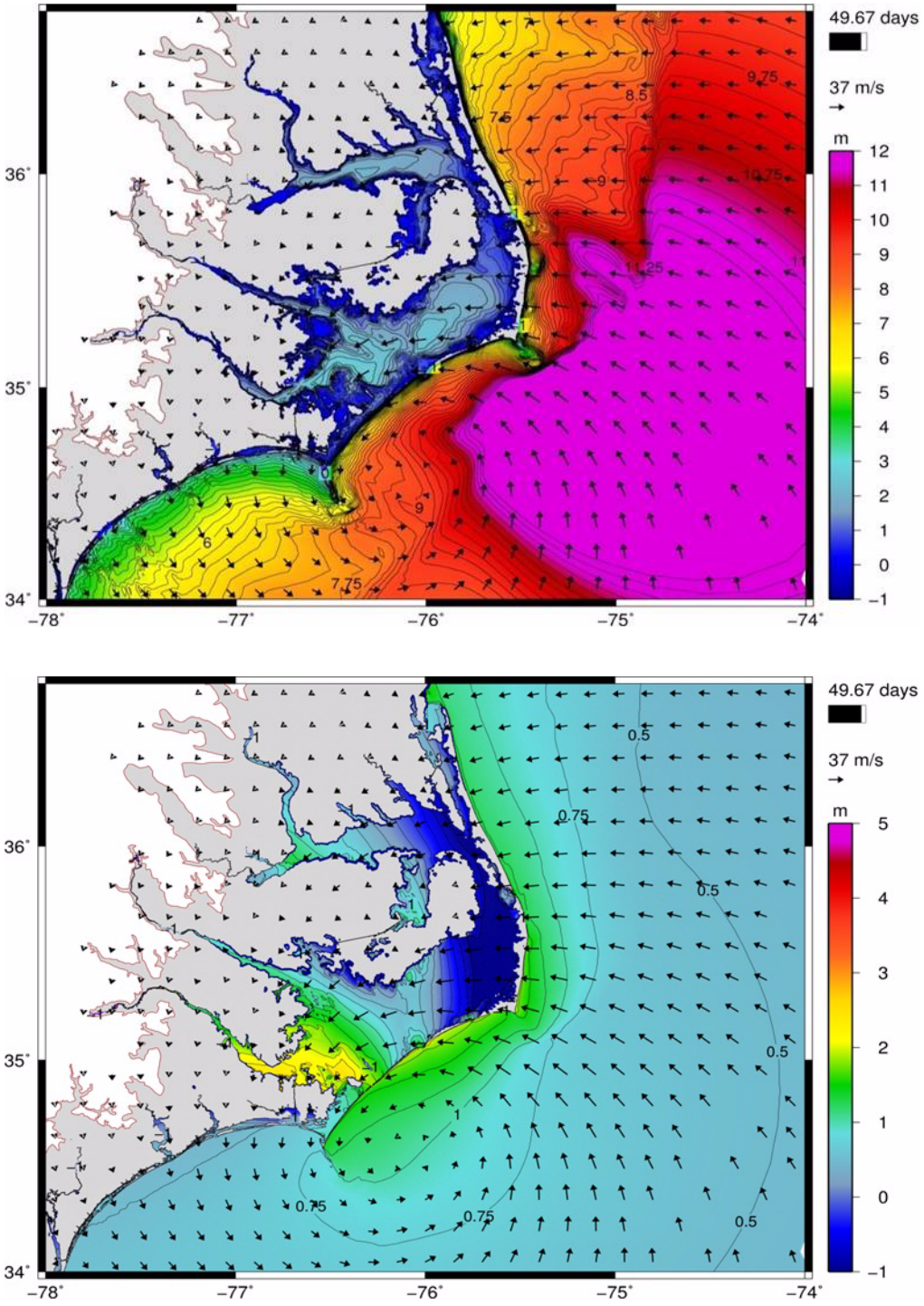

Figure 6.44 Significant wave heights (top) and water surface elevations (bottom) 49.67 days into the Hurricane Isabel simulation. The wind vectors are shown on each plot, and this time corresponds to slightly before Hurricane Isabel makes landfall on the Outer Banks on September 18, 2003.

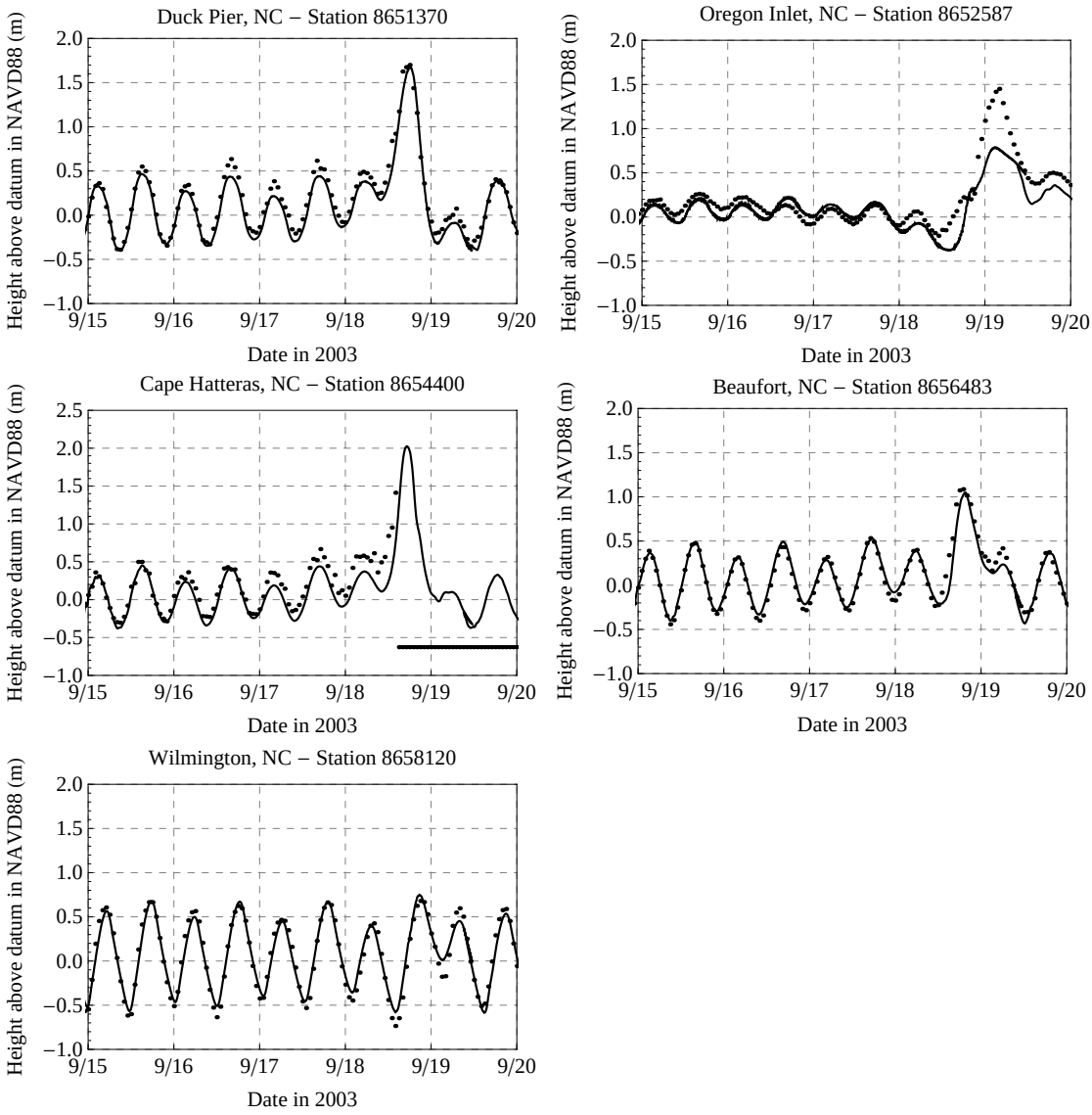

Figure 6.45 ADCIRC (solid) results for Hurricane Isabel compared to NOAA tidal station (dots) measurements.

halfway between Duck Pier and Cape Hatteras. The ADCIRC tides and storm surge are an accurate representation of the measured values during Hurricane Isabel at all of the locations except for Oregon Inlet. ADCIRC underpredicts the maximum water surface elevation by about 0.75 m at Oregon Inlet[a]. The timing and peak of the surge at Duck Pier and Beaufort are captured by ADCIRC. Additionally, the model does a decent job at Cape

a. The results for Oregon Inlet have subsequently been improved through local improvements to the ADCIRC grid in the area around Oregon Inlet [*Luettich*, personal communication, 2011].

Hatteras. Unfortunately, the tidal station at Cape Hatteras did not record the peak surge from Isabel, because it was not recording data at the time of the peak surge. Wilmington, NC did not experience significant surge from Isabel because it was on the west side of the storm and was about 100 miles away from the center track of the storm. However, the tides were accurately represented by ADCIRC for the Wilmington station.

Wave heights computed by SWAN were compared to NDBC wave data. A comparison of the wave results for the Hurricane Isabel hindcast is shown in Figure 6.46. The results at stations 41001 and 41002 are included in *Van Cooten et al.* [2011]. For reference, the Diamond Shoals buoy is located on the continental shelf south-southeast of Cape Hatteras and the Frying Pan Shoals buoy is located on the continental shelf southeast of Wilmington, as shown in the left panel of Figure 6.43. The two other buoy locations are in deeper water seaward of the continental shelf.

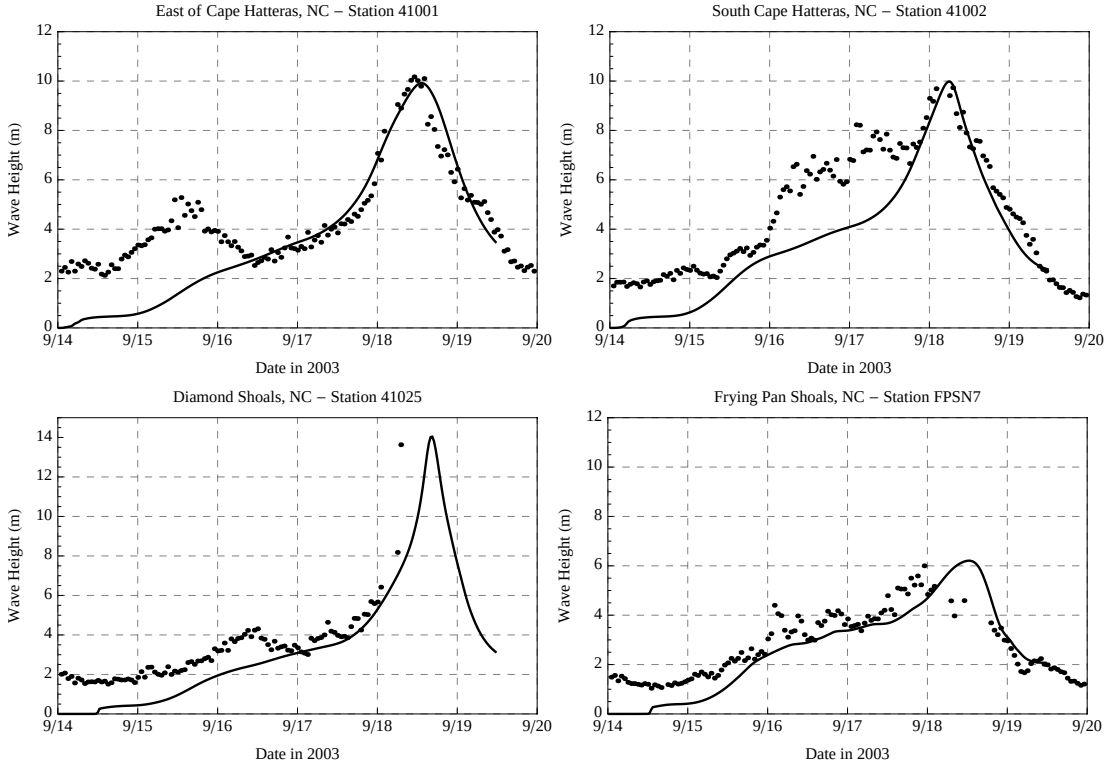

Figure 6.46 Comparison of SWAN (lines) and NOAA (dots) wave height results for Hurricane Isabel.

The results show good agreement between the measured wave heights and the wave heights computed in the model hindcast. Specifically, the peak wave heights for the deep water locations off Cape Hatteras were captured by the model. The wave results are under-predicted, across the board, for early times (before September 16th) because the wind forcing (and SWAN computations) started at the beginning of the day on September 14, 2003. As one would expect, it takes time for the wave heights to ramp up and approach the actual values. The results are not as good for the buoys in the shallower depths as for the deep water locations. Specifically, for Frying Pan Shoals, the SWAN results have the correct magnitude, but the timing of the peak is off by about 12 hours. For Diamond Shoals, the buoy stopped recording on September 18, so the last value in the record is the one exceeding 13 m that is in agreement with the peak computed by SWAN. However, the SWAN wave heights reach that level at a later time, and it is unknown whether or not the last record from the buoy was the maximum experienced at that location.

The river portion of the ADCIRC domain was assessed by comparing ADCIRC results to daily data from USGS gauge locations. The seven gauge locations within the ADCIRC domain are shown in Figure 6.47. The daily data was used so there would be consistency from location to location. Higher frequency discharge data is available through the USGS instantaneous data archive and the stage (and water surface elevation) can be obtained using the discharge data in conjunction with a rating curve. However, the discharge data is not available for all the stations on the Tar River. Furthermore, for these locations, the temporal variation in discharge is not particularly large. Therefore, the high temporal resolution data from the instantaneous data archive is not necessary to evaluate hindcast results for rainfall-induced flooding from tropical systems in this geographical

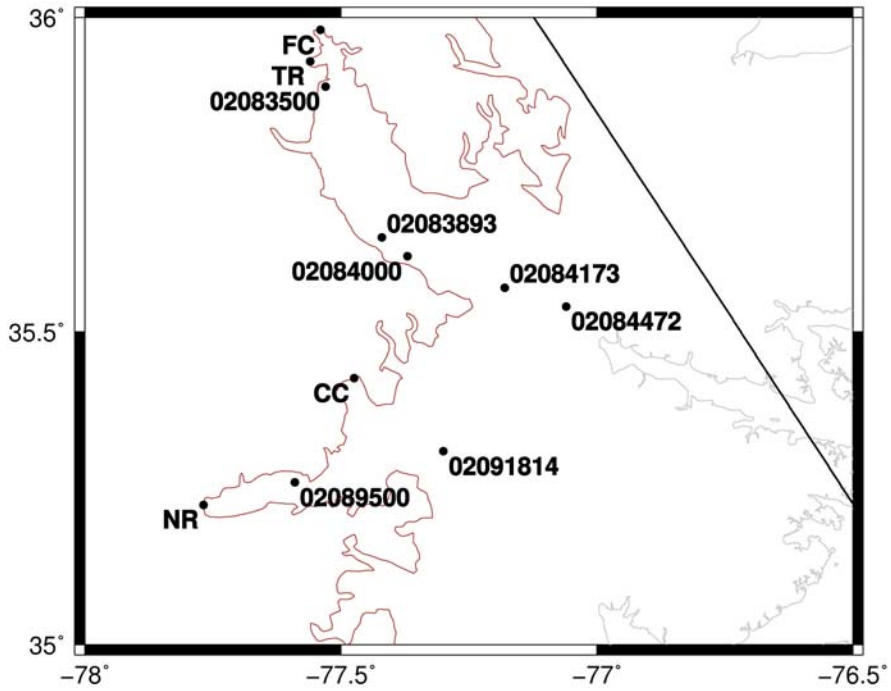

Figure 6.47 Hand-off locations (NR = Neuse River, CC = Contentnea Creek, TR = Tar River, and FC = Fishing Creek) and USGS gauge locations (8-digit numbers) on the Tar and Neuse Rivers within the ADCIRC domain.

area. However, the instantaneous data archive was used to determine the timing of the peak surge at Washington in order to compare to the timing of the surge modeled in ADCIRC.

The locations of the gauge locations on the Tar River, from upstream to downstream, are Tar River at Tarboro (02083500), Tar River at US 264 near Rock Springs (02083893), Tar River at Greenville (02084000), Tar River at SR 1565 near Grimesland (02084173) and Pamlico River at Washington (02084472). Elevation and discharge results are available at Tarboro, Greenville and Washington. Thus, water surface elevation and discharge results from ADCIRC are compared to USGS values for those three locations. At the gauges near Rock Springs and Grimesland, only stage results are available, so only water surface elevation comparisons are done at those two locations.

The comparisons for the river locations on the Tar River are shown in Figure 6.48.

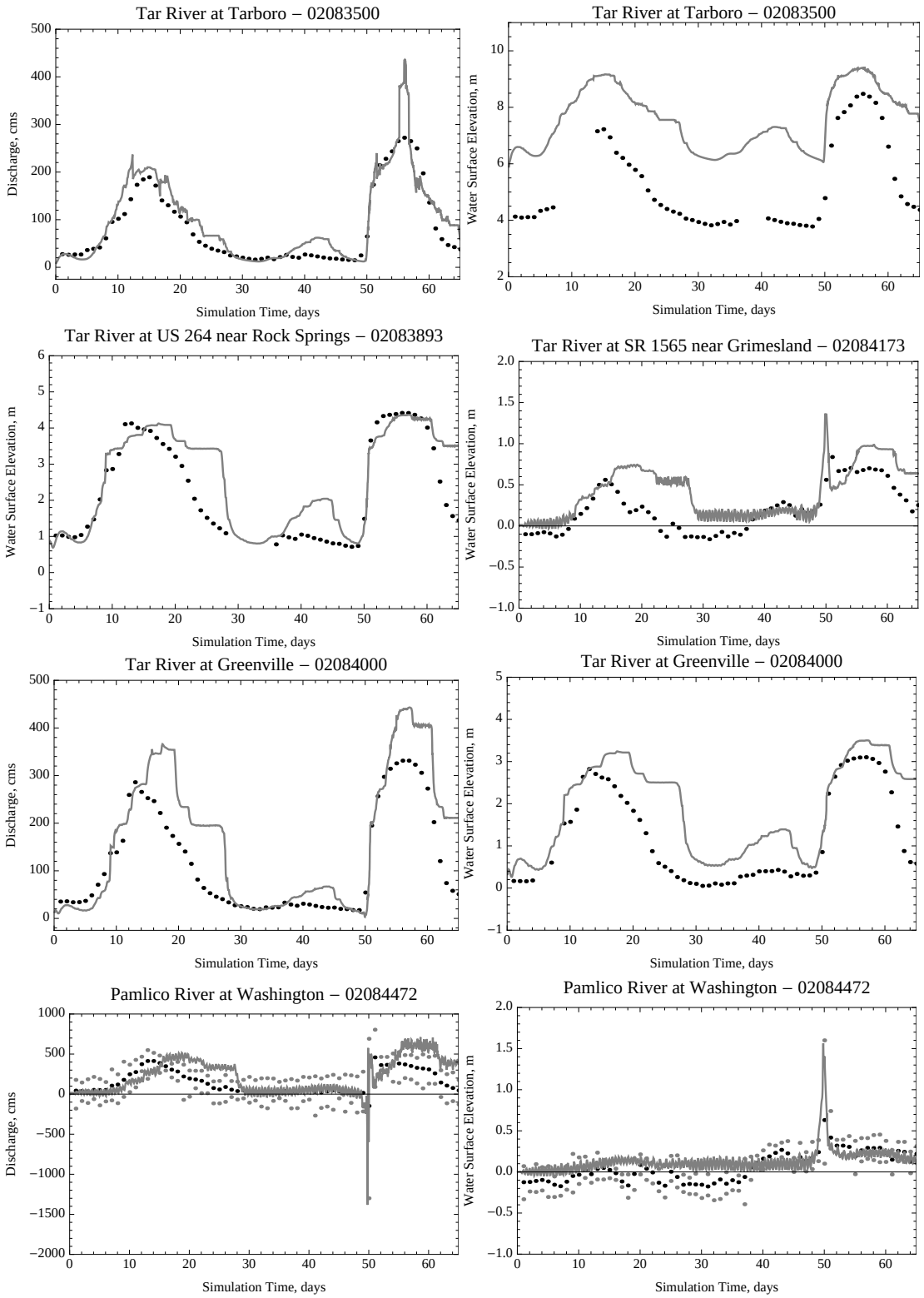

Figure 6.48 Hurricane Isabel hindcast comparison between ADCIRC results (lines) and USGS daily gauge data (black dots are mean, while the gray dots for Washington are max. and min.) for locations on the Tar-Pamlico River. The left panels are discharge, while the WSE is shown on the right, except for the second row of panel (both elevation).

Before starting discussion of results, it is worth pointing out that the daily USGS values are plotted at the end of the day for which they occur. For example, the first day of the simulation is July 31, 2003. The mean USGS values for that day are reported at the 1.0 day time in the graph. However, the USGS results for North Carolina use eastern time, rather than UTC. The offset for eastern daylight time (EDT), compared to UTC, is -4 hours. Noon EDT is 16 hours into the day in UTC. Rather than report the USGS value for July 31 at 0.67 days into the simulation, it is reported at 1.0 days.

The Nash-Sutcliffe model efficiency coefficient, E, was computed for each of the locations within the domain where USGS discharge data was available. The efficiency coefficient is given by (6.7), where Q_o^k and Q_m^k are the observed and modeled discharge at time k, and $\overline{Q_o}$ is the mean observed discharge [*Nash* 1970].

$$E = 1 - \frac{\sum_k (Q_o^k - Q_m^k)^2}{\sum_k (Q_o^k - \overline{Q_o})^2} \tag{6.7}$$

The efficiency coefficient was calculated using mean USGS and ADCIRC values for the last 60 full days of the simulation. The first four full days were ignored to allow the model to have time to spin-up the river conditions. The time offset was accounted for in computing the daily mean ADCIRC discharge values. The Nash-Sutcliffe model efficiency coefficients for the Hurricane Isabel hindcast are listed in Table 6.9. The efficiency coefficient ranges in value from $-\infty$ to 1. A value of 1 results from a perfect match between observed and modeled discharge. An efficiency of zero signifies the model performance is equivalent to the observation mean. Negative values occur when the model predictions are worse than the observation mean.

Table 6.9 Nash-Sutcliffe model efficiency coefficients for the Hurricane Isabel hindcast using USGS mean daily discharge values and mean daily ADCIRC discharge results.

USGS Gage	02083500	02084000	02084472	02089500	02091814
E	0.832	0.423	-0.268	-1.27	-5.61

At Tarboro (02083500), the discharge results match fairly well, as shown in Table 6.9 and Figure 6.48. The efficiency of the coupled model at Tarboro is 0.832. There are some instances of overprediction of discharge by ADCIRC that cause the efficiency to drop below 1, but the model results are significantly more accurate than the mean of the observed data. However, the errors that are present are good examples of ADCIRC river issues that have been presented earlier in the chapter. The largest error occurs at the peak discharge resulting from the Hurricane Isabel precipitation. The ADCIRC result shows an overprediction of the peak discharge of about 50%. Analysis of discharge results for cross-sections upstream of Tarboro shows that the spike in the discharge results at Tarboro is a result of a gain in volume as the flood wave moves downstream. The amplified peak is not present in the signal just downstream of the confluence of the Tar River and Fishing Creek.

The water surface elevation results for the Tar River at Tarboro show that the error is larger at lower flows than at higher flows. When the discharge is at baseflow levels (around day 35 of the simulation), the water surface elevation in ADCIRC is about 6 m, while the USGS results give a value around 4 m. However, at the peak flow resulting from Hurricane Isabel, even though the discharge is too high, the water surface elevation error is only about 1 m.

The next station downstream on the Tar River, USGS 02083893, shows that the ADCIRC elevation results match the USGS results throughout the simulation. The largest

error occurs in the week prior to the landfall of Hurricane Isabel when the elevations in ADCIRC are too large. The ADCIRC flow results were higher than the USGS values at Tarboro for this time as well. The elevation errors at station 02083893 are probably a result of erroneous discharge values, possibly due to errors in the boundary forcing from HL-RDHM. Referring back to Figure 6.40, there is more discharge in the boundary time series from HL-RDHM for the Tar River hand-off point at day 40 than at days 30-50. The USGS discharge and elevation results do not show an increase in discharge or elevation around day 40. Therefore, it stands to reason that there is an error in the HL-RDHM forcing provided to ADCIRC.

The results for the Tar River at Greenville (0208400) are also, generally, good. However, the peak flows are too high, which result in the Nash-Sutcliffe efficiency being significantly lower than at Tarboro (0.423 vs. 0.832). The overly-high model discharges are a result of mass balance error for rivers in ADCIRC. Comparing the peak flows at Greenville to those at Tarboro, the peak discharge rates for the first flood wave (10-15 days into the simulation) are almost twice as high at Greenville as at Tarboro. The USGS data shows higher flow rates as well. However, there is not currently a physical mechanism in ADCIRC to amplify flows via lateral inflows, i.e., the tributaries that provide additional flow to the Tar River between Tarboro and Greenville are not modeled in ADCIRC. Additionally, precipitation over the ADCIRC domain is not used. Thus, the increase in flow rates is a result of mass balance error caused by wet/dry algorithm idiosyncrasies for floodplain inundation.

The elevation errors are relatively small, compared to the Tarboro gauge location. However, for the time period 30-35 days into the simulation, the flow rates are approxi-

mately equal. There is an error of approximately 0.5 m for the elevations associated with those small discharges. As expected, based on comparisons to NCFMP cross-sections in Section 6.2.5, ADCIRC overpredicts the elevation for low flows. At both 13 and 53 days into the simulation, the flow rates (slightly less than 300 cms) are approximately equal and the water surface elevations agree.

The results for the station near Grimesland (02084173) show similar elevation errors to the results at Greenville. Specifically, the water surface elevations are overpredicted after the peaks in the USGS elevation results. This is a result of the mass balance error from inundation upstream. Additionally, the results for Grimesland show the tidal signal at low flows. The peak flows mask the tidal signal. Furthermore, just before 50 days into the simulation, there is a spike in the water surface elevations resulting from the Hurricane Isabel storm surge. The mean stage values provided by the USGS do not accurately represent the peak surge values, at least as represented in the ADCIRC hindcast. This is not particularly surprising because the peak surge does not span an entire day. Thus, the mean water surface elevation will be less than the peak surge. The tidal signal is not present in the USGS results because the mean daily data is used, so the tidal signal is averaged out.

The last station on the Tar River is the station for the Pamlico River at Washington (02084472). The maximum, minimum and mean stage and discharge values are available at Washington. The mean values are plotted with black dots and the maximum and minimum values are shown with gray dots. The same trends are continued at Washington. There is an overprediction in discharge after the peaks that contributes to the negative Nash-Sutcliffe efficiency of -0.268. On the other hand, there is excellent agreement of the peak elevation and minimum discharge related to the Hurricane Isabel storm surge. In fact,

the minimum peak discharge from the instantaneous data archive results occurs at the time that corresponds to 49.896 days into the ADCIRC simulation. Presumably, the minimum discharge occurs at the same time as the peak surge. The peak surge in the ADCIRC simulation occurs 49.833 days into the simulation. Therefore, at the USGS gage location at Washington, the peak water surface elevation and timing for the surge is almost exactly reproduced. Additionally, the peak negative discharge calculated from the ADCIRC output is in good agreement with the USGS value. However, the maximum USGS discharge values immediately after Hurricane Isabel passes are higher than the ADCIRC flow rates.

The elevation and discharge comparisons for the two stations on the Neuse River are shown in Figure 6.49. Kinston, NC (02089500) is above the confluence of the Neuse River and Contentnea Creek, while Fort Barnwell, NC (02091814) is just downstream of the confluence. Thus, it is not surprising that the flow rates are higher at Fort Barnwell than they are at Kinston. However, the peak flow during the event before Isabel is almost 500 cms at Kinston, whereas the peak discharge at the hand-off point on the Neuse, for the same event, is less than 300 cms. This is another example of mass balance errors for rivers in ADCIRC. The Nash-Sutcliffe efficiencies for the locations on the Neuse River show the model is less accurate than the observation mean. The calibrated HL-RDHM model generally produces high Nash-Sutcliffe efficiency values. Therefore, the negative efficiency values are probably due to issues with river routing in ADCIRC, as has been discussed previously.

Using Figure 6.49, it is difficult to ascertain how the water surface elevations compare for similar flow rates for the two stations on the Neuse River because the discharge results do not match. The best point for comparisons is at Kinston, just prior to the drastic

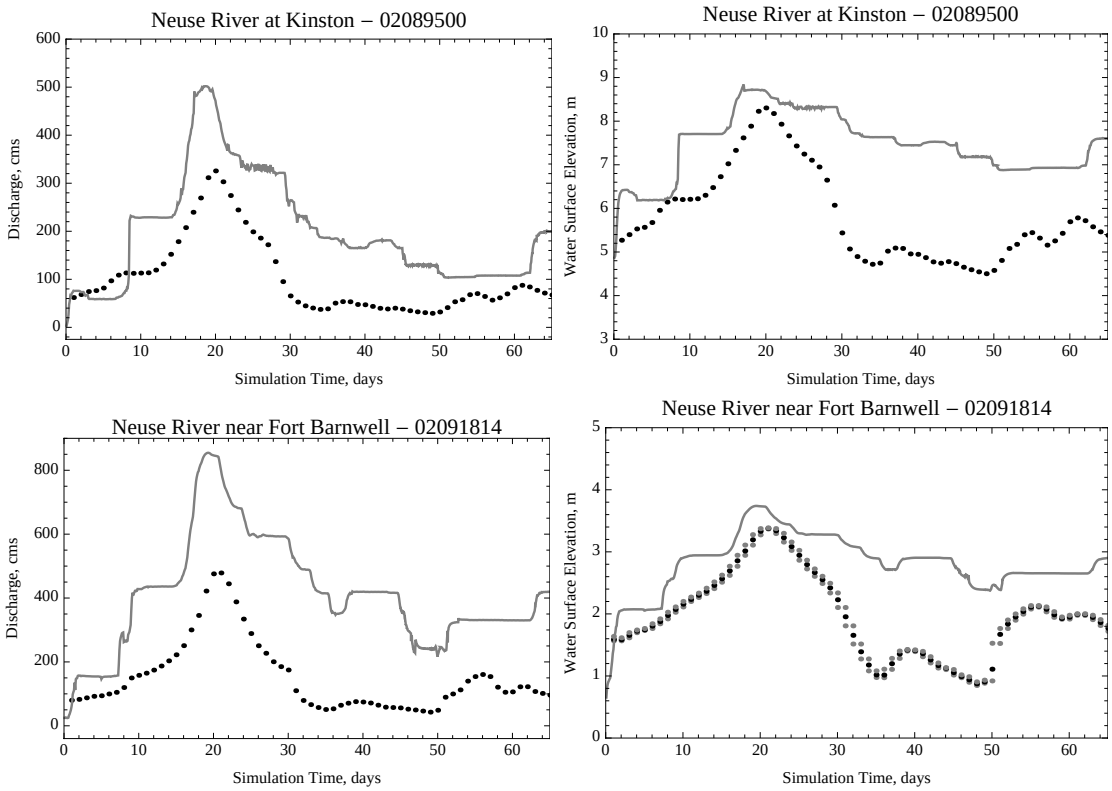

Figure 6.49 Hurricane Isabel hindcast comparison between ADCIRC results (lines) and USGS gage data (dots) for locations on the Neuse River.

rise in discharge around day eight of the simulation. The water surface elevations are similar even though the ADCIRC discharge is lower than the USGS discharge. This shows ADCIRC overpredicts water surface elevation for low discharge values at Kinston, which is consistent with results throughout this chapter.

In order to compare the water surface elevations for the ADCIRC grid to those for the USGS stations, the elevation and discharge time series were used to create rating curves for the locations on the Neuse River. The rating curves are shown in Figure 6.50, with the ADCIRC points plotted in gray and the USGS points shown in black. The rating curves show that the water surface elevations are overpredicted by ADCIRC for flows less than 300 cms at Kinston, with errors close to 1 m for low flows, while ADCIRC overpredicts water surface elevations for flows less than approximately 80 cms at the gauge location

near Fort Barnwell. At low flows, the water surface elevations are better for the Fort Barnwell gauge location than the Kinston location. However, ADCIRC underpredicts the water surface elevation at Fort Barnwell by about a third of a meter for higher flows between 300 and 500 cms. It is noteworthy that looped rating curves, shown by the USGS data, are also produced by ADCIRC.

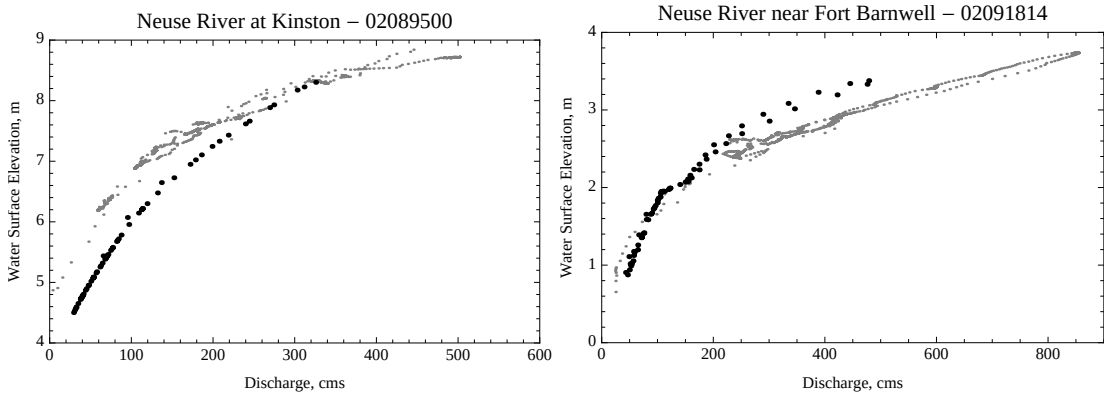

Figure 6.50 Rating curves for the USGS locations on the Neuse in the ADCIRC domain. The gray points are water surface elevation and discharge pairs from the ADCIRC hindcast for Hurricane Isabel and the black points are USGS mean daily values.

6.6 Analysis of ADCIRC River Results

The previous section details results from hindcasts of Hurricane Floyd, Hurricane Isabel and Tropical Storm Alberto. The results show significant mass balance errors occur for river discharges in ADCIRC when the flow leaves the main channel and enters the floodplain. In this section, the focus will shift from presentation of the results for the rivers in the ADCIRC domain to analysis of the river results and errors.

6.6.1 River Reach Delineations

The locations of the cross-sections used to compute the discharge for the rivers in the ADCIRC domain are shown in Table 6.7 and Table 6.8. The cross-section locations are shown graphically in Figure 6.51, along with the maximum extent of inundation for the Tar

and Neuse River basins during the Hurricane Floyd hindcast. For this analysis, river reaches are defined between consecutive sections on the Tar and Neuse Rivers as outlined in Table 6.10 (Tar) and Table 6.11 (Neuse). For this analysis, two different lengths will be utilized for reach length and slope calculations. The first is the length along one edge of the main channel in the ADCRIC grid. This is similar to the thalweg length, that is the length along the deepest part of the channel. Herein, this length will be referred to as the channel length and denoted as L_0. The other length is analogous to the valley length, which gives the distance from the top of the reach to the bottom along the valley centerline. There is not a well-defined valley for the Tar or Neuse River within the ADCIRC domain, so the valley length is an estimate. The valley length is an estimate of the distance along the centerline of the river inundation during high flow events; the valley length does not follow the sinuosity of the channel. The valley length gives a better estimate for the length of the floodplain and the flow length for high flow conditions. This length will be referred to as the valley length and denoted as L_v [*Rosgen* 1996].

The difference between the channel length and the valley length is shown graphically in Figure 6.52. The white line is indicative of the valley length. The valley length line is relatively straight and independent of the local sinuosity of the river. Thus, for sinuous stretches, the valley length can be considerably shorter than the channel length. For this reach, the fourth reach on the Neuse River, the channel length is 9.90 km, whereas the valley length is about 5.56 km. While the channel length is determined from the ADCIRC grid, there is variability in the estimated valley lengths because the points are not defined.

The mean channel slope, $\overline{S_0}$, is calculated using the channel length of the reach and the change in elevation. The change in elevation is calculated using nodes at the beginning

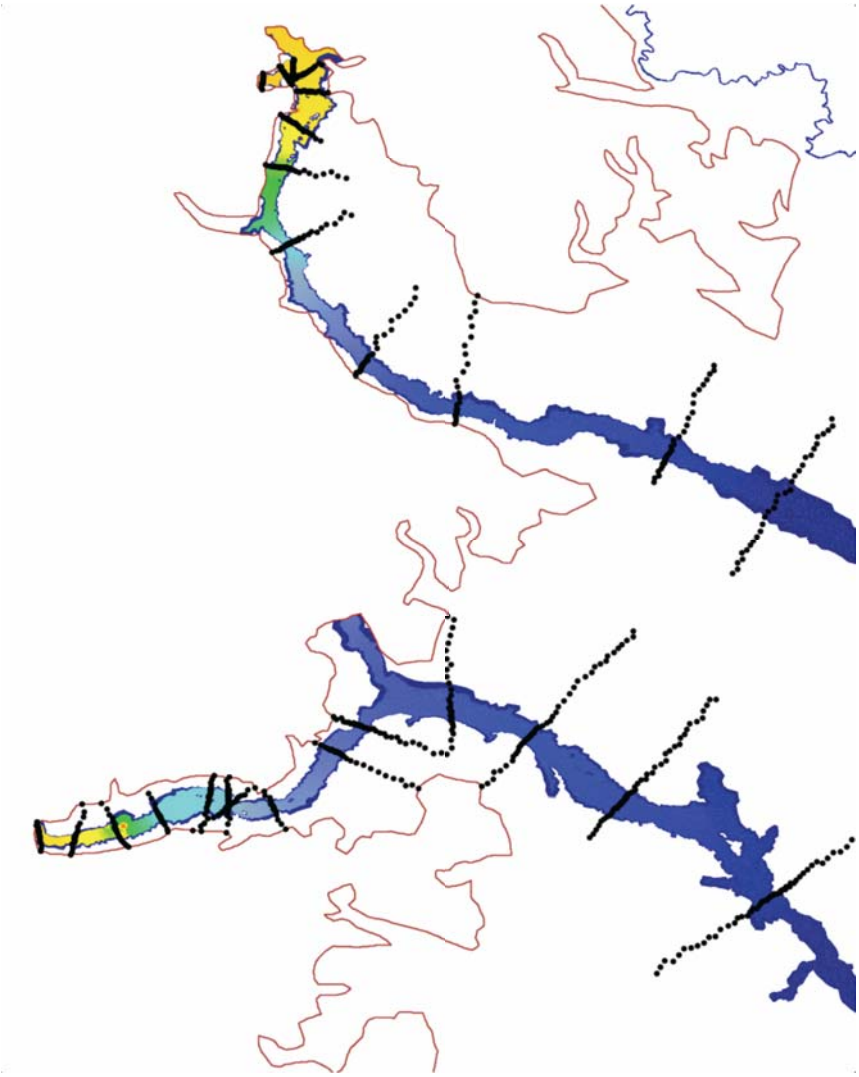

Figure 6.51 Maximum extent of inundation on the Tar and Neuse Rivers during the Hurricane Floyd hindcast. The black dots show the locations of nodes in the cross-sections to compute discharge.

and end of each reach. Herein, the nodes defining the left side of each of the rivers (facing upstream) will be used to determine the elevation change and channel length. This selection is somewhat arbitrary. The right side of each river could have been used just as easily. However, because of the adjustments to the main channel river nodes described in Section 6.2.5, the channel lengths and elevation changes are similar based on the geometry of the rivers in the modified ADCIRC grid, so the choice is inconsequential.

The standard deviation of the channel slope, σ_{slope}, is computed using (6.8), where

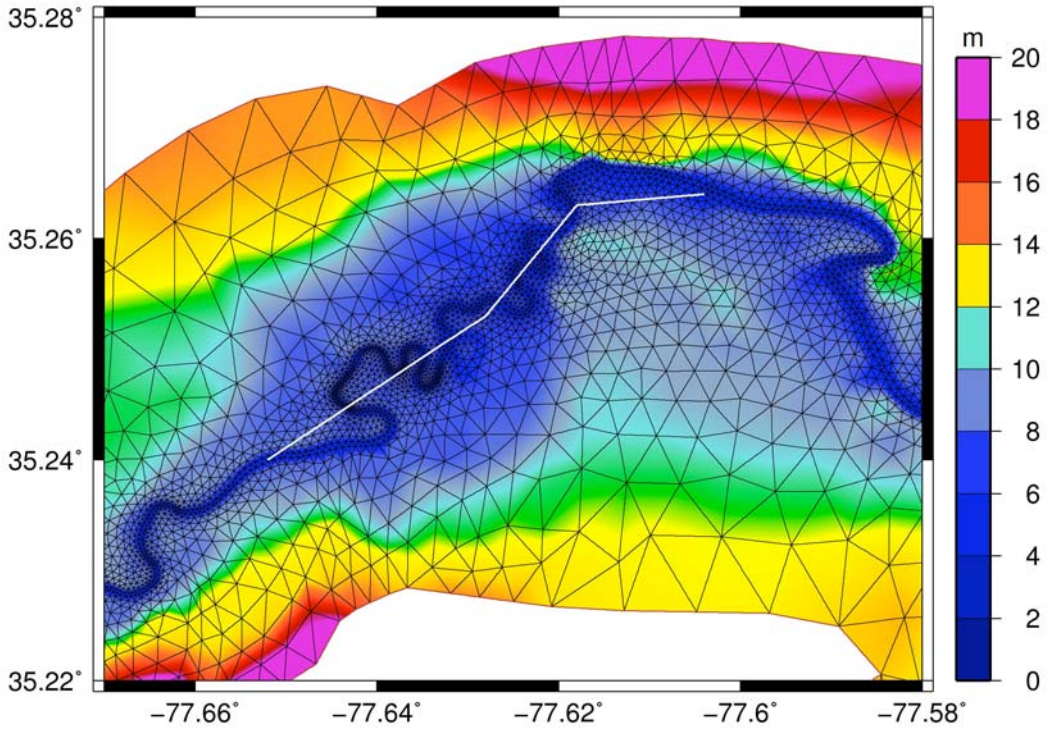

Figure 6.52 The path used to compute the valley length (shown in white) for the fourth reach on the Neuse River overlain on the ADCIRC grid. The channel length is calculated as the sum of the line segments defining one side of the main channel and tracks channel sinuosity.

n is the number of segments (element edges) in the reach along the left side of the channel, S_{0_i} is the slope of a given segment, $\overline{S_0}$ is the mean channel slope, and $(\Delta x)_i$ is the length of the segment.

$$\sigma_{slope} = \sqrt{\frac{\sum_{i=1}^{n} (\Delta x)_i (S_{0_i} - \overline{S_0})^2}{\sum_{i=1}^{n} (\Delta x)_i}} \qquad \textbf{(6.8)}$$

The values in Table 6.10 and Table 6.11 are the reach channel length, channel slope and standard deviation of channel slope for reaches on the Tar and Neuse Rivers in the ADCIRC grid. It should be noted that the tributaries are not analyzed in this section. Therefore, some of the cross-sections presented in Section 6.5 will not be used here.

Table 6.10 Tar River reach delineation and physical properties. The length, mean slope and slope standard deviation are based on the elevations for the nodes that define the left side of the channel (facing upstream). The values are similar to the values based on the nodes defining the right side of the channel.

Tar Reach ID	Upstream Section	Downstream Section	Channel Length (km)	Mean Channel Slope (m/km)	Channel Slope Standard Deviation (m/km)
1	Tar 1	Tar 2	3.16	0.430	0.420
2	Tar 2	Tar 3	2.40	0.261	0.706
3	Tar 7	Tar 8	2.96	-0.0873	0.188
4	Tar 8	Tar 9	7.24	0.0738	0.327
5	Tar 9	Tar 10	5.70	0.0625	0.340
6	Tar 10	Tar 11	9.09	0.0724	0.356
7	Tar 11	Tar 12	16.32	0.124	0.258
8	Tar 12	Tar 13	12.29	0.202	0.489
9	Tar 13	Tar 14	22.52	0.0840	0.235

Using the valley length to characterize the reach, the change in elevation for the reach is the same, so the mean valley slope, $\overline{S_v}$, can be computed, as shown in (6.9), using the mean channel slope, channel length and valley length.

$$\overline{S_v} = \frac{L_0}{L_v}\overline{S_0} \tag{6.9}$$

Additionally, the sinuosity of the reach, denoted by SI and given by (6.10), can be evaluated using the ratio of the two lengths.

$$SI = \frac{L_0}{L_v} \tag{6.10}$$

The mean valley slope and sinuosity of each reach are listed in Table 6.12.

Table 6.11 Neuse River reach delineation and physical properties. The length, mean slope and slope standard deviation are based on the elevations for the nodes that define the left side of the channel (facing upstream). The values are similar to the values based on the nodes defining the right side of the channel.

Neuse Reach ID	Upstream Section	Downstream Section	Channel Length (km)	Mean Channel Slope (m/km)	Channel Slope Standard Deviation (m/km)
1	Neuse 1	Neuse 2	4.33	0.0863	0.136
2	Neuse 2	Neuse 3	5.68	0.284	0.478
3	Neuse 3	Neuse 4	6.47	0.192	0.680
4	Neuse 4	Neuse 5	9.90	0.0824	0.784
5	Neuse 5	Neuse 7	3.52	0.0512	0.494
6	Neuse 7	Neuse 8	4.84	0.160	0.503
7	Neuse 8	Neuse 9	10.33	0.103	0.425
8	Neuse 9	Neuse 10	5.10	0.164	0.303
9	Neuse 13	Neuse 14	7.42	0.172	0.276
10	Neuse 14	Neuse 15	12.35	-0.0109	0.487
11	Neuse 15	Neuse 16	19.66	0.0851	0.258

The geometric analysis shows that the slopes and sinuosity vary throughout the grid. The Tar River is steepest and most sinuous near the hand-off point. The two steepest stretches on the Neuse River are also in the uppermost areas (near the hand-off point on the Neuse River). Additionally, the Neuse River is most sinuous upstream of Kinston. And, generally, the Neuse River is more sinuous than the Tar River. There is also quite a bit of scatter in the slopes, as shown by the relatively high standard deviation values for the slopes. The distribution of slopes for two reaches on the Tar River are shown in Figure 6.53. The first reach on the Tar River is the reach with the largest slope. And, the majority of the

Table 6.12 Tar and Neuse River reach properties based on the valley characteristics for the reach.

Tar ID	Valley Length (km)	Mean Valley Slope (m/km)	Sinuosity		Neuse ID	Valley Length (km)	Mean Valley Slope (m/km)	Sinuosity
1	2.07	0.656	1.53		1	3.30	0.113	1.31
2	1.50	0.418	1.60		2	3.70	0.436	1.54
3	2.16	-0.120	1.37		3	4.34	0.286	1.49
4	5.80	0.0921	1.25		4	5.56	0.147	1.78
5	5.53	0.0644	1.03		5	2.62	0.0688	1.34
6	8.75	0.0752	1.04		6	4.33	0.0179	1.12
7	14.61	0.139	1.12		7	8.11	0.131	1.27
8	9.90	0.251	1.24		8	3.50	0.239	1.46
9	20.19	0.0937	1.12		9	7.04	0.181	1.05
					10	10.51	-0.0128	1.18
					11	16.35	0.102	1.20

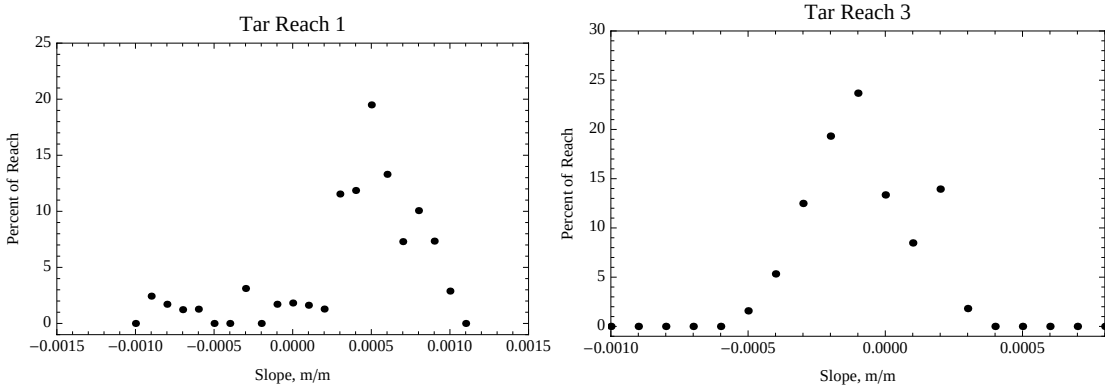

Figure 6.53 Distribution of slopes for two different reaches on the Tar River. The dots show the percentage of a given reach for different slopes. The slope for each individual segment was placed in the closest bin (rounded to 0.0001). For example, approximately 19.5% of Tar Reach 1 has a slope between 0.00045 and 0.00055.

slopes are between 0.0003 and 0.001 m/m. However, there are numerous individual segments with adverse slopes as well. For the third reach delineated on the Tar River, the overall slope is negative. However, the distribution is more symmetric than for the first Tar

River reach. Additionally, the most severe adverse slopes are less than the most severe adverse slopes for reach 1.

6.6.2 Mass Errors for Each Reach

For a given storm and reach, the total mass error per reach length, ε_{reach}, is calculated using (6.11), where $Q_{T_{start}}$ is the total volume of discharge through the section at the upstream end of the reach, $Q_{T_{end}}$ is the total discharge through the section at the end of the reach and L_v is the valley length of the reach. Multiplication by 100 is used to convert the error to a percent error.

$$\varepsilon_{reach} = 100\left(\left(\frac{Q_{T_{end}}}{Q_{T_{start}}}\right)^{1/L_v} - 1\right) \tag{6.11}$$

The mass balance error in each of the reaches for each of the storms is listed in Table 6.13 (Tar) and Table 6.14 (Neuse). The results show the stretch with the largest error

Table 6.13 Percent mass balance error per km, calculated using (6.11), of reach valley length for Tar River reaches.

Tar Reach ID	Hurricane Floyd	Hurricane Isabel	T.S. Alberto	Mean of Events[a]
1	2.192	0.185	0.209	0.862
2	10.653	16.387	14.714	13.918
3	-1.012	0.869	-2.272	-0.805
4	1.346	0.718	3.966	2.010
5	-0.976	-0.388	-2.750	-1.371
6	-0.132	0.839	1.035	0.581
7	0.764	1.528	1.021	1.105
8	1.705	2.236	2.068	2.003
9	0.215	-0.021	0.063	0.086

a. Arithmetic mean of the errors for the three events.

Table 6.14 Percent mass balance error per km, calculated using (6.11), of reach valley length for Neuse River reaches.

Neuse Reach ID	Hurricane Floyd	Hurricane Isabel	T.S. Alberto	Mean of Events
1	3.056	6.834	6.331	5.407
2	2.196	9.758	5.215	5.723
3	0.932	4.752	0.913	2.199
4	3.265	3.226	4.846	3.779
5	-1.101	-3.817	-2.908	-2.609
6	-0.340	1.981	1.446	1.029
7	1.287	2.895	1.932	2.038
8	0.793	1.811	0.672	1.092
9	-0.091	0.328	0.190	0.142
10	-0.057	0.232	0.141	0.105
11	-0.034	-0.488	-0.423	-0.315

on the Tar River is reach 2. There is also significant gain in mass in the reach just upstream of Tarboro (reach 4) and the two upstream of Greenville (reaches 7 and 8). On the Neuse River, the mass gain generally occurs at the highest rate in the most upstream areas, which causes the flow rate to be significantly overpredicted at Kinston. The mass balance in the stretch of the Neuse River downstream of Kinston is better than the mass balance between the hand-off point and Kinston. It is worth noting that the sixth cross-section on the Neuse River was not used to create reaches. The fifth reach on the Neuse uses sections 5 and 7. The sixth section was included only because it is was desired to have a section for the Kinston USGS gage location. However, the sections in close proximity upstream and downstream were included because the location of the Kinston gauge is not a good location for a cross-section in ADCIRC. In particular, the Neuse River is very sinuous near Kinston and it was difficult to cut a section that would be approximately perpendicular to the flow

for major flood events like Hurricane Floyd. The Neuse River passes through the sixth cross-section three times.

The mass errors on the Tar and Neuse Rivers do not correlate particularly well with distance from the hand-off point. And, while the error on the Neuse River is generally less for Floyd, showing a bias towards less error for larger flows, the results are mixed for the Tar River. It seems reasonable that the percent error might be less for larger flows, depending on the extent of wetting that occurs for a given storm. The current theory is that poor handling of inundation causes the mass balance problems. If the extent of wetting correlates with mass balance error, and the extent of wetting is relatively unchanged despite a higher volume, the percent mass error will be less for the larger flood.

6.6.3 Correlation Between Reach Slope and Mass Error

In an attempt to find an indicator for river mass balance error, the reach mass error was graphed against the mean valley slope. The initial thought was that lower river slopes may result in higher floodplain inundation, thus resulting in increased mass balance error for reaches with small slopes. The Tar River data is shown in Figure 6.54. Generally, the opposite is true. If the points for the reach with the largest slope are neglected, the error seems to increase with river reach slope. However, the correlation is fairly weak, especially considering the near zero mass error for the reach with the largest slope. And, for that reach, the mass error is only significant for Hurricane Floyd. The error for Hurricane Isabel and Tropical Storm Alberto is less than 0.25% per km.

The comparison of mass error to reach slope for the Neuse River is shown in Figure 6.55. The mass error is fairly high for the steepest reach, and the reach with the

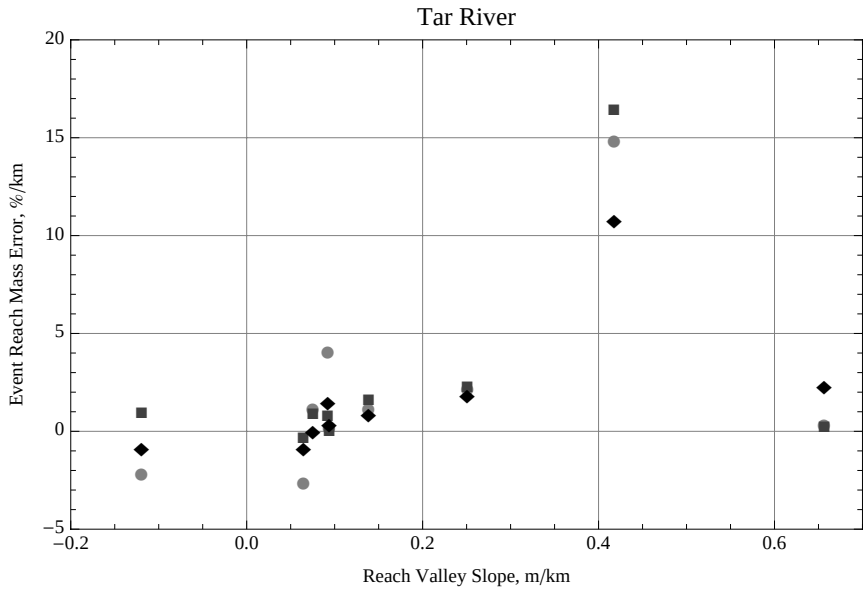

Figure 6.54 Reach mass error against reach valley slope for Tar River reaches for Hurricane Floyd (black diamonds), Hurricane Isabel (dark gray squares) and Tropical Storm Alberto (gray circles).

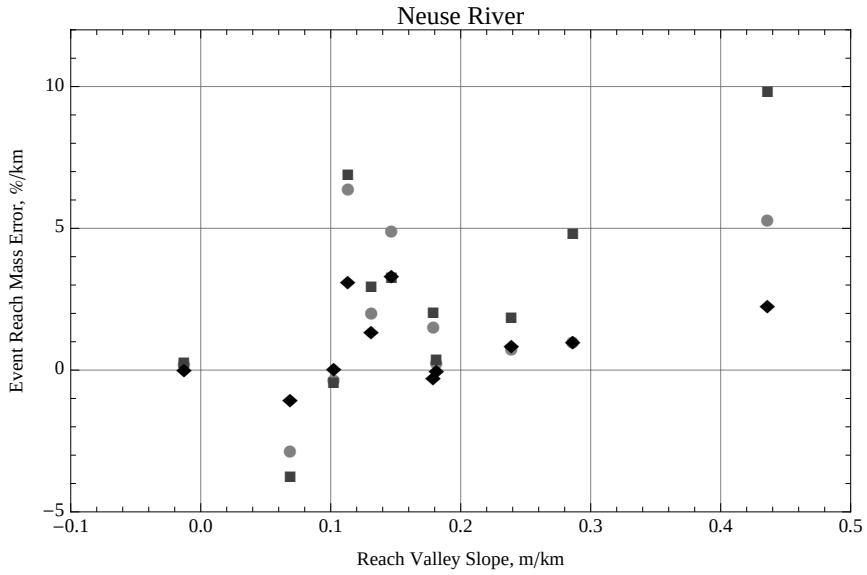

Figure 6.55 Reach mass error against reach valley slope for Neuse River reaches for Hurricane Floyd (black diamonds), Hurricane Isabel (dark gray squares) and Tropical Storm Alberto (gray circles).

smallest slope has almost no mass error. However, there are a number of reaches with mean slopes around 0.1 m/km and a wide array of reach mass error rates. So, while there may be a correlation between reach slope and ADCIRC mass error, it is not apparent from this

analysis. However, it is also unclear if the mean valley slope in the ADCIRC grid, even after the modifications to the river node elevations, is a satisfactory representation of the actual valley slopes, which may be related to the floodplain extents.

The comparisons of the reach mass error rates to the standard deviation of the reach channel slope are shown in Figure 6.56. Again, there does not seem to be a significant

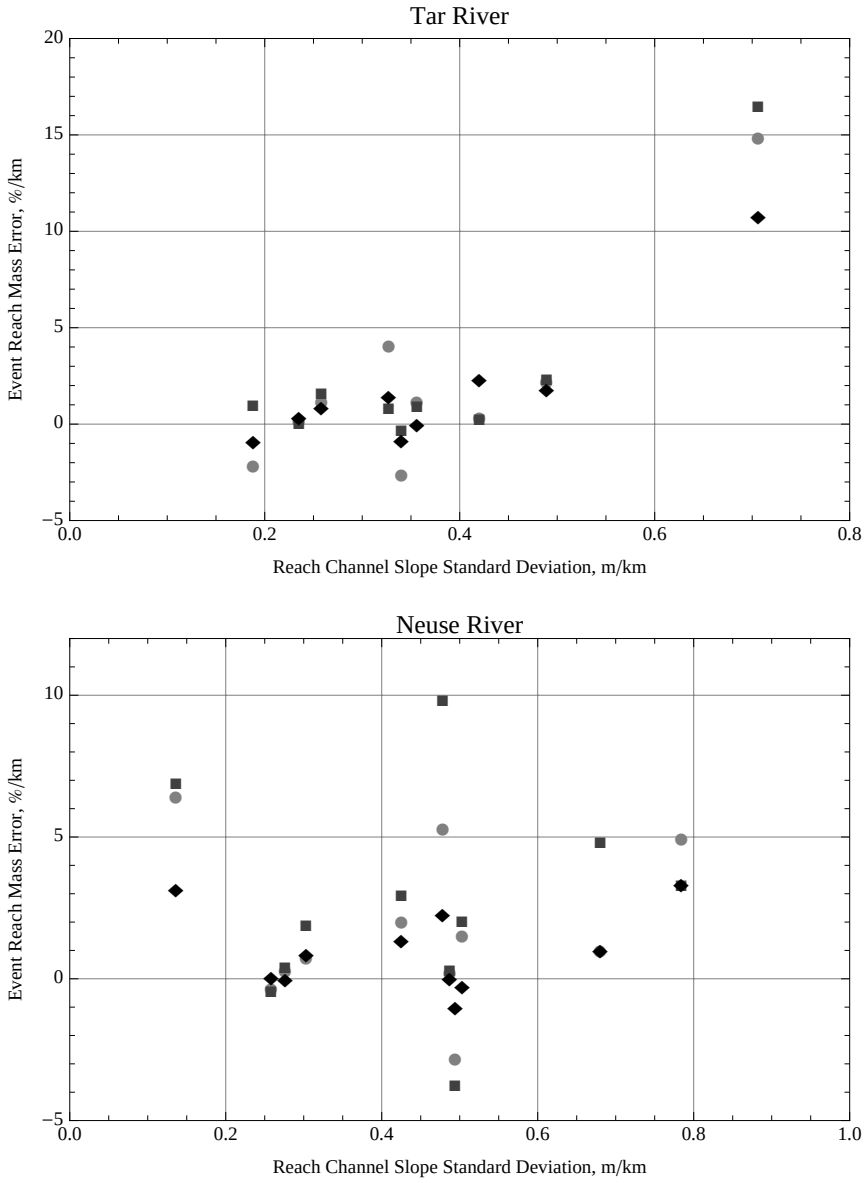

Figure 6.56 Reach mass error against standard deviation of channel slope for the Tar (top) and Neuse (bottom) River reaches for Hurricane Floyd (black diamonds), Hurricane Isabel (dark gray squares) and Tropical Storm Alberto (gray circles).

correlation. In fact, if the reach on the Tar River with the largest standard deviation is ignored, there is no distinct trend. A positive correlation based on the results for one reach does not seem justified. The results on the Neuse River support the findings for the Tar River. Specifically, there is not a discernible trend. As with the river slope, the standard deviation of the river slope is based on the representation of the Tar and Neuse Rivers in the ADCIRC grid, which may or may not be fair representation of the actual rivers. In fact, it is hard to imagine that the actual bottom slopes of the Tar and Neuse Rivers are accurately represented by the ADCIRC river bottom slopes. It is more likely that the floodplains are accurately represented in the ADCIRC grid than the main river. Attempting to characterize the floodplain based on the ADCIRC representation of the main river may not be meaningful.

6.6.4 Correlation Between Sinuosity and Mass Balance Error

A comparison of the event mass error to the sinuosity of the reaches is shown in Figure 6.57. Unlike the slope and standard deviation of the slope, the sinuosity of the rivers in ADCIRC is a reasonable representation of the actual sinuosity on the Tar and Neuse Rivers. As was the case for slope and standard deviation, there is not a significant pattern.

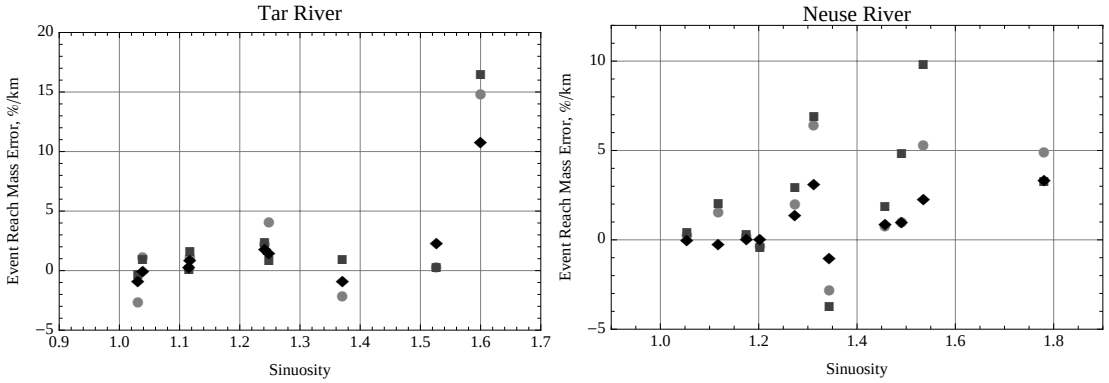

Figure 6.57 Reach mass error versus sinuosity of the channel for the Tar (left panel) and Neuse (right panel) River reaches for Hurricane Floyd (black diamonds), Hurricane Isabel (dark gray squares) and Tropical Storm Alberto (gray circles).

The relatively high rate of mass error in the most sinuous reach on the Tar River creates the illusion of an upward trend that is not supported by the rest of the data. For the results on the Neuse River, there appears to be a more widespread correlation between reach sinuosity and mass balance error. Generally, the more sinuous stretches of the Neuse River have more mass balance error.

6.6.5 Correlation Between Inundation Area and Mass Balance Error

The maximum extent of inundation for the Hurricane Floyd hindcast was shown previously in Figure 6.51. The inundation extent and cross-section locations were used to estimate the inundation area using the polygon feature in Google Earth Pro that allows the extents of inundation to be delineated and calculates the area extent inside the polygon. Then, the mass error per area was computed using the total discharge rates and the inundation area, A_{inun}, using (6.12).

$$\varepsilon_A = \frac{Q_{T_{end}} - Q_{T_{start}}}{A_{inun}} \tag{6.12}$$

It is worth noting that the inundation area includes the areal extent of the river under low flow conditions. However, the main channel width is small in comparison to the average inundation width, especially for an event like Hurricane Floyd (40 m versus 2 km). The ε_A values for each of the reaches on the Tar and Neuse Rivers can be seen in Figure 6.58.

The average inundation width was generally around 2 km. However, the reach with the smallest average inundation width (0.771 km), based on the inundation area and valley length, is the second reach on the Tar River. This is the reach with the largest mass error per valley length on either the Tar or the Neuse River. Additionally, there is a wide variation in

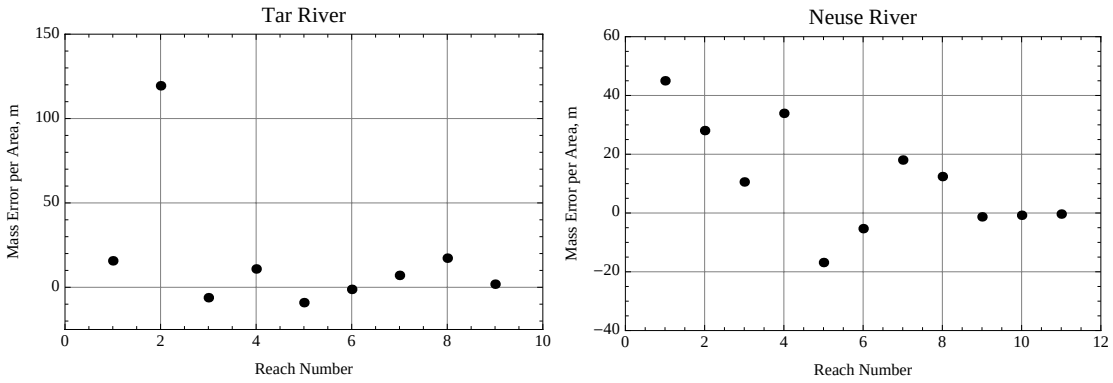

Figure 6.58 Mass error per inundation area for each reach on the Tar and Neuse River during the Hurricane Floyd hindcast.

mass error per area on both the Tar and Neuse Rivers, which suggests that the total inundation area is not a good indicator of mass balance error.

The limited amount of detailed analysis of mass balance river errors has been confined to idealized domains previously. Additionally, the analysis has focused on mass balance and relation to model instability. The first instance was a result of instability in attempts to use sequential wetting to wet an initially dry river. The second instance was during attempts to optimize parameter selection for river inundation simulations. In both cases, instability resulted as a consequence of sequential dam break-type wetting.

During the river initialization application, water entered at the boundary where there were initially wet elements (because the discharge boundary condition will not enter the domain if the boundary elements are dry). An idealized domain with a constant bottom slope was used, so the water travelled downstream, wetting elements during the propagation. However, over time, the amount of water immediately behind the wetting front would increase and, eventually, cause the simulation to terminate.

A similar problem resulted during the river inundation simulations. Again, an idealized channel was used. And, as long as the flow was confined to the main channel (which

was initialized wet) the mass balance during the simulation was close to perfect. However, when the flow rate was increased to initiate floodplain inundation, the inundation would move downstream along the floodplain and the water would build up behind the floodplain dam break wetting front. Eventually, the errors reached a level that cause the simulation to terminate.

The Tar and Neuse River systems are much more complex than the idealized domains. As such, they may have geometric irregularities that curb the sequential dam break wetting that causes simulation termination using the idealized grid. However, the mechanism causing mass balance error and instability in the idealized simulations may also be present in the simulations for coastal North Carolina. But, due to the non-idealized nature of the ADCIRC grid for simulations for North Carolina, the mechanism may be regulated by the local floodplain and channel geometry to maintain stability. The valley slope, standard deviation of channel slope, sinuosity and inundation extent may not be good indicators of sequential dam break locations that cause substantial mass balance errors.

6.6.6 Nash-Sutcliffe Efficiencies and Elevation Errors

Previously, the Nash-Sutcliffe efficiency values were reported for the Hurricane Isabel hindcast. The efficiencies were computed for the last 45 full days of the simulations for Hurricane Floyd and Tropical Storm Alberto and tabulated in Table 6.15, along with the values for the last 60 full days of the Hurricane Isabel hindcast. As with the results for Hurricane Isabel, the first four full days were ignored to allow the rivers time to spin-up. The Nash-Sutcliffe efficiency at Washington is not available for Hurricane Floyd because there are not USGS discharge values available for that time period. The results are fairly consistent from event to event. In general, the efficiency values are lower for locations

Table 6.15 Nash-Sutcliffe model efficiency coefficients for the Hurricane Floyd, Hurricane Isabel, and Tropical Storm Alberto hindcasts, at USGS discharge gauge locations on the Tar and Neuse Rivers within the ADCIRC domain.

USGS Gauge	02083500	02084000	02084472	02089500	02091814
Hurricane Floyd	0.751	0.731	N/A	-0.788	-0.272
Hurricane Isabel	0.832	0.423	-0.268	-1.27	-5.61
T.S. Alberto	0.922	0.748	-0.591	-1.72	-7.79

farther from the hand-off point. However, for Hurricane Floyd, the efficiency values are very close for the Tar River at Tarboro and Greenville and the efficiency is higher at Fort Barnwell than at Kinston.

Figure 6.59 shows a comparison of discharge results for Hurricane Floyd. The USGS daily mean discharge values (dots) and ADCIRC discharge values (lines) are shown. The results are similar for the two locations on the Tar River. There is underprediction ahead of the rising limb and slight overprediction of the peak flow. Then, the recession is too fast during the falling limb. The results for the Neuse River are significantly worse than the results for the Tar River. Some of this error is due to mass balance problems within the ADCIRC domain. However, the peak forcing (approximately 1200 cms) is also higher than the peak discharge at Kinston. Furthermore, the second peak seen in the ADCIRC discharge results at Kinston is a result of a second peak in the HL-RDHM boundary forcing.

The second HL-RDHM peak is error in the hydrologic model hindcast. Future work to quantify ADCIRC skill in riverine areas should incorporate information about error in boundary conditions provided by the hydrologic models. The hand-off points were not placed at USGS gauge locations, such as the Tar River at Tarboro, to allow those gauge

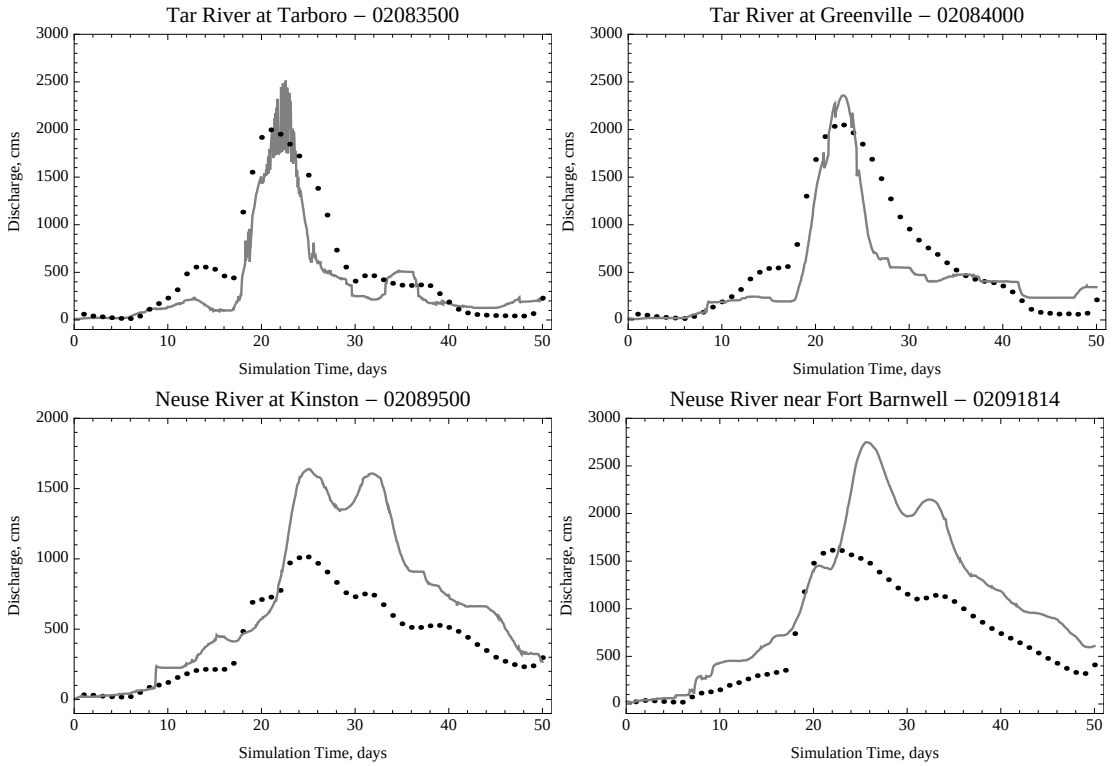

Figure 6.59 Hurricane Floyd hindcast comparison between ADCIRC results (lines) and USGS gauge location data (dots) for locations on the Tar and Neuse Rivers.

locations to be used as validation points for ADCIRC simulations. There are no actual discharge or water surface elevation values available at the hand-off points, but the accuracy of the boundary conditions provided can be assessed using stations upstream and downstream of the hand-off points on the rivers and tributaries.

The discharge comparisons for Tropical Storm Alberto are shown in Figure 6.60. The results are satisfactory at Tarboro. At Greenville, the peak is represented reasonably well, but there is overprediction of flow towards the end of the simulation that is less prevalent at Tarboro. The error in overprediction at Washington is significantly higher than the error at Greenville and is due to higher flow rates in ADCIRC at Washington, whereas the flow rates from the USGS stations are comparable. In other words, the actual flow rates at Greenville and Washington are similar, but ADCIRC has higher flows at Washington than

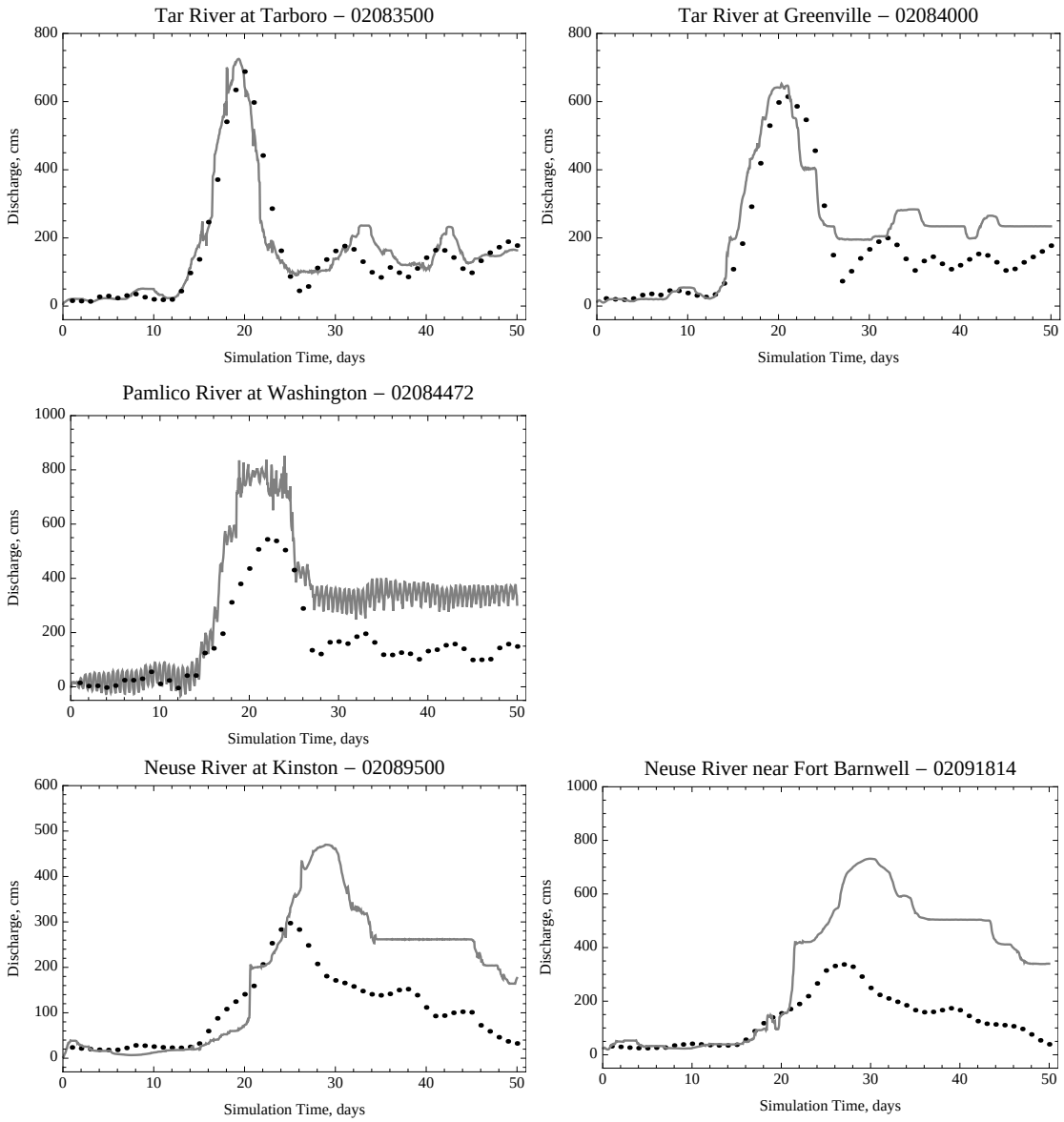

Figure 6.60 Tropical Storm Alberto hindcast comparison between ADCIRC results (lines) and USGS gauge location data (dots) for locations on the Tar and Neuse Rivers.

at Greenville, as a result of the mass balance error, which causes the larger discharge over-prediction at the Washington gauge location. The overprediction on the Neuse River is also a result of ADCIRC error, because the peak flow in the HL-RDHM boundary condition is comparable to the expected peak flow at Kinston.

The maximum elevation and inundation extent in the areas upstream of Kinston during the Tropical Storm Alberto hindcast are shown in Figure 6.61. In the middle of the

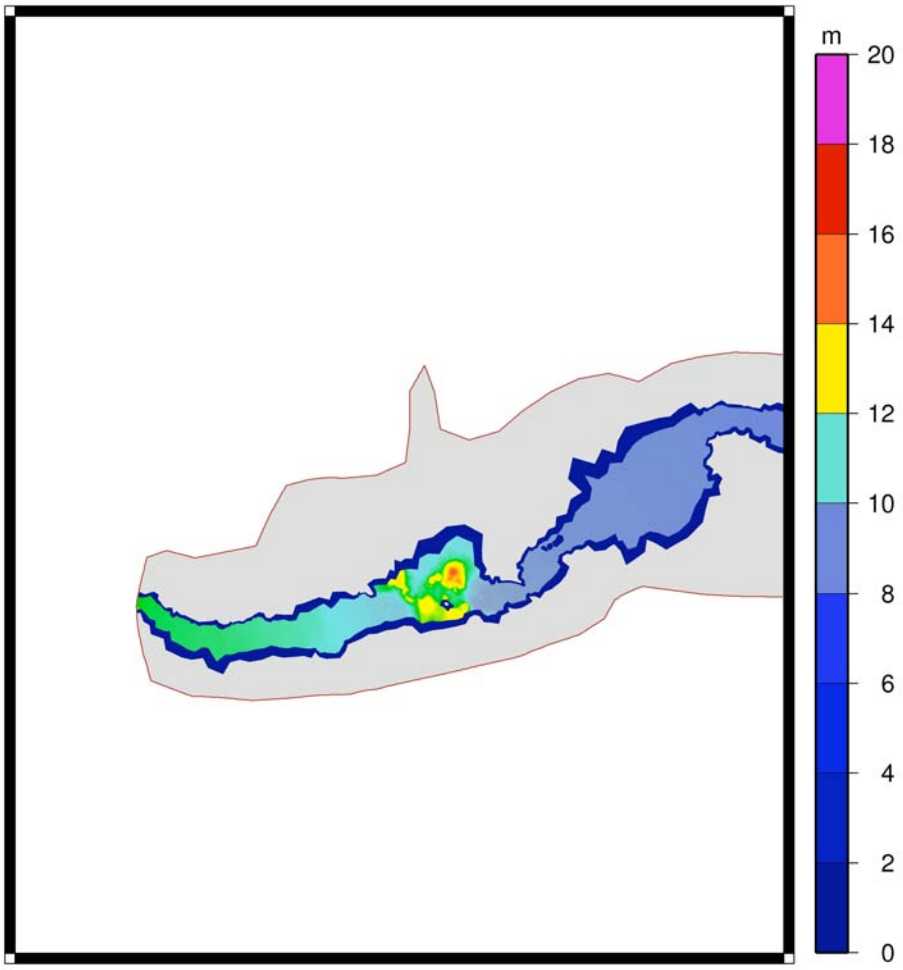

Figure 6.61 Maximum elevation during the ADCIRC hindcast of Tropical Storm Alberto for areas on the Neuse River upstream of Kinston.

image, there is an area of red and yellow that signifies maximum elevations that are much greater than the maximum elevations at other locations in the immediate vicinity. This particular location is on the outside of a horseshoe bend in a sinuous area. This elevation error may be at least partially responsible for the overpredicted flow rates downstream.

A quantitative analysis of the water surface elevation error throughout the simulation was not completed for two reasons. First, data is missing for different USGS gage locations at different times during the simulations. This difficulty could be overcome by estimating values for the missing points using the discharge value in conjunction with a

rating curve. The second reason is the larger obstacle. The water surface elevation results are coupled to the discharge results. Given the large amount of error in the discharge results, especially for the locations on the Neuse River, an error metric using only the water surface elevation results would not be particularly useful. Instead, comparison of rating curves using the USGS and ADCIRC data will be completed in the next section.

The water surface elevation results for select USGS gage locations for Hurricane Floyd and Tropical Storm Alberto are presented in Figure 6.62 and Figure 6.63, respectively. For Hurricane Floyd, the peak water surface elevation is underpredicted using ADCIRC for the three locations analyzed. The peak discharge for the Tar River was a good representation of the actual flow experienced during Floyd, so the underprediction in peak elevation means there is a problem with the ADCIRC grid. At the peak flow, ADCIRC

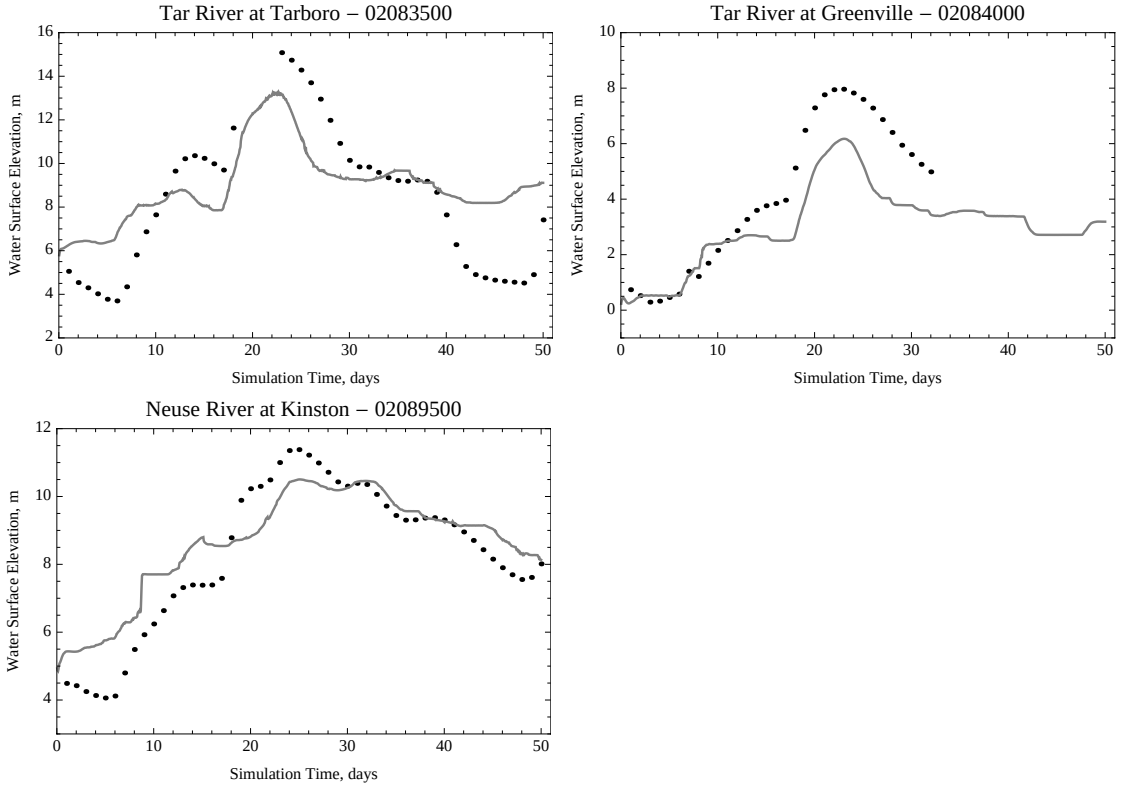

Figure 6.62 Hurricane Floyd hindcast comparison between ADCIRC water surface elevation results (lines) and USGS gage location data (dots) for locations on the Tar and Neuse Rivers.

underpredicts the water surface elevation by about 2 m. That amount of difference has large impacts on the amount of inundation. The inundation may be underpredicted, depending on the tool used to convert stage to inundation. The underprediction for the Neuse River at Kinston is worse than Figure 6.62 suggests. The underprediction is about 1 m. However, the peak flow in ADCIRC is significantly overpredicted. The elevation error would be much larger if the flow rate was represented more accurately.

The elevation results for Tropical Storm Alberto, Figure 6.63, show that ADCIRC underpredicts the elevation at Tarboro and Greenville for the peak flow rates. The results for the locations on the Neuse River are generally decent. The water surface elevation is too high at low flows, which is expected. However, the overprediction for the last half of the simulation is due, at least in part, to overpredicted discharge rates.

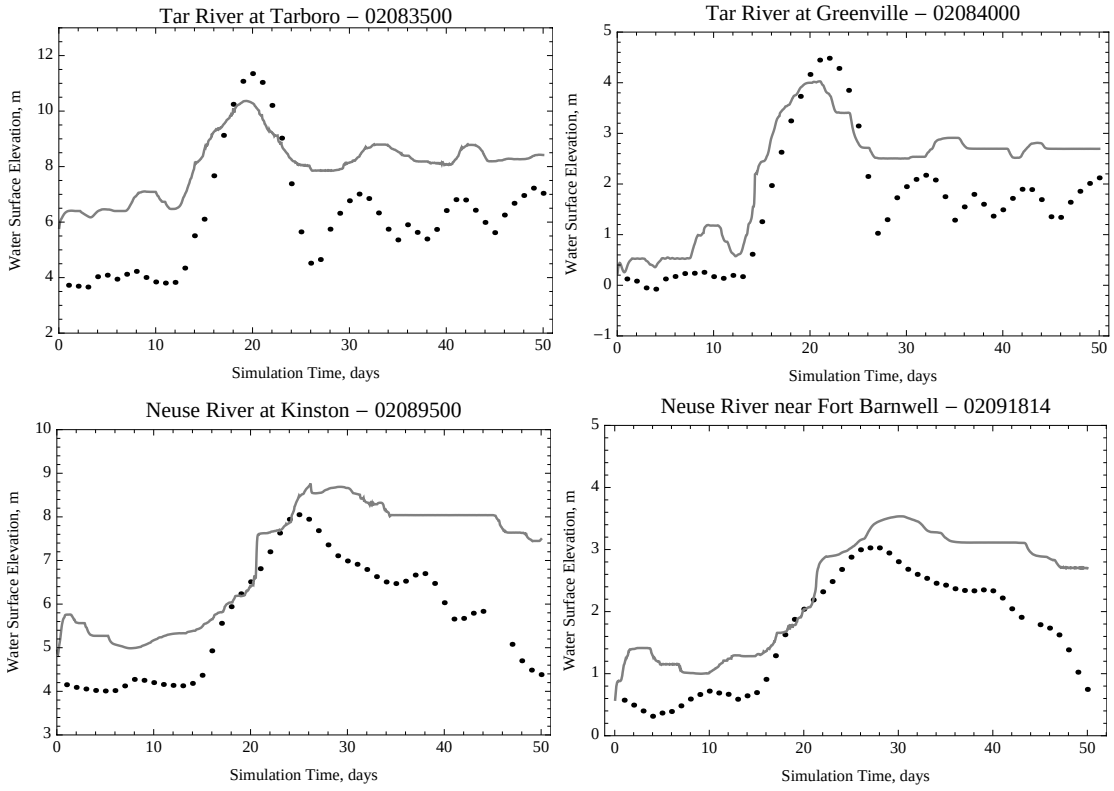

Figure 6.63 Tropical Storm Alberto hindcast comparison between ADCIRC water surface elevation results (lines) and USGS gage location data (dots) for locations on the Tar and Neuse Rivers.

6.6.7 Rating Curves at USGS Gage Locations

In order to isolate the error in water surface elevation predicted for a given flow rate, rating curves were developed from the USGS and ADCIRC data. Rating curves for the Neuse River at Kinston and Fort Barnwell were presented previously for the Isabel hindcast results. The left panels in Figure 6.64 shows the rating curves created using USGS mean daily values (black dots) and ADCIRC results (gray dots). The results for Hurricane Floyd were used to create the rating curves for Tarboro, Greenville and Kinston. Hurricane Floyd results were used because the results provided a larger range of values. The stage values were not available at Fort Barnwell for Hurricane Floyd, so the Hurricane Isabel results were used. As such, the rating curve for Fort Barnwell is a reproduction of the right panel in Figure 6.50, presented in the Hurricane Isabel hindcast section.

The idealized rating curve comparisons between curves based on uniform flow analysis of the ADCIRC grid and NCFMP sections are shown on the right side of Figure 6.64. The idealized comparison from the location closest to each of the USGS gauge locations was selected. It is worth noting that the water surface elevation is significantly underpredicted in ADCIRC for high flows at Tarboro, Greenville and Kinston. This result is consistent with the idealized analysis, which suggests ADCIRC will underpredict maximum water surface elevation for high flows, compared to the NCFMP elevations. The idealized results predict that the same underprediction would not occur at Fort Barnwell, although the lack of availability of water surface elevations for Hurricane Floyd makes evaluation of this prediction difficult.

The actual rating curves give insight into the skill of ADCIRC at predicting water surface elevations, if the flow rates are accurately represented. Generally, ADCIRC will

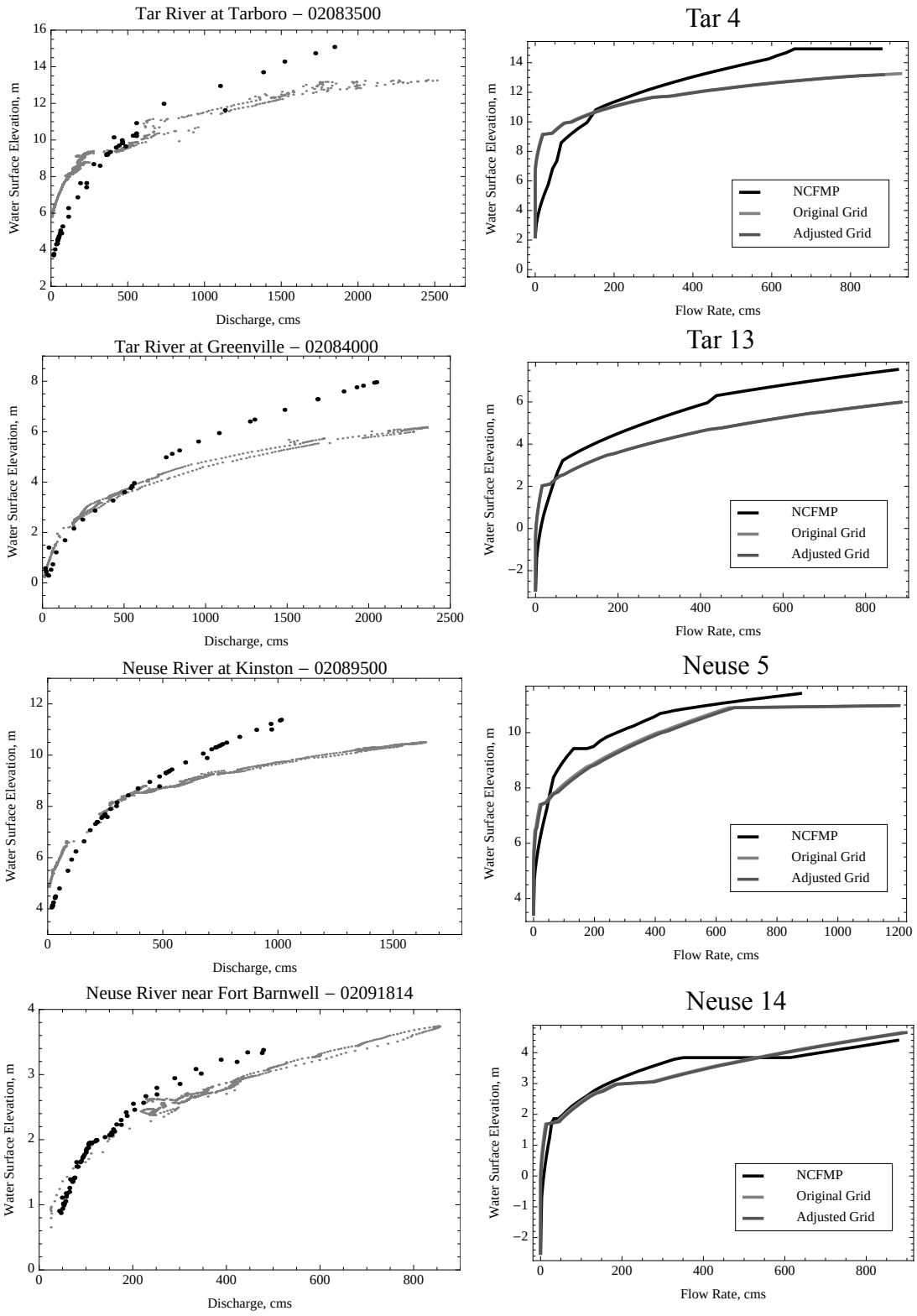

Figure 6.64 Comparison of actual USGS (black dots) and ADCIRC (gray dots) rating curves (left panels) to idealized NCFMP and ADCIRC rating curves for the Tar River (Tarboro, Greenville) and the Neuse River (Kinston, Fort Barnwell).

perform satisfactorily for flood flows as long as they are not too extreme. The elevation errors predicted by the rating curves are fairly low for flow rates of 100-500 cms. Additionally, the consistency between the actual rating curves and the idealized rating curves suggests the high-resolution NCFMP data could be used to improve the ADCIRC grid in the future. Furthermore, the NCFMP cross-sections could be used to generate rating curves to compare to ADCIRC results for stretches of the rivers that do not have USGS gauge locations.

6.7 Conclusions

A coupled model has been set up to model inundation in the Tar-Pamlico River/ Neuse River/Pamlico Sound area of coastal North Carolina. Results from a simulation using the tightly coupled ADCIRC+SWAN version of ADCIRC to hindcast Hurricane Isabel produce realistic water surface elevations and wave heights in the Atlantic Ocean, outer banks and at Washington at the mouth of the Tar-Pamlico River.

While the model was able to capture the waves and surge for Hurricane Isabel in the coastal areas of the domain, there is room for improvement in results for the river portion of the domain. The main problem is related to the current treatment of wetting and drying within ADCIRC. The current system requires elements to either be wet or dry. Elements cannot be partially wet. Therefore, it is not currently possible to match the actual river rating curves for the entire range of reasonable flows. The current ADCIRC grid overpredicts the water surface elevations at low flows.

Additionally, ADCIRC has mass balance problems. Specifically, for out-of-bank flows, the amount of mass grows with distance downstream. However, on the positive side,

ADCIRC is able to model flow in small rivers and obtain good mass balance near the boundary for specified river boundary forcings. Additionally, the modeled water surface elevations are generally fairly good for relatively high flows, which are the flow rates of concern for this modeling effort.

CHAPTER 7. Summary and Future Work

7.1 Summary

Near the end of Chapter 1, the impetus for this study related to use of ADCIRC for modeling inundation in the coastal plain was presented:

> *The hypothesis driving this work is that systematic improvements and additions to the ADCIRC hydrodynamic model can improve forecasting and hindcasting of coastal flood inundation, as well as be useful in future studies of theoretical storms.*

The work completed for and presented in this dissertation culminated in the Hurricane Isabel hindcast that demonstrated the capability of ADCIRC to model total water level and storm surge inundation in coastal North Carolina. This application included use of a variable G formulation and discharge boundary conditions on the Tar and Neuse Rivers from HL-RDHM.

The effects of the numerical parameter, G, on ADCIRC solutions are investigated in Chapter 2, Chapter 3 and Chapter 4. In Chapter 2, constant G values, a variable G formula based on dispersion analysis by *Atkinson et al.* [2004], and a variable G formula suggested by Westerink (based on experience modeling with ADCIRC) were applied to a variety of test cases. Additionally, Fourier analysis was applied to analyze the propagation characteristics of ADCIRC. The results show elevation fields, velocity fields and mass residuals are all impacted by specification of G. Furthermore, similar results can be obtained between constant and variable G specifications, with lower average G values for

the variable G simulations, by selectively increasing G for certain nodes at certain instances of time. However, the analysis in Chapter 2 did not result in the generation of an optimal parameterization of G.

The failure of the analysis in Chapter 2 to yield the desired final product, an automated routine for computing variable G that can be effectively applied to a wide range of applications, was a catalyst for the analysis in Chapter 3 and Chapter 4, which focus on the application of the forward sensitivity method to 1-D ADCIRC. Unlike Fourier and dispersion analysis, the forward sensitivity method is applicable to non-linear systems.

In Chapter 3, the forward sensitivity method, which has not previously been applied to GWCE-based shallow water models, is applied to the linearized version of 1-D ADCIRC with constant G parameterization. The linear, constant G case was chosen for the initial analysis due to its relative simplicity. The analysis shows spurious, short-wavelength oscillations appear in the nodal sensitivity results when G is set too high. Spurious, short-wavelength oscillations result from application of the continuous Galerkin finite element method to the primitive continuity and momentum equations; use of the GWCE alleviates the presence of the oscillations as long as G is not too high. As G is increased too much, a threshold is exceeded that results in the presence of spurious oscillations. Additionally, by combining the computed sensitivities with errors between the model results and observations, corrections can be calculated. In this work, the data assimilation process consisted of generating least-squares corrections.

The forward sensitivity method analysis in Chapter 3 is extended to a three-coefficient, variable G parameterization for non-linear 1-D ADCIRC in Chapter 4. The elevation and velocity sensitivities to the coefficients in the G parameterization are analyzed. Addi-

tionally, mass residual sensitivity to G is assessed. Least-squares corrections based on results and sensitivities are computed.

The results from Chapter 3 and Chapter 4 show the elevation and velocity sensitivity to G generally decrease as G increases; increases to coefficients that increase G also decrease sensitivities. Eventually, as G gets too high, spurious oscillations are generated. Both of these facets of the sensitivities have implications for the least-squares corrections that are generated. The decrease in sensitivity to G as G increases results in undercorrections when G is lower than the optimal value and overcorrections when G is higher than the optimal value. However, as long as the initial G value is not too far away from the target value, the target value can be recovered using sequential optimization.

When G causes the GWCE to become "too primitive," the sensitivities are no longer representative of the change in the fields (elevations and velocities) with G on a larger scale. Thus, the least-squares corrections generated using the sensitivities may be erroneous, in that they do not result in G being corrected towards the target value. For some G values, the sensitivities for consecutive nodes are 180 degrees out-of-phase, i.e., the sensitivities at one node are positive when the sensitivities at the next node are negative and vice-versa. The errors compared to observations, however, do not follow the same trend; the errors are often still fairly consistent. The least-squares corrections for G, based on the errors and sensitivities, have opposite signs for those nodes. Thus, understanding of the system under investigation is essential when attempting to correct G using the data assimilation step in the FSM.

The analysis of sensitivity of mass residuals to G in Chapter 4 shows the forward sensitivity method is effective for computing sensitivity of mass residuals. Additionally,

least-squares corrections to G can be computed that result in decreased local mass balance error. However, changes to G that cause a decrease in mass residual for one element do not necessarily result in decreased local mass error throughout the domain, or even immediately adjacent to the element where the decrease occurs.

The last two chapters focus on model coupling; the end goal of the coupling was to have a hydrologic model coupled to ADCIRC to produce total water level predictions for coastal inundation. The 1-D coupling analysis in Chapter 5 suggested the utility of one-way coupling from a hydrologic model to ADCIRC using discharge boundary conditions at a hand-off point upstream of major backwater effects. ADCIRC produced better elevation and velocity results when discharge was used as the upstream boundary condition than when elevations from the channel routing model were specified. Additionally, as long as the hand-off point was upstream of major backwater effects, the complexity of the momentum equation in the channel routing algorithm did not greatly impact ADCIRC results for the coupled model. Therefore, the 2-D coupled modeling in Chapter 6 was completed with ADCIRC handling areas affected by storm surge inundation and receiving discharge values, from a hydrologic model using kinematic wave routing, at the river boundaries in the grid.

The 2-D studies show promising results for discharge boundary conditions in ADCIRC as a way of incorporating hydrologic model results to model total water level in the coastal plain. The discharge is applied to the main river nodes to avoid potential mass balance problems resulting from the lateral extent of the river (at the boundary) not being known throughout the simulation a priori. Analysis of the discharge through cross-sections in the first few kilometers inside the boundary show the specified discharge rate is accu-

rately brought into the ADCIRC domain. Furthermore, the Hurricane Isabel hindcast results show ADCIRC accurately models total water level along the outer banks of North Carolina and in the Pamlico Sound at the end of the Tar-Pamlico River. Unfortunately, severe mass balance errors, due to the wet/dry algorithms operating within the river portion of the ADCIRC domain, detract from the utility of the coupled system because the water surface elevation and discharge values are overpredicted in areas downstream from the hand-off points, such as Greenville, Kinston and Fort Barnwell. The deficiencies in the current system point to areas for future research.

7.2 Future Work

As was the case with this dissertation, the future work can be divided into two main sections. First, extension of the FSM to the 2-D ADCIRC model would allow the sensitivity of elevations, velocity and mass residual to G to be analyzed in more realistic domains. Additionally, the impact of different geometric (e.g., grid size) and flow (e.g., bottom friction and vorticity) variables within a G parameterization could be assessed. Furthermore, the elevation data available would allow for meaningful data assimilation and parameter correction estimation.

While parameter estimation for the variable G formulation is an interesting and important topic, the more pressing area of concern is mass balance in rivers. Analyses point to the current wetting and drying implementation as the culprit for the mass balance errors. The current ADCIRC system uses a step-wise wetting and drying procedure [*Luettich* 1995; *Dietrich* 2004]. An element is treated as either completely wet or completely dry, and elements become wet when a sufficient water surface gradient is reached. While results are

generally adequate for the flooding-type wetting applications most commonly encountered in ADCIRC applications, the Tar and Neuse Rivers are subject to both flooding-type wetting and dam break-type wetting. Dam break-type wetting occurs when the water is moving from a location of higher elevation to a location of lower elevation, while flooding-type wetting is the opposite situation.

Partially wet elements have been successfully incorporated into shallow water codes [*Bates* 1999; *Defina* 1994, 2000; *Hervouet* 1999]. Partially wet element implementations utilize a scaling parameter on the accumulation term of the continuity equation that results in a physically-realistic relationship between accumulation and water depth in an element. Partially wet elements may be useful in representing low flows in rivers because the entire elements are not required to be wet. Initial 1-D testing shows promising results for flooding-type wetting in ADCIRC using partially wet elements, and simulations have also produced reasonable results for 1-D dam break-type wetting using mass balance as the criterion for flood propagation [*Dick* 2011]. Both flooding- and dam break-type wetting and drying are necessary for accurate representation of rivers in ADCIRC.

References

Abbott M.B., Bathurst J.C., Cunge J.A., O'Connell P.E., Rasmussen J., 1986a. An introduction to the European Hydrological System-Système Hydrologique Européen, "SHE", 1: History and philosophy of a physically-based, distributed modelling system. *Journal of Hydrology*, 87(1-2): 45-59.

Abbott M.B., Bathurst J.C., Cunge J.A., O'Connell P.E., Rasmussen J., 1986b. An introduction to the European Hydrological System-Système Hydrologique Européen, "SHE", 2: Structure of a physically-based, distributed modelling system. *Journal of Hydrology*, 87(1-2): 61-77.

Atkinson J.H., Westerink J.J., Hervouet J.M., 2004. Similarities between the quasi-bubble and the generalized wave continuity equation solutions to the shallow water equations. *International Journal for Numerical Methods in Fluids*, 45(7): 689-714.

Bales J.D, 2003. Effects of Hurricane Floyd inland flooding, September-October 1999, on tributaries to Pamlico Sound, North Carolina, *Estuaries and Coasts*, 26(5): 1319-1328.

Bales J.D., Oblinger C.J., Sallenger A.H., 2000. Two months of flooding in eastern North Carolina, September-October 1999: Hydrologic, water-quality, and geologic effects of Hurricanes Dennis, Floyd, and Irene. USGS Water Resources Investigations Report 00-4093. 4 April 2011 <http://pubs.usgs.gov/wri/wri004093/flooding.html>.

Bates P.D., Anderson M.G., 1993. A two-dimensional finite-element model for river flow inundation. In *Proceedings of the Royal Society London A: Mathematical, Physical, and Engineering Sciences*, 440(1909): 481-491.

Bates P.D., De Roo A.P.J., 2000. A simple raster-based model for flood inundation simulation. *Journal of Hydrology,* 236(1-2): 54-77.

Bates P.D., Hervouet J.M., 1999. A new method for moving-boundary hydrodynamic problems in shallow water. In *Proceedings of the Royal Society London A: Mathematical, Physical, and Engineering Sciences*, 455: 3107-3128.

Bates P.D., Stewart M.D., Siggers G.B., Smith C.N., Hervouet J.M., Sellin R.J.H., 1998. Internal and external validation of a two-dimensional finite element code for river flood simulations. In *Proceedings of the Institute of Civil Engineers, Water Maritime and Energy*, 130: 127-141.

Bedient P.B., Holder A., Benavides J.A., Vieux B.E., 2003. Radar-based flood warning

system applied to Tropical Storm Allison. *Journal of Hydrologic Engineering,* 8(6): 308-318.

Bedient P.B., Huber W.C., 2002. *Hydrology and Floodplain Analysis: 3rd Edition*. Prentice-Hall Inc., Upper Saddle River, New Jersey.

Blanton B.O., Luettich R.A., 2008. North Carolina coastal flood analysis system model grid generation. Technical Report TR-08-05, RENCI Technical Report Series: 18 p.

Brunner G.W., 2001. *HEC-RAS River Analysis System: Hydraulic Reference Manual, Version 3.0*.

Brunner G.W., 2002. *HEC-RAS River Analysis System: User Manual, Version 3.1*.

Bunya S., Dietrich J.C., Westerink J.J., Ebersole B.A., Smith J.M., Atkinson J.H., Jensen R., Resio D.T., Luettich R.A., Dawson C., Cardone V.J., Cox A.T., Powell M.D., Westerink H.J., Roberts H.J., 2010. A high-resolution coupled riverine flow, tide, wind, wind wave and storm surge model for southern Louisiana and Mississippi: Part I - Model development and validation. *Monthly Weather Review*, 138: 345-377.

Carpenter T.M., Georgakakos K.P., 2004. Continuous streamflow simulation with the HRCDHM distributed hydrologic model. *Journal of Hydrology*, 298(1-4): 61-79.

Carpenter T.M., Georgakakos K.P., 2006. Intercomparison of lumped versus distributed hydrologic model ensemble simulations on operational forecast scales. *Journal of Hydrology*, 329(1-2): 174-185.

Chaudhry M.H., 1993. *Open-Channel Flow*. Prentice-Hall Inc., Englewood Cliffs, New Jersey.

Chen F., Didhia J., 2001. Coupling an advanced land surface-hydrology model with the Penn State-NCAR MM5 modeling system; Part 1: Model implementation and sensitivity. *Monthly Weather Review*, 129(4): 569-585.

Dawson C., Kubatko E.J., Westerink J.J., Trahan C., Mirabito C., Michoski C., Panda N., 2010. Discontinuous Galerkin methods for modeling hurricane storm surge. *Advances in Water Resources*, in-press.

Defina, A., 2000. Two-dimensional shallow flow equations for partially dry areas. *Water Resources Research*, 36(11): 3251-3264.

Defina, A., D'Alpaos L., Matticchio B., 1994. "A new set of equations for very shallow water and partially dry areas suitable to 2D numerical models." In *Modelling Flood Propagation Over Initially Dry Areas (ed. P. Molinaro and L. Natale)*, ASCE, New York: 72-81.

Dick C.G., 2011. *Implementation and analysis of a new wetting and drying framework for*

GWCE-based hydrodynamic models. Master's thesis, University of Oklahoma.

Dietrich J.C., Bunya S., Westerink J.J., Ebersole B.A., Smith J.M., Atkinson J.H., Jensen R., Resio D.T., Luettich R.A., Dawson C., Cardone V.J., Cox A.T., Powell M.D., Westerink H.J., Roberts H.J., 2010a. A high-resolution coupled riverine flow, tide, wind, wind wave and storm surge model for southern Louisiana and Mississippi: Part II - Synoptic description and analyses of Hurricanes Katrina and Rita. *Monthly Weather Review*, 138: 378-404.

Dietrich J.C., Kolar R.L., Dresback K.M., 2008. Mass residuals as a criterion for mesh refinement in continuous Galerkin shallow water models. *Journal of Hydraulic Engineering*, 134(5): 520-532.

Dietrich J.C., Kolar R.L., Luettich R.A., 2004. Assessment of ADCIRC's wetting and drying algorithm. *Developments in Water Science*, 55: 1767-1778.

Dietrich J.C., Zijlema M., Westerink J.J., Holthuijsen L.H., Dawson C., Luettich R.A., Jensen R., Smith J.M., Stelling G.S., Stone G.W., 2010b. Modeling hurricane waves and storm surge using integrally-coupled, scalable computations. *Coastal Engineering*, (in-review).

Dresback K.M., 2005. *Algorithmic improvements and analyses of the generalized wave continuity equation based model, ADCIRC*. Ph.D. dissertation, University of Oklahoma.

Dresback K.M., Kolar R.L., Blain C.A., Szpilka C.M., Luettich R.A., Shay T., 2010. Development and applications of the coupled HYCOM and ADCIRC system. In Spaulding, editor, *ECM 11 Conference Proceedings*: 259-277.

Fang Z., Bedient P.B., Benavides J., Zimmer A.L., 2008. Enhanced radar-based flood alert system and floodplain map library. *Journal of Hydrologic Engineering*, 13(10): 926-938.

Feldman A., H.E.C. (US), 2000. *Hydrologic Modeling System HEC-HMS: Technical Reference Manual*. US Army Corps of Engineers, Hydrologic Engineering Center.

Fleming J.G., Fulcher C.W., Luettich R.A., Estrade B.D., Allen G.D., Winer H.S., 2008. A real time storm surge forecasting system using ADCIRC. In Spaulding, editor, *ECM 10 Conference Proceedings*: 893-912.

Fritz H.M., Blount C., Sokoloski R., Singleton J., Fuggle A., McAdoo B.G., Moore A., Grass C., Tate B., 2007. Hurricane Katrina storm surge distribution and field observations on the Mississippi Barrier Islands. *Estuarine, Coastal and Shelf Science*, 74(1-2): 12-20.

Frohn L.M., Christensen J.H., Brandt J., 2002. Development of a high-resolution nested air pollution model: The numerical approach. *Journal of Computational Physics*, 179(1):

68-94.

Galland J.C., Goutal N., Hervouet J.M., 1991. TELEMAC: A new numerical model for solving shallow-water equations. *Advances in Water Resources*, 14(3): 138-148.

Gutro R., 2009. NASA - Hurricane Season 2009: Hurricane Ida (Atlantic Ocean). NASA's Goddard Space Flight Center. 24 March 2011 <www.nasa.gov/mission_pages/hurricanes/archives/2009/h2009_Ida.html>.

Hagen S.C., Westerink J.J., Kolar R.L., 2000. One-dimensional finite element grids based on a localized truncation error analysis. *International Journal for Numerical Methods in Fluids*, 32: 241-261.

Hervouet J.M., Janin J.M., 1994. "Finite element algorithms for modeling flood propagation." In *Modelling Flood Propagation Over Initially Dry Areas (ed. P. Molinaro and L. Natale)*, ASCE, New York: 102-108.

Hervouet J.M., Van Haren L., 1996. Recent advances in numerical methods for fluid flows. In *Floodplain Processes (ed. Anderson et al.)*, Wiley, Chichester: 183-214.

Horritt M.S., Bates P.D., 2002. Evaluation of 1D and 2D numerical models for prediction river flood inundation. *Journal of Hydrology*, 268(1-4): 87-99.

Hydrology Laboratory (HL), 2008. *Hydrology Laboratory - Research Distributed Hydrologic Model (HL-RDHM) User Manual*. National Weather Service, Office of Hydrologic Development, Hydrology Laboratory, v.2.4.2.

Kinnmark I.P.E., 1986. The Shallow Water Wave Equations: Formulations, Analysis and Applications. Volume 15 of *Lecture Notes in Engineering* (ed. C.A. Brebbia and S.A. Orszag)15. Springer-Verlag, Berlin, 187 pp.

Kolar R.L., Westerink J.J., 2000. A look back at 20 years of gwc-based shallow water models. In *Proceedings of the XIII International Conference on Computational Methods in Water Resources*, Calgary, Alberta, Canada: 899-906.

Kolar R.L., Westerink J.J., Cantekin M.E., Blain C.A., 1994. Aspects of nonlinear simulations using shallow water models based on the wave continuity equation. *Computers and Fluids* 23(3): 523-538.

Koren V.S., Reed S., Smith M., Zhang Z., Seo D.J., 2004. Hydrology laboratory research modeling system (HL-RMS) of the U.S. National Weather Service. *Journal of Hydrology*, 291(3-4): 297-318.

Kubatko E.J., Westerink J.J., Dawson C., 2006. *hp* Discontinuous Galerkin methods for advection dominated problems in shallow water flow. *Computer Methods in Applied Mechanics and Engineering*, 196(1-3): 437-451.

Lakshmivarahan S., Lewis J.M., 2010. Forward Sensitivity Approach to Dynamic Data Assimilation. *Advances in Meteorology*: 12 p.

Lewis J.M., Lakshmivarahan S., Dhall S.K., 2006. *Dynamic Data Assimilation: A Least-Squares Approach*. Cambridge University Press.

Luettich R.A., Westerink J.J., 1995. Implementation and testing of elemental flooding and drying in the ADCIRC hydrodynamic model. Technical report, Final report for the Department of Army, Contract Number DACW39-94-M-5869.

Luettich R.A., Westerink J.J., 2004. Formulation and numerical implementation of the 2D/3D ADCIRC finite element model version 44.XX. Technical report, Available on the web at <http://adcirc.org/adcirc_theory_2004_12_08.pdf>.

Luettich R.A., Westerink J.J., Scheffner N.W., 1992. ADCIRC: an advanced three-dimensional circulation model for shelves, coasts and estuaries; Report 1: Theory and methodology of ADCIRC-2DDI and ADCIRC-3DL. Technical Report DRP-92-6, Department of the Army, US Army Corps of Engineers, Waterways Experiment Station, Vicksburg, MS.

Lynch D.R., Gray W.G., 1979. A wave equation model for finite element tidal computations. *Computers and Fluids*, 7(3): 207-228.

Massey T.C., Blain C.A., 2005. In search of a consistent and conservative mass flux for the GWCE. *Computer Methods in Applied Mechanics and Engineering*, 195: 571-587.

Mattocks C., Forbes C., 2008. A real-time, event-triggered storm surge forecasting system for the state of North Carolina. *Ocean Modelling*, 25(3-4): 95-119.

Moreda F., Koren V., Zhang Z., Reed S., Smith M., 2006. Parameterization of distributed hydrological models: Learning from the experiences of lumped modeling. *Journal of Hydrology*, 320(1-2): 218-237.

Nash J.E., Sutcliffe J.V., 1970. River flow forecasting through conceptual models part I - A discussion of principles. *Journal of Hydrology*, 10(3): 282-290.

Ng B., Turner A., Tyler A.O., Falconer R.A., Millward G.E., 1996. Modelling contaminant geochemistry in estuaries. *Water Research*, 30(1): 63-74.

Pasch R.J., Kimberlain T.B., Stewart S.R., 1999. Preliminary report: Hurricane Floyd, 7-17 September, 1999. National Hurricane Center Document. 4 April 2011 <http://www.nhc.noaa.gov/1999floyd.html>.

Pritchard D.W., 1971. Two dimensional models. In Ward and Espey, editors, *Estuarine Modeling*, Water Quality Office, Environmental Protection Agency, NTIS Publication No. PB206-807.

Qu Y., 2005. *An integrated hydrologic model for multi-process simulation using semi-discrete finite volume approach*. Ph.D. dissertation, The Pennsylvania State University.

Qu Y., Duffy C.J., 2007. A semidiscrete finite volume formulation for multiprocess watershed simulation. *Water Resources Research*; 43: 18 p.

Reed S.M., Koren V., Smith M., Zhang Z., Moreda F., Seo D., DMIP Participants, 2004. Overall distributed model intercomparison project results. *Journal of Hydrology*, 298: 27-60.

Refsgaard J.C., Storm B., Refsgaard A., 1995. Recent developments of the Systeme Hydrologique Europeen (SHE) towards the MIKE SHE. *International Association of Hydrological Sciences*, 231: 427-434.

Rosgen D.L., Silvey H.L., 1996. *Applied River Morphology.* Wildland Hydrology, Pagosa Springs, Colorado.

Sherman L.K., 1932. Streamflow from rainfall by the unit-graph method. *Eng. News-Rec.*, 108: 501-505.

Smith M.B., Seo D., Koren V., Reed S., Zhang Z., Duan Q., Moreda F., Cong S., 2004. The distributed model intercomparison project (DMIP): Motivation and experiment design. *Journal of Hydrology*, 298(1-4): 4-26.

Szpilka CM, 2005. *Development and Analysis of Algorithmic Improvements for the ADCIRC Hydrodynamic Model*. Ph.D. dissertation, University of Oklahoma.

Tannehill J.C., Anderson D.A., Pletcher R.H., 1997. *Computational Fluid Mechanics and Heat Transfer: Second Edition*. Taylor & Francis, Philadelphia, Pennsylvania.

US Army Corps of Engineers (USACE), 2009. Performance Evaluation of the New Orleans and Southern Louisiana Hurricane Protection System, Final Report of the Interagency Performance Evaluation Task (IPET) Force.

Van Cooten S., Co-authors, 2011. The CI-FLOW Project: Tracking Precipitation from the Sky to the Summit to the Sea. *Bulletin of the American Meteorological Society*, in-review.

Velleux M.L., England J.F., Julien P.Y., 2006. *TREX Watershed Modeling Framework User's Manual: Model Theory and Description*. Colorado State University Department of Civil Engineering, Fort Collins, CO.

Vergara H.J., Hong Y., Gourley J.J., Zhang Y., Anagnostou E.N., 2010. Evaluating flood prediction skill of TMPA rainfall products over Tar River basin using a distributed hydrologic model. In *AGU Fall Meeting Abstracts*.

Vieux B.E., 2001. *Distributed Hydrologic Modeling Using GIS*, volume 38 of *Water Science and Technology Library*. Kluwer Academic Publishers.

Vieux B.E., Cui Z., Gaur A., 2004. Evaluation of a physics-based distributed hydrologic model for flood forecasting. *Journal of Hydrology*, 298(1-4): 155-177.

Vieux B.E., Vieux J.E., 2002. V*flo*: A real-time distributed hydrologic model. In *Proceedings of the 2nd Federal Interagency Hydrologic Modeling Conference*.

Westerink J.J., Luettich R.A., Scheffner N.W., 1994. ADCIRC: An advanced three-dimensional circulation model for shelves, coasts and estuaries; Report 2: User's manual for ADCIRC-2DDI. Technical Report DRP-92-6, Department of the Army, US Army Corps of Engineers, Waterways Experiment Station, Vicksburg, MS.

Westerink J.J., Luettich R.A., Feyen J.C., Atkinson J.H., Dawson C., Roberts H.J., Powell M.D., Dunion J.P., Kubatko E.J., Pourtaheri H., 2008. A basin- to channel-scale unstructured grid hurricane storm surge model applied to southern Louisiana. *Monthly Weather Review*, 136(3): 833-864.

Yeh G.T., Huang G., Zhang F., Cheng H.P., Lin H.C., 2005. WASH123D: A numerical model of flow, thermal transport, and salinity, sediment, and water quality transport in watershed systems of 1-D stream-river network, 2-D overland regime, and 3-D subsurface media. Technical report, Office of Research and Development, US Environmental Protection Agency.

Zijlema M., 2010. Computation of wind-wave spectra in coastal waters with SWAN on unstructured grids. *Coastal Engineering*, 57(3): 267-277.

Appendix A. Nomenclature

Symbols

Roman Letters

A	SWE system matrix for $k+1$ time level ($R^{2n \times 2n}$ where n is the number of nodes in the domain)
A	cross-sectional flow area for hydraulic routing
A_e	area of element
A_{JJW}	coefficient multiplier in Westerink variable G formula
B	SWE system matrix for time level k ($R^{2n \times 2n}$ where n is the number of nodes in the domain)
C	SWE system matrix for time level $k-1$ ($R^{2n \times 2n}$ where n is the number of nodes in the domain)
C_f	bottom friction coefficient
G	numerical parameter in the generalized wave continuity equation
H	sensitivity vector ($R^{n \times p}$ where n is the number of sensitivity values for each of the p parameters)
H	total fluid depth, equals $h + \zeta$
L	symbol for primitive continuity equation
$\mathbf{M}^{\mathrm{c}}$	symbol for primitive momentum equation, conservative form
Q_{net}	net flux out of the element
S_0	bottom slope for channel routing models
S_f	friction slope for channel routing
T	time period for wave period, except in the section for Fourier analysis of the finite difference approximation to the SWE
W	symbol for the wave continuity equation
W^G	symbol for the generalized wave continuity equation
c	vector of variables consisting of the water surface elevations and velocities (R^{2n} where n is the number of nodes in the domain)

e	error value calculated using one observation and one model result
$\mathbf{e}$	error vector defined as the difference between observations and model results, $\mathbf{e} = \mathbf{z} - \mathbf{c}$ (R^n where n is the length of the observation vector)
$\mathbf{f}$	Coriolis parameter, equals $2\Omega \sin\phi$
$\mathbf{f}_{bc}^{k+1}$	specified boundary forcing at time $k+1$ (R^{2n} where n is the number of nodes in the domain)
g	magnitude of gravity $\|\mathbf{g}\|$
h	bathymetry
h	depth of flow for channel routing models
j	spatial index
k	temporal index
k_n	coefficient in Manning's equation equal to 1.0 for units in meters and 1.49 for units in feet
m	the number of elements necessary to represent a wave
n	Manning's roughness value
P	wetted perimeter of channel cross-section
q	unit discharge equal to the product of velocity and depth, $q = uh$
R	hydraulic radius equal to the flow area divided by the wetted perimeter, $R = A/P$
t	time
u	depth-averaged velocity component in the x-coordinate direction
w	single sensitivity to G defined as $(\partial c_j^k)/(\partial G)$
$\mathbf{w}$	vector of sensitivity to G defined as $(\partial \mathbf{c}^k)/(\partial G)$ (R^{2n} where n is the number of nodes in the domain)
$\mathbf{v}$	velocity of the fluid in 2D u, v
x	Cartesian space coordinate
$\mathbf{z}$	observation vector (R^n where n is the number of observations)

Greek Letters

α_{JHA}	scaling factor for variable formula based on Quasi-Bubble
ε	lateral eddy viscosity
ε_d	nodal mass balance residual difference
ε_n	nodal mass balance residual
ε_v	mass balance residual

ζ	surface elevation above the datum
λ	propagation factor
λ'	discrete propagation factor
λ_d	amplification factor
τ	2D bottom friction term, which is determined from either a linear relationship or through the Chezy formulation
ω	wave frequency
θ	time-weighting parameter for Euler time stepping
θ_d	phase change per time step
σ	wave number
ψ	term to account for wind stress and atmospheric pressure variations in the momentum equation
ι	$\sqrt{-1}$

Special Symbols and Operators

∇	nabla (grad) operator
$\nabla\bullet$	divergence operator

Appendix B. Discrete Time Formulation for the Forward Sensitivity Method

B.1 Introduction

The discrete time formulation of the forward sensitivity method presented in this appendix is based on the work presented in *Lakshmivarahan and Lewis* [2010].

B.2 Model System

The system of equations for the 1-D version of ADCIRC, consisting of the generalized wave continuity and momentum equations, requires three time levels due to the second derivative of elevation with respect to time in the GWCE. The ADCIRC model equations can be written succinctly, as in (B.1), where $\beta \in R^{n \times n}$ is a coefficient matrix, $\mathbf{c}^k \in R^n$ is the solution vector consisting of the water surface elevations and depth-averaged velocities, $\alpha \in R^p$ is the control vector, and $M_1, M_2 : R^n \times R^p \rightarrow R^n$ are the components of the system at the current and past time levels.

$$\beta \mathbf{c}^{k+1} = M_1(\mathbf{c}^k, \alpha) + M_2(\mathbf{c}^{k-1}, \alpha) \qquad \textbf{(B.1)}$$

B.3 Forward Sensitivity Functions

The forward sensitivity functions for the discrete time system can be found by aggregating the individual components. To begin, consider the i^{th} component of (B.1), as

shown in (B.2), where β_i is the i^{th} row of the coefficient matrix β.

$$\beta_i \mathbf{c}^{k+1} = M_{1i}(\mathbf{c}^k, \alpha) + M_{2i}(\mathbf{c}^{k-1}, \alpha) \tag{B.2}$$

B.3.1 Sensitivity to the Control Vector

Differentiation with respect to the j^{th} component of the control vector, as in (B.3), results in (B.4), where the terms on the RHS are given by (B.5) and (B.6).

$$\frac{\partial}{\partial \alpha_j}(\beta_i \mathbf{c}^{k+1}) = \frac{\partial}{\partial \alpha_j}[M_{1i}(\mathbf{c}^k, \alpha) + M_{2i}(\mathbf{c}^{k-1}, \alpha)] \tag{B.3}$$

$$\sum_{r=1}^{n} \frac{\partial \beta_{ir}}{\partial \alpha_j} \cdot \mathbf{c}_r^{k+1} + \sum_{r=1}^{n} \beta_{ir} \cdot \frac{\partial \mathbf{c}_r^{k+1}}{\partial \alpha_j} = \frac{\partial M_{1i}(\mathbf{c}^k, \alpha)}{\partial \alpha_j} + \frac{\partial M_{2i}(\mathbf{c}^{k-1}, \alpha)}{\partial \alpha_j} \tag{B.4}$$

$$\frac{\partial M_{1i}(\mathbf{c}^k, \alpha)}{\partial \alpha_j} = \sum_{r=1}^{n} \frac{\partial M_{1i}(\mathbf{c}^k, \alpha)}{\partial \mathbf{c}_r^k} \cdot \frac{\partial \mathbf{c}_r^k}{\partial \alpha_j} + \frac{\partial M_{1i}(\mathbf{c}^k, \alpha)}{\partial \alpha_j} \tag{B.5}$$

$$\frac{\partial M_{2i}(\mathbf{c}^{k-1}, \alpha)}{\partial \alpha_j} = \sum_{r=1}^{n} \frac{\partial M_{2i}(\mathbf{c}^{k-1}, \alpha)}{\partial \mathbf{c}_r^{k-1}} \cdot \frac{\partial \mathbf{c}_r^{k-1}}{\partial \alpha_j} + \frac{\partial M_{2i}(\mathbf{c}^{k-1}, \alpha)}{\partial \alpha_j} \tag{B.6}$$

Defining the sensitivity of the solution to parameter α_j to be $\vartheta_{ij}^k = \frac{\partial \mathbf{c}_i^k}{\partial \alpha_j}$, (B.4) can be rewritten as (B.7).

$$\sum_{r=1}^{n} \frac{\partial \beta_{ir}}{\partial \alpha_j} \cdot \mathbf{c}_r^{k+1} + \sum_{r=1}^{n} \beta_{ir} \vartheta_{rj}^{k+1} = \sum_{r=1}^{n} \frac{\partial M_{1i}}{\partial \mathbf{c}_r^k} \vartheta_{rj}^k + \frac{\partial M_{1i}}{\partial \alpha_j} + \sum_{r=1}^{n} \frac{\partial M_{2i}}{\partial \mathbf{c}_r^{k-1}} \vartheta_{rj}^{k-1} + \frac{\partial M_{2i}}{\partial \alpha_j} \tag{B.7}$$

The equations can then be combined, as shown in (B.8), where $D_c(M_1) = \left[\frac{\partial M_{1i}}{\partial \mathbf{c}_r^k}\right] \in R^{n \times n}$ and $D_\alpha(M_1) = \left[\frac{\partial M_{1i}}{\partial \alpha_j}\right] \in R^{n \times p}$ are Jacobians of M_1 with respect to $\mathbf{c}$ and α, respectively.

$$D_\alpha(\beta \mathbf{c}^{k+1}) + \beta \vartheta^{k+1} = D_c(M_1)\vartheta^k + D_\alpha(M_1) + D_c(M_2)\vartheta^{k-1} + D_\alpha(M_2) \tag{B.8}$$

The updated sensitivity can be isolated by moving the first term on the LHS of (B.8) to the

RHS, resulting in (B.9).

$$\beta \vartheta^{k+1} = -D_\alpha(\beta \mathbf{c}^{k+1}) + D_c(M_1)\vartheta^k + D_\alpha(M_1) + D_c(M_2)\vartheta^{k-1} + D_\alpha(M_2) \qquad \textbf{(B.9)}$$

If the initial elevation and velocity fields do not depend on the control vector (i.e., $(\partial \mathbf{c}_i^0)/(\partial \alpha_j) = 0$), the initial conditions for the sensitivities are $\vartheta^{-1} = \vartheta^0 = 0$.

B.3.2 Sensitivity to the Initial Conditions

Generation of the equation for evolution of the sensitivity to the initial conditions follows the same procedure used to generate the equation for the sensitivity to the control vector. Differentiation of (B.2) with respect to the j^{th} element of the initial condition, $\mathbf{c}_j^0$, results in (B.10).

$$\sum_{r=1}^{n} \beta_{ir} \cdot \frac{\partial \mathbf{c}_r^{k+1}}{\partial \mathbf{c}_j^0} = \sum_{r=1}^{n} \frac{\partial M_{1i}(\mathbf{c}^k, \alpha)}{\partial \mathbf{c}_r^k} \cdot \frac{\partial \mathbf{c}_r^k}{\partial \mathbf{c}_j^0} + \sum_{r=1}^{n} \frac{\partial M_{2i}(\mathbf{c}^{k-1}, \alpha)}{\partial \mathbf{c}_r^{k-1}} \cdot \frac{\partial \mathbf{c}_r^{k-1}}{\partial \mathbf{c}_j^0} \qquad \textbf{(B.10)}$$

This expression contains fewer terms than the equation for the evolution of the sensitivity to the control vector because the elements of the control are assumed to be independent of the initial conditions. Defining the sensitivity of an element of the solution to an element of the initial condition as $\omega_{ij}^k = (\partial \mathbf{c}_i^k)/(\partial \mathbf{c}_j^0)$ allows the equations to be aggregated in matrix form as (B.11).

$$\beta \omega^{k+1} = D_c(M_1)\omega^k + D_c(M_2)\omega^{k-1} \qquad \textbf{(B.11)}$$

In this case, the initial conditions for the sensitivities are identity matrices, i.e. $\omega^{-1} = \omega^0 = I$.

B.4 Model Errors

Let $z_j^k \in R$ be an observation at time level k and spatial location j. The observation

is a function of the true state of the system, $\hat{\mathbf{c}}$, as well as the unobservable noise in the system. This is shown in (B.12), where $h(\hat{\mathbf{c}})$ is the mapping from the model space to the observation space and v_j^k is the noise in the observation.

$$z_j^k = h(\hat{\mathbf{c}}) + v_j^k \tag{B.12}$$

For the studies included in this dissertation, the observations are values from model output. Thus, the noise in the observations is negligible, so (B.12) reduces to (B.13).

$$z_j^k = h(\hat{\mathbf{c}}) \tag{B.13}$$

Furthermore, the model output for the simulation to generate observations is taken as the true state of the system. Therefore, there is a direct mapping from the model space to the observation space, i.e. $z_j^k = c_j$. For the case of observations at m time levels at spatial location j, the observation vector is $\mathbf{z}_j \in R^m$.

B.4.1 Error Based on One Observation

The model error, e_j^k, is found by computing the difference between the observation and the model predicted value, $h(\mathbf{c})$, as shown in (B.14).

$$e_j^k = z_j^k - h(\mathbf{c}) \tag{B.14}$$

However, there is a direct mapping from the model space to the observation space. Therefore, the model-predicted value is just a value from the model at the appropriate combination of space and time, $h(\mathbf{c}) = c_j^k$, and the model error is given by (B.15).

$$e_j^k = z_j^k - c_j^k \tag{B.15}$$

B.4.2 Error Based on Multiple Observations at One Spatial Location

For spatial location j, the model error vector based on observations and model

results at m time levels is given by (B.16), where $\mathbf{c}_j, \mathbf{e}_j, \mathbf{z}_j \in R^m$.

$$\mathbf{e}_j = \mathbf{z}_j - \mathbf{c}_j \tag{B.16}$$

B.5 First-Order Corrections

Using a standard Taylor series expansion, the change, Δf, in the solution $f(t) = f(t, a)$ resulting from a change in a of δa is given by (B.17), where $\delta^j f$ is the j^{th} variation of $f(t)$.

$$\Delta f = f(t, a + \delta a) - f(t, a) = \sum_j \delta^j f \tag{B.17}$$

Analysis in this dissertation is limited to first-order analysis, with Δf approximated by the first variation, δf, i.e., $\Delta f \approx \delta f$.

The evolution of the ADCIRC model results depends on the initial conditions and control parameters. Thus, $\mathbf{c}^k = \mathbf{c}(t, \mathbf{c}^0, \alpha)$. Therefore, at a given time, the change in the model state depends on perturbations to both the initial conditions and the control vector, as shown in (B.18), where $D_{c^0}(\mathbf{c}) \in R^{n \times n}$ and $D_\alpha(\mathbf{c}) \in R^{n \times p}$ are the Jacobians of the model state with respect to the initial condition and the control vector, respectively.

$$\Delta \mathbf{c} \approx \delta \mathbf{c} = D_{c^0}(\mathbf{c}) \delta \mathbf{c}^0 + D_\alpha(\mathbf{c}) \delta \alpha \tag{B.18}$$

However, these Jacobians are simply the sensitivity functions presented previously.

B.5.1 Corrections Based on One Observation

The goal of the correction process is to generate a correction to eliminate the model error, i.e. $\delta c_j^k = e_j^k$. Applying (B.18) to a given error value, at node j and time k, results in (B.19), where the j subscript on the Jacobian indicates the j^{th} row of each respective

Jacobian matrix.

$$e_j^k = D_{c^0{}_j}(\mathbf{c}^k)\delta\mathbf{c}^0 + D_{\alpha_j}(\mathbf{c}^k)\delta\alpha \tag{B.19}$$

(B.19) can be rewritten as (B.20), where $\mathbf{H}_j^k = [D_{c^0{}_j}(\mathbf{c}^k), D_{\alpha_j}(\mathbf{c}^k)]$ and $\varsigma = [(\delta\mathbf{c}^0)^T, (\delta\alpha)^T]^T$.

$$e_j^k = \mathbf{H}_j^k\varsigma \tag{B.20}$$

The correction vector, ς, is given by solution of the inverse problem. The least-squares solution is given by (B.21).

$$\varsigma_{LS} = [(\mathbf{H}_j^k)^T(\mathbf{H}_j^k)]^{-1}(\mathbf{H}_j^k)^T e_j^k \tag{B.21}$$

B.5.2 Corrections Based on Multiple Observations at One Location

Frequently, multiple observations are available at a given spatial location. One example is the collection of the temporal evolution of water surface elevation values measured by a tidal gauge. As before, the goal of the correction process is to generate a correction to minimize model error. Applying (B.18) to error values at node j results in (B.22), where $\mathbf{H}_{1_j}$ and $\mathbf{H}_{2_j}$ are given by (B.23) and (B.24), respectively.

$$\mathbf{e}_j = \mathbf{H}_{1_j}\delta\mathbf{c}^0 + \mathbf{H}_{2_j}\delta\alpha \tag{B.22}$$

$$\mathbf{H}_{1_j} = [(D_{c^0{}_j}(\mathbf{c}^{t_1}))^T, (D_{c^0{}_j}(\mathbf{c}^{t_2}))^T, \ldots, (D_{c^0{}_j}(\mathbf{c}^{t_N}))^T]^T \tag{B.23}$$

$$\mathbf{H}_{2_j} = [(D_{\alpha_j}(\mathbf{c}^{t_1}))^T, (D_{\alpha_j}(\mathbf{c}^{t_2}))^T, \ldots, (D_{\alpha_j}(\mathbf{c}^{t_N}))^T]^T \tag{B.24}$$

(B.22) can be rewritten as (B.25), where $\mathbf{H}_j = [\mathbf{H}_{1_j}, \mathbf{H}_{2_j}]$ and $\varsigma = [(\delta\mathbf{c}^0)^T, (\delta\alpha)^T]^T$.

$$\mathbf{e}_j = \mathbf{H}_j\varsigma \tag{B.25}$$

The correction vector, ς, is given by solution of the inverse problem. The least-squares

solution is given by (B.26).

$$\varsigma_{LS} = [(\mathbf{H}_j)^T(\mathbf{H}_j)]^{-1}(\mathbf{H}_j)^T\mathbf{e}_j \quad \textbf{(B.26)}$$

Appendix C. Forward Sensitivity Method Results for Linear 1-D ADCIRC with Constant G

C.1 Linear Sloping Domain

C.1.1 Elevation and Elevation Sensitivity Results

The results presented in this section are for four different simulations on the linear sloping domain. All the simulations utilized a constant G value of $0.001\ s^{-1}$. Additionally, the simulations were performed using the explicit version of ADCIRC. The difference between the simulations was the number of nodes used to discretize the domain and, thus, the element size. The base domain consists of 21 nodes (20 elements). The three other domains had 11, 41 and 81 nodes, respectively.

The elevation results are shown in Figure C.1 and Figure C.2. There are eight lines on each plot. The four solid lines are the elevation results for the different simulations, which have units of m. The four dashed lines are the corresponding elevation sensitivity results which have units of ms. The black, dark gray, gray and light gray lines are for the 11, 21, 41 and 81 node simulations, respectively. Additionally, the node number listed on each of the panels is the node number associated with the 21 node grid. For instance, in the sixth panel of Figure C.1, the label is "Node 11." The results are for the 6th, 11th, 21st and 41st nodes in the 11, 21, 41 and 81 node domains.

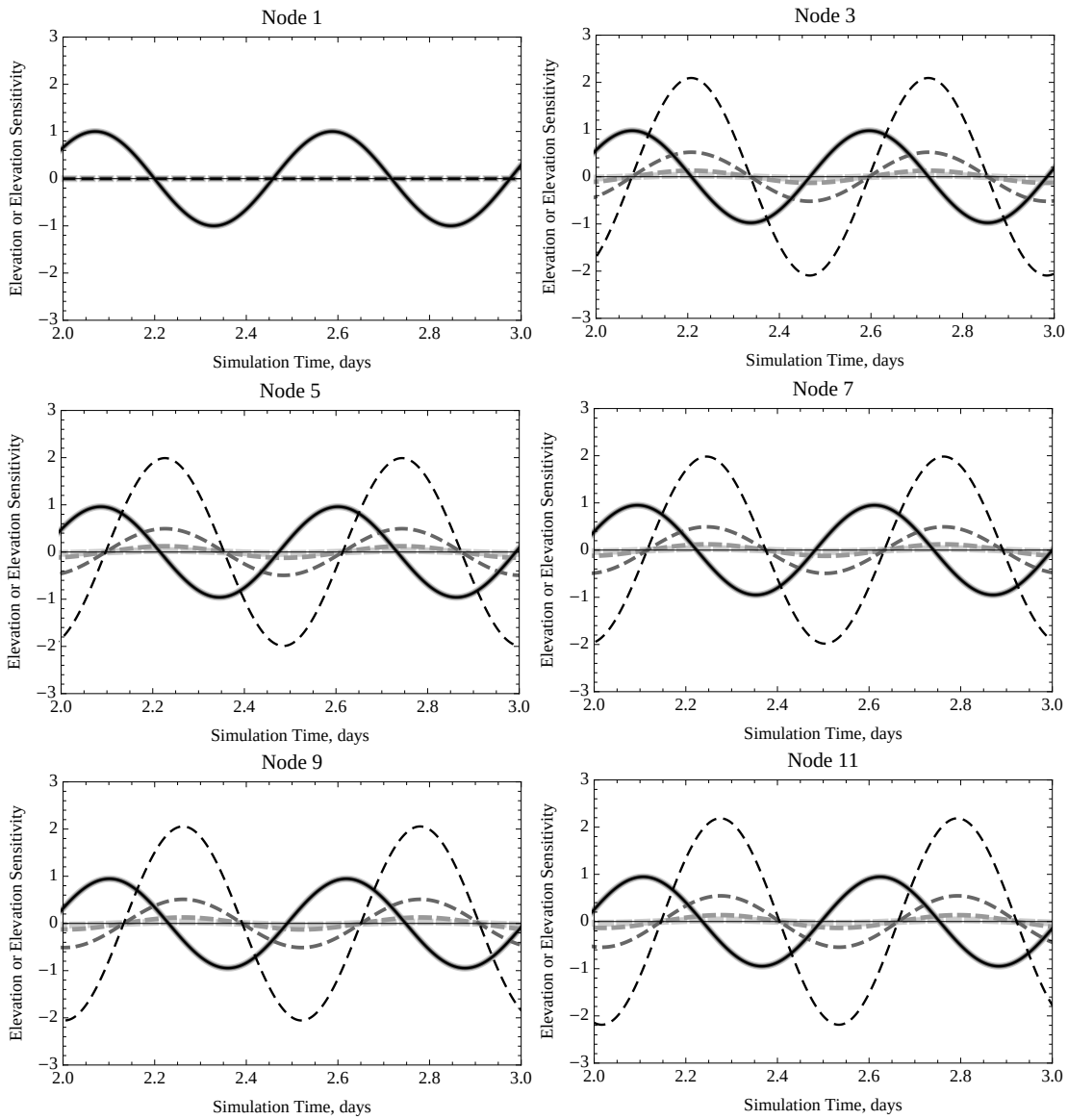

Figure C.1 Elevation and elevation sensitivity results for a simulation on the linear sloping domain using a G value of 0.001 s^{-1}. The solid lines depict the elevation results, which have units of m. The dashed lines show the temporal evolution of the sensitivity of the elevation to G. The units for elevation sensitivity to G are ms. The node number listed in the title for each panel is the node number in the 21 node grid associated with a given location (i.e., a fixed coordinate). The black lines are for results from the 11 node grid. The dark gray, gray and light gray lines depict results from the 21, 41 and 81 node grids, respectively.

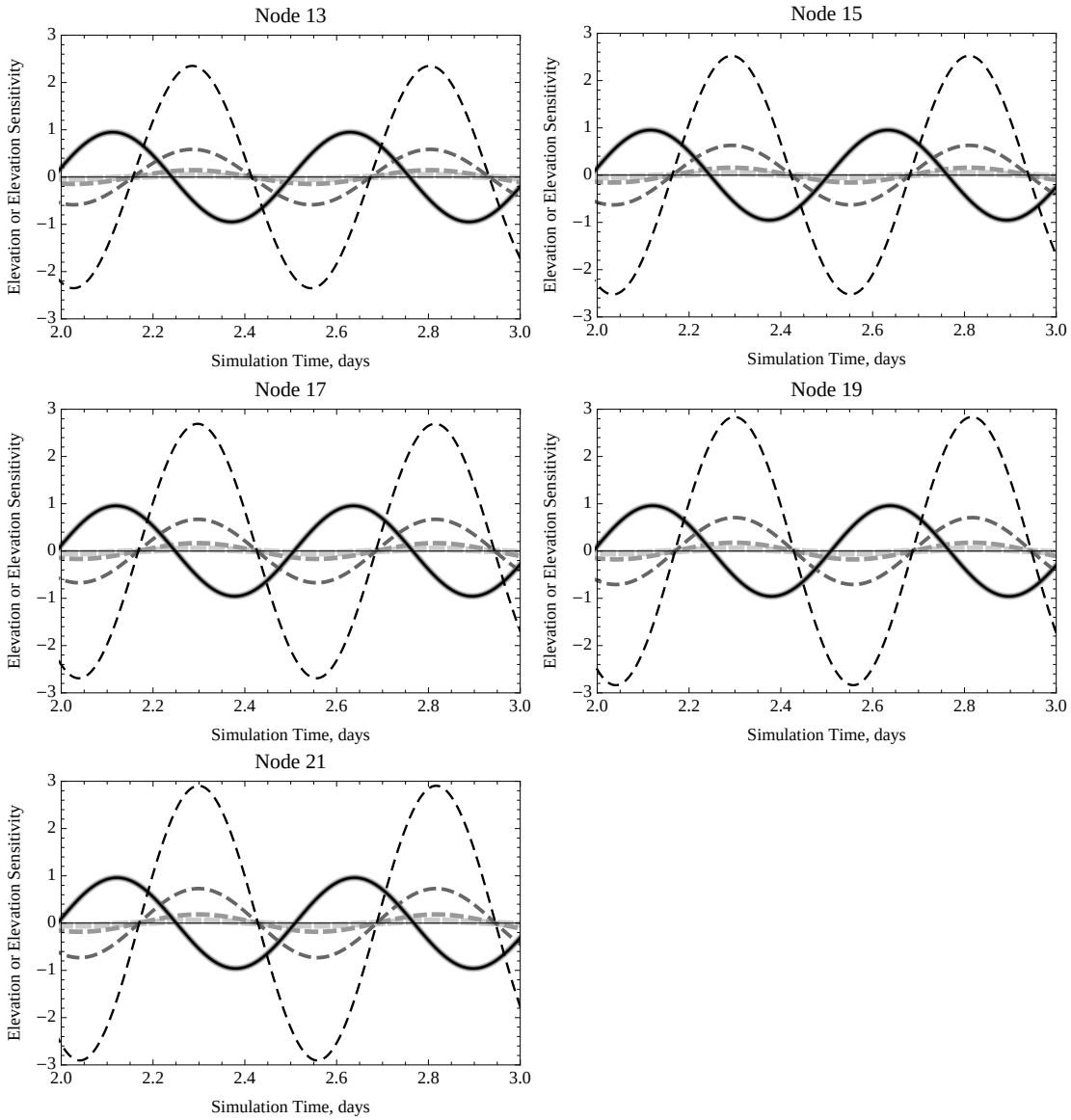

Figure C.2 Elevation and elevation sensitivity results for a simulation on the linear sloping domain using a G value of 0.001 s^{-1}. Specifics about the panels can be found in the caption for Figure C.1.

C.1.2 Velocity and Velocity Sensitivity Results

The results presented in this section are for four different simulations on the linear sloping domain. All the simulations used a constant G value of $0.001\ s^{-1}$. The difference between the simulations was the number of nodes used to discretize the domain and, thus, the element size. The base domain consists of 21 nodes (20 elements). The three other

domains had 11, 41 and 81 nodes, respectively.

The results are shown in Figure C.3 and Figure C.4. There are eight lines on each plot. The four solid lines are the velocity results for the different simulations, which have units of m/s. The four dashed lines are the corresponding velocity sensitivity results which have units of m. The black, dark gray, gray and light gray lines are for the 11, 21, 41 and 81 node simulations, respectively. Additionally, the node number listed on each of the panels is the node number associated with the 21 node grid. For instance, in the sixth panel of Figure C.3, the label is "Node 11." The results are for the 6th, 11th, 21st and 41st nodes in the 11, 21, 41 and 81 node domains.

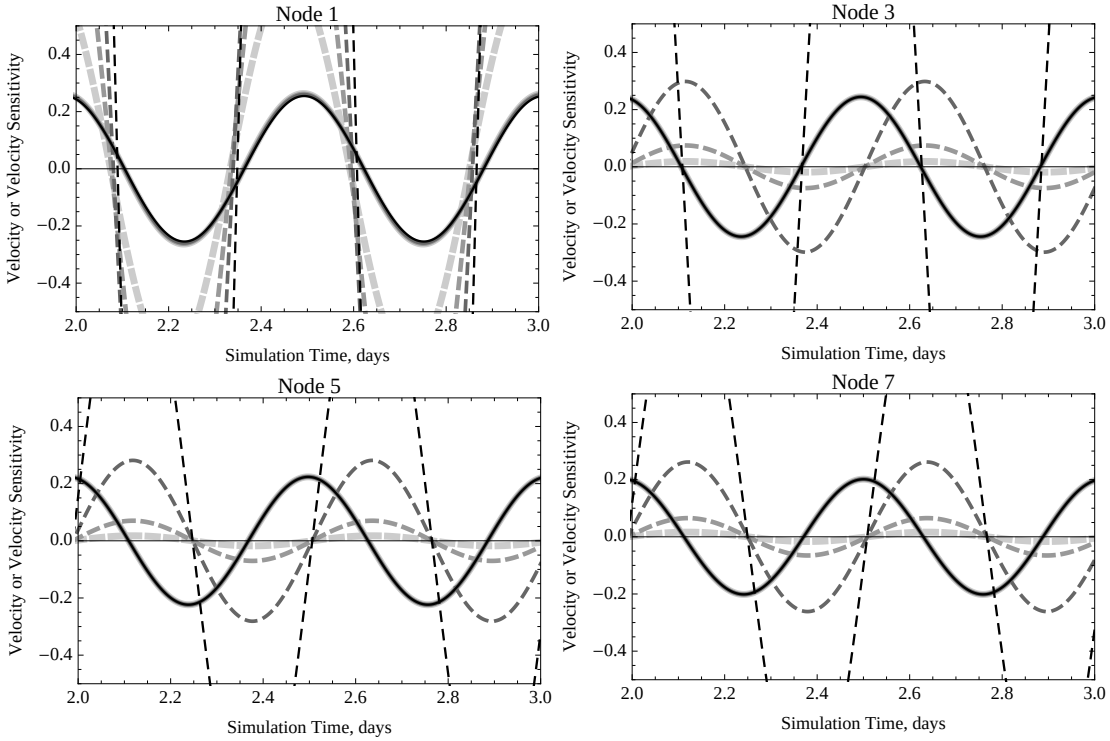

Figure C.3 Velocity and velocity sensitivity results for a simulation on the linear sloping domain using a *G* value of 0.001 s^{-1}. The solid lines depict the velocity results, which have units of m / s. The dashed lines show the temporal evolution of the sensitivity of the velocity to *G*. The units for velocity sensitivity to *G* are m. The node number listed in the title for each panel is the node number in the 21 node grid associated with a given location (i.e., a fixed coordinate). The black lines are for results from the 11 node grid. The dark gray, gray and light gray lines depict results from the 21, 41 and 81 node grids, respectively.

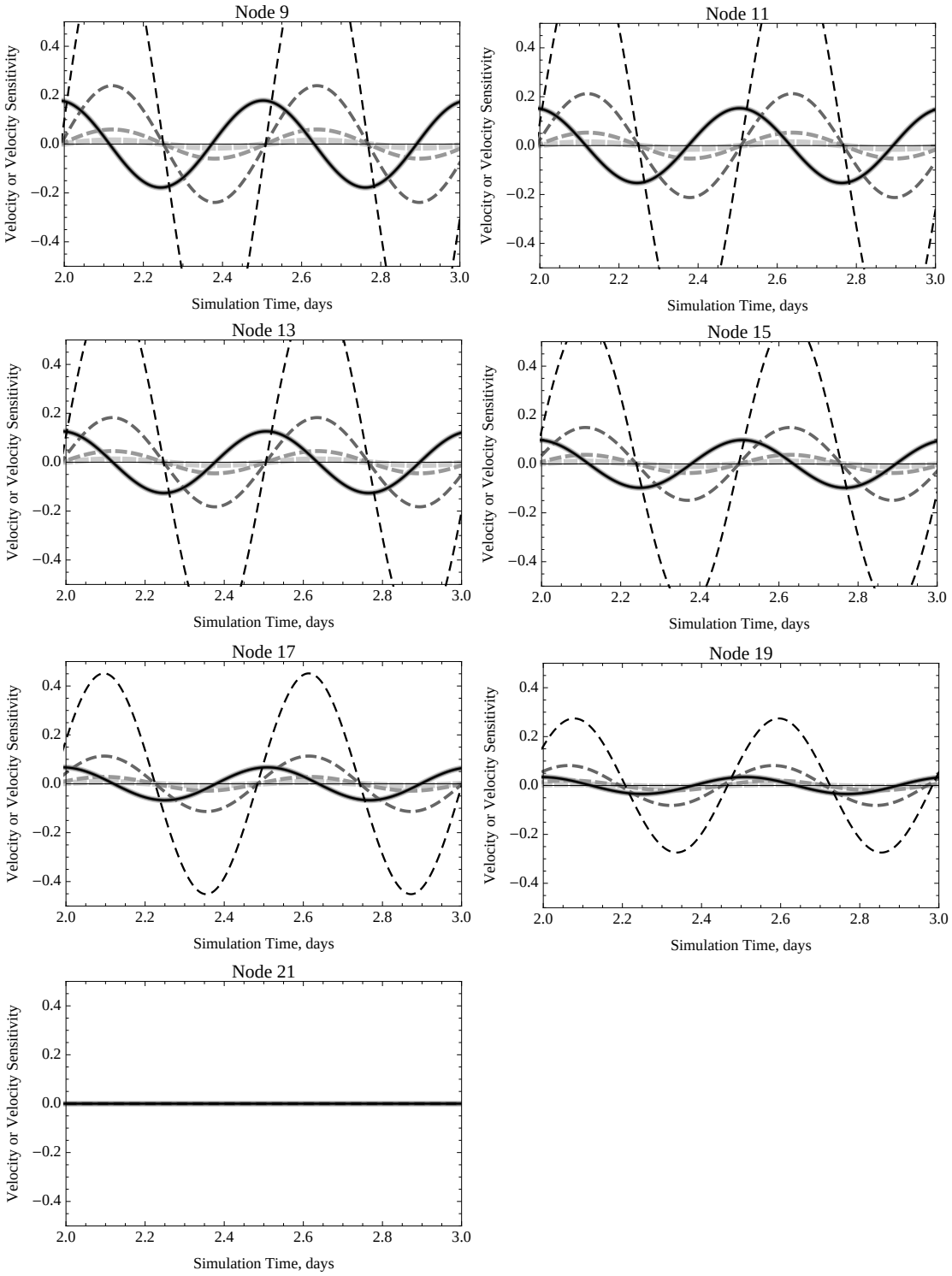

Figure C.4 Velocity and velocity sensitivity results for a simulation on the linear sloping domain using a G value of 0.001 s^{-1}. Specifics about the panels can be found in the caption for Figure C.3.

C.2 Seamount Domain Using "Non-Primitive" G Value

C.2.1 Elevation and Elevation Sensitivity Results

The results presented in this section are for three different simulations on variations of the seamount domain. All the simulations used the explicit version of the code with a constant G value of $0.001\ s^{-1}$. The difference between the simulations was the number of nodes used to discretize the domain and, thus, the element size. The base domain consists of 31 nodes (30 elements). The two other domains had 16 and 61 nodes, respectively. The time step for these simulations was 1 s. This allowed the explicit code to be stable at a G value that was not stable with a time step of 5 s.

The elevation results are shown in Figure C.5, Figure C.6 and Figure C.7. There are six lines on each plot. The three solid lines are the elevation results for the different simulations, which have units of m. Note that the water surface elevation values have been multiplied by 10 so it is easier to see the temporal (within a given panel) and spatial (comparing panels) variation in the results. The three dashed lines are the corresponding elevation sensitivity results which have units of ms. The elevation sensitivities are not scaled. The black, dark gray and light gray lines are for the 16, 31 and 61 node simulations, respectively. Additionally, the node number listed on each of the panels is the node number associated with the 31 node grid. For instance, in the sixth panel of Figure C.15, the label is "Node 11." The results are for the 6th, 11th and 21st nodes in the 16, 31 and 61 node domains.

Unlike in the linear sloping domain case presented earlier, there are instances where geometry of the domain varies slightly between the coarsest grid and the two finer grids. The break points between the sections for the original grid are at node 1, 11, 16, 21, 26 and

31. These correspond to nodes 1, 21, 31, 41, 51 and 61 for the grid with 61 nodes. However, for the grid with just 16 nodes, the break points occur at nodes 1, 6, 9, 11, 14 and 31. In the grid with 16 nodes, node 9 is the first node on the seamount. On the original grid, node 16 is the first node on the seamount. The x-position of node 9 in the 16-node grid is the same as node 17 in the 31-node grid. For the comparisons, the break points were used as controls, so the graph labeled "Node 16" consists of results from node 9, node 16 and node 31 for the three grids. Comparisons are made for each of the points in the coarsest domain. The point used from the 31 node grid is the closest node corresponding to the same location along a given linear stretch. The node from the 61 node grid is the node from the same x-position as the node from the 31 node grid.

C.2.2 Velocity and Velocity Sensitivity Results

The results presented in this section are for three different simulations on variations of the seamount domain. All the simulations were with a constant G value of 0.001 s^{-1}. The difference between the simulations was the number of nodes used to discretize the domain and, thus, the element size. The base domain consists of 31 nodes (30 elements). The two other domains had 16 and 61 nodes, respectively.

The velocity results are shown in Figure C.8, Figure C.9 and Figure C.10. There are six lines on each plot. The three solid lines are the velocity results for the different simulations, which have units of m/s. As with the elevations, the velocities are multiplied by 10. The three dashed lines are the corresponding velocity sensitivity results (not scaled) which have units of m. The black, dark gray and light gray lines are for the 16, 31 and 61 node simulations, respectively. Additionally, the node number listed on each of the panels is the node number associated with the 31 node grid. For instance, in the sixth panel of

Figure C.18, the label is “Node 11.” The results are for the 6th, 11th and 21st nodes in the 16, 31 and 61 node domains.

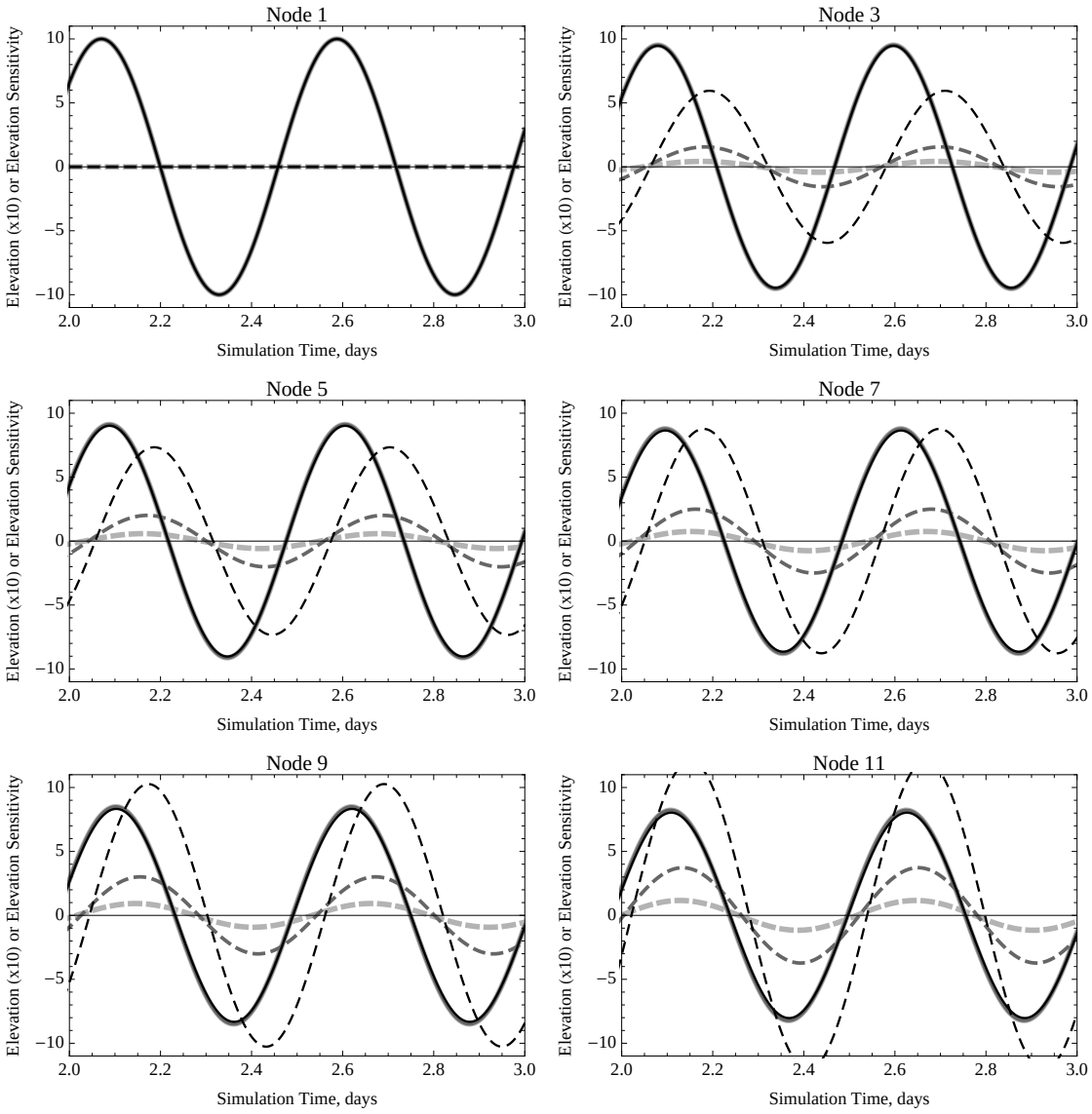

Figure C.5 Elevation and elevation sensitivity results for a simulation on the seamount domain using a *G* value of 0.001 s^{-1}. The solid lines depict the elevation results, which have units of m. The dashed lines show the temporal evolution of the sensitivity of the elevation to *G.* The units for elevation sensitivity to *G* are ms. The node number listed in the title for each panel is the node number in the 31 node grid associated with a given location (i.e., a fixed coordinate). The black lines are for results from the 16 node grid. The dark gray and light gray lines depict results from the 31 and 61 node grids, respectively.

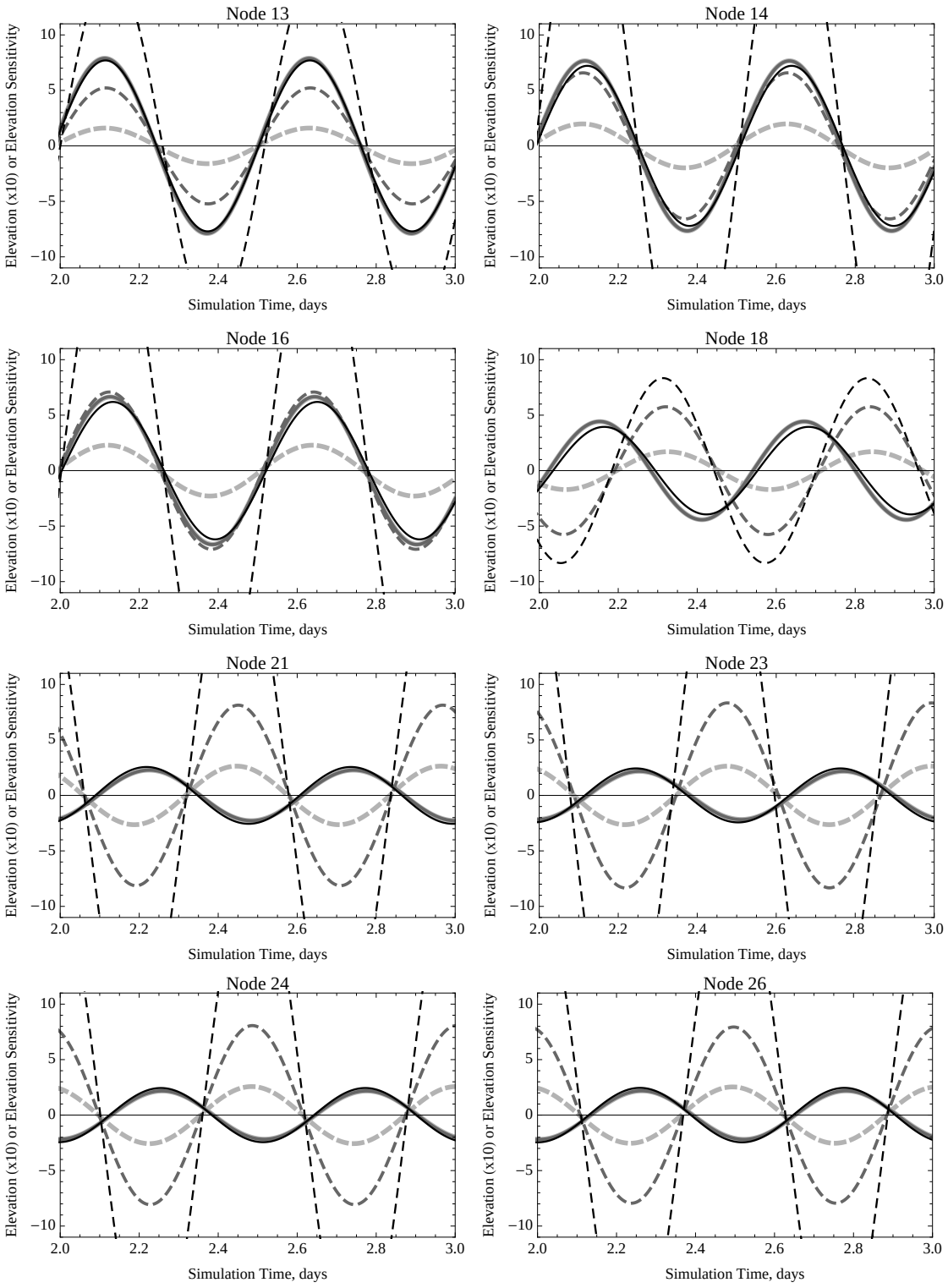

Figure C.6 Elevation and elevation sensitivity results for a simulation on the seamount domain using a G value of 0.001 s^{-1}. Specifics about the panels can be found in the caption for Figure C.5.

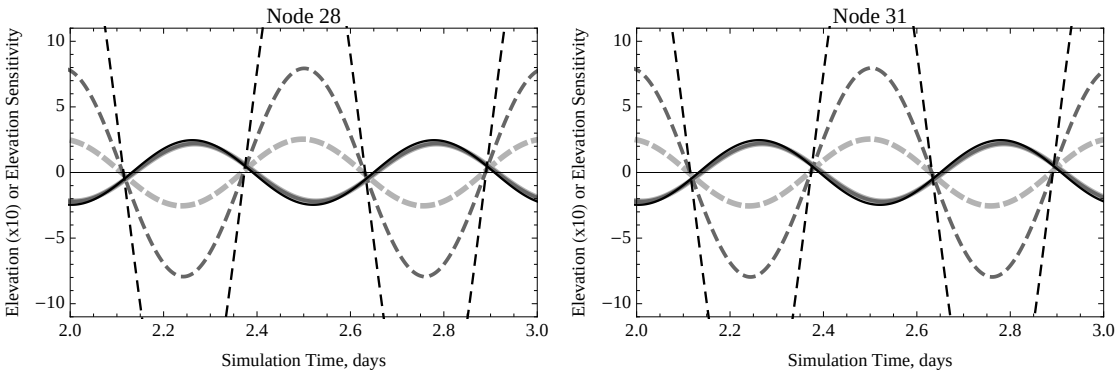

Figure C.7 Elevation and elevation sensitivity results for a simulation on the seamount domain using a G value of 0.001 s^{-1}. Specifics about the panels can be found in the caption for Figure C.5.

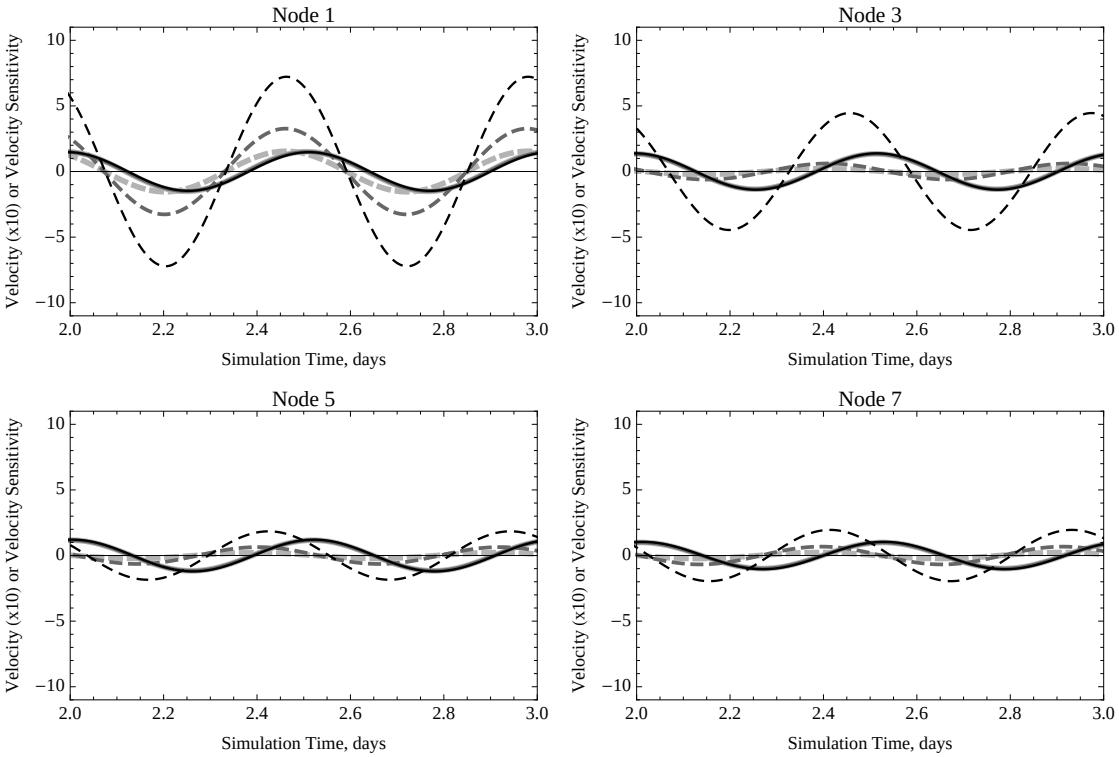

Figure C.8 Velocity and velocity sensitivity results for a simulation on the seamount domain using a G value of 0.001 s^{-1}. The solid lines depict the velocity results, which have units of m / s. The dashed lines show the temporal evolution of the sensitivity of the velocity to G. The units for velocity sensitivity to G are m. The node number listed in the title for each panel is the node number in the 31 node grid associated with a given location (i.e., a fixed coordinate). The black lines are for results from the 16 node grid. The dark gray and light gray lines depict results from the 31 and 61 node grids, respectively.

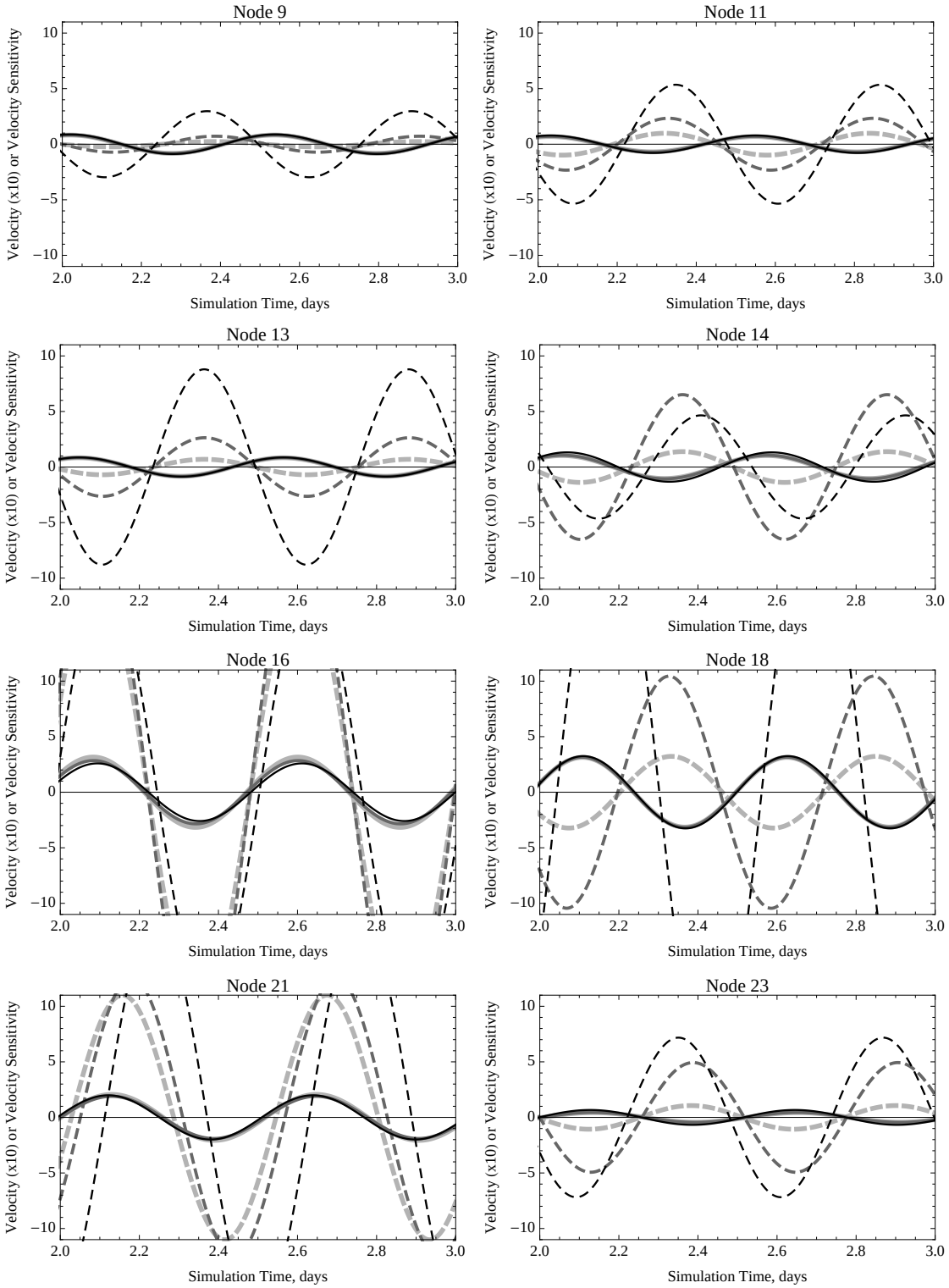

Figure C.9 Velocity and velocity sensitivity results for a simulation on the seamount domain using a G value of 0.001 s^{-1}. Specifics about the panels can be found in the caption for Figure C.8.

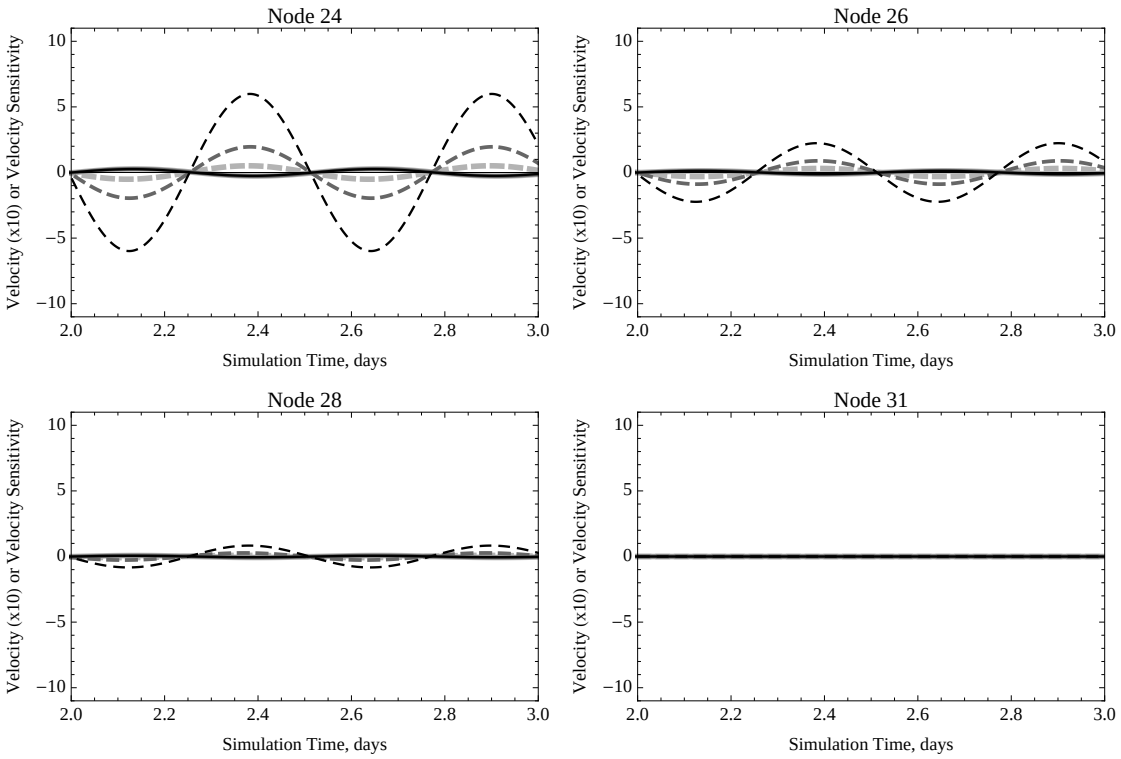

Figure C.10 Velocity and velocity sensitivity results for a simulation on the seamount domain using a G value of 0.001 s^{-1}. Specifics about the panels can be found in the caption for Figure C.8.

C.2.3 Mass Balance and Mass Balance Sensitivity Results

The results presented in this section are for three different simulations on variations of the seamount domain. All the simulations used a constant G value of 0.001 s^{-1}. The difference between the simulations was the number of nodes used to discretize the domain and, thus, the element size. The base domain consists of 31 nodes (30 elements). The two other domains had 16 and 61 nodes, respectively.

The results for mass balance and mass balance sensitivity are elementally-based. The elements used for the comparisons are the elements to the left of the nodes evaluated for the comparisons previously. For instance, the last element in the deep portion of the domain oceanward of the seamount is element 5 in the 16 node grid, element 10 in the 31

node grid and element 20 in the 61 node grid. Consistent with previous presentations in this appendix, the label in the figure corresponds to the element from the 31-node grid. In this case, this comparison receives the label “Element 10.” The line color scheme is also consistent with previous results for the seamount. The black, dark gray and light gray lines (solid and dashed) are used to illustrate results from the 16-node, 31-node and 61-node grids.

Previously, elevation results were shown with solid lines, while elevation sensitivity results were depicted using dashed lines. Likewise, velocity results were provided using solid lines, while the velocity sensitivity to G was shown using dashed lines. For the mass balance and mass balance sensitivity presentation, the mass balance is shown in the left panel, while the mass balance sensitivity is shown in the corresponding right panel. The accumulation term is shown using a solid line, while the net flux term is delineated with dashing. The mass balance sensitivity graphics use the same template, with sensitivity of the accumulation term to G shown in solid lines and sensitivity of the net flux term to G rendered using dashed lines. The first three comparisons are shown in Figure C.11. The rest of the comparisons are presented in Figure C.12 through Figure C.14.

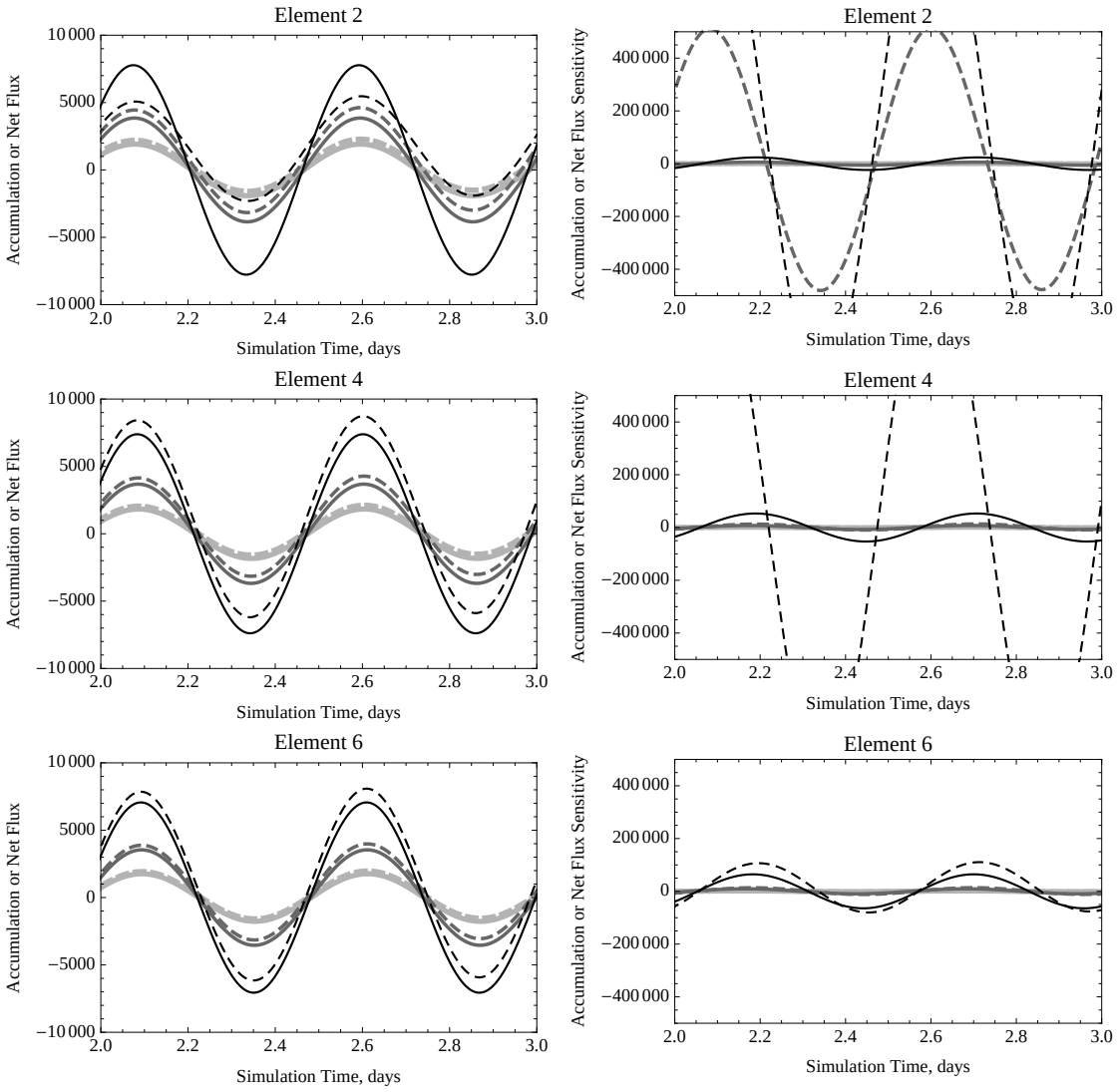

Figure C.11 Mass balance (left panels) and mass balance sensitivity (right panels) results for a simulation on the seamount domain using a G value of 0.001 s^{-1}. The mass balance terms have units of m^2, while the mass balance sensitivity results have units of m^2s. The solid lines show the accumulation results, while the dashed lines show the net flux terms. The element number listed in the title for each panel is the node number in the 31 node grid associated with a given location. The black lines are for results from the 16 node grid. The dark gray and light gray lines depict results from the 31 and 61 node grids, respectively.

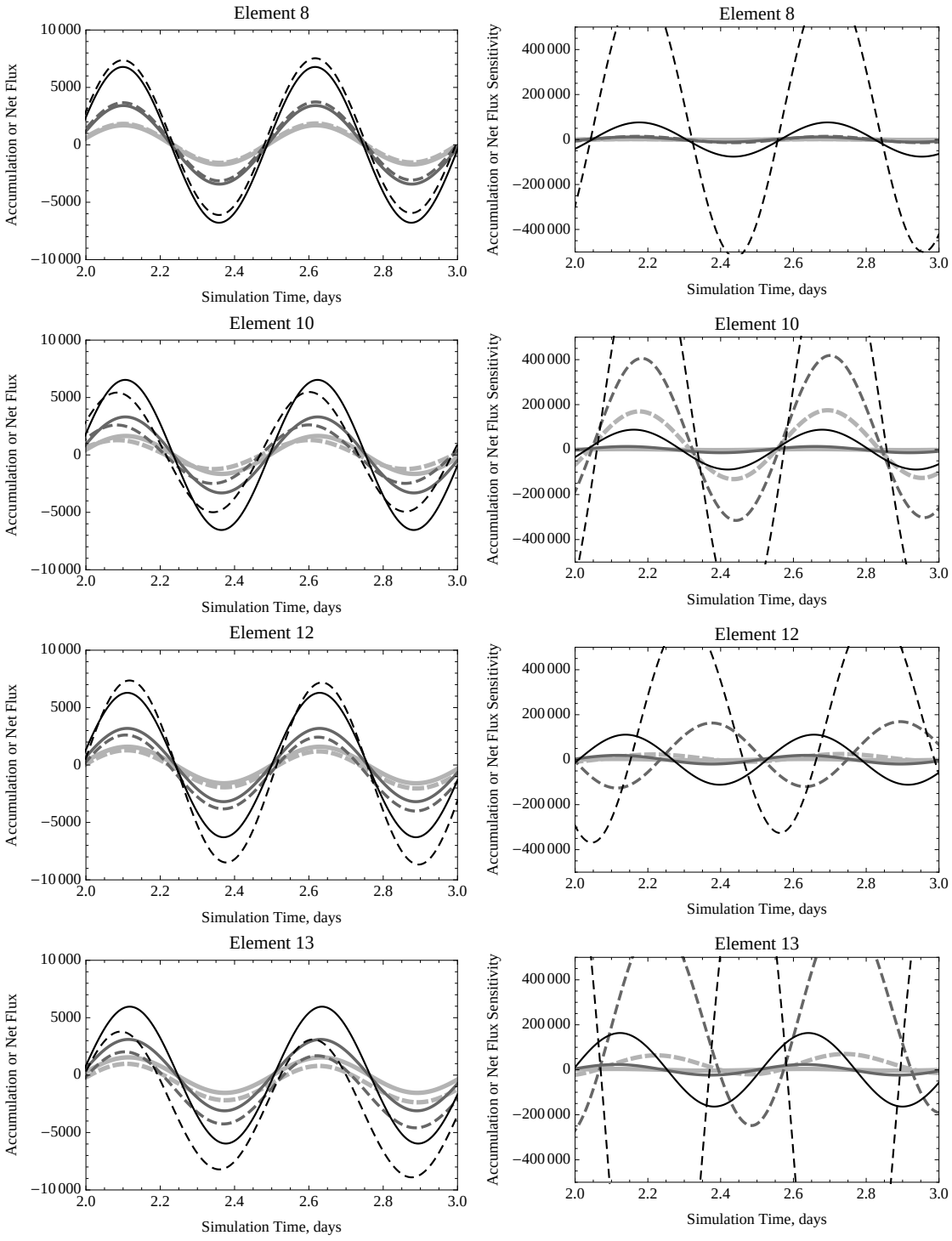

Figure C.12 Mass balance (left panels) and mass balance sensitivity (right panels) results for a simulation on the seamount domain using a G value of 0.001 s^{-1}. Specifics about the panels can be found in the caption for Figure C.11.

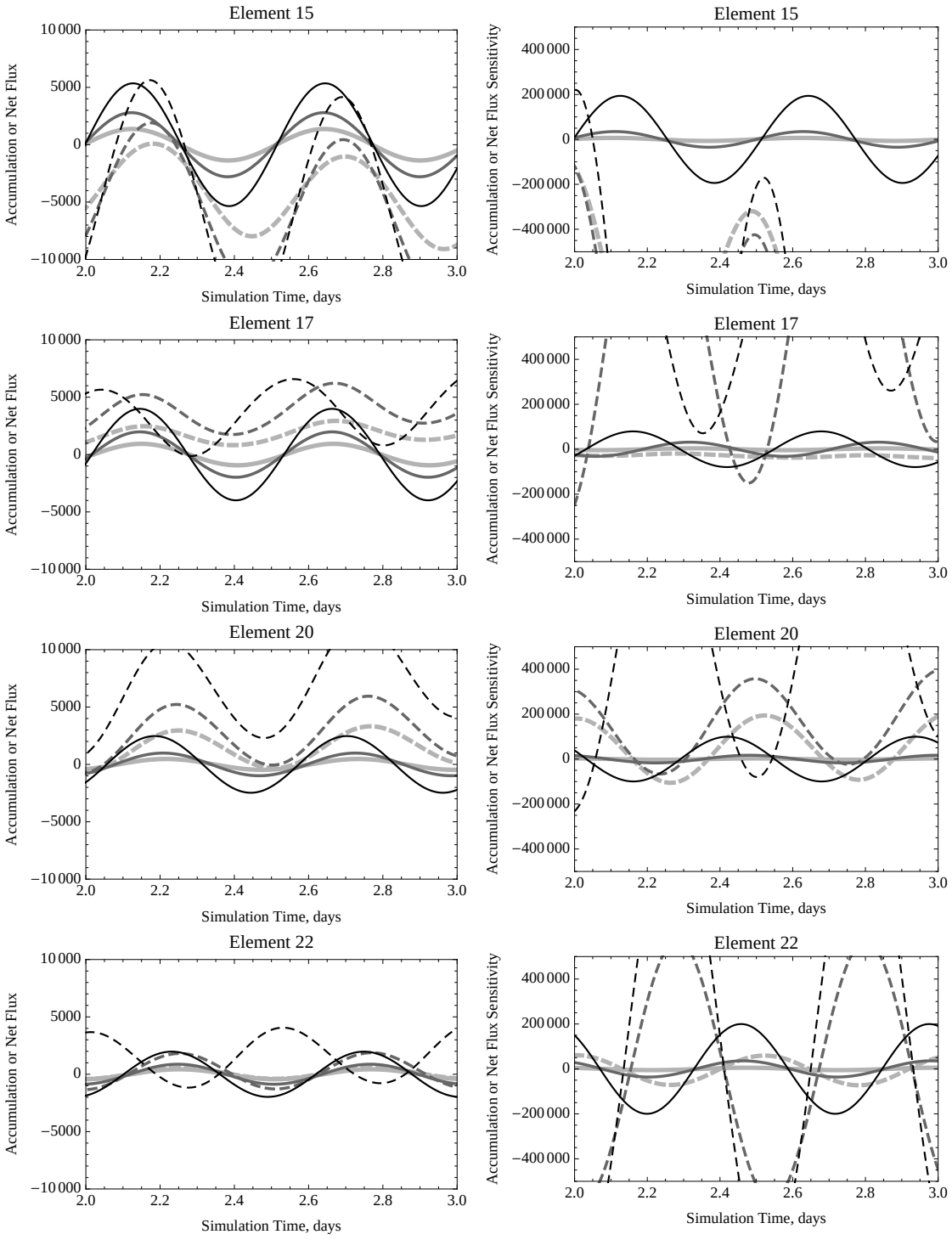

Figure C.13 Mass balance (left panels) and mass balance sensitivity (right panels) results for a simulation on the seamount domain using a G value of 0.001 s^{-1}. Specifics about the panels can be found in the caption for Figure C.11.

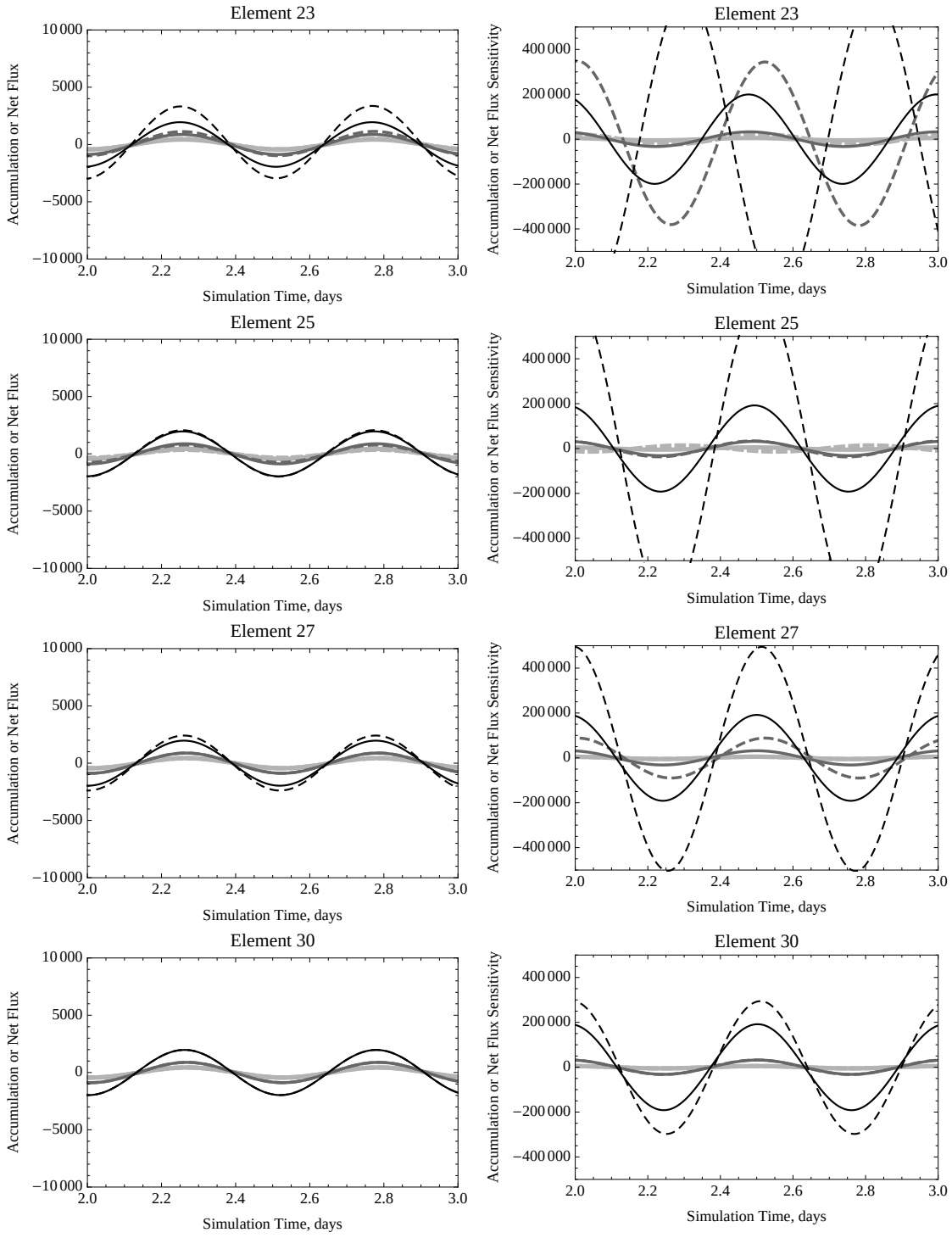

Figure C.14 Mass balance (left panels) and mass balance sensitivity (right panels) results for a simulation on the seamount domain using a G value of 0.001 s^{-1}. Specifics about the panels can be found in the caption for Figure C.11.

C.3 Seamount Domain Using "Primitive" G Value

C.3.1 Elevation and Elevation Sensitivity Results

The results presented in this section are for three different simulations on variations of the seamount domain. All the simulations used the explicit version of the code with a constant G value of 0.01 s^{-1}. The difference between the simulations was the number of nodes used to discretize the domain and, thus, the element size. The base domain consists of 31 nodes (30 elements). The two other domains had 16 and 61 nodes, respectively. The time step for these simulations was one second.

The elevation results are shown in Figure C.15, Figure C.16 and Figure C.17. There are six lines on each plot. The three solid lines are the elevation results for the different simulations, which have units of m. The three dashed lines are the corresponding elevation sensitivity results which have units of ms. The black, dark gray and light gray lines are for the 16, 31 and 61 node simulations, respectively. Additionally, the node number listed on each of the panels is the node number associated with the 31 node grid. For instance, in the sixth panel of Figure C.15, the label is "Node 11." The results are for the 6th, 11th and 21st nodes in the 16, 31 and 61 node domains.

Unlike in the linear sloping domain case presented earlier, there are instances where the geometry of the domain varies slightly between the coarsest grid and the two finer grids. The break points between the sections for the original grid are at node 1, 11, 16, 21, 26 and 31. These correspond to nodes 1, 21, 31, 41, 51 and 61 for the grid with 61 nodes. However, for the grid with just 16 nodes, the break points occur at nodes 1, 6, 9, 11, 14 and 31. In the grid with 16 nodes, node 9 is the first node on the seamount. On the original grid, node 16 is the first node on the seamount. The x-position of node 9 in the 16-node grid is the same

as node 17 in the 31-node grid. For the comparisons, the break points were used as controls, so the graph labeled “Node 16” consists of results from node 9, node 16 and node 31 for the three grids. Comparisons are made for each of the points in the coarsest domain. The point used from the 31 node grid is the closest node corresponding to the same location along a given linear stretch. The node from the 61 node grid is the node from the same x-position as the node from the 31 node grid.

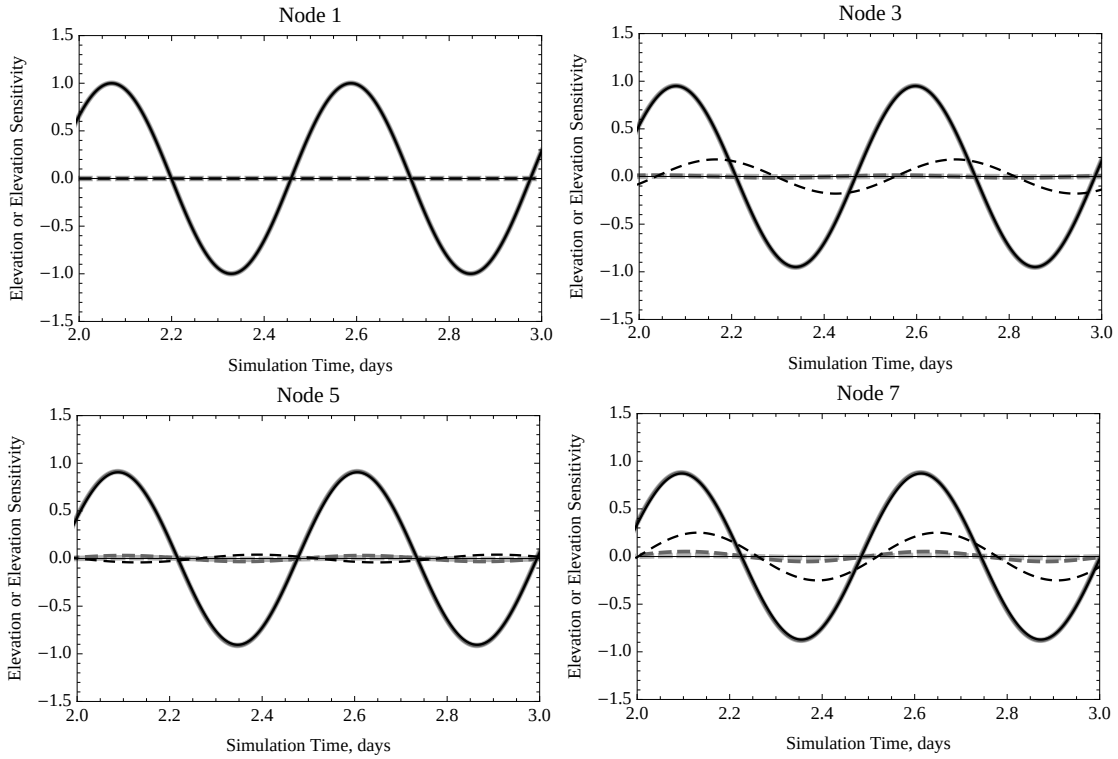

Figure C.15 Elevation and elevation sensitivity results for a simulation on the seamount domain using a G value of 0.01 s^{-1}. The solid lines depict the elevation results, which have units of m. The dashed lines show the temporal evolution of the sensitivity of the elevation to G. The units for elevation sensitivity to G are ms. The node number listed in the title for each panel is the node number in the 31 node grid associated with a given location. The black lines are for results from the 16 node grid. The dark gray and light gray lines depict results from the 31 and 61 node grids, respectively.

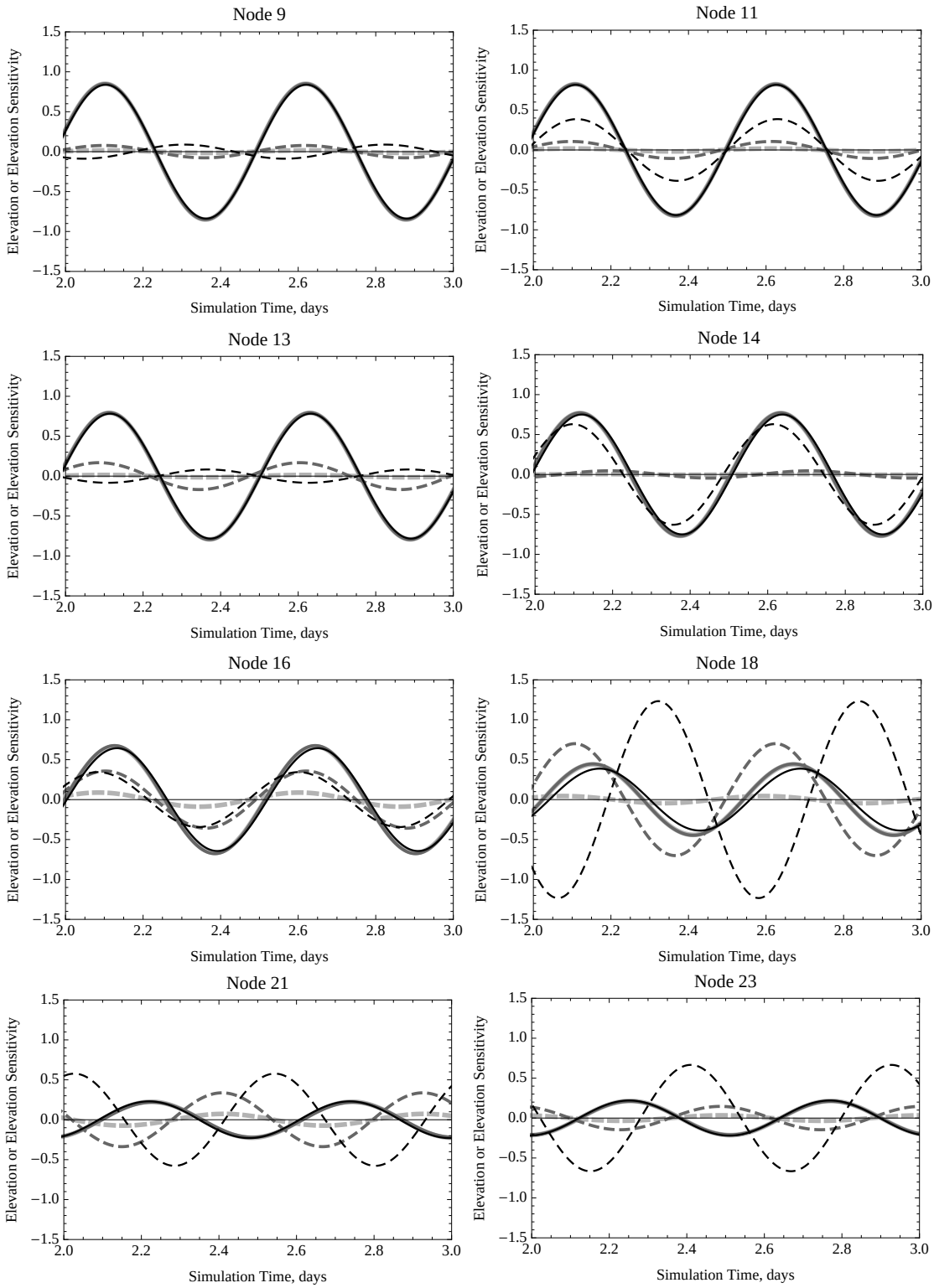

Figure C.16 Elevation and elevation sensitivity results for a simulation on the seamount domain using a G value of 0.01 s^{-1}. Specifics about the panels can be found in the caption for Figure C.15.

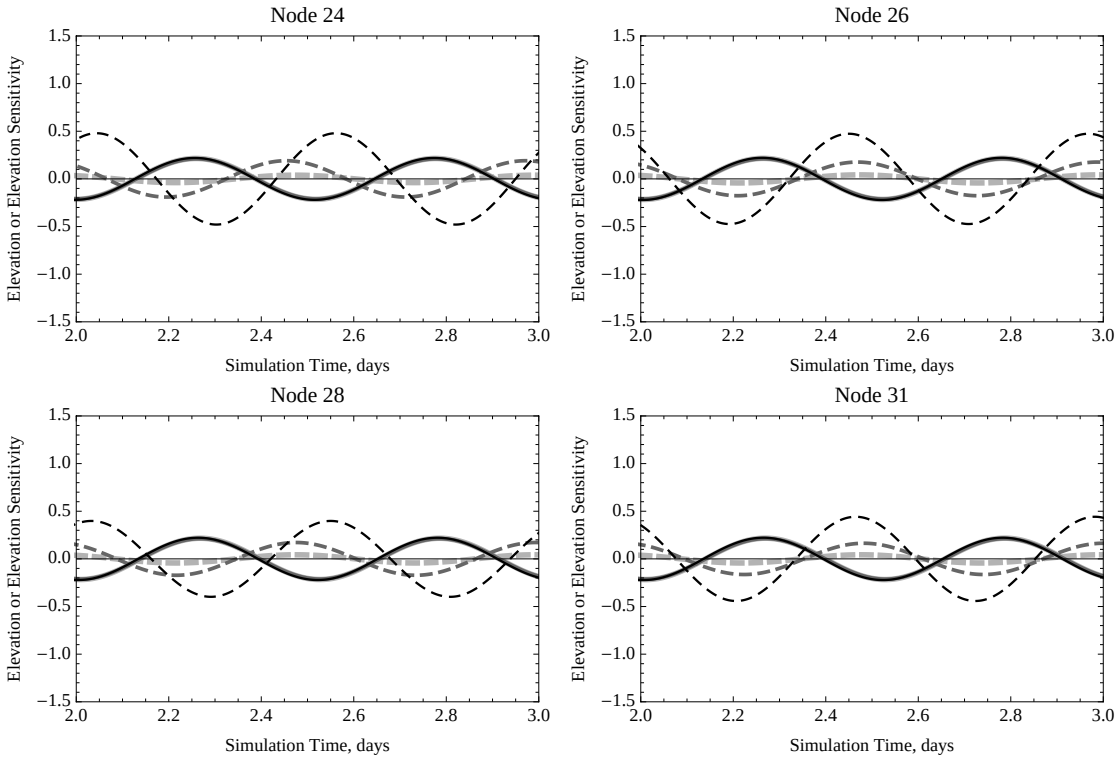

Figure C.17 Elevation and elevation sensitivity results for a simulation on the seamount domain using a G value of 0.01 s^{-1}. Specifics about the panels can be found in the caption for Figure C.15.

C.3.2 Velocity and Velocity Sensitivity Results

The results presented in this section are for three different simulations on variations of the seamount domain. All the simulations used a constant G value of 0.01 s^{-1}. The difference between the simulations was the number of nodes used to discretize the domain and, thus, the element size. The base domain consists of 31 nodes (30 elements). The two other domains had 16 and 61 nodes, respectively.

The velocity results are shown in Figure C.18, Figure C.19 and Figure C.20. There are six lines on each plot. The three solid lines are the velocity results for the different simulations, which have units of m/s. The three dashed lines are the corresponding velocity sensitivity results which have units of m. The black, dark gray and light gray lines are for the 16, 31 and 61 node simulations, respectively. Additionally, the node number listed on

each of the panels is the node number associated with the 31 node grid. For instance, in the sixth panel of Figure C.18, the label is “Node 11.” The results are for the 6th, 11th and 21st nodes in the 16, 31 and 61 node domains.

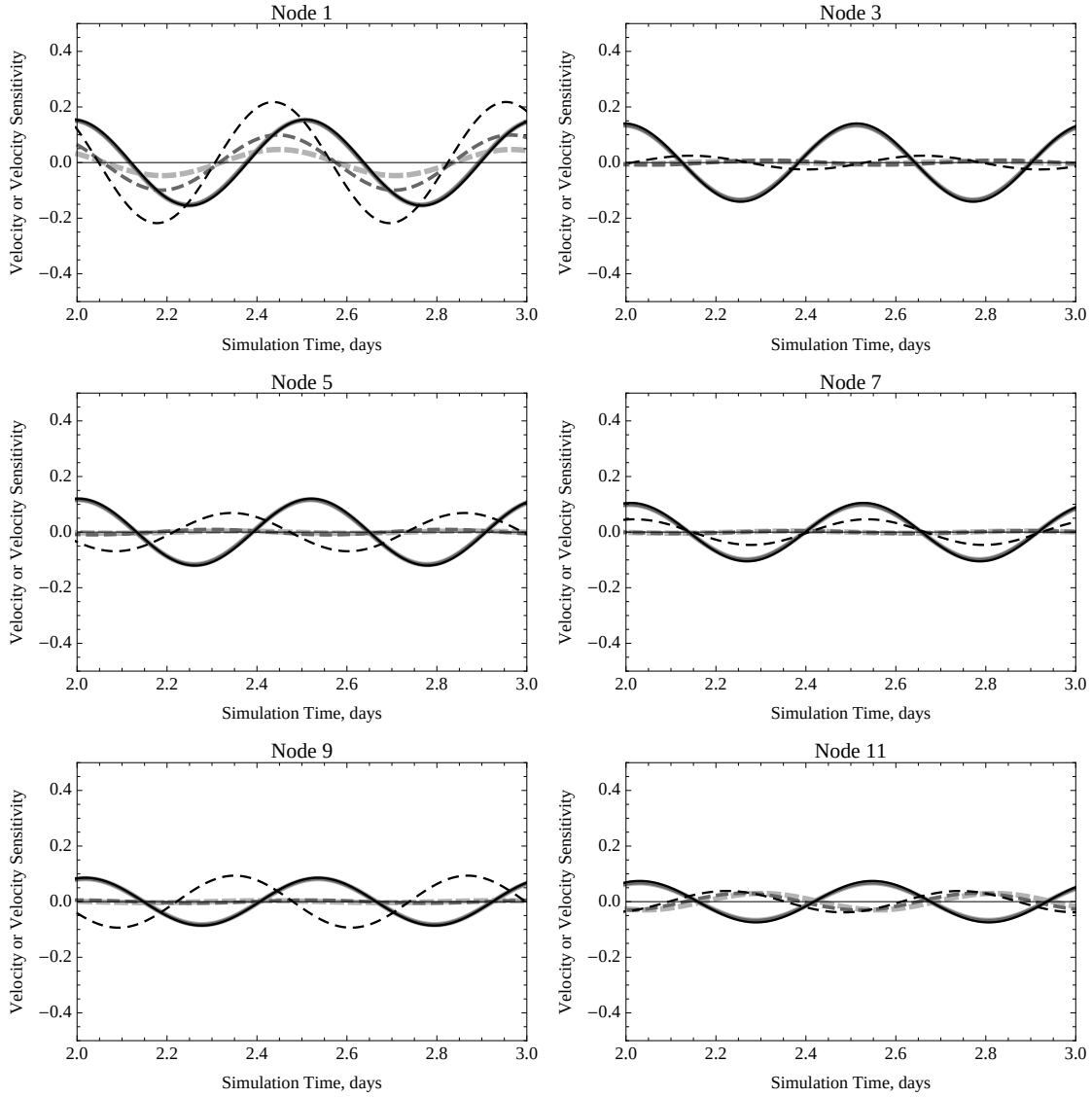

Figure C.18 Velocity and velocity sensitivity results for a simulation on the seamount domain using a G value of 0.01 s^{-1}. The solid lines depict the velocity results, which have units of m / s. The dashed lines show the temporal evolution of the sensitivity of the velocity to G. The units for velocity sensitivity to G are m. The node number listed in the title for each panel is the node number in the 31 node grid associated with a given location. The black lines are for results from the 16 node grid. The dark gray and light gray lines depict results from the 31 and 61 node grids, respectively.

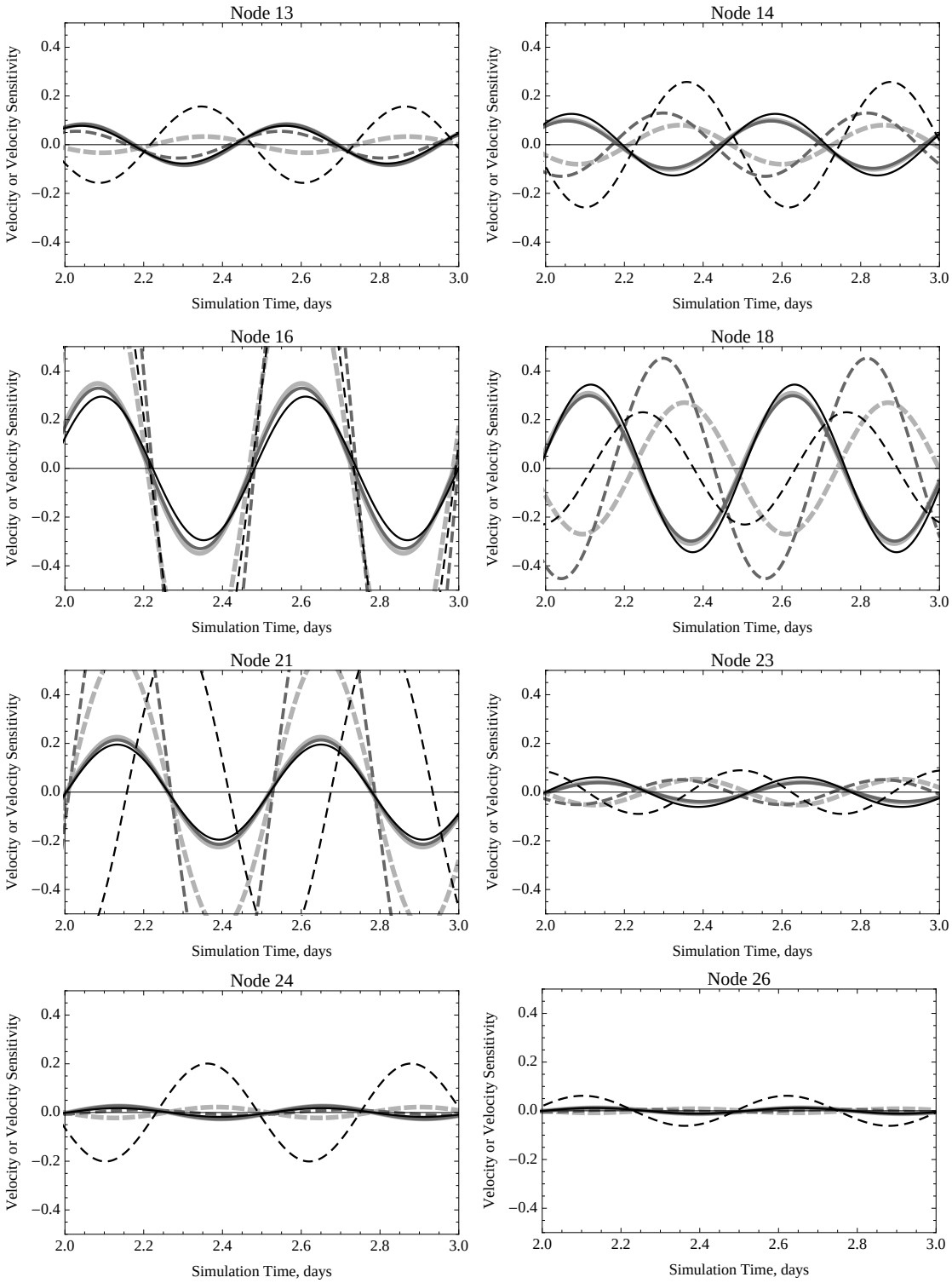

Figure C.19 Velocity and velocity sensitivity results for a simulation on the seamount domain using a G value of 0.01 s^{-1}. Specifics about the panels can be found in the caption for Figure C.18.

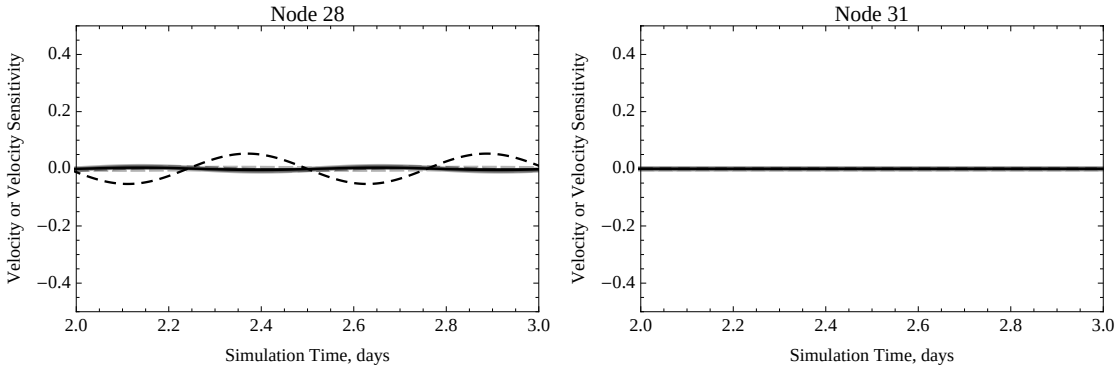

Figure C.20 Velocity and velocity sensitivity results for a simulation on the seamount domain using a G value of 0.01 s^{-1}. Specifics about the panels can be found in the caption for Figure C.18.

C.3.3 Mass Balance and Mass Balance Sensitivity Results

The results presented in this section are for three different simulations on variations of the seamount domain. All the simulations used a constant G value of 0.01 s^{-1}. The difference between the simulations was the number of nodes used to discretize the domain and, thus, the element size. The base domain consists of 31 nodes (30 elements). The two other domains had 16 and 61 nodes, respectively.

The results for mass balance and mass balance sensitivity are elementally-based. The elements used for the comparisons are the elements to the left of the nodes evaluated for the comparisons previously. For instance, the last element in the deep portion of the domain oceanward of the seamount is element 5 in the 16 node grid, element 10 in the 31 node grid and element 20 in the 61 node grid. Consistent with previous presentations in this appendix, the label in the figure corresponds to the element from the 31-node grid. In this case, this comparison receives the label "Element 10." The line color scheme is also consistent with previous results for the seamount. The black, dark gray and light gray lines (solid and dashed) are used to illustrate results from the 16-node, 31-node and 61-node grids.

Previously, elevation results were shown with solid lines, while elevation sensitivity results were depicted using dashed lines. Likewise, velocity results were provided using solid lines, while the velocity sensitivity to G was shown using dashed lines. For the mass balance and mass balance sensitivity presentation, the mass balance is shown in the left panel, while the mass balance sensitivity is shown in the corresponding right panel. The accumulation term is shown using a solid line, while the net flux term is delineated with dashing. The mass balance sensitivity graphics use the same template, with sensitivity of the accumulation term to G shown in solid lines and sensitivity of the net flux term to G rendered using dashed lines. The first three comparisons are shown in Figure C.21. The rest of the comparisons are presented in Figure C.22 through Figure C.24.

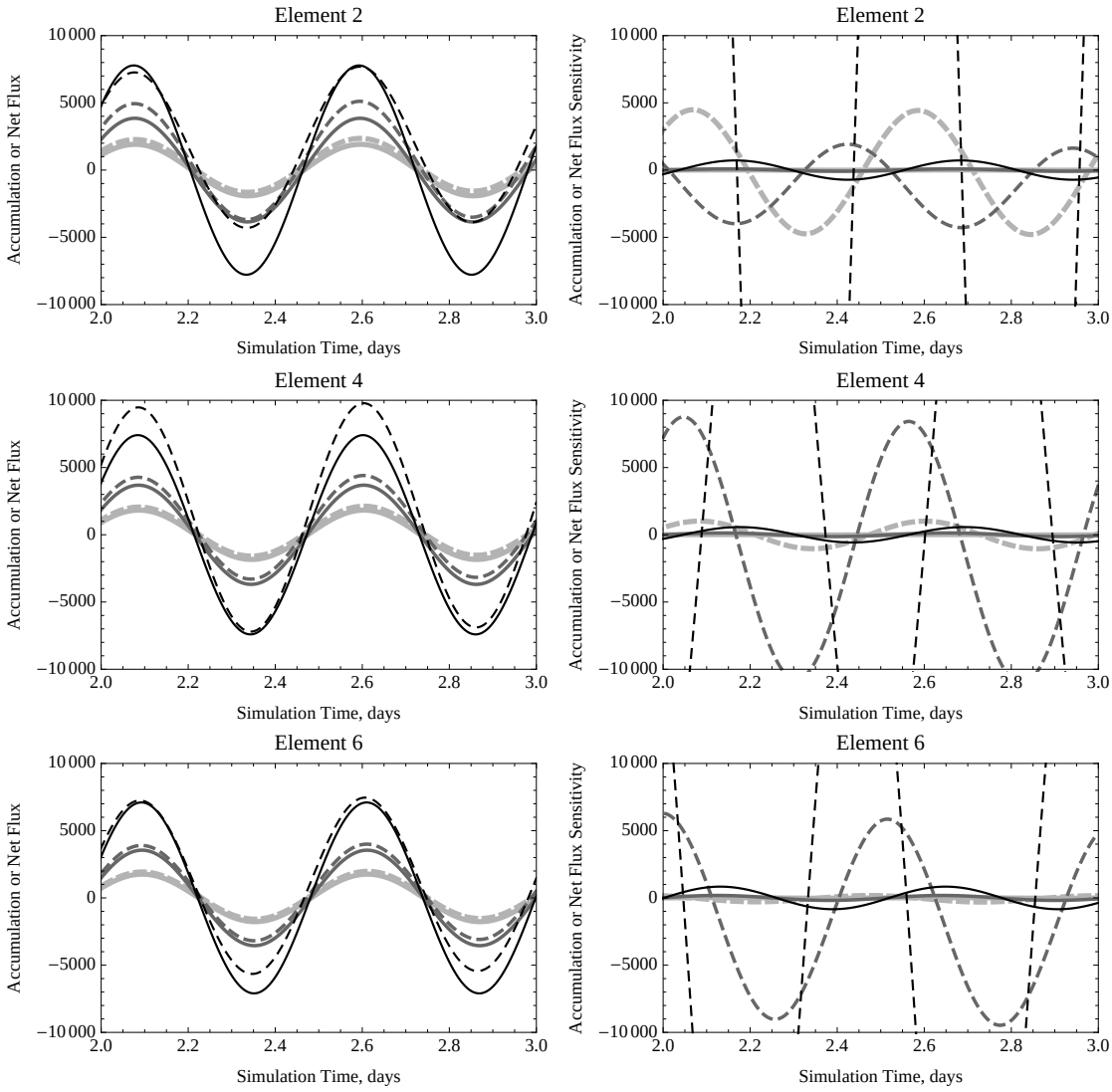

Figure C.21 Mass balance (left panels) and mass balance sensitivity (right panels) results for a simulation on the seamount domain using a G value of 0.01 s^{-1}. The mass balance terms have units of m^2 while the mass balance sensitivity results have units of m^2s. The solid lines show the accumulation results while the dashed lines show the net flux terms. The element number listed in the title for each panel is the node number in the 31 node grid associated with a given location. The black lines are for results from the 16 node grid. The dark gray and light gray lines depict results from the 31 and 61 node grids, respectively.

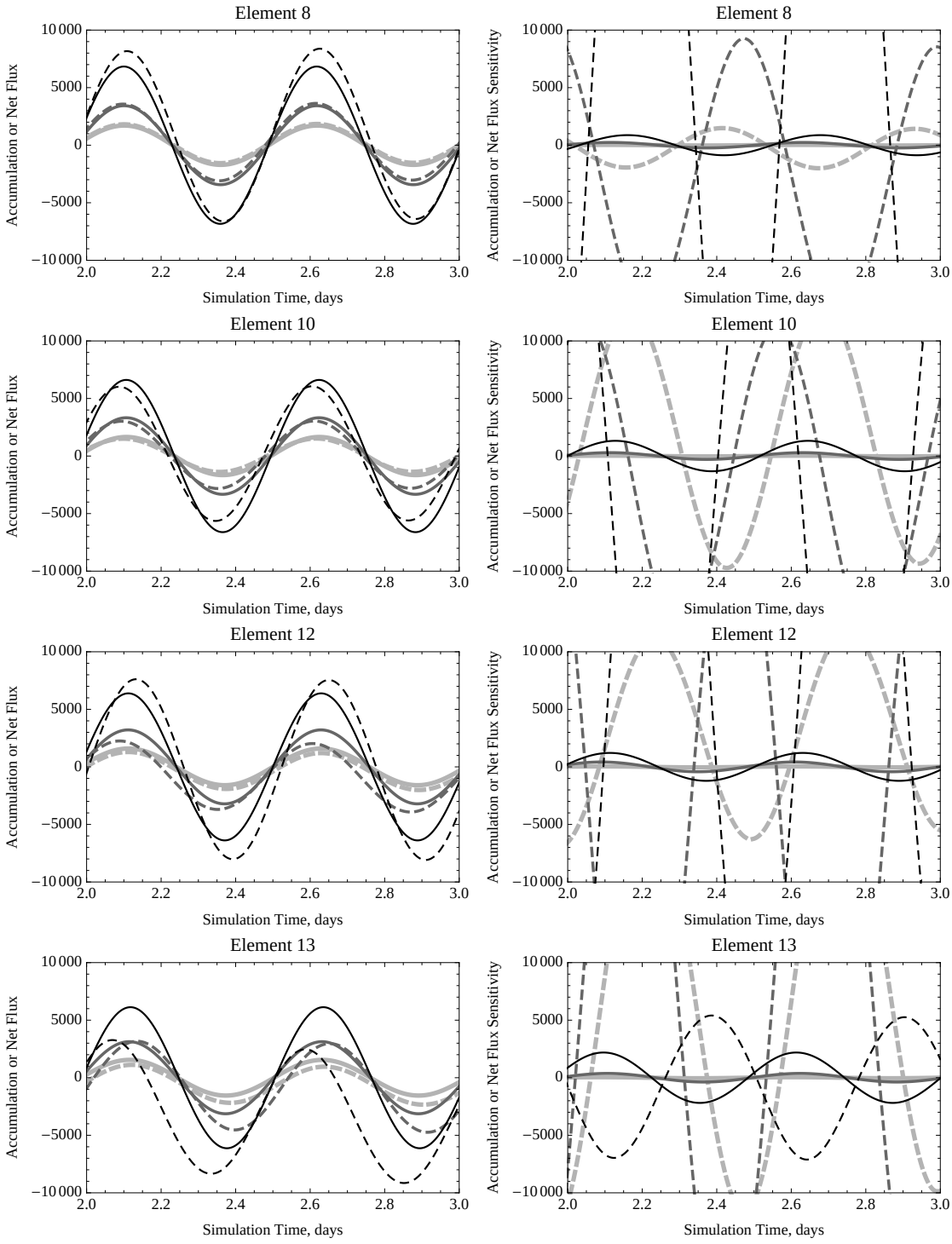

Figure C.22 Mass balance (left panels) and mass balance sensitivity (right panels) results for a simulation on the seamount domain using a G value of 0.01 s^{-1}. Specifics about the panels can be found in the caption for Figure C.21.

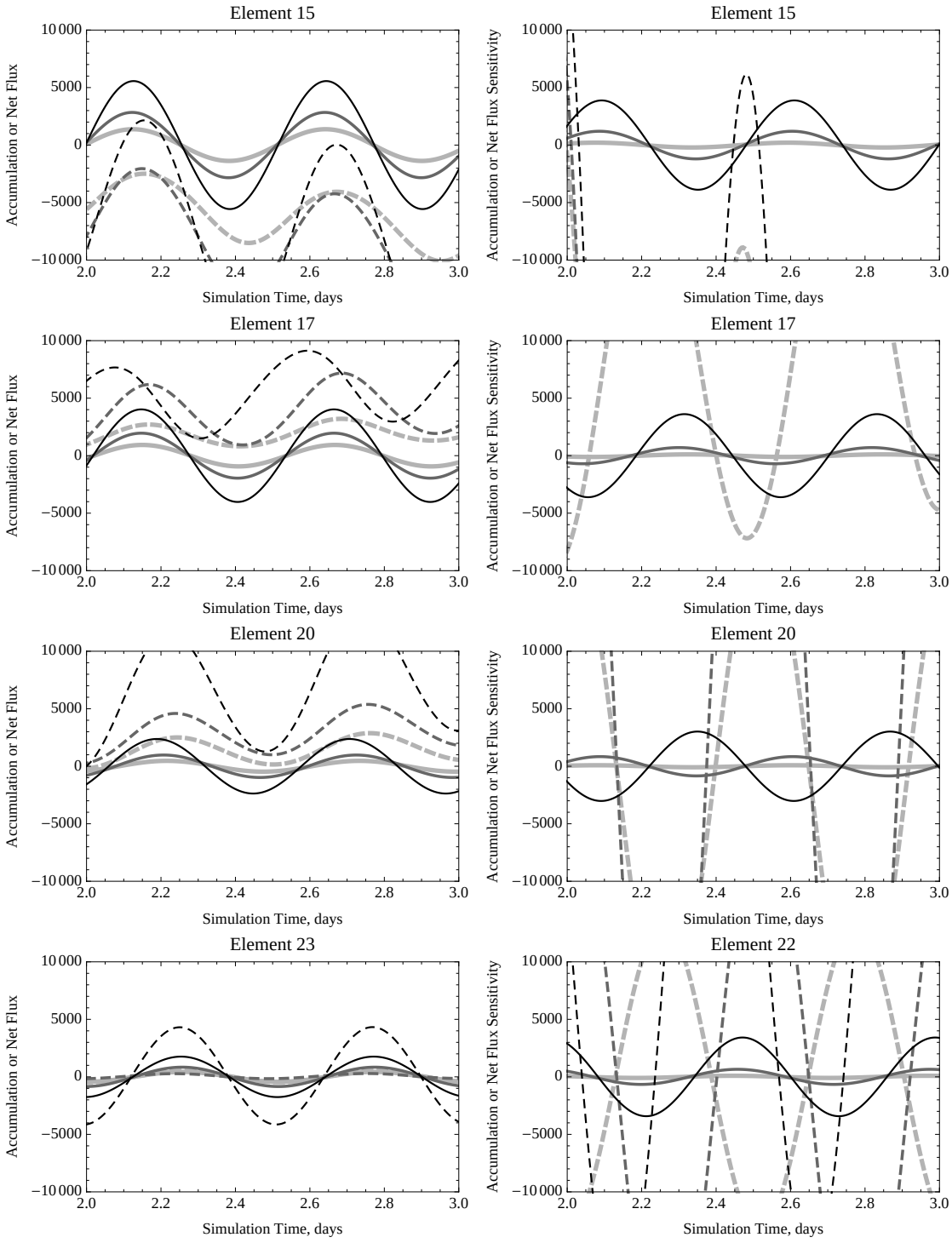

Figure C.23 Mass balance (left panels) and mass balance sensitivity (right panels) results for a simulation on the seamount domain using a G value of 0.01 s^{-1}. Specifics about the panels can be found in the caption for Figure C.21.

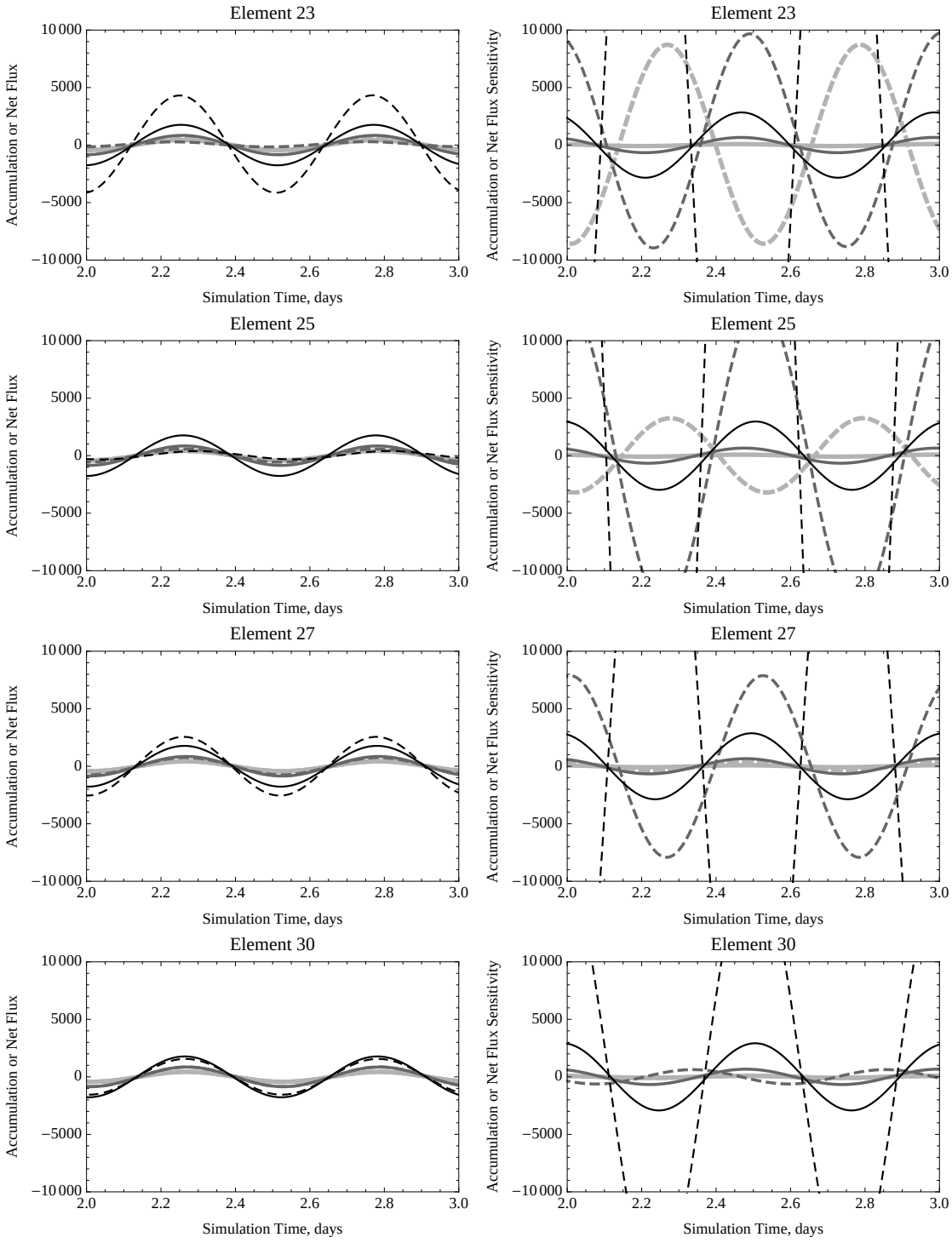

Figure C.24 Mass balance (left panels) and mass balance sensitivity (right panels) results for a simulation on the seamount domain using a G value of 0.01 s^{-1}. Specifics about the panels can be found in the caption for Figure C.21.

Appendix D. Derivation of Equations and Sensitivities for Non-Linear 1-D ADCIRC Using a Variable G Parameterization

D.1 Elemental Equations

The elemental equations for 1-D GWCE and NCM, as presented in Chapter 4, are given by (D.1) and (D.2), respectively.

$$\left(1+\frac{G\Delta t}{2}\right)\mathbf{M}^{L}_{i,j}\zeta^{k+1}_{j} = 2\mathbf{M}^{L}_{i,j}\zeta^{k}_{j}+\left(\frac{G\Delta t}{2}-1\right)\mathbf{M}^{L}_{i,j}\zeta^{k-1}_{j}+\Delta t^{2}(Hu)_{e}(G)^{k}_{j}\mathbf{M}^{5}_{i,j}- \quad \textbf{(D.1)}$$

$$\Delta t^{2}(Huu)^{k}_{j}\mathbf{M}^{3}_{i,j}-g\Delta t^{2}\mathbf{M}^{2}_{i,j}\zeta^{k}_{j}-\frac{g\Delta t^{2}}{2}(\zeta^{2})^{k}_{j}\mathbf{M}^{3}_{i,j}-\varepsilon\Delta t\mathbf{M}^{3}_{i,j}\zeta^{k}_{j}+\varepsilon\Delta t\mathbf{M}^{3}_{i,j}\zeta^{k-1}_{j}+$$

$$\Delta t^{2}[(G-\tau)(Hu)]^{k}_{j}\mathbf{M}^{4}_{i,j}$$

$$\left(1+\frac{\tau\Delta t}{2}\right)\mathbf{M}^{L}_{i,j}u^{k+1}_{j} = \left(1-\frac{\tau\Delta t}{2}\right)\mathbf{M}^{L}_{i,j}u^{k}_{j}-\frac{\Delta t}{2}(u^{2})^{k}_{j}\mathbf{M}^{5}_{i,j}-g\Delta t^{2}\zeta^{k}_{j}\mathbf{M}^{5}_{i,j}-\varepsilon\Delta t\mathbf{M}^{3}_{i,j}u^{k}_{j} \quad \textbf{(D.2)}$$

where $\mathbf{M}^{L}_{i,j} = \Delta x\begin{bmatrix}1/2 & 0\\ 0 & 1/2\end{bmatrix}$, $\mathbf{M}^{2}_{i,j} = \frac{h_j+h_{j+1}}{2\Delta x}\begin{bmatrix}1 & -1\\ -1 & 1\end{bmatrix}$, $\mathbf{M}^{3}_{i,j} = \frac{1}{\Delta x}\begin{bmatrix}1 & -1\\ -1 & 1\end{bmatrix}$, $\mathbf{M}^{4}_{i,j} = \frac{1}{2}\begin{bmatrix}-1 & -1\\ 1 & 1\end{bmatrix}$ and $\mathbf{M}^{5}_{i,j} = \frac{1}{2}\begin{bmatrix}-1 & 1\\ -1 & 1\end{bmatrix}$. Again, constant grid spacing has been utilized.

D.2 Matrix Assembly

Using 5 nodes (4 elements) to discretize the domain allows the system matrices to be of reasonable size. Assembly results in (D.3) for the GWCE and (D.4) for the NCM.

$$\left(1+\frac{G\Delta t}{2}\right)\begin{bmatrix}1&0&0&0&0\\0&2&0&0&0\\0&0&2&0&0\\0&0&0&2&0\\0&0&0&0&1\end{bmatrix}\begin{bmatrix}\zeta_1\\\zeta_2\\\zeta_3\\\zeta_4\\\zeta_5\end{bmatrix}^{k+1} = 2\begin{bmatrix}1&0&0&0&0\\0&2&0&0&0\\0&0&2&0&0\\0&0&0&2&0\\0&0&0&0&1\end{bmatrix}\begin{bmatrix}\zeta_1\\\zeta_2\\\zeta_3\\\zeta_4\\\zeta_5\end{bmatrix}^{k} + \left(\frac{G\Delta t}{2}-1\right)\begin{bmatrix}1&0&0&0&0\\0&2&0&0&0\\0&0&2&0&0\\0&0&0&2&0\\0&0&0&0&1\end{bmatrix}\begin{bmatrix}\zeta_1\\\zeta_2\\\zeta_3\\\zeta_4\\\zeta_5\end{bmatrix}^{k-1} - \quad \textbf{(D.3)}$$

$$\frac{2\varepsilon\Delta t}{(\Delta x)^2}\begin{bmatrix}1&-1&0&0&0\\-1&2&-1&0&0\\0&-1&2&-1&0\\0&0&-1&2&-1\\0&0&0&-1&1\end{bmatrix}\begin{bmatrix}\zeta_1\\\zeta_2\\\zeta_3\\\zeta_4\\\zeta_5\end{bmatrix}^{k} -$$

$$\frac{g(\Delta t)^2}{(\Delta x)^2}\begin{bmatrix}h_1+h_2&-(h_1+h_2)&0&0&0\\-(h_1+h_2)&h_1+2h_2+h_3&-(h_2+h_3)&0&0\\0&-(h_2+h_3)&h_2+2h_3+h_4&-(h_3+h_4)&0\\0&0&-(h_3+h_4)&h_3+2h_4+h_5&-(h_4+h_5)\\0&0&0&-(h_4+h_5)&h_4+h_5\end{bmatrix}\begin{bmatrix}\zeta_1\\\zeta_2\\\zeta_3\\\zeta_4\\\zeta_5\end{bmatrix}^{k} +$$

$$\frac{2\varepsilon\Delta t}{(\Delta x)^2}\begin{bmatrix}1&-1&0&0&0\\-1&2&-1&0&0\\0&-1&2&-1&0\\0&0&-1&2&-1\\0&0&0&-1&1\end{bmatrix}\begin{bmatrix}\zeta_1\\\zeta_2\\\zeta_3\\\zeta_4\\\zeta_5\end{bmatrix}^{k-1} - \frac{2(\Delta t)^2}{(\Delta x)^2}\begin{bmatrix}1&-1&0&0&0\\-1&2&-1&0&0\\0&-1&2&-1&0\\0&0&-1&2&-1\\0&0&0&-1&1\end{bmatrix}\begin{bmatrix}(Huu)_1\\(Huu)_2\\(Huu)_3\\(Huu)_4\\(Huu)_5\end{bmatrix}^{k} +$$

$$\frac{(\Delta t)^2}{2\Delta x}\begin{bmatrix}-(H_1u_1+H_2u_2)&H_1u_1+H_2u_2&0&0&0\\-(H_1u_1+H_2u_2)&H_1u_1-H_3u_3&H_2u_2+H_3u_3&0&0\\0&-(H_2u_2+H_3u_3)&H_2u_2-H_4u_4&H_3u_3+H_4u_4&0\\0&0&-(H_3u_3+H_4u_4)&H_3u_3-H_5u_5&H_4u_4+H_5u_5\\0&0&0&-(H_4u_4+H_5u_5)&H_4u_4+H_5u_5\end{bmatrix}\begin{bmatrix}G_1\\G_2\\G_3\\G_4\\G_5\end{bmatrix}^{k} -$$

$$\frac{g(\Delta t)^2}{(\Delta x)^2}\begin{bmatrix}1&-1&0&0&0\\-1&2&-1&0&0\\0&-1&2&-1&0\\0&0&-1&2&-1\\0&0&0&-1&1\end{bmatrix}\begin{bmatrix}\zeta_1^2\\\zeta_2^2\\\zeta_3^2\\\zeta_4^2\\\zeta_5^2\end{bmatrix}^{k} + \frac{(\Delta t)^2}{\Delta x}\begin{bmatrix}-1&-1&0&0&0\\1&0&-1&0&0\\0&1&0&-1&0\\0&0&1&0&-1\\0&0&0&1&1\end{bmatrix}\left(\begin{bmatrix}(GHu)_1\\(GHu)_2\\(GHu)_3\\(GHu)_4\\(GHu)_5\end{bmatrix}^{k} - \begin{bmatrix}(\tau Hu)_1\\(\tau Hu)_2\\(\tau Hu)_3\\(\tau Hu)_4\\(\tau Hu)_5\end{bmatrix}^{k}\right)$$

$$\left(1+\frac{\tau\Delta t}{2}\right)\begin{bmatrix}1&0&0&0&0\\0&2&0&0&0\\0&0&2&0&0\\0&0&0&2&0\\0&0&0&0&1\end{bmatrix}\begin{bmatrix}u_1\\u_2\\u_3\\u_4\\u_5\end{bmatrix}^{k+1} = \left(1-\frac{\tau\Delta t}{2}\right)\begin{bmatrix}1&0&0&0&0\\0&2&0&0&0\\0&0&2&0&0\\0&0&0&2&0\\0&0&0&0&1\end{bmatrix}\begin{bmatrix}u_1\\u_2\\u_3\\u_4\\u_5\end{bmatrix}^{k} - \tag{D.4}$$

$$\frac{\Delta t}{4\Delta x}\begin{bmatrix}-(u_1+u_2) & u_1+u_2 & 0 & 0 & 0\\ -(u_1+u_2) & u_1-u_3 & u_2+u_3 & 0 & 0\\ 0 & -(u_2+u_3) & u_2-u_4 & u_3+u_4 & 0\\ 0 & 0 & -(u_3+u_4) & u_3-u_5 & u_4+u_5\\ 0 & 0 & 0 & -(u_4+u_5) & u_4+u_5\end{bmatrix}\begin{bmatrix}u_1\\u_2\\u_3\\u_4\\u_5\end{bmatrix}^{k} -$$

$$\frac{g\Delta t}{\Delta x}\begin{bmatrix}-1&1&0&0&0\\-1&0&1&0&0\\0&-1&0&1&0\\0&0&-1&0&1\\0&0&0&-1&1\end{bmatrix}\begin{bmatrix}\zeta_1\\\zeta_2\\\zeta_3\\\zeta_4\\\zeta_5\end{bmatrix}^{k} - \frac{2\varepsilon\Delta t}{(\Delta x)^2}\begin{bmatrix}1&-1&0&0&0\\-1&2&-1&0&0\\0&-1&2&-1&0\\0&0&-1&2&-1\\0&0&0&-1&1\end{bmatrix}\begin{bmatrix}u_1\\u_2\\u_3\\u_4\\u_5\end{bmatrix}^{k}$$

D.3 System Equations

As stated in Chapter 4, the system can be written for each node as shown in (D.5).

$$\beta_j(G)c_j^{k+1} = M_{1j}(\mathbf{c}^k, G) + M_{2j}(\mathbf{c}^{k-1}, G) \tag{D.5}$$

The entire system can be written similarly, as shown in (D.6).

$$\beta(G)\mathbf{c}^{k+1} = M_1(\mathbf{c}^k, G) + M_2(\mathbf{c}^{k-1}, G) \tag{D.6}$$

However, presentation is done more easily if the equations for elevations (from the GWCE) and velocities (from the NCM) are kept separate.

The GWCE system can be rewritten as

$$\beta_G(G)\zeta^{k+1} = \zeta_{bc}^{k+1} + \sum_{i=1}^{8}\mathbf{M}_{1iG} + \sum_{i=1}^{2}\mathbf{M}_{2iG} \tag{D.7}$$

where the $\mathbf{M}_{1iG}$ terms in the GWCE are at the current time level and the $\mathbf{M}_{2iG}$ terms are

at the previous time level. The terms are as follows:

$$\beta_G(G) = \begin{bmatrix} 1 \\ 2\left(1 + \frac{G_2 \Delta t}{2}\right) \\ 2\left(1 + \frac{G_3 \Delta t}{2}\right) \\ 2\left(1 + \frac{G_4 \Delta t}{2}\right) \\ \left(1 + \frac{G_5 \Delta t}{2}\right) \end{bmatrix} \tag{D.8}$$

$$\zeta_{bc}^{k+1} = \begin{bmatrix} \zeta_1^{k+1} \\ 0 \\ 0 \\ 0 \\ 0 \end{bmatrix} \tag{D.9}$$

$$\mathbf{M}_{11G} = \begin{bmatrix} 0 \\ 4\zeta_2 \\ 4\zeta_3 \\ 4\zeta_4 \\ 2\zeta_5 \end{bmatrix}^k \tag{D.10}$$

$$\mathbf{M}_{12G} = -\frac{2\varepsilon \Delta t}{(\Delta x)^2} \begin{bmatrix} 0 \\ -\zeta_1 + 2\zeta_2 - \zeta_3 \\ -\zeta_2 + 2\zeta_3 - \zeta_4 \\ -\zeta_3 + 2\zeta_4 - \zeta_5 \\ -\zeta_4 + \zeta_5 \end{bmatrix}^k \tag{D.11}$$

$$\mathbf{M}_{13G} = -\frac{g(\Delta t)^2}{(\Delta x)^2}\begin{bmatrix} 0 \\ -(h_1+h_2)\zeta_1+(h_1+2h_2+h_3)\zeta_2-(h_2+h_3)\zeta_3 \\ -(h_2+h_3)\zeta_2+(h_2+2h_3+h_4)\zeta_3-(h_3+h_4)\zeta_4 \\ -(h_3+h_4)\zeta_3+(h_3+2h_4+h_5)\zeta_4-(h_4+h_5)\zeta_5 \\ -(h_4+h_5)\zeta_4+(h_4+h_5)\zeta_5 \end{bmatrix}^k \quad \textbf{(D.12)}$$

$$\mathbf{M}_{14G} = -\frac{2(\Delta t)^2}{(\Delta x)^2}\begin{bmatrix} 0 \\ -(Huu)_1+2(Huu)_2-(Huu)_3 \\ -(Huu)_2+2(Huu)_3-(Huu)_4 \\ -(Huu)_3+2(Huu)_4-(Huu)_5 \\ -(Huu)_4+(Huu)_5 \end{bmatrix}^k \quad \textbf{(D.13)}$$

$$\mathbf{M}_{15G} = \frac{(\Delta t)^2}{2\Delta x}\begin{bmatrix} 0 \\ -(H_1u_1+H_2u_2)G_1+(H_1u_1-H_3u_3)G_2+(H_2u_2+H_3u_3)G_3 \\ -(H_2u_2+H_3u_3)G_2+(H_2u_2-H_4u_4)G_3+(H_3u_3+H_4u_4)G_4 \\ -(H_3u_3+H_4u_4)G_3+(H_3u_3-H_5u_5)G_4+(H_4u_4+H_5u_5)G_5 \\ -(H_4u_4+H_5u_5)G_4+(H_4u_4+H_5u_5)G_5 \end{bmatrix}^k \quad \textbf{(D.14)}$$

$$\mathbf{M}_{16G} = -\frac{g(\Delta t)^2}{(\Delta x)^2}\begin{bmatrix} 0 \\ -(\zeta_1)^2+2(\zeta_2)^2-(\zeta_3)^2 \\ -(\zeta_2)^2+2(\zeta_3)^2-(\zeta_4)^2 \\ -(\zeta_3)^2+2(\zeta_4)^2-(\zeta_5)^2 \\ -(\zeta_4)^2+(\zeta_5)^2 \end{bmatrix}^k \quad \textbf{(D.15)}$$

$$\mathbf{M}_{17G} = \frac{(\Delta t)^2}{\Delta x}\begin{bmatrix} 0 \\ (GHu)_1-(GHu)_3 \\ (GHu)_2-(GHu)_4 \\ (GHu)_3-(GHu)_5 \\ (GHu)_4+(GHu)_5 \end{bmatrix}^k \quad \textbf{(D.16)}$$

$$\mathbf{M}_{18G} = -\frac{(\Delta t)^2}{\Delta x}\begin{bmatrix} 0 \\ (\tau Hu)_1 - (\tau Hu)_3 \\ (\tau Hu)_2 - (\tau Hu)_4 \\ (\tau Hu)_3 - (\tau Hu)_5 \\ (\tau Hu)_4 + (\tau Hu)_5 \end{bmatrix}^k \tag{D.17}$$

$$\mathbf{M}_{21G} = \begin{bmatrix} 0 \\ 2\left(\frac{G_2\Delta t}{2} - 1\right)\zeta_2 \\ 2\left(\frac{G_3\Delta t}{2} - 1\right)\zeta_3 \\ 2\left(\frac{G_4\Delta t}{2} - 1\right)\zeta_4 \\ \left(\frac{G_5\Delta t}{2} - 1\right)\zeta_5 \end{bmatrix}^{k-1} \tag{D.18}$$

$$\mathbf{M}_{22G} = \frac{2\varepsilon\Delta t}{(\Delta x)^2}\begin{bmatrix} 0 \\ -\zeta_1 + 2\zeta_2 - \zeta_3 \\ -\zeta_2 + 2\zeta_3 - \zeta_4 \\ -\zeta_3 + 2\zeta_4 - \zeta_5 \\ -\zeta_4 + \zeta_5 \end{bmatrix}^{k-1} \tag{D.19}$$

Similarly, the NCM system can be rewritten as

$$\beta_M(G)\mathbf{u}^{k+1} = \sum_{i=1}^{4} \mathbf{M}_{1iM} \tag{D.20}$$

where the $\mathbf{M}_{1iM}$ terms in the momentum equation are at the current time level. The terms are as follows:

$$\beta_M(G) = \begin{bmatrix} \left(1+\frac{\tau\Delta t}{2}\right) \\ 2\left(1+\frac{\tau\Delta t}{2}\right) \\ 2\left(1+\frac{\tau\Delta t}{2}\right) \\ 2\left(1+\frac{\tau\Delta t}{2}\right) \\ 1 \end{bmatrix} \tag{D.21}$$

$$\mathbf{M}_{11M} = \begin{bmatrix} \left(1-\frac{\tau\Delta t}{2}\right)u_1 \\ 2\left(1-\frac{\tau\Delta t}{2}\right)u_2 \\ 2\left(1-\frac{\tau\Delta t}{2}\right)u_3 \\ 2\left(1-\frac{\tau\Delta t}{2}\right)u_4 \\ 0 \end{bmatrix}^k \tag{D.22}$$

$$\mathbf{M}_{12M} = -\frac{\Delta t}{4\Delta x}\begin{bmatrix} -(u_1+u_2)u_1+(u_1+u_2)u_2 \\ -(u_1+u_2)u_1+(u_1-u_3)u_2+(u_2+u_3)u_3 \\ -(u_2+u_3)u_2+(u_2-u_4)u_3+(u_3+u_4)u_4 \\ -(u_3+u_4)u_3+(u_3-u_5)u_4+(u_4+u_5)u_5 \\ 0 \end{bmatrix}^k \tag{D.23}$$

$$\mathbf{M}_{13M} = -\frac{g\Delta t}{\Delta x}\begin{bmatrix} -\zeta_1+\zeta_2 \\ -\zeta_1+\zeta_3 \\ -\zeta_2+\zeta_4 \\ -\zeta_3+\zeta_5 \\ 0 \end{bmatrix}^k \tag{D.24}$$

$$\mathbf{M}_{14M} = -\frac{2\varepsilon\Delta t}{(\Delta x)^2}\begin{bmatrix} u_1 - u_2 \\ -u_1 + 2u_2 - u_3 \\ -u_2 + 2u_3 - u_4 \\ -u_3 + 2u_4 - u_5 \\ 0 \end{bmatrix}^k \quad \textbf{(D.25)}$$

D.4 Sensitivity to G

As noted in Chapter 4, the sensitivity to each of the coefficients in the parameterization for G are given by (D.26).

$$\frac{\partial\beta(G)}{\partial\alpha_i}\mathbf{c}^{k+1} + \beta(G)\frac{\partial\mathbf{c}^{k+1}}{\partial\alpha_i} = D_c(M_1)\frac{\partial\mathbf{c}^k}{\partial\alpha_i} + D_{\alpha_i}(M_1) + D_c(M_2)\frac{\partial\mathbf{c}^{k-1}}{\partial\alpha_i} + D_{\alpha_i}(M_2) \quad \textbf{(D.26)}$$

where $D_c(M_1) = [\partial M_{1i}/\partial c_j] \in R^{2n\times 2n}$, $D_c(M_2) = [\partial M_{2i}/\partial c_j] \in R^{2n\times 2n}$, $D_{\alpha_i}(M_1) = [\partial M_{1j}/\partial\alpha_i] \in R^{2n}$, and $D_{\alpha_i}(M_2) = [\partial M_{2j}/\partial c_i] \in R^{2n}$.

Following the format used previously, the derivatives and Jacobians will be shown for the individual terms in the GWCE and NCM.

$$\frac{\partial\beta_G(G)}{\partial\alpha_i} = \begin{bmatrix} 0 \\ \Delta t\dfrac{\partial G_2}{\partial\alpha_i} \\ \Delta t\dfrac{\partial G_3}{\partial\alpha_i} \\ \Delta t\dfrac{\partial G_4}{\partial\alpha_i} \\ \dfrac{\Delta t}{2}\dfrac{\partial G_5}{\partial\alpha_i} \end{bmatrix}^k \quad \textbf{(D.27)}$$

$$\frac{\partial \zeta_{bc}^{k+1}}{\partial \alpha_i} = \begin{bmatrix} 0 \\ 0 \\ 0 \\ 0 \\ 0 \end{bmatrix} \tag{D.28}$$

$$D_x(\mathbf{M}_{11G}) = \begin{bmatrix} 0 & 0 & 0 & 0 & 0 & 0 & 0 & 0 & 0 & 0 \\ 0 & 4 & 0 & 0 & 0 & 0 & 0 & 0 & 0 & 0 \\ 0 & 0 & 4 & 0 & 0 & 0 & 0 & 0 & 0 & 0 \\ 0 & 0 & 0 & 4 & 0 & 0 & 0 & 0 & 0 & 0 \\ 0 & 0 & 0 & 0 & 2 & 0 & 0 & 0 & 0 & 0 \end{bmatrix} \tag{D.29}$$

$$D_x(\mathbf{M}_{12G}) = -\frac{2\varepsilon\Delta t}{(\Delta x)^2}\begin{bmatrix} 0 & 0 & 0 & 0 & 0 & 0 & 0 & 0 & 0 & 0 \\ -1 & 2 & -1 & 0 & 0 & 0 & 0 & 0 & 0 & 0 \\ 0 & -1 & 2 & -1 & 0 & 0 & 0 & 0 & 0 & 0 \\ 0 & 0 & -1 & 2 & -1 & 0 & 0 & 0 & 0 & 0 \\ 0 & 0 & 0 & -1 & 1 & 0 & 0 & 0 & 0 & 0 \end{bmatrix} \tag{D.30}$$

$$D_x(\mathbf{M}_{13G}) = -\frac{g(\Delta t)^2}{(\Delta x)^2}\begin{bmatrix} 0 & 0 & 0 & 0 & 0 & 0 & 0 & 0 & 0 & 0 \\ -(h_1+h_2) & h_1+2h_2+h_3 & -(h_2+h_3) & 0 & 0 & 0 & 0 & 0 & 0 & 0 \\ 0 & -(h_2+h_3) & h_2+2h_3+h_4 & -(h_3+h_4) & 0 & 0 & 0 & 0 & 0 & 0 \\ 0 & 0 & -(h_3+h_4) & h_3+2h_4+h_5 & -(h_4+h_5) & 0 & 0 & 0 & 0 & 0 \\ 0 & 0 & 0 & -(h_4+h_5) & h_4+h_5 & 0 & 0 & 0 & 0 & 0 \end{bmatrix} \tag{D.31}$$

$$D_x(\mathbf{M}_{14G}) = -\frac{2(\Delta t)^2}{(\Delta x)^2}\begin{bmatrix} 0 & 0 & 0 & 0 & 0 & 0 & 0 & 0 & 0 & 0 \\ -(u_1)^2 & 2(u_2)^2 & -(u_3)^2 & 0 & 0 & -2(Hu)_1 & 4(Hu)_2 & -2(Hu)_3 & 0 & 0 \\ 0 & -(u_2)^2 & 2(u_3)^2 & -(u_4)^2 & 0 & 0 & -2(Hu)_2 & 4(Hu)_3 & -2(Hu)_4 & 0 \\ 0 & 0 & -(u_3)^2 & 2(u_4)^2 & -(u_5)^2 & 0 & 0 & -2(Hu)_3 & 4(Hu)_4 & -2(Hu)_5 \\ 0 & 0 & 0 & -(u_4)^2 & (u_5)^2 & 0 & 0 & 0 & -2(Hu)_4 & 2(Hu)_5 \end{bmatrix}^k \tag{D.32}$$

$$D_x(\mathbf{M}_{15G}) = \frac{(\Delta t)^2}{2\Delta x} \tag{D.33}$$

$$\begin{bmatrix} 0 & 0 & 0 & 0 & 0 & 0 & 0 & 0 & 0 & 0 \\ u_1(G_2-G_1) & u_2(G_3-G_1) & u_3(G_3-G_2) & 0 & 0 & H_1(G_2-G_1) & H_2(G_3-G_1) & H_3(G_3-G_2) & 0 & 0 \\ 0 & u_2(G_3-G_2) & u_3(G_4-G_2) & u_4(G_4-G_3) & 0 & 0 & H_2(G_3-G_2) & H_3(G_4-G_2) & H_4(G_4-G_3) & 0 \\ 0 & 0 & u_3(G_4-G_3) & u_4(G_5-G_3) & u_5(G_5-G_4) & 0 & 0 & H_3(G_4-G_3) & H_4(G_5-G_3) & H_5(G_5-G_4) \\ 0 & 0 & 0 & u_4(G_5-G_4) & u_5(G_5-G_4) & 0 & 0 & 0 & H_4(G_5-G_4) & H_5(G_5-G_4) \end{bmatrix}^k$$

$$D_x(\mathbf{M}_{16G}) = -\frac{g(\Delta t)^2}{(\Delta x)^2}\begin{bmatrix} 0 & 0 & 0 & 0 & 0 & 0\,0\,0\,0\,0 \\ -2\zeta_1 & 4\zeta_2 & -2\zeta_3 & 0 & 0 & 0\,0\,0\,0\,0 \\ 0 & -2\zeta_2 & 4\zeta_3 & -2\zeta_4 & 0 & 0\,0\,0\,0\,0 \\ 0 & 0 & -2\zeta_3 & 4\zeta_4 & -2\zeta_5 & 0\,0\,0\,0\,0 \\ 0 & 0 & 0 & -2\zeta_4 & 2\zeta_5 & 0\,0\,0\,0\,0 \end{bmatrix}^k \quad \textbf{(D.34)}$$

$$D_x(\mathbf{M}_{17G}) = \frac{(\Delta t)^2}{\Delta x}\begin{bmatrix} 0 & 0 & 0 & 0 & 0 & 0 & 0 & 0 & 0 & 0 \\ (Gu)_1 & 0 & -(Gu)_3 & 0 & 0 & (GH)_1 & 0 & -(GH)_3 & 0 & 0 \\ 0 & (Gu)_2 & 0 & -(Gu)_4 & 0 & 0 & (GH)_2 & 0 & -(GH)_4 & 0 \\ 0 & 0 & (Gu)_3 & 0 & -(Gu)_5 & 0 & 0 & (GH)_3 & 0 & -(GH)_5 \\ 0 & 0 & 0 & (Gu)_4 & (Gu)_5 & 0 & 0 & 0 & (GH)_4 & (GH)_5 \end{bmatrix}^k \quad \textbf{(D.35)}$$

$$D_x(\mathbf{M}_{18G}) = \quad \textbf{(D.36)}$$

$$-\frac{(\Delta t)^2}{\Delta x}\begin{bmatrix} 0 & 0 & 0 & 0 & 0 & 0 & 0 & 0 & 0 & 0 \\ (\tau u)_1 & 0 & -(\tau u)_3 & 0 & 0 & (\tau H)_1 & 0 & -(\tau H)_3 & 0 & 0 \\ 0 & (\tau u)_2 & 0 & -(\tau u)_4 & 0 & 0 & (\tau H)_2 & 0 & -(\tau H)_4 & 0 \\ 0 & 0 & (\tau u)_3 & 0 & -(\tau u)_5 & 0 & 0 & (\tau H)_3 & 0 & -(\tau H)_5 \\ 0 & 0 & 0 & (\tau u)_4 & (\tau u)_5 & 0 & 0 & 0 & (\tau H)_4 & (\tau H)_5 \end{bmatrix}^k$$

$$D_x(\mathbf{M}_{21G}) = \begin{bmatrix} 0 & 0 & 0 & 0 & 0 & 0\,0\,0\,0\,0 \\ 0 & 2\left(\frac{G_2\Delta t}{2}-1\right) & 0 & 0 & 0 & 0\,0\,0\,0\,0 \\ 0 & 0 & 2\left(\frac{G_3\Delta t}{2}-1\right) & 0 & 0 & 0\,0\,0\,0\,0 \\ 0 & 0 & 0 & 2\left(\frac{G_4\Delta t}{2}-1\right) & 0 & 0\,0\,0\,0\,0 \\ 0 & 0 & 0 & 0 & \frac{G_5\Delta t}{2}-1 & 0\,0\,0\,0\,0 \end{bmatrix}^{k-1} \quad \textbf{(D.37)}$$

$$D_x(\mathbf{M}_{22G}) = \frac{2\varepsilon\Delta t}{(\Delta x)^2}\begin{bmatrix} 0 & 0 & 0 & 0 & 0 & 0 & 0 & 0 & 0 & 0 \\ -1 & 2 & -1 & 0 & 0 & 0 & 0 & 0 & 0 & 0 \\ 0 & -1 & 2 & -1 & 0 & 0 & 0 & 0 & 0 & 0 \\ 0 & 0 & -1 & 2 & -1 & 0 & 0 & 0 & 0 & 0 \\ 0 & 0 & 0 & -1 & 1 & 0 & 0 & 0 & 0 & 0 \end{bmatrix} \tag{D.38}$$

$$\frac{\partial \beta_M(G)}{\partial \alpha_i} = \begin{bmatrix} 0 \\ 0 \\ 0 \\ 0 \\ 0 \end{bmatrix} \tag{D.39}$$

$$D_x(\mathbf{M}_{11M}) = \left(1 - \frac{\tau\Delta t}{2}\right)\begin{bmatrix} 0 & 0 & 0 & 0 & 0 & 1 & 0 & 0 & 0 & 0 \\ 0 & 0 & 0 & 0 & 0 & 0 & 2 & 0 & 0 & 0 \\ 0 & 0 & 0 & 0 & 0 & 0 & 0 & 2 & 0 & 0 \\ 0 & 0 & 0 & 0 & 0 & 0 & 0 & 0 & 2 & 0 \\ 0 & 0 & 0 & 0 & 0 & 0 & 0 & 0 & 0 & 0 \end{bmatrix} \tag{D.40}$$

$$D_x(\mathbf{M}_{12M}) = -\frac{\Delta t}{4\Delta x}\begin{bmatrix} 0 & 0 & 0 & 0 & 0 & -2u_1 & 2u_2 & 0 & 0 & 0 \\ 0 & 0 & 0 & 0 & 0 & -2u_1 & 0 & 2u_3 & 0 & 0 \\ 0 & 0 & 0 & 0 & 0 & 0 & -2u_2 & 0 & 2u_4 & 0 \\ 0 & 0 & 0 & 0 & 0 & 0 & 0 & -2u_3 & 0 & 2u_5 \\ 0 & 0 & 0 & 0 & 0 & 0 & 0 & 0 & 0 & 0 \end{bmatrix}^k \tag{D.41}$$

$$D_x(\mathbf{M}_{13M}) = -\frac{g\Delta t}{\Delta x}\begin{bmatrix} -1 & 1 & 0 & 0 & 0 & 0 & 0 & 0 & 0 & 0 \\ -1 & 0 & 1 & 0 & 0 & 0 & 0 & 0 & 0 & 0 \\ 0 & -1 & 0 & 1 & 0 & 0 & 0 & 0 & 0 & 0 \\ 0 & 0 & -1 & 0 & 1 & 0 & 0 & 0 & 0 & 0 \\ 0 & 0 & 0 & 0 & 0 & 0 & 0 & 0 & 0 & 0 \end{bmatrix} \tag{D.42}$$

$$D_x(\mathbf{M}_{14M}) = -\frac{2\varepsilon\Delta t}{(\Delta x)^2}\begin{bmatrix} 0 & 0 & 0 & 0 & 0 & 1 & -1 & 0 & 0 & 0 \\ 0 & 0 & 0 & 0 & 0 & -1 & 2 & -1 & 0 & 0 \\ 0 & 0 & 0 & 0 & 0 & 0 & -1 & 2 & -1 & 0 \\ 0 & 0 & 0 & 0 & 0 & 0 & 0 & -1 & 2 & -1 \\ 0 & 0 & 0 & 0 & 0 & 0 & 0 & 0 & 0 & 0 \end{bmatrix} \tag{D.43}$$

The Jacobians with respect to the coefficients in the G parameterization will not be shown. Rather, the derivative with respect to a given coefficient, α_i, will be shown. The GWCE and NCM have been combined for the following terms.

$$\frac{\partial M_1}{\partial \alpha_i} = \frac{(\Delta t)^2}{2\Delta x}\begin{bmatrix} 0 \\ -(H_1u_1 + H_2u_2)\dfrac{\partial G_1}{\partial \alpha_i} + (H_1u_1 - H_3u_3)\dfrac{\partial G_2}{\partial \alpha_i} + (H_2u_2 + H_3u_3)\dfrac{\partial G_3}{\partial \alpha_i} \\ -(H_2u_2 + H_3u_3)\dfrac{\partial G_2}{\partial \alpha_i} + (H_2u_2 - H_4u_4)\dfrac{\partial G_3}{\partial \alpha_i} + (H_3u_3 + H_4u_4)\dfrac{\partial G_4}{\partial \alpha_i} \\ -(H_3u_3 + H_4u_4)\dfrac{\partial G_3}{\partial \alpha_i} + (H_3u_3 - H_5u_5)\dfrac{\partial G_4}{\partial \alpha_i} + (H_4u_4 + H_5u_5)\dfrac{\partial G_5}{\partial \alpha_i} \\ -(H_4u_4 + H_5u_5)\dfrac{\partial G_4}{\partial \alpha_i} + (H_4u_4 + H_5u_5)\dfrac{\partial G_5}{\partial \alpha_i} \\ 0 \\ 0 \\ 0 \\ 0 \\ 0 \end{bmatrix}^k + \textbf{(D.44)}$$

$$\frac{(\Delta t)^2}{\Delta x}\begin{bmatrix} 0 \\ H_1u_1\dfrac{\partial G_1}{\partial \alpha_i} - H_3u_3\dfrac{\partial G_3}{\partial \alpha_i} \\ H_2u_2\dfrac{\partial G_2}{\partial \alpha_i} - H_4u_4\dfrac{\partial G_4}{\partial \alpha_i} \\ H_3u_3\dfrac{\partial G_3}{\partial \alpha_i} - H_5u_5\dfrac{\partial G_5}{\partial \alpha_i} \\ H_4u_4\dfrac{\partial G_4}{\partial \alpha_i} + H_5u_5\dfrac{\partial G_5}{\partial \alpha_i} \\ 0 \\ 0 \\ 0 \\ 0 \\ 0 \end{bmatrix}^k$$

$$\frac{\partial M_2}{\partial \alpha_i} = \begin{bmatrix} 0 \\ \Delta t \zeta_2 \dfrac{\partial G_2}{\partial \alpha_i} \\ \Delta t \zeta_3 \dfrac{\partial G_3}{\partial \alpha_i} \\ \Delta t \zeta_4 \dfrac{\partial G_4}{\partial \alpha_i} \\ \dfrac{\Delta t}{2} \zeta_5 \dfrac{\partial G_5}{\partial \alpha_i} \\ 0 \\ 0 \\ 0 \\ 0 \\ 0 \end{bmatrix}^{k-1} \tag{D.45}$$

Appendix E. 1-D Coupling Results on Variable Sloping Domain

E.1 Hydraulic Simulations Using Full-Domain ADCIRC Forcing

The simulations in this section were performed using the constant unit discharge upstream boundary condition and the 2.5 day water surface elevation ocean boundary condition (Figure 5.8) presented in Chapter 5.

E.1.1 Kinematic Wave Channel Routing

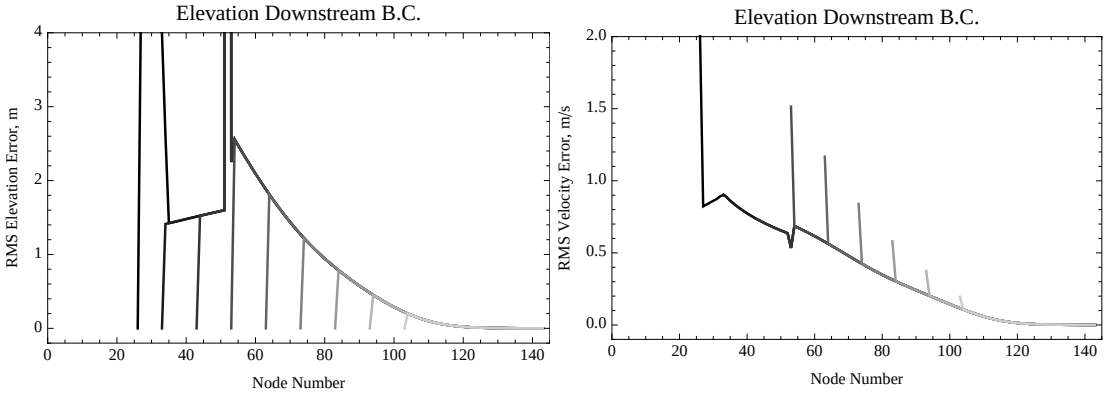

Figure E.1 Elevation and velocity $RMSE_t$ for the kinematic wave channel routing model on the variable sloping domain. The downstream boundary conditions come from a full-domain ADCIRC simulation. Each of the nine different lines corresponds to a simulation with a different hand-off point. The darkest lines show results for the simulation with the most oceanward hand-off point. The lines get successively lighter as the hand-off point is moved upstream.

E.1.2 Diffusive Wave Channel Routing

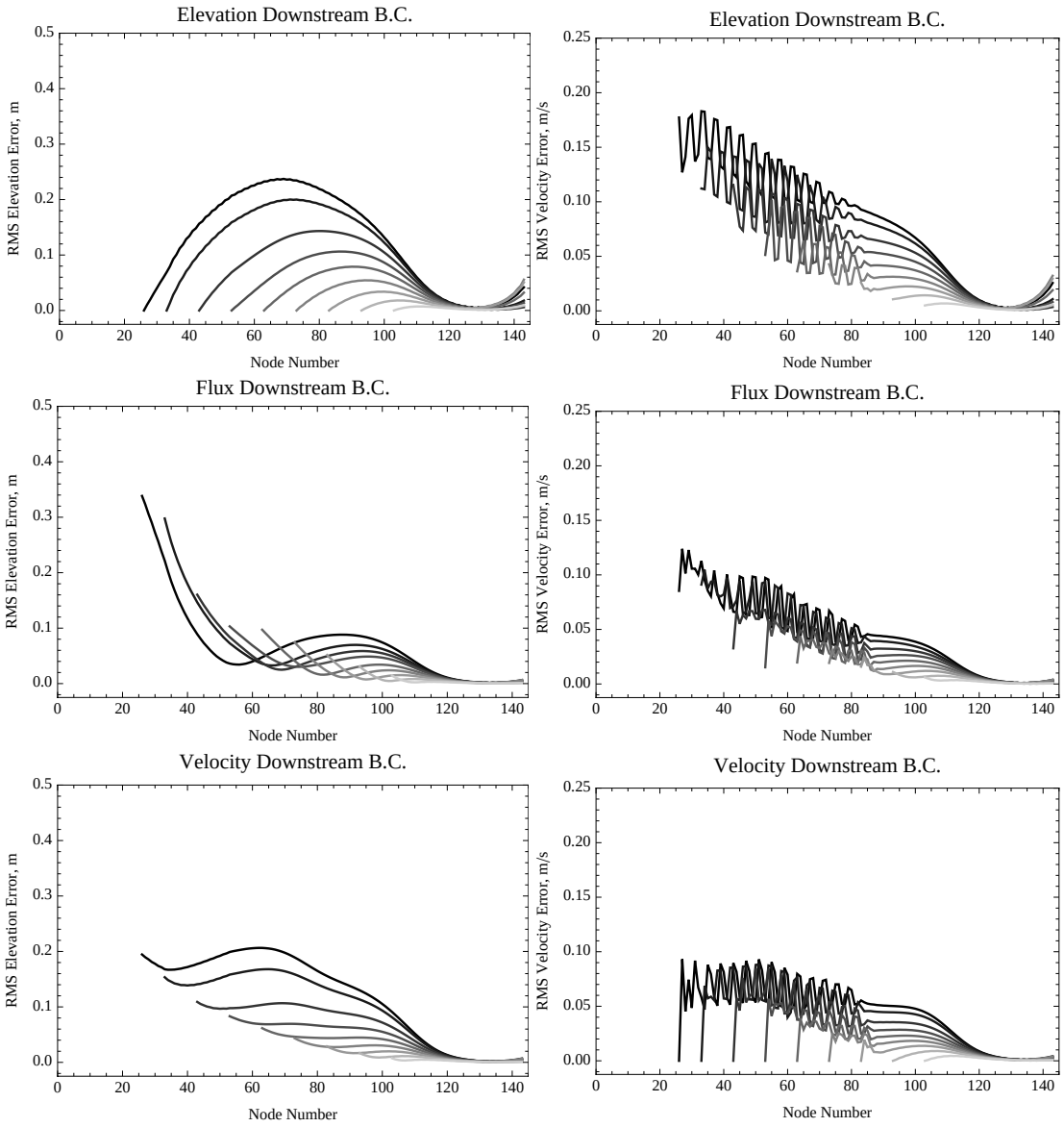

Figure E.2 Elevation and velocity $RMSE_t$ for the diffusive wave channel routing model on the variable sloping domain. The downstream boundary conditions come from a full-domain ADCIRC simulation.

E.1.3 Dynamic Wave Channel Routing

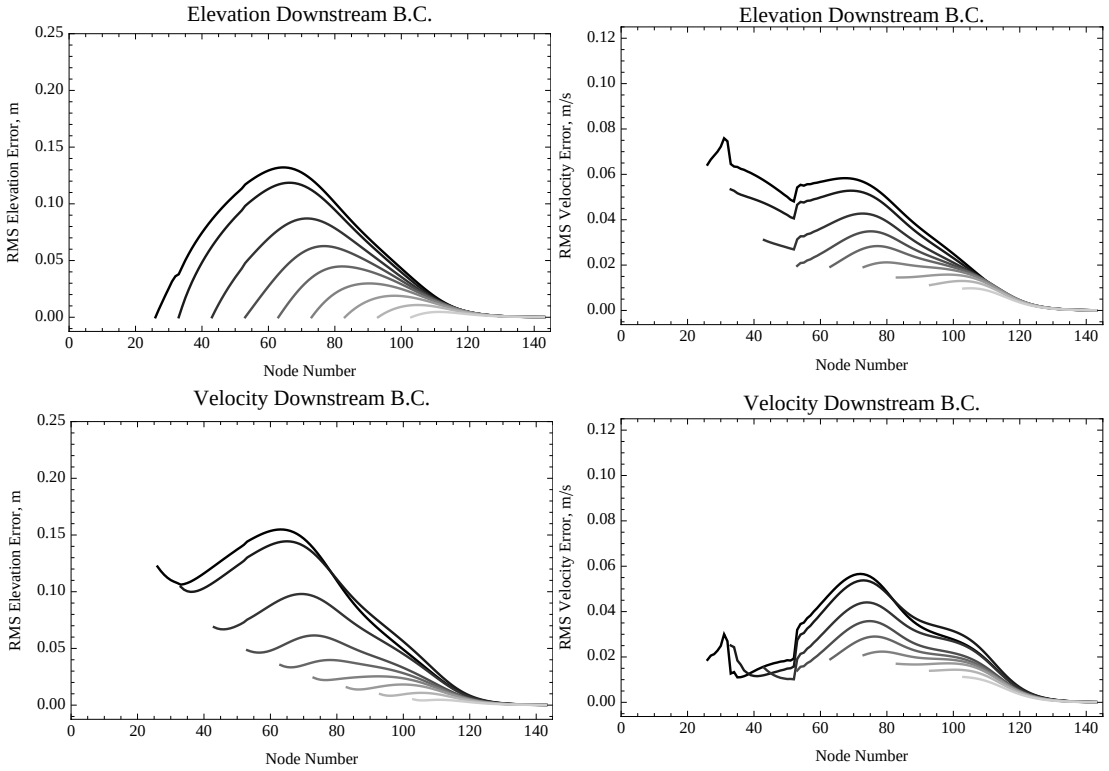

Figure E.3 Elevation and velocity $RMSE_t$ for the dynamic wave channel routing model on the variable sloping domain. The downstream boundary conditions come from a full-domain ADCIRC simulation.

E.2 ADCIRC Simulations Using Full-Domain Hydraulic Forcing

The simulations in this section used the constant unit discharge upstream and the 2.5 day water surface elevation ocean boundary conditions presented in Chapter 5.

E.2.1 Full-Domain Comparisons

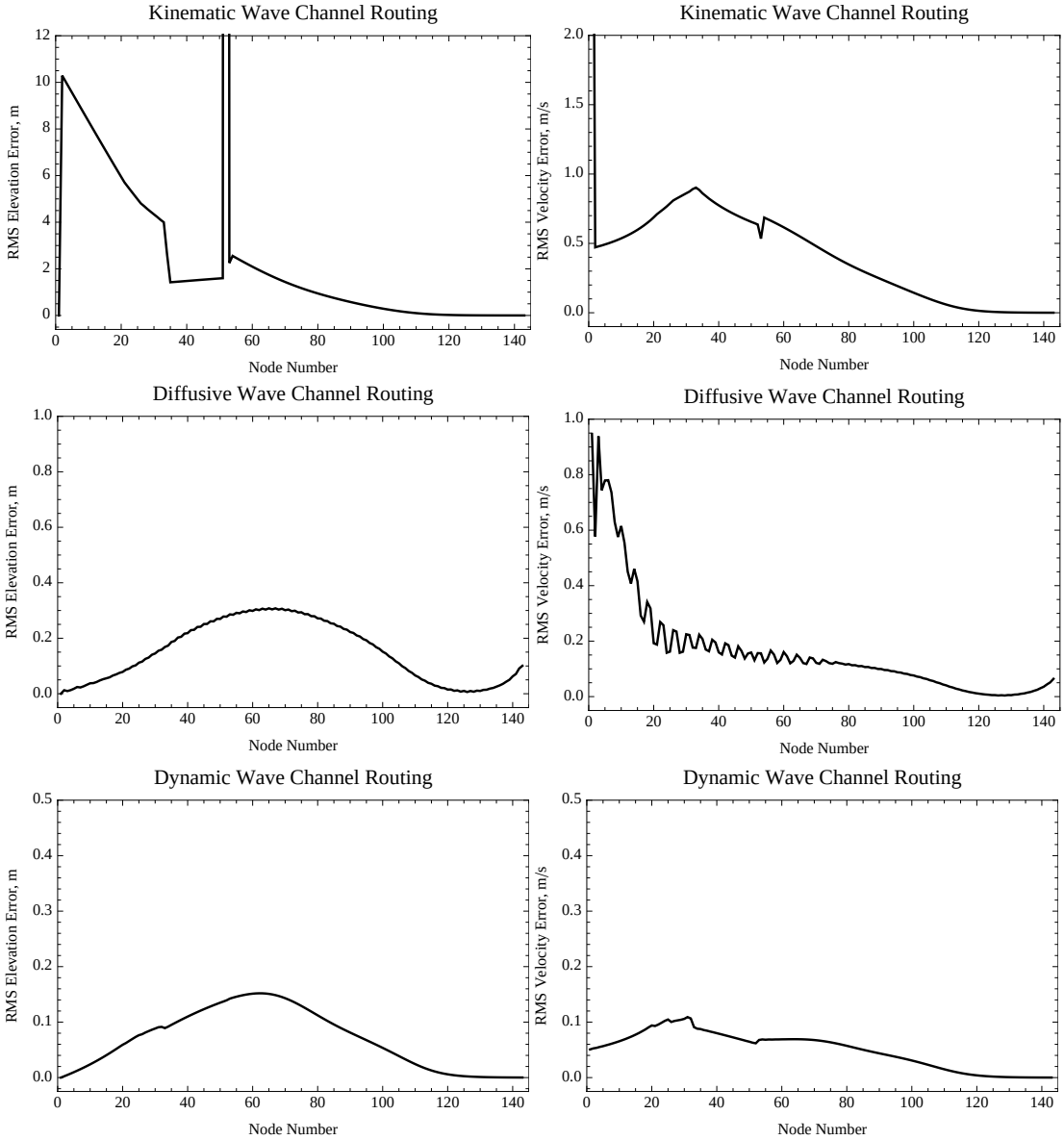

Figure E.4 Elevation and velocity $RMSE_t$ for the full-domain channel routing models on the variable sloping domain. The full-domain ADCIRC simulation results are used as the true solution.

E.2.2 ADCIRC Forced with Upstream Elevation Boundary Conditions from Channel Routing Models

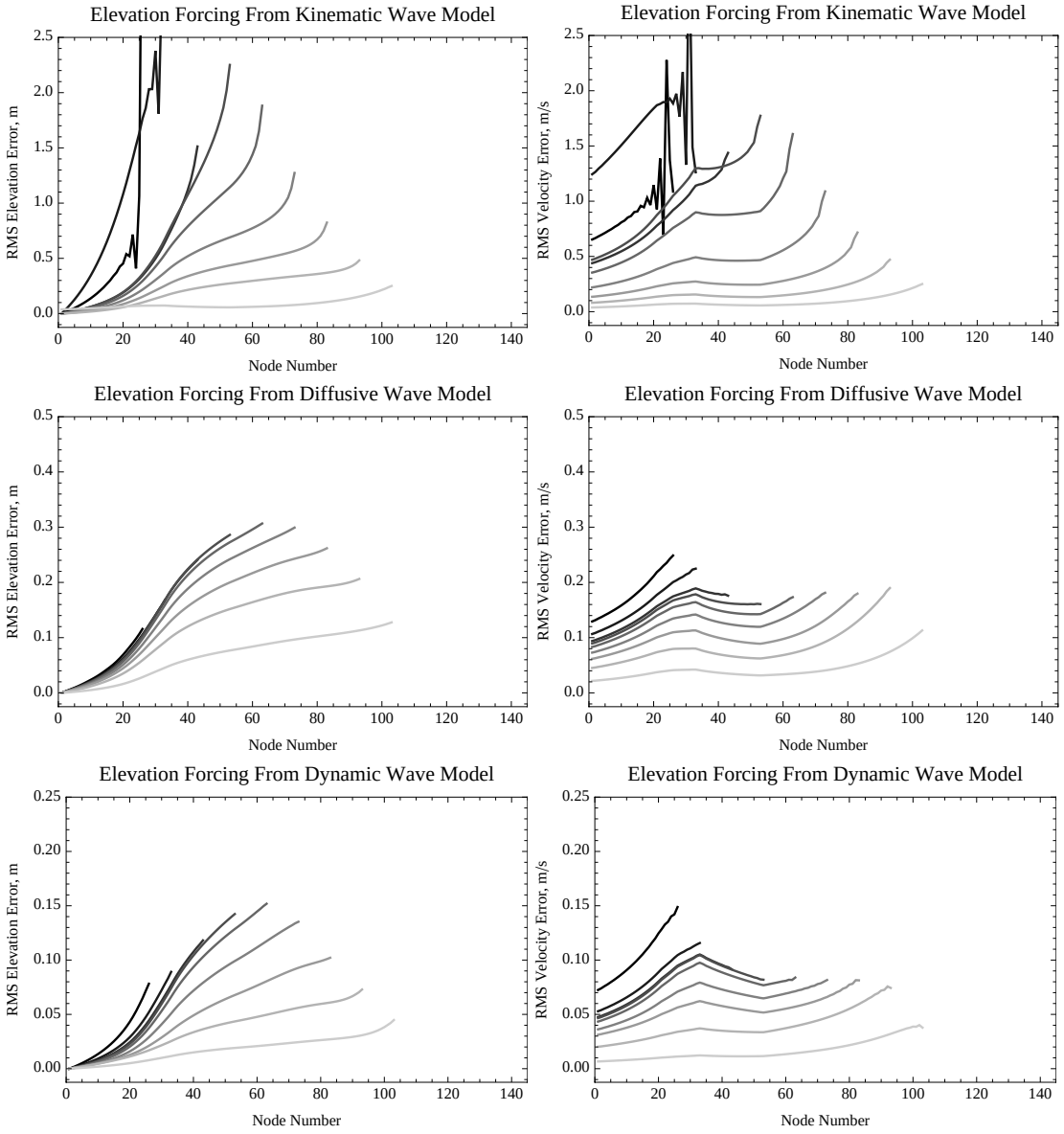

Figure E.5 Elevation and velocity $RMSE_t$ for ADCIRC on the variable sloping domain. The upstream boundary conditions come from the full-domain channel routing simulations.

E.2.3 ADCIRC Forced with Upstream Boundary Condition from Dynamic Wave Model

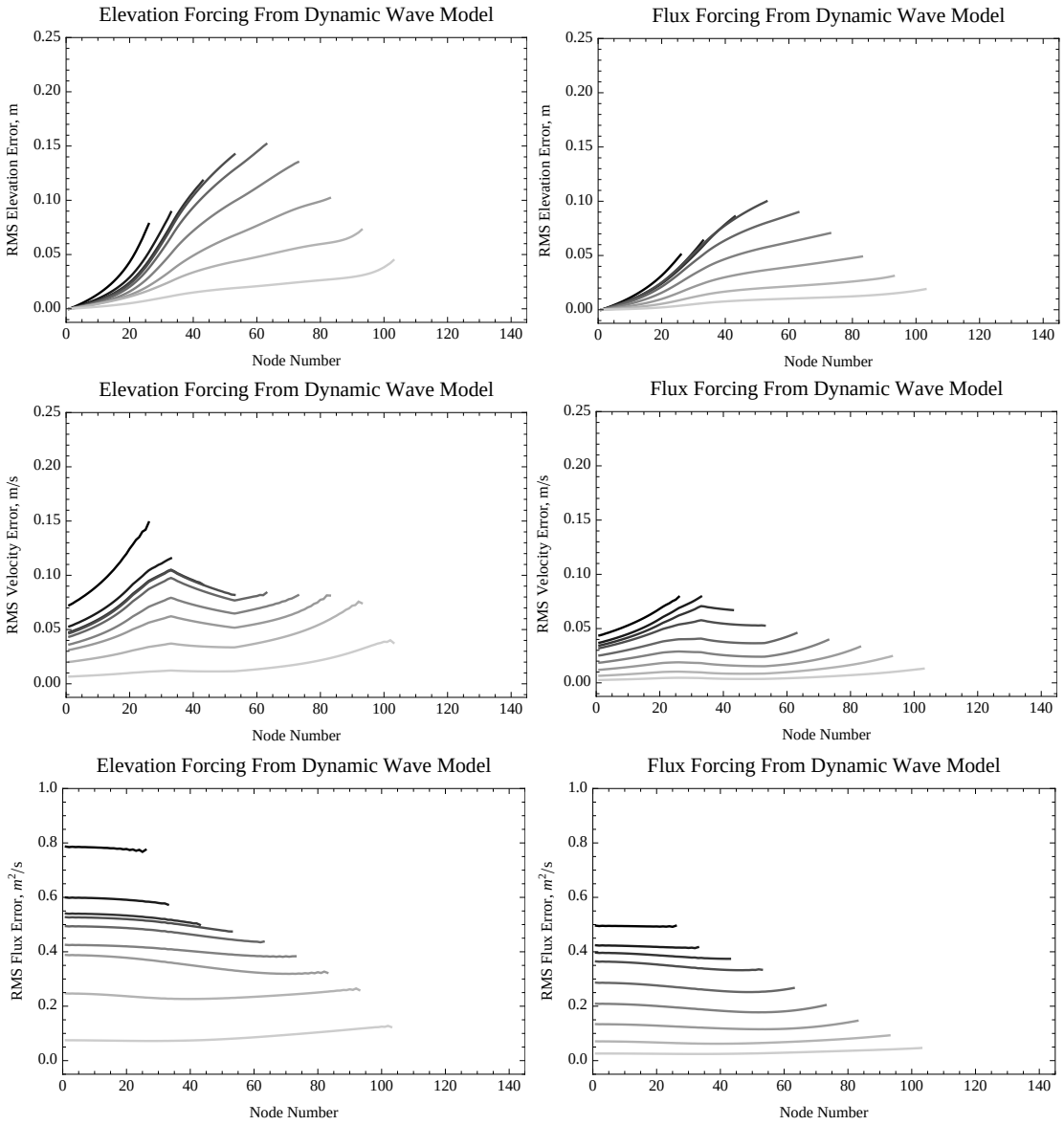

Figure E.6 Elevation, velocity and flux $RMSE_t$ for ADCIRC on the variable sloping domain. The upstream boundary conditions from the full-domain dynamic wave channel routing simulation.

E.2.4 ADCIRC Forced with Upstream Boundary Condition from ADCIRC Model

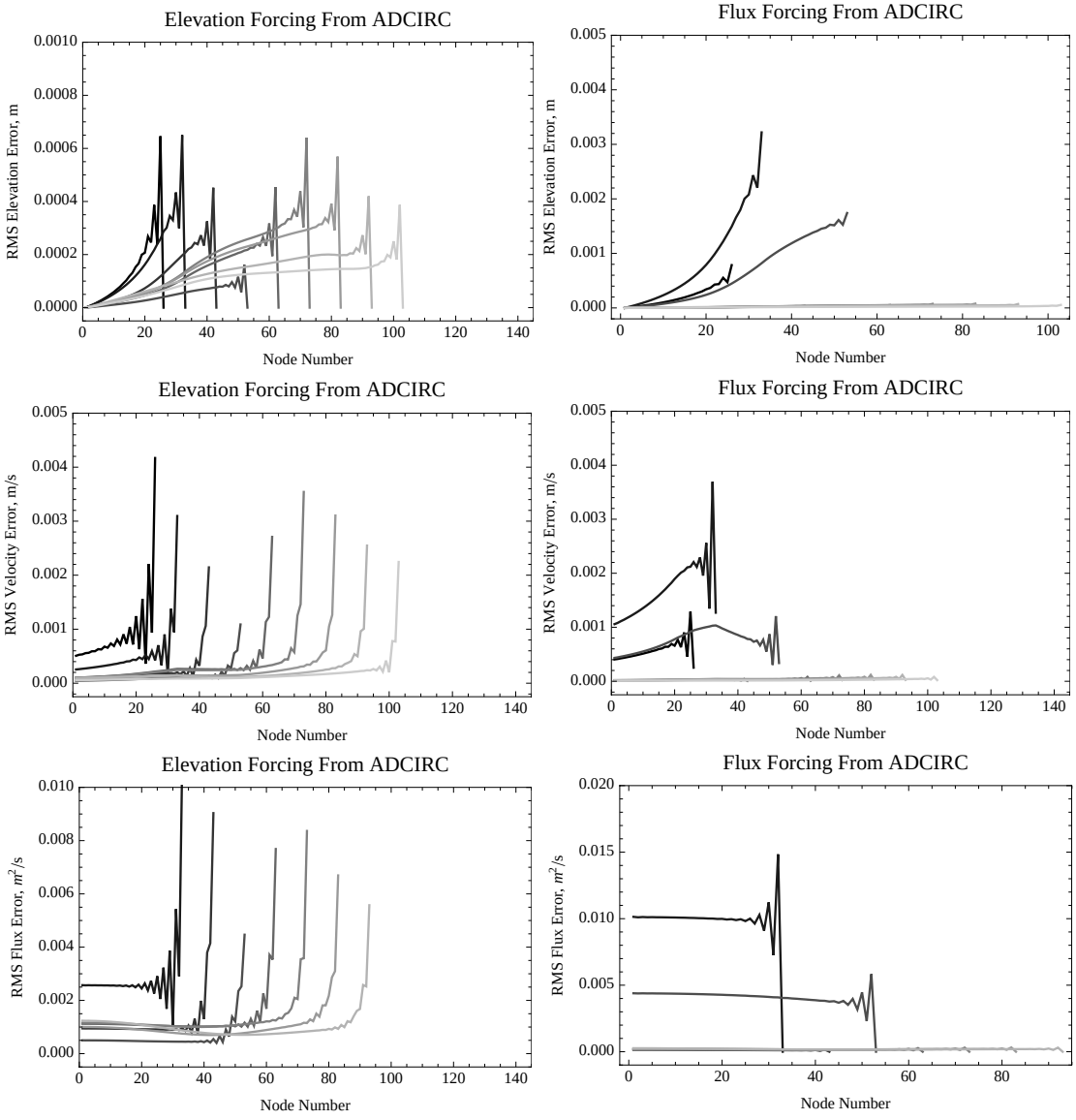

Figure E.7 Elevation, velocity and flux $RMSE_t$ for ADCIRC on the variable sloping domain. The upstream boundary conditions from the full-domain ADCIRC simulation.

E.3 Simulations Using Boundary Forcing from Partial-Domain Simulations

The 5.0 day simulations in this section use the non-constant unit discharge upstream (Figure 5.19) and WSE ocean (Figure 5.18) boundary conditions presented in Chapter 5.

E.3.1 ADCIRC Forced with Upstream Boundary Condition from Partial-Domain Dynamic Wave Model

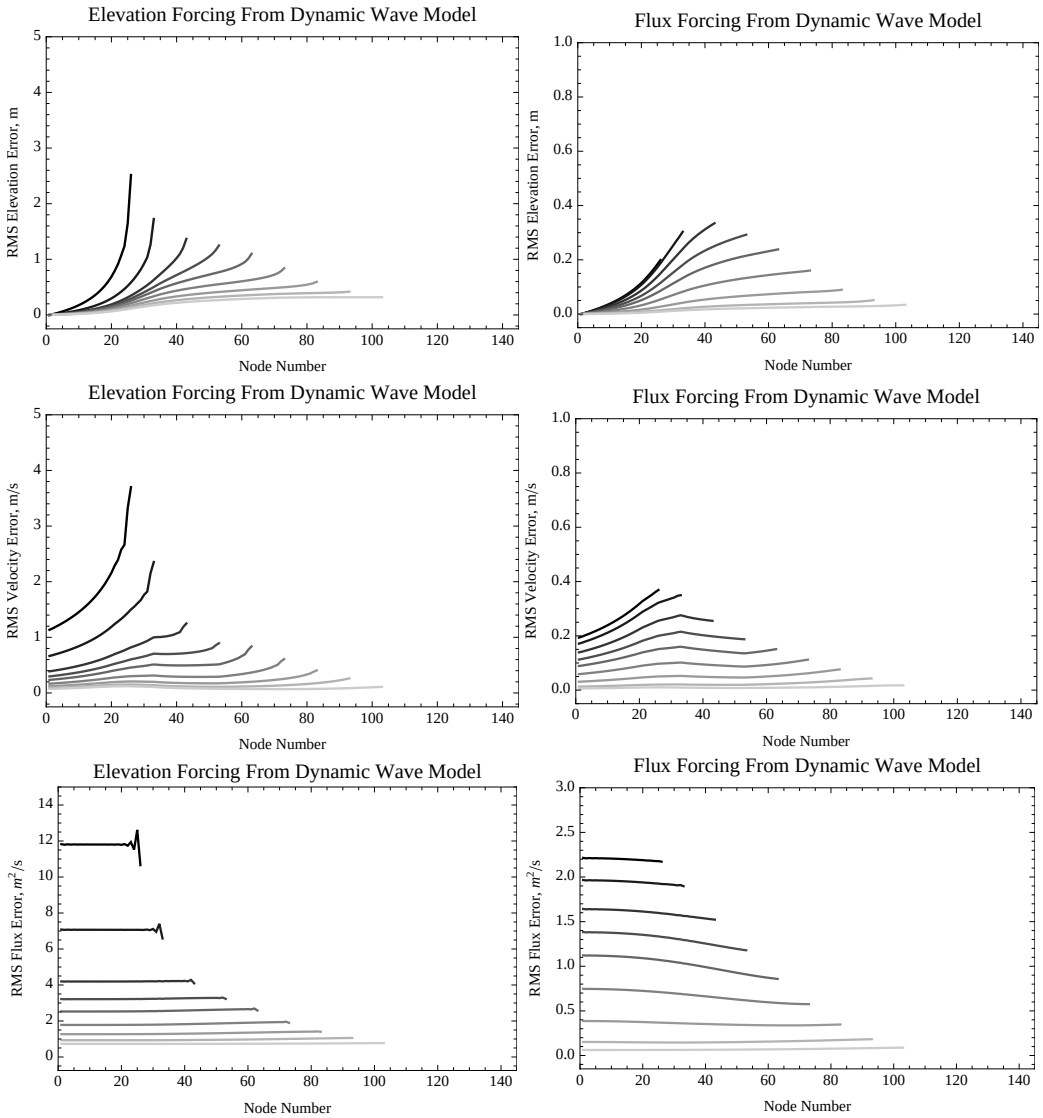

Figure E.8 Elevation, velocity and flux $RMSE_t$ for ADCIRC on the variable sloping domain. The upstream boundary conditions come from partial-domain dynamic wave channel routing simulations.

E.3.2 Dynamic Wave Hydraulic Model Forced with Downstream Elevation from ADCIRC

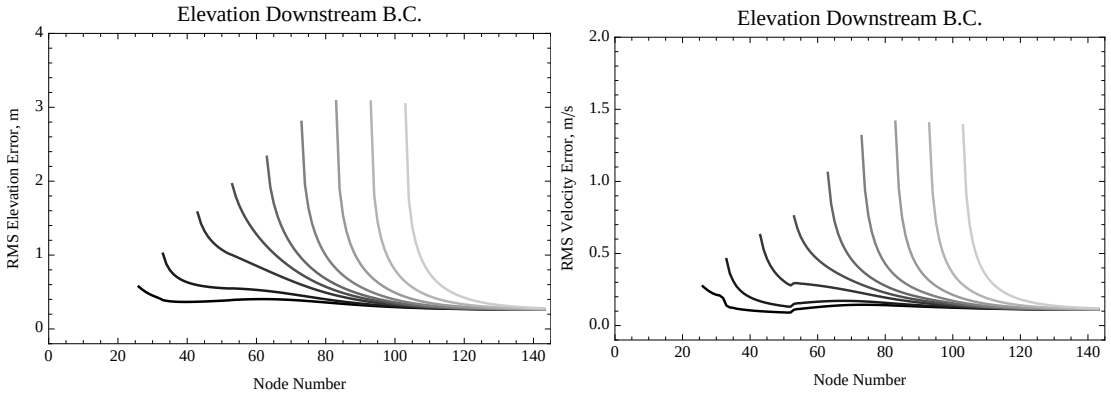

Figure E.9 Elevation and velocity $RMSE_t$ for the dynamic wave hydraulic model on the variable sloping domain. The downstream boundary conditions come from the partial-domain ADCIRC simulation.

E.4 Two-Way Coupling of ADCIRC to the Dynamic Wave Hydraulic Model

The simulations in this section were 5.0 day simulations using the 5.0 day water surface elevation ocean boundary condition. The first set simulations used a constant unit discharge (2.0 m^2/s) and the second set used the non-constant unit discharge hydrograph.

E.4.1 Constant Upstream Discharge

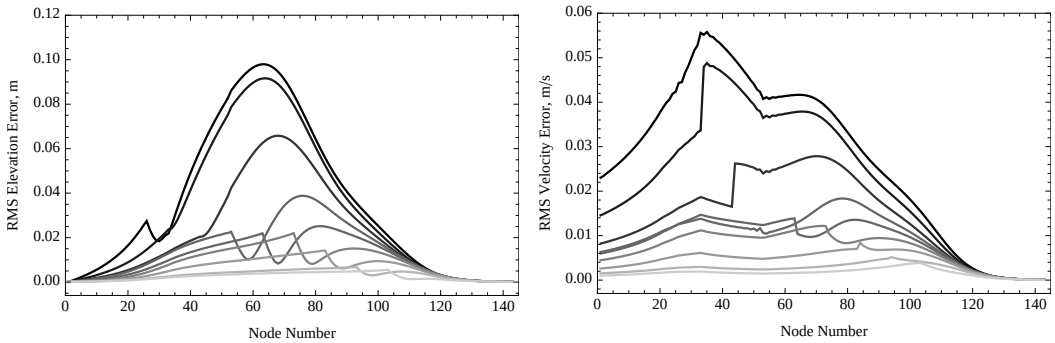

Figure E.10 Elevation and velocity $RMSE_t$ for the two-way coupled model on the variable sloping domain. The coupled model is compared to the full-domain ADCIRC simulation to compute the errors.

E.4.2 Non-Constant Upstream Discharge

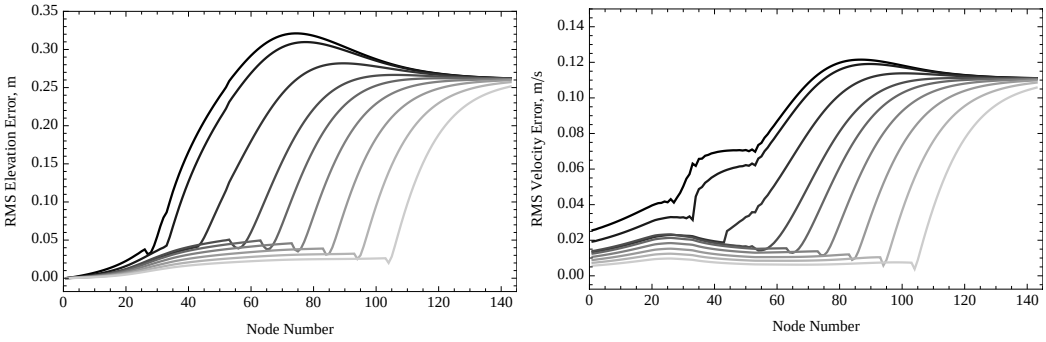

Figure E.11 Elevation and velocity $RMSE_t$ for the two-way coupled model on the variable sloping domain. The coupled model is compared to the full-domain ADCIRC simulation to compute the errors.

Appendix F. Comparison of ADCIRC Grid Geometry to North Carolina Floodplain Mapping Program Cross-Sections

F.1 Locations for Comparisons

HEC-RAS cross-sections provided by the North Carolina Floodplain Mapping Program (NCFMP) were used to evaluate the river geometry representation in the ADCIRC grid. The locations were estimated using descriptions of distances from landmarks on the NCFMP stations. The nineteen locations used on the Tar River are shown in Figure F.1. The twenty locations used on the Neuse River are shown in Figure F.2.

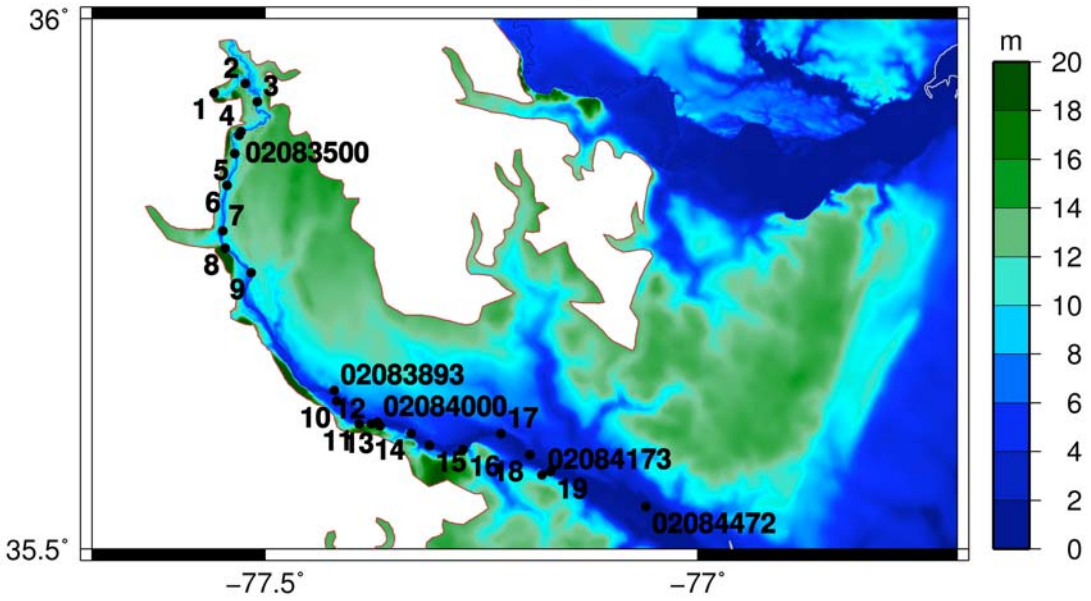

Figure F.1 NCFMP to ADCIRC grid comparison locations and USGS gauge station locations (8-digit numbers) on the Tar River.

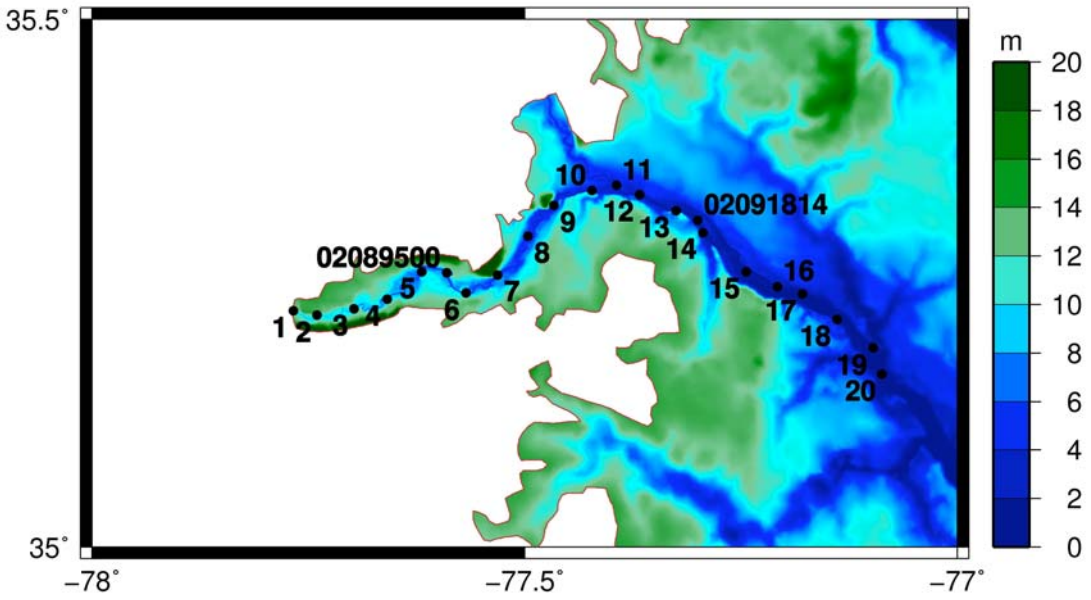

Figure F.2 NCFMP to ADCIRC grid comparison locations and USGS gauge station locations (8-digit numbers) on the Neuse River.

F.2 Idealized Water Surface Elevation vs. Discharge Plots for Locations on the Tar River

The water surface elevation vs. discharge plots for the sections were developed using a bottom slope of 0.00015 and a Manning's roughness value of 0.025. The water surface elevation values are based on uniform flow depth for a given flow rate. The plots for the first eight locations on the Tar River can be found in Figure F.3. The comparisons for locations nine through sixteen are shown in Figure F.4. The data for the last three sections on the Tar River is plotted in Figure F.5.

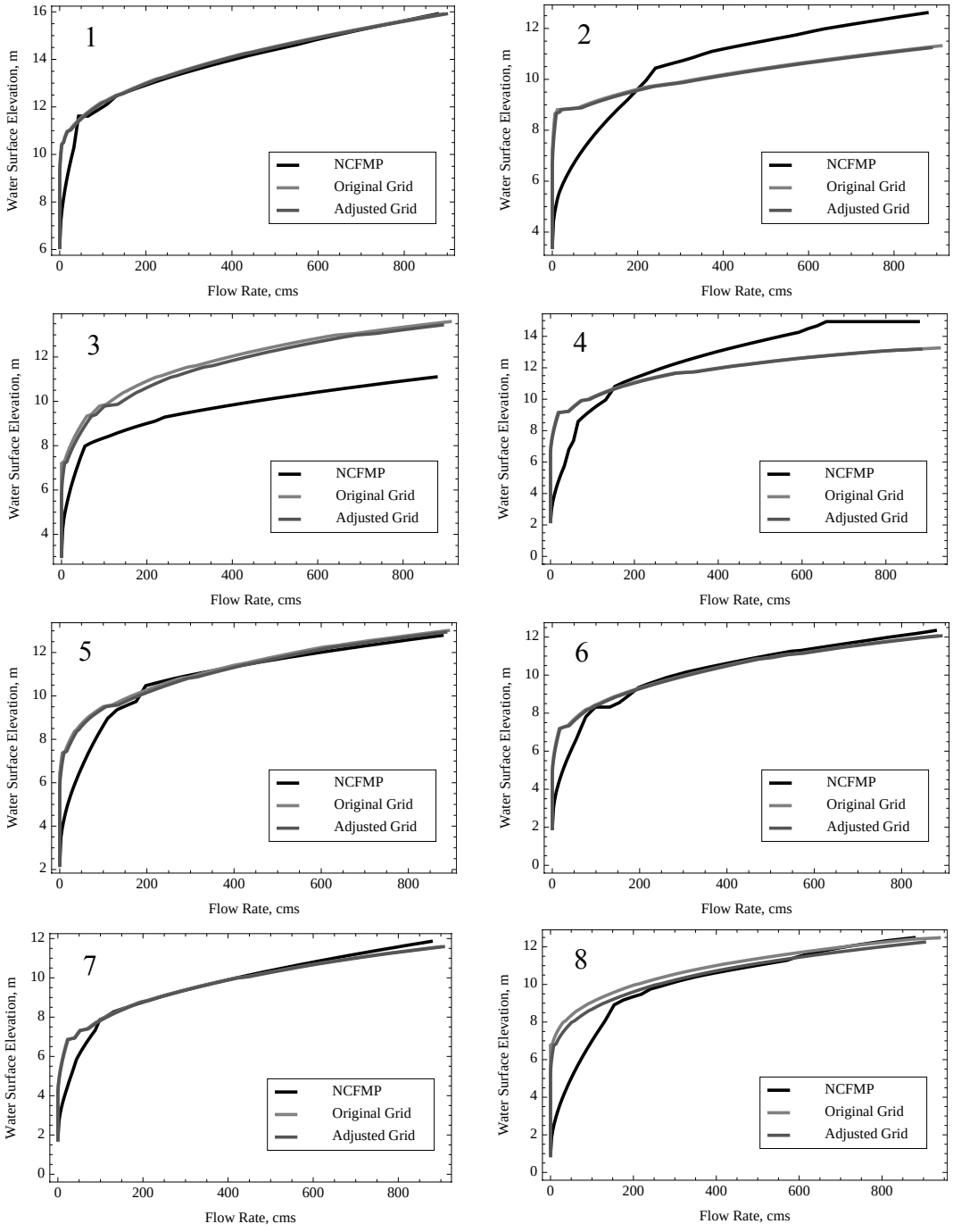

Figure F.3 Water surface elevation vs. discharge plots to compare the ADCIRC cross-section to the actual channel cross-sections (from NCFMP data) for the first eight locations on the Tar River.

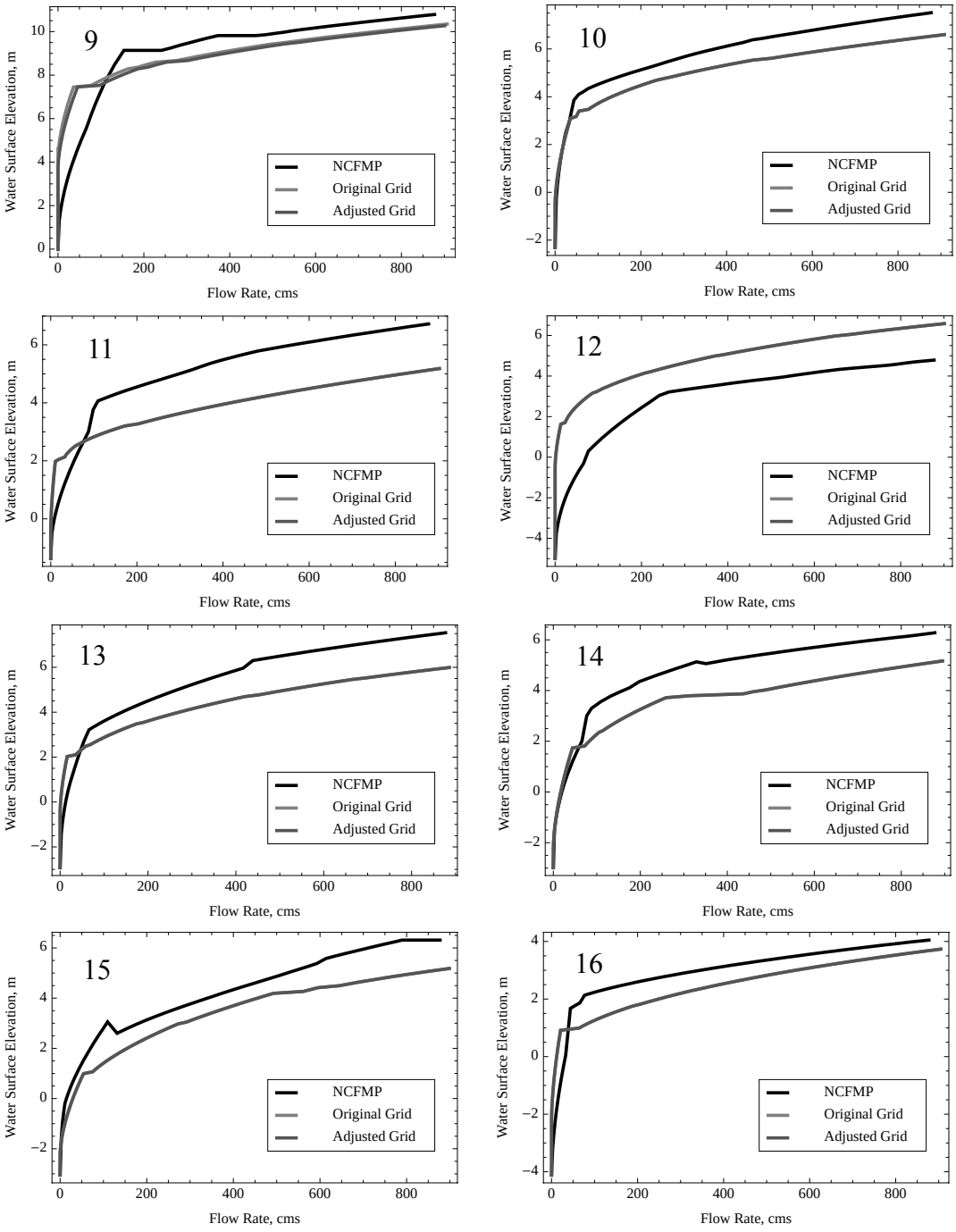

Figure F.4 Water surface elevation vs. discharge plots to compare the ADCIRC cross-section to the actual channel cross-sections (from NCFMP data) for locations nine through sixteen on the Tar River.

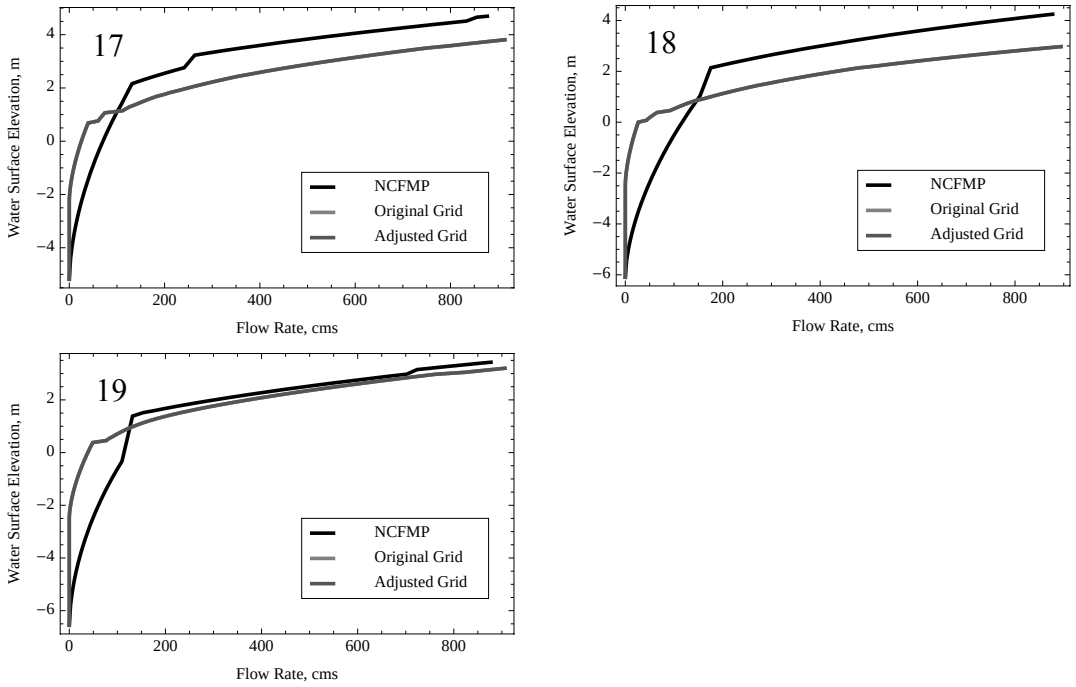

Figure F.5 Water surface elevation vs. discharge plots to compare the ADCIRC cross-section to the actual channel cross-sections (from NCFMP data) for locations seventeen through nineteen on the Tar River.

F.3 Idealized Water Surface Elevation vs. Discharge Plots for Locations on the Neuse River

The plots for the first eight locations on the Neuse River can be found in Figure F.6. The comparisons for locations nine through sixteen are shown in Figure F.7. The data for the last four sections on the Neuse River is plotted in Figure F.8.

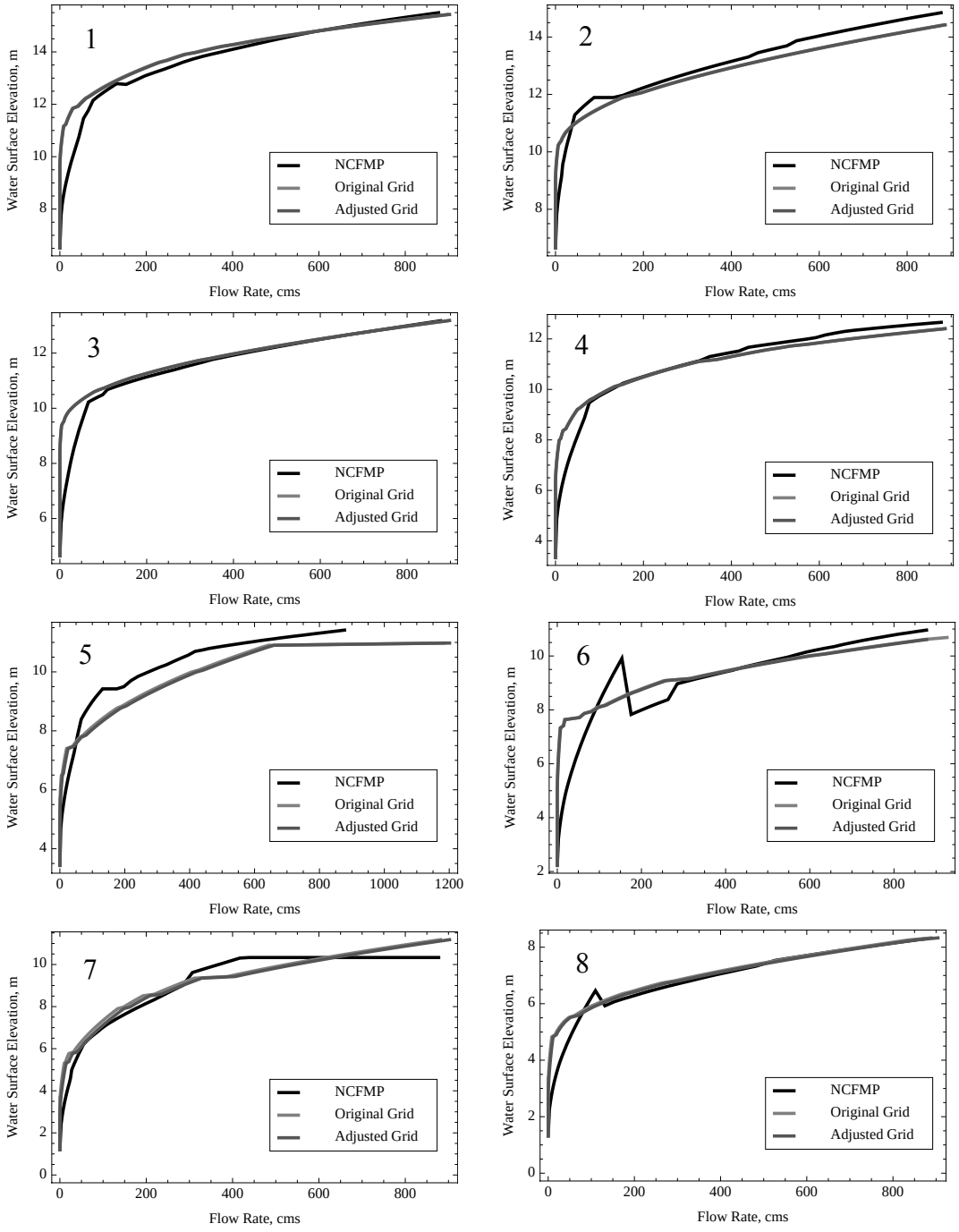

Figure F.6 Water surface elevation vs. discharge plots to compare the ADCIRC cross-section to the actual channel cross-sections (from NCFMP data) for the first eight locations on the Neuse River.

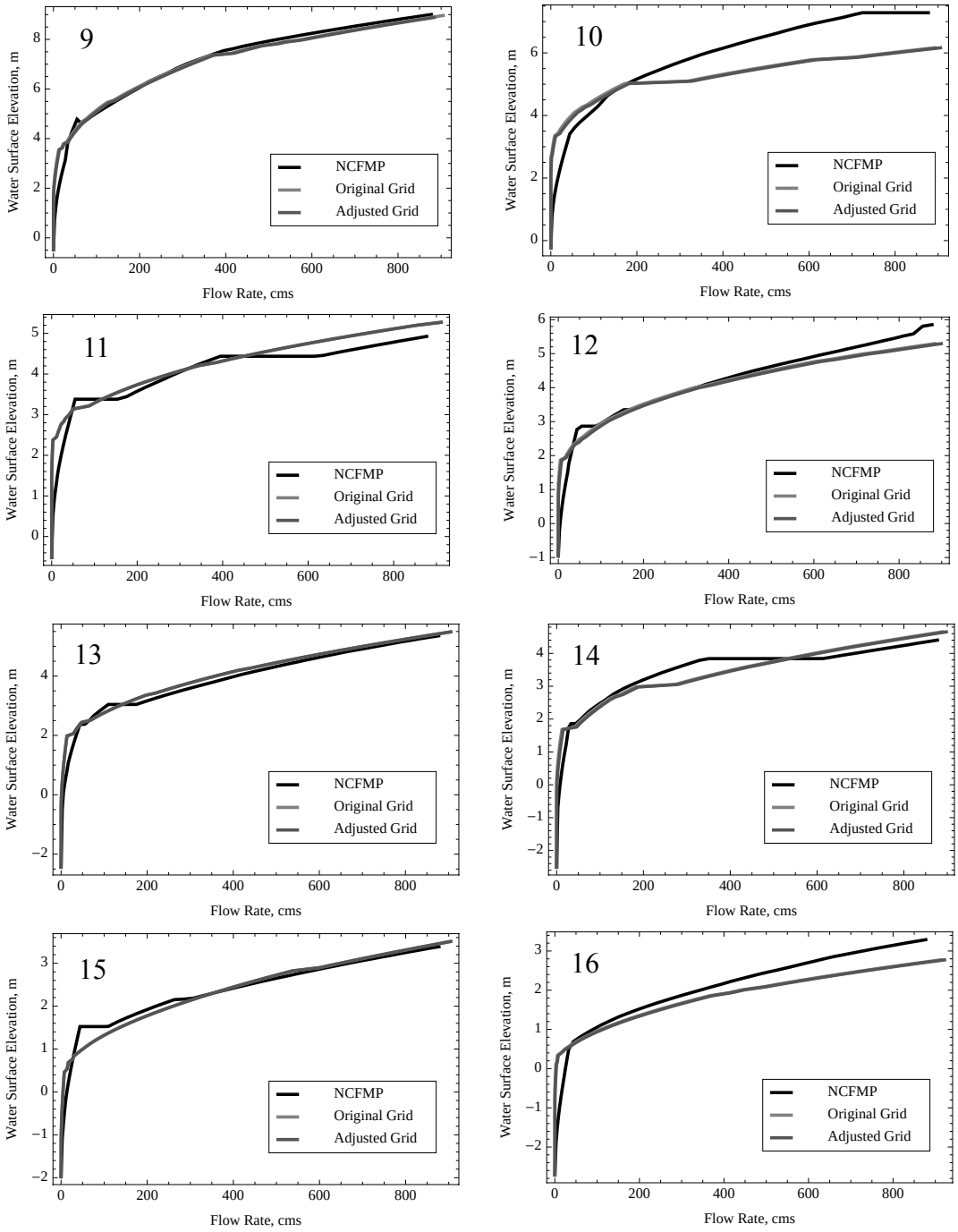

Figure F.7 Water surface elevation vs. discharge plots to compare the ADCIRC cross-section to the actual channel cross-sections (from NCFMP data) for locations nine through sixteen on the Neuse River.

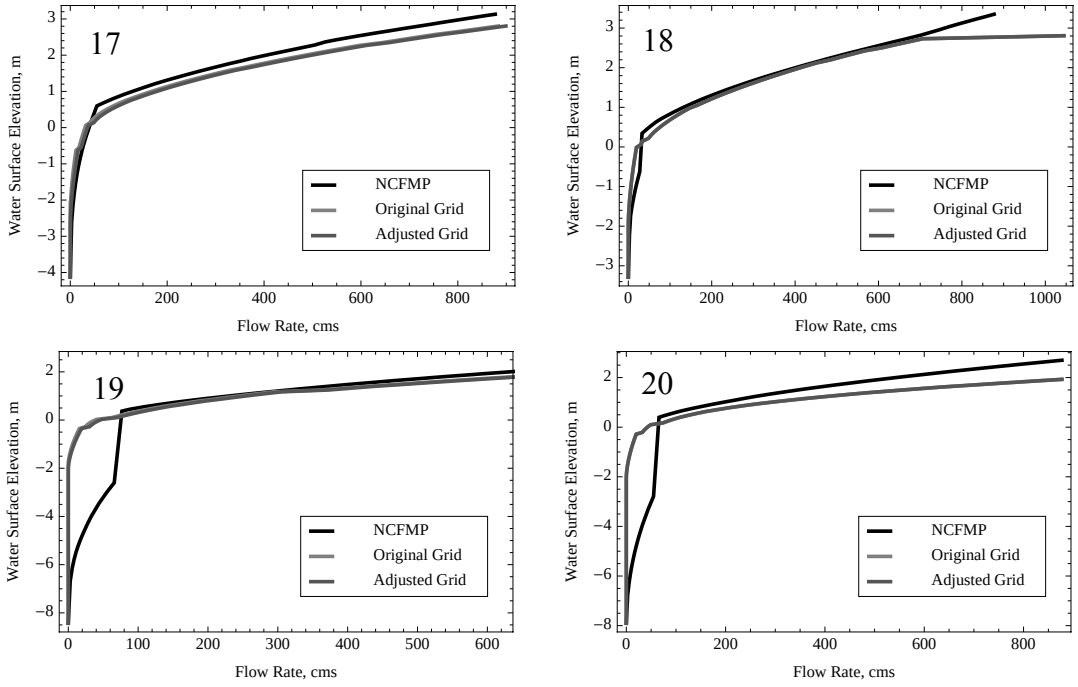

Figure F.8 Water surface elevation vs. discharge plots to compare the ADCIRC cross-section to the actual channel cross-sections (from NCFMP data) for locations seventeen through twenty on the Neuse River.